frontiers | Research Topics

RNA modifications and epitranscriptomics - volume II

Edited by
Giovanni Nigita, Xiao Han, Ernesto Picardi and Kunqi Chen

Published in
Frontiers in Genetics
Frontiers in Cell and Developmental Biology

ISSN 1664-8714
ISBN 978-2-8325-2777-1
DOI 10.3389/978-2-8325-2777-1

About Frontiers

Frontiers is more than just an open access publisher of scholarly articles: it is a pioneering approach to the world of academia, radically improving the way scholarly research is managed. The grand vision of Frontiers is a world where all people have an equal opportunity to seek, share and generate knowledge. Frontiers provides immediate and permanent online open access to all its publications, but this alone is not enough to realize our grand goals.

Frontiers journal series

The Frontiers journal series is a multi-tier and interdisciplinary set of open-access, online journals, promising a paradigm shift from the current review, selection and dissemination processes in academic publishing. All Frontiers journals are driven by researchers for researchers; therefore, they constitute a service to the scholarly community. At the same time, the *Frontiers journal series* operates on a revolutionary invention, the tiered publishing system, initially addressing specific communities of scholars, and gradually climbing up to broader public understanding, thus serving the interests of the lay society, too.

Dedication to quality

Each Frontiers article is a landmark of the highest quality, thanks to genuinely collaborative interactions between authors and review editors, who include some of the world's best academicians. Research must be certified by peers before entering a stream of knowledge that may eventually reach the public - and shape society; therefore, Frontiers only applies the most rigorous and unbiased reviews. Frontiers revolutionizes research publishing by freely delivering the most outstanding research, evaluated with no bias from both the academic and social point of view. By applying the most advanced information technologies, Frontiers is catapulting scholarly publishing into a new generation.

What are Frontiers Research Topics?

Frontiers Research Topics are very popular trademarks of the *Frontiers journals series*: they are collections of at least ten articles, all centered on a particular subject. With their unique mix of varied contributions from Original Research to Review Articles, Frontiers Research Topics unify the most influential researchers, the latest key findings and historical advances in a hot research area.

Find out more on how to host your own Frontiers Research Topic or contribute to one as an author by contacting the Frontiers editorial office: frontiersin.org/about/contact

RNA modifications and epitranscriptomics - volume II

Topic editors

Giovanni Nigita — The Ohio State University, United States
Xiao Han — Fuzhou University, China
Ernesto Picardi — University of Bari Aldo Moro, Italy
Kunqi Chen — Fujian Medical University, China

Citation

Nigita, G., Han, X., Picardi, E., Chen, K., eds. (2023). *RNA modifications and epitranscriptomics - volume II*. Lausanne: Frontiers Media SA.
doi: 10.3389/978-2-8325-2777-1

Table of contents

05 Editorial: RNA modifications and epitranscriptomics, Volume II
Kunqi Chen, Ernesto Picardi, Xiao Han and Giovanni Nigita

07 Association Among the Gut Microbiome, the Serum Metabolomic Profile and RNA m^{6}A Methylation in Sepsis-Associated Encephalopathy
Hui Wang, Qing Wang, Jingjing Chen and Cunrong Chen

19 Identification of RNA Methylation-Related lncRNAs Signature for Predicting Hot and Cold Tumors and Prognosis in Colon Cancer
Rong He, Changfeng Man, Jiabin Huang, Lian He, Xiaoyan Wang, Yakun Lang and Yu Fan

38 The Potential Role of m6A RNA Methylation in the Aging Process and Aging-Associated Diseases
Jin Sun, Bokai Cheng, Yongkang Su, Man Li, Shouyuan Ma, Yan Zhang, Anhang Zhang, Shuang Cai, Qiligeer Bao, Shuxia Wang and Ping Zhu

56 The Alteration of m^{6}A Modification at the Transcriptome-Wide Level in Human Villi During Spontaneous Abortion in the First Trimester
Jiajie She, Kaifen Tan, Jie Liu, Shuo Cao, Zengguang Li, You Peng, Zhuoyu Xiao, Ruiying Diao and Liping Wang

67 A novel prognostic signature based on N7-methylguanosine-related long non-coding RNAs in breast cancer
Zhidong Huang, Kaixin Lou and Hong Liu

82 Identification and functional analysis of m^{6}A in the mammary gland tissues of dairy goats at the early and peak lactation stages
Shujun Wang, Lu Zhang, Rong Xuan, Qing Li, Zhibin Ji, Tianle Chao, Jianmin Wang and Chunlan Zhang

97 Comprehensive analysis of m5C-Related lncRNAs in the prognosis and immune landscape of hepatocellular carcinoma
Qian Lu, Lianyu Liu, Shuai Wang, Qi Zhang and Li Li

119 Development of necroptosis-related gene signature to predict the prognosis of colon adenocarcinoma
Miaomiao Li, Tianyang Zhang and Wei Chen

133 PLP1 may serve as a potential diagnostic biomarker of uterine fibroids
Lei Cai, Zhiqi Liao, Shiyu Li, Ruxing Wu, Jie Li, Fang Ren and Hanwang Zhang

145 METTL16 regulates m^{6}A methylation on chronic hepatitis B associated gene HLA-DPB1 involved in liver fibrosis
Haibing Gao, Xiangmei Wang, Huaxi Ma, Shenglong Lin, Dongqing Zhang, Wenjun Wu, Ziyuan Liao, Mengyun Chen, Qin Li, Minghua Lin and Dongliang Li

154 Prognostic analysis of m6A-related genes as potential biomarkers in idiopathic pulmonary fibrosis
Zhiqiang Wang, Lanyu Shen, Junjie Wang, Jiaqian Huang, Huimin Tao and Xiumin Zhou

167 ADAR RNA editing on antisense RNAs results in apparent U-to-C base changes on overlapping sense transcripts
Riccardo Pecori, Isabel Chillón, Claudio Lo Giudice, Annette Arnold, Sandra Wüst, Marco Binder, Marco Marcia, Ernesto Picardi and Fotini Nina Papavasiliou

180 Identification and experimental validation of key m6A modification regulators as potential biomarkers of osteoporosis
Yanchun Qiao, Jie Li, Dandan Liu, Chenying Zhang, Yang Liu and Shuguo Zheng

198 MiRNA-Seq reveals key MicroRNAs involved in fat metabolism of sheep liver
Xiaojuan Fei, Meilin Jin, Zehu Yuan, Taotao Li, Zengkui Lu, Huihua Wang, Jian Lu, Kai Quan, Junxiang Yang, Maochang He, Tingpu Wang, Yuqin Wang and Caihong Wei

frontiers | Frontiers in Genetics

TYPE Editorial
PUBLISHED 07 June 2023
DOI 10.3389/fgene.2023.1229046

OPEN ACCESS

EDITED AND REVIEWED BY
William C. Cho,
QEH, Hong Kong SAR, China

*CORRESPONDENCE
Xiao Han,
hanxiao@fzu.edu.cn
Giovanni Nigita,
giovanni.nigita@osumc.edu

RECEIVED 25 May 2023
ACCEPTED 30 May 2023
PUBLISHED 07 June 2023

CITATION
Chen K, Picardi E, Han X and Nigita G (2023), Editorial: RNA modifications and epitranscriptomics, Volume II.
Front. Genet. 14:1229046.
doi: 10.3389/fgene.2023.1229046

Editorial: RNA modifications and epitranscriptomics, Volume II

Kunqi Chen[1], Ernesto Picardi[2], Xiao Han[3]* and Giovanni Nigita[4]*

[1]Key Laboratory of Gastrointestinal Cancer, Ministry of Education, School of Basic Medical Sciences, Fujian Medical University, Fuzhou, China, [2]Department of Biosciences, Biotechnology and Environment, University of Bari Aldo Moro, Bari, Italy, [3]College of Biological Science and Engineering, Fuzhou University, Fuzhou, China, [4]Department of Cancer Biology and Genetics and Comprehensive Cancer Center, The Ohio State University, Columbus, OH, United States

KEYWORDS

RNA methylation, RNA editing, psuedourylation, epitranscriptomics, RNA modification, RNA

Editorial on the Research Topic
RNA modifications and epitranscriptomics, Volume II

RNA modifications have been proven to be an important complement to epigenetics. Currently, at least 170 types of RNA modifications have been identified among all three life domains. In the past decade, several molecular functions of RNA modifications have been unveiled, including RNA structure switches, RNA stability, RNA export, and translation. RNA modification-associated biological processes such as neuro and embryo development, cell cycle, and stress response were also investigated. Additionally, aberrant RNA modifications have been observed in multiple diseases and are considered as potential therapeutic targets. However, compared with well-studied DNA modifications and posttranslational modifications, the biological meanings of RNA modifications have not been yet deciphered in detail. To facilitate the understanding of RNA modifications and their biological roles, we collected 14 articles on this Research Topic, including 13 research articles and a review.

Pecori et al. provide unique work on this Research Topic, focusing on the RNA editing mechanism. Based on high-throughput sequencing methods, the authors found putative U-to-C editing sites. A more in-depth analysis revealed that such sites may be misinterpreted as novel modification events, resulting instead from A-to-I editing on overlapping antisense RNAs that are transcribed from the same loci. Their findings were experimentally validated by RT–qPCR and editing quantification.

Noncentral nervous system sepsis can cause sepsis-related encephalopathy (SAE), a brain dysfunction disease. To identify the potential biomarkers and association among the gut microbiome, serum metabolomic profile, and RNA m6A methylation in SAE patients, Wang H. et al. collected twenty patients with and without SAE. In this work, authors integrated multiple experimental methods, such as ELISA, RT–qPCR, 16S rDNA sequencing, and LC-MS/MS. The ELISA and RT–qPCR results showed positive correlations between IL-6, ICAM-5, and the m6A methyltransferase METTL3, while the m6A demethylase FTO was decreased in SAE patients. Interestingly, a positive correlation between the abundance of *Acinetobacter* and the expression of METTL3 was also observed, which affected the diversity of the gut microbiome. In general, m6A regulators could be used for SAE screening.

Three studies used high-throughput sequencing to show the landscape of posttranscriptional regulation. She et al. provided an epitranscriptome profile in villous tissues from spontaneous abortion (SA). They applied MeRIP-seq to detect methylation

regions and integrated bioinformatics analysis. Based on the sequencing results, the authors suggest that the methylation distribution and motifs differ in SA and normal conditions. In the conjoint analysis of meRIP-seq and RNA-seq, the enriched gene ontology and KEGG pathways also differed between SA and normal conditions. Additionally, their results suggested that m6A modification plays an important role in SA by regulating lysine degradation and the Hippo signaling pathway. In summary, the authors believe their findings provide an alternative therapeutic target for spontaneous abortion.

Wang S. et al. presented the epitranscriptome of the mammary gland tissues of dairy goats at different lactation stages. They applied MeRIP-seq to show 2,476 and 1,451 m6A methylation peaks during the early and peak stages of lactation, respectively. The distribution of m6A peaks among transcriptomes differs at the early and peak stages, whereas the motif is similar in different stages. The differentially methylated genes were further analyzed by gene ontology and KEGG pathway analyses, and the results suggest that hypo- or hypermethylated genes participate in biological processes, such as cell apoptosis, cell growth processes, cellular components, or biogenesis. Finally, the hub genes show that HRAS, JUN, and EGFR may play the most important roles in the lactation stages.

miRNA is another type of posttranscriptional regulation. Fei et al. used high-throughput miRNA-seq to analyze differentially expressed miRNAs in the liver tissue between Hu (short/fat-tailed) sheep and Tibetan (short/thin-tailed) sheep. Compared with Hu sheep, six upregulated and five downregulated miRNAs were observed in Tibetan sheep. Miranda and RNAhybrid were used to predict the target of miRNA. The differentially expressed miRNAs and their target genes were integrated into gene ontology and KEGG pathway analysis. In addition to bioinformatics analysis, oar-miR-432-regulated SIRT1 was validated by Western blotting. In general, authors believe their work could provide a theory to study the fat metabolism of sheep.

Two works focused on colon cancer. He et al. provided a bioinformatics analysis to show the potential association between RNA methylation and lncRNAs in colon cancer, which could be biomarkers for hot and cold tumors and prognosis. They used RNA-seq data from the colon cancer cohort from TCGA and identified m1A/m5C/m6A/m7G-related lncRNAs based on Pearson correlation. In a further step, univariate Cox regression analysis was applied to identify 23 RNA modification-related lncRNAs with prognostic value. Additionally, the patients classified into different groups based on RNA modification-related lncRNAs had different clinical characteristics in immune microenvironmental infiltration and immunotherapy response. The authors believe their work will contribute to personalized treatment regimens. Other works presented by Li et al. analyzed the necroptosis-related genes in the colon cancer cohort and the potential association between necroptosis-related genes and RNA modifications.

Gao et al. and Lu et al. showed that m6A and m5C participate in the development of liver disease, respectively. Gao et al. used wet lab methodologies to identify that the m6A methyltransferase METTL16 contributes to liver fibrosis in chronic hepatitis B infection. Lu et al. used bioinformatics analysis to identify m5C-related lncRNAs in hepatocellular carcinoma.

Bioinformatics analysis with experimental verification was integrated into osteoporosis, breast cancer, and uterine fibroids studies. Qiao et al. analyzed high-throughput sequencing data to show that m6A regulators are biomarkers in osteoporosis, which was validated by experiments. Huang et al. used TCGA-BRCA RNA-seq data to identify m7G-related lncRNAs and validated them by RT–qPCR. Cai et al. analyzed previously published DNA and RNA methylation profiles to study uterine fibroids and validated them by experiments to identify PLP1 as a biomarker. Another work presented by Wang Z. et al. used different datasets to build a prediction model for the prognosis of idiopathic pulmonary fibrosis and validation.

Sun et al. provided a review article to summarize the roles of m6A methylation in aging and aging-associated diseases, including tumors, neurodegenerative diseases, diabetes, and cardiovascular diseases. In addition, the authors also discussed the association between m6A methylation and autophagy, inflammation, oxidative stress, and DNA damage. Considering the importance of m6A in aging and disease development, the authors suggest that m6A-related drugs should be developed to address the challenges of aging.

Generally, in this Research Topic, 13 articles focused on posttranscriptional regulation-related biological processes or disease development covering m1A/m5C/m6A/m7G, and one article studied the mechanism of RNA editing. We hope our Research Topic enhances our understanding of RNA modifications.

Author contributions

All authors listed have made a substantial, direct, and intellectual contribution to the work and approved it for publication.

Conflict of interest

The authors declare that the research was conducted in the absence of any commercial or financial relationships that could be construed as a potential conflict of interest.

Publisher's note

frontiers in Genetics

ORIGINAL RESEARCH
published: 30 March 2022
doi: 10.3389/fgene.2022.859727

Association Among the Gut Microbiome, the Serum Metabolomic Profile and RNA m^{6}A Methylation in Sepsis-Associated Encephalopathy

*Hui Wang, Qing Wang, Jingjing Chen and Cunrong Chen**

Department of Intensive Care Medicine, Union Hospital Affiliated to Fujian Medical University, Fuzhou, China

Objective: To investigate the relationship among the gut microbiome, serum metabolomic profile and RNA m6A methylation in patients with sepsis-associated encephalopathy (SAE), 16S rDNA technology, metabolomics and gene expression validation were applied.

Methods: Serum and feces were collected from patients with and without (SAE group and non-SAE group, respectively, n = 20). The expression of serum markers and IL-6 was detected by enzyme-linked immunosorbent assay (ELISA), and blood clinical indicators were detected using a double antibody sandwich immunochemiluminescence method. The expression of RNA m^{6}A regulator were checked by Q-RTPCR. The gut microbiome was analyzed by 16S rDNA sequencing and the metabolite profile was revealed by liquid chromatography-mass spectrometry (LC-MS/MS).

Results: In the SAE group, the IL-6, ICAM-5 and METTL3 levels were significantly more than those in the non-SAE group, while the FTO levels were significantly decreased in the SAE group. The diversity was decreased in the SAE gut microbiome, as characterized by a profound increase in commensals of the *Acinetobacter*, *Methanobrevibacter*, and *Syner-01 genera*, a decrease in [*Eubacterium*]_*hallii*_group, while depletion of opportunistic organisms of the *Anaerofilum*, *Catenibacterium*, and *Senegalimassilia* genera were observed in both groups. The abundance of *Acinetobacter* was positively correlated with the expression of METTL3. The changes between the intestinal flora and the metabolite profile showed a significant correlation. *Sphingorhabdus* was negatively correlated with 2-ketobutyric acid, 9-decenoic acid, and L-leucine, and positively correlated with Glycyl-Valine *[Eubacterium]_hallii*_group was positively correlated with 2-methoxy-3-methylpyazine, acetaminophen, and synephrine acetonide.

Conclusion: The gut microbiota diversity was decreased. The serum metabolites and expression of RNA m6A regulators in PBMC were significantly changed in the SAE group compared to the non-SAE group. The results revealed that serum and fecal biomarkers could be used for SAE screening.

Keywords: sepsis-associated encephalopathy, gut microbiota, serum metabolomic, 16S rDNA, rna m6a

OPEN ACCESS

Edited by:
Xiao Han,
Fuzhou University, China

Reviewed by:
Xianlin Han,
Peking Union Medical College Hospital (CAMS), China
Cong Chen,
Chinese Academy of Medical Sciences and Peking Union Medical College, China

****Correspondence:***
Cunrong Chen
chencunrong789@fjmu.edu.cn

Specialty section:
This article was submitted to RNA, a section of the journal Frontiers in Genetics

Received: *21 January 2022*
Accepted: *14 February 2022*
Published: *30 March 2022*

Citation:
Wang H, Wang Q, Chen J and Chen C (2022) Association Among the Gut Microbiome, the Serum Metabolomic Profile and RNA m^{6}A Methylation in Sepsis-Associated Encephalopathy. Front. Genet. 13:859727. doi: 10.3389/fgene.2022.859727

INTRODUCTION

Sepsis-related encephalopathy (SAE) is a severe disease with brain dysfunction, mainly caused by non-central nervous system sepsis (Guo et al., 2021). The clinical manifestation of SAE are a disturbance of consciousness, mild cognitive impairment, delirium, and coma (Tomasi et al., 2017). The fatality rate of SAE is as high as 30–70%, seriously affecting the survival of patients (Kempker and Martin, 2016). At present, electroencephalogram (EEG), transcranial Doppler, and a series of serum markers (including intercellular adhesion molecule-5 [ICAM-5] and soluble protein-100β [S-100β]) have certain value in the early diagnosis, evaluation, prognosis, and other aspects of SAE. However, prospective studies with large samples are lacking, and there is currently no targeted therapy available for the early prevention and symptomatic treatment of SAE (Harding et al., 2016; Falck et al., 2017). SAE is a pathological state, but its pathogenesis is not yet fully understood. The occurrence of SAE is believed to be related to the nonspecific inflammation and noninflammatory response of brain cells. The pathogenic basis of SAE is the change in the metabolic function of brain cells following brain injury (Flierl et al., 2010; Sallam et al., 2016; Khaertynov et al., 2017). Neuroinflammation is the main mechanism which recently are reported related to RNA m^{6}A methylation underlying the development of SAE (Ji et al., 2015; Nardelli et al., 2016). Therefore, anti-neuroinflammation could be a key factor in improving this syndrome.

The gut microbiota is involved in the nervous system, apoptosis, immunity, metabolism, blood brain barrier, and other brain functions through the gut-brain axis. Abnormal changes in gut microbes are closely related to brain diseases such as cognitive dysfunction (Erny et al., 2015; Chu et al., 2019). The cholinergic anti-inflammatory pathway is an important pathway through which the intestinal flora affect brain function, and is known as the bacterium-entero-brain axis. Cholinergic anti-inflammatory pathways could regulate inflammatory responses in central nervous system and the peripheral tissues (Ertle et al., 2021; Melo et al., 2021; Wedn et al., 2021). The function of the central choline system is closely related to the higher functions of the brain, such as awakening, learning, memory, sleep, and sensorimotor functions. An excessive inflammatory response is an underlying mechanism of the development of SAE, and studies have shown that the electrical stimulation of cholinergic nerves can reduce the occurrence of SAE by inhibiting the inflammatory response (Wang et al., 2016; Hering and Winklewski, 2017; Hoover et al., 2017).

With the widespread application and continuous development of molecular-based technology, metabolomics analysis has been increasingly applied in various studies, the results of which can lay a theoretical foundation for clarifying the mechanisms of numerous diseases (Hara et al., 2015; Zhu et al., 2019; Bai et al., 2021). From the gut microbiome, tryptophan-derived AHR ligands in the CNS can regulate astrocyte function to inhibit inflammation and neurodegeneration (Rothhammer et al., 2016). Metabolites of intestinal flora, such as neurotransmitter short-chain fatty acids, can participate in neural activation and regulate the synaptic activity of proximal neurons of the intestinal nervous system, which are related to many psychiatric diseases (Sajdel-Sulkowska, 2021; Wang et al., 2021).

In recent years, many studies have shown that RNA m6A epigenetics can participate in the regulation of the occurrence and development of a variety of diseases, and more and more evidence shows that metabolism, intestinal flora and RNA epigenetics build a complex cross regulatory network (Jabs et al., 2020; Luo et al., 2021; Yao et al., 2021; Tang et al., 2022). The main regulatory factors of rnam6a in human body have been gradually revealed, including RNA methyltransferase, demethylase protein and so on. Especially m6A in SAE, there is no research on the relationship between these factors.

In this study, we performed 16S rDNA combined with LC-MS/MS to identify differences in the metabolites in the sera of patients with and without SAE. This study was conducted to study the associations among gut microbiome, metabolites and RNA m6A regulators in SAE, and to give new theoretical support for diagnosis and treatment of SAE.

MATERIALS AND METHODS

Study Subjects

Twenty patients with SAE who were admitted to the Union Hospital affiliated to Fujian Medical University from January 2021 to July 2021 were included in the study group, and 20 patients without encephalopathy and sepsis (non-SAE) who were admitted during the same period were included in the control group.

The patients were classified following an examination of symptoms, signs, blood, biochemistry, and laboratory culture. The inclusion criteria were patients who met the diagnostic criteria for sepsis (patients with confirmed severe sepsis were transferred to the ICU for treatment); patients with SAE confirmed by craniocerebral imaging and EEG; age >18 years old; and patients with no previous history of CNS diseases and complete clinical data. Patients with the following conditions were excluded: combined liver and kidney failure, heart failure, and shock; coagulation mechanism disorders; uremia encephalopathy, drug poisoning, cerebral infarction, cerebral hemorrhage, and cerebral tumor; and severe cognitive impairment.

This study was approved by the Ethical Review Committee of the Union Hospital affiliated to Fujian Medical University, and informed consent was obtained from each study participant.

Deoxyribonucleic Acid Extraction

Stool sampling cups were used to collect fecal samples from the patients in both groups (n = 20 per group). A commercial kit (Tiangen, Beijing, China) was used to extract the microbial genomic DNA from each fecal sample (250–500 mg) (TGuide S96 Soil/fecal genomic DNA).

Ribonucleic Acid Extraction and Q-RTPCR

The total RNA was extracted according to the instructions of the kit. After extraction, the total RNA was extracted with 20 μL total

RNA, including RNA, was obtained by elution with ldepc water (pure water without RNA enzyme). RNA purity and concentration were measured on nanodrop. Reverse transcription kits, primers, probes and real-time quantitative RT qPCR kits were purchased from Applied Biosystems. Take 200 ng of total RNA from each group and add 15 μL Reverse transcription reaction was carried out in the RT reaction system. Real time quantitative RT qPCR was performed by fluorescence quantitative PCR. The total RT qPCR reaction system was 20 μL. Of which 2 × taqman Master Mix 10 μL, cDNA 1 33 μL. TaqMan primer and probe 1 μL and autoclaved deionized water 7 67 μL. Reaction conditions: 95°C for 10 min; 95 °C for 15 s, 60°C for 60 s, 40 cycles. Each reaction is provided with 3 multiple holes, and the difference of CQ value between multiple holes is no more than 1, which is used for data analysis and calculate the average CQ value.

16S rDNA Sequencing

The 16S rDNA sequencing experiment was performed using BIOTREE (Shanghai, China). Using the primers 338F and 806R to amplify the V3/V4 region of the 16S rDNA genes. The primer sequences were as follows: F: 5′-ACTCCTACG GGAGGCAGCA-3′, R: 5′-GGACTACHVGGGTWTCTAAT-3′. The established libraries were inspected first, and the qualified libraries were sequenced with an Illumina NovaSeq 6,000 (Illumina). FastQC (0.11.9), Trimmomatic (version 0.33), UCHIME (version 8.1), USEARCH (version 10.0), QIIME, and R packages (v3.2.0) were used to perform bioinformatic analysis. The data was available in public database PRJCA007583 (https://ngdc.cncb.ac.cn/).

For the metastats analysis, a *t*-test was performed to obtain the *p* and the Q values. Finally, according to the *p* or Q value, the relevant species were screened, and the default value was $p \geq 0.05$.

The default parameters for LEfSe to detect taxa with rich differences between groups. Only those taxa with a log linear discriminant analysis (LDA) score >4 were ultimately considered.

Metabolite Extraction

The LC-MS/MS nontarget metabolomics experiment was conducted using BIOTREE (Shanghai, China). Briefly, extract solution (1 volume acetonitrile: 1 volume methanol) was added to 50 μL sample. Then, the sample was rotated for 30 s and sonicated for 10 min, before precipitating the proteins. Finally, the sample was centrifuged to collect the supernatant for the next experiments.

LC-MS/MS

LC-MS/MS was processed on an UHPLC system (Vanquish, Thermo Fisher Scientific). The UPLC BEH Amide column coupled to the Q Exactive HFX mass spectrometer (Orbitrap MS, Thermo) was used. All steps were common procedure processed by company.

Data Preprocessing and Annotation

ProteoWizard was used to convert the data into the mzXML format, and the R program package (kernel XCMS) was used for peak recognition, peak alignment, and peak integration. Then, it matches with the BiotreeDB (V2.1) self-built two-level mass spectrometry database for material annotation.

Enzyme-Linked Immunosorbent Assay

Blood samples were collected from the two groups for ELISA (n = 20 for each group). On the first day after the diagnosis of SAE and non-SAE, 5 ml of fasting peripheral venous blood was sampled from the patients in the morning, and low-molecular-weight heparin was inserted into the anticoagulant vacuum vein collection. The blood was obtained by centrifugation and collecting the supernatant. ELISA was used to determine the levels of BDNF, NSE, ICAM-5, and S-100β (i.e., S-100β [F0027-B, F0161-B, F11072-B, F11076-B]; Fankew, Shanghai FANKEL Industrial Co., Ltd., China) in the blood samples. All experiments were repeated three times.

Detection of Blood Clinical Indicators

The white blood cell (WBC) and neutrophil (NEUT) levels were measured by UniCel® DxH 800 Coulter® (Beckman Coulter, Inc., United States). The procalcitonin (PCT) level was measured by a double antibody sandwich immunochemiluminescence method (VIDAS 30, Shanghai Fengyue Trading Co., Ltd., China), and the interleukin-6 (IL-6) (ab178013, Abcam, United States) level was measured by ELISA. All experiments were repeated three times.

Statistical Analysis

The measurement data are presented as the mean ± the standard deviation. The enumeration data are described as percentage, and the χ^2 test was used for inter-group comparison. p-values < 0.05 indicated statistically significant differences.

RESULT

Patient Characteristics

Twenty patients from each group were selected for clinicopathological analysis. There were no significant differences in sex, age, basic disease (e.g., hypertension and diabetes), or infection site (i.e., respiratory tract, gastrointestinal tract, urinary system, and blood flow) between the two groups (**Table 1**). The WBC, NEUT, PCT, and IL-6 levels were significantly increased in the SAE group. We used ELISA to further analyze the levels of serum makers in the two groups. In the SAE group, the expression levels of BDNF, NSE, S-100β, and ICAM-5 were significantly higher than those in the non-SAE group (**Figures 1A–D**). In the SAE group, the expression level of METTL3 was increased while FTO was decreased (**Figure 1E**). Other m^{6}A regulators have no significant difference.

Analysis of the Diversity of Gut Microbiota

To understand the diversity of the intestinal microbiota of patients with SAE, the fecal microorganisms in both groups were analyzed by 16S rDNA sequencing. The rank abundance curve showed that all samples contained high species richness and evenness (**Figure 2A**). The alpha indexes (i.e., Chao1, PD whole, Shannon, and Simpson index) showed that compared to the non-SAE group, the fecal microbial diversity of the SAE group did not significantly decrease (**Figure 2B**). Analysis of the taxonomic composition on the basis of the OTUs showed 769 common microbial species in the feces of both groups (**Figure 2C**). Six and

TABLE 1 | Analysis of general patient data.

	SAE (*n* = 20)	Non-SAE (*n* = 20)	χ2/t/z	*p*
Gender [n/%]			0.107	0.744
Male	13 (65%)	12 (60%)		
Female	7 (35%)	8 (40%)		
Age	62.3 ± 13.55	62.45 ± 12.50	−0.036	0.971
Basic disease [n/%]				
Hypertension	4 (20%)	6 (30%)	0.533	0.465
Diabetes	2 (10%)	3 (15%)	0.000	1.000
Other	17 (85%)	19 (95%)	0.278	0.605
Infection Site [n/%]				
Respiratory Tract	19 (95%)	16 (80%)	0.914	0.342
Gastrointestinal Tract	5 (25%)	5 (25%)	0.000	1.000
Urinary System	1 (5%)	1 (5%)	0.000	1.000
Blood Flow	1 (5%)	1 (5%)	0.000	1.000
Serum Biochemicals				
WBC(×109/L)	15 (9.17)	8 (4.17)	−2.137	0.033*
NEUT (×109/L)	14 (9.17)	7 (3.12)	−2.53	0.011*
PCT (ng/ml)	20 (6.57)	2 (0.8)	−3.194	0.001**
IL-6 (pg/ml)	784 (214,5000)	228 (81,611)	−2.336	0.02*

WBC:white blood cell count; NEUT: neutrophil count; PCT: procalcitonin; IL-6: Interleukin-6. *p < *0.05*, **p < *0.01*.

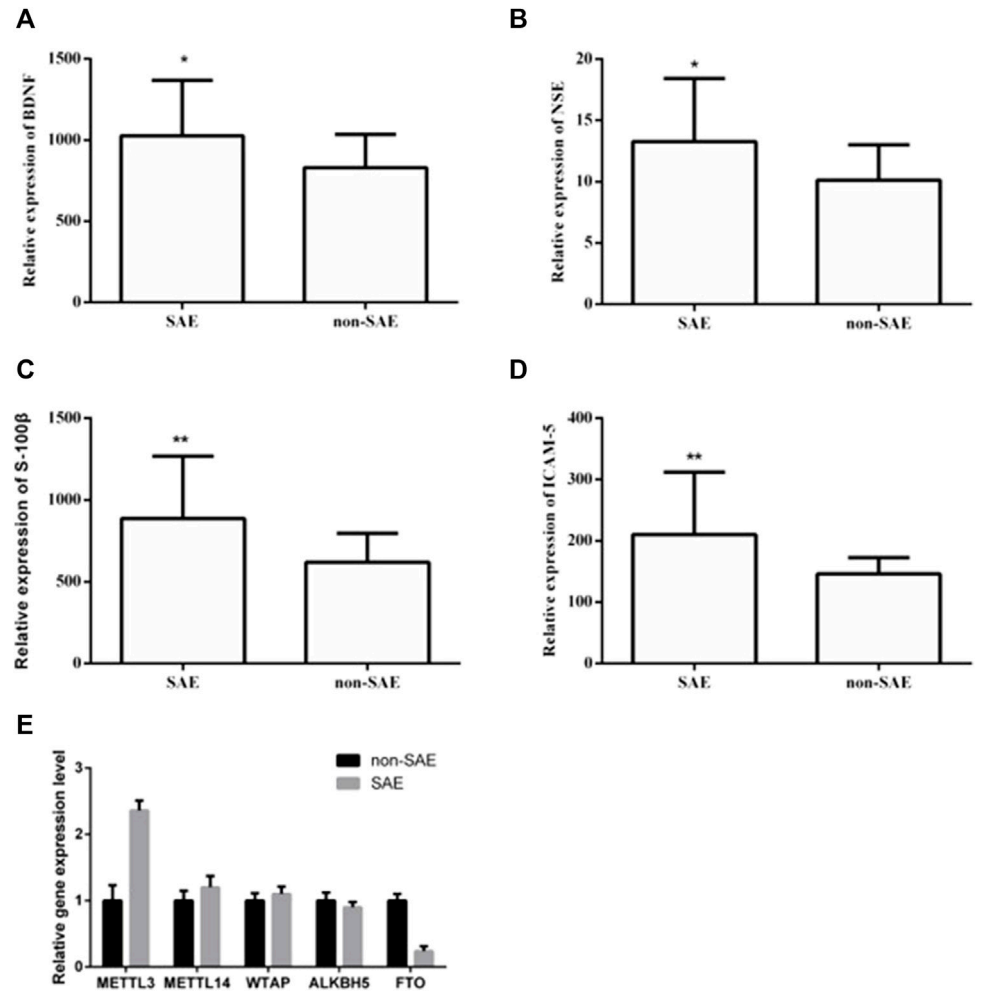

FIGURE 1 | The expression levels of BDNF, NSE, S-100β, ICAM-5, METTL3 and FTO in blood. The expression levels of BDNF **(A)**, NSE **(B)**, S-100β **(C)**, ICAM-5 **(D)**. * and ** indicates $p < 0.05$ and 0.01 respectively.

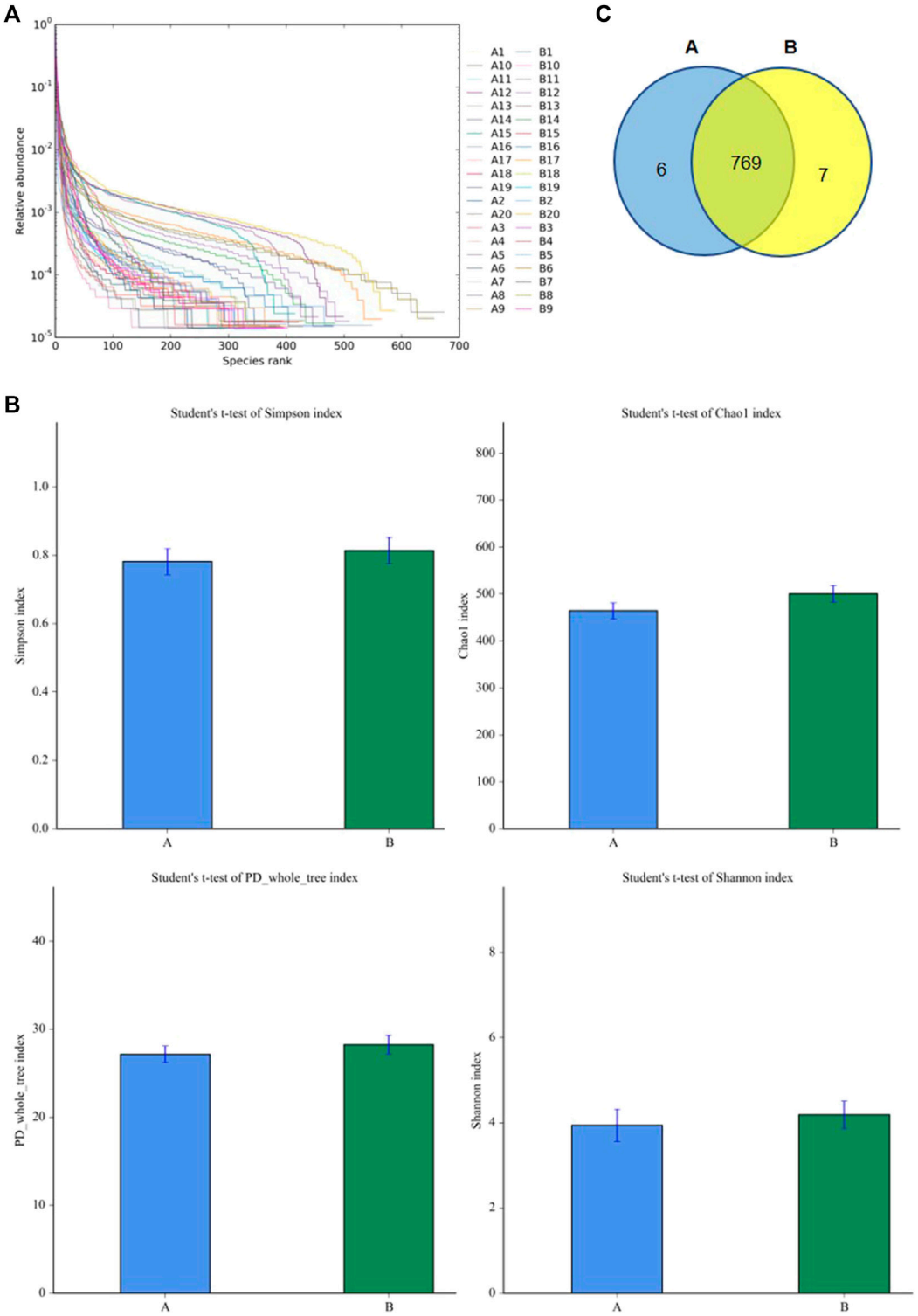

FIGURE 2 | Diversities of fecal microbiome. **(A)** The rank abundance curve. **(B)** The changes of Chao 1 index. **(C)** Venn diagram. A: SAE group; B: nonSAE group.

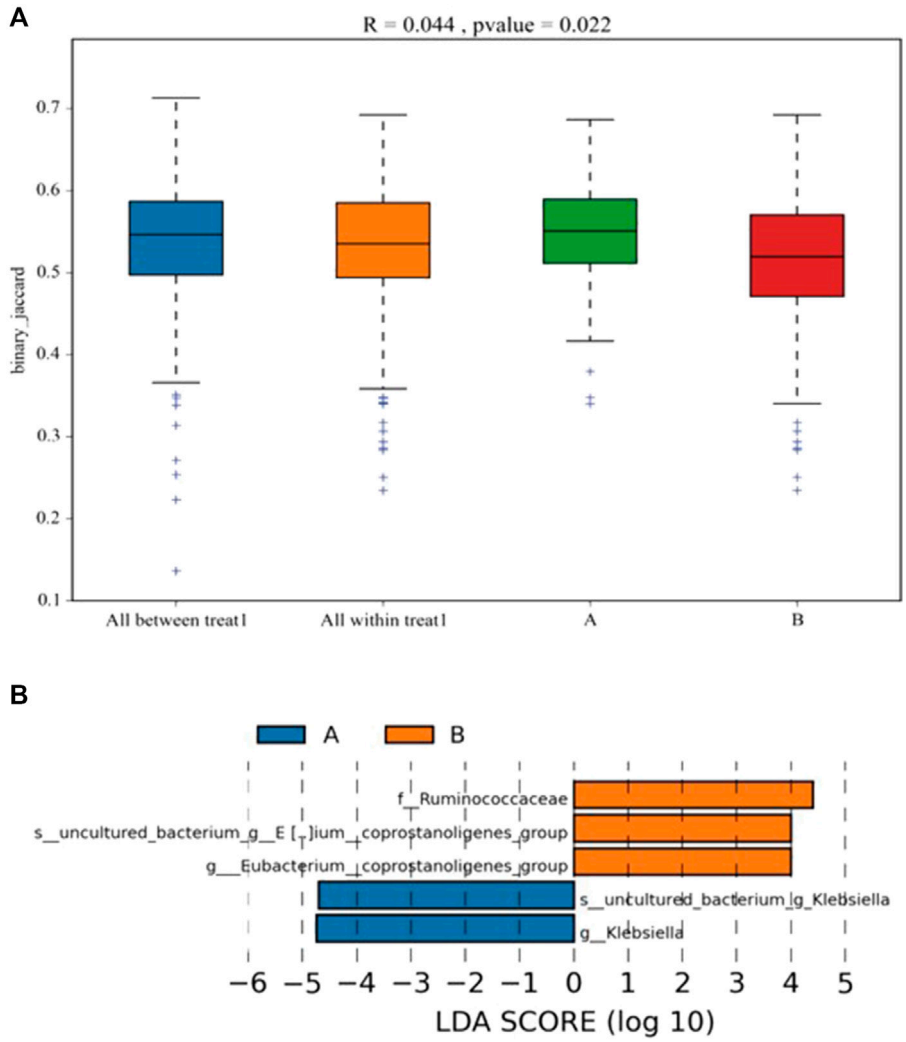

FIGURE 3 | Analysis of the differential microbial in fecal. **(A)** the differentia in two groups (ANOSIM). **(B)** LDA score displays the different microbiota ($p < 0.05$). Orange represents increase, and blue represents decrease. A: SAE group; B: nonSAE group.

seven species-specific microorganisms were found in the SAE and non-SAE groups, respectively (**Figure 2C**).

Differences in the Intestinal Microbiota Between the Sepsis-Related Encephalopathy and Non-Sepsis-Related Encephalopathy Groups

ANOSIM was performed to analyze the similarity between multi-dimensional data groups. The R value was 0.044, and the *p* value was 0.022; these values indicated that no significant differences between and within groups, with high inspection reliability (**Figure 3A**). LEfSe analysis showed five differential biomarkers between the SAE and non-SAE groups (LDA score >4). Compared to the SAE group, the genera *Eubacterium_coprostanoligenes*, *Eubacterium_coprostanoligenes*_group [*Eubacterium*]_*hallii*_group, and f_Ruminococcaceae were higher in the non-SAE group, while the genera g_*Klebsiella* and s_uncultured_bacterium_g_*Klebsiella* were lower in the non-SAE group (**Figure 3B**). Metastat analysis revealed 16 different genera between the two groups, showing a remarkable increase in commensals in the *Acinetobacter*, *Methanobrevibacter*, and *Syner-01* but depletion of opportunistic organisms in *Anaerofilum*, *Catenibacterium*, and *Senegalimassilia* in the two groups.

Serum Metabolomic Profiles of the Sepsis-Related Encephalopathy and Non-Sepsis-Related Encephalopathy Groups

The serum metabolic profile was examined using high-throughput LC/MS. The PCA score indicated that clustering of the QC samples in the positive- or negative-ion mode had

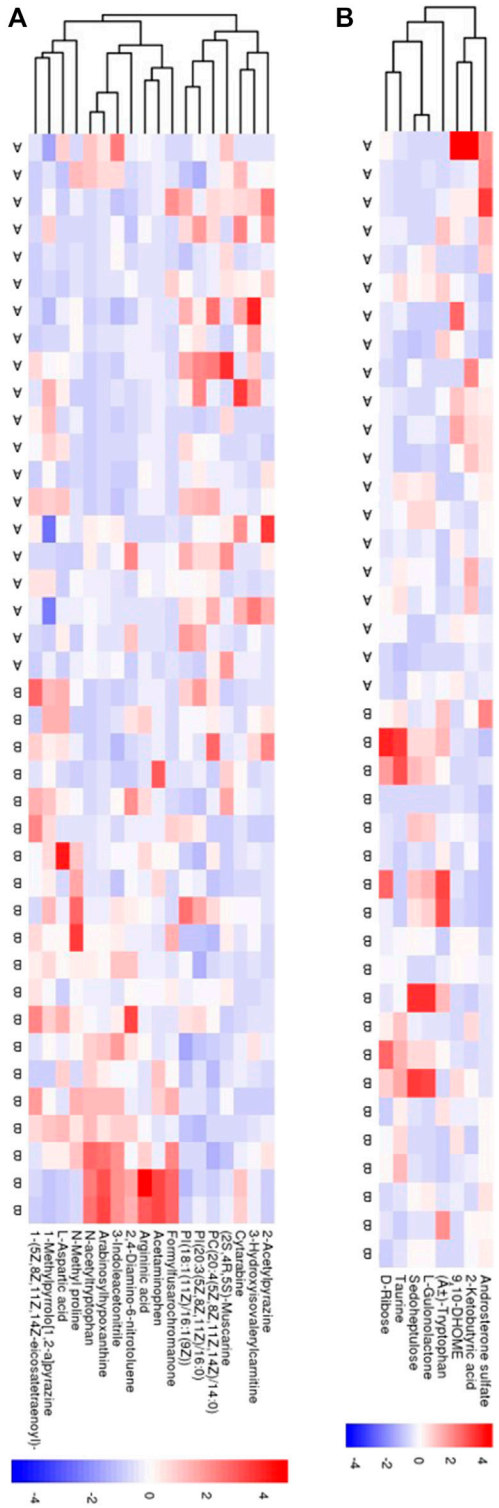

FIGURE 4 | Serum metabolomic analyses. **(A,B)** The PCA score plot and the PLS-DA scores plot in positive ion model and in negative ion mode, respectively. **(C,D)** Heatmaps of 18 metabolites and 8 metabolites in positive ion model and in negative ion model, respectively. Blue circle: QC sample, green circle: nonSAE group, red circle: SAE group. A: SAE group; B: nonSAE group.

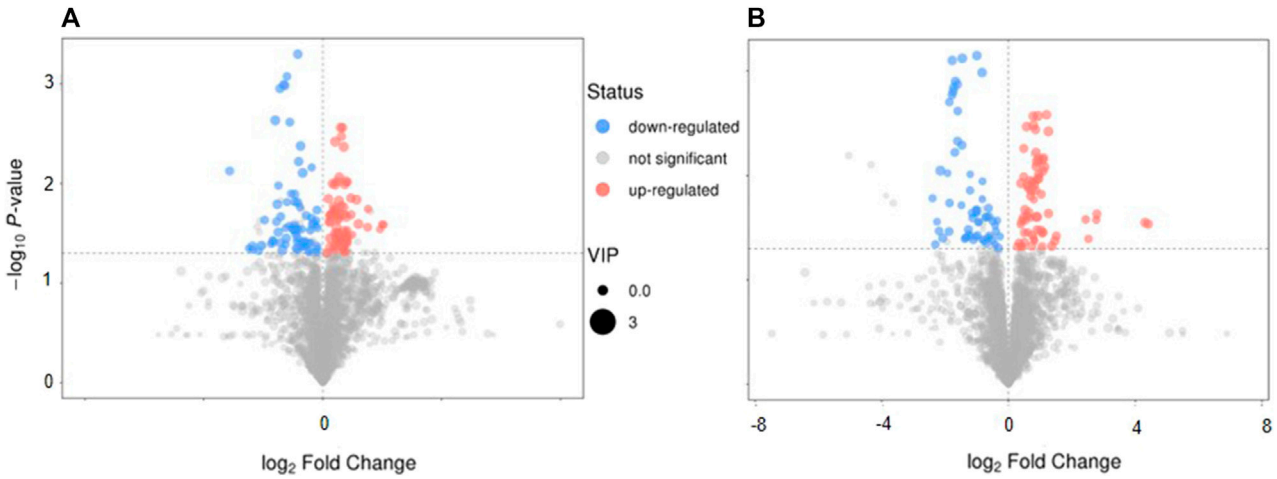

FIGURE 5 | The characteristics and pathway of serum metabolites. **(A,B)** Volcano map in positive-ion model and in negative-ion model, respectively. **(C,D)** The different metabolites pathway related with SAE were confirmed, in positive ion model and in negative ion model, respectively. Red: up-regulation, blue: down-regulation, gray: not significant, *$p < 0.05$.

good stability (**Supplemental Figure 1 and 2**). The PLS-DA score could separate the SAE group from the non-SAE group according to the difference between the two groups in either the positive- or negative-ion mode (**Supplemental Figure 1 and 2**). The heatmap showed that in the positive-ion and negative-ion mode, there were 300 (MS2 score >0.8) (**Figure 4A**) and 158 (MS2 score >0.8) potential biomarkers in the SAE group, respectively (**Figure 4B**).

Serum Metabolomic Profiles of the Sepsis-Related Encephalopathy and Non-Sepsis-Related Encephalopathy Groups

The volcano plot showed that 143 of the detected serum metabolites changed significantly in the positive-ion mode (**Figure 5A**), among which 18 metabolites matched the MS2 name, and 7 and 11 metabolites were downregulated and upregulated, respectively. In the negative-ion mode, 129 of the detected serum metabolites changed significantly (**Figure 5B**), among which, 8 metabolites matched the MS2 name, and 3 and 5 metabolites were upregulated and downregulated, respectively. In addition, the main metabolic pathways for enriching differential metabolites were analyzed. Thirteen metabolic pathways (**Supplemental Figure 3A**) (e.g., cyanoamino acid, aspartate, alanine, and pantothenate and glutamate metabolism, and CoA biosynthesis) and six metabolic pathways (**Supplemental Figure 3B**) (e.g., linoleic acid, taurine, and hypotaurine metabolism and pentose phosphate pathway) were observed.

Correlation Between Gut Microbiota and Serum Metabolites

We next investigated the possible correlation of changes in the metabolites and the intestinal microbiome spectra. The differences in the intestinal flora and serum metabolites between the two groups were analyzed by Spearman's correlation coefficient, and were found to have a significant correlation (**Figure 6**). Furthermore, we found the abundance of *Acinetobacter* was positively correlated with the expression of METTL3, the person correlation factor r was 0.436 with significance ($p = 0.03$).

In the positive-ion mode, the [*Eubacterium*]_*hallii*_group was positively correlated with 2-methoxy-3-methylpyazine, acetaminophen, and synephrine acetonide; *Sphingorhabdus* was positively correlated with glycyl-valine; and the [*Eubacterium*]_*coprostanoligenes*_group was positively correlated with 2-methoxy-3-methylpyazine and synephrine acetonide.

In the negative-ion mode, *Sphingorhabdus* was negatively correlated with 2-ketobutyric acid, 9-decenoic acid, and L-leucine. In addition, uncultured_bacterium_f_Family_XVIII and uncultured_bacterium_c_0319-7L14 were positively correlated with 2-ketobutyric acid. There was a positive correlation between *Dorea* and sedoheptulose, and *Syner-01* and L-leucine.

DISCUSSION

SAE is a diffuse brain dysfunction, mainly caused by non-central nervous system sepsis. The reasons for this process may include brain inflammation, neurotransmitter dysfunction, and abnormal activation of microglia (Mazeraud et al., 2020).

In our study, the SAE group was found to have a higher expression level of WBC, NEUT, PCT, and IL-6 than the non-SAE group, which was consistent with the findings of previous studies (Jun and Wen Zhenjie, 2020; Zhao et al., 2020; Deng et al., 2021). Studies have shown that the levels of serum NSE, S-100β, and IL-6 were obviously increased in the SAE group; thus, S-100β, serum NSE, and IL-6 levels were significantly correlated with SAE (Tomasi et al., 2017; Guo et al., 2021). A previous study demonstrated that the BDNF levels of patients with SAE were higher than those of patients with sepsis alone (Wen Zhenjie, 2018). In this study, the levels of BDNF, NSE, ICAM-5, and S-

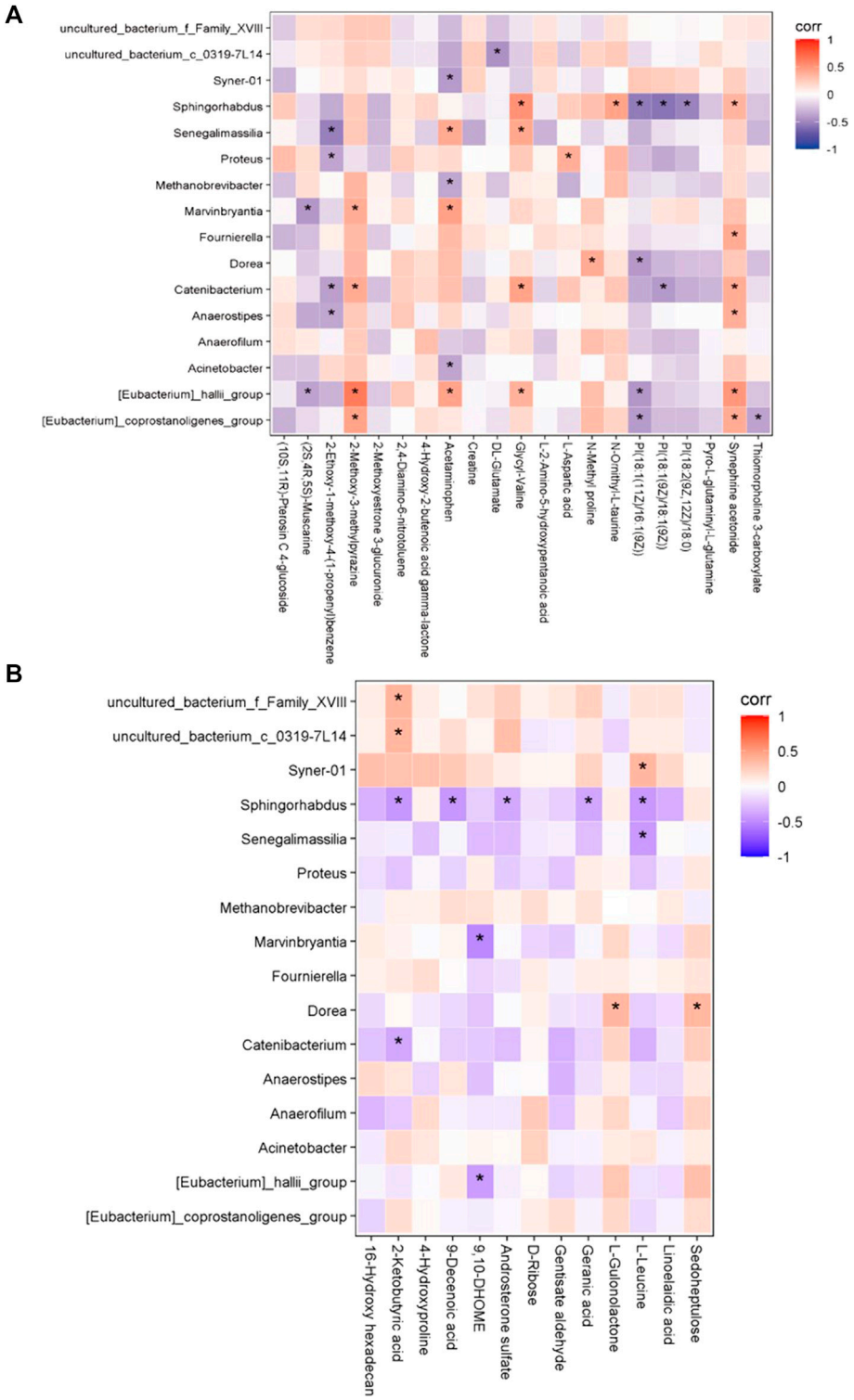

FIGURE 6 | The correlation between gut microbiome and serum metabolomic. **(A)** In positive ion model **(B)** In negative ion model. Red: up-regulation, blue: down-regulation, gray: not significant, *$p < 0.05$.

100β in the SAE group were obviously increased, consistent with the findings of previous studies. In addition, we found that the expression of mettl3 and FTO changed. Previous studies have shown that RNA m6A is widely involved in the occurrence and development of various diseases. This result also implies its association with metabolism and intestinal flora in diseases.

SAE is a pathological state, and its pathogenesis remains ambiguous. At present, it remains necessary to use advanced technology to conduct research to clarify its exact molecular mechanism. This research was performed to better understand the pathogenesis of SAE, and to bring new theoretical support for diagnosis and treatment of SAE. To our knowledge, this is the first study to combine LC–MS/MS metabolomics and 16S rDNA sequencing to analyze the exact molecular mechanism of SAE.

The gut microbiota can regulate the biological processes of the nervous system, apoptosis, immunity, metabolism, the blood brain barrier, and other brain functions through the gut-brain axis. Abnormal changes in these microorganisms are closely related to various brain diseases. With the occurrence of sepsis, the abundance of intestinal flora in the population and rats undergoes specific changes, mainly at the genus level. The proportion of *Alistipes* has risen significantly, contrary to the significant decrease in *Faecalibacterium* (Li et al., 2018). The brain function of rats in the sepsis group decreased with the change in the intestinal flora. Intestinal flora has also been demonstrated to impact SAE via the vagus nerve, with an increase in Firmicutes phylum and a decrease in Proteobacteria phylum observed in the fecal microbiota transplantation groups compared to the lipopolysaccharide group (Liu et al., 2020). Probiotics could protect the sepsis patients from cognitive impairment through reversing the abnormalities in the intestinal flora (Li et al., 2019). Our research revealed that the diversity of the intestinal flora was reduced in the SAE group. In the SAE and non-SAE groups, a substantial increase in commensals in *Acinetobacter*, *Methanobrevibacter*, and *Syner-01* was found, but opportunistic organisms in the *Anaerofilum*, *Catenibacterium*, and *Senegalimassilia* were depleted. The results indicated that the gut microbiota diversity and number were decreased in patients with SAE, which is in line with the results of previous studies.

The host converts intestinal flora metabolites directly or indirectly into nutrients (Mizock, 1990; Jonas et al., 2018). Host cells have various biological functions, and SAE tissue and cell abnormalities can be detected using metabolomics methods, the results of which may contribute to the discovery of new indicators for early diagnosis or therapy of SAE. The concentrations of all aromatic amino acids in cerebrospinal fluid are upregulated in hepatic encephalopathy, whereas in patients with sepsis, only the phenylalanine levels are elevated (Yen et al., 2015). According to the Glasgow Coma Score (GCS), patients with SAE are divided into 15, 12–14, 9–11, and 3–8 groups, with 63 different metabolites observed between the SAE and control groups. The common metabolites in all groups were as follows: for the group with GCS = 15 points, 4-hydroxyphenylacetic acid; GCS = 12–14 points, carbostyril and 3-ethyl-4,7-dimethoxy (35.8%); GCS = 9–11 points, malic acid peak 1; GCS = 3–8 points, oxalic acid. The GCS was also related to the concentration of 4-hydroxyphenylacetic acid (Zhu et al., 2019). In this study, 272 different metabolites and 19 different metabolic pathways were found between the SAE and non-SAE groups. The results showed that the metabolic pathways were abundant in tryptophan metabolism and primary bile acid biosynthesis, which was inconsistent with the results of previous studies.

We found that bacteria and metabolites were correlated in preterm infant feces, and previous studies have shown that bacterial metabolism has an impact on metabolite abundance in humans and mice (Dodd et al., 2017; Stephen et al., 2018). In this study, *Sphingorhabdus* was negatively correlated with 2-ketobutyric acid, 9-decenoic acid, and L-leucine but positively correlated with glycyl-valine. Moreover [*Eubacterium*]_*hallii*_group was positively correlated with 2-methoxy-3-methylpyazine, acetaminophen, and synephrine acetonide. In addition, abundance of [*Eubacterium*]_*hallii*_group was significantly decreased in SAE. This suggest that the correlation may play role in SAE development.

In line with previous studies, our results indicated that the gut microbiota diversity and number were downregulated in the patients with SAE.

CONCLUSION

In conclusion, in patients with SAE, the diversity and quantity of intestinal flora were downregulated, and bacteria were increased or depleted, accompanied by changes in the serum metabolic map. Our results uncovered the relationship between intestinal flora and serum metabolites in patients with SAE, which may provide theoretical support for the diagnosis and treatment of SAE.

DATA AVAILABILITY STATEMENT

The datasets presented in this study can be found in online repositories. The names of the repository/repositories and accession number(s) can be found below: https://ngdc.cncb.ac.cn/, PRJCA007583.

ETHICS STATEMENT

The studies involving human participants were reviewed and approved by the Ethical Review Committee of the Union Hospital affiliated to Fujian Medical University. The patients/participants provided their written informed consent to participate in this study.

AUTHOR CONTRIBUTIONS

CC and HW designed the project. HW performed all experiments. QW and JC helped data analysis. HW and CC worte the manuscript.

FUNDING

The study was supported by Fujian science and technology planning project-guiding (key) of social development (2019Y0023).

SUPPLEMENTARY MATERIAL

The Supplementary Material for this article can be found online at https://www.frontiersin.org/articles/10.3389/fgene.2022.859727/full#supplementary-material

REFERENCES

Bai, X., Jia, J., Kang, Q., Fu, Y., Zhou, Y., Zhong, Y., et al. (2021). Integrated Metabolomics and Lipidomics Analysis Reveal Remodeling of Lipid Metabolism and Amino Acid Metabolism in Glucagon Receptor–Deficient Zebrafish. *Front Cel Dev Biol* 8, 605979. doi:10.3389/fcell.2020.605979

Chu, C., Murdock, M. H., Jing, D., Won, T. H., Chung, H., Kressel, A. M., et al. (2019). The Microbiota Regulate Neuronal Function and Fear Extinction Learning. *Nature* 574 (7779), 543–548. doi:10.1038/s41586-019-1644-y

Deng, X., Zou, Q., Zheng, S., and Wang, H. (2021). Protective Effect and Mechanism of Angong Niuhuang Pill in Sepsis-Associated Brain Dysfunction of Rats. *Zhonghua Wei Zhong Bing Ji Jiu Yi Xue* 33 (8), 979–984. doi:10.3760/cma.j.cn121430-20210506-00659

Dodd, D., Spitzer, M. H., Van Treuren, W., Merrill, B. D., Hryckowian, A. J., Higginbottom, S. K., et al. (2017). A Gut Bacterial Pathway Metabolizes Aromatic Amino Acids into Nine Circulating Metabolites. *Nature* 551, 648. doi:10.1038/nature24661

Erny, D., Hrabě de Angelis, A. L., Jaitin, D., Wieghofer, P., Staszewski, O., David, E., et al. (2015). Host Microbiota Constantly Control Maturation and Function of Microglia in the CNS. *Nat. Neurosci.* 18, 965. doi:10.1038/nn.4030

Ertle, C. M., Rommel, F. R., Tumala, S., Moriwaki, Y., Klein, J., Kruse, J., et al. (2021). New Pathways for the Skin's Stress Response: The Cholinergic Neuropeptide SLURP-1 Can Activate Mast Cells and Alter Cytokine Production in Mice. *Front. Immunol.* 12, 631881. doi:10.3389/fimmu.2021.631881

Falck, M., Osredkar, D., Maes, E., Flatebø, T., Wood, T. R., Sabir, H., et al. (2017). Hypothermic Neuronal Rescue from Infection-Sensitised Hypoxic-Ischaemic Brain Injury Is Pathogen Dependent. *Dev. Neurosci.* 39, 238. doi:10.1159/000455838

Flierl, M. A., Rittirsch, D., Huber-Lang, M. S., and Stahel, P. F. (2010). Pathophysiology of Septic Encephalopathy - an Unsolved Puzzle. *Crit. Care* 14 (3), 165. doi:10.1186/cc9035

Guo, W., Li, Y., and Li, Q. (2021). Relationship between miR-29a Levels in the Peripheral Blood and Sepsis-Related Encephalopathy. *Am. J. Transl Res.* 13 (7), 7715–7722. eCollection 2021.

Hara, N., Chijiiwa, M., Yara, M., Ishida, Y., Ogiwara, Y., Inazu, M., et al. (2015). Metabolomic Analyses of Brain Tissue in Sepsis Induced by Cecal Ligation Reveal Specific Redox Alterations-Protective Effects of the Oxygen Radical Scavenger Edaravone. *Scavenger Edaravone.* 44 (6), 578–584. doi:10.1097/shk.0000000000000465

Harding, B., Conception, K., Li, Y., and Zhang, L. (2016). Glucocorticoids Protect Neonatal Rat Brain in Model of Hypoxic-Ischemic Encephalopathy (HIE). *Ijms* 18 (1), 17. doi:10.3390/ijms18010017

Hering, D., and Winklewski, P. J. (2017). Autonomic Nervous System in Acute Kidney Injury. *Clin. Exp. Pharmacol. Physiol.* 44, 162. doi:10.1111/1440-1681.12694

Hoover, D. B., Brown, T. C., Miller, M. K., Schweitzer, J. B., and Williams, D. L. (2017). Loss of Sympathetic Nerves in Spleens from Patients with End Stage Sepsis. *Front. Immunol.* 8, 1712. doi:10.3389/fimmu.2017.01712

Jabs, S., Biton, A., Bécavin, C., Nahori, M.-A., Ghozlane, A., Pagliuso, A., et al. (2020). Impact of the Gut Microbiota on the m6A Epitranscriptome of Mouse Cecum and Liver. *Nat. Commun.* 11 (1), 1344. doi:10.1038/s41467-020-15126-x

Ji, M. H., Qiu, L. L., Tang, H., Ju, L. S., Sun, X. R., Zhang, H., et al. (2015). Sepsis-induced Selective Parvalbumin Interneuron Phenotype Loss Andcognitive Impairments May Be Mediated by NADPH-Oxidase 2 Activation in Mice. *J. Neuroinflammation* 12, 182. doi:10.1186/s12974-015-0401-x

Jonas, Z., Jackson, M. A., Kastenmüller, G., Mangino, M., Long, T., Telenti, A., et al. (2018). The Fecal Metabolome as a Functional Readout of the Gut Microbiome. *Nat. Genet.* 50 (6), 790–795. doi:10.1038/s41588-018-0135-7

Jun, C., and Wen Zhenjie, L. Y. (2020). The Change of Serum Calcitonin Original Value to Evaluate the Prognosis of Sepsis Correlation Encephalopathy. *China Med. Guide* 17, 38–39. doi:10.3760/cma.j.issn.2095-4352.2016.08.004

Kempker, J. A., and Martin, G. S. (2016). The Changing Epidemiology and Definitions of Sepsis. *Clin. Chest Med.* 37, 165–179. doi:10.1016/j.ccm.2016.01.002

Khaertynov, K. S., Boichuk, S. V., Khaiboullina, S. F., Anokhin, V. A., Andreeva, A. A., Lombardi, V. C., et al. (2017). Comparative Assessment of Cytokine Pattern in Early and Late Onset of Neonatal Sepsis. *J. Immunol. Res.* 2017, 1–8. doi:10.1155/2017/8601063

Li, S., Lv, J., Li, J., Zhao, Z., Guo, H., Zhang, Y., et al. (2018). Intestinal Microbiota Impact Sepsis Associated Encephalopathy via the Vagus Nerve. *Neurosci. Lett.* 662, 98. doi:10.1016/j.neulet.2017.10.008

Li, X., Cao, Z., Yang, Y., Chen, L., Liu, J., Lin, Q., et al. (2019). Correlation between Jejunal Microbial Diversity and Muscle Fatty Acids Deposition in Broilers Reared at Different Ambient Temperatures. *Sci. Rep.* 9, 11022. doi:10.1038/s41598-019-47323-0

Liu, J., Jin, Y., Li, H., Yu, J., Gong, T., Gao, X., et al. (2020). Probiotics Exert Protective Effect against Sepsis-Induced Cognitive Impairment by Reversing Gut Microbiota Abnormalities. *J. Agric. Food Chem.* 68 (50), 14874–14883. doi:10.1021/acs.jafc.0c06332

Luo, J., Yu, J., and Peng, X. (2021). Could Partial Nonstarch Polysaccharides Ameliorate Cancer by Altering m6A RNA Methylation in Hosts through Intestinal Microbiota? *Crit. Rev. Food Sci. Nutr.*, 1–16. doi:10.1080/10408398.2021.1927975

Mazeraud, A., Righy, C., Bouchereau, E., Benghanem, S., Bozza, F. A., and Sharshar, T. (2020). Septic-Associated Encephalopathy: a Comprehensive Review. *Neurotherapeutics* 17 (Suppl. 2), 392. doi:10.1007/s13311-020-00862-1

Melo, G. D. D., Lazarini, F., Larrous, F., Feige, L., Kornobis, E., Levallois, S., et al. (2021). Attenuation of Clinical and Immunological Outcomes during SARS-CoV-2 Infection by Ivermectin. *EMBO Mol. Med.* 13, e14122. doi:10.15252/emmm.202114122

Mizock, B. A. (1990). Septic Encephalopathy. Evidence for Altered Phenylalanine Metabolism and Comparison with Hepatic Encephalopathy. *Arch. Intern. Med.* 150 (2), 443–449. doi:10.1001/archinte.150.2.443

Nardelli, P., Vincent, J. A., Powers, R., Cope, T. C., and Rich, M. M. (2016). Reduced Motor Neuron Excitability Is an Important Contributor to Weakness in a Rat Model of Sepsis. *Exp. Neurol.* 282, 1–8. doi:10.1016/j.expneurol.2016.04.020

Rothhammer, V., Mascanfroni, I. D., Bunse, L., Takenaka, M. C., Kenison, J. E., Mayo, L., et al. (2016). Type I Interferons and Microbial Metabolites of Tryptophan Modulate Astrocyte Activity and central Nervous System Inflammation via the Aryl Hydrocarbon Receptor. *Nat. Med.* 22, 586. doi:10.1038/nm.4106

Sajdel-Sulkowska, E. M. (2021). Neuropsychiatric Ramifications of COVID-19: Short-Chain Fatty Acid Deficiency and Disturbance of Microbiota-Gut-Brain Axis Signaling. *Biomed. Res. Int.* 2021, 7880448. doi:10.1155/2021/7880448

Sallam, M. Y., El-Gowilly, S. M., Abdel-Galil, A.-G. A., and El-Mas, M. M. (2016). Central GABAA Receptors Are Involved in Inflammatory and Cardiovascular Consequences of Endotoxemia in Conscious Rats. *Naunyn-schmiedeberg's Arch. Pharmacol.* 389 (3), 279–288. doi:10.1007/s00210-015-1201-7

Stephen, W., Osborne, S., Enriquez, C., Bixby, C., Arrieta, A., Whiteson, K., et al. (2018). The Microbiome and Metabolome of Preterm Infant Stool Are Personalized and Not Driven by Health Outcomes, Including Necrotizing Enterocolitis and Late-Onset Sepsis. *mSphere* 3, e00104. doi:10.1128/mSphere.00104-18

Tang, F., Chen, L., Gao, H., Xiao, D., and Li, X. (2022). m6A: An Emerging Role in Programmed Cell Death. *Front. Cel Dev. Biol.* 10, 817112. doi:10.3389/fcell.2022.817112

Tomasi, C. D., Vuolo, F., Generoso, J., Soares, M., Barichello, T., Quevedo, J., et al. (2017). Biomarkers of Delirium in a Low-Risk Community-Acquired Pneumonia-Induced Sepsis. *Mol. Neurobiol.* 54 (1), 722–726. doi:10.1007/s12035-016-9708-6

Wang, D.-W., Yin, Y.-M., and Yao, Y.-M. (2016). Vagal Modulation of the Inflammatory Response in Sepsis. *Int. Rev. Immunol.* 35 (5), 415–433. doi:10.3109/08830185.2015.1127369

Wang, Q., Davis, P. B., Qi, X., Chen, S. G., Gurney, M. E., Perry, G., et al. (2021). Gut-microbiota-microglia-brain Interactions in Alzheimer's Disease: Knowledge-Based, Multi-Dimensional Characterization. *Alz Res. Ther.* 13 (1), 177. doi:10.1186/s13195-021-00917-1

Wedn, A. M., El-Bassossy, H. M., Eid, A. H., and El-Mas, M. M. (2021). Modulation of Preeclampsia by the Cholinergic Anti-inflammatory Pathway: Therapeutic Perspectives. *Biochem. Pharmacol.* 192 (3), 114703. doi:10.1016/j.bcp.2021.114703

Wen Zhenjie, L. Y. (2018). The Role and Mechanism of Intestinal flora in Sepsis Associated Encephalopathy through Cholinergic Anti-inflammatory Pathway. *Hebei Med. Univ.* 11, 1357–1360.

Yao, L., Man, C. F., He, R., He, L., Huang, J. B., Xiang, S. Y., et al. (2021). The Interaction between N6-Methyladenosine Modification and Non-coding RNAs in Gastrointestinal Tract Cancers. *Front. Oncol.* 11, 784127. doi:10.3389/fonc.2021.784127

Yen, S., McDonald, J. A. K., Schroeter, K., Oliphant, K., Sokolenko, S., Blondeel, E. J. M., et al. (2015). Metabolomic Analysis of Human Fecal Microbiota: A Comparison of Feces-Derived Communities and Defined Mixed Communities. *J. Proteome Res.* 14 (3), 1472–1482. doi:10.1021/pr5011247

Zhao, X., Li, X., and Xiao, H. (2020). Correlation Analysis between Serum NSE, S100β, IL-6 and Sepsis Associated Encephalopath in Burn Patients. *The Chin. J. Burns Wounds Surf. ulcers* 32, 406–408. doi:10.3969/j.issn.1001-0726.2020.06.009

Zhu, J., Zhang, M., Han, T., Wu, H., Xiao, Z., Lin, S., et al. (2019). Exploring the Biomarkers of Sepsis-Associated Encephalopathy (SAE): Metabolomics Evidence from Gas Chromatography-Mass Spectrometry. *Biomed. Res. Int.* 2019, 1–10. doi:10.1155/2019/2612849

Conflict of Interest: The authors declare that the research was conducted in the absence of any commercial or financial relationships that could be construed as a potential conflict of interest.

Publisher's Note: All claims expressed in this article are solely those of the authors and do not necessarily represent those of their affiliated organizations, or those of the publisher, the editors and the reviewers. Any product that may be evaluated in this article, or claim that may be made by its manufacturer, is not guaranteed or endorsed by the publisher.

frontiers | Frontiers in Genetics

ORIGINAL RESEARCH
published: 06 April 2022
doi: 10.3389/fgene.2022.870945

Identification of RNA Methylation-Related lncRNAs Signature for Predicting Hot and Cold Tumors and Prognosis in Colon Cancer

Rong He[1†], Changfeng Man[1†], Jiabin Huang[1], Lian He[1], Xiaoyan Wang[2], Yakun Lang[1] and Yu Fan[1*]*

[1]Cancer Institute, The Affiliated People's Hospital of Jiangsu University, Zhenjiang, China, [2]Department of Gastroenterology, The Affiliated Suqian First People's Hospital of Nanjing Medical University, Suqian, China

OPEN ACCESS

Edited by:
Giovanni Nigita,
The Ohio State University,
United States

Reviewed by:
Wallax Ferreira,
Evandro Chagas Institute, Brazil
Kunqi Chen,
Fujian Medical University, China

***Correspondence:**
Yu Fan
yuf12345@ujs.edu.cn
Yakun Lang
lyk11223@sina.com

[†]These authors have contributed equally to this work and share first authorship

Specialty section:
This article was submitted to RNA, a section of the journal Frontiers in Genetics

Received: *07 February 2022*
Accepted: *21 March 2022*
Published: *06 April 2022*

Citation:
He R, Man C, Huang J, He L, Wang X, Lang Y and Fan Y (2022) Identification of RNA Methylation-Related lncRNAs Signature for Predicting Hot and Cold Tumors and Prognosis in Colon Cancer. Front. Genet. 13:870945. doi: 10.3389/fgene.2022.870945

N6-methyladenosine (m6A), N1-methyladenosine (m1A), 5-methylcytosine (m5C), and 7-methylguanosine (m7G) are the major forms of RNA methylation modifications, which are closely associated with the development of many tumors. However, the prognostic value of RNA methylation-related long non-coding RNAs (lncRNAs) in colon cancer (CC) has not been defined. This study summarised 50 m6A/m1A/m5C/m7G-related genes and downloaded 41 normal and 471 CC tumor samples with RNA-seq data and clinicopathological information from The Cancer Genome Atlas (TCGA) database. A total of 1057 RNA methylation-related lncRNAs (RMlncRNAs) were identified with Pearson correlation analysis. Twenty-three RMlncRNAs with prognostic values were screened using univariate Cox regression analysis. By consensus clustering analysis, CC patients were classified into two molecular subtypes (Cluster 1 and Cluster 2) with different clinical outcomes and immune microenvironmental infiltration characteristics. Cluster 2 was considered to be the "hot tumor" with a better prognosis, while cluster 1 was regarded as the "cold tumor" with a poorer prognosis. Subsequently, we constructed a seven-lncRNA prognostic signature using the least absolute shrinkage and selection operator (LASSO) Cox regression. In combination with other clinical traits, we found that the RNA methylation-related lncRNA prognostic signature (called the "RMlnc-score") was an independent prognostic factor for patients with colon cancer. In addition, immune infiltration, immunotherapy response analysis, and half-maximum inhibitory concentration (IC50) showed that the low RMlnc-score group was more sensitive to immunotherapy, while the high RMlnc-score group was sensitive to more chemotherapeutic agents. In summary, the RMlnc-score we developed could be used to predict the prognosis, immunotherapy response, and drug sensitivity of CC patients, guiding more accurate, and personalized treatment regimens.

Keywords: colon cancer, RNA methylation, long non-coding RNA, immunotherapy, tumor immune microenvironment

INTRODUCTION

Colon cancer (CC), a common gastrointestinal malignancy, is the third leading cause of cancer-related mortality, and morbidity worldwide (Siegel et al., 2022). Although patient prognosis has significantly improved with the advances in surgery, radiotherapy, and chemotherapy techniques, the 5-years survival rate for patients with advanced CC is only 10% (Su and Zhang, 2017). In recent years, immunotherapy has shown excellent anti-tumor efficacy in many types of malignancies, such as colon cancer, head and neck tumors, melanoma, kidney cancer, and lung cancer (Constantinidou et al., 2019; Morse et al., 2020). However, not all CC patients respond to immunotherapy. Patients who benefit from immunotherapy are mainly those with mismatch repair-deficient (dMMR) or microsatellite instability-high (MSI-H), with an efficacy rate of only 30–40%, and this population represents only a small fraction of those with advanced CC(Le et al., 2017; Morse et al., 2020). Other immunotherapeutic biomarkers include tumor mutational burden (TMB) and programmed cell death ligand-1 (PD-L1) expression (Chan et al., 2019; Luchini et al., 2019; Sagredou et al., 2021). However, the above markers have significant limitations in clinical application, and there exist some patients who are negative for the above markers and can also benefit from PD-1/PD-L1 based immunotherapy (Liu et al., 2019; He et al., 2021). Therefore, it is urgent to find some novel and effective biomarkers to detect the prognosis of CC and to guide immunotherapy regimens.

RNA methylation is considered an important process in epigenetic regulation, which occurs in mRNA and in ncRNA (Xu et al., 2021). Various forms of RNA methylation exist depending on the site of methylation, including N1-methyladenosine (m1A), 5-methylcytosine (m5C), N6-methyladenosine (m6A), 7-methylguanosine (m7G), and 2-O-dimethyladenosine (m6Am) (Xie et al., 2020). RNA methylation is involved in various physiological and pathological processes, and its dysregulation is closely associated with the development of human cancer. For example, the m6A-related regulator METTL3 was found to be highly expressed in several types of cancers and associated with poor prognosis, including gastric cancer (Wang et al., 2020), liver cancer (Chen et al., 2018), and colon cancer (Li et al., 2019a). The m5C-related factors form a tumor microenvironment suitable for migration and metastasis of various cancer cells by regulating some known tumor promoters, such as HDGF, TGF-β, FGF2, and G3BP1(Zhang et al., 2021c). The m1A demethylase ALKBH3, also known as prostate cancer antigen 1 (PCA-1), in addition to being exceptionally abundant in prostate cancer (Konishi et al., 2005), the oncogenic role of m1A demethylation has been found in colon (Zhao et al., 2019), breast (Woo and Chambers, 2019), and lung cancers (Tasaki et al., 2011). METTL1/WDR4-mediated enhancement of m7G modification improves translation efficiency and is associated with poor prognosis in several cancers (Katsara and Schneider, 2021). In addition, recent studies have demonstrated that RNA methylation can play a critical role in tumor immunity by affecting immune cell maturation and RNA immunogenicity, which provides a new direction for future cancer immunotherapy (Zhang et al., 2021a).

Long non-coding RNAs (lncRNAs) are a class of non-protein-coding RNAs with transcripts longer than 200 nt, mainly involved in epigenetic regulation, transcriptional, and post-transcriptional regulation (Cao et al., 2019). Increasing evidence suggests that lncRNAs play an integral role in the development and progression of several cancers, including colon cancer, suggesting that they could serve as novel biomarkers, and therapeutic targets (Meng et al., 2021; Dong et al., 2022; Shen et al., 2022). In recent years, studies on the relationship between RNA methylation and lncRNA in tumors have become the hot topic. For example, NSUN2-mediated m5C methylation of lncRNA H19 may contribute to the development and growth of hepatocellular carcinoma by affecting the interaction with oncoprotein G3BP1 (Sun et al., 2020). ALKBH5 promotes the invasion and metastasis of gastric cancer cells by demethylating lncRNA NEAT1 (Zhang et al., 2019). Wang et al. developed an m5C-related lncRNA prognostic model to predict patient prognosis (Wang et al., 2021b). Zhang et al. constructed a risk model including 31 m6A-related lncRNAs in colon cancer that could be used to predict patient prognosis (Zhang et al., 2021b). However, studies including four major (m6A, m1A, m5C, and m7G) RNA methylation modification-related lncRNAs in tumors have remained relatively rare so far. In this study, we collected transcriptomic data and clinical information from CC patients and performed a series of bioinformatic analyses to understand the expression of m6A, m1A, m5C, and m7G-RNA methylation modification-related lncRNAs and their impact in CC, and to elucidate the potential mechanisms of prognosis. The significance and originality of this study is that it further reveals a potential link between RNA methylation modification patterns and tumor microenvironment and clinical treatment response. This novel signature can be used to assess the sensitivity of CC patients to immunotherapy and chemotherapy.

MATERIALS AND METHODS

Data Acquisition and Processing

Transcriptome profiling data, somatic mutation data, and corresponding clinical data for the TCGA-CORD cohort were downloaded from The Cancer Genome Atlas (TCGA) database (https://cancergenome.nih.gov/), including data from 471 CC and 41 normal case samples. Gene expression profiles were then fully annotated with the Gencode project (Frankish et al., 2019) and distinguished into mRNAs and lncRNAs profiles. The GSE17536 dataset (N = 177) was obtained from Gene Expression Omnibus (GEO, http://www.ncbi.nlm.nih.gov/geo) as an external validation set to better verify the role of target lncRNAs.

Differential Expression and Mutational Analysis of RNA Methylation Regulators

Through the review of the latest literature, a total of 50 m6A-, m1A-, m5C-, and m7G-RNA methylation regulators were obtained. Among them, 25 m6A regulators (METTL3, METTL14, METTL16, WTAP, KIAA1429, VIRMA, RBM1, RBM15,

RBM15B, and ZC3H13, FTO, ALKBH5, YTHDC1, YTHDC2, YTHDF1, YTHDF2, YTHDF3 IGF2BP1, IGF2BP2, IGF2BP3, HNRNPA2B1, HNRNPC, HNRNPG, RBMX, LRPPRC, and FMR1) (Li et al., 2019b; Hu et al., 2019; An and Duan, 2022), 13 m1A regulators (TRMT6, TRMT61A, TRMT61B, TRMT61C, TRMT10C, BMT2 RRP8, YTHDF1, YTHDF2, YTHDF3, and YTHDC1, ALKBH1, and ALKBH3) (Xie et al., 2020; Song et al., 2021a), 14 m5C regulators (NOP2, NSUN1, NSUN2, NSUN3, NSUN4, NSUN5, NSUN7, DNMT1, TRDMT1, DNMT3A, DNMT3B, TET2, YBX1, and ALYREF) (Meng et al., 2021), and 2 m7G regulators (METTL1 and WDR4) (Tomikawa, 2018) were included. RNA methylation regulators differentially expressed in colon cancer and normal tissues in the TCGA-CORD cohort were identified using the "limma" package. The "maftools" package was used to generate mutation maps of RNA methylation regulators in CC patients. CNV altered positions of RNA methylation regulators on 23 chromosomes were mapped using the "RCircos" package.

Identification of RNA Methylation-Related lncRNA and Analysis of Their Prognostic Value

Pearson correlation analysis was used to screen for lncRNAs co-expressed with differentially expressed RNA methylation-related genes (|Pearson R|>0.5 and p-value <0.001). Univariate Cox regression analysis was performed to screen for RMlncRNAs significantly associated with OS ($p < 0.05$), and the Sankey diagram was mapped by the "ggalluvial" R package. The Wilcoxon test was used to detect differences in the expression of prognosis-related RMlncRNAs between tumor tissues and normal tissues.

Consistent Clustering of RNA Methylation-Related lncRNAs

Based on the expression of RMlncRNAs with prognostic value, unsupervised consensus clustering was performed using "ConsensusClusterPlus" on 433 colon cancer patients to identify potential molecular subtypes (Wilkerson and Hayes, 2010). R packages " survival" and "survminer" were used to analyze the prognosis of samples with different molecular subtypes. Clinical data were included and analyzed for differences in molecular subtypes by using the "heatmap" R package for distinct clinicopathological features. The proportion of 22 tumor-infiltrating immune cells (TICs) in each sample was quantified using the CIBERSORT algorithm (Newman et al., 2015). The ESTIMATE algorithm was used to calculate the tumor microenvironment (TME) score (including immune score, stromal score, ESTIMATE score, and tumor purity) for each sample (Yoshihara et al., 2013). In addition, we synthesized 38 immune checkpoint genes from the literature and examined the expression of these checkpoint genes among molecular subtypes (Pardoll, 2012; Nirschl and Drake, 2013).

Construction and Validation of RNA Methylation-Related lncRNA Signature

The TCGA-CORD cohort was randomly divided into a training set and a test set (1:1 ratio). A minimum absolute shrinkage and selection operator (LASSO) Cox regression analysis was used to narrow down candidate lncRNAs and develop an RNA methylation-related lncRNA signature (we named it RMlnc-score). The formula is as follows: RMlnc-score = Σ ($\beta i \times$ Expi) (β: coefficients, Exp: lncRNA expression level). Patients were then divided into high RMlnc-score and low RMlnc-score groups based on the median value of RMlnc-score. Kaplan-Meier survival curves were plotted using the R package "survival" to describe the overall survival difference between the high and low score groups. Receiver operating characteristic curves (ROC) analysis was performed to evaluate its sensitivity and accuracy. Heatmaps were generated to reveal differences in signature lncRNA expression in the low and high RMlnc-score groups.

Analysis of the Prognostic Value and Clinical Relevance for the RMlnc-Score

The student's t-test was used to assess the relationship between RMlnc-score and clinical characteristics. In addition, survival analysis was performed to further elucidate the relationship between RMlnc-score by sex (male and female), age (≤65 and >65 years), T-stage (T1-2 and T3-4), N-stage (N0 and N1-2), M-stage (M0 and M1), and grade (stages I-II and stages III-IV) in each subgroup for prognostic ability. Subsequently, univariate and multivariate Cox regression analyses were used to determine the relationship and independence between clinicopathological characteristics and RMlnc-score. A nomogram and calibration curves were then constructed based on independent prognostic factors from multivariate Cox regression analysis to predict the probability of survival at 1, 3, and 5 years in CC patients. The GSE17536 dataset was used as an external validation cohort to further assess the prognostic value and clinical relevance of model lncRNAs.

Principal Component Analysis and Assessment of Immune Cell Infiltration

The R package "scatterplot3d" was used to perform PCA analysis to explore potential differences between high and low RMlnc-score groups. To analyze the correlation between RMlnc-score and TICs, we used different software (including ssGSEA, xCELL, Timer, Quantiseq, MCPcounter, EPIC, CIBERSORT-ABS, and CIBERSORT) to comprehensively analyze of immune cell infiltration.

Assessment of Response to Anti-Tumor Therapy

The tumor immune dysfunction and exclusion (TIDE) algorithm (Fu et al., 2020) was used to assess the potential response of colon cancer patients in the different RMlnc-score groups to immunotherapy. Data from the Genomics of Drug Sensitivity in Cancer (GDSC) database were used to predict the response of CC patients to chemotherapeutic drug therapy. The "pRRophetic" R package (Geeleher et al., 2014) was used to calculate the half-maximal inhibitory concentration (IC50) of common chemotherapeutic agents.

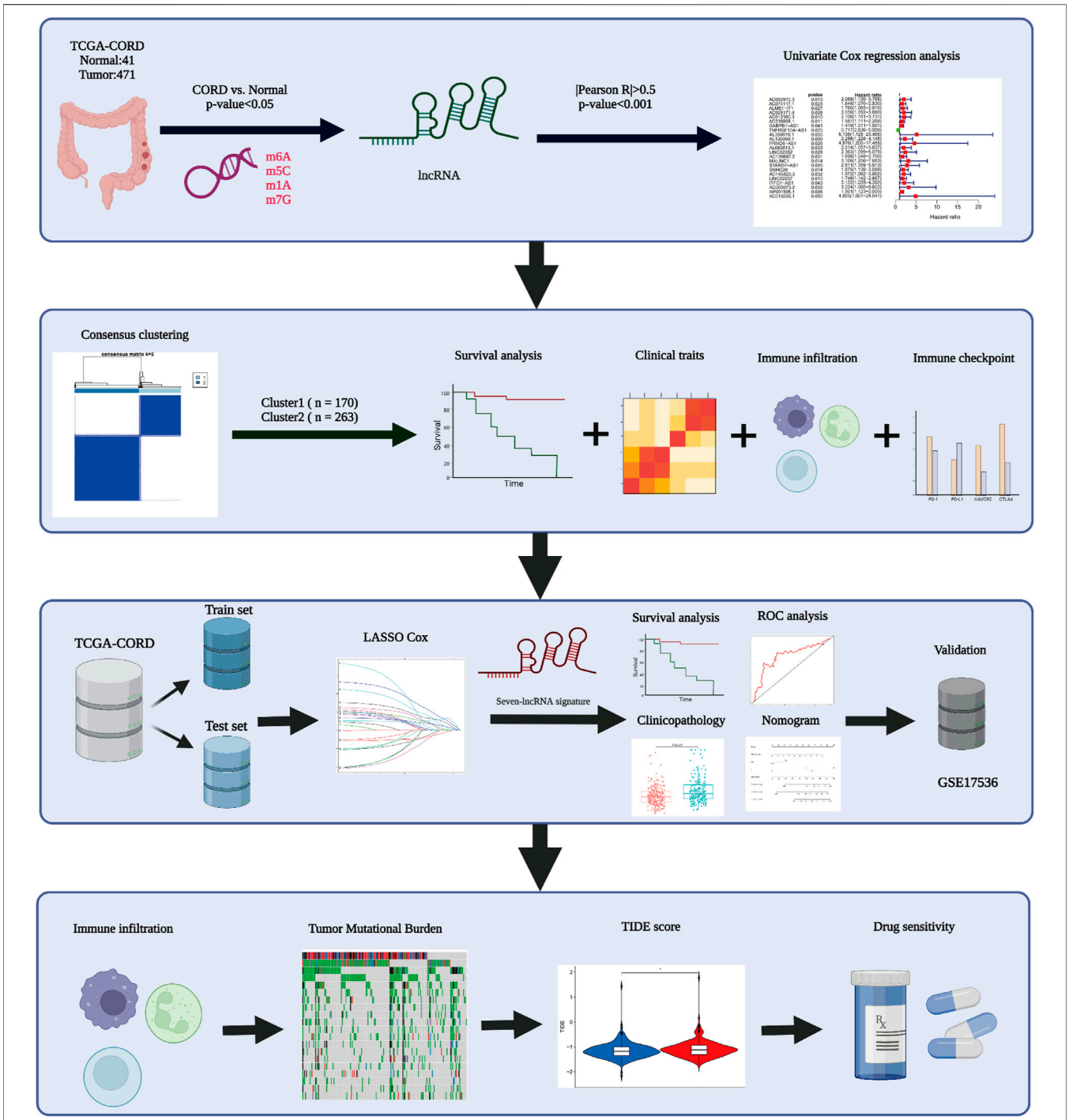

FIGURE 1 | Workflow diagram of this study.

Prediction of RNA Methylation Modification Sites on 7 lncRNAs

m6A-Atlas (Tang et al., 2021) and SRAMP(Zhou et al., 2016) were used to predict the m6A site of the lncRNAs; m5C-Atlas (Ma et al., 2022) and RNAm5Cfinder (Li et al., 2018) were used to predict the m5C site of the lncRNAs; m7GHub (Song et al., 2020) and iRNA-m7G (Chen et al., 2019) databases were used to predict the m7G site of the lncRNAs.

Statistical Analysis

All statistical analyses were performed using R software (v4.0.2). p values < 0.05 were considered statistically significant if not explicitly stated.

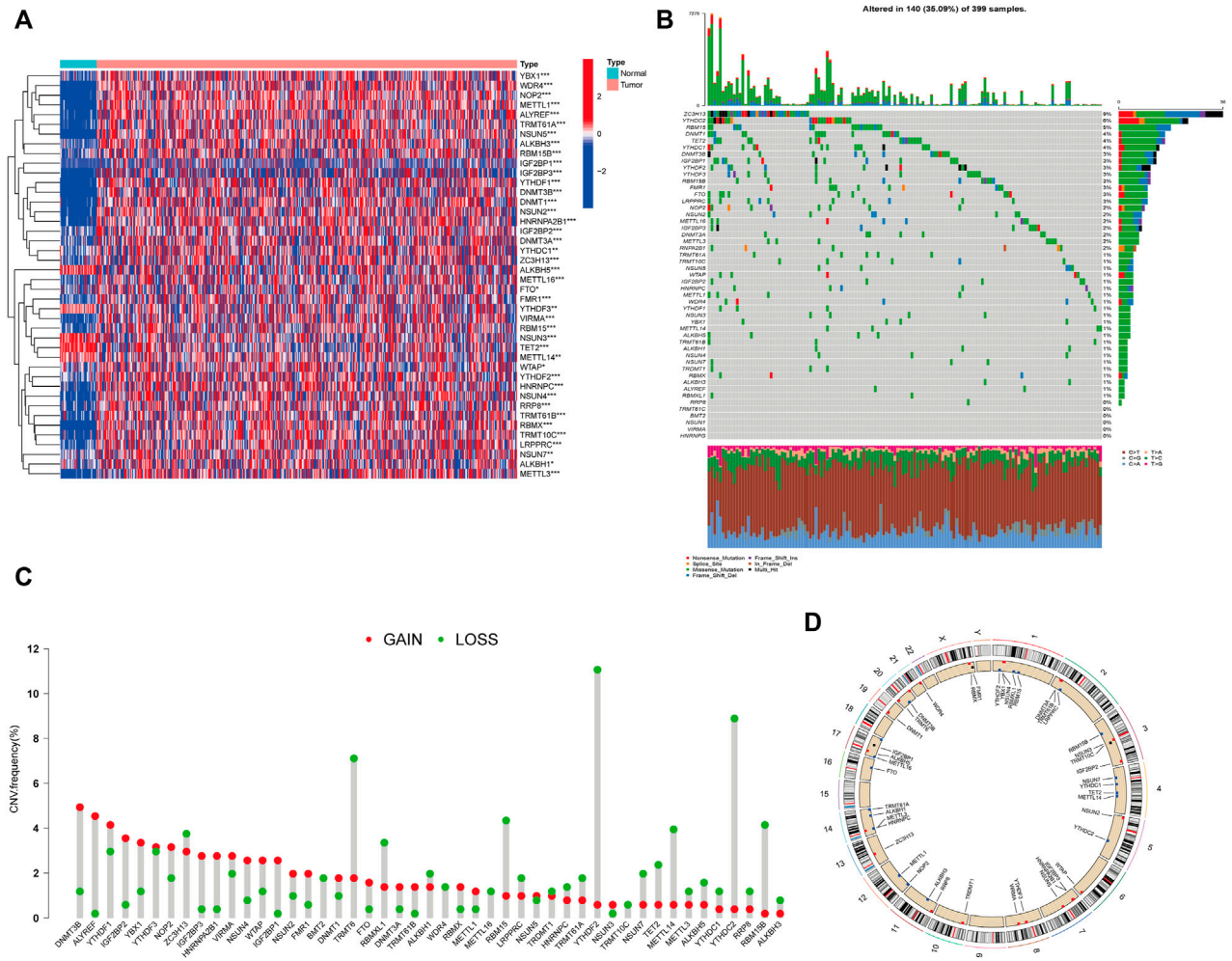

FIGURE 2 | Characteristics and differences of RNA methylation-related regulators in CC. **(A)** Heatmap of differential expression of RNA methylation-related regulators between normal (n = 41) and colon cancer tissues (n = 471) in the TCGA-CORD cohort. **(B)** Mutation waterfall plots of 399 colon cancer patients from the TCGA-CORD cohort. **(C)** Copy number variation (CNV) frequency of RNA methylation-related regulators in the TCGA-CORD cohort. **(D)** The location of CNV alterations of RNA methylation-associated regulators on chromosomes in the TCGA-CORD cohort. *p<0.05; **p<0.01; ***p<0.001.

RESULTS

Landscape of RNA Methylation Regulator Expression and Gene Mutation in CC

The workflow of this study is illustrated in **Figure 1**. First, we investigated the expression of 50 m1A-, m5C-, m6A-, and m7G-RNA methylation regulatory genes in the TCGA-CORD cohort (**Figure 2A**). The results showed that there were 42 differentially expressed RNA methylation regulatory genes. Among them, 37 regulators were highly expressed in colon cancer tissues, and five were lowly expressed in colon cancer tissues. Next, we investigated the incidence of somatic mutations and copy number variations for 50 regulators in TCGA-CORD. A total of 140 of 399 samples (35.09%) experienced genetic alterations in RNA methylation regulators (**Figure 2B**). Among them, ZC3H13 (9%) was the gene with the highest mutation frequency, followed by YTHDC2 (6%), and RBM15 (5%.) The investigation of CNV alteration frequency revealed that all RNA methylation regulators were found to show prevalent CNV alterations. Among them, DNMT3B, ALYREF, YTHDF1/3, IGF2BP2/3, YBX1, and HNRNPA2B1 showed significant copy number amplification, while TRMT6, YTHDF2, YTHDC2, and RBM15/15B showed remarkable copy number deletions (**Figure 2C**). **Figure 2D** shows the location of CNV changes in RNA methylation regulators on chromosomes. The above analysis revealed a high degree of heterogeneity in the expression and inherited variation status of RNA methylation in CC, demonstrating that RNA methylation-related regulators may play a pivotal position in the occurrence and development of CC.

Identification of RNA Methylation-Related lncRNAs in CC Patients

We identified 1,057 lncRNAs significantly associated with 42 differentially expressed RNA methylation regulators by using

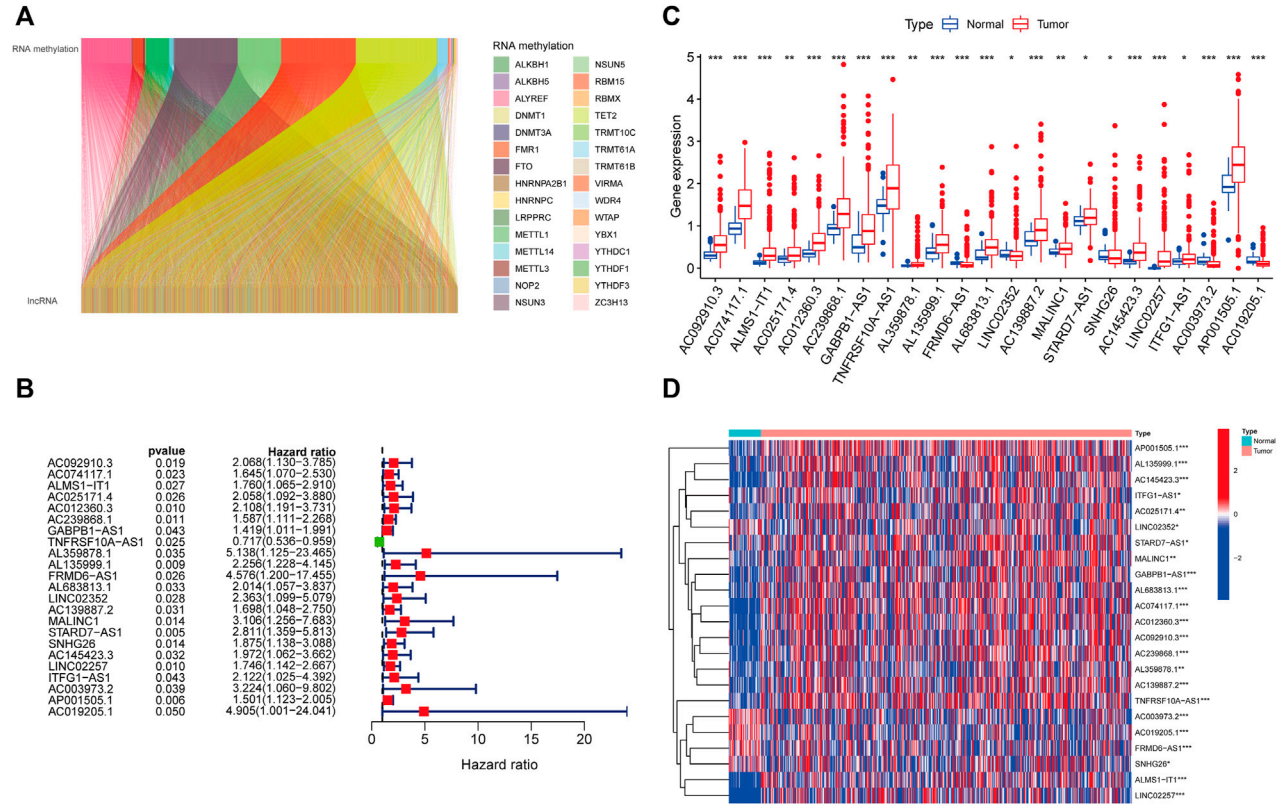

FIGURE 3 | Identification of prognostic value of RNA methylation-related lncRNAs. **(A)** 1,057 lncRNAs were co-expressed with differentially expressed RNA methylation-related regulators. **(B)** Univariate Cox regression analysis screened 23 lncRNAs with prognostic value. **(C,D)** The boxplot and heatmap of 23 lncRNAs with prognostic value differentially expressed between 41 normal and 471 tumor tissues in the TCGA-CORD cohort. *p<0.05; **p<0.01; ***p<0.001; ns, no sense.

Pearson correlation analysis and defined them as RMlncRNAs. Based on the mRNA-lncRNA co-expression pattern, we constructed a Sankey diagram to show their linkage (**Figure 3A**). After excluding normal tissues or patients lacking survival data, we merged survival information with RMlncRNA expression data of colon cancer patients (final number of patients = 433). Subsequently, we performed univariate Cox regression analysis and found that 23 RMlncRNAs were significantly associated with OS of colon cancer patients ($p < 0.05$, **Figure 3B**). Among them, only TNFRSF10A-AS1 was identified as a protective factor with a risk ratio (HR) < 1, while all others were considered as risk factors. The bar graph and heatmap showed significant differences in the expression of these 23 prognosis-related RMlncRNAs between normal and colon cancer tissues (**Figures 3C, D**).

Molecular Subtypes Mediated by 23 Prognosis-Related RMlncRNAs

Based on the expression levels of 23 prognosis-related RMlncRNAs in CC samples, we clustered 433 samples by an unsupervised clustering approach to further elucidate the biological differences between subgroups. Our results showed that K = 2 was the optimal number of clusters with the highest correlation within groups and the least interference between groups (**Figures 4A–C**). Therefore, CC patients were divided into two subgroups: Cluster1 ($n = 170$) and Cluster2 ($n = 263$). The survival analysis results showed a significant survival advantage for Cluster2 patients ($p = 0.021$, **Figure 4D**). The heatmap showed differences in prognosis-related RMlncRNA expression between subgroups (**Figure 4E**), and most RMlncRNAs were highly expressed in Cluster1. In addition, we found that patients with distant metastasis (M1) were more represented in Cluster1 ($p < 0.05$), while other clinicopathological features were not significantly different between the two subgroups.

Characterization of Immune Microenvironmental Infiltration Between the Distinct Clusters

We further explored the differences in immune microenvironment characteristics between distinct clusters to understand the interactions between RNA methylation-related lncRNAs and the immune microenvironment (TME). The results of CIBERSORT analysis (**Figure 5A**) showed that 8 of the 22 immune infiltrating cells differed between clusters, with T cells CD8, T cells regulatory (Tregs), NK cells resting, NK cells

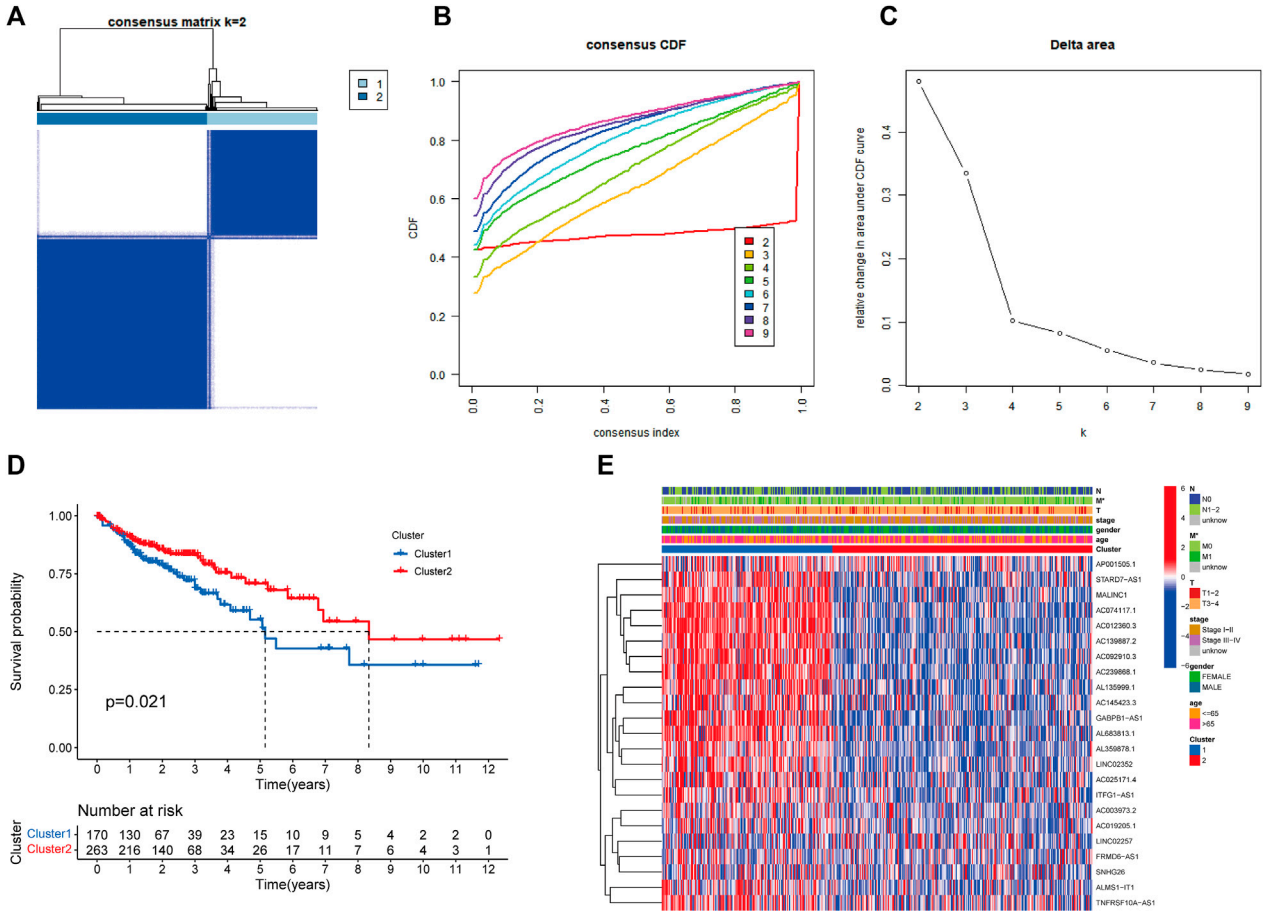

FIGURE 4 | Overall survival and clinical characteristics of different subgroups of CC. **(A)** Consensus matrix at optimal $k = 2$. **(B)** The cumulative distribution function (CDF) from $k = 2$ to 9. **(C)** Relative variation of the area under the CDF region at $k = 2$–9. **(D)** Kaplan-Meier curves of the overall survival (OS) time of cluster 1 and cluster 2 ($p = 0.021$). **(E)** Heatmap of clinical characteristics and 23 prognostic lncRNA expressions among the two clusters. *p<0.05.

activated, monocytes, dendritic cells resting, and neutrophils showed more infiltration in Cluster2, while only T cells CD4 memory activated were highly enriched in Cluster1. The percentages of 22 immune cell types in GC patients between the two clusters are shown in **Figure 5B**. ESTIMATE analysis showed (**Figure 5C**) that the immune score ($p < 0.001$), stromal score ($p = 0.0062$), and ESTIMATE score ($p < 0.001$) were significantly higher in Cluster2 than Cluster1, while the tumor purity in Cluster1 ($p < 0.001$) was considerably higher than Cluster2. In addition, we tried to determine the correlation between subgroups and some immune checkpoints. We found remarkable differences in the expression levels of 18 immune checkpoint genes between the two subtypes ($p < 0.05$). The expression levels of PD-1, PD-L1, HAVCR2, CTLA4, LDHA, LGALS9, TNFRSF18, YTHDF1, LAG3, CD40, TNFRSF4, TNFRSF9, CD86, B2M, and CD8A were higher in Cluster2, whereas PDCD1LG2, IL12A, PVR, and JAK1 were higher in Cluster 2 (**Figure 5D**). Previous studies have shown that high immune scores and activation of suppressive immune checkpoints (like HAVCR2, PD-L1, CTLA-4) play a crucial role in "hot tumors" (Zhan et al., 2021). "Hot tumors" are more likely to benefit from immune checkpoint blockade (ICB) therapy, whereas "cold tumors" with low levels of immune infiltration are more likely to become resistant to immunotherapy (Galon and Bruni, 2019). Therefore, we may consider cluster 1 as the "cold tumor" and cluster 2 as the "hot tumor", which may predict different immunotherapy responses.

Construction and Validation of RNA Methylation-Related lncRNA Prognostic Signature

The 433 colon cancer patients were randomly divided into a training set ($n = 217$) and a test set ($n = 216$). To avoid overfitting, we screened the seven most powerful prognostic RMlncRNAs by LASSO regression analysis, which were used to construct the RNA methylation-related lncRNA prognostic signature (RMlnc-score) (**Figures 6A, B**). The correlation coefficients are shown in **Table 1**. Patients were classified into low RMlnc-score and high RMlnc-score groups according to the cut-off values of RMlnc-score. The RMlnc-score for each patient was calculated as follows:RMlnc-score=(0.0645*ALMS1-IT1 expression) + (−0.1268*TNFRSF10A-

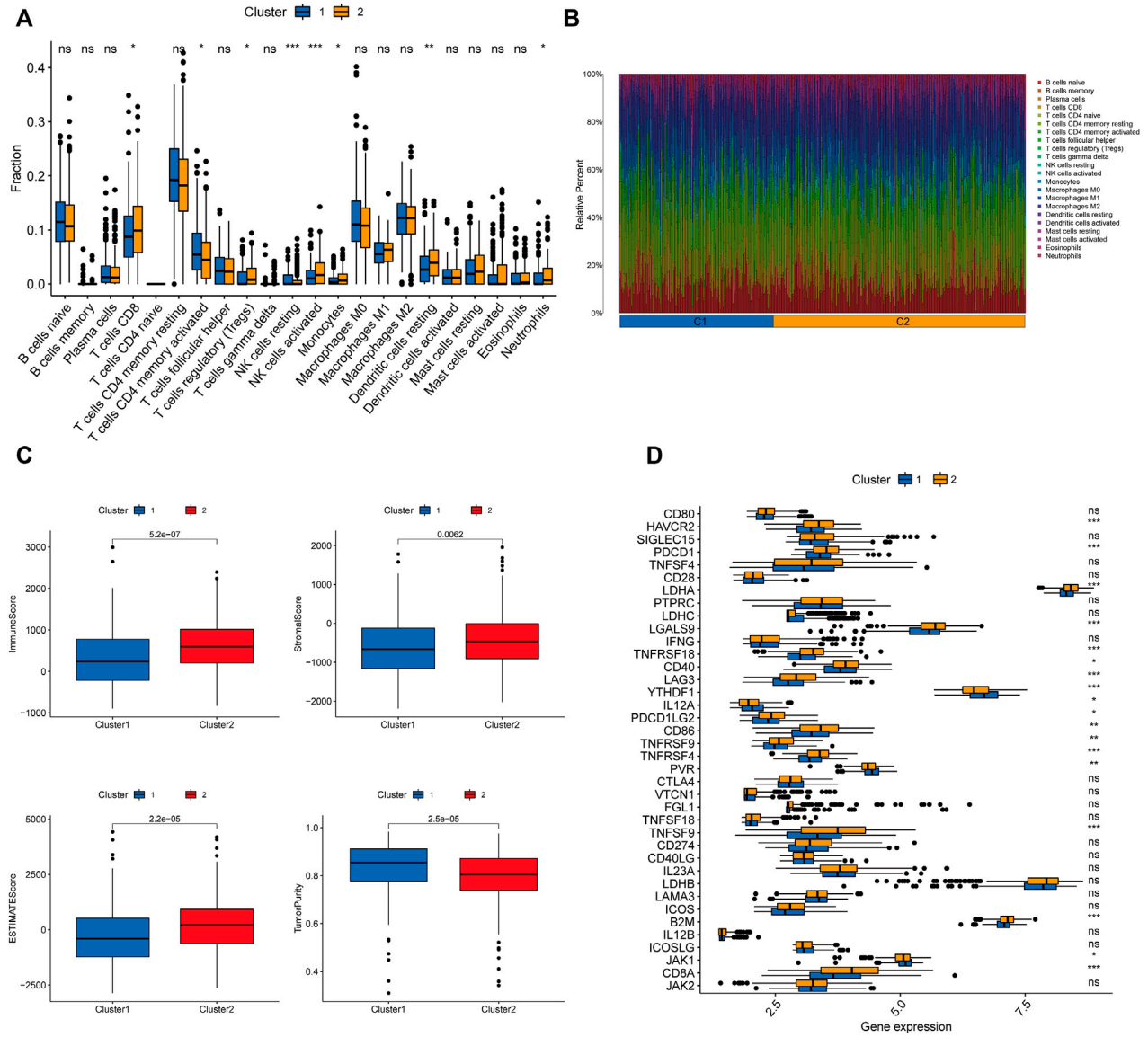

FIGURE 5 | Characterization of TME cell infiltration in different clusters. **(A)** CIBERSORT analysis of the abundance of 22 tumor-infiltrating immune cells (TICs) infiltration between the two groups. **(B)** The bar graph displaying the ratio of 22 TICs types for CC patients in cluster 1 and cluster 2. **(C)** The violin plots depicting the difference in tumor microenvironment scores (including immune score, stromal score, ESTIMATE score, and tumor purity) between the two clusters. **(D)** Expression of 32 immune checkpoint genes between the two clusters. $*p < 0.05$; $**p < 0.01$; $***p < 0.001$;ns, no sense.

AS1 expression) + (0.6464*FRMD6-AS1 expression) + (0.6173*STARD7-AS1) + (0.4430*LINC02257 expression) + (0.2254*AP001505.1 expression) + (0.2329*AC019205.1 expression). The Kaplan-Meier curves showed that in the training set ($p < 0.001$, **Figure 6C**) and test set ($p = 0.002$, **Figure 6D**), patients in the high RMlnc-score group had a worse prognosis compared to the low RMlnc-score group. The area under the curve (AUC) for 5-years overall survival (OS) was 0.741 and 0.734 for the training and test sets, respectively (**Figures 6E, F**). In the overall cohort (**Figure 6G**), the RMlnc-score (our study) had an AUC of 0.737 at 5-years overall survival, which was substantially higher than ChaiLncSig (AUC = 0.653), YunLncSig (AUC = 0.658), and ZhangLncSig (AUC = 0.659). This suggests that the RMlnc-score has higher accuracy in predicting survival compared to three recently published lncRNA signatures for colon cancer (Chai et al., 2021; Yun and Yang, 2021; Zhang et al., 2021d). The survival status and RMlnc-score score curves for the training and test sets showed (**Figure 6H, I**, 7I) that RMlnc-score was proportional to the number of deaths in CC patients. The heatmaps showed (**Figures 6J, K**) that the expression of ALMS1-IT1, FRMD6-AS1, STARD7-AS1, LINC02257, AP001505.1, and AC019205.1 was upregulated in the high RMlnc-score group, while TNFRSF10A-AS1 was upregulated in the low RMlnc -score group was up-regulated. In addition, we performed a validation analysis of the signature

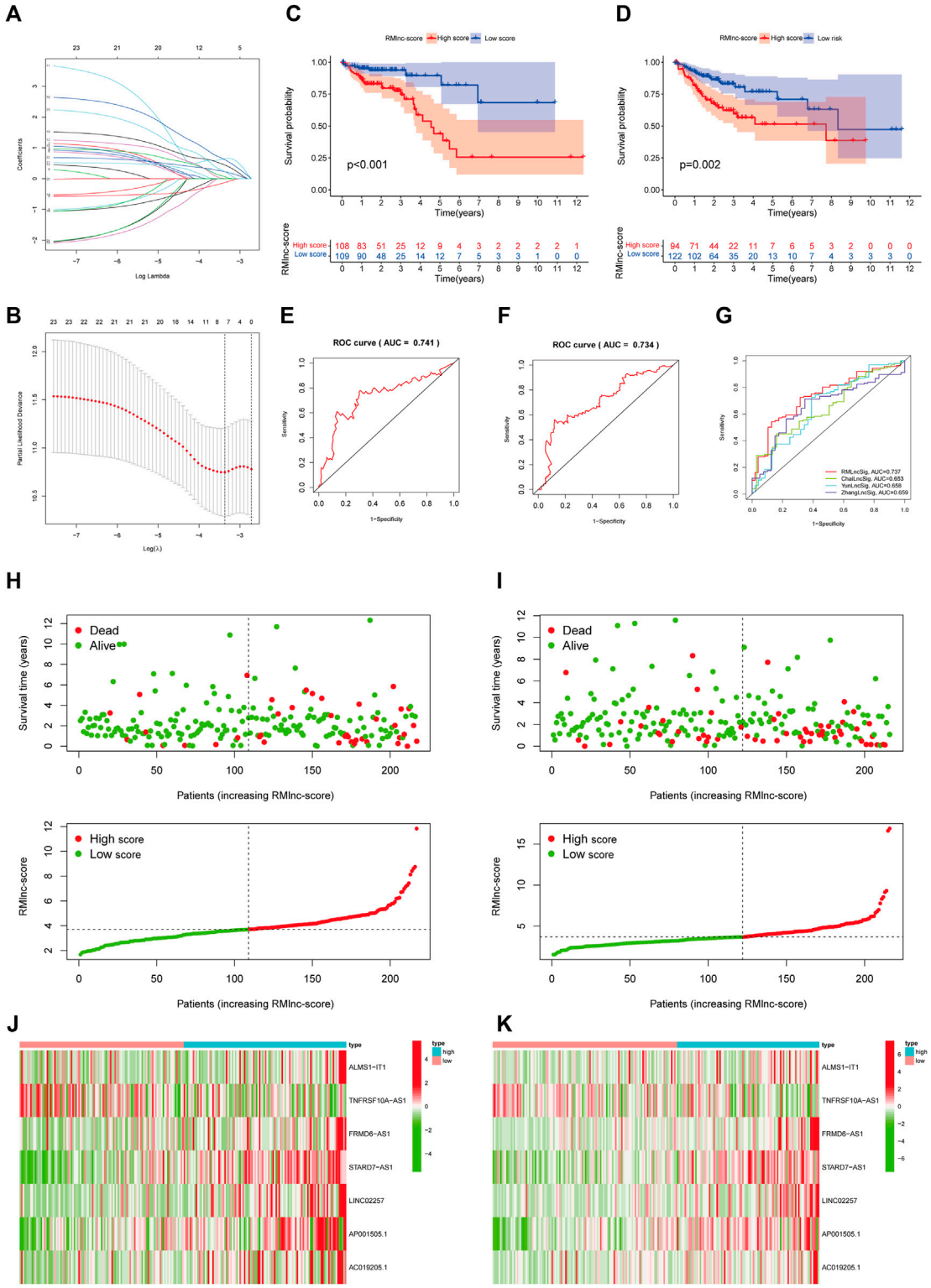

FIGURE 6 | RNA methylation-related lncRNA prognostic signature. **(A,B)** Seven optimal RNA methylation-related lncRNAs were found using the least absolute shrinkage and selection operator (LASSO) cox regression. **(C,D)** Kaplan-Meier curves for overall survival in the training and test sets. **(E,F)** ROC curves were used to predict the 5-years survival of patients in the training and test sets. The AUC was 0.741 in the training set and 0.734 in the test set. **(G)** Comparison of RMlinc-score with other prognostic evaluation models. **(H,I)** Survival status and RMlinc-score curves in the training and test sets. **(J,K)** Heatmap of RNA methylation-related lncRNAs expression in the training and test sets.

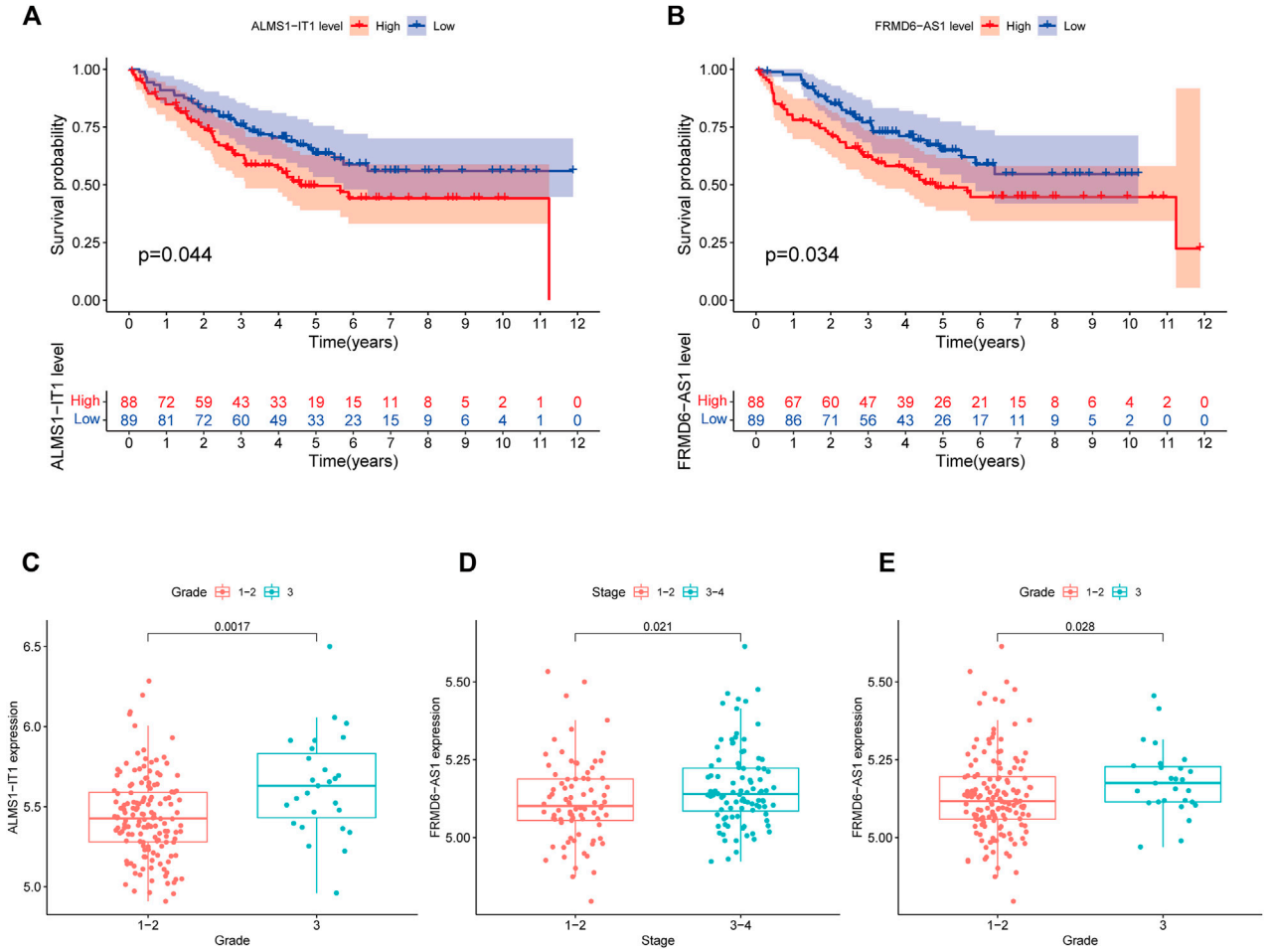

FIGURE 7 | Validation of lncRNA prognostic signatures in the GEO cohort. **(A)** Kaplan-Meier survival curve of ALMS1-IT1. **(B)** Kaplan-Meier survival curves of FRMD6-AS1. **(C)** Correlation between ALMS1-IT1 expression and grade. **(D)** Correlation between FRMD6-AS1 expression and stage. **(E)** Correlation between FRMD6-AS1 expression and grade.

lncRNA in the GSE17536 cohort. However, due to fewer non-coding genes in the microarray data, we only detected ALMS1-IT1 and FRMD6-AS1. Our results showed that high expression of ALMS1-IT1 (p = 0.044) and FRMD6-AS1 (p = 0.034) was significantly associated with poor prognosis of patients (**Figures 7A, B**). High expression of ALMS1-IT1 was associated with high grade (p = 0.0017, **Figure 7C**) and high expression of FRMD6-AS1 was associated with high stage (p = 0.021, **Figure 7D**) and high grade (p = 0.028, **Figure 7E**).

TABLE 1 | The correlation coefficients of 7 RNA methylation-related lncRNAs.

Gene	Coef
ALMS1-IT1	0.064532959
TNFRSF10A-AS1	−0.12683763
FRMD6-AS1	0.64643134
STARD7-AS1	0.617319233
LINC02257	0.443023664
AP001505.1	0.225414755
AC019205.1	0.232908459

Independent Prognostic and Clinical Correlation Analysis

Stratified survival analysis in combination with clinical characteristics (**Figures 8A–L**) showed that in age>65 (p < 0.001), age ≤ 65 (p < 0.001), male (p < 0.001), female (p = 0.004), stage III-IV (p = 0.002), T3-4 (p < 0.001), M0 (p < 0.001), and N1-2 (p < 0.001) subgroups of patients, survival was significantly lower in the high RMlnc-score group than in the low RMlnc-score group. By comparing the RMlnc-score of patients in different groups, we found that RMlnc-score increased with increasing T-stage, N-stage, M-stage, and clinical stage, while no significant differences were seen for age and gender (**Figures 8M–R**). Univariate Cox regression analysis showed that age, stage, T-stage, N-stage, M-stage, and RMlnc-score (all p < 0.001) were strongly associated with prognosis (**Figure 9A**). Multivariate Cox regression analysis confirmed that

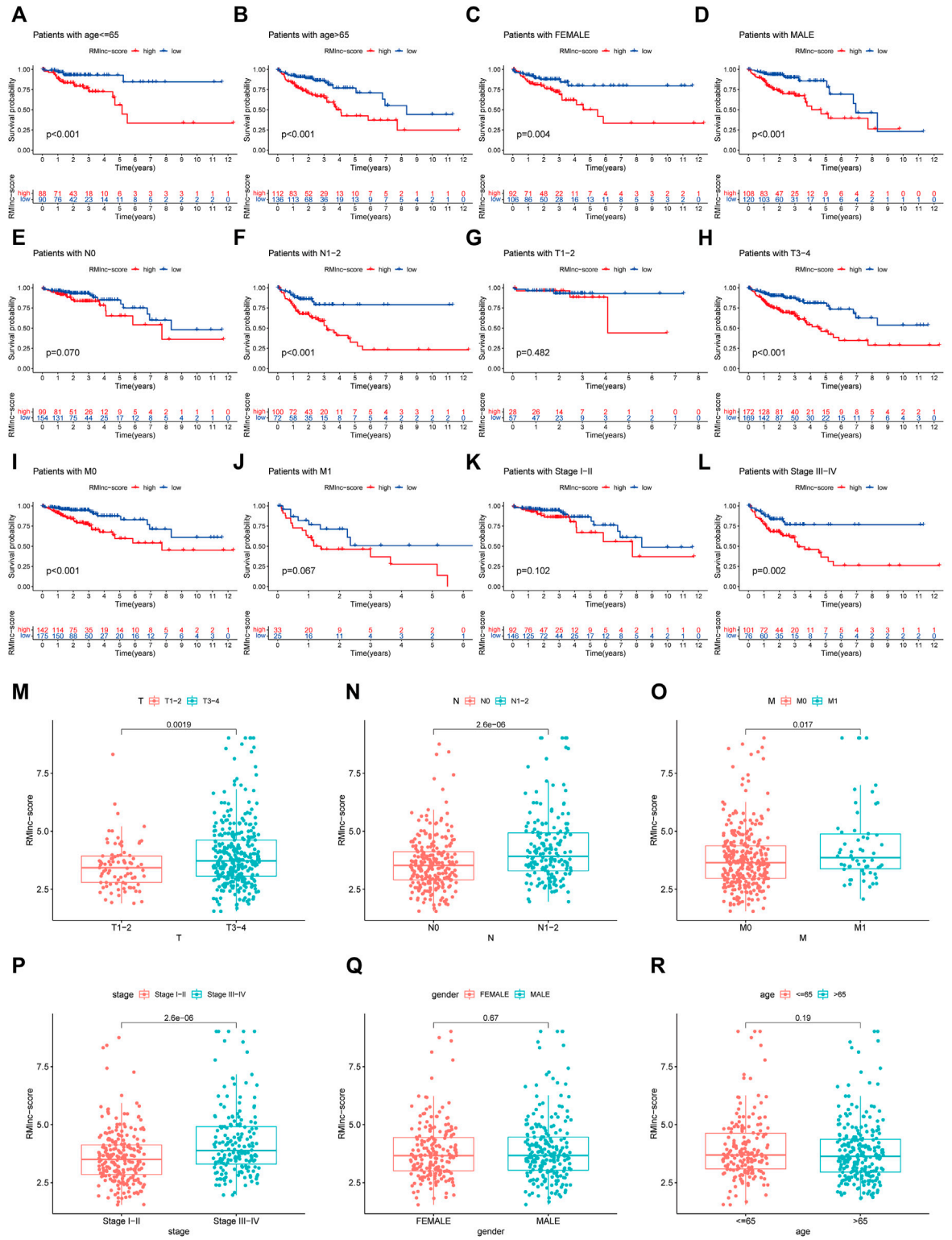

FIGURE 8 | Correlation of clinical characteristics with RMlnc-score by subgroup analysis. Kaplan-Meier curves stratified by **(A,B)** age, **(C,D)** sex, **(E,F)** N stage, **(G,H)** T stage, **(I,J)** M stage, and **(K,L)** clinical stage. **(M–R)** Differential analysis of RMlnc-score for different subgroups.

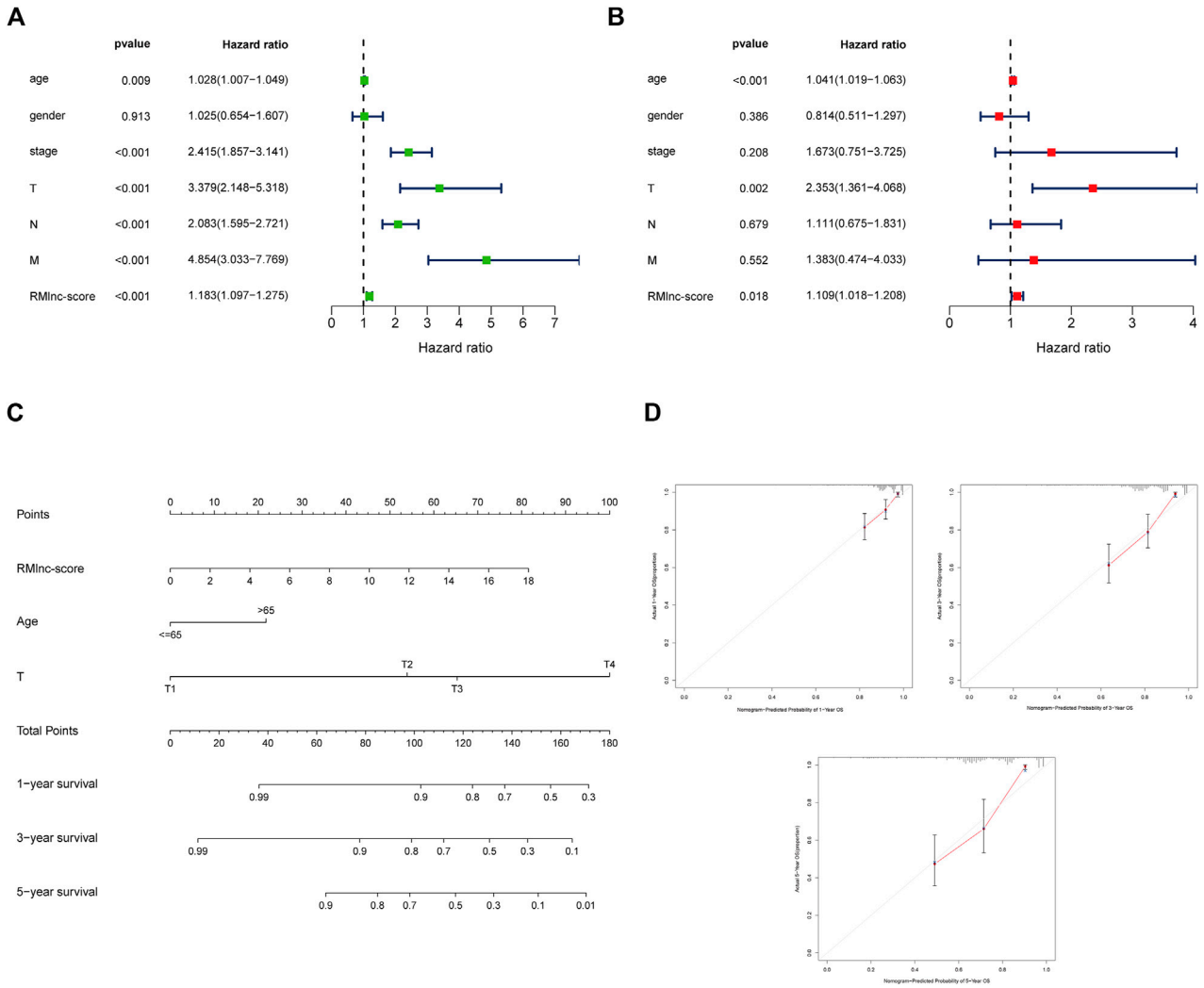

FIGURE 9 | Establishment of nomogram for predicting OS in colon cancer patients. **(A)** Univariate Cox regression analysis of clinical characteristics and RMlnc-score in CC samples. **(B)** Multivariate Cox regression analysis of clinical characteristics and RMlnc-score in CC samples. **(C)** The nomogram with multiple independent predictors, including age, T-stage, and RMlnc-score, was employed to predict 1-, 3-, and 5-years OS in patients with colon cancer. **(D)** Calibration curves of the nomogram for predicting 1,3,5-years OS.

age, T-stage, and RMlnc-score were independent prognostic factors for CC patients (**Figure 9B**). Based on the three independent prognostic factors in the multivariate Cox regression analysis, we created a nomogram capable of predicting the incidence of OS in CC patients at 1, 3, and 5 years (**Figure 9C**). The calibration curve demonstrated the high accuracy and sensitivity of this nomogram (**Figure 9D**).

PCA Analysis and Immune Microenvironment Characterization

The results of principal component analysis (PCA) showed no significant differences between the high RMlnc-score group and the low RMlnc-score group in the expression of all genes (**Figure 10A**), RNA methylation-related genes (**Figure 10B**), and RNA methylation-related lncRNAs (**Figure 10C**). However, in the expression of the seven lncRNAs used in the prognostic model (**Figure 10D**), there was a significant difference between the high RMlnc-score and low RMlnc-score groups. We also explored whether our model could predict immune cell infiltration in CC. The bubble plot (**Figure 10E**) showed that RMlnc-score was positively correlated with $CD4^+$ T cells, cancer-associated fibroblast (CAFs), myeloid dendritic cell, macrophage M0, NK cell activated, hematopoietic stem cell while negative correlation with CD4+8 cell, monocyte, neutrophil, and B cell plasma. The ssGSEA results (**Figure 10F**) showed that some immune cells, including dendritic cells (DCs), activated dendritic cells (aDCs), immature dendritic cells (iDCs), mast cells, neutrophils, NK cells, and type 2 T helper were significantly increased in the low RMlnc-score group, and some pathways associated with immune function, namely APC co-stimulation, C-C chemokine receptor, and cytolytic activity, were significantly activated in the low RMlnc-score group.

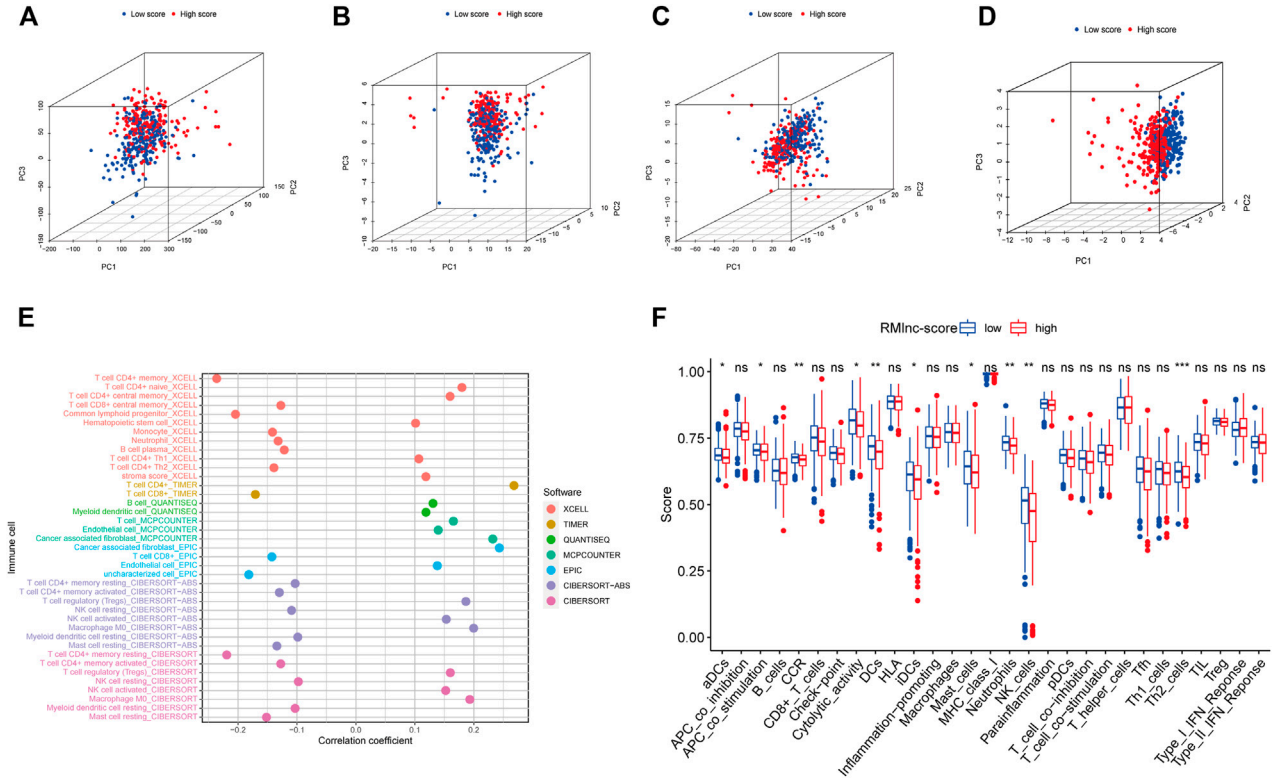

FIGURE 10 | The principal component analysis and immune microenvironment differences of high and low RMlnc-score groups. Principal component analysis between low RMlnc-score and high RMlnc-score groups based on the expression of **(A)** all genes, **(B)** RNA methylation-related genes, and **(C)** RNA methylation-related lncRNAs and the **(D)** seven lncRNAs of prognostic signature. **(E)** Correlation between RMlnc-score and tumor-infiltrating immune cells. The correlation coefficient higher than 0 indicated positive correlation and lower than 0 denoted negative correlation. **(F)** Differences in immune cells and immune function between the high RMlnc-score and low RMlnc-score groups. *p<0.05; **p<0.01; ***p<0.001; ns, no sense.

Immunotherapy Response Analysis

TMB and MSI have been reported to be predictive biomarkers of immunotherapeutic response (Ock et al., 2017; Vandekerkhove et al., 2021). Therefore, we first compared somatic mutations in high RMlnc-score and low RMlnc-score and visualized the top 20 genes with the highest mutation frequency (**Figures 11A, B**). However, there was no significant difference in tumor mutational load between the high RMlnc-score and low RMlnc-score groups (**Figure 11C**). We then compared the differences in MSI distribution between the different scoring groups and found that the low RMlnc-score group was associated with higher microsatellite instability (MSI) (**Figure 11D**). TIDE, a novel predictive marker of immunotherapy, was better than known immunotherapy biomarkers (including TMB and PD-L1 expression) for response to immunotherapy in certain tumors (Wang et al., 2019). Higher TIDE scores indicate that tumor cells are more likely to induce immune escape, thus indicating a lower response rate to immunotherapy. Surprisingly, we found that patients in the low RMlnc-score group had significantly lower TIDE scores (including T cell dysfunction and exclusion scores) than those in the high RMlnc-score group (**Figures 11E–G**). The above findings suggested that RMlnc-score correlates with the response of CC patients to immunotherapy and may help predict the efficacy of ICB immunotherapy.

Drug Sensitivity Analysis

To explore the effect of RMlnc-score on drug response, we compared the half-maximal inhibitory concentration (IC50) of the commonly used drugs in both groups. The results showed that the IC50 values of bicalutamide, lapatinib, sorafenib, metformin, and temsirolimus were higher in the high RMlnc-score group, indicating that patients in the low-scoring group were more sensitive to these five drugs. In contrast, axitinib, bexarotene, bosutinib, elesclomol, embelin, etoposide, imatinib, lenalidomide, methotrexate, midostaurin, nilotinib, pazopanib, shikonin, vinblastine, vinorelbine, and vorinostat had higher IC50 in patients with low RMlnc-score, implying that patients in the high RMlnc-score group were more sensitive to these drugs (**Figure 12**).

Analysis of RNA Methylation Modification Sites

After scanning the m6A-Atlas, m5C-Atlas, and m7GHub databases, we eventually obtained six m6A, nine m5C, and one m7G modification sites on STARD7-AS1 and five m5C modification sites on FRMD6-AS1, which have been experimentally validated (**Supplementary Table S1**). Then, we also utilized the widely used bioinformatics tools SRAMP,

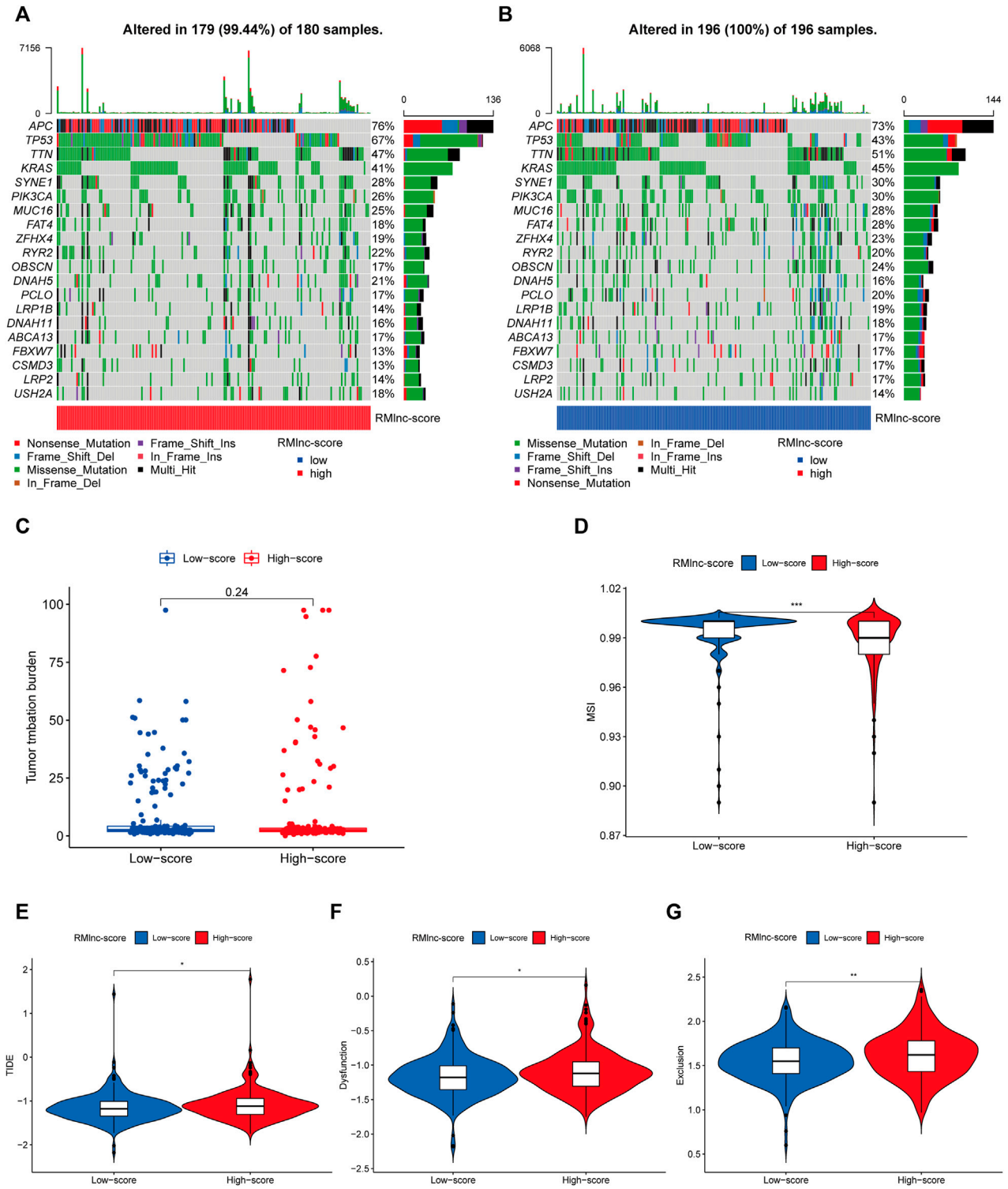

FIGURE 11 | Predictability of immunotherapy response in the prognostic signature. **(A,B)** Waterfall plot of the tumor mutational burden (TMB) landscape in the high RMInc-score and low RMInc-score groups presenting the top 20 genes with the highest mutation frequency. **(C)** Differences in TMB of colon cancer patients in the high and low RMInc-score groups. **(D)** Differences in microsatellite instability (MSI) of colon cancer patients in high and low RMInc-score groups. **(E-G)** TIDE prediction scores (including TIDE score, dysfunction score, and exclusion score) between high RMInc-score and low RMInc-score groups. *p<0.05; **p<0.01.

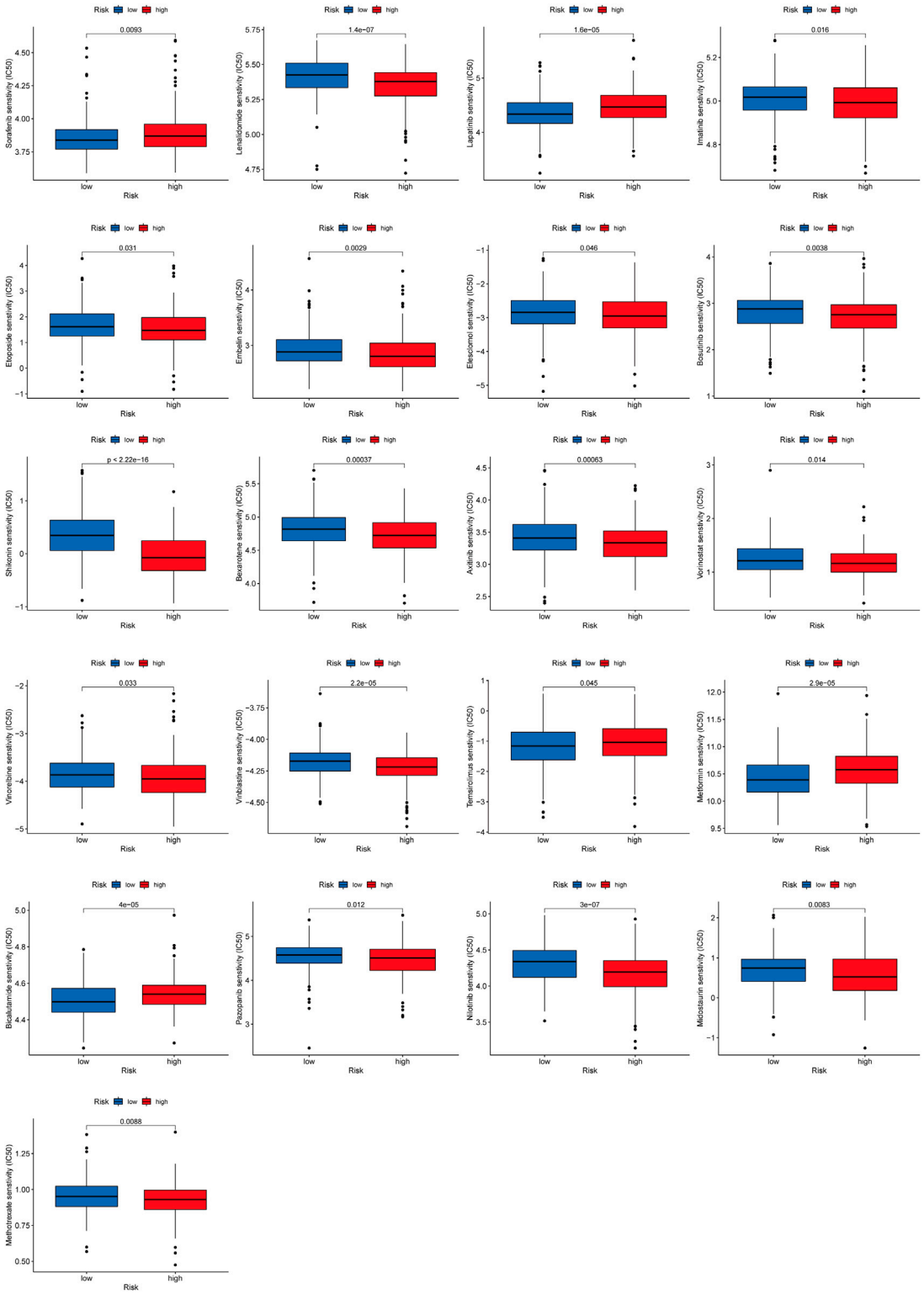

FIGURE 12 | Anti-tumor drug sensitivity in high RMlnc-score and low RMlnc-score populations.

RNAm5Cfinder, and iRNA-m7G to predict potential m6A, m5C, and m7G modification sites on our seven lncRNAs. Some meaningful results showed that all seven lncRNAs were potentially methylated (**Supplementary Table S2**).

DISCUSSION

CC is a highly complex and heterogeneous tumor characterized by high morbidity and poor prognosis (Kumar et al., 2021). Chemotherapy for CC has progressed in recent years, but tumor resistance is frequent when traditional histological and anatomical classifications are used to guide anti-tumor therapy. Therefore, accurate identification of molecular subtypes of CC is vital to guide individualized treatment. Although previous studies have also identified several prognostic signatures of CC for the stratification of colon cancer patients, considerable heterogeneity remains between subtypes (Cui et al., 2021; Song et al., 2021b). Therefore, more accurate prognostic signatures of CC are urgently needed to improve patient survival. An increasing number of studies have shown that RNA methylation modifications (including m6A, m5C, m1A, and m7G) play an essential role in tumor progression and influence specific biological processes by interacting with lncRNAs (Chen et al., 2021; Yao et al., 2021). Huang et al. constructed an m5C-associated lncRNA prognostic signature that accurately predicted breast cancer patient's prognosis and immune microenvironment characteristics (Huang et al., 2021). A recent study has identified the critical role of m6A/m5C/m1A-related lncRNA-based prognostic signature in predicting molecular subtypes and prognosis of head and neck tumors (Wang et al., 2021a). However, to the best of our knowledge, no prognostic signature based on m6A/m1A/m5C/m7G-related lncRNAs has been found to be accurate and applicable to CC patients.

In this study, we first identified 1057 RNA methylation-associated lncRNAs in the TCGA-CORD cohort, 23 of which were confirmed with prognostic value. In addition, we defined two clusters by consensus clustering analysis to investigate potential molecular subtypes of CC. The results showed that the subtypes were strongly correlated with tumor stage and OS, with cluster 2 having better OS and less distant metastasis than cluster 1, reflecting the association between RNA methylation-associated lncRNAs and CC progression and prognosis. Recent studies have shown that RNA methylation and lncRNAs play a critical regulatory role in the immune system, especially in immune cell infiltration and anti-tumor immune responses (Li et al., 2017; Wu et al., 2020; Eptaminitaki et al., 2021). Based on these findings, we obtained TME scores and immune microenvironmental landscapes for each CC sample to investigate the relationship between clusters, TME, and immune checkpoints. The results showed that TME scores, immune infiltrating cells, and immune checkpoints differed significantly between the two clusters. Among them, cluster 2 had a significantly higher immune score, stromal score, and ESTIMATE score than cluster 1, while cluster 1 had a higher tumor purity than cluster 2. The majority of immune infiltrating cells were enriched in cluster 2, including T cells CD8, Tregs, NK cells resting, NK cells activated, Monocytes Dendritic cells resting, and Neutrophils. In addition, we found that 15 out of 18 differentially expressed immune checkpoint molecules (including PD-1, PD-L1, HAVCR2, CTLA4, LDHA, LGALS9, TNFRSF18, YTHDF1, LAG3, CD40, TNFRSF4, TNFRSF9, CD86, B2M, and CD8A) were highly expressed in cluster 2. It was reported that high PD-L1 expression/infiltrating tumors with high immune scores are usually considered hot tumors which are sensitive to immunotherapy. In contrast, low PD-L1 expression/non-infiltrating tumors with low immune scores are typically regarded as cold tumors which are less effective for immunotherapy (Kuriyama et al., 2020). Therefore, we identified cluster 2 as "hot tumor" and cluster 1 as "cold tumor," corresponding to different prognoses and immunotherapeutic responses.

Among the 23 RNA methylation-related lncRNAs, seven lncRNAs were used to generate prognostic gene signatures that stratified CC patients into low RMlnc-score and high RMlnc-score groups with different OS. The survival time of patients in the high RMlnc-score group was significantly shorter than that in the low RMlnc-score group, both in the training and test sets, which also demonstrated that the prognostic model consisting of all seven lncRNAs could well predict the prognosis of CC patients. We validated the predictive ability of RMlnc-score in patients stratified based on clinicopathological parameters. We noticed that RMlnc-score showed a strong positive correlation with tumor progression (T3-4, N1-2, M1, and stage III-IV). Univariate and multivariate cox regression analyses showed that RMlnc-score, age, and T-stage were available as independent prognostic factors for OS in CC patients. By integrating these independent prognostic factors, we constructed nomograms that could predict 1-, 3-, and 5-years survival in CC patients, which were highly accurate and reliable in estimating individual survival rates. Notably, we further validated the correlation of our signature lncRNA with clinicopathological features in the GSE17536 cohort. We detected that high expression of lncRNAs ALMS1-IT1 and FRMD6-AS1 was associated with poorer prognosis and poorer differentiation. High FRMD6-AS1 expression was also associated with higher clinical stage. Previous studies have shown that upregulation of ALMS1-IT1 can promote lung cancer progression by mediating AVL9 activation of the cell cycle protein-dependent kinase pathway (Luan et al., 2021). Li et al. constructed a ferroptosis-related lncRNA prognostic signature that also included ALMS1-IT1 and found it to be strongly associated with poor prognosis in colon cancer (Li et al., 2022). These findings validated the oncogenic properties of ALMS1-IT1 and are consistent with our results. Unfortunately, there are few studies on the remaining lncRNAs. Therefore, we anticipated that our results would help to demonstrate the prognostic value of these RNA methylation-related lncRNAs, thus providing insights into their potential role in carcinogenesis and progression of CC.

Currently, only a minority of CC patients have responded to immunotherapy in clinical practice. Thus, it is necessary to assess the value of prognostic characteristics in predicting response to

immunotherapy. The effectiveness of immunotherapy is influenced by the immunogenicity of the tumor microenvironment, which is why understanding TME is essential for evaluating immunotherapy (Turley et al., 2015). The ssGSEA results showed that the low RMlnc-score group had a greater enrichment of immune-related cells and immune-related pathways, including dendritic cells (DCs), activated dendritic cells (aDCs), immature dendritic cells (iDCs), mast cells, neutrophils, NK cells, type 2 T helper, APC co-stimulation, C-C chemokine receptor, and cytolytic activity. The above results indicated that patients with low RMlnc-score had higher immunogenicity and better immunotherapy response.

Drug efficacy is related to drug sensitivity and individual differences in patients, and targeting the appropriate subpopulation will improve drug efficacy. Therefore, we further analyzed the sensitivity of patients in distinct RMlnc-score groups to anti-tumor drugs. Prediction of chemotherapy drug sensitivity showed that bicalutamide, lapatinib, sorafenib, metformin, and temsirolimus were the ideal choices for CC patients in the low RMlnc-score group. At the same time, axitinib, bexarotene, bosutinib, elesclomol,embelin, etoposide, imatinib, lenalidomide, methotrexate, midostaurin, nilotinib, pazopanib, shikonin, vinblastine, vinorelbine, and vorinostat may work better in patients in the high RMlnc-score group.

However, our study has some limitations. First, this is a retrospective analysis based on an online public database, and we used internal validation methods in the TCGA cohort and external validation in the GSE17536 independent cohort, but large-scale prospective data are still needed to validate our prognostic signature. In addition, the potential mechanism of RMlnc-score may need further validation by *in vitro* and *in vivo* experiments.

CONCLUSION

In summary, our study elucidated that RNA methylation-related lncRNAs and can predict the prognosis of CC patients and guide more effective and personalized treatment strategies by identifying hot and cold tumors. Targeting RNA methylation and lncRNAs would be a promising way to overcome individual treatment failure and improve patient prognosis.

DATA AVAILABILITY STATEMENT

The original contributions presented in the study are included in the article/**Supplementary Material**, further inquiries can be directed to the corresponding author/s.

AUTHOR CONTRIBUTIONS

RH wrote the article; RH, CM, LH, and JH processed the data analysis; CM, XW, YL, and YF conceived of this study; YF revised the final manuscript. The authors read and approved the final manuscript.

FUNDING

This work was supported by Jiangsu Innovative Team Leading Talent Fund (CXTDC2016006, QNRC2016446), Jiangsu 333 Talent Fund (BRA2020016), Jiangsu Provincial Key Research and Development Special Fund (BE2015666), Jiangsu Six High Peak Talent Fund (WSW-205, WSW236), Zhenjiang Key Research and Development Fund (SH2021038), Suqian Science and Technology Support Project Fund (K201907).

ACKNOWLEDGMENTS

The authors would like to give their sincere appreciation to the reviewers for their helpful comments on this article and research groups for the TCGA and CEO, which provided data for this collection.

SUPPLEMENTARY MATERIAL

The Supplementary Material for this article can be found online at: https://www.frontiersin.org/articles/10.3389/fgene.2022.870945/full#supplementary-material

REFERENCES

An, Y., and Duan, H. (2022). The Role of m6A RNA Methylation in Cancer Metabolism. *Mol. Cancer* 21 (1), 14. doi:10.1186/s12943-022-01500-4

Cao, S.-Q., Zheng, H., Sun, B.-C., Wang, Z.-L., Liu, T., Guo, D.-H., et al. (2019). Long Non-Coding RNA Highly Up-Regulated in Liver Cancer Promotes Exosome Secretion. *World J. Gastroenterol.* 25 (35), 5283–5299. doi:10.3748/wjg.v25.i35.5283

Chai, X.-K., Qi, W., Zou, C.-Y., He, C.-X., Su, M., and Zhao, D.-Q. (2021). Potential Prognostic Value of a Seven m6A-Related LncRNAs Signature and the Correlative Immune Infiltration in Colon Adenocarcinoma. *Front. Genet.* 12, 774010. doi:10.3389/fgene.2021.774010

Chan, T. A., Yarchoan, M., Jaffee, E., Swanton, C., Quezada, S. A., Stenzinger, A., et al. (2019). Development of Tumor Mutation burden as an Immunotherapy Biomarker: Utility for the Oncology Clinic. *Ann. Oncol.* 30 (1), 44–56. doi:10.1093/annonc/mdy495

Chen, K., Song, B., Tang, Y., Wei, Z., Xu, Q., Su, J., et al. (2021). RMDisease: A Database of Genetic Variants that Affect RNA Modifications, with Implications for Epitranscriptome Pathogenesis. *Nucleic Acids Res.* 49 (D1), D1396–d1404. doi:10.1093/nar/gkaa790

Chen, M., Wei, L., Law, C.-T., Tsang, F. H.-C., Shen, J., Cheng, C. L.-H., et al. (2018). RNA N6-Methyladenosine Methyltransferase-Like 3 Promotes Liver Cancer Progression through YTHDF2-Dependent Posttranscriptional Silencing of SOCS2. *Hepatology* 67 (6), 2254–2270. doi:10.1002/hep.29683

Chen, W., Feng, P., Song, X., Lv, H., and Lin, H. (2019). iRNA-m7G: Identifying N7-Methylguanosine Sites by Fusing Multiple Features. *Mol. Ther. - Nucleic Acids* 18, 269–274. doi:10.1016/j.omtn.2019.08.022

Constantinidou, A., Alifieris, C., and Trafalis, D. T. (2019). Targeting Programmed Cell Death -1 (PD-1) and Ligand (PD-L1): A new era in Cancer Active Immunotherapy. *Pharmacol. Ther.* 194, 84–106. doi:10.1016/j.pharmthera.2018.09.008

Cui, Z., Sun, G., Bhandari, R., Lu, J., Zhang, M., Bhandari, R., et al. (2021). Comprehensive Analysis of Glycolysis-Related Genes for Prognosis, Immune Features, and Candidate Drug Development in Colon Cancer. *Front. Cel Dev. Biol.* 9, 684322. doi:10.3389/fcell.2021.684322

Dong, L., Liu, D., Jing, D., Xu, H., Zhang, C., Qi, D., et al. (2022). LncRNA ARST Is a Novel Prognostic and Diagnostic Biomarker for Colorectal Cancer. *Cancer Manag. Res.* 14, 19–24. doi:10.2147/cmar.S338997

Eptaminitaki, G. C., Wolff, N., Stellas, D., Sifakis, K., and Baritaki, S. (2021). Long Non-Coding RNAs (lncRNAs) in Response and Resistance to Cancer Immunosurveillance and Immunotherapy. *Cells* 10 (12), 3313. doi:10.3390/cells10123313

Frankish, A., Diekhans, M., Ferreira, A.-M., Johnson, R., Jungreis, I., Loveland, J., et al. (2019). GENCODE Reference Annotation for the Human and Mouse Genomes. *Nucleic Acids Res.* 47 (D1), D766–d773. doi:10.1093/nar/gky955

Fu, J., Li, K., Zhang, W., Wan, C., Zhang, J., Jiang, P., et al. (2020). Large-Scale Public Data Reuse to Model Immunotherapy Response and Resistance. *Genome Med.* 12 (1), 21. doi:10.1186/s13073-020-0721-z

Galon, J., and Bruni, D. (2019). Approaches to Treat Immune Hot, Altered and Cold Tumours with Combination Immunotherapies. *Nat. Rev. Drug Discov.* 18 (3), 197–218. doi:10.1038/s41573-018-0007-y

Geeleher, P., Cox, N. J., and Huang, R. (2014). Clinical Drug Response Can Be Predicted Using Baseline Gene Expression Levels and *In Vitro* Drug Sensitivity in Cell Lines. *Genome Biol.* 15 (3), R47. doi:10.1186/gb-2014-15-3-r47

He, Y., Wang, L., Li, X., Zhang, T., Song, T., Zhang, J., et al. (2021). Rectosigmoid-Junction Squamous Cell Carcinoma with pMMR/MSS Achieved a Partial Response Following PD-1 Blockade Combined with Chemotherapy: A Case Report. *Front. Oncol.* 11, 596342. doi:10.3389/fonc.2021.596342

Hu, B.-B., Wang, X.-Y., Gu, X.-Y., Zou, C., Gao, Z.-J., Zhang, H., et al. (2019). N6-Methyladenosine (m6A) RNA Modification in Gastrointestinal Tract Cancers: Roles, Mechanisms, and Applications. *Mol. Cancer* 18 (1), 178. doi:10.1186/s12943-019-1099-7

Huang, Z., Pan, J., Wang, H., Du, X., Xu, Y., Wang, Z., et al. (2021). Prognostic Significance and Tumor Immune Microenvironment Heterogenicity of m5C RNA Methylation Regulators in Triple-Negative Breast Cancer. *Front. Cel Dev. Biol.* 9, 657547. doi:10.3389/fcell.2021.657547

Katsara, O., and Schneider, R. J. (2021). m7G tRNA Modification Reveals New Secrets in the Translational Regulation of Cancer Development. *Mol. Cel* 81 (16), 3243–3245. doi:10.1016/j.molcel.2021.07.030

Konishi, N., Nakamura, M., Ishida, E., Shimada, K., Mitsui, E., Yoshikawa, R., et al. (2005). High Expression of a New Marker PCA-1 in Human Prostate Carcinoma. *Clin. Cancer Res.* 11 (14), 5090–5097. doi:10.1158/1078-0432.Ccr-05-0195

Kumar, N., Thomas, A., Madhu, S., Ramos, M. R. D., Shen, L., Tan, J. Y. H., et al. (2021). Analysis of Unplanned Hospital Readmissions up to 2-Years after Metastatic Spine Tumour Surgery. *Eur. Spine J.* 30, 2887–2895. doi:10.1007/s00586-021-06723-5

Kuriyama, K., Higuchi, T., Yokobori, T., Saito, H., Yoshida, T., Hara, K., et al. (2020). Uptake of Positron Emission Tomography Tracers Reflects the Tumor Immune Status in Esophageal Squamous Cell Carcinoma. *Cancer Sci.* 111 (6), 1969–1978. doi:10.1111/cas.14421

Le, D. T., Durham, J. N., Smith, K. N., Wang, H., Bartlett, B. R., Aulakh, L. K., et al. (2017). Mismatch Repair Deficiency Predicts Response of Solid Tumors to PD-1 Blockade. *Science* 357 (6349), 409–413. doi:10.1126/science.aan6733

Li, H.-B., Tong, J., Zhu, S., Batista, P. J., Duffy, E. E., Zhao, J., et al. (2017). m6A mRNA Methylation Controls T Cell Homeostasis by Targeting the IL-7/STAT5/SOCS Pathways. *Nature* 548 (7667), 338–342. doi:10.1038/nature23450

Li, J., Huang, Y., Yang, X., Zhou, Y., and Zhou, Y. (2018). RNAm5Cfinder: A Web-Server for Predicting RNA 5-methylcytosine (m5C) Sites Based on Random Forest. *Sci. Rep.* 8 (1), 17299. doi:10.1038/s41598-018-35502-4

Li, N., Shen, J., Qiao, X., Gao, Y., Su, H.-B., and Zhang, S. (2022). Long Non-Coding RNA Signatures Associated with Ferroptosis Predict Prognosis in Colorectal Cancer. *Int. J. Gen. Med.* 15, 33–43. doi:10.2147/ijgm.S331378

Li, T., Hu, P.-S., Zuo, Z., Lin, J.-F., Li, X., Wu, Q.-N., et al. (2019a). METTL3 Facilitates Tumor Progression via an m6A-IGF2BP2-dependent Mechanism in Colorectal Carcinoma. *Mol. Cancer* 18 (1), 112. doi:10.1186/s12943-019-1038-7

Li, Y., Xiao, J., Bai, J., Tian, Y., Qu, Y., Chen, X., et al. (2019b). Molecular Characterization and Clinical Relevance of m6A Regulators across 33 Cancer Types. *Mol. Cancer* 18 (1), 137. doi:10.1186/s12943-019-1066-3

Liu, X., Yao, J., Song, L., Zhang, S., Huang, T., and Li, Y. (2019). Local and Abscopal Responses in Advanced Intrahepatic Cholangiocarcinoma with Low TMB, MSS, pMMR and Negative PD-L1 Expression Following Combined Therapy of SBRT with PD-1 Blockade. *J. Immunotherapy Cancer* 7 (1), 204. doi:10.1186/s40425-019-0692-z

Luan, T., Zhang, T. Y., Lv, Z. H., Guan, B. X., Xu, J. Y., Li, J., et al. (2021). The lncRNA ALMS1-IT1 May Promote Malignant Progression of Lung Adenocarcinoma via AVL9-Mediated Activation of the Cyclin-Dependent Kinase Pathway. *FEBS Open Bio* 11 (5), 1504–1515. doi:10.1002/2211-5463.13140

Luchini, C., Bibeau, F., Ligtenberg, M. J. L., Singh, N., Nottegar, A., Bosse, T., et al. (2019). ESMO Recommendations on Microsatellite Instability Testing for Immunotherapy in Cancer, and its Relationship with PD-1/PD-L1 Expression and Tumour Mutational burden: A Systematic Review-Based Approach. *Ann. Oncol.* 30 (8), 1232–1243. doi:10.1093/annonc/mdz116

Ma, J., Song, B., Wei, Z., Huang, D., Zhang, Y., Su, J., et al. (2022). m5C-Atlas: A Comprehensive Database for Decoding and Annotating the 5-Methylcytosine (m5C) Epitranscriptome. *Nucleic Acids Res.* 50 (D1), D196–d203. doi:10.1093/nar/gkab1075

Meng, L., Zhang, Q., and Huang, X. (2021). Abnormal 5-Methylcytosine lncRNA Methylome Is Involved in Human High-Grade Serous Ovarian Cancer. *Am. J. Transl Res.* 13 (12), 13625–13639. https://pubmed.ncbi.nlm.nih.gov/35035702/

Morse, M. A., Hochster, H., and Benson, A. (2020). Perspectives on Treatment of Metastatic Colorectal Cancer with Immune Checkpoint Inhibitor Therapy. *Oncologist* 25 (1), 33–45. doi:10.1634/theoncologist.2019-0176

Newman, A. M., Liu, C. L., Green, M. R., Gentles, A. J., Feng, W., Xu, Y., et al. (2015). Robust Enumeration of Cell Subsets from Tissue Expression Profiles. *Nat. Methods* 12 (5), 453–457. doi:10.1038/nmeth.3337

Nirschl, C. J., and Drake, C. G. (2013). Molecular Pathways: Coexpression of Immune Checkpoint Molecules: Signaling Pathways and Implications for Cancer Immunotherapy. *Clin. Cancer Res.* 19 (18), 4917–4924. doi:10.1158/1078-0432.Ccr-12-1972

Ock, C.-Y., Hwang, J.-E., Keam, B., Kim, S.-B., Shim, J.-J., Jang, H.-J., et al. (2017). Genomic Landscape Associated with Potential Response to Anti-CTLA-4 Treatment in Cancers. *Nat. Commun.* 8 (1), 1050. doi:10.1038/s41467-017-01018-0

Pardoll, D. M. (2012). The Blockade of Immune Checkpoints in Cancer Immunotherapy. *Nat. Rev. Cancer* 12 (4), 252–264. doi:10.1038/nrc3239

Sagredou, S., Dalezis, P., Papadopoulou, E., Voura, M., Deligiorgi, M. V., Nikolaou, M., et al. (2021). Effects of a Novel Thiadiazole Derivative with High Anticancer Activity on Cancer Cell Immunogenic Markers: Mismatch Repair System, PD-L1 Expression, and Tumor Mutation Burden. *Pharmaceutics* 13 (6), 885. doi:10.3390/pharmaceutics13060885

Shen, D., Ding, L., Lu, Z., Wang, R., Yu, C., Wang, H., et al. (2022). METTL14-Mediated Lnc-LSG1 m6A Modification Inhibits Clear Cell Renal Cell Carcinoma Metastasis via Regulating ESRP2 Ubiquitination. *Mol. Ther. - Nucleic Acids* 27, 547–561. doi:10.1016/j.omtn.2021.12.024

Siegel, R. L., Miller, K. D., Fuchs, H. E., and Jemal, A. (2022). Cancer Statistics, 2022. *CA Cancer J. Clin.* 72 (1), 7–33. doi:10.3322/caac.21708

Song, B., Tang, Y., Chen, K., Wei, Z., Rong, R., Lu, Z., et al. (2020). m7GHub: Deciphering the Location, Regulation and Pathogenesis of Internal mRNA N7-Methylguanosine (m7G) Sites in Human. *Bioinformatics* 36 (11), 3528–3536. doi:10.1093/bioinformatics/btaa178

Song, P., Tayier, S., Cai, Z., and Jia, G. (2021a). RNA Methylation in Mammalian Development and Cancer. *Cell Biol Toxicol* 37 (6), 811–831. doi:10.1007/s10565-021-09627-8

Song, W., Ren, J., Xiang, R., Kong, C., and Fu, T. (2021b). Identification of Pyroptosis-Related Subtypes, the Development of a Prognosis Model, and Characterization of Tumor Microenvironment Infiltration in Colorectal Cancer. *Oncoimmunology* 10 (1), 1987636. doi:10.1080/2162402x.2021.1987636

Su, M., and Zhang, Q. (2017). Deficiency of Gap Junction Composed of Connexin43 Contributes to Oxaliplatin Resistance in colon Cancer Cells. *Oncol. Lett.* 14 (3), 3669–3674. doi:10.3892/ol.2017.6598

Sun, Z., Xue, S., Zhang, M., Xu, H., Hu, X., Chen, S., et al. (2020). Aberrant NSUN2-Mediated m5C Modification of H19 lncRNA Is Associated with Poor Differentiation of Hepatocellular Carcinoma. *Oncogene* 39 (45), 6906–6919. doi:10.1038/s41388-020-01475-w

Tang, Y., Chen, K., Song, B., Ma, J., Wu, X., Xu, Q., et al. (2021). m6A-Atlas: A Comprehensive Knowledgebase for Unraveling the N6-Methyladenosine

(m6A) Epitranscriptome. *Nucleic Acids Res.* 49 (D1), D134–d143. doi:10.1093/nar/gkaa692

Tasaki, M., Shimada, K., Kimura, H., Tsujikawa, K., and Konishi, N. (2011). ALKBH3, a Human AlkB Homologue, Contributes to Cell Survival in Human Non-Small-Cell Lung Cancer. *Br. J. Cancer* 104 (4), 700–706. doi:10.1038/sj.bjc.6606012

Tomikawa, C. (2018). 7-Methylguanosine Modifications in Transfer RNA (tRNA). *Int. J. Mol. Sci.* 19 (12), 4080. doi:10.3390/ijms19124080

Turley, S. J., Cremasco, V., and Astarita, J. L. (2015). Immunological Hallmarks of Stromal Cells in the Tumour Microenvironment. *Nat. Rev. Immunol.* 15 (11), 669–682. doi:10.1038/nri3902

Vandekerkhove, G., Lavoie, J.-M., Annala, M., Murtha, A. J., Sundahl, N., Walz, S., et al. (2021). Plasma ctDNA Is a Tumor Tissue Surrogate and Enables Clinical-Genomic Stratification of Metastatic Bladder Cancer. *Nat. Commun.* 12 (1), 184. doi:10.1038/s41467-020-20493-6

Wang, E., Li, Y., Ming, R., Wei, J., Du, P., Zhou, P., et al. (2021a). The Prognostic Value and Immune Landscapes of a m6A/m5C/m1A-Related LncRNAs Signature in Head and Neck Squamous Cell Carcinoma. *Front. Cel Dev. Biol.* 9, 718974. doi:10.3389/fcell.2021.718974

Wang, K., Zhong, W., Long, Z., Guo, Y., Zhong, C., Yang, T., et al. (2021b). 5-Methylcytosine RNA Methyltransferases-Related Long Non-Coding RNA to Develop and Validate Biochemical Recurrence Signature in Prostate Cancer. *Front. Mol. Biosci.* 8, 775304. doi:10.3389/fmolb.2021.775304

Wang, Q., Chen, C., Ding, Q., Zhao, Y., Wang, Z., Chen, J., et al. (2020). METTL3-mediated m6A Modification of HDGF mRNA Promotes Gastric Cancer Progression and Has Prognostic Significance. *Gut* 69 (7), 1193–1205. doi:10.1136/gutjnl-2019-319639

Wang, S., He, Z., Wang, X., Li, H., and Liu, X.-S. (2019). Antigen Presentation and Tumor Immunogenicity in Cancer Immunotherapy Response Prediction. *Elife* 8, e49020. doi:10.7554/eLife.49020

Wilkerson, M. D., and Hayes, D. N. (2010). ConsensusClusterPlus: A Class Discovery Tool with Confidence Assessments and Item Tracking. *Bioinformatics* 26 (12), 1572–1573. doi:10.1093/bioinformatics/btq170

Woo, H.-H., and Chambers, S. K. (2019). Human ALKBH3-Induced m1A Demethylation Increases the CSF-1 mRNA Stability in Breast and Ovarian Cancer Cells. *Biochim. Biophys. Acta (Bba) - Gene Regul. Mech.* 1862 (1), 35–46. doi:10.1016/j.bbagrm.2018.10.008

Wu, M., Fu, P., Qu, L., Liu, J., and Lin, A. (2020). Long Noncoding RNAs, New Critical Regulators in Cancer Immunity. *Front. Oncol.* 10, 550987. doi:10.3389/fonc.2020.550987

Xie, S., Chen, W., Chen, K., Chang, Y., Yang, F., Lin, A., et al. (2020). Emerging Roles of RNA Methylation in Gastrointestinal Cancers. *Cancer Cel Int* 20 (1), 585. doi:10.1186/s12935-020-01679-w

Xu, Y., Zhang, M., Zhang, Q., Yu, X., Sun, Z., He, Y., et al. (2021). Role of Main RNA Methylation in Hepatocellular Carcinoma: N6-Methyladenosine, 5-Methylcytosine, and N1-Methyladenosine. *Front. Cel Dev. Biol.* 9, 767668. doi:10.3389/fcell.2021.767668

Yao, L., Man, C.-F., He, R., He, L., Huang, J.-B., Xiang, S.-Y., et al. (2021). The Interaction between N6-Methyladenosine Modification and Non-Coding RNAs in Gastrointestinal Tract Cancers. *Front. Oncol.* 11, 784127. doi:10.3389/fonc.2021.784127

Yoshihara, K., Shahmoradgoli, M., Martínez, E., Vegesna, R., Kim, H., Torres-Garcia, W., et al. (2013). Inferring Tumour Purity and Stromal and Immune Cell Admixture from Expression Data. *Nat. Commun.* 4, 2612. doi:10.1038/ncomms3612

Yun, D., and Yang, Z. (2021). Identification of a Four-lncRNA Prognostic Signature for Colon Cancer Based on Genome Instability. *J. Oncol.* 2021, 7408893. doi:10.1155/2021/7408893

Zhan, L., Zhang, J., Zhu, S., Liu, X., Zhang, J., Wang, W., et al. (2021). N6-Methyladenosine RNA Modification: An Emerging Immunotherapeutic Approach to Turning up Cold Tumors. *Front. Cel Dev. Biol.* 9, 736298. doi:10.3389/fcell.2021.736298

Zhang, J., Guo, S., Piao, H.-y., Wang, Y., Wu, Y., Meng, X.-y., et al. (2019). ALKBH5 Promotes Invasion and Metastasis of Gastric Cancer by Decreasing Methylation of the lncRNA NEAT1. *J. Physiol. Biochem.* 75 (3), 379–389. doi:10.1007/s13105-019-00690-8

Zhang, M., Song, J., Yuan, W., Zhang, W., and Sun, Z. (2021a). Roles of RNA Methylation on Tumor Immunity and Clinical Implications. *Front. Immunol.* 12, 641507. doi:10.3389/fimmu.2021.641507

Zhang, P., Liu, G., and Lu, L. (2021b). N6-Methylandenosine-Related lncRNA Signature Is a Novel Biomarkers of Prognosis and Immune Response in Colon Adenocarcinoma Patients. *Front. Cel Dev. Biol.* 9, 703629. doi:10.3389/fcell.2021.703629

Zhang, Q., Liu, F., Chen, W., Miao, H., Liang, H., Liao, Z., et al. (2021c). The Role of RNA m5C Modification in Cancer Metastasis. *Int. J. Biol. Sci.* 17 (13), 3369–3380. doi:10.7150/ijbs.61439

Zhang, W., Fang, D., Li, S., Bao, X., Jiang, L., and Sun, X. (2021d). Construction and Validation of a Novel Ferroptosis-Related lncRNA Signature to Predict Prognosis in Colorectal Cancer Patients. *Front. Genet.* 12, 709329. doi:10.3389/fgene.2021.709329

Zhao, Y., Zhao, Q., Kaboli, P. J., Shen, J., Li, M., Wu, X., et al. (2019). m1A Regulated Genes Modulate PI3K/AKT/mTOR and ErbB Pathways in Gastrointestinal Cancer. *Translational Oncol.* 12 (10), 1323–1333. doi:10.1016/j.tranon.2019.06.007

Zhou, Y., Zeng, P., Li, Y.-H., Zhang, Z., and Cui, Q. (2016). SRAMP: Prediction of Mammalian N6-Methyladenosine (m6A) Sites Based on Sequence-Derived Features. *Nucleic Acids Res.* 44 (10), e91. doi:10.1093/nar/gkw104

Conflict of Interest: The authors declare that the research was conducted in the absence of any commercial or financial relationships that could be construed as a potential conflict of interest.

Publisher's Note: All claims expressed in this article are solely those of the authors and do not necessarily represent those of their affiliated organizations, or those of the publisher, the editors and the reviewers. Any product that may be evaluated in this article, or claim that may be made by its manufacturer, is not guaranteed or endorsed by the publisher.

frontiers | Frontiers in Genetics

REVIEW
published: 20 April 2022
doi: 10.3389/fgene.2022.869950

The Potential Role of m6A RNA Methylation in the Aging Process and Aging-Associated Diseases

Jin Sun[1,2], Bokai Cheng[1,2], Yongkang Su[1,2], Man Li[1,2], Shouyuan Ma[3], Yan Zhang[4], Anhang Zhang[1,2], Shuang Cai[1,2], Qiligeer Bao[1,2], Shuxia Wang[1,2] and Ping Zhu[1,2]**

[1]Department of Geriatrics, The Second Medical Center and National Clinical Research Center for Geriatric Diseases, Chinese PLA General Hospital, Beijing, China, [2]Medical School of Chinese PLA, Beijing, China, [3]Department of Geriatric Cardiology, The Second Medical Center, Chinese PLA General Hospital, Beijing, China, [4]Department of Outpatient, The First Medical Center, Chinese PLA General Hospital, Beijing, China

N6-methyladenosine (m^6A) is the most common and conserved internal eukaryotic mRNA modification. m^6A modification is a dynamic and reversible post-transcriptional regulatory modification, initiated by methylase and removed by RNA demethylase. m^6A-binding proteins recognise the m^6A modification to regulate gene expression. Recent studies have shown that altered m^6A levels and abnormal regulator expression are crucial in the ageing process and the occurrence of age-related diseases. In this review, we summarise some key findings in the field of m^6A modification in the ageing process and age-related diseases, including cell senescence, autophagy, inflammation, oxidative stress, DNA damage, tumours, neurodegenerative diseases, diabetes, and cardiovascular diseases (CVDs). We focused on the biological function and potential molecular mechanisms of m^6A RNA methylation in ageing and age-related disease progression. We believe that m^6A modification may provide a new target for anti-ageing therapies.

Keywords: N6-methyladenosine, aging, aging-related disease, epigenetics, RNA methylation

OPEN ACCESS

Edited by:
Giovanni Nigita,
The Ohio State University,
United States

Reviewed by:
Xiangting Wang,
University of Science and Technology of China, China
Piyush Khandelia,
Birla Institute of Technology and Science, India

***Correspondence:**
Ping Zhu
zhuping301hospital@163.com
Shuxia Wang
wangsx301@163.com

Specialty section:
This article was submitted to Epigenomics and Epigenetics, a section of the journal Frontiers in Genetics

Received: *05 February 2022*
Accepted: *31 March 2022*
Published: *20 April 2022*

Citation:
Sun J, Cheng B, Su Y, Li M, Ma S, Zhang Y, Zhang A, Cai S, Bao Q, Wang S and Zhu P (2022) The Potential Role of m6A RNA Methylation in the Aging Process and Aging-Associated Diseases. Front. Genet. 13:869950. doi: 10.3389/fgene.2022.869950

1 INTRODUCTION

Ageing is a process of molecular and cellular damage accumulating over time, leading to a progressive decline in physical and mental capacity and an increased risk of disease and death (Borghesan et al., 2020). At present, changes in molecular and cellular ageing processes are believed to be the basis of age-related diseases, including cell senescence, autophagy, inflammation, oxidative stress, DNA damage, telomere depletion, protease inactivation, and epigenetic disorders (Ungvari et al., 2020). Ageing is the greatest risk factor for most chronic diseases, leading to morbidity and mortality (Kennedy et al., 2014). Presently, the field of ageing has focused on understanding the molecular mechanisms that regulate the ageing process and identifying biomarkers that could help to predict age-related processes. New therapeutic targets mainly focus on improving the health of the elderly population.

Epigenetics regulate gene and non-coding RNA expression without altering primary DNA sequences through many mechanisms, such as DNA methylation, histone modification, and nucleosome localisation (Portela and Esteller, 2010). Epigenetic imprinting persists during development and can be passed on to the offspring (Fraga et al., 2005; Kaminsky et al., 2009). Known epigenetic mechanisms include DNA methylation, histone modification, chromatin remodelling, and RNA methylation (Wang and Chang, 2018). At present, it is believed that during the ageing process, a decrease in histone synthesis and a change in chromatin structure

leads to a general loss of structural heterochromatin (Lee et al., 2020). Histone variants have also been observed in ageing organisms, which have different primary sequences and properties compared to typical histones, thus changing the gene transcription program (Henikoff and Smith, 2015). In addition, the ageing process involves DNA methylation changes (Day et al., 2013; Horvath, 2015; Unnikrishnan et al., 2019), ATP-dependent chromatin remodelling (Clapier et al., 2017), histone modifications (including methylation, acetylation, ubiquitination) (Lawrence et al., 2016), and miRNA changes (Huan et al., 2018).

As one of the most common post-transcriptional modifications in eukaryotic mRNA, N6-methyladenosine (m^6A) adds a methyl group to the nitrogen-containing base at the sixth position of the adenine residue of RNA. It was first found in the eukaryotic mRNA of Novikov hepatoma cells and mouse L cells (Desrosiers et al., 1974; Schäfer, 1982). m^6A modification has a conservative identification motif, RRACH (R = G/A, H = A/C/U) (Csepany et al., 1990). The evolutionary conservatism and dynamic reversibility of its modification make it unique for gene expression regulation. m^6A RNA methylation has become a key regulator of various post-transcriptional gene regulation processes and acts as a translation initiation mechanism in protein synthesis (Karthiya and Khandelia, 2020). In addition, numerous reports have indicated that m^6A modification may cause important changes in the ageing process and affect the occurrence and development of many age-related diseases. In this review, we focused on m^6A RNA methylation mechanisms related to the ageing process and emphasised their significance in age-related diseases. We believe that m^6A RNA methylation is a potential target for treating age-related diseases.

2 OVERVIEW OF N6-METHYLADENOSINE MODIFICATION

RNA modification is a post-transcriptional process that regulates gene expression by binding to proteins without involving the RNA sequence. More than 160 types of RNA modifications, ubiquitous in both coding and non-coding RNA, have been identified. First discovered in 1974, m^6A modification refers to the methylation of the sixth nitrogen atom of adenylate. It is considered the most abundant internal modification in eukaryotic mRNA (Desrosiers et al., 1974). With recent improvements in detection techniques, such as high-throughput sequencing, the study of m^6A RNA methylation is booming. Presently, it has been reported that there are three m^6A residues per average mRNA transcript in mammalian cells (Dominissini et al., 2012). In addition to mRNA, m^6A RNA methylation covers almost all types of RNA, including transfer RNAs (tRNAs), ribosomal RNAs (rRNAs), cyclic RNAs (circRNAs), microRNAs, and small nucleolar RNA (snoRNA) (Sergiev et al., 2016).

m^6A RNA methylation is a dynamic and reversible RNA modification, and its function is determined by three types of enzymes: RNA methyltransferase, RNA demethylase, and m^6A-binding proteins (**Figure 1**) (Fu et al., 2014). m^6A modification is crucial in regulating gene expression, splicing, RNA editing, RNA stability, controlling mRNA lifespan and degradation, and mediating ring RNA translation (Zhao et al., 2017). In addition, m^6A modification is related to many physiological processes, pathological processes, and human diseases, including the circadian rhythm (Zhong et al., 2018), reproductive system development (Hongay and Orr-Weaver, 2011; Hsu et al., 2017; Ivanova et al., 2017; Kasowitz et al., 2018), haematopoietic system development (Wang et al., 2014a; Zhang et al., 2017), nervous system development and degeneration (Hess et al., 2013; Lence et al., 2016; Li et al., 2017a; Yen and Chen, 2021), cardiovascular diseases (CVDs) (Chen et al., 2021a), nutritional and metabolic diseases (Wu et al., 2020a), and tumorigenesis (Wang et al., 2020a; Zhou et al., 2020).

2.1 RNA Methyltransferases

RNA methyltransferases, including RNA methyltransferase-like protein 3 (METTL3) (Bokar et al., 1997), RNA methyltransferase-like protein 14 (METTL14) (Liu et al., 2014), Wilms' tumour 1-associating protein (WTAP) (Agarwala et al., 2012), RNA-binding motif protein 15 (RBM15) and its analogue RBM15B (Patil et al., 2016), Vir-like m^6A RNA methyltransferase associated protein (VIRMA)/KIAA1429 (Schwartz et al., 2014), Zinc finger CCCH domain-containing protein 13 (ZC3H13) (Wen et al., 2018), RNA methyltransferase-like protein 16 (METTL16) (Pendleton et al., 2017), and RNA methyltransferase-like protein 5 (METTL5) (van Tran et al., 2019; Richard et al., 2019), mediate m^6A modification, are mainly located in nuclear speckles, and are called "m^6A writers." Among these, METTL3 was the first key RNA methyltransferase and core RNA methyltransferase subunit of m^6A methylation. It is critical in the occurrence of m^6A modifications and participates in various physiological processes (Bokar et al., 1997). Abnormal METTL3 expression changes m^6A RNA methylation levels. As the structural support for METTL3, METTL14 is co-located in the nucleus in a 1:1 ratio and forms a stable RNA methyltransferase complex responsible for m^6A modification (Liu et al., 2014). WTAP in the RNA methyltransferase complex is primarily used as a connecting protein between METTL3 and METTL14. WTAP lacks a conserved catalytic methylation domain and cannot catalyse m^6A modification, but its deletion significantly affects m^6A modification levels and physiological processes, such as embryonic differentiation (Ping et al., 2014). METTL3/METTL14/WTAP is considered to be the core RNA methyltransferase component, and in recent years, some studies have reported new RNA methyltransferase complex components, such as RBM15/15B, which assists in the binding of METTL3 and WTAP, and its deletion leads to damage to X-inactive specific transcript (XIST)-mediated gene silencing on the X chromosome (Knuckles et al., 2018). ZC3H13 (Wen et al., 2018), VIRMA (Yue et al., 2018), and other proteins also participate in m^6A RNA methylation as cofactors of the m^6A RNA methyltransferase complex. In addition, Warda et al. (2017) reported on an independent m^6A writer, METTL16, finding that its binding site does not overlap with the METTL3/METTL14

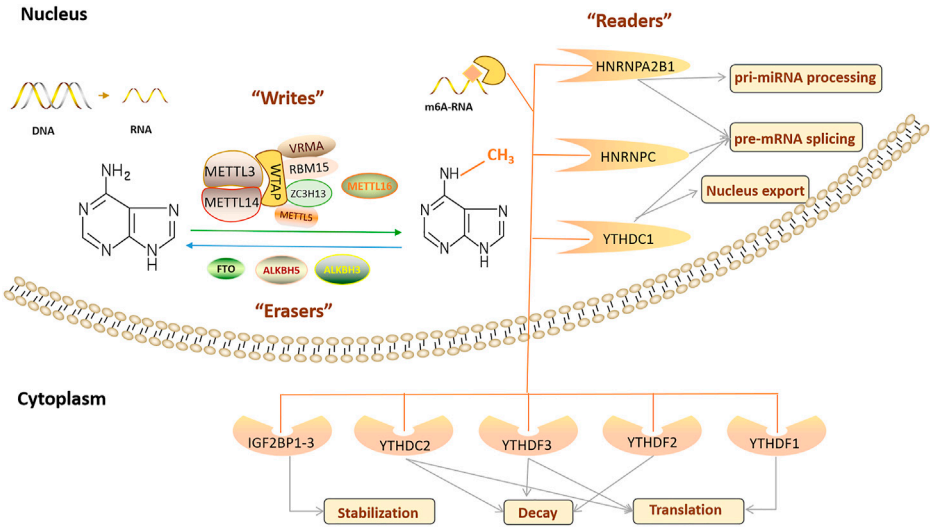

FIGURE 1 | Regulation of the m6A modification and the function of the m6A regulators.

methylation complex, and it regulates the stability and splicing of mRNA by catalysing m^6A modification in snoRNAs, U6 small nuclear RNAs (snRNAs), and other long non-coding RNAs (lncRNAs). There are continuous reports of new RNA methyltransferases, such as METTL5, the enzyme responsible for 18S rRNA m^6A modification, and ZCCHC4, a confirmed 28S rRNA m^6A modification enzyme (van Tran et al., 2019; Richard et al., 2019). Some studies reported that WTAP interacts with many proteins and lncRNAs, of which more than 100 may bind to METTL3 or METTL14 (Schöller et al., 2018). Therefore, "writer" may include the reported proteins and other components that need further exploration.

2.2 RNA Demethylases

RNA demethylases, including fat mass and obesity-related proteins (FTO) (Jia et al., 2011), AlkB homologue 5 (ALKBH5) (Huang et al., 2020a), and AlkB homologue 3 (ALKBH3) (Ueda et al., 2017; Sun et al., 2019), can remove the m^6A modification. They are called "m^6A erasers" and are located in nuclear spots with RNA methyltransferase. In 2011, FTO was identified as the first m^6A RNA demethylase, verifying that m^6A RNA methylation is a dynamic and reversible RNA modification. FTO-mediated m^6A demethylation acts in various biological processes, inhibiting peroxisome proliferator-activated receptor (PPARβ/δ) and AMP-activated protein kinase (AMPK) pathways, disrupting skeletal muscle lipid utilisation, inhibiting macrophage lipid influx by downregulating PPARγ protein expression, and accelerating cholesterol outflow *via* AMPK phosphorylation. Thus, foam cell formation and atherosclerosis development were inhibited (Yang et al., 2022). FTO regulates the alternative splicing of RUNT-related transcription factor 1 (RUNX1) through m^6A modifications (Zhao et al., 2014), whereas FTO regulates fat formation and deposition by altering the expression of PPARγ (Lee et al., 2011) and angiopoietin-like 4 (ANGPTL4) (Wang et al., 2015a). In addition, FTO is widely involved in regulating the cell cycle (Li et al., 2019a), tumour growth (Li et al., 2019b), proliferation and migration (Tang et al., 2019), stem cell maintenance (Su et al., 2020) and other biological processes.

ALKBH5 is the second m^6A RNA demethylase and is expressed in most tissues, especially the testes (Aik et al., 2014). ALKBH5 inactivation increases m^6A RNA methylation levels, leading to male-mouse infertility (Tang et al., 2018a). In addition, ALKBH3 has recently been considered a new m^6A RNA demethylase that preferentially catalyses m^6A demethylation in tRNA (Ueda et al., 2017; Woo and Chambers, 2019).

2.3 N6-Methyladenosine Binding Proteins

The "m^6A writers" and "m^6A erasers" determine whether RNA is methylated, but m^6A-binding proteins ("m^6A readers") determine the final biological function of m^6A modification. "m^6A readers" recognise and bind to an m^6A modified transcript, then regulate mRNA stability (Zhao et al., 2014), mRNA splicing (Xiao et al., 2016), mRNA structure (Spitale et al., 2015), mRNA output (Roundtree et al., 2017), translation efficiency (Wang et al., 2015b) and microRNA (miRNA) biogenesis (Alarcón et al., 2015). "Readers" include proteins containing YTH domains (YTHDF1/2/3 and YTHDC1/2), heterogeneous ribonucleoproteins including heterogenous nuclear ribonucleoprotein (HNRNP) C (HNRNPC), HNRNP G (HNRNPG), and HNRNP A2B1 (HNRNPA2B1), and insulin-like growth factor 2 binding proteins (IGF2BPs), which are members of a protein family involved in regulating some aspects of ageing. Different "readers" have different cellular localisations and thus perform various biological functions. YTH domain containing 1 (YTHDC1) regulates mRNA splicing by recruiting the splicing factor serine- and arginine-rich splicing factor 3 (SRSF3) or blocking serine- and arginine-rich splicing factor 10 (SRSF10) in the nucleus (Xiao et al., 2016). In addition, it

TABLE 1 | The role of m^6A modification in the fundamental processes.

The Processes related to aging	m^6A regulator	Organism	Role in processes	Mechanism	Reference
Autophagy	MTC	Cells, Drosophila	Suppression	Promote the degradation of ATG transcripts	Tang et al. (2021)
	METTL14	Leydig Cells	Suppression	Reduce AMPK activity	Chen et al. (2021b)
	ALKBH5	Leydig Cells	Promotion	Promote the activity of AMPK	Chen et al. (2021b)
		ovarian cancer cells	Suppression	Regulation of bcl-2 expression	Zhu et al. (2019)
	FTO, YTHDF2	Cells	Promotion	Increase the expression of ULK1	Jin et al. (2018)
Inflammation	METTL3	Cells	Promotion	Regulate alternative splicing of MyD88	Feng et al. (2018)
	METTL14	Endothelial cell, mice	Promotion	Promote FOXO1 expression	Jian et al. (2020)
	ALKBH5	HK-2 cells	Promotion	Up-regulate MALAT1 expression by demethylation	Zhu and Lu, (2020)
	FTO	Cells	Promotion	Promote M1 and M2 macrophage activation	Gu et al. (2020)
	RBM4, YTHDF2	Cells	Suppression	Decrease m^6A modified STAT1 mRNA levels and inhibite the polarization of M1 macrophages	Huangfu et al. (2020)
Oxidative stress	METTL3	mRTECs	Suppression	Regulate Keap1-Nrf2 pathway	Wang et al. (2019c)
	METTL14	Cardiomyocytes, mice	Suppression	Regulate Wnt1/β-Catenin Signaling Pathway	Pang et al. (2021)
	WTAP	Cells and rat	Promotion	Regulate m^6A modification of ATF4 mRNA	Wang et al. (2021)
	FTO	Cell, human samples	Promotion	Increased the translation efficiency of PGC1αmRNA	Zhuang et al. (2019)
	YTHDF1/3	Cells	Promotion	Promote stress granule formation	Fu and Zhuang, (2020)
DNA damage	METTL3, YTHDC1	Cells	Suppression	Modulates accumulation of DNA-RNA hybrids at DSBs sites and recruit RAD51 and BRCA1	Zhang et al. (2020c)
	METTL3/14, YTHDC1	Cells	Suppression	Active on ssDNA and lesion-containing dsDNA	Yu et al. (2021)
	YTHDF1	Cells, mice	Suppression	Upregulates HR-related factors RAD51 and BRCA1	Sun et al. (2022)
Cell senescence	METTL3	Cells	Promotion	Target NF-κB, drives the senescence-associated secretory phenotype	Liu et al. (2021)
	METTL14	Clinical Sample	Promotion	Participates in the TNF-α-induced m^6A modification of miR-34a-5p to promote cell senescence	Zhu et al. (2021b)
	FTO	Granulosa cells	Suppression	Regulates the expression of FOS	Jiang et al. (2021)
	METTL3, IGF2BP2	hMSC	Suppression	Stabilizate of the MIS12 transcript	Wu et al. (2020b)

increases the output of circRNA NOP2/SUN domain family, member 2 (circNSUN2) in the cytoplasm by interacting with nuclear output factor 1 (Chen et al., 2019a). HNRNPA2B1 and HNRNPC are also located in the nucleus. HNRNPA2B1 regulates RNA splicing and promotes miRNA maturation by recognising pri-miRNA markers and interacting with DiGeorge syndrome critical region 8 (DGCR8) (Zhao et al., 2017). HNRNPC selectively recognizes m^6A modified transcripts to promote pre-RNA processing (Liu et al., 2015). YTHDF1/2/3, YTH domain containing 2 (YTHDC2), and IGF2BP1/2/3 are localised in the cytoplasm. YTH domain family protein 1 (YTHDF1) initiates RNA translation by interacting with translation initiation factors and ribosomes, whereas YTH domain family protein 2 (YTHDF2) selectively binds m^6A modified transcripts and accelerates their degradation (Wang et al., 2015b). On the other hand, YTH domain family protein 3 (YTHDF3) and YTHDF1/2 play a synergistic role, not only promoting YTHDF1-mediated translation but also affecting the decline in YTHDF2-mediated m^6A modification (Wang et al., 2014b; Shi et al., 2017). Like YTHDF3, YTHDC2 is an RNA helicase, and its helix-unwinding region contributes to RNA binding and promotes mRNA translation or degradation (Hsu et al., 2017). Other proteins located in the cytoplasm are IGF2BP1–3, which recognise and bind to m^6A modified transcripts, thus enhancing mRNA stability (Huang et al., 2018).

3 N6-METHYLADENOSINE CHANGES IN MOLECULAR PROCESSES ASSOCIATED WITH AGEING

Many studies have confirmed that m^6A methylation regulates several physiological processes that are crucial in the ageing process. Here, we focused on the mechanisms of m^6A RNA methylation in autophagy, inflammation, oxidative stress, DNA damage, and cell senescence (**Table 1**).

3.1 N6-Methyladenosine and Autophagy

Autophagy is a highly conserved intracellular clearance mechanism regulated by various proteins and is important for maintaining homeostasis in the internal environment. The mammalian target of rapamycin (mTOR) is a key factor in autophagy regulation. Protein kinase B (AKT) and mitogen-activated protein kinase (MAPK) signalling pathways activate

mTOR to inhibit autophagy, whereas AMPK and p53 pathways negatively regulate mTOR to promote autophagy (Alers et al., 2012). After mTOR inactivation, UNC-51-like kinase 1/2 (ULK1/2) is activated and binds to the focal adhesion kinase family interacting protein of 200 kDa (FIP200) to form a ULK1 complex with autophagy-related 13 (ATG13) proteins, promoting autophagosome formation (Codogno et al., 2011). m^6A methylation and related regulators regulate autophagy by regulating ATG expression or by affecting autophagy-related signalling pathways. In 2018, Jin et al. first reported a positive regulatory effect of FTO on autophagy, accomplished by affecting the abundance of Unc-51 like autophagy activating kinase 1 (ULK1) (Jin et al., 2018). Another RNA demethylase, ALKBH5, has been shown to enhance autophagy by reducing m^6A methylation in FIP200 transcripts (Li et al., 2020), suggesting a negative correlation between m^6A modification and autophagy. A study of RNA methyltransferases further confirmed this. METTL3 upregulates methylation and triggers YTHDF1 and Forkhead box O3 (FOXO3) binding to promote the translation of FOXO mRNA. FOXO further blocks ATG gene expression to inhibit autophagy (Lin et al., 2020). A decrease in METTL14 levels increases the stability of calcium/calmodulin-dependent protein kinase 2 (CAMKK2) mRNA and activates the AMPK and ULK1 complex to initiate autophagy (Chen et al., 2021b).

Abnormal autophagy can lead to diseases, some of which may be associated with ageing. Studies have shown that autophagy decreases with age. Increasing autophagy levels can inhibit the accumulation of damaged proteins, delay the occurrence of degenerative changes, and prolong life (Rubinsztein et al., 2011; Papp et al., 2016). There is evidence that autophagy regulates some age-related diseases in lower organisms (such as *Drosophila* and *Caenorhabditis elegans*), but this hypothesis has not been confirmed in mammals. Accelerating ageing by decreasing autophagy is controversial. Nevertheless, several studies have reported that deleting autophagy proteins leads to the accumulation of misfolded proteins and abnormal mitochondria in cells, resulting in premature senescence, organ dysfunction, and eventually the development of various ageing-related diseases, such as neurodegenerative diseases, cancer, CVDs, and metabolic syndrome (Linton et al., 2015; Guo et al., 2018; Luo et al., 2020). In summary, autophagy regulation is closely related to ageing, in which m^6A modification plays an important role. Therefore, further studies on the relationship between m^6A modification and autophagy in ageing may provide a new method for anti-ageing research.

3.2 N6-Methyladenosine and Inflammation

RNA methylation is involved in inflammation. m^6A methylation affects pathways related to metabolic reprogramming, stress response, and ageing by regulating type I interferon (IFN) mRNA stability (Rubio et al., 2018). Lipopolysaccharides (LPSs) induce inflammation. It has been found that LPS stimulation promotes METTL3 expression and biological activity in macrophages, and METTL3 overexpression alleviates lipopolysaccharide-induced inflammation through the nuclear factor-κB (NF-κB) signalling pathway, further confirming the relationship between m^6A methylation and inflammation (Wang et al., 2019a). In addition, the interaction between m^6A modification and inflammation is crucial for various diseases to occur. YTHDF2 deletion aggravates the inflammatory state and metastasis of human hepatocellular carcinoma cells (Hou et al., 2019). After an ischaemic stroke, FTO expression is downregulated, and m^6A methylation is increased in the main inflammatory pathways, including interleukin (IL)-6 cytokines, tumour necrosis factor (TNF), toll-like receptor (TLR), and NF-κB signalling pathways (Chokkalla et al., 2019). It has been suggested that m^6A may regulate secondary brain injury after cerebral ischaemia by affecting inflammation.

In summary, m^6A methylation affects inflammation under physiological and pathological conditions. Presently, the chronic inflammatory state is considered one of the characteristics of ageing, namely "inflammatory ageing" (inflamm-ageing), which is mainly characterised by inflammatory cell infiltration and an increase in pro-inflammatory factors [TNF-α, IL-1β, IL-6, C-reactive protein (CRP), etc.] Although most current studies on the relationship between m^6A modification and inflammation are based on specific diseases and signalling pathways, the study of epigenetic changes in inflammation potentiates the development of effective drugs with specific anti-ageing targets.

3.3 N6-Methyladenosine and Mitochondria: Oxidative Stress

Oxidative damage accumulates with ageing in many species and tissues. RNA modification is mobilised to activate or inhibit stress-resistant signalling pathways (Peters et al., 2021). Li et al. (2017b) found that the activities of METTL3/METLL14, p21, and senescence-related β-galactosidase (SA-βGAL) increased significantly after oxidative damage stimulated HCT116 $p53^{-/-}$cells, indicating that METTL3/METLL14 may trigger the p53 independent effect of ageing in the oxidative damage response, which needs to be further tested. Arsenite et al. stimulated human keratinocytes to induce reactive oxygen species (ROS) production, increasing WTAP, METTL14, and total m^6A expression levels (Zhao et al., 2019). FTO induces oxidative stress and increases ROS levels by reducing m^6A methylation of peroxisome proliferator-activated receptor gamma coactivator-1 alpha (PGC1α) (an important regulator of mitochondrial metabolism that is also affected by the ageing process) and increasing PGC1α mRNA translation efficiency.

3.4 N6-Methyladenosine and DNA Damage

DNA damage refers to changes in DNA structure caused by physical or chemical stimuli in the environment. The persistence of DNA damage can lead to a prolonged DNA damage response (DDR) and induce senescence (Di Micco et al., 2021). m^6A is critical in DNA damage and repair. It has been reported that METTL3/METTL14 and METTL16 are recruited to DNA damage sites to facilitate DNA repair and the DDR by adjusting m^6A modifications under ultraviolet (UV) radiation

stimulation (Svobodová Kovaříková et al., 2020). This repair is carried out through the nucleotide excision repair (NER) pathway because knockout of the non-homologous end junction (NHEJ) enzyme SUV391H/H2 does not affect m^6A recruitment under UV stimulation (Svobodová Kovaříková et al., 2020).

3.5 N6-Methyladenosine and Cell Senescence

Cell senescence results from many processes, including telomere wear, macromolecular damage, and oncogene-activated signal transduction (Childs et al., 2015). Senescent cells widely exist in ageing and diseased tissues, secreting numerous pro-inflammatory cytokines, called the ageing-associated secretory phenotype [senescence-associated secretory phenotype (SASP)]. These cytokines regulate the tissue microenvironment and affect how nearby normal cells function. Studies have shown that senescent cells are involved in atherosclerosis (Ito et al., 2014), Alzheimer's disease (AD) (Boccardi et al., 2015), Parkinson's disease (PD) (Chinta et al., 2013), chronic obstructive pulmonary disease (Barnes et al., 2019), insulin resistance (Aravinthan et al., 2015), age-related chronic inflammation (Campisi and Robert, 2014), cancer (Calcinotto et al., 2019), osteoporosis (Farr and Khosla, 2019), and loss of haematopoietic stem cell function (de Haan and Lazare, 2018) in the elderly.

In 2017, Li et al. (2017b) reported a link between m^6A methylation and cellular senescence. They found that p21 protein methylation increased with m^6A methylation, whereas the p21 mRNA level was not affected by m^6A, suggesting that m^6A methylation regulates p21 translation. In another study, breast cancer cells were exposed to sublethal concentrations of ammonium trifluoride (SFN). m^6A methylation levels decreased, the activity of SA-βGAL increased, and p53, p21, and p27 protein levels increased, but the corresponding mRNA levels remained unchanged. SFN may lead to senescence by reducing m^6A methylation levels (Lewinska et al., 2017). Min et al. reported an m^6A RNA modification map of human peripheral blood mononuclear cells (PBMCs) from young and old groups. They found that the total level of m^6A modification in PBMCs of the elderly was significantly lower than that in the young PBMCs, while the expression of m^6A modified transcripts was higher than that of unmodified transcripts (Min et al., 2018). Shafik et al. have reported dynamic changes in m^6A RNA methylation during brain ageing. In their study, they compared the m^6A spectra of Brodmann area 9 (BA9) in the cerebral cortex of 6-week-old and 52-week-old mice and post-mortem pubertal and elderly human brains, and the results showed that the m^6A modification sites were significantly increased with increasing age, both in mice and humans. Functional enrichment analysis showed that differential m^6A loci mainly occurred in the untranslated regions of genes that affect ageing-related pathways, which are related to the strong negative effect of mRNA expression (Shafik et al., 2021).

A recent study reported that METTL3 downregulation decreased m^6A modification of human bone marrow mesenchymal stem cells (hMSC) with premature senescence, and hMSCs showed accelerated ageing after METTL3 gene knockout. The m^6A modifications in Hutchinson-Gilford progeria (HGPS) and Werner syndrome (WS) increased with METTL3 overexpression and delayed disease progression. They identified MIS12 as the specific target of m^6A modification deletion in the premature ageing process using RNA sequencing (RNA-seq) and m^6A methylation RNA immunoprecipitation sequencing (MERIP-seq) analysis. m^6A deletion accelerates hMSC ageing, while IGF2BP2 recognises and stabilizes m^6A modified MIS12 mRNA to prevent accelerating senescence in hMSCs. Based on the above results, Wu et al. (2020b) proposed a regulatory model in which METTL3-mediated m^6A modification improves the stability of IGF2BP2-mediated MIS12 mRNA, thus reversing the ageing phenotype of hMSCs.

Cellular senescence is an important component of the ageing process. Selective clearance of senescent cells is currently the focus of anti-senescence research. Senolytics (a mixture of dasatinib and quercetin), agents that target cellular senescence, have completed small clinical trials in patients with idiopathic fibrosis with promising efficacy and safety results (Justice et al., 2019). The results need to be validated in larger samples and populations with other age-related diseases. The link between m^6A methylation and cellular senescence may provide novel therapeutic targets for localising senescent cells, with important clinical implications.

4 N6-METHYLADENOSINE CHANGES IN AGEING ASSOCIATED DISEASES/ DISORDERS

The study of m^6A RNA methylation and the ageing process has laid the foundation for more comprehensive and in-depth exploration into the epigenetic mechanisms of various ageing-related diseases. At present, several studies focus on the role of m^6A RNA methylation in ageing-related pathological processes, such as cancer. Here, we summarise the latest reports on m^6A modification and ageing-related diseases, focusing on cancer, neurodegenerative diseases, diabetes mellitus, and CVDs (**Table 2**).

4.1 Cancer

In recent years, many studies on m^6A RNA methylation have reported that changes in m^6A modification levels and the imbalance of regulatory factors are related to the activation and inhibition of cancer-related signalling pathways. Therefore, m^6A modification is widely involved in the occurrence (Uddin et al., 2021), progression (Wang et al., 2020a), and drug resistance of cancer (Huang et al., 2020a) and may be a promising biomarker and potential therapeutic target for the diagnosis and prognosis of many kinds of tumours. High METTL3 (Vu et al., 2017), WTAP (Bansal et al., 2014; Naren et al., 2021), FTO (Li et al., 2017c), ALKBH5 (Shen et al., 2020a; Wang et al., 2020b), and YTHDF2 (Paris et al., 2019) expression has been observed in all subtypes of acute myelogenous leukaemia (AML), and high WTAP (Naren et al., 2021), ALKBH5 (Shen et al., 2020a; Wang et al., 2020b) and

TABLE 2 | The functional roles of RNA m^6A modification in various types of human disease.

Age-related disease	Organism	Role in disease	m^6A regulator	Functional in disease	Ref
Cancer:					
Respiratory neoplasms					
Lung cancer	Clinical Samples; cells	Oncogene	METTL3; FTO; YTHDF1/2; IGF2BP1	Promote LC growth and progress; induce invasion and metastasis of NSCLC	(Lin et al., 2016; Chen et al., 2020a), (Liu et al., 2018a; Chen et al., 2018; Müller et al., 2019)
	Cells	Suppressor	ALKBH5	Inhibits tumor growth and metastasis	Jin et al. (2020)
Nasopharyngeal carcinoma	Cells	Oncogene	METTL3	Promote proliferation and invasion of NPC cells	Zheng et al. (2019)
Leukemia	Clinical Samples; cells; mice	Oncogene	METTL3; METTL14; WTAP; YTHDF1; FTO; IGF2BP1	Promote AML cells proliferation and leukemia cells self-renewal, growth and metabolism	(Bansal et al., 2014; Vu et al., 2017; Li et al., 2018a; Weng et al., 2018)
Gastroinestinal tumor					
Hepatocellular carcinoma	Clinical Samples; cells; mice	Oncogene	METTL3; METTL14; YTHDF1; KIAA1429; WTAP; YTHDF2	Induce HCC cells proliferation, migration, invasion and metastasis	(Chen et al., 2018; Cheng et al., 2019; Müller et al., 2019)
	Cells; mice	Suppressor	METTL14	Suppress tumor invasion and metastasis	Ma et al. (2017)
Gastric carcinoma	Cells, Clinical samples	Oncogene	METTL3; ALKBH5	Promote proliferation, tumor angiogenesis, invasion and metastasis of GC	(Zhang et al., 2019a; Wang et al., 2020e)
Colorectal cancer	Cells, Clinical samples, mice	Oncogene	METTL3; FTO; WTAP; YTHDC2; YTHDF1; IGF2BPs	Promote the proliferation, migration, invasion and EMT of CRC cells	(Tanabe et al., 2016; Zhang et al., 2016; Shen et al., 2018; Wu et al., 2019b; Li et al., 2019c)
	Cells, clinical samples	Suppressor	METTL3; METTL14	Suppress CRC proliferation and migration	(Deng et al., 2019; Chen et al., 2020b)
Pancreatic cancer	Cells, clinical samples	Oncogene	METTL3; YTHDF2	Promote cell proliferation, migration, and invasion	(Chen et al., 2017; Zhang et al., 2019b)
	Cells, clinical samples	Suppressor	ALKBH5; YTHDF2	Suppress cancer migration, invasion, and EMT	(Chen et al., 2017; He et al., 2018)
Urological cancers					
Bladder cancer	Cells, clinical samples, mice	Oncogene	METTL3; FTO; ALKBH5	Promote BC cells proliferation, colony formation, invasion and metastasis; inhibit cell apoptosis	(Cai et al., 2018; Wang et al., 2020f)
	Clinical samples	Suppressor	METTL14	Inhibit bladder TIC self-renewal and tumorigenesis	Gu et al. (2019)
Renal cell cancer	Cells, clinical samples, mice	Oncogene	WTAP	Enhance cell proliferation abilities	Tang et al. (2018b)
	Cells, clinical samples, mice	Suppressor	METTL3; FTO	Suppress tumor growth, proliferation, migration, invasion function and cell cycle of RCC and induce apoptosis	(Li et al., 2017d; Zhuang et al., 2019)
Prostate cancer	Cells	Oncogene	METTL3; YTHDF2	Promote tumor cells proliferation, survival, colony formation, and migration	Cai et al. (2019)
Reproductive neoplasms					
Breast cancer	Cells, clinical samples, mice	Oncogene	METTL3; FTO; ALKBH5	Promote BC cells proliferation, colony formation and metastasis; inhibit the apoptosis	(Niu et al., 2019; Wang et al., 2020f)
Ovarian cancer	Cells, clinical samples, mice	Oncogene	METTL3; ALKBH5; IGF2BP1	Promote the proliferation and invasion *in vitro* and *in vivo*	(Hua et al., 2018; Müller et al., 2019)
Cervical carcinom	Cells, clinical samples	Oncogene	FTO	Promote cell proliferation and migration; induce resistance	Zou et al. (2019)
Endometrial cancer	Cells, clinical samples, mice	Suppressor	METTL3/METTL14	Inhibit the proliferation and tumorigenicity	Liu et al. (2018b)
Skin tumors					
Melanoma	Cells, clinical samples, mice	Oncogene	FTO	Increase tumor growth	Yang et al. (2019a)
	Cells, clinical samples, mice	Suppressor	YTHDF1	Restrain cell growth and migratory ability	Jia et al. (2019)
Squamous cell carcinoma	Cells, clinical samples, mice	Oncogene	METTL3	Promote tumorigenicity	Zhou et al. (2019)
Neurodegenerative diseases:					
Alzheimer's disease	Mice, clinical samples	Up-regulation	METTL3; IGF2BP2; RBM15B	—	(Han et al., 2020; Deng et al., 2021)
	Cells, mice, clinical samples	Down-regulation	METTL3; FTO	—	(Huang et al., 2020b; Han et al., 2020), (Zhao et al., 2021)
Parkinson's disease	Cells	Down-regulation	HNRNPC	—	Quan et al. (2021)

(Continued on following page)

TABLE 2 | (*Continued*) The functional roles of RNA m^6A modification in various types of human disease.

Age-related disease	Organism	Role in disease	m^6A regulator	Functional in disease	Ref
Cardiovascular disease:					
Hypertension	Rat	—	—	The m^6A methylation level reduce	Wu et al. (2019a)
Cardiac hypertrophy	Cells, mice	Up-regulation	METTL3; FTO	Promote cardiomyocyte hypertrophy both *in vitro* and *in vivo*	(Gan et al., 2013; Dorn et al., 2019), (Berulava et al., 2020)
Heart failure	Clinical samples and mice	Up-regulation	METTL3, METTL4, KIAA1429, FTO, YTHDF2	Data from MeRIP-seq	Zhang et al. (2021)
	Clinical sample, preclinical pig, mice, cells	Down-regulation	FTO	Increase m^6A in RNA and decrease cardiomyocyte contractile function	Mathiyalagan et al. (2019)
Atherosclerosis	Cells, mice, clinical sample	Up-regulation	METTL3, METTL14, IGF2BP1	Promote cardiovascular endothelial cell proliferation and invasion; aggravates endothelial inflammation, angiogenesis and atherosclerosis	(Zhang et al., 2020b; Jian et al., 2020; Dong et al., 2021)
Diabete mellitus	Clinical sample, cells	Up-regulation	FTO, METTL3	Induce mRNA expression of FOXO1, G6PC, and DGAT2	(Yang et al., 2019b; Yang et al., 2020b)
	Cells, mice, clinical sample	Down-regulation	METTL3, METTL14	regulated functional maturation and mass expansion of neonatal β-cells	(De Jesus et al., 2019; Liu et al., 2019; Men et al., 2019; Wang et al., 2020d)

IGF2BP1 expression (Elcheva et al., 2020) are related to the poor prognosis of AML patients. The same phenomenon has been observed in solid tumours. METTL3, RBM15, KIAA1429, YTHDF1, YTHDF2, HNRNPA2B1, HNRNPC, and IGF2BP1/2/3 expression levels in lung cancer tissues are significantly higher than those in normal tissues (Shi et al., 2019; Zhang et al., 2020a; Li and Zhan, 2020; Sheng et al., 2020).

METTL3 may regulate the growth, differentiation, and apoptosis of AML cells by affecting the phosphoinositide 3-kinases (PI3K)/AKT pathway (Vu et al., 2017). Mechanistically, METTL3 promotes c-MYC, B-cell CLL/lymphoma 2 (BCL2), and phosphatase and tensin homologue (PTEN) mRNA translation by regulating m^6A modification levels. Deleting METTL3 increases phosphorylated AKT (p-AKT) levels. METTL3 also regulates drug resistance and invasiveness of lung cancer cells by inducing m^6A modification of enhancer of zeste homologue 2 (EZH2) mRNA in A549 cells (Chen et al., 2020a). In addition, it has been reported that the tumour suppressor miR-33a targets the 3′-UTR of METTL3 mRNA to reduce METTL3 expression, thus inhibiting A549 and NCI-H460 cell proliferation (Du et al., 2017). This suggests that METTL3 may be a new target for lung cancer therapy. Recently, Yankova et al. found that STM2457, a small molecule METTL3 inhibitor, reduced AML growth and increased apoptosis by reducing the expression of an mRNA known to cause leukaemia. Further animal experiments showed that STM2457 prolongs the survival time of various AML mouse models (Yankova et al., 2021). METTL14 acts in various solid tumours and leukaemia through different mechanisms. METTL14 expression is downregulated in AML cells. However, it still plays a carcinogenic role in AML. METTL14 increases MYB/MYC expression through the SPI1-METTL14-MYB/MYC signal axis to promote AML occurrence (Weng et al., 2018). METTL14 inhibits the migration and invasion of renal cancer cells by downregulating purinergic receptor P2X 6 (P2RX6) protein translation and ATP-P2RX6-Ca^{2+}-p-$ERK_{1/2}$-MMP9 signalling in renal cell carcinomas (Wang et al., 2019b).

The RNA demethylases FTO and ALKBH5 are also crucial in tumours. FTO may act as a tumour promoter. FTO increases the expression of myeloid zinc finger 1 (MZF1) by reducing m^6A mRNA modification, and promotes lung cancer progression (Liu et al., 2018a). Knockdown of FTO increases the expression of tumour suppressor genes ASB2 and retinoic acid receptor alpha (RARA) and inhibits AML proliferation and differentiation (Li et al., 2017c). It also reduces the mRNA stability of ubiquitin-specific protease (USP7) and inhibits cancer cell growth (Li et al., 2019b).

In addition, some studies have focused on the function of m^6A-binding proteins in tumours. YTHDF1 and YTHDF2 can be used as oncogenes and tumour suppressors. YTHDF1 deficiency regulates the transformation efficiency of cyclin-dependent kinase 2 (CDK2), cyclin-dependent kinase 4 (CDK4), and cyclin D1 (CCND1) through the Keap1-Nrf2-AKR1C1 pathway to inhibit tumour cell proliferation and xenograft tumorigenesis. YTHDF1 deletion also inhibits new lung adenocarcinoma (ADC) progression (Shi et al., 2019). However, the study also found that YTHDF1 knockdown leads to cell resistance to cisplatin, whereas high YTHDF1 expression leads to better clinical outcomes (Shi et al., 2019). The results of studies on the role of YTHDF2 in lung cancer are complex. One study reported that YTHDF2 promotes METTL3-induced tumorigenesis by increasing suppressor of cytokine signalling 2 (SOCS2) degradation (Chen et al., 2018). However, another study found that YTHDF2 overexpression inhibits non-small cell lung cancer (NSCLC) cell growth and invasion by promoting a decrease in yes-associated protein (YAP) mRNA in NSCLC cells (Jin et al., 2020). However, these studies have repeatedly confirmed the dual role of YTHDF1/2 in

tumorigenesis and progression. IGF2BP1 exerts its carcinogenic function by regulating the expression of key transcriptional and metabolic factors, such as TNF receptor 2 (TNFR2), MYB, and MYC (Li et al., 2018a; Paris et al., 2019; Elcheva et al., 2020).

At present, m^6A modification and its regulatory factors have proven to be crucial in the occurrence, metastasis, immune escape, and drug resistance of various tumours, including haematological tumours (Vu et al., 2017), respiratory tumours [lung cancer (Du et al., 2018) and nasopharyngeal carcinoma (Zheng et al., 2019)], digestive tract tumours (gastric cancer (Yang et al., 2020a), colorectal cancer (Ni et al., 2019; Shen et al., 2020b; Chen et al., 2021c), pancreatic cancer (Geng et al., 2020), and hepatocellular carcinoma (Chen and Wong, 2020)), urinary tumours [bladder cancer (Han et al., 2019), renal cell carcinoma (Zhuang et al., 2019), and prostate cancer (Zhu et al., 2021a)], reproductive system tumours [breast cancer (Cai et al., 2018), cervical squamous cell carcinoma (Wang et al., 2020c), epithelial ovarian cancer (Hua et al., 2018), and endometrial cancer (Liu et al., 2018b)], skin tumours [melanoma (Yang et al., 2019a; Jia et al., 2019), skin squamous cell carcinoma (Zhou et al., 2019)], and glioblastoma (Cui et al., 2017). Current research results show that m^6A regulators may play a dual role in the pathogenesis of tumours, not only as oncogenes but as tumour suppressors. The biological effects of the same m^6A regulator are different in different tumours. Some studies have reported the opposite role for an m^6A regulator in the same cancer. In short, m^6A modification can be used as a marker for a variety of tumours to diagnose and evaluate prognosis and potential therapeutic targets. However, our understanding of the role of m^6A modification in tumours is still in its infancy. Numerous studies are still needed to explore the exact molecular mechanism of m^6A and tumours to develop new targeted drugs for clinical treatment.

4.2 Diabetes Mellitus

m^6A plays an important role in the pathogenesis of type 2 diabetes mellitus (T2D). It has been reported that the mRNA expression of RNA demethylase FTO in T2D patients is upregulated compared with that in a normal control group, inducing the increased expression of key genes involved in glucose and fat metabolisms, such as FOXO1, FASN, G6PC, and DGAT2. This suggests that FTO participates in glucose metabolism by regulating target gene expression (Yang et al., 2019b). In addition, some studies have found that METTL3/14 expression in the β cells of T2D patients and diabetic mice is decreased, leading to decreased β cell proliferation and impaired insulin secretion by reducing the m^6A modification levels of several transcripts related to cell cycle progression, insulin secretion, and insulin/IGF1-AKT-PDX1 pathway (De Jesus et al., 2019; Wang et al., 2020d). In addition, loss of METTL3/14 is associated with abnormal glucose tolerance, hyperglycaemia, and hypoinsulinemia in neonatal mice (Liu et al., 2019; Men et al., 2019; Wang et al., 2020d). A recent study found that METTL3 mRNA and miR-25-3p expression were downregulated in PBMCs and retinal pigment epithelial (RPE) cells stimulated by high glucose. RPE cells overexpressing METTL3 could upregulate p-AKT levels through the miR-25-3p/PTEN axis, thus rescuing the viability of RPE cells stimulated by high glucose (Zha et al., 2020). However, inconsistently, Yang et al. found that METTL3 expression was upregulated in human diabetic cataract tissue samples and high glucose-induced human lens epithelial cells (HLECs), and the total level of m^6A modification increased (Yang et al., 2020b). In summary, m^6A modification is involved in the occurrence of T2D and its related complications. It is expected to provide a new diagnostic and treatment strategy for T2D and its complications.

4.3 Neurodegenerative Diseases

Currently, m^6A modification is considered very important for nervous system development (Hess et al., 2013; Lence et al., 2016; Li et al., 2017a). In addition, some studies have found that abnormal m^6A modifications are related to degenerative changes in the nervous system. Neurodegenerative diseases, including AD and PD, are caused by the gradual loss of neuronal structure or function. It has been reported that m^6A modification levels are downregulated in 6-hydroxydopamine (6-OHDA)-treated PC12 cells and rat striatum, whereas 6-OHDA increases the level of oxidative stress and Ca^{2+} influx by inducing N-methyl-D-aspartate (NMDA) receptor one expression, leading to the death of dopaminergic neurons that eventually develops into PD (Chen et al., 2019b). In addition, some studies have focused on the correlation between m^6A modification and AD. Compared with the control group, METTL3 expression in the cerebral cortex and hippocampus of AD model mice was upregulated, FTO expression was downregulated, and modification levels were significantly increased, suggesting that m^6A methylation promotes AD development (Han et al., 2020). Mechanistic studies have reported that FTO activates the TSC1-mTOR-Tau signalling pathway by reducing m^6A modification levels and then participates in the occurrence of AD (Li et al., 2018b; Annapoorna et al., 2019; Chen et al., 2019b). However, FTO expression was increased in the brains of ternary transgenic AD mice, and conditional knockout of FTO in the neurons of AD mice improved their cognitive ability (Li et al., 2018b). Previous studies have reported that FTO is associated with structural brain atrophy in healthy elderly subjects (Ho et al., 2010), and a prospective cohort study also found that FTO interacts with apolipoprotein E (APOE) to increase the risk of dementia, especially AD (Keller et al., 2011). In summary, the above studies showed that m^6A modification is related to neurodegenerative changes, and its regulatory factors may be used as candidate therapeutic targets for neurodegenerative diseases. However, its role and mechanism need further exploration.

4.4 CVDs

Age is an independent risk factor for CVDs. Studies have shown that m^6A modification may affect the occurrence and development of various CVDs. The level of m^6A RNA methylation in pericytes of spontaneously hypertensive rats was decreased, suggesting that m^6A is involved in blood pressure regulation (Wu et al., 2019a). In addition, under pressure overload stimulation, METTL3 induces compensatory cardiac hypertrophy by regulating the m^6A modification of kinase

and intracellular signal pathway transcripts. However, mice with conditional knockout of the METTL3 gene show the morphology and function of heart failure after stress or ageing stimulation (Dorn et al., 2019). Another study found that FTO expression increased after adipose factor-induced cardiomyocyte hypertrophy, whereas FTO knockout inhibited the hypertrophy of neonatal rat cardiomyocytes (Gan et al., 2013). Berulava et al. (2020) further confirmed these results. They found that the ejection fraction was significantly decreased in cardiomyocyte-specific knockout FTO mice, and heart failure progressed faster (Gan et al., 2013). However, another study found that increasing FTO expression in the hearts of mice with heart failure prevented the myocardial contractile transcript from degrading by reducing its m^{6}A modification then reducing the decrease in myocardial contractility caused by ischaemia (Mathiyalagan et al., 2019). These studies suggest that m^{6}A modification and its regulatory factors are crucial in maintaining normal myocardial homeostasis, compensatory myocardial hypertrophy, and heart failure progression.

In addition, m^{6}A also acts in atherosclerosis progression. METTL14 increases the expression of mature miR-19a by upregulating the m^{6}A modification of miR-19a and accelerates the proliferation of cardiovascular endothelial cells (Zhang et al., 2020b). Additionally, a study reported that METTL14 mediates endothelial cell inflammation, interacts with FOXO1, and promotes vascular cell adhesion molecule 1 (VCAM-1) and intercellular adhesion molecule 1 (ICAM-1) transcription, while METTL14 knockout inhibits the progression of atherosclerotic plaques in mice (Jian et al., 2020). It is believed that m^{6}A modification affects the process of atherosclerosis by regulating cardiovascular endothelial proliferation and endothelial cell inflammation.

In summary, numerous studies have confirmed the correlation between m^{6}A modification and CVDs, but further research needs to verify its established molecular changes and pathological process. In addition, most of the current reports focus on METTL3 and FTO, and the role of other m^{6}A regulators, such as m^{6}A binding proteins in CVDs, is still unclear. m^{6}A modification still needs further exploration to provide a new treatment strategy for CVDs.

5 CONCLUSION AND PERSPECTIVES

Alterations in the epigenetic transcriptome are key regulators of gene expression and cellular physiology. m^{6}A, the most abundant internal modification of mRNAs and lncRNAs, is widely involved in regulating various cellular processes. Therefore, exploring the changes and molecular mechanisms of m^{6}A modification in a pathological state and developing new targeted drugs will provide a new strategy for the early diagnosis and accurate treatment of diseases in the future.

Although several studies have reported on the functional role of m^{6}A RNA methylation in ageing and related diseases, many major knowledge gaps remain to be filled. First, numerous studies have confirmed the correlation between m^{6}A and age-related diseases. However, current research results are controversial. In tumours, for example, the same m^{6}A regulatory factor may play different roles in different tumour types. For instance, METTL14 promotes the migration and invasion of breast cancer (Yi et al., 2020), whereas METTL14 downregulates the cancer-causing long-chain non-coding RNA X-inactive specific transcript (lncRNA XIST) and inhibits tumour proliferation and metastasis in colon cancer (Yang et al., 2020c). This may be due to the difference in disease types, but research on m^{6}A is still in its infancy. The level of m^{6}A modification, the biological role of regulatory factors in the occurrence and development of various diseases, and their molecular mechanisms require further study. There is still a way to go before m^{6}A related drugs can be applied. Second, the epigenetic clock based on the DNA methylation site is recognised as the most promising marker of ageing and has been used to evaluate anti-ageing efficacy. m^{6}A, a methylated form of epigenetics and DNA methylation, has been shown to function in ageing and ageing-related diseases. Whether it cooperates with DNA methylation to regulate gene expression during ageing or whether it has a potential relationship with other types of RNA modification or epigenetic methods remains to be further studied.

In addition, several reports have shown that m^{6}A modification has great potential as a diagnostic marker and therapeutic target in the treatment of anti-ageing and age-related diseases, but few have identified inhibitors specifically targeting m^{6}A regulatory proteins. Previous studies have found that the natural product rhein competitively binds the FTO active site *in vitro* (Chen et al., 2012), inhibits inflammation (Hu et al., 2019) and improves virus-induced lung injury (Shen et al., 2019). However, it is unclear whether m^{6}A methylation regulation mediates these effects. Therefore, more drugs modified by m^{6}A are required to fill this gap. In addition, the exact function of each m^{6}A regulatory factor is not consistent in different cells, diseases, and even different stages of disease development. Our understanding of this is not comprehensive, which is also a challenge for applying m^{6}A in anti-ageing therapy.

AUTHOR CONTRIBUTIONS

JS proposed the idea and drafted the manuscript, BC, YS, ML, SM, and YZ revised and corrected the initial manuscript, AZ, SC, and QB were involved in the accumulation of the relevant references, SW and PZ contributed to the conception of the study and helped perform the revision with constructive discussions. All authors read and approved the final manuscript.

FUNDING

This study was supported by the "National Key R&D Program of China" (Funding No. 2020YFC2008900), co-funded by Logistics Scientific Research Project of the Chinese PLA (Funding No.19BJZ30), National defense science and technology innovation projects (Funding No. 19-163-15-ZD-009-001-10) and Health care project of Second Medical Center of PLA General Hospital (Funding No. NLBJ-2019012).

REFERENCE

Agarwala, S. D., Blitzblau, H. G., Hochwagen, A., and Fink, G. R. (2012). RNA Methylation by the MIS Complex Regulates a Cell Fate Decision in Yeast. *Plos Genet.* 8 (6), e1002732. doi:10.1371/journal.pgen.1002732

Aik, W., Scotti, J. S., Choi, H., Gong, L., Demetriades, M., Schofield, C. J., et al. (2014). Structure of Human RNA N6-Methyladenine Demethylase ALKBH5 Provides Insights into its Mechanisms of Nucleic Acid Recognition and Demethylation. *Nucleic Acids Res.* 42 (7), 4741–4754. doi:10.1093/nar/gku085

Alarcón, C. R., Lee, H., Goodarzi, H., Halberg, N., and Tavazoie, S. F. (2015). N6-methyladenosine marks Primary microRNAs for Processing. *Nature* 519 (7544), 482–485. doi:10.1038/nature14281

Alers, S., Löffler, A. S., Wesselborg, S., and Stork, B. (2012). Role of AMPK-mTOR-Ulk1/2 in the Regulation of Autophagy: Cross Talk, Shortcuts, and Feedbacks. *Mol. Cel Biol* 32 (1), 2–11. doi:10.1128/mcb.06159-11

Annapoorna, P. K., Iyer, H., Parnaik, T., Narasimhan, H., Bhattacharya, A., and Kumar, A. (2019). FTO: An Emerging Molecular Player in Neuropsychiatric Diseases. *Neuroscience* 418, 15–24. doi:10.1016/j.neuroscience.2019.08.021

Aravinthan, A., Challis, B., Shannon, N., Hoare, M., Heaney, J., and Alexander, G. J. M. (2015). Selective Insulin Resistance in Hepatocyte Senescence. *Exp. Cel. Res.* 331 (1), 38–45. doi:10.1016/j.yexcr.2014.09.025

Bansal, H., Yihua, Q., Iyer, S. P., Ganapathy, S., Proia, D., Penalva, L. O., et al. (2014). WTAP Is a Novel Oncogenic Protein in Acute Myeloid Leukemia. *Leukemia* 28 (5), 1171–1174. doi:10.1038/leu.2014.16

Barnes, P. J., Baker, J., and Donnelly, L. E. (2019). Cellular Senescence as a Mechanism and Target in Chronic Lung Diseases. *Am. J. Respir. Crit. Care Med.* 200 (5), 556–564. doi:10.1164/rccm.201810-1975TR

Berulava, T., Buchholz, E., Elerdashvili, V., Pena, T., Islam, M. R., Lbik, D., et al. (2020). Changes in m6A RNA Methylation Contribute to Heart Failure Progression by Modulating Translation. *Eur. J. Heart Fail.* 22 (1), 54–66. doi:10.1002/ejhf.1672

Boccardi, V., Pelini, L., Ercolani, S., Ruggiero, C., and Mecocci, P. (2015). From Cellular Senescence to Alzheimer's Disease: The Role of Telomere Shortening. *Ageing Res. Rev.* 22, 1–8. doi:10.1016/j.arr.2015.04.003

Bokar, J. A., Shambaugh, M. E., Polayes, D., Matera, A. G., and Rottman, F. M. (1997). Purification and cDNA Cloning of the AdoMet-Binding Subunit of the Human mRNA (N6-Adenosine)-Methyltransferase. *Rna* 3 (11), 1233–1247.

Borghesan, M., Hoogaars, W. M. H., Varela-Eirin, M., Talma, N., and Demaria, M. (2020). A Senescence-Centric View of Aging: Implications for Longevity and Disease. *Trends Cell Biology* 30 (10), 777–791. doi:10.1016/j.tcb.2020.07.002

Cai, J., Yang, F., Zhan, H., Situ, J., Li, W., Mao, Y., et al. (2019). RNA m6A Methyltransferase METTL3 Promotes the Growth of Prostate Cancer by Regulating Hedgehog Pathway. *Ott* 12, 9143–9152. doi:10.2147/ott.S226796

Cai, X., Wang, X., Cao, C., Gao, Y., Zhang, S., Yang, Z., et al. (2018). HBXIP-elevated Methyltransferase METTL3 Promotes the Progression of Breast Cancer via Inhibiting Tumor Suppressor Let-7g. *Cancer Lett.* 415, 11–19. doi:10.1016/j.canlet.2017.11.018

Calcinotto, A., Kohli, J., Zagato, E., Pellegrini, L., Demaria, M., and Alimonti, A. (2019). Cellular Senescence: Aging, Cancer, and Injury. *Physiol. Rev.* 99 (2), 1047–1078. doi:10.1152/physrev.00020.2018

Campisi, J., and Robert, L. (2014). Cell Senescence: Role in Aging and Age-Related Diseases. *Interdiscip. Top. Gerontol.* 39, 45–61. doi:10.1159/000358899

Chen, B., Ye, F., Yu, L., Jia, G., Huang, X., Zhang, X., et al. (2012). Development of Cell-Active N6-Methyladenosine RNA Demethylase FTO Inhibitor. *J. Am. Chem. Soc.* 134 (43), 17963–17971. doi:10.1021/ja3064149

Chen, H., Gao, S., Liu, W., Wong, C.-C., Wu, J., Wu, J., et al. (2021). RNA N6-Methyladenosine Methyltransferase METTL3 Facilitates Colorectal Cancer by Activating the m6A-GLUT1-mTORC1 Axis and Is a Therapeutic Target. *Gastroenterology* 160 (4), 1284–1300. e1216. doi:10.1053/j.gastro.2020.11.013

Chen, J., Sun, Y., Xu, X., Wang, D., He, J., Zhou, H., et al. (2017). YTH Domain Family 2 Orchestrates Epithelial-Mesenchymal Transition/proliferation Dichotomy in Pancreatic Cancer Cells. *Cell Cycle* 16 (23), 2259–2271. doi:10.1080/15384101.2017.1380125

Chen, M., Wei, L., Law, C.-T., Tsang, F. H.-C., Shen, J., Cheng, C. L.-H., et al. (2018). RNA N6-Methyladenosine Methyltransferase-like 3 Promotes Liver Cancer Progression through YTHDF2-dependent Posttranscriptional Silencing of SOCS2. *Hepatology* 67 (6), 2254–2270. doi:10.1002/hep.29683

Chen, M., and Wong, C.-M. (2020). The Emerging Roles of N6-Methyladenosine (m6A) Deregulation in Liver Carcinogenesis. *Mol. Cancer* 19 (1), 44. doi:10.1186/s12943-020-01172-y

Chen, R.-X., Chen, X., Xia, L.-P., Zhang, J.-X., Pan, Z.-Z., Ma, X.-D., et al. (2019). N6-methyladenosine Modification of circNSUN2 Facilitates Cytoplasmic export and Stabilizes HMGA2 to Promote Colorectal Liver Metastasis. *Nat. Commun.* 10 (1), 4695. doi:10.1038/s41467-019-12651-2

Chen, W. W., Qi, J. W., Hang, Y., Wu, J. X., Zhou, X. X., Chen, J. Z., et al. (2020). Simvastatin Is Beneficial to Lung Cancer Progression by Inducing METTL3-Induced m6A Modification on EZH2 mRNA. *Eur. Rev. Med. Pharmacol. Sci.* 24 (8), 4263–4270. doi:10.26355/eurrev_202004_21006

Chen, X., Xu, M., Xu, X., Zeng, K., Liu, X., Sun, L., et al. (2020). METTL14 Suppresses CRC Progression via Regulating N6-methyladenosine-dependent Primary miR-375 Processing. *Mol. Ther.* 28 (2), 599–612. doi:10.1016/j.ymthe.2019.11.016

Chen, X., Yu, C., Guo, M., Zheng, X., Ali, S., Huang, H., et al. (2019). Down-Regulation of m6A mRNA Methylation Is Involved in Dopaminergic Neuronal Death. *ACS Chem. Neurosci.* 10 (5), 2355–2363. doi:10.1021/acschemneuro.8b00657

Chen, Y.-s., Ouyang, X.-p., Yu, X.-h., Novák, P., Zhou, L., He, P.-p., et al. (2021). N6-Adenosine Methylation (m6A) RNA Modification: an Emerging Role in Cardiovascular Diseases. *J. Cardiovasc. Trans. Res.* 14, 857–872. doi:10.1007/s12265-021-10108-w

Chen, Y., Wang, J., Xu, D., Xiang, Z., Ding, J., Yang, X., et al. (2021). m6A mRNA Methylation Regulates Testosterone Synthesis through Modulating Autophagy in Leydig Cells. *Autophagy* 17 (2), 457–475. doi:10.1080/15548627.2020.1720431

Cheng, X., Li, M., Rao, X., Zhang, W., Li, X., Wang, L., et al. (2019). KIAA1429 Regulates the Migration and Invasion of Hepatocellular Carcinoma by Altering m6A Modification of ID2 mRNA. *Ott* 12, 3421–3428. doi:10.2147/ott.S180954

Childs, B. G., Durik, M., Baker, D. J., and van Deursen, J. M. (2015). Cellular Senescence in Aging and Age-Related Disease: from Mechanisms to Therapy. *Nat. Med.* 21 (12), 1424–1435. doi:10.1038/nm.4000

Chinta, S. J., Lieu, C. A., Demaria, M., Laberge, R.-M., Campisi, J., and Andersen, J. K. (2013). Environmental Stress, Ageing and Glial Cell Senescence: a Novel Mechanistic Link to Parkinson's Disease? *J. Intern. Med.* 273 (5), 429–436. doi:10.1111/joim.12029

Chokkalla, A. K., Mehta, S. L., Kim, T., Chelluboina, B., Kim, J., and Vemuganti, R. (2019). Transient Focal Ischemia Significantly Alters the M 6 A Epitranscriptomic Tagging of RNAs in the Brain. *Stroke* 50 (10), 2912–2921. doi:10.1161/strokeaha.119.026433

Clapier, C. R., Iwasa, J., Cairns, B. R., and Peterson, C. L. (2017). Mechanisms of Action and Regulation of ATP-dependent Chromatin-Remodelling Complexes. *Nat. Rev. Mol. Cel Biol* 18 (7), 407–422. doi:10.1038/nrm.2017.26

Codogno, P., Mehrpour, M., and Proikas-Cezanne, T. (2011). Canonical and Non-canonical Autophagy: Variations on a Common Theme of Self-Eating? *Nat. Rev. Mol. Cel Biol* 13 (1), 7–12. doi:10.1038/nrm3249

Csepany, T., Lin, A., Baldick, C. J., Jr., and Beemon, K. (1990). Sequence Specificity of mRNA N6-Adenosine Methyltransferase. *J. Biol. Chem.* 265 (33), 20117–20122. doi:10.1016/s0021-9258(17)30477-5

Cui, Q., Shi, H., Ye, P., Li, L., Qu, Q., Sun, G., et al. (2017). m 6 A RNA Methylation Regulates the Self-Renewal and Tumorigenesis of Glioblastoma Stem CellsA RNA Methylation Regulates the Self-Renewal and Tumorigenesis of Glioblastoma Stem Cells. *Cel Rep.* 18 (11), 2622–2634. doi:10.1016/j.celrep.2017.02.059

Day, K., Waite, L. L., Thalacker-Mercer, A., West, A., Bamman, M. M., Brooks, J. D., et al. (2013). Differential DNA Methylation with Age Displays Both Common and Dynamic Features across Human Tissues that Are Influenced by CpG Landscape. *Genome Biol.* 14 (9), R102. doi:10.1186/gb-2013-14-9-r102

de Haan, G., and Lazare, S. S. (2018). Aging of Hematopoietic Stem Cells. *Blood* 131 (5), 479–487. doi:10.1182/blood-2017-06-746412

De Jesus, D. F., Zhang, Z., Kahraman, S., Brown, N. K., Chen, M., Hu, J., et al. (2019). m6A mRNA Methylation Regulates Human β-cell Biology in Physiological States and in Type 2 diabetesA mRNA Methylation Regulates Human β-Cell Biology in Physiological States and in Type 2 Diabetes. *Nat. Metab.* 1 (8), 765–774. doi:10.1038/s42255-019-0089-9

Deng, R., Cheng, Y., Ye, S., Zhang, J., Huang, R., Li, P., et al. (2019). m6A Methyltransferase METTL3 Suppresses Colorectal Cancer Proliferation and

Migration through P38/ERK pathwaysA Methyltransferase METTL3 Suppresses Colorectal Cancer Proliferation and Migration through P38/ERK Pathways. *Ott* 12, 4391–4402. doi:10.2147/ott.S201052

Deng, Y., Zhu, H., Xiao, L., Liu, C., Liu, Y.-L., and Gao, W. (2021). Identification of the Function and Mechanism of m6A Reader IGF2BP2 in Alzheimer's Disease. *Aging* 13 (21), 24086–24100. doi:10.18632/aging.203652

Desrosiers, R., Friderici, K., and Rottman, F. (1974). Identification of Methylated Nucleosides in Messenger RNA from Novikoff Hepatoma Cells. *Proc. Natl. Acad. Sci. U.S.A.* 71 (10), 3971–3975. doi:10.1073/pnas.71.10.3971

Di Micco, R., Krizhanovsky, V., Baker, D., and d'Adda di Fagagna, F. (2021). Cellular Senescence in Ageing: from Mechanisms to Therapeutic Opportunities. *Nat. Rev. Mol. Cel Biol* 22 (2), 75–95. doi:10.1038/s41580-020-00314-w

Dominissini, D., Moshitch-Moshkovitz, S., Schwartz, S., Salmon-Divon, M., Ungar, L., Osenberg, S., et al. (2012). Topology of the Human and Mouse m6A RNA Methylomes Revealed by m6A-Seq. *Nature* 485 (7397), 201–206. doi:10.1038/nature11112

Dong, G., Yu, J., Shan, G., Su, L., Yu, N., and Yang, S. (2021). N6-Methyladenosine Methyltransferase METTL3 Promotes Angiogenesis and Atherosclerosis by Upregulating the JAK2/STAT3 Pathway via m6A Reader IGF2BP1. *Front. Cel Dev. Biol.* 9, 731810. doi:10.3389/fcell.2021.731810

Dorn, L. E., Lasman, L., Chen, J., Xu, X., Hund, T. J., Medvedovic, M., et al. (2019). The N 6 -Methyladenosine mRNA Methylase METTL3 Controls Cardiac Homeostasis and Hypertrophy. *Circulation* 139 (4), 533–545. doi:10.1161/circulationaha.118.036146

Du, M., Zhang, Y., Mao, Y., Mou, J., Zhao, J., Xue, Q., et al. (2017). MiR-33a Suppresses Proliferation of NSCLC Cells via Targeting METTL3 mRNA. *Biochem. biophysical Res. Commun.* 482 (4), 582–589. doi:10.1016/j.bbrc.2016.11.077

Du, Y., Hou, G., Zhang, H., Dou, J., He, J., Guo, Y., et al. (2018). SUMOylation of the m6A-RNA Methyltransferase METTL3 Modulates its Function. *Nucleic Acids Res.* 46 (10), 5195–5208. doi:10.1093/nar/gky156

Elcheva, I. A., Wood, T., Chiarolanzio, K., Chim, B., Wong, M., Singh, V., et al. (2020). RNA-binding Protein IGF2BP1 Maintains Leukemia Stem Cell Properties by Regulating HOXB4, MYB, and ALDH1A1. *Leukemia* 34 (5), 1354–1363. doi:10.1038/s41375-019-0656-9

Farr, J. N., and Khosla, S. (2019). Cellular Senescence in Bone. *Bone* 121, 121–133. doi:10.1016/j.bone.2019.01.015

Feng, Z., Li, Q., Meng, R., Yi, B., and Xu, Q. (2018). METTL 3 Regulates Alternative Splicing of MyD88 upon the Lipopolysaccharide-induced Inflammatory Response in Human Dental Pulp Cells. *J. Cel Mol Med* 22 (5), 2558–2568. doi:10.1111/jcmm.13491

Fraga, M. F., Ballestar, E., Paz, M. F., Ropero, S., Setien, F., Ballestar, M. L., et al. (2005). Epigenetic Differences Arise during the Lifetime of Monozygotic Twins. *Proc. Natl. Acad. Sci. U.S.A.* 102 (30), 10604–10609. doi:10.1073/pnas.0500398102

Fu, Y., Dominissini, D., Rechavi, G., and He, C. (2014). Gene Expression Regulation Mediated through Reversible m6A RNA Methylation. *Nat. Rev. Genet.* 15 (5), 293–306. doi:10.1038/nrg3724

Fu, Y., and Zhuang, X. (2020). m6A-binding YTHDF Proteins Promote Stress Granule Formation. *Nat. Chem. Biol.* 16 (9), 955–963. doi:10.1038/s41589-020-0524-y

Gan, X. T., Zhao, G., Huang, C. X., Rowe, A. C., Purdham, D. M., and Karmazyn, M. (2013). Identification of Fat Mass and Obesity Associated (FTO) Protein Expression in Cardiomyocytes: Regulation by Leptin and its Contribution to Leptin-Induced Hypertrophy. *PloS one* 8 (9), e74235. doi:10.1371/journal.pone.0074235

Geng, Y., Guan, R., Hong, W., Huang, B., Liu, P., Guo, X., et al. (2020). Identification of m6A-Related Genes and m6A RNA Methylation Regulators in Pancreatic Cancer and Their Association with Survival. *Ann. Transl Med.* 8 (6), 387. doi:10.21037/atm.2020.03.98

Gu, C., Wang, Z., Zhou, N., Li, G., Kou, Y., Luo, Y., et al. (2019). Mettl14 Inhibits Bladder TIC Self-Renewal and Bladder Tumorigenesis through N6-Methyladenosine of Notch1. *Mol. Cancer* 18 (1), 168. doi:10.1186/s12943-019-1084-1

Gu, X., Zhang, Y., Li, D., Cai, H., Cai, L., and Xu, Q. (2020). N6-methyladenosine Demethylase FTO Promotes M1 and M2 Macrophage Activation. *Cell Signal.* 69, 109553. doi:10.1016/j.cellsig.2020.109553

Guo, F., Liu, X., Cai, H., and Le, W. (2018). Autophagy in Neurodegenerative Diseases: Pathogenesis and Therapy. *Brain Pathol.* 28 (1), 3–13. doi:10.1111/bpa.12545

Han, J., Wang, J.-z., Yang, X., Yu, H., Zhou, R., Lu, H.-C., et al. (2019). METTL3 Promote Tumor Proliferation of Bladder Cancer by Accelerating Pri-miR221/222 Maturation in m6A-dependent Manner. *Mol. Cancer* 18 (1), 110. doi:10.1186/s12943-019-1036-9

Han, M., Liu, Z., Xu, Y., Liu, X., Wang, D., Li, F., et al. (2020). Abnormality of m6A mRNA Methylation Is Involved in Alzheimer's Disease. *Front. Neurosci.* 14, 98. doi:10.3389/fnins.2020.00098

He, Y., Hu, H., Wang, Y., Yuan, H., Lu, Z., Wu, P., et al. (2018). ALKBH5 Inhibits Pancreatic Cancer Motility by Decreasing Long Non-coding RNA KCNK15-AS1 Methylation. *Cell Physiol Biochem* 48 (2), 838–846. doi:10.1159/000491915

Henikoff, S., and Smith, M. M. (2015). Histone Variants and Epigenetics. *Cold Spring Harb Perspect. Biol.* 7 (1), a019364. doi:10.1101/cshperspect.a019364

Hess, M. E., Hess, S., Meyer, K. D., Verhagen, L. A. W., Koch, L., Brönneke, H. S., et al. (2013). The Fat Mass and Obesity Associated Gene (Fto) Regulates Activity of the Dopaminergic Midbrain Circuitry. *Nat. Neurosci.* 16 (8), 1042–1048. doi:10.1038/nn.3449

Ho, A. J., Stein, J. L., Hua, X., Lee, S., Hibar, D. P., Leow, A. D., et al. (2010). A Commonly Carried Allele of the Obesity-Related FTO Gene Is Associated with Reduced Brain Volume in the Healthy Elderly. *Proc. Natl. Acad. Sci. U S A.* 107 (18), 8404–8409. doi:10.1073/pnas.0910878107

Hongay, C. F., and Orr-Weaver, T. L. (2011). Drosophila Inducer of MEiosis 4 (IME4) Is Required for Notch Signaling during Oogenesis. *Proc. Natl. Acad. Sci. U.S.A.* 108 (36), 14855–14860. doi:10.1073/pnas.1111577108

Horvath, S. (2015). Erratum to: DNA Methylation Age of Human Tissues and Cell Types. *Genome Biol.* 16 (1), 96. doi:10.1186/s13059-015-0649-6

Hou, J., Zhang, H., Liu, J., Zhao, Z., Wang, J., Lu, Z., et al. (2019). YTHDF2 Reduction Fuels Inflammation and Vascular Abnormalization in Hepatocellular Carcinoma. *Mol. Cancer* 18 (1), 163. doi:10.1186/s12943-019-1082-3

Hsu, P. J., Zhu, Y., Ma, H., Guo, Y., Shi, X., Liu, Y., et al. (2017). Ythdc2 Is an N6-Methyladenosine Binding Protein that Regulates Mammalian Spermatogenesis. *Cell Res* 27 (9), 1115–1127. doi:10.1038/cr.2017.99

Hu, F., Zhu, D., Pei, W., Lee, I., Zhang, X., Pan, L., et al. (2019). Rhein Inhibits ATP-Triggered Inflammatory Responses in Rheumatoid Rat Fibroblast-like Synoviocytes. *Int. immunopharmacology* 75, 105780. doi:10.1016/j.intimp.2019.105780

Hua, W., Zhao, Y., Jin, X., Yu, D., He, J., Xie, D., et al. (2018). METTL3 Promotes Ovarian Carcinoma Growth and Invasion through the Regulation of AXL Translation and Epithelial to Mesenchymal Transition. *Gynecol. Oncol.* 151 (2), 356–365. doi:10.1016/j.ygyno.2018.09.015

Huan, T., Chen, G., Liu, C., Bhattacharya, A., Rong, J., Chen, B. H., et al. (2018). Age-associated microRNA Expression in Human Peripheral Blood Is Associated with All-Cause Mortality and Age-Related Traits. *Aging Cell* 17 (1), e12687. doi:10.1111/acel.12687

Huang, H., Camats-Perna, J., Medeiros, R., Anggono, V., and Widagdo, J. (2020b). Altered Expression of the m6A Methyltransferase METTL3 in Alzheimer's Disease. *eNeuro* 7 (5), 0125–220. doi:10.1523/eneuro.0125-20.2020

Huang, H., Weng, H., and Chen, J. (2020a). m6A Modification in Coding and Non-coding RNAs: Roles and Therapeutic Implications in CancerA Modification in Coding and Non-coding RNAs: Roles and Therapeutic Implications in Cancer. *Cancer cell* 37 (3), 270–288. doi:10.1016/j.ccell.2020.02.004

Huang, H., Weng, H., Sun, W., Qin, X., Shi, H., Wu, H., et al. (2018). Recognition of RNA N6-Methyladenosine by IGF2BP Proteins Enhances mRNA Stability and Translation. *Nat. Cel Biol* 20 (3), 285–295. doi:10.1038/s41556-018-0045-z

Huangfu, N., Zheng, W., Xu, Z., Wang, S., Wang, Y., Cheng, J., et al. (2020). RBM4 Regulates M1 Macrophages Polarization through Targeting STAT1-Mediated Glycolysis. *Int. immunopharmacology* 83, 106432. doi:10.1016/j.intimp.2020.106432

Ito, T. K., Yokoyama, M., Yoshida, Y., Nojima, A., Kassai, H., Oishi, K., et al. (2014). A Crucial Role for CDC42 in Senescence-Associated Inflammation and Atherosclerosis. *PloS one* 9 (7), e102186. doi:10.1371/journal.pone.0102186

Ivanova, I., Much, C., Di Giacomo, M., Azzi, C., Morgan, M., Moreira, P. N., et al. (2017). The RNA M 6 A Reader YTHDF2 Is Essential for the Post-transcriptional Regulation of the Maternal Transcriptome and Oocyte Competence. *Mol. Cel.* 67 (6), 1059–1067. e1054. doi:10.1016/j.molcel.2017.08.003

Jia, G., Fu, Y., Zhao, X., Dai, Q., Zheng, G., Yang, Y., et al. (2011). N6-methyladenosine in Nuclear RNA Is a Major Substrate of the Obesity-Associated FTO. *Nat. Chem. Biol.* 7 (12), 885–887. doi:10.1038/nchembio.687

Jia, R., Chai, P., Wang, S., Sun, B., Xu, Y., Yang, Y., et al. (2019). m6A Modification Suppresses Ocular Melanoma through Modulating HINT2 mRNA Translation. *Mol. Cancer* 18 (1), 161. doi:10.1186/s12943-019-1088-x

Jian, D., Wang, Y., Jian, L., Tang, H., Rao, L., Chen, K., et al. (2020). METTL14 Aggravates Endothelial Inflammation and Atherosclerosis by Increasing FOXO1 N6-Methyladeosine Modifications. *Theranostics* 10 (20), 8939–8956. doi:10.7150/thno.45178

Jiang, Z.-x., Wang, Y.-n., Li, Z.-y., Dai, Z.-h., He, Y., Chu, K., et al. (2021). The m6A mRNA Demethylase FTO in Granulosa Cells Retards FOS-dependent Ovarian Aging. *Cell Death Dis* 12 (8), 744. doi:10.1038/s41419-021-04016-9

Jin, D., Guo, J., Wu, Y., Yang, L., Wang, X., Du, J., et al. (2020). m6A Demethylase ALKBH5 Inhibits Tumor Growth and Metastasis by Reducing YTHDFs-Mediated YAP Expression and Inhibiting miR-107/lats2-Mediated YAP Activity in NSCLCA Demethylase ALKBH5 Inhibits Tumor Growth and Metastasis by Reducing YTHDFs-Mediated YAP Expression and Inhibiting miR-107/lats2-Mediated YAP Activity in NSCLC. *Mol. Cancer* 19 (1), 40. doi:10.1186/s12943-020-01161-1

Jin, S., Zhang, X., Miao, Y., Liang, P., Zhu, K., She, Y., et al. (2018). m6A RNA Modification Controls Autophagy through Upregulating ULK1 Protein abundanceA RNA Modification Controls Autophagy through Upregulating ULK1 Protein Abundance. *Cel Res* 28 (9), 955–957. doi:10.1038/s41422-018-0069-8

Justice, J. N., Nambiar, A. M., Tchkonia, T., LeBrasseur, N. K., Pascual, R., Hashmi, S. K., et al. (2019). Senolytics in Idiopathic Pulmonary Fibrosis: Results from a First-In-Human, Open-Label, Pilot Study. *EBioMedicine* 40, 554–563. doi:10.1016/j.ebiom.2018.12.052

Kaminsky, Z. A., Tang, T., Wang, S.-C., Ptak, C., Oh, G. H. T., Wong, A. H. C., et al. (2009). DNA Methylation Profiles in Monozygotic and Dizygotic Twins. *Nat. Genet.* 41 (2), 240–245. doi:10.1038/ng.286

Karthiya, R., and Khandelia, P. (2020). m6A RNA Methylation: Ramifications for Gene Expression and Human Health. *Mol. Biotechnol.* 62 (10), 467–484. doi:10.1007/s12033-020-00269-5

Kasowitz, S. D., Ma, J., Anderson, S. J., Leu, N. A., Xu, Y., Gregory, B. D., et al. (2018). Nuclear m6A Reader YTHDC1 Regulates Alternative Polyadenylation and Splicing during Mouse Oocyte Development. *Plos Genet.* 14 (5), e1007412. doi:10.1371/journal.pgen.1007412

Keller, L., Xu, W., Wang, H.-X., Winblad, B., Fratiglioni, L., and Graff, C. (2011). The Obesity Related Gene, FTO, Interacts with APOE, and Is Associated with Alzheimer's Disease Risk: a Prospective Cohort Study. *Jad* 23 (3), 461–469. doi:10.3233/jad-2010-101068

Kennedy, B. K., Berger, S. L., Brunet, A., Campisi, J., Cuervo, A. M., Epel, E. S., et al. (2014). Geroscience: Linking Aging to Chronic Disease. *Cell* 159 (4), 709–713. doi:10.1016/j.cell.2014.10.039

Knuckles, P., Lence, T., Haussmann, I. U., Jacob, D., Kreim, N., Carl, S. H., et al. (2018). Zc3h13/Flacc Is Required for Adenosine Methylation by Bridging the mRNA-Binding Factor Rbm15/Spenito to the m6A Machinery Component Wtap/Fl(2)d. *Genes Dev.* 32 (5-6), 415–429. doi:10.1101/gad.309146.117

Lawrence, M., Daujat, S., and Schneider, R. (2016). Lateral Thinking: How Histone Modifications Regulate Gene Expression. *Trends Genet.* 32 (1), 42–56. doi:10.1016/j.tig.2015.10.007

Lee, E. K., Lee, M. J., Abdelmohsen, K., Kim, W., Kim, M. M., Srikantan, S., et al. (2011). miR-130 Suppresses Adipogenesis by Inhibiting Peroxisome Proliferator-Activated Receptor γ Expression. *Mol. Cel Biol* 31 (4), 626–638. doi:10.1128/mcb.00894-10

Lee, J.-H., Kim, E. W., Croteau, D. L., and Bohr, V. A. (2020). Heterochromatin: an Epigenetic point of View in Aging. *Exp. Mol. Med.* 52 (9), 1466–1474. doi:10.1038/s12276-020-00497-4

Lence, T., Akhtar, J., Bayer, M., Schmid, K., Spindler, L., Ho, C. H., et al. (2016). m6A Modulates Neuronal Functions and Sex Determination in DrosophilaA Modulates Neuronal Functions and Sex Determination in Drosophila. *Nature* 540 (7632), 242–247. doi:10.1038/nature20568

Lewinska, A., Adamczyk-Grochala, J., Kwasniewicz, E., and Wnuk, M. (2017). Downregulation of Methyltransferase Dnmt2 Results in Condition-dependent Telomere Shortening and Senescence or Apoptosis in Mouse Fibroblasts. *J. Cel Physiol* 232 (12), 3714–3726. doi:10.1002/jcp.25848

Li, G., Song, Y., Liao, Z., Wang, K., Luo, R., Lu, S., et al. (2020). Bone-derived Mesenchymal Stem Cells Alleviate Compression-Induced Apoptosis of Nucleus Pulposus Cells by N6 Methyladenosine of Autophagy. *Cel Death Dis* 11 (2), 103. doi:10.1038/s41419-020-2284-8

Li, H., Ren, Y., Mao, K., Hua, F., Yang, Y., Wei, N., et al. (2018). FTO Is Involved in Alzheimer's Disease by Targeting TSC1-mTOR-Tau Signaling. *Biochem. biophysical Res. Commun.* 498 (1), 234–239. doi:10.1016/j.bbrc.2018.02.201

Li, J., Zhu, L., Shi, Y., Liu, J., Lin, L., and Chen, X. (2019). m6A Demethylase FTO Promotes Hepatocellular Carcinoma Tumorigenesis via Mediating PKM2 Demethylation. *Am. J. Transl Res.* 11 (9), 6084–6092.

Li, J., Han, Y., Zhang, H., Qian, Z., Jia, W., Gao, Y., et al. (2019). The m6A Demethylase FTO Promotes the Growth of Lung Cancer Cells by Regulating the m6A Level of USP7 mRNA. *Biochem. biophysical Res. Commun.* 512 (3), 479–485. doi:10.1016/j.bbrc.2019.03.093

Li, L., Zang, L., Zhang, F., Chen, J., Shen, H., Shu, L., et al. (2017). Fat Mass and Obesity-Associated (FTO) Protein Regulates Adult Neurogenesis. *Hum. Mol. Genet.* 26 (13), 2398–2411. doi:10.1093/hmg/ddx128

Li, N., and Zhan, X. (2020). Identification of Pathology-specific Regulators of m6A RNA Modification to Optimize Lung Cancer Management in the Context of Predictive, Preventive, and Personalized Medicine. *EPMA J.* 11 (3), 485–504. doi:10.1007/s13167-020-00220-3

Li, Q., Li, X., Tang, H., Jiang, B., Dou, Y., Gorospe, M., et al. (2017). NSUN2-Mediated m5C Methylation and METTL3/METTL14-Mediated m6A Methylation Cooperatively Enhance P21 Translation. *J. Cel. Biochem.* 118 (9), 2587–2598. doi:10.1002/jcb.25957

Li, T., Hu, P.-S., Zuo, Z., Lin, J.-F., Li, X., Wu, Q.-N., et al. (2019). METTL3 Facilitates Tumor Progression via an m6A-igf2bp2-dependent Mechanism in Colorectal Carcinoma. *Mol. Cancer* 18 (1), 112. doi:10.1186/s12943-019-1038-7

Li, X., Tang, J., Huang, W., Wang, F., Li, P., Qin, C., et al. (2017). The M6A Methyltransferase METTL3: Acting as a Tumor Suppressor in Renal Cell Carcinoma. *Oncotarget* 8 (56), 96103–96116. doi:10.18632/oncotarget.21726

Li, Z., Qian, P., Shao, W., Shi, H., He, X. C., Gogol, M., et al. (2018). Suppression of m6A Reader Ythdf2 Promotes Hematopoietic Stem Cell Expansion. *Cel Res* 28 (9), 904–917. doi:10.1038/s41422-018-0072-0

Li, Z., Weng, H., Su, R., Weng, X., Zuo, Z., Li, C., et al. (2017). FTO Plays an Oncogenic Role in Acute Myeloid Leukemia as a N 6 -Methyladenosine RNA Demethylase. *Cancer cell* 31 (1), 127–141. doi:10.1016/j.ccell.2016.11.017

Lin, S., Choe, J., Du, P., Triboulet, R., and Gregory, R. I. (2016). The M 6 A Methyltransferase METTL3 Promotes Translation in Human Cancer Cells. *Mol. Cel.* 62 (3), 335–345. doi:10.1016/j.molcel.2016.03.021

Lin, Z., Niu, Y., Wan, A., Chen, D., Liang, H., Chen, X., et al. (2020). RNA M 6 A Methylation Regulates Sorafenib Resistance in Liver Cancer through FOXO 3-mediated Autophagy. *Embo J.* 39 (12), e103181. doi:10.15252/embj.2019103181

Linton, P.-J., Gurney, M., Sengstock, D., Mentzer, R. M., Jr., and Gottlieb, R. A. (2015). This Old Heart: Cardiac Aging and Autophagy. *J. Mol. Cell. Cardiol.* 83, 44–54. doi:10.1016/j.yjmcc.2014.12.017

Liu, J., Eckert, M. A., Harada, B. T., Liu, S.-M., Lu, Z., Yu, K., et al. (2018). m6A mRNA Methylation Regulates AKT Activity to Promote the Proliferation and Tumorigenicity of Endometrial cancerA mRNA Methylation Regulates AKT Activity to Promote the Proliferation and Tumorigenicity of Endometrial Cancer. *Nat. Cel Biol* 20 (9), 1074–1083. doi:10.1038/s41556-018-0174-4

Liu, J., Luo, G., Sun, J., Men, L., Ye, H., He, C., et al. (2019). METTL14 Is Essential for β-cell Survival and Insulin Secretion. *Biochim. Biophys. Acta (Bba) - Mol. Basis Dis.* 1865 (9), 2138–2148. doi:10.1016/j.bbadis.2019.04.011

Liu, J., Ren, D., Du, Z., Wang, H., Zhang, H., and Jin, Y. (2018). m 6 A Demethylase FTO Facilitates Tumor Progression in Lung Squamous Cell Carcinoma by Regulating MZF1 expressionA Demethylase FTO Facilitates Tumor Progression in Lung Squamous Cell Carcinoma by Regulating MZF1 Expression. *Biochem. biophysical Res. Commun.* 502 (4), 456–464. doi:10.1016/j.bbrc.2018.05.175

Liu, J., Yue, Y., Han, D., Wang, X., Fu, Y., Zhang, L., et al. (2014). A METTL3-METTL14 Complex Mediates Mammalian Nuclear RNA N6-Adenosine Methylation. *Nat. Chem. Biol.* 10 (2), 93–95. doi:10.1038/nchembio.1432

Liu, N., Dai, Q., Zheng, G., He, C., Parisien, M., and Pan, T. (2015). N6-methyladenosine-dependent RNA Structural Switches Regulate RNA-Protein Interactions. *Nature* 518 (7540), 560–564. doi:10.1038/nature14234

Liu, P., Li, F., Lin, J., Fukumoto, T., Nacarelli, T., Hao, X., et al. (2021). m6A-independent Genome-wide METTL3 and METTL14 Redistribution Drives the Senescence-

Associated Secretory phenotypeA-independent Genome-wide METTL3 and METTL14 Redistribution Drives the Senescence-Associated Secretory Phenotype. *Nat. Cel Biol* 23 (4), 355–365. doi:10.1038/s41556-021-00656-3

Luo, R., Su, L.-Y., Li, G., Yang, J., Liu, Q., Yang, L.-X., et al. (2020). Activation of PPARA-Mediated Autophagy Reduces Alzheimer Disease-like Pathology and Cognitive Decline in a Murine Model. *Autophagy* 16 (1), 52–69. doi:10.1080/15548627.2019.1596488

Ma, J. z., Yang, F., Zhou, C. c., Liu, F., Yuan, J. h., Wang, F., et al. (2017). METTL14 Suppresses the Metastatic Potential of Hepatocellular Carcinoma by Modulating N 6 -methyladenosine-dependent Primary MicroRNA Processing. *Hepatology* 65 (2), 529–543. doi:10.1002/hep.28885

Mathiyalagan, P., Adamiak, M., Mayourian, J., Sassi, Y., Liang, Y., Agarwal, N., et al. (2019). FTO-dependent N 6 -Methyladenosine Regulates Cardiac Function during Remodeling and Repair. *Circulation* 139 (4), 518–532. doi:10.1161/circulationaha.118.033794

Men, L., Sun, J., Luo, G., and Ren, D. (2019). Acute Deletion of METTL14 in β-Cells of Adult Mice Results in Glucose Intolerance. *Endocrinology* 160 (10), 2388–2394. doi:10.1210/en.2019-00350

Min, K.-W., Zealy, R. W., Davila, S., Fomin, M., Cummings, J. C., Makowsky, D., et al. (2018). Profiling of m6A RNA Modifications Identified an Age-Associated Regulation of AGO2 mRNA Stability. *Aging Cell* 17 (3), e12753. doi:10.1111/acel.12753

Müller, S., Glaß, M., Singh, A. K., Haase, J., Bley, N., Fuchs, T., et al. (2019). IGF2BP1 Promotes SRF-dependent Transcription in Cancer in a m6A- and miRNA-dependent Manner. *Nucleic Acids Res.* 47 (1), 375–390. doi:10.1093/nar/gky1012

Naren, D., Yan, T., Gong, Y., Huang, J., Zhang, D., Sang, L., et al. (2021). High Wilms' Tumor 1 Associating Protein Expression Predicts Poor Prognosis in Acute Myeloid Leukemia and Regulates m6A Methylation of MYC mRNA. *J. Cancer Res. Clin. Oncol.* 147 (1), 33–47. doi:10.1007/s00432-020-03373-w

Ni, W., Yao, S., Zhou, Y., Liu, Y., Huang, P., Zhou, A., et al. (2019). Long Noncoding RNA GAS5 Inhibits Progression of Colorectal Cancer by Interacting with and Triggering YAP Phosphorylation and Degradation and Is Negatively Regulated by the m6A Reader YTHDF3. *Mol. Cancer* 18 (1), 143. doi:10.1186/s12943-019-1079-y

Niu, Y., Lin, Z., Wan, A., Chen, H., Liang, H., Sun, L., et al. (2019). RNA N6-Methyladenosine Demethylase FTO Promotes Breast Tumor Progression through Inhibiting BNIP3. *Mol. Cancer* 18 (1), 46. doi:10.1186/s12943-019-1004-4

Pang, P., Qu, Z., Yu, S., Pang, X., Li, X., Gao, Y., et al. (2021). Mettl14 Attenuates Cardiac Ischemia/Reperfusion Injury by Regulating Wnt1/β-Catenin Signaling Pathway. *Front. Cel Dev. Biol.* 9, 762853. doi:10.3389/fcell.2021.762853

Papp, D., Kovács, T., Billes, V., Varga, M., Tarnóci, A., Hackler, L., Jr., et al. (2016). AUTEN-67, an Autophagy-Enhancing Drug Candidate with Potent Antiaging and Neuroprotective Effects. *Autophagy* 12 (2), 273–286. doi:10.1080/15548627.2015.1082023

Paris, J., Morgan, M., Campos, J., Spencer, G. J., Shmakova, A., Ivanova, I., et al. (2019). Targeting the RNA m6A Reader YTHDF2 Selectively Compromises Cancer Stem Cells in Acute Myeloid Leukemia. *Cell stem cell* 25 (1), 137–148. e136. doi:10.1016/j.stem.2019.03.021

Patil, D. P., Chen, C.-K., Pickering, B. F., Chow, A., Jackson, C., Guttman, M., et al. (2016). m6A RNA Methylation Promotes XIST-Mediated Transcriptional repressionA RNA Methylation Promotes XIST-Mediated Transcriptional Repression. *Nature* 537 (7620), 369–373. doi:10.1038/nature19342

Pendleton, K. E., Chen, B., Liu, K., Hunter, O. V., Xie, Y., Tu, B. P., et al. (2017). The U6 snRNA M 6 A Methyltransferase METTL16 Regulates SAM Synthetase Intron Retention. *Cell* 169 (5), 824–835. e814. doi:10.1016/j.cell.2017.05.003

Peters, A., Nawrot, T. S., and Baccarelli, A. A. (2021). Hallmarks of Environmental Insults. *Cell* 184 (6), 1455–1468. doi:10.1016/j.cell.2021.01.043

Ping, X.-L., Sun, B.-F., Wang, L., Xiao, W., Yang, X., Wang, W.-J., et al. (2014). Mammalian WTAP Is a Regulatory Subunit of the RNA N6-Methyladenosine Methyltransferase. *Cel Res* 24 (2), 177–189. doi:10.1038/cr.2014.3

Portela, A., and Esteller, M. (2010). Epigenetic Modifications and Human Disease. *Nat. Biotechnol.* 28 (10), 1057–1068. doi:10.1038/nbt.1685

Quan, W., Li, J., Liu, L., Zhang, Q., Qin, Y., Pei, X., et al. (2021). Influence of N6-Methyladenosine Modification Gene HNRNPC on Cell Phenotype in Parkinson's Disease. *Parkinson's Dis.* 2021, 1–10. doi:10.1155/2021/9919129

Richard, E. M., Polla, D. L., Assir, M. Z., Contreras, M., Shahzad, M., Khan, A. A., et al. (2019). Bi-allelic Variants in METTL5 Cause Autosomal-Recessive Intellectual Disability and Microcephaly. *Am. J. Hum. Genet.* 105 (4), 869–878. doi:10.1016/j.ajhg.2019.09.007

Roundtree, I. A., Luo, G.-Z., Zhang, Z., Wang, X., Zhou, T., Cui, Y., et al. (2017). YTHDC1 Mediates Nuclear export of N6-Methyladenosine Methylated mRNAs. *Elife* 6. doi:10.7554/eLife.31311

Rubinsztein, D. C., Mariño, G., and Kroemer, G. (2011). Autophagy and Aging. *Cell* 146 (5), 682–695. doi:10.1016/j.cell.2011.07.030

Rubio, R. M., Depledge, D. P., Bianco, C., Thompson, L., and Mohr, I. (2018). RNA M6 A Modification Enzymes Shape Innate Responses to DNA by Regulating Interferon β. *Genes Dev.* 32 (23-24), 1472–1484. doi:10.1101/gad.319475.118

Schäfer, K. P. (1982). RNA Synthesis and Processing Reactions in a Subcellular System from Mouse L Cells. *Hoppe-Seyler´s Z. für physiologische Chem.* 363 (1), 33–44. doi:10.1515/bchm2.1982.363.1.33

Schöller, E., Weichmann, F., Treiber, T., Ringle, S., Treiber, N., Flatley, A., et al. (2018). Interactions, Localization, and Phosphorylation of the m6A Generating METTL3-METTL14-WTAP Complex. *Rna* 24 (4), 499–512. doi:10.1261/rna.064063.117

Schwartz, S., Mumbach, M. R., Jovanovic, M., Wang, T., Maciag, K., Bushkin, G. G., et al. (2014). Perturbation of m6A Writers Reveals Two Distinct Classes of mRNA Methylation at Internal and 5′ Sites. *Cel Rep.* 8 (1), 284–296. doi:10.1016/j.celrep.2014.05.048

Sergiev, P. V., Golovina, A. Y., Osterman, I. A., Nesterchuk, M. V., Sergeeva, O. V., Chugunova, A. A., et al. (2016). N6-Methylated Adenosine in RNA: From Bacteria to Humans. *J. Mol. Biol.* 428 (10 Pt B), 2134–2145. doi:10.1016/j.jmb.2015.12.013

Shafik, A. M., Zhang, F., Guo, Z., Dai, Q., Pajdzik, K., Li, Y., et al. (2021). N6-methyladenosine Dynamics in Neurodevelopment and Aging, and its Potential Role in Alzheimer's Disease. *Genome Biol.* 22 (1), 17. doi:10.1186/s13059-020-02249-z

Shen, C., Sheng, Y., Zhu, A. C., Robinson, S., Jiang, X., Dong, L., et al. (2020). RNA Demethylase ALKBH5 Selectively Promotes Tumorigenesis and Cancer Stem Cell Self-Renewal in Acute Myeloid Leukemia. *Cell stem cell* 27 (1), 64–80. e69. doi:10.1016/j.stem.2020.04.009

Shen, C., Xuan, B., Yan, T., Ma, Y., Xu, P., Tian, X., et al. (2020). m6A-dependent Glycolysis Enhances Colorectal Cancer progressionA-dependent Glycolysis Enhances Colorectal Cancer Progression. *Mol. Cancer* 19 (1), 72. doi:10.1186/s12943-020-01190-w

Shen, C., Zhang, Z., Xie, T., Ji, J., Xu, J., Lin, L., et al. (2019). Rhein Suppresses Lung Inflammatory Injury Induced by Human Respiratory Syncytial Virus through Inhibiting NLRP3 Inflammasome Activation via NF-Kb Pathway in Mice. *Front. Pharmacol.* 10, 1600. doi:10.3389/fphar.2019.01600

Shen, X. P., Ling, X., Lu, H., Zhou, C. X., Zhang, J. K., and Yu, Q. (2018). Low Expression of microRNA-1266 Promotes Colorectal Cancer Progression via Targeting FTO. *Eur. Rev. Med. Pharmacol. Sci.* 22 (23), 8220–8226. doi:10.26355/eurrev_201812_16516

Sheng, H., Li, Z., Su, S., Sun, W., Zhang, X., Li, L., et al. (2020). YTH Domain Family 2 Promotes Lung Cancer Cell Growth by Facilitating 6-phosphogluconate Dehydrogenase mRNA Translation. *Carcinogenesis* 41 (5), 541–550. doi:10.1093/carcin/bgz152

Shi, H., Wang, X., Lu, Z., Zhao, B. S., Ma, H., Hsu, P. J., et al. (2017). YTHDF3 Facilitates Translation and Decay of N6-Methyladenosine-Modified RNA. *Cel Res* 27 (3), 315–328. doi:10.1038/cr.2017.15

Shi, Y., Fan, S., Wu, M., Zuo, Z., Li, X., Jiang, L., et al. (2019). YTHDF1 Links Hypoxia Adaptation and Non-small Cell Lung Cancer Progression. *Nat. Commun.* 10 (1), 4892. doi:10.1038/s41467-019-12801-6

Spitale, R. C., Flynn, R. A., Zhang, Q. C., Crisalli, P., Lee, B., Jung, J.-W., et al. (2015). Structural Imprints *In Vivo* Decode RNA Regulatory Mechanisms. *Nature* 519 (7544), 486–490. doi:10.1038/nature14263

Su, R., Dong, L., Li, Y., Gao, M., Han, L., Wunderlich, M., et al. (2020). Targeting FTO Suppresses Cancer Stem Cell Maintenance and Immune Evasion. *Cancer cell* 38 (1), 79–96. e11. doi:10.1016/j.ccell.2020.04.017

Sun, T., Wu, R., and Ming, L. (2019). The Role of m6A RNA Methylation in Cancer. *Biomed. Pharmacother.* 112, 108613. doi:10.1016/j.biopha.2019.108613

Sun, Y., Dong, D., Xia, Y., Hao, L., Wang, W., and Zhao, C. (2022). YTHDF1 Promotes Breast Cancer Cell Growth, DNA Damage Repair and Chemoresistance. *Cel Death Dis* 13 (3), 230. doi:10.1038/s41419-022-04672-5

Svobodová Kovaříková, A., Stixová, L., Kovařík, A., Komůrková, D., Legartová, S., Fagherazzi, P., et al. (2020). N6-Adenosine Methylation in RNA and a Reduced m3G/TMG Level in Non-coding RNAs Appear at Microirradiation-Induced DNA Lesions. *Cells* 9 (2), 360. doi:10.3390/cells9020360

Tanabe, A., Tanikawa, K., Tsunetomi, M., Takai, K., Ikeda, H., Konno, J., et al. (2016). RNA Helicase YTHDC2 Promotes Cancer Metastasis via the Enhancement of the Efficiency by Which HIF-1α mRNA Is Translated. *Cancer Lett.* 376 (1), 34–42. doi:10.1016/j.canlet.2016.02.022

Tang, C., Klukovich, R., Peng, H., Wang, Z., Yu, T., Zhang, Y., et al. (2018). ALKBH5-dependent m6A Demethylation Controls Splicing and Stability of Long 3′-UTR mRNAs in Male Germ Cells. *Proc. Natl. Acad. Sci. U.S.A.* 115 (2), E325–e333. doi:10.1073/pnas.1717794115

Tang, H.-W., Weng, J.-H., Lee, W. X., Hu, Y., Gu, L., Cho, S., et al. (2021). mTORC1-chaperonin CCT Signaling Regulates M 6 A RNA Methylation to Suppress Autophagy. *Proc. Natl. Acad. Sci. U.S.A.* 118 (10), e2021945118. doi:10.1073/pnas.2021945118

Tang, J., Wang, F., Cheng, G., Si, S., Sun, X., Han, J., et al. (2018). Wilms' Tumor 1-associating Protein Promotes Renal Cell Carcinoma Proliferation by Regulating CDK2 mRNA Stability. *J. Exp. Clin. Cancer Res.* 37 (1), 40. doi:10.1186/s13046-018-0706-6

Tang, X., Liu, S., Chen, D., Zhao, Z., and Zhou, J. (2019). The Role of the Fat Mass and Obesity-associated P-rotein in the P-roliferation of P-ancreatic C-ancer C-ells. *Oncol. Lett.* 17 (2), 2473–2478. doi:10.3892/ol.2018.9873

Uddin, M. B., Wang, Z., and Yang, C. (2021). The m6A RNA Methylation Regulates Oncogenic Signaling Pathways Driving Cell Malignant Transformation and Carcinogenesis. *Mol. Cancer* 20 (1), 61. doi:10.1186/s12943-021-01356-0

Ueda, Y., Ooshio, I., Fusamae, Y., Kitae, K., Kawaguchi, M., Jingushi, K., et al. (2017). AlkB Homolog 3-mediated tRNA Demethylation Promotes Protein Synthesis in Cancer Cells. *Sci. Rep.* 7, 42271. doi:10.1038/srep42271

Ungvari, Z., Tarantini, S., Sorond, F., Merkely, B., and Csiszar, A. (2020). Mechanisms of Vascular Aging, A Geroscience Perspective. *J. Am. Coll. Cardiol.* 75 (8), 931–941. doi:10.1016/j.jacc.2019.11.061

Unnikrishnan, A., Freeman, W. M., Jackson, J., Wren, J. D., Porter, H., and Richardson, A. (2019). The Role of DNA Methylation in Epigenetics of Aging. *Pharmacol. Ther.* 195, 172–185. doi:10.1016/j.pharmthera.2018.11.001

van Tran, N., Ernst, F. G. M., Hawley, B. R., Zorbas, C., Ulryck, N., Hackert, P., et al. (2019). The Human 18S rRNA m6A Methyltransferase METTL5 Is Stabilized by TRMT112. *Nucleic Acids Res.* 47 (15), 7719–7733. doi:10.1093/nar/gkz619

Vu, L. P., Pickering, B. F., Cheng, Y., Zaccara, S., Nguyen, D., Minuesa, G., et al. (2017). The N6-Methyladenosine (m6A)-Forming Enzyme METTL3 Controls Myeloid Differentiation of normal Hematopoietic and Leukemia Cells. *Nat. Med.* 23 (11), 1369–1376. doi:10.1038/nm.4416

Wang, C.-Y., Shie, S.-S., Wen, M.-S., Hung, K.-C., Hsieh, I.-C., Yeh, T.-S., et al. (2015). Loss of FTO in Adipose Tissue Decreases Angptl4 Translation and Alters Triglyceride Metabolism. *Sci. Signal.* 8 (407), ra127. doi:10.1126/scisignal.aab3357

Wang, H., Xu, B., and Shi, J. (2020). N6-methyladenosine METTL3 Promotes the Breast Cancer Progression via Targeting Bcl-2. *Gene* 722, 144076. doi:10.1016/j.gene.2019.144076

Wang, J., Ishfaq, M., Xu, L., Xia, C., Chen, C., and Li, J. (2019). METTL3/m6A/miRNA-873-5p Attenuated Oxidative Stress and Apoptosis in Colistin-Induced Kidney Injury by Modulating Keap1/Nrf2 Pathway. *Front. Pharmacol.* 10, 517. doi:10.3389/fphar.2019.00517

Wang, J., Li, Y., Wang, P., Han, G., Zhang, T., Chang, J., et al. (2020). Leukemogenic Chromatin Alterations Promote AML Leukemia Stem Cells via a KDM4C-ALKBH5-AXL Signaling Axis. *Cell stem cell* 27 (1), 81–97. e88. doi:10.1016/j.stem.2020.04.001

Wang, J., Yan, S., Lu, H., Wang, S., and Xu, D. (2019). METTL3 Attenuates LPS-Induced Inflammatory Response in Macrophages via NF-Kb Signaling Pathway. *Mediators Inflamm.* 2019, 1–8. doi:10.1155/2019/3120391

Wang, J., Zhang, J., Ma, Y., Zeng, Y., Lu, C., Yang, F., et al. (2021). WTAP Promotes Myocardial Ischemia/reperfusion Injury by Increasing Endoplasmic Reticulum Stress via Regulating m6A Modification of ATF4 mRNA. *Aging* 13 (8), 11135–11149. doi:10.18632/aging.202770

Wang, K. C., and Chang, H. Y. (2018). Epigenomics. *Circ. Res.* 122 (9), 1191–1199. doi:10.1161/circresaha.118.310998

Wang, Q., Chen, C., Ding, Q., Zhao, Y., Wang, Z., Chen, J., et al. (2020). METTL3-mediated m6A Modification of HDGF mRNA Promotes Gastric Cancer Progression and Has Prognostic Significance. *Gut* 69 (7), 1193–1205. doi:10.1136/gutjnl-2019-319639

Wang, Q., Guo, X., Li, L., Gao, Z., Su, X., Ji, M., et al. (2020). N6-methyladenosine METTL3 Promotes Cervical Cancer Tumorigenesis and Warburg Effect through YTHDF1/HK2 Modification. *Cel Death Dis* 11 (10), 911. doi:10.1038/s41419-020-03071-y

Wang, Q., Zhang, H., Chen, Q., Wan, Z., Gao, X., and Qian, W. (2019). Identification of METTL14 in Kidney Renal Clear Cell Carcinoma Using Bioinformatics Analysis. *Dis. markers* 2019, 1–11. doi:10.1155/2019/5648783

Wang, T., Kong, S., Tao, M., and Ju, S. (2020). The Potential Role of RNA N6-Methyladenosine in Cancer Progression. *Mol. Cancer* 19 (1), 88. doi:10.1186/s12943-020-01204-7

Wang, X., Lu, Z., Gomez, A., Hon, G. C., Yue, Y., Han, D., et al. (2014). N6-methyladenosine-dependent Regulation of Messenger RNA Stability. *Nature* 505 (7481), 117–120. doi:10.1038/nature12730

Wang, X., Zhao, B. S., Roundtree, I. A., Lu, Z., Han, D., Ma, H., et al. (2015). N6-methyladenosine Modulates Messenger RNA Translation Efficiency. *Cell* 161 (6), 1388–1399. doi:10.1016/j.cell.2015.05.014

Wang, Y., Li, Y., Toth, J. I., Petroski, M. D., Zhang, Z., and Zhao, J. C. (2014). N6-methyladenosine Modification Destabilizes Developmental Regulators in Embryonic Stem Cells. *Nat. Cel Biol* 16 (2), 191–198. doi:10.1038/ncb2902

Wang, Y., Sun, J., Lin, Z., Zhang, W., Wang, S., Wang, W., et al. (2020). m6A mRNA Methylation Controls Functional Maturation in Neonatal Murine β-CellsA mRNA Methylation Controls Functional Maturation in Neonatal Murine β-Cells. *Diabetes* 69 (8), 1708–1722. doi:10.2337/db19-0906

Warda, A. S., Kretschmer, J., Hackert, P., Lenz, C., Urlaub, H., Höbartner, C., et al. (2017). Human METTL16 Is a N 6 -methyladenosine (M 6 A) Methyltransferase that Targets pre-mRNAs and Various Non-coding RNAs. *EMBO Rep.* 18 (11), 2004–2014. doi:10.15252/embr.201744940

Wen, J., Lv, R., Ma, H., Shen, H., He, C., Wang, J., et al. (2018). Zc3h13 Regulates Nuclear RNA m6A Methylation and Mouse Embryonic Stem Cell Self-Renewal. *Mol. Cel* 69 (6), 1028–1038. e1026. doi:10.1016/j.molcel.2018.02.015

Weng, H., Huang, H., Wu, H., Qin, X., Zhao, B. S., Dong, L., et al. (2018). METTL14 Inhibits Hematopoietic Stem/Progenitor Differentiation and Promotes Leukemogenesis via mRNA m6A Modification. *Cell stem cell* 22 (2), 191–205. e199. doi:10.1016/j.stem.2017.11.016

Woo, H.-H., and Chambers, S. K. (2019). Human ALKBH3-Induced m1A Demethylation Increases the CSF-1 mRNA Stability in Breast and Ovarian Cancer Cells. *Biochim. Biophys. Acta (Bba) - Gene Regul. Mech.* 1862 (1), 35–46. doi:10.1016/j.bbagrm.2018.10.008

Wu, J., Frazier, K., Zhang, J., Gan, Z., Wang, T., and Zhong, X. (2020). Emerging Role of M 6 A RNA Methylation in Nutritional Physiology and Metabolism. *Obes. Rev.* 21 (1), e12942. doi:10.1111/obr.12942

Wu, Q., Yuan, X., Han, R., Zhang, H., and Xiu, R. (2019). Epitranscriptomic Mechanisms of N6-Methyladenosine Methylation Regulating Mammalian Hypertension Development by Determined Spontaneously Hypertensive Rats Pericytes. *Epigenomics* 11 (12), 1359–1370. doi:10.2217/epi-2019-0148

Wu, Y., Yang, X., Chen, Z., Tian, L., Jiang, G., Chen, F., et al. (2019). m6A-induced lncRNA RP11 Triggers the Dissemination of Colorectal Cancer Cells via Upregulation of Zeb1A-Induced lncRNA RP11 Triggers the Dissemination of Colorectal Cancer Cells via Upregulation of Zeb1. *Mol. Cancer* 18 (1), 87. doi:10.1186/s12943-019-1014-2

Wu, Z., Shi, Y., Lu, M., Song, M., Yu, Z., Wang, J., et al. (2020). METTL3 Counteracts Premature Aging via m6A-dependent Stabilization of MIS12 mRNA. *Nucleic Acids Res.* 48 (19), 11083–11096. doi:10.1093/nar/gkaa816

Xiao, W., Adhikari, S., Dahal, U., Chen, Y.-S., Hao, Y.-J., Sun, B.-F., et al. (2016). Nuclear M 6 A Reader YTHDC1 Regulates mRNA Splicing. *Mol. Cel* 61 (4), 507–519. doi:10.1016/j.molcel.2016.01.012

Yang, J., Liu, J., Zhao, S., and Tian, F. (2020). N6-Methyladenosine METTL3 Modulates the Proliferation and Apoptosis of Lens Epithelial Cells in Diabetic Cataract. *Mol. Ther. - Nucleic Acids* 20, 111–116. doi:10.1016/j.omtn.2020.02.002

Yang, S., Wei, J., Cui, Y.-H., Park, G., Shah, P., Deng, Y., et al. (2019). m6A mRNA Demethylase FTO Regulates Melanoma Tumorigenicity and Response to Anti-PD-1 blockadeA mRNA Demethylase FTO Regulates Melanoma Tumorigenicity and Response to Anti-PD-1 Blockade. *Nat. Commun.* 10 (1), 2782. doi:10.1038/s41467-019-10669-0

Yang, X., Zhang, S., He, C., Xue, P., Zhang, L., He, Z., et al. (2020). METTL14 Suppresses Proliferation and Metastasis of Colorectal Cancer by Down-Regulating Oncogenic Long Non-coding RNA XIST. *Mol. Cancer* 19 (1), 46. doi:10.1186/s12943-020-1146-4

Yang, Y., Shen, F., Huang, W., Qin, S., Huang, J.-T., Sergi, C., et al. (2019). Glucose Is Involved in the Dynamic Regulation of m6A in Patients with Type 2 Diabetes. *J. Clin. Endocrinol. Metab.* 104 (3), 665–673. doi:10.1210/jc.2018-00619

Yang, Z., Jiang, X., Li, D., and Jiang, X. (2020). HBXIP Promotes Gastric Cancer via METTL3-Mediated MYC mRNA m6A Modification. *Aging* 12 (24), 24967–24982. doi:10.18632/aging.103767

Yang, Z., Yu, G.-l., Zhu, X., Peng, T.-h., and Lv, Y.-c. (2022). Critical Roles of FTO-Mediated mRNA m6A Demethylation in Regulating Adipogenesis and Lipid Metabolism: Implications in Lipid Metabolic Disorders. *Genes Dis.* 9 (1), 51–61. doi:10.1016/j.gendis.2021.01.005

Yankova, E., Blackaby, W., Albertella, M., Rak, J., De Braekeleer, E., Tsagkogeorga, G., et al. (2021). Small-molecule Inhibition of METTL3 as a Strategy against Myeloid Leukaemia. *Nature* 593 (7860), 597–601. doi:10.1038/s41586-021-03536-w

Yen, Y.-P., and Chen, J.-A. (2021). The m6A Epitranscriptome on Neural Development and Degeneration. *J. Biomed. Sci.* 28 (1), 40. doi:10.1186/s12929-021-00734-6

Yi, D., Wang, R., Shi, X., Xu, L., Yilihamu, Y. e., and Sang, J. (2020). METTL14 Promotes the Migration and Invasion of Breast Cancer Cells by Modulating N6-methyladenosine and hsa-miR-146a-5p E-xpression. *Oncol. Rep.* 43 (5), 1375–1386. doi:10.3892/or.2020.7515

Yu, D., Horton, J. R., Yang, J., Hajian, T., Vedadi, M., Sagum, C. A., et al. (2021). Human MettL3-MettL14 RNA Adenine Methyltransferase Complex Is Active on Double-Stranded DNA Containing Lesions. *Nucleic Acids Res.* 49 (20), 11629–11642. doi:10.1093/nar/gkab460

Yue, Y., Liu, J., Cui, X., Cao, J., Luo, G., Zhang, Z., et al. (2018). VIRMA Mediates Preferential m6A mRNA Methylation in 3′UTR and Near Stop Codon and Associates with Alternative Polyadenylation. *Cell Discov* 4, 10. doi:10.1038/s41421-018-0019-0

Zha, X., Xi, X., Fan, X., Ma, M., Zhang, Y., and Yang, Y. (2020). Overexpression of METTL3 Attenuates High-Glucose Induced RPE Cell Pyroptosis by Regulating miR-25-3p/PTEN/Akt Signaling cascade through DGCR8. *Aging* 12 (9), 8137–8150. doi:10.18632/aging.103130

Zhang, B., Xu, Y., Cui, X., Jiang, H., Luo, W., Weng, X., et al. (2021). Alteration of m6A RNA Methylation in Heart Failure with Preserved Ejection Fraction. *Front. Cardiovasc. Med.* 8, 647806. doi:10.3389/fcvm.2021.647806

Zhang, B. Y., Han, L., Tang, Y. F., Zhang, G. X., Fan, X. L., Zhang, J. J., et al. (2020). METTL14 Regulates M6A Methylation-Modified Primary miR-19a to Promote Cardiovascular Endothelial Cell Proliferation and Invasion. *Eur. Rev. Med. Pharmacol. Sci.* 24 (12), 7015–7023. doi:10.26355/eurrev_202006_21694

Zhang, C., Chen, L., Peng, D., Jiang, A., He, Y., Zeng, Y., et al. (2020). METTL3 and N6-Methyladenosine Promote Homologous Recombination-Mediated Repair of DSBs by Modulating DNA-RNA Hybrid Accumulation. *Mol. Cel.* 79 (3), 425–442. e427. doi:10.1016/j.molcel.2020.06.017

Zhang, C., Chen, Y., Sun, B., Wang, L., Yang, Y., Ma, D., et al. (2017). m6A Modulates Haematopoietic Stem and Progenitor Cell specificationA Modulates Haematopoietic Stem and Progenitor Cell Specification. *Nature* 549 (7671), 273–276. doi:10.1038/nature23883

Zhang, J., Bai, R., Li, M., Ye, H., Wu, C., Wang, C., et al. (2019). Excessive miR-25-3p Maturation via N6-Methyladenosine Stimulated by Cigarette Smoke Promotes Pancreatic Cancer Progression. *Nat. Commun.* 10 (1), 1858. doi:10.1038/s41467-019-09712-x

Zhang, J., Guo, S., Piao, H.-y., Wang, Y., Wu, Y., Meng, X.-y., et al. (2019). ALKBH5 Promotes Invasion and Metastasis of Gastric Cancer by Decreasing Methylation of the lncRNA NEAT1. *J. Physiol. Biochem.* 75 (3), 379–389. doi:10.1007/s13105-019-00690-8

Zhang, J., Tsoi, H., Li, X., Wang, H., Gao, J., Wang, K., et al. (2016). Carbonic Anhydrase IVinhibits colon Cancer Development by Inhibiting the Wnt Signalling Pathway through Targeting the WTAP-WT1-TBL1 axis. *Gut* 65 (9), 1482–1493. doi:10.1136/gutjnl-2014-308614

Zhang, Y., Liu, X., Liu, L., Li, J., Hu, Q., and Sun, R. (2020). Expression and Prognostic Significance of m6A-Related Genes in Lung Adenocarcinoma. *Med. Sci. Monit.* 26, e919644. doi:10.12659/msm.919644

Zhao, B. S., Roundtree, I. A., and He, C. (2017). Post-transcriptional Gene Regulation by mRNA Modifications. *Nat. Rev. Mol. Cel Biol* 18 (1), 31–42. doi:10.1038/nrm.2016.132

Zhao, F., Xu, Y., Gao, S., Qin, L., Austria, Q., Siedlak, S. L., et al. (2021). METTL3-dependent RNA m6A Dysregulation Contributes to Neurodegeneration in Alzheimer's Disease through Aberrant Cell Cycle Events. *Mol. Neurodegeneration* 16 (1), 70. doi:10.1186/s13024-021-00484-x

Zhao, T., Li, X., Sun, D., and Zhang, Z. (2019). Oxidative Stress: One Potential Factor for Arsenite-Induced Increase of N6-Methyladenosine in Human Keratinocytes. *Environ. Toxicol. Pharmacol.* 69, 95–103. doi:10.1016/j.etap.2019.04.005

Zhao, X., Yang, Y., Sun, B.-F., Shi, Y., Yang, X., Xiao, W., et al. (2014). FTO-dependent Demethylation of N6-Methyladenosine Regulates mRNA Splicing and Is Required for Adipogenesis. *Cel Res* 24 (12), 1403–1419. doi:10.1038/cr.2014.151

Zheng, Z.-Q., Li, Z.-X., Zhou, G.-Q., Lin, L., Zhang, L.-L., Lv, J.-W., et al. (2019). Long Noncoding RNA FAM225A Promotes Nasopharyngeal Carcinoma Tumorigenesis and Metastasis by Acting as ceRNA to Sponge miR-590-3p/miR-1275 and Upregulate ITGB3. *Cancer Res.* 79 (18), 4612–4626. doi:10.1158/0008-5472.Can-19-0799

Zhong, X., Yu, J., Frazier, K., Weng, X., Li, Y., Cham, C. M., et al. (2018). Circadian Clock Regulation of Hepatic Lipid Metabolism by Modulation of m6A mRNA Methylation. *Cel Rep.* 25 (7), 1816–1828. e1814. doi:10.1016/j.celrep.2018.10.068

Zhou, R., Gao, Y., Lv, D., Wang, C., Wang, D., and Li, Q. (2019). METTL3 Mediated m6A Modification Plays an Oncogenic Role in Cutaneous Squamous Cell Carcinoma by Regulating ΔNp63. *Biochem. biophysical Res. Commun.* 515 (2), 310–317. doi:10.1016/j.bbrc.2019.05.155

Zhou, Z., Lv, J., Yu, H., Han, J., Yang, X., Feng, D., et al. (2020). Mechanism of RNA Modification N6-Methyladenosine in Human Cancer. *Mol. Cancer* 19 (1), 104. doi:10.1186/s12943-020-01216-3

Zhu, H., Gan, X., Jiang, X., Diao, S., Wu, H., and Hu, J. (2019). ALKBH5 Inhibited Autophagy of Epithelial Ovarian Cancer through miR-7 and BCL-2. *J. Exp. Clin. Cancer Res.* 38 (1), 163. doi:10.1186/s13046-019-1159-2

Zhu, H., Sun, B., Zhu, L., Zou, G., and Shen, Q. (2021). N6-Methyladenosine Induced miR-34a-5p Promotes TNF-α-Induced Nucleus Pulposus Cell Senescence by Targeting SIRT1. *Front. Cel Dev. Biol.* 9, 642437. doi:10.3389/fcell.2021.642437

Zhu, K., Li, Y., and Xu, Y. (2021). The FTO m6A Demethylase Inhibits the Invasion and Migration of Prostate Cancer Cells by Regulating Total m6A Levels. *Life Sci.* 271, 119180. doi:10.1016/j.lfs.2021.119180

Zhu, S., and Lu, Y. (2020). Dexmedetomidine Suppressed the Biological Behavior of HK-2 Cells Treated with LPS by Down-Regulating ALKBH5. *Inflammation* 43 (6), 2256–2263. doi:10.1007/s10753-020-01293-y

Zhuang, C., Zhuang, C., Luo, X., Huang, X., Yao, L., Li, J., et al. (2019). N6-methyladenosine Demethylase FTO Suppresses clear Cell Renal Cell Carcinoma through a Novel FTO-PGC-1α Signalling axis. *J. Cel Mol Med* 23 (3), 2163–2173. doi:10.1111/jcmm.14128

Zou, D., Dong, L., Li, C., Yin, Z., Rao, S., and Zhou, Q. (2019). The m6A Eraser FTO Facilitates Proliferation and Migration of Human Cervical Cancer Cells. *Cancer Cel Int* 19, 321. doi:10.1186/s12935-019-1045-1

Conflict of Interest: The authors declare that the research was conducted in the absence of any commercial or financial relationships that could be construed as a potential conflict of interest.

Publisher's Note: All claims expressed in this article are solely those of the authors and do not necessarily represent those of their affiliated organizations, or those of the publisher, the editors and the reviewers. Any product that may be evaluated in this article, or claim that may be made by its manufacturer, is not guaranteed or endorsed by the publisher.

GLOSSARY

6-OHDA 6-hydroxydopamine
AD Alzheimer's disease
ADC adenocarcinoma
AKT Protein kinase B
ALKBH3 AlkB homologue 3
ALKBH5 AlkB homologue 5
AML acute myeloid leukaemia
AMPK AMP-activated protein kinase
ANGPTL4 angiopoietin-like 4
APOE apolipoprotein E
ASB2 ankyrin repeat and SOCS box containing 2
ATG13 autophagy-related 13
BA9 Brodmann area 9
BCL2 B-cell CLL/lymphoma 2
CAMKK2 calcium/calmodulin-dependent protein kinase kinase 2
CCND1 cyclin D1
CDK2 cyclin-dependent kinase 2
CDK4 cyclin-dependent kinase 4
circNSUN2 circRNA NOP2/SUN domain family, member 2
circRNA cyclic RNA
CRP C-reactive protein
CVD cardiovascular disease
DDR DNA damage response
DGCR8 DiGeorge syndrome critical region 8
DNMT3A DNA methyltransferase 3α
EGFR epidermal growth factor
EZH2 enhancer of zeste homologue 2
FIP200 family interacting protein of 200kDa
FOXO3 Forkhead box O3
FTO fat mass and obesity-related proteins
HDF human diploid fibroblasts
HGPS Hutchinson-Gilford progeria
HLEC human lens epithelial cell
hMSC human bone marrow mesenchymal stem cell
HNRNPC heterogeneous nuclear ribonucleoprotein C
HNRNPG heterogeneous nuclear ribonucleoprotein G
HNRNPA2B1 heterogeneous nuclear ribonucleoprotein A2B1
ICAM-1 intercellular adhesion molecule 1
IFN: interferon
IGF2BP insulin-like growth factor 2 binding protein
IL Interleukin
LPS Lipopolysaccharides
lncRNA long non-coding RNA;
lncRNA XIST long-chain non-coding RNA X-inactive specific transcript
m6A N6-methyladenosine; MAPK: mitogen-activated protein kinase
MERIP-seq m6A methylation RNA immunoprecipitation sequencing
METTL3 RNA methyltransferase-like protein 3
METTL5 RNA methyltransferase-like protein 5
METTL14 RNA methyltransferase-like protein 14
METTL16 RNA methyltransferase-like protein 16
miRNA microRNA
MK2 MAPKAPK2
mTOR mammalian target of rapamycin
MZF1 myeloid zinc finger 1
NER nucleotide excision repair
NF-κB nuclear factor-κB
NHEJ non-homologous end junction
NMDA N-methyl-D-aspartate
NSCLC non-small cell lung cancer
P13K phosphoinositide 3-kinases
P2RX6 purinergic receptor P2X 6
p-AKT phosphorylated AKT
PBMC peripheral blood mononuclear cell
PD Parkinson's disease
PGC1α peroxisome proliferator-activated receptor gamma coactivator-1 alpha
PPARβ/δ peroxisome proliferator-activated receptor
PTEN phosphatase and tensin homologue
RARA retinoic acid receptor alpha
RBM15 RNA -binding motif protein 15
RNA-seq RNA sequencing
ROS reactive oxygen species
RPE retinal pigment epithelial
rRNA ribosomal RNA
RUNX1 RUNT-related transcription factor 1
SA-βGAL senescence-related β-galactosidase
SAM S-Adenosyl Methionine
SASP senescence-associated secretory phenotype
SFN ammonium trifluoride
snoRNA small nucleolar molecule RNA
snRNA small nuclear RNA
SOCS2 suppressor of cytokine signalling 2
SRSF10 serine- and arginine-rich splicing factor 10
SRSF3 serine- and arginine-rich splicing factor 3
T2D type 2 diabetes mellitus
TAZ PDZ binding motif-based transcriptional coactivator

TLR toll-like receptors
TNF tumour necrosis factor
TNFR2 tumour necrosis factor receptor 2
tRNA transfer RNA
ULK1 Unc-51 like autophagy activating kinase 1
ULK1/2 UNC-51-like kinase
USP7 ubiquitin specific protease 7
UV ultraviolet
VCAM-1 vascular cell adhesion molecule 1
VIRMA Vir-like m6A RNA methyltransferase associated protein
WS Werner syndrome
WTAP Wilms' tumour 1-associating protein
XIST X-inactive specific transcript
YAP yes associated protein
YTHDC1 YTH domain containing 1
YTHDC2 YTH domain containing 2
YTHDF1 YTH domain family protein 1
YTHDF2 YTH domain family protein 2
YTHDF3 YTH domain family protein 3
ZCCH4 zinc finger CCHC-type containing 4
ZC3H13 zinc finger CCCH domain-containing protein 13

frontiers | Frontiers in Genetics

ORIGINAL RESEARCH
published: 08 June 2022
doi: 10.3389/fgene.2022.861853

The Alteration of m^{6}A Modification at the Transcriptome-Wide Level in Human Villi During Spontaneous Abortion in the First Trimester

Jiajie She[1,2†], Kaifen Tan[3†], Jie Liu[4†], Shuo Cao[3], Zengguang Li[3], You Peng[3], Zhuoyu Xiao[3], Ruiying Diao[1] and Liping Wang[1*]*

[1]The First Affiliated Hospital of Shenzhen University, Reproductive Medicine Centre, Shenzhen Second People's Hospital, Shenzhen, China, [2]Shenzhen Institutes of Advanced Technology, Chinese Academy of Sciences, Shenzhen, China, [3]Department of Developmental Biology, School of Basic Medical Sciences, Southern Medical University, Guangzhou, China, [4]Department of Obstetrics and Gynecology, Nanfang Hospital, Southern Medical University, Guangzhou, China

A growing number of studies have demonstrated that N6 methyladenine (m^{6}A) acts as an important role in the pathogenesis of reproductive diseases. Therefore, it is essential to profile the genome-wide m^{6}A modifications such as in spontaneous abortion. In this study, due to the trace of human villi during early pregnancy, we performed high-throughput sequencing in villous tissues from spontaneous abortion (SA group) and controls with induced abortion (normal group) in the first trimester. Based on meRIP-seq data, 18,568 m^{6}A peaks were identified. These m^{6}A peaks were mainly located in the coding region near the stop codon and were mainly characterized by AUGGAC and UGGACG motif. Compared with normal group, the SA group had 2,159 significantly upregulated m^{6}A peaks and 281 downregulated m^{6}A peaks. Biological function analyses revealed that differential m^{6}A-modified genes were mainly involved in the Hippo and Wnt signaling pathways. Based on the conjoint analysis of meRIP-seq and RNA-seq data, we identified thirty-five genes with differentially methylated m^{6}A peaks and synchronously differential expression. And these genes were mainly involved in the Wnt signaling pathway, phosphatase activity regulation, protein phosphatase inhibitor activity, and transcription inhibitor activity. This study is the first to profile the transcriptome-wide m^{6}A methylome in spontaneous abortion during early pregnancy, which provide novel insights into the pathogenesis and treatment of spontaneous abortion in the first trimester.

Keywords: N6 methyladenine (m^{6}A), spontaneous abortion, early pregnancy, MeRIP-seq, villous tissues

OPEN ACCESS

Edited by:
Xiao Han,
Fuzhou University, China

Reviewed by:
Tianshun Gao,
Sun Yat-Sen University, China
Cecilia Battistelli,
Sapienza University of Rome, Italy

****Correspondence:***
Ruiying Diao
15889753127@163.com
Liping Wang
wlp18665070696@163.com

†These authors have contributed equally to this work

Specialty section:
This article was submitted to Epigenomics and Epigenetics, a section of the journal Frontiers in Genetics

Received: *25 January 2022*
Accepted: *25 April 2022*
Published: *08 June 2022*

Citation:
She J, Tan K, Liu J, Cao S, Li Z, Peng Y, Xiao Z, Diao R and Wang L (2022) The Alteration of m^{6}A Modification at the Transcriptome-Wide Level in Human Villi During Spontaneous Abortion in the First Trimester. Front. Genet. 13:861853. doi: 10.3389/fgene.2022.861853

INTRODUCTION

Spontaneous abortion (SA) is considered to be one of the most common and severe complications during early pregnancy, which affects 10–15% of pregnant women (Rossen et al., 2018). The etiology of SA is multifactorial, which mainly includes endocrine abnormalities, immune abnormalities, abnormal uterine anatomy, prethrombotic state, chromosome abnormality and infection factors. There may still be other unknown factors contributing to SA, so further investigation is needed. To date, the role of some epigenetic modifications (DNA methylation, histone modification, and non-coding RNA) in SA has been well identified (Liu et al., 2018; Wang et al., 2019; Chen et al., 2021). As the most abundant epigenetic

modification of mRNA in eukaryotic cells, m^{6}A modification affects the stability (Wang et al., 2014; Ke et al., 2017; Huang et al., 2020), translation (Meyer et al., 2015; Wang et al., 2015; Shi et al., 2017), and splicing of mRNA (Xiao et al., 2016; Pendleton et al., 2017). Although previous studies have also illuminated that m^{6}A modification plays important roles in the regulation of immune function and inflammatory response, the relationship between m^{6}A methylation and SA remains to be elucidated.

As known, the m^{6}A modification includes three main components: 1) "writers", the methyltransferase complex, such as METTL3 (methyltransferase-like 3), METTL14 (methyltransferase-like 14) (Wang et al., 2016), and METTL16 (methyltransferase-like 16) (Mendel et al., 2018); 2) 'readers', RNA binding proteins, including YTHDF1/2/3 (YTH-family proteins 1/2/3), and YTHDC1/2 (YTH domain containing proteins 1/2) (Xu et al., 2015; Gao et al., 2019), and IGF2BP1/2/3 (insulin-like growth factor 2 mRNA binding proteins 1/2/3) (Huang et al., 2020); 3) "erasers", demethylases, including ALKBH5 (alkB homolog 5) (Zheng et al., 2013) and FTO (fat mass and obesity-associated protein) (Jia et al., 2011). Recently, studies have shown that YTHDF2 can regulate oocyte maturation in female mice and negatively regulate the JAK-STAT pathway to affect the development of mouse nervous system (Ivanova et al., 2017). Wang et al. found that FTO can inhibit the expression level of myogenin, and thus inhibit the differentiation of muscle cells. Li et al. found that ALKBH5 might inhibit the invasion of trophoblast cells in patients with recurrent pregnancy loss, inhibit trophoblast invasion and thus affect mRNA stability. Furthermore, m^{6}A modification has also been confirmed to be associated with embryonic stem cell differentiation (Aguilo et al., 2015; Geula et al., 2015), hematopoietic system development (Zhang et al., 2017), myogenesis (Wang et al., 2017), and early embryonic development (Sui et al., 2020). Xia's lab mapped the transcriptome-wide m^{6}A profiles of major fetal tissues including human placenta (Xiao et al., 2019), but the m^{6}A methylome in human villi during spontaneous abortion in the first trimester has not been characterized.

In this study, due to the trace of early villous tissue, we performed high-throughput sequencing to determine the transcriptome-wide m^{6}A methylome in human villi from patients with spontaneous abortion and controls with induced abortion in the first trimester. Using MeRIP-seq data, we further identified differential m^{6}A peaks in villous tissue based on the comparison of spontaneous abortion and induced abortion samples. Then, we identified differentially expressed genes using RNA-seq data. Finally, the conjoint analysis of MeRIP-seq and RNA-seq revealed some genes with differentially methylated m^{6}A peaks and synchronously differential expression, which might provide an alternative strategy for the therapy and prevention of spontaneous abortion.

MATERIALS AND METHODS

Samples Collection

Villous tissues from patients with spontaneous abortion and controls with induced abortion used in this research were obtained with written informed consent from all participants. All tissues were approved by the Medicine Ethics Committee of Shenzhen Second People's Hospital (Approval number, 20210517001-FS01). The inclusion criteria were: (1) Patients who were clinically diagnosed with spontaneous abortion for the first time or healthy women who underwent voluntary induced abortion; (2) Age between 18 and 35; (3) Gestational ages between 6-8 weeks. The exclusion criteria were: (1) Patients with fetal chromosomal or congenital abnormalities; (2) Patients with abnormal uterine structures; (3) Patients with polycystic ovary syndrome, endometriosis, and thyroid disease; (4) Patients with vaginitis. Three spontaneous abortion samples and three induced abortion samples were obtained from elective terminations of apparently normal pregnancies. These samples were further used for MeRIP-seq. The villous tissue was rinsed in precooled normal saline three times, while the tissue with a diameter of 1 mm was cut with ophthalmic scissors. After the tissue was mixed in Trizol solution in a volume ratio of 1:10, it was ground to homogenate with a freeze grinder, and the left tissue was frozen in liquid nitrogen.

MeRIP Sequencing

Total RNA from each sample was isolated using TRIzol reagent (Invitrogen) and fragmented into ~100-nucleotide-long fragments by zinc acetate. Next, Affinity-purified anti-m^{6}A polyclonal antibodies (Abcam) were used for immunoprecipitation to analyze approximately 300 μg of fragmented RNA. After stringent washing with a high-salt buffer (400 mM NaCl, 0.05% NP-40, 10 mM Tris–HCl), competitive buffer (150 mM NaCl, 0.05% NP-40, 10 mM Tris–HCl, 0.25 mg ml−1 mix of adenosine, uridine, guanosine and cytidine), high-detergent buffer (150 mM NaCl, 0.5% NP-40,10 mM Tris–HCl), and immunoprecipitation buffer (150 mM NaCl, 0.05% NP-40, 10 mM Tris–HCl), bound RNA was eluted by competition with 1 mg ml−1 N6-methyladenosine (Selleckchem) and used for library construction using the NEBNext Ultra RNA Library Prep Kit v2 for Illumina. After removal of ribosomal RNA using the Epicentre Ribo-zero rRNA Removal Kit (Epicentre), total RNA from each tissue was fragmented and a library was constructed using the NEBNext Ultra RNA Library Prep Kit v2 for Illumina (New England Biolabs) as input RNA. RNA-seq libraries of m^{6}A antibody-enriched mRNAs and input mRNAs were prepared. Sequencing was carried out using an Illumina Hiseq 4000 platform according to the manufacturer's instructions.

Data Analysis

Trimmomatic (v.0.27) (Bolger et al., 2014) was used for quality control of paired-end sequencing data. Reads that mapped to rRNA and tRNA sequences (obtained from the UCSC gene annotation (hg38)) using bowtie2 (v.2.3.4) (Langmead and Salzberg, 2013) were discarded, and the remaining reads were aligned to the GRCh38 using hisat2-align (v.2.1.0) (Kim et al., 2015). Unique reads with high mapping quality were retained using Picard (v.2.16.0) and SAMtools (v.1.7.0). MACS2 (v.2.1.1) (Gaspar, 2018) was used to identify m^{6}A peaks with the parameter '--nomodel' and '-q 0.05'. ExomePeak2 package

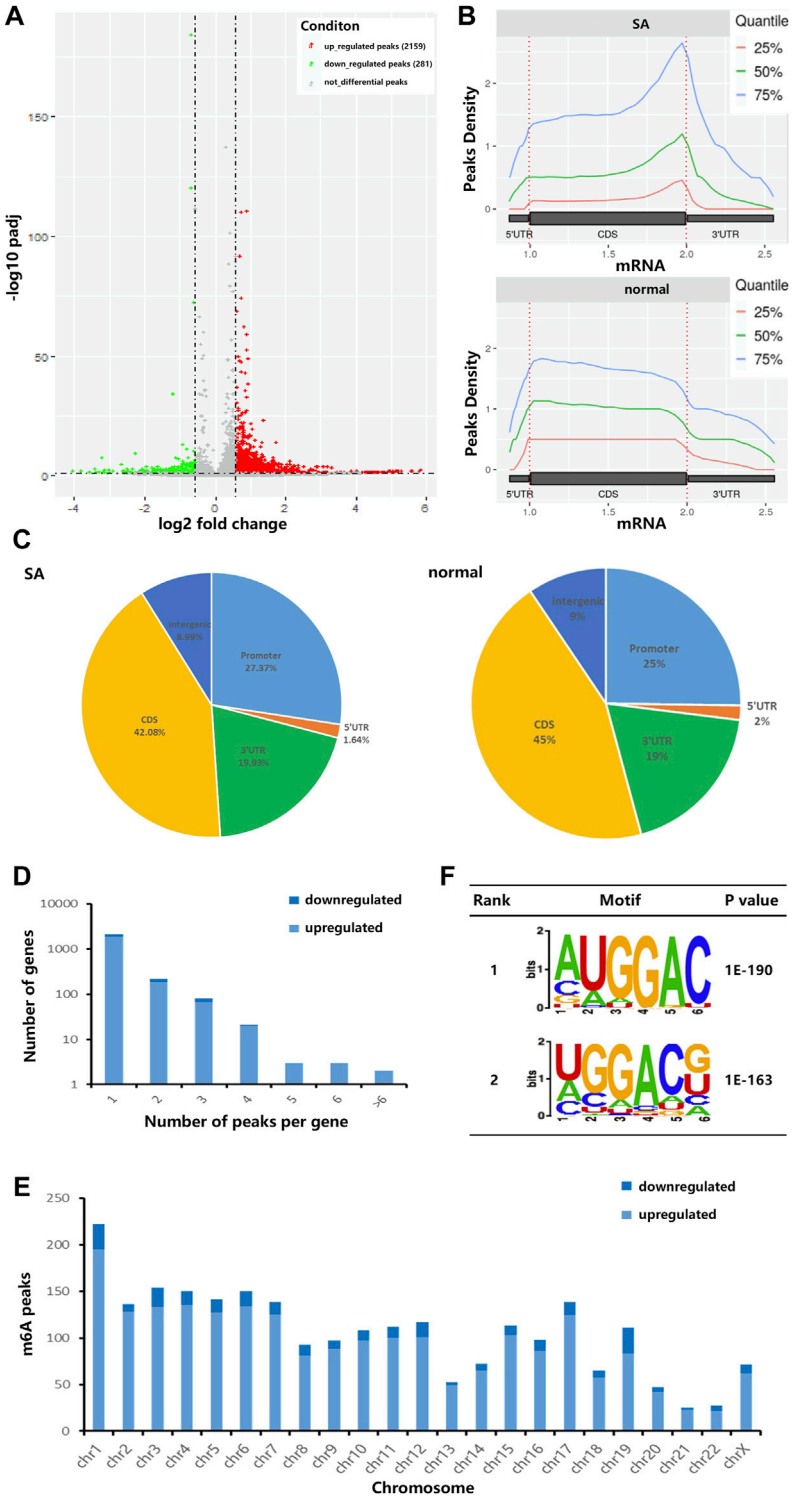

FIGURE 1 | Characteristics of m^{6}A methylation in human villi during spontaneous abortion in the first trimester. **(A)** Volcano plots showing the significantly altered m^{6}A peaks. **(B)** Accumulation of the region of average m^{6}A peaks along with all transcripts in SA group and normal group. **(C)** Pie charts showing the distribution of m^{6}A peaks in SA group and normal group. **(D)** The distribution of altered m^{6}A peaks per gene. **(E)** The distributions of altered m^{6}A peaks in all chromosomes. **(F)** The top two m^{6}A motifs enriched from the altered m^{6}A peaks.

TABLE 1 | Top 20 altered m^{6}A peaks in human villi during spontaneous abortion in the first trimester.

Chr	Peak start	Peak end	Peak region	Gene name	Regulation	Log2(FC)	P value
chr4	158,171,401	158,172,272	intron	FAM198B	up	5.830	5.76E-03
chr4	119,033,176	119,033,301	3′ UTR	MYOZ2	up	5.829	4.81E-03
chr4	453,467	453,542	intron	ABCA11P	up	5.778	8.64E-03
chr1	169,376,663	169,377,063	exon	NME7	up	5.586	8.54E-03
chrX	101,488,487	101,488,537	non-coding	ARMCX4	up	5.580	7.82E-03
chr4	37,020,627	37,022,548	TTS	LOC100508631	up	5.563	8.18E-03
chr16	69,356,783	69,357,056	exon	TMED6	up	5.263	1.13E-02
chr8	18,221,796	18,221,846	5′ UTR	NAT1	up	5.198	1.48E-02
chr9	88,462,616	88,475,585	intron	NXNL2	up	5.165	1.59E-02
chr4	13,615,416	13,615,466	exon	BOD1L1	up	5.157	1.38E-02
chr4	372,742	375,592	3′ UTR	MIR571	down	–4.054	7.14E-03
chr11	78,658,228	78,658,303	exon	NARS2	down	–3.808	1.70E-02
chr16	12,572,889	12,573,014	3′ UTR	MIR4718	down	–3.588	3.27E-02
chr3	37,819,313	37,819,463	3′ UTR	ITGA9-AS1	down	–3.415	1.37E-03
chr7	83,135,139	83,135,189	exon	PCLO	down	–3.388	2.05E-02
chr1	241,595,581	241,595,642	TTS	CHML	down	–3.307	2.46E-02
chr1	147,757,292	147,758,409	3′ UTR	GJA5	down	–3.233	4.10E-08
chrX	72,204,881	72,204,956	3′ UTR	PIN4	down	–3.199	4.94E-02
chr3	37,819,488	37,819,538	3′ UTR	ITGA9-AS1	down	–3.167	2.36E-03
chr22	30,663,347	30,663,422	TTS	DUSP18	down	–3.159	2.39E-02

3′UTR, 3′untranslated region; 5′UTR, 5′untranslated region; TTS, transcription termination site.

(v.1.2.0) (Meng et al., 2014) was used for the identification of differentially methylated peaks. The GFF annotation file was referred to determine the strand information of m^{6}A peaks. The findMotifsGenome.pl Perl script from the Homer software suite was used for motif search with the "-mask -rna -len 6" parameters. Genomic locations were split into CDS, 5′UTR, 3′UTR, promoter (2 kb upstream and 100 bp downstream of the TSS), and intergenic regions. The distribution of m^{6}A peaks on mRNA was analyzed using the R package Guitar (v.1.7.0) (Cui et al., 2016). Differentially expressed genes were identified using the RNA-seq data (the corresponding MeRIP-seq input library data) by the R package DEseq2 (v.1.32.0) (Love et al., 2014). The R package clusterProfiler (v.4.1.3) (Wu et al., 2021) was used to calculate the biological significance of differentially methylated genes and differentially expressed genes through the Gene Ontology (GO) database and the latest Kyoto Encyclopedia of Genes and Genomes (KEGG) database.

The Construction of Hub Gene Network

The STRING (v11.5) (https://string-db.org/cgi/input.pl) (Szklarczyk et al., 2021) has been widely applied to construct a protein-protein interaction (PPI) network. Based on those DEGs, the "Multiple proteins" option was selected. The minimum required interaction score was set as "high confidence (0.700)" and a PPI network was constructed. And then, the cytoHubba (Chin et al., 2014) was employed to identify hub genes. The eccentricity algorithm was selected and twenty top-ranked genes were chosen as hub genes. Finally, Cytoscape (v3.9.0) (Demchak et al., 2014) was used to visualize the hub gene network.

Statistical Analyses

The *t*-test was used for comparing the statistical significance between two groups. For each analysis, $p < 0.05$ was considered as statistically significant.

Data Availability

The raw sequencing and processed data reported in this study have been deposited in the Sequence Read Archive (SRA) and Gene Expression Omnibus (GEO) database and are accessible at https://dataview.ncbi.nlm.nih.gov/object/PRJNA786693 and https://www.ncbi.nlm.nih.gov/geo/query/acc.cgi?acc=GSE193052, respectively.

RESULTS

Profiles of m^{6}A Modification in Human Villi With Spontaneous Abortion in the First Trimester

Due to the trace of early villous tissue, we performed a micro MeRIP-seq analysis of villous tissues from three patients with spontaneous abortion (SA group) and three controls with induced abortion (normal group) in the first trimester. We detected a total of 18,568 m^{6}A peaks in these two groups by R package exomePeak2. As shown in **Figure 1A**, compared with normal group, SA group had 2,159 significantly upregulated m^{6}A peaks, which corresponded to transcripts of 2,087 genes, and 281 significantly downregulated m^{6}A peaks, which corresponded to transcripts of 311 genes ($|\log2\text{ (fold change)}| > 0.585$ and $p < 0.05$). The top 20 altered m^{6}A peaks were listed in **Table 1**. Then, we investigated the distribution of m^{6}A peaks in the SA and normal group and found that m^{6}A peaks in the SA and normal group were primarily enriched in the coding sequence (CDS) near the stop codon and the whole CDS region, respectively (**Figure 1B**). However, m^{6}A peaks in the SA group showed a distinct pattern from m^{6}A peaks in the normal group with a relative decrease in the number of m^{6}A peaks in the coding sequence (CDS) (42.08 *vs.* 45%) and 5′ untranslated region (5′UTR) (1.64 *vs.* 2%) and a relative increase in the 3′

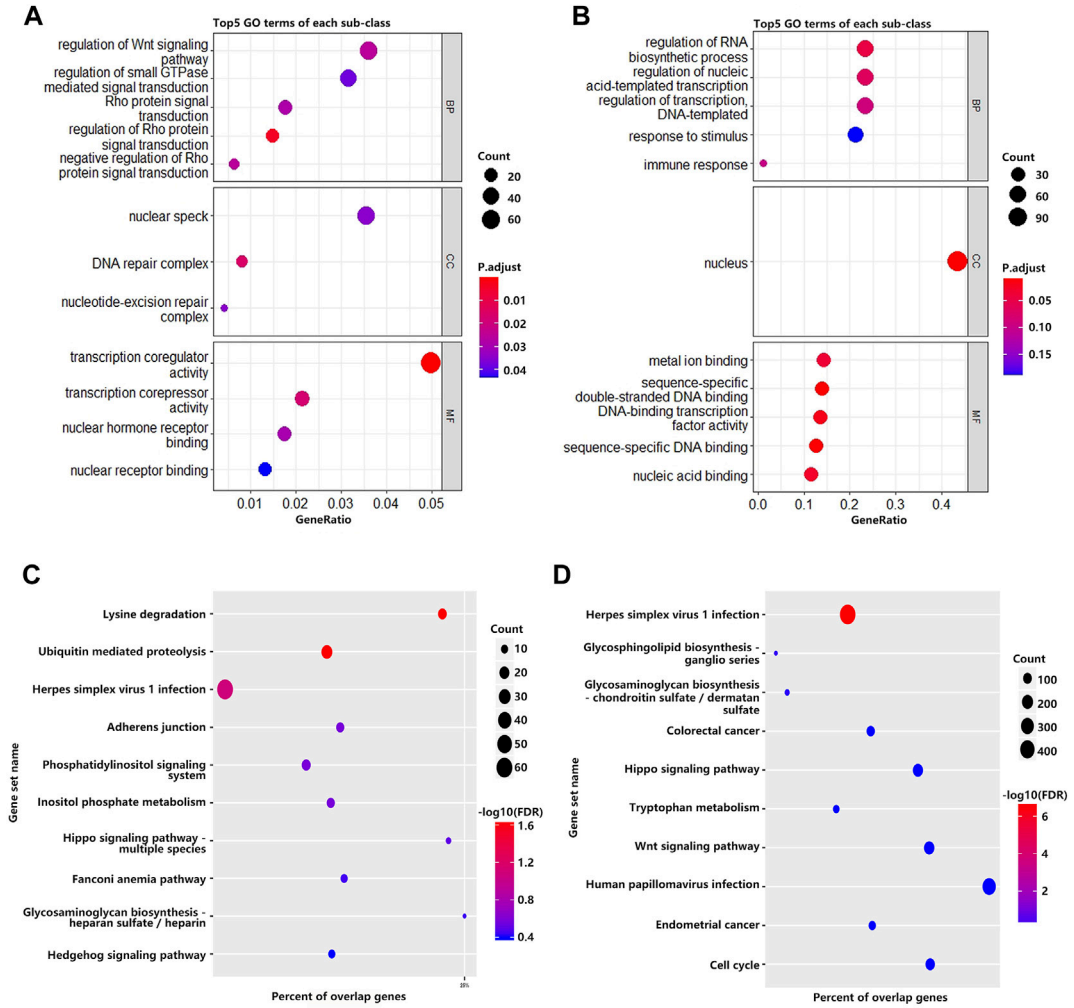

FIGURE 2 | GO and KEGG pathway enrichment analyses of differentially methylated mRNA. **(A)** The top 5 GO terms of genes with significantly upregulated m^{6}A peaks. **(B)** The top 5 GO terms of genes with significantly downregulated m^{6}A peaks. **(C)** The top 10 KEGG pathways of genes with significantly upregulated m^{6}A peaks. **(D)** The top 10 KEGG pathways of genes with significantly downregulated m^{6}A peaks.

untranslated region (3′UTR) (19.93 *vs.* 19%) (**Figure 1C**). By analyzing the distribution of m^{6}A peaks per gene, we found that most genes only had one corresponding m^{6}A peak (1,878/236 genes with upregulated and downregulated peaks, respectively) (**Figure 1D**). Furthermore, dysregulated m^{6}A peaks were found in all chromosomes, except chrY, and were mainly found in chr1, chr2, chr3, chr4, chr5, chr6, chr7, chr17 (**Figure 1E**). Moreover, the m^{6}A peaks were mainly characterized by AUGGAC and UGGACG motif (**Figure 1F**).

GO and KEGG Pathway Enrichment Analysis of Differentially m^{6}A-Modified mRNA

To investigate the biological significance of m^{6}A modification in villous tissues of patients with spontaneous abortion and controls with induced abortion in the first trimester, we performed GO and KEGG pathway enrichment analyses of differentially methylated mRNAs. GO ontology was classified into three categories: biological process (BP), cellular component (CC), and molecular function (MF). The top five significantly enriched BPs, CCs, and MFs of genes with upregulated and downregulated m^{6}A peaks were shown in **Figures 2A,B**, respectively. The results in **Figure 2A** indicated that GO terms such as the regulation of Wnt signaling pathway, Rho protein signal transduction, transcription coregulator activity, and transcription corepressor activity were significantly enriched, and GO terms such as regulation of RNA biosynthetic process, regulation of nucleic acid-templated transcription and DNA-binding transcription factor activity were significantly enriched in **Figure 2B**. For KEGG pathway enrichment analysis, we found that genes with upregulated m^{6}A peaks in villous tissues of patients with spontaneous abortion in the first trimester were significantly associated with the lysine degradation, ubiquitin-mediated proteolysis, herpes simplex virus 1 infection, adherens junction, phosphatidylinositol signaling system, inositol

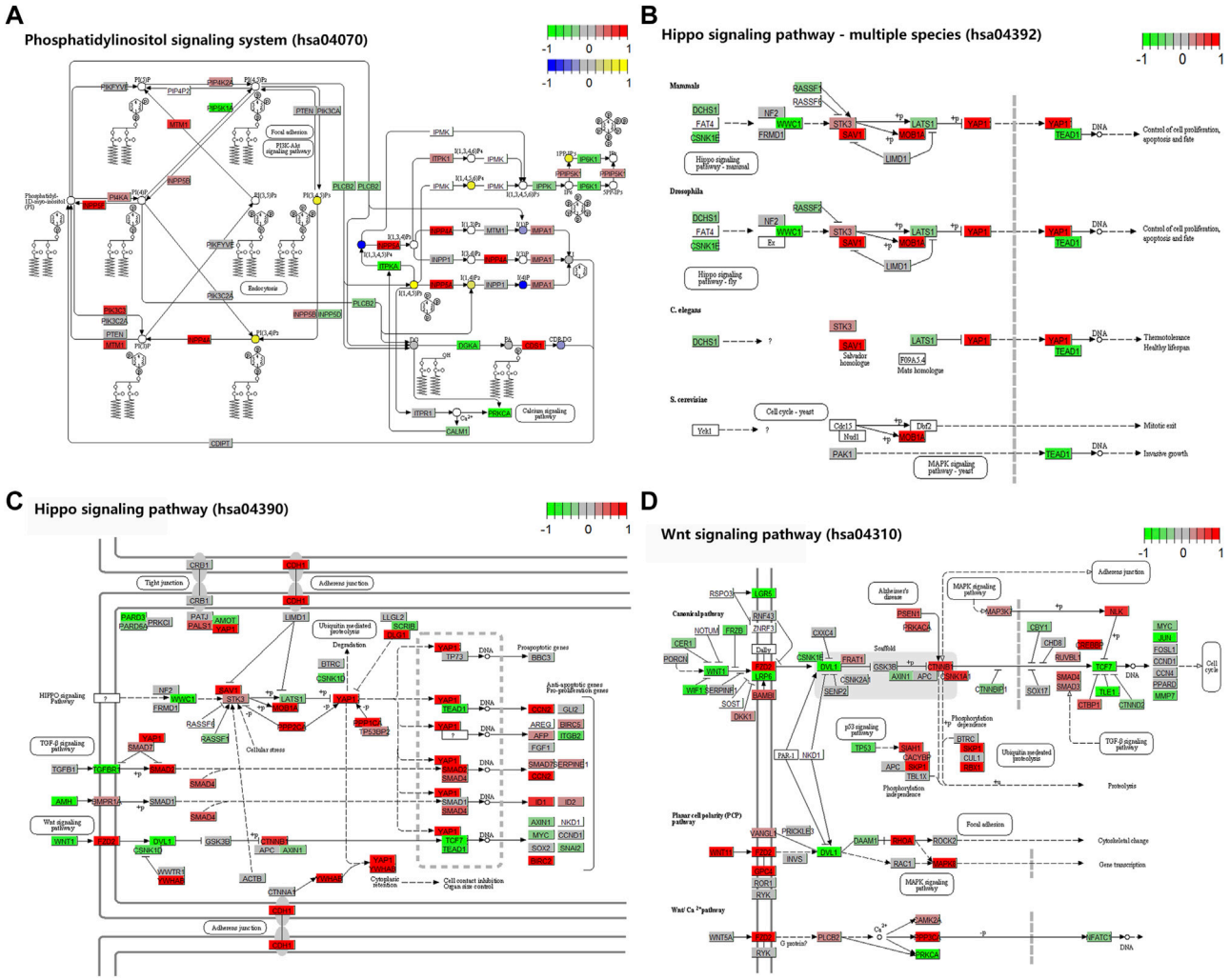

FIGURE 3 | Four major KEGG pathways. **(A)** Phosphatidylinositol signaling system. **(B)** Hippo signaling pathway–multiple species. **(C)** Hippo signaling pathway. **(D)** Wnt signaling pathway. The colors in the graph from red to green indicate the change from high to low in m^{6}A dysregulation on genes. The colors in the graph from yellow to blue indicate the change from high to low in m^{6}A dysregulation on compounds.

phosphate metabolism, and Hippo signaling pathway - multiple species (**Figure 2C**). Genes with downregulated m^{6}A peaks were significantly associated with herpes simplex virus 1 infection, glycosphingolipid biosynthesis-ganglio series, Hippo signaling pathway, tryptophan metabolism, and Wnt signaling pathway (**Figure 2D**). The enrichment of genes in the four major pathways is shown in **Figure 3**.

Overview of mRNA Expression Profiles and Conjoint Analysis of meRIP-Seq and RNA-Seq

Through RNA-seq (meRIP-seq input library), we detected the transcriptome profiles of villous tissues from patients with spontaneous abortion and controls with induced abortion in the first trimester. R package DESeq2 was used to detect differentially expressed genes (DEGs). Compared with normal group, SA group had 254 significantly upregulated genes and 133 significantly downregulated genes (| log2 (fold change) | > 0.585 and $p < 0.05$; **Figures 4A,B**). The MA plot was visualized for these DEGs (**Supplementary Figure S1**). The top 20 DEGs are listed in **Table 2**. The top 5 significantly enriched BPs, CCs, and MFs of genes with upregulated and downregulated expressed genes and top 10 KEGG pathways were displayed in **Supplementary Figure S2**. Based on these DEGs, we construct a PPI network through the STRING database. The hub genes selected from the PPI network are visualized in **Supplementary Figure S3**. According to the eccentricity scores, we identified twenty hub genes with highest confidence scores from the network, and found that most of hub genes were related to immune response and embryonic development. Then, we conducted conjoint analysis of the MeRIP-seq and RNA-seq data and explored the relationship between differential m^{6}As and host gene expression level. We found that the expression level of host gene of differential m^{6}As

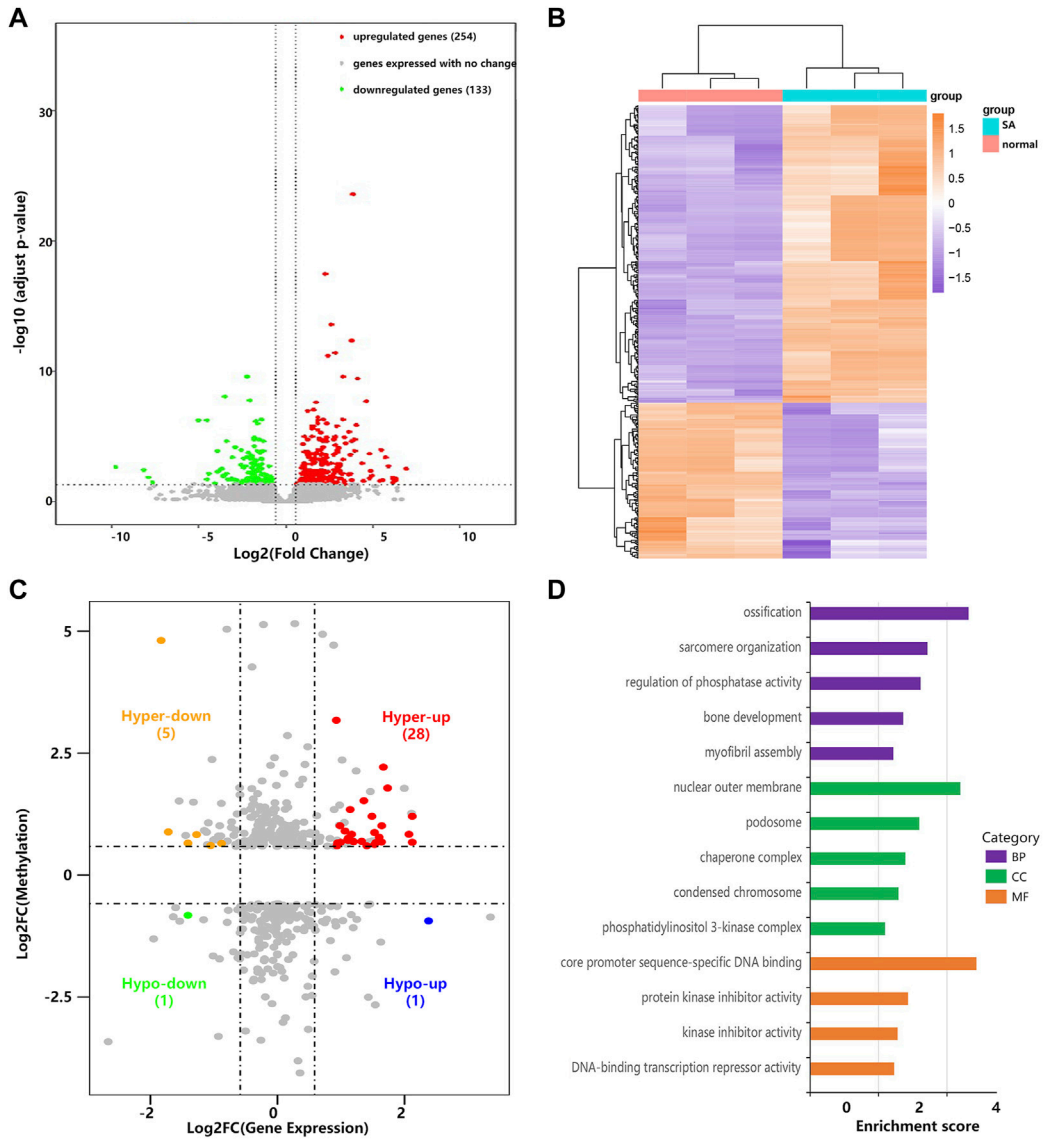

FIGURE 4 | Conjoint analysis of MeRIP-seq and RNA-seq data. **(A)** Volcano plots showing the differentially expressed genes in villous tissues of SA group compared with normal group. **(B)** Heatmap plots showing the differentially expressed genes in villous tissues of SA group compared with normal group. **(C)** Four-quadrant plots showing the distribution of genes with significant changes in both the m^{6}A modification and mRNA levels. **(D)** The top 5 GO terms of genes with significant changes in both the m^{6}A modification and mRNA levels.

was lower in both SA group and normal group compared with constitutive m^{6}As (**Supplementary Figure S4**). Dividing all differentially methylated m^{6}A peaks with all differentially expressed mRNAs into four groups (hyper-up, hyper-down, hypo-up, and hypo-down), we identified 34 hypermethylated m^{6}A peaks in mRNAs that were significantly upregulated (28; hyper-up) or downregulated (6; hyper-down), while 2 hypomethylated m^{6}A peaks in mRNAs that were significantly upregulated (1; hypo-up) or downregulated (1; hypo-down) (**Figure 4C**, **Supplementary Table S1**). Finally, we performed GO and KEGG pathway enrichment analysis to explore the biological function of those genes (35) with differentially methylated m^{6}A peaks and differential expression. The top 5 significantly enriched BPs, CCs, and MFs indicated that these genes were mainly enriched in the ossification (BP category), nuclear outer membrane (CC category), and core promoter sequence-specific DNA binding (MF) (**Figure 4D**). However, no KEGG pathways were significantly enriched.

DISCUSSION

In this study, we performed high-throughput sequencing to reveal the m^{6}A transcriptome-wide map in human villi during spontaneous abortion in the first trimester. Using the MeRIP-seq data, we found 2,398 genes corresponding to 2,440 altered

TABLE 2 | The top 20 differentially expressed mRNAs in human villi during spontaneous abortion in the first trimester.

Gene name	Log2(FC)	Regulation	Location	Strand	P-value
LILRB4	6.994372489	up	chr19:54643889-54670359	+	2.56E-05
KRT6A	6.408677648	up	chr12:52487174-52493257	–	0.000353
TMEM176B	6.402794137	up	chr7:150791285-150801360	–	0.000225
TMEM176A	6.289546685	up	chr7:150800403-150805120	+	0.000221
WNT10A	6.231355116	up	chr2:218880363-218899581	+	0.000217
CTD-2020K17.3	6.217088894	up	chr17:45238028-45241734	–	0.000581
CXCL10	6.158743623	up	chr4:76021117-76023497	–	0.000178
TNC	5.941216251	up	chr9:115019578-115118257	–	1.42E-05
CD300E	5.778269717	up	chr17:74609887-74623738	–	2.10E-06
CXCL9	5.640406283	up	chr4:76001275-76007488	–	0.000375
HBE1	–13.27930895	down	chr11:5268345-5505617	–	1.55E-06
HBZ	–9.7258281	down	chr16:152687-154503	+	1.59E-05
SLC4A1	–8.109924704	down	chr17:44248385-44268141	–	3.30E-05
SPTB	–7.906942374	down	chr14:64746283-64879883	–	0.000189
COX4I2	–7.653108088	down	chr20:31637888-31645006	+	0.000574
LINC02484	–4.950756206	down	chr4:34120894-34269747	–	7.19E-10
ADAMTS18	–4.478881307	down	chr16:77247813-77435114	–	0.000323
RAPGEF4	–4.44120067	down	chr2:172735274-173052893	+	6.25E-10
GOLGA2P7	–4.061744557	down	chr15:84199311-84230136	–	0.000712
AGTR1	–3.91772292	down	chr3:148697784-148743008	+	4.73E-05

m^{6}A peaks, which were highly enriched by the m^{6}A consensus motif (RRACH). The enrichment was not perfectly overlapping the RRACH motif described in literature, which might be related to the parameters (-mask -rna -len 6) used for motif search. These genes were mainly involved in lysine degradation, Hippo signaling pathway, ubiquitin-mediated proteolysis, and glycosphingolipid and glycosaminoglycan biosynthesis. Through conjoint analysis of meRIP-seq and RNA-seq data, we identified 35 genes with differentially methylated m^{6}A peaks and synchronously differential expression, which revealed the relationship between m^{6}A methylation and gene expression. These genes were enriched in the Wnt signaling pathway, phosphatase activity regulation, protein phosphatase inhibitor activity, and transcription inhibitor activity. It was recently reported that m^{6}A inhibition through targeted strategies was effective in counteracting different diseases, such as myeloid leukaemia. This could provide a background for the development of therapeutics and for further investigations in the future (Bedi et al., 2020; Garbo et al., 2021; Moroz-Omori et al., 2021; Yankova et al., 2021).

The cellular mechanisms underlying SA are the proliferation and apoptosis of cytotrophoblasts and human decidual cells (Cinar et al., 2012). Studies have shown that at 6-8 weeks in the first trimester of pregnancy, the expression level of TIMP-1 (tissue inhibitor of MMP-2) in villous tissue is significantly decreased, which leads to the abnormal invasion of trophoblast cells, and thus leads to spontaneous abortion (Kesanakurti et al., 2013). As reported, the high expression of e-cadherin (E-cad) in villous tissue affects the invasion of trophoblast, making it difficult for placenta implantation, resulting in spontaneous abortion (Li et al., 2017). MiR126, located in the region of epidermal growth factor-like domain 7 (EGFL7), negatively regulates vascular endothelial growth factor (VEGF), which reduces shallow implantation of trophoblasts, and finally leads to spontaneous abortion (Schmidt et al., 2007).

Basing on the MeRIP-seq data, we identified some differentially methylated mRNAs which were closely linked to many important pathways. KEGG pathway enrichment analysis results indicated that genes with upregulated m^{6}A modification sites were involved in the regulation of lysine degradation. Some studies have confirmed the relationship between lysine metabolism and early embryo development. Studies illuminated that lysine deprivation during low-protein diets could adversely affect early embryo development (Van Winkle et al., 2020). Lysine was specific to LSD1, a demethylase, which regulated the expression and appropriate timing of key developmental regulators during early embryonic development (Foster et al., 2010). Our results indicated that m^{6}A modification might affect early embryonic development by regulating lysine degradation. For these genes with upregulated m^{6}A modification sites, another related pathway was Hippo signaling pathway. Hippo signaling plays a critical role in early embryonic development as low Hippo activity is required for trophoblast differentiation and high Hippo activity permits inner cell mass formation (Wu and Guan, 2021). During murine preimplantation embryogenesis, Hippo signaling pathway is known to play a significant role in lineage segregation and henceforth the formation of blastocysts (Sasaki, 2015). Our results suggested that modulating m^{6}A modifications of the Hippo signaling pathway might be a possible therapy for in human villi during spontaneous abortion in the first trimester in the future.

In addition, another related pathway was ubiquitin-mediated proteolysis. Studies suggested that ubiquitin-mediated proteolysis could be used to regulate Hippo signaling and thus participate in early embryonic development (Ma et al., 2018). Therefore, m^{6}A modification might affect ubiquitin-mediated proteolysis to regulate Hippo signaling and thus regulate early embryonic development. Genes with downregulated m^{6}A modification sites were mainly enriched in glycosphingolipid and

glycosaminoglycan biosynthesis. Glycosphingolipids (GSLs) were a class of ceramide-based glycolipids essential for embryo development in mammals (Yamashita et al., 1999; Russo et al., 2016), whether glycosaminoglycan (GAG) biosynthetic was important for mouse embryonic stem cells (mESCs) (Nairn et al., 2007). Based on our results, we hypothesized that m^{6}A modification might influence the expression level of some genes related to glycosphingolipid and glycosaminoglycan biosynthesis and thus influence embryo development.

Through the conjoint analysis of MeRIP-seq and RNA-seq data, thirty-five genes with differentially methylated m^{6}A peaks and synchronously differential expression in spontaneous abortion were discovered (**Supplementary Table S1**). Among these genes, IGFBP3, C/EBPβ may be regulated by m^{6}A modification of mRNAs. IGFBP3 (Insulin-like growth factor binding protein 3) with high expression level suggested betted oocyte maturation and early embryo development (Wang et al., 2006). IGFBP3 is highly expressed in the endometrium and at the maternal-fetal interface, which promoted the matrix metalloproteinases 2 (MMP2) expression and cell migration in both human endometrial stromal cells (HESCs) and primary human decidual stromal cells (HDSCs) (Luo et al., 2020). Combined with our results, m^{6}A modification may promote the expression of IGFBP3 and thus promote the high expression of MMP2 and the low expression of its tissue inhibitors TIMP-1, and finally lead to spontaneous abortion. CCAAT/enhancer binding protein β (C/EBPβ) is the earliest marker of enveloping layer (EVL) and is essential for EVL differentiation in zebrafish (Zhang et al., 2021). Studies indicated that C/EBPβ transcription factor could inhibit the mRNA decay of IL-8 and thus repress the inflammatory response (Zhang et al., 2010). Moreover, C/EBPβ is also a biomarker of endometrial receptivity and plays a conserved functional role during embryo implantation (Kannan et al., 2010). Combined with our results, altered m^{6}A modification may influence the expression of C/EBPβ, regulate embryo implantation and thus influence early embryo development. However, detailed molecular mechanisms are still unknown and further exploration deserves careful consideration in the future.

CONCLUSION

Here, we systematically investigated the whole-transcriptome m^{6}A profile of human villous tissues during spontaneous abortion in the first trimester, revealing a dynamic m^{6}A methylation landscape in spontaneous abortion for the first time. Based on the conjoint analysis of MeRIP-seq and RNA-seq data, many genes with differentially methylated m^{6}A peaks and synchronously differential expression were discovered. It indicated a potential link between m^{6}A methylation and mRNA expression, and might provide an alternative therapeutic strategy for spontaneous abortion. In addition, the m^{6}A modification profile might provide novel insights into the pathogenesis and treatment of spontaneous abortion during early pregnancy.

DATA AVAILABILITY STATEMENT

The original contributions presented in the study are publicly available. This data can be found here: https://www.ncbi.nlm.nih.gov/Traces/study/?acc=SRP350117&o=acc_s%3

ETHICS STATEMENT

The studies involving human participants were reviewed and approved by Medicine Ethics Committee of Shenzhen Second People's Hospital. The patients/participants provided their written informed consent to participate in this study.

AUTHOR CONTRIBUTIONS

JS performed sample collection, data analysis and wrote the first draft. KT and YP conducted the whole experiment together. JL and ZX contributed to the sample collection. SC, and ZL gave advice for the data analysis. LW and RD gave constructive advice for the whole project.

FUNDING

This work was supported by the grants from the Science and Technology Innovation Committee of Shenzhen (JCYJ20190806165007495), the Shenzhen Foundation of Science and Technology (JCYJ20210324103606017), and the Guangdong Basic and Applied Basic Research Foundation (2019A1515011693).

SUPPLEMENTARY MATERIAL

The Supplementary Material for this article can be found online at: https://www.frontiersin.org/articles/10.3389/fgene.2022.861853/full#supplementary-material

REFERENCES

Aguilo, F., Zhang, F., Sancho, A., Fidalgo, M., Di Cecilia, S., Vashisht, A., et al. (2015). Coordination of m(6)A mRNA Methylation and Gene Transcription by ZFP217 Regulates Pluripotency and Reprogramming. *Cell Stem Cell* 17, 689–704. doi:10.1016/j.stem.2015.09.005

Bedi, R. K., Huang, D., Eberle, S. A., Wiedmer, L., Śledź, P., and Caflisch, A. (2020). Small-Molecule Inhibitors of METTL3, the Major Human Epitranscriptomic Writer. *ChemMedChem* 15, 744–748. doi:10.1002/cmdc.202000011

Bolger, A. M., Lohse, M., and Usadel, B. (2014). Trimmomatic: A Flexible Trimmer for Illumina Sequence Data. *Bioinformatics* 30, 2114–2120. doi:10.1093/bioinformatics/btu170

Chen, X., Guo, D.-Y., Yin, T.-L., and Yang, J. (2021). Non-Coding RNAs Regulate Placental Trophoblast Function and Participate in Recurrent Abortion. *Front. Pharmacol.* 12, 646521. doi:10.3389/fphar.2021.646521

Chin, C.-H., Chen, S.-H., Wu, H.-H., Ho, C.-W., Ko, M.-T., and Lin, C.-Y. (2014). cytoHubba: Identifying Hub Objects and Sub-Networks from Complex Interactome. *BMC Syst. Biol.* 8, S11. doi:10.1186/1752-0509-8-S4-S11

Cinar, O., Kara, F., and Can, A. (2012). Potential Role of Decidual Apoptosis in the Pathogenesis of Miscarriages. *Gynecol. Endocrinol.* 28, 382–385. doi:10.3109/09513590.2011.633127

Cui, X., Wei, Z., Zhang, L., Liu, H., Sun, L., Zhang, S.-W., et al. (2016). Guitar: An R/Bioconductor Package for Gene Annotation Guided Transcriptomic Analysis of RNA-Related Genomic Features. *BioMed Res. Int.* 2016, 8367534. doi:10.1155/2016/8367534

Demchak, B., Hull, T., Reich, M., Liefeld, T., Smoot, M., Ideker, T., et al. (2014). Cytoscape: The Network Visualization Tool for GenomeSpace Workflows. *F1000Res* 3, 151. doi:10.12688/f1000research.4492.2

Foster, C. T., Dovey, O. M., Lezina, L., Luo, J. L., Gant, T. W., Barlev, N., et al. (2010). Lysine-Specific Demethylase 1 Regulates the Embryonic Transcriptome and CoREST Stability. *Mol. Cell. Biol.* 30, 4851–4863. doi:10.1128/mcb.00521-10

Gao, Y., Pei, G., Li, D., Li, R., Shao, Y., Zhang, Q. C., et al. (2019). Multivalent m6A Motifs Promote Phase Separation of YTHDF Proteins. *Cell Res.* 29, 767–769. doi:10.1038/s41422-019-0210-3

Garbo, S., Zwergel, C., and Battistelli, C. (2021). m6A RNA Methylation and Beyond - The Epigenetic Machinery and Potential Treatment Options. *Drug Discov. Today* 26, 2559–2574. doi:10.1016/j.drudis.2021.06.004

Gaspar, J. M. (2018). Improved Peak-Calling with MACS2. bioRxiv. doi:10.1101/496521

Geula, S., Moshitch-Moshkovitz, S., Dominissini, D., Mansour, A. A., Kol, N., Salmon-Divon, M., et al. (2015). m6A mRNA Methylation Facilitates Resolution of Naïve Pluripotency Toward Differentiation. *Science* 347, 1002–1006. doi:10.1126/science.1261417

Huang, H., Weng, H., Sun, W., Qin, X., Shi, H., Wu, H., et al. (2020). Publisher Correction: Recognition of RNA N6-Methyladenosine by IGF2BP Proteins Enhances mRNA Stability and Translation. *Nat. Cell Biol.* 22, 1288. doi:10.1038/s41556-020-00580-y

Ivanova, I., Much, C., Di Giacomo, M., Azzi, C., Morgan, M., Moreira, P. N., et al. (2017). The RNA m6A Reader YTHDF2 Is Essential for the Post-Transcriptional Regulation of the Maternal Transcriptome and Oocyte Competence. *Mol. Cell.* 67, 1059–1067. doi:10.1016/j.molcel.2017.08.003

Jia, G., Fu, Y., Zhao, X., Dai, Q., Zheng, G., Yang, Y., et al. (2011). N6-Methyladenosine in Nuclear RNA is a Major Substrate of the Obesity-Associated FTO. *Nat. Chem. Biol.* 7, 885–887. doi:10.1038/nchembio.687

Kannan, A., Fazleabas, A. T., Bagchi, I. C., and Bagchi, M. K. (2010). The Transcription Factor C/EBPβ is a Marker of Uterine Receptivity and Expressed at the Implantation Site in the Primate. *Reprod. Sci.* 17, 434–443. doi:10.1177/1933719110361384

Ke, S., Pandya-Jones, A., Saito, Y., Fak, J. J., Vågbø, C. B., Geula, S., et al. (2017). m6A mRNA Modifications are Deposited in Nascent Pre-mRNA and are not Required for Splicing but Do Specify Cytoplasmic Turnover. *Genes Dev.* 31, 990–1006. doi:10.1101/gad.301036.117

Kesanakurti, D., Chetty, C., Dinh, D. H., Gujrati, M., and Rao, J. S. (2013). Role of MMP-2 in the Regulation of IL-6/Stat3 Survival Signaling via Interaction with α5β1 Integrin in Glioma. *Oncogene* 32, 327–340. doi:10.1038/onc.2012.52

Kim, D., Langmead, B., and Salzberg, S. L. (2015). HISAT: A Fast Spliced Aligner with Low Memory Requirements. *Nat. Methods* 12 (4), 357–360. doi:10.1038/nmeth.3317

Langmead, B., and Salzberg, S. (2013). Fast Gapped-Read Alignment with Bowtie 2. *Nat. Methods* 9 (4), 357–359. doi:10.1038/nmeth.1923

Li, P., Shi, Y., Shuai, H., Cai, Y., Lu, W., Wang, G., et al. (2017). Alterted SLIT2/ROBO1 Signalling is Linked to Impaired Placentation of Missed and Threatened Miscarriage in Early Pregnancy. *Histopathology* 71, 543–552. doi:10.1111/his.13250

Liu, Y., Tang, Y., Ye, D., Ma, W., Feng, S., Li, X., et al. (2018). Impact of Abnormal DNA Methylation of Imprinted Loci on Human Spontaneous Abortion. *Reprod. Sci.* 25, 131–139. doi:10.1177/1933719117704906

Love, M. I., Huber, W., and Anders, S. (2014). Moderated Estimation of Fold Change and Dispersion for RNA-Seq Data With DESeq2. *Genome Biology* 15, 550. doi:10.1186/s13059-014-0550-8

Luo, J., Zhu, H., Chang, H. M., Lin, Y. M., Yang, J., and Leung, P. C. K. (2020). The Regulation of IGFBP3 by BMP2 Has a Role in Human Endometrial Remodeling. *FASEB J.* 34, 15462–15479. doi:10.1096/fj.202000508R

Ma, X., Guo, X., Richardson, H. E., Xu, T., and Xue, L. (2018). POSH Regulates Hippo Signaling Through Ubiquitin-Mediated Expanded Degradation. *Proc. Natl. Acad. Sci. U.S.A.* 115, 2150–2155. doi:10.1073/pnas.1715165115

Mendel, M., Chen, K.-M., Homolka, D., Gos, P., Pandey, R. R., McCarthy, A. A., et al. (2018). Methylation of Structured RNA by the m6A Writer METTL16 Is Essential for Mouse Embryonic Development. *Mol. Cell* 71, 986–1000. doi:10.1016/j.molcel.2018.08.004

Meng, J., Lu, Z., Liu, H., Zhang, L., Zhang, S., Chen, Y., et al. (2014). A Protocol for RNA Methylation Differential Analysis with MeRIP-Seq Data and exomePeak R/Bioconductor Package. *Methods* 69, 274–281. doi:10.1016/j.ymeth.2014.06.008

Meyer, K. D., Patil, D. P., Zhou, J., Zinoviev, A., Skabkin, M. A., Elemento, O., et al. (2015). 5′ UTR m6A Promotes Cap-Independent Translation. *Cell* 163, 999–1010. doi:10.1016/j.cell.2015.10.012

Moroz-Omori, E. V., Huang, D., Kumar Bedi, R., Cheriyamkunnel, S. J., Bochenkova, E., Dolbois, A., et al. (2021). METTL3 Inhibitors for Epitranscriptomic Modulation of Cellular Processes. *ChemMedChem* 16, 3035–3043. doi:10.1002/cmdc.202100291

Nairn, A. V., Kinoshita-Toyoda, A., Toyoda, H., Xie, J., Harris, K., Dalton, S., et al. (2007). Glycomics of Proteoglycan Biosynthesis in Murine Embryonic Stem Cell Differentiation. *J. Proteome Res.* 6, 4374–4387. doi:10.1021/pr070446f

Pendleton, K. E., Chen, B., Liu, K., Hunter, O. V., Xie, Y., Tu, B. P., et al. (2017). The U6 snRNA m6A Methyltransferase METTL16 Regulates SAM Synthetase Intron Retention. *Cell* 169, 824–835. doi:10.1016/j.cell.2017.05.003

Rossen, L. M., Ahrens, K. A., and Branum, A. M. (2018). Trends in Risk of Pregnancy Loss Among US Women, 1990-2011. *Paediatr. Perinat. Epidemiol.* 32, 19–29. doi:10.1111/ppe.12417

Russo, D., Parashuraman, S., and D'Angelo, G. (2016). Glycosphingolipid-Protein Interaction in Signal Transduction. *Int. J. Mol. Sci.* 17, 1732. doi:10.3390/ijms17101732

Sasaki, H. (2015). Position- and Polarity-Dependent Hippo Signaling Regulates Cell Fates in Preimplantation Mouse Embryos. *Semin. Cell Dev. Biol.* 47-48, 80–87. doi:10.1016/j.semcdb.2015.05.003

Schmidt, M., Paes, K., De Mazière, A., Smyczek, T., Yang, S., Gray, A., et al. (2007). EGFL7 Regulates the Collective Migration of Endothelial Cells by Restricting Their Spatial Distribution. *Development* 134, 2913–2923. doi:10.1242/dev.002576

Shi, H., Wang, X., Lu, Z., Zhao, B. S., Ma, H., Hsu, P. J., et al. (2017). YTHDF3 Facilitates Translation and Decay of N6-Methyladenosine-Modified RNA. *Cell Res.* 27, 315–328. doi:10.1038/cr.2017.15

Sui, X., Hu, Y., Ren, C., Cao, Q., Zhou, S., Cao, Y., et al. (2020). METTL3-Mediated m6A Is Required for Murine Oocyte Maturation and Maternal-To-Zygotic Transition. *Cell Cycle* 19, 391–404. doi:10.1080/15384101.2019.1711324

Szklarczyk, D., Gable, A. L., Nastou, K. C., Lyon, D., Kirsch, R., Pyysalo, S., et al. (2021). The STRING Database in 2021: Customizable Protein-Protein Networks, and Functional Characterization of User-Uploaded Gene/Measurement Sets. *Nucleic Acids Res.* 49, D605–D612. doi:10.1093/nar/gkaa1074

Van Winkle, L. J., Galat, V., and Iannaccone, P. M. (2020). Lysine Deprivation During Maternal Consumption of Low-Protein Diets Could Adversely Affect Early Embryo Development and Health in Adulthood. *Int. J. Environ. Res. Public Health* 17, 5462. doi:10.3390/ijerph17155462

Wang, J., Yang, J., Yan, Y., Zhu, Z., Mu, Y., Wang, X., et al. (2019). Effect of Adoptive Transfer of CD4+CD25+Foxp3+ Treg Induced by Trichostatin A on the Prevention of Spontaneous Abortion. *J. Reprod. Immunol.* 131, 30–35. doi:10.1016/j.jri.2018.12.002

Wang, T., Chang, C., Wu, H., Chiu, Y., Chen, C., and Wang, H. (2006). Insulin-Like Growth Factor-II (IGF-II), IGF-Binding Protein-3 (IGFBP-3), and IGFBP-4 in Follicular Fluid are Associated with Oocyte Maturation and Embryo Development. *Fertil. Steril.* 86, 1392–1401. doi:10.1016/j.fertnstert.2006.03.064

Wang, X., Feng, J., Xue, Y., Guan, Z., Zhang, D., Liu, Z., et al. (2016). Structural Basis of N^6-Adenosine Methylation by the METTL3–METTL14 Complex Chemical Modifications of RNA Have Essential Roles in a Vast Range of Cellular Processes. *Nature* 534 (7608), 575–578. doi:10.1038/nature18298

Wang, X., Huang, N., Yang, M., Wei, D., Tai, H., Han, X., et al. (2017). FTO is Required for Myogenesis by Positively Regulating mTOR-PGC-1α Pathway-Mediated Mitochondria Biogenesis. *Cell Death Dis.* 8, e2702. doi:10.1038/cddis.2017.122

Wang, X., Lu, Z., Gomez, A., Hon, G. C., Yue, Y., Han, D., et al. (2014). N^6-Methyladenosine-Dependent Regulation of Messenger RNA Stability. *Nature* 505, 117–120. doi:10.1038/nature12730

Wang, X., Zhao, B. S., Roundtree, I. A., Lu, Z., Han, D., Ma, H., et al. (2015). N^6-Methyladenosine Modulates Messenger RNA Translation Efficiency. *Cell* 161, 1388–1399. doi:10.1016/j.cell.2015.05.014

Wu, T., Hu, E., Xu, S., Chen, M., Guo, P., Dai, Z., et al. (2021). ClusterProfiler 4.0: A Universal Enrichment Tool for Interpreting Omics Data. *Innovation(China)* 2, 100141. doi:10.1016/j.xinn.2021.100141

Wu, Z., and Guan, K.-L. (2021). Hippo Signaling in Embryogenesis and Development. *Trends Biochem. Sci.* 46, 51–63. doi:10.1016/j.tibs.2020.08.008

Xiao, S., Cao, S., Huang, Q., Xia, L., Deng, M., Yang, M., et al. (2019). The RNA N^6-Methyladenosine Modification Landscape of Human Fetal Tissues. *Nat. Cell Biol.* 21, 651–661. doi:10.1038/s41556-019-0315-4

Xiao, W., Adhikari, S., Dahal, U., Chen, Y.-S., Hao, Y.-J., Sun, B.-F., et al. (2016). Nuclear m6A Reader YTHDC1 Regulates mRNA Splicing. *Mol. Cell* 61, 507–519. doi:10.1016/j.molcel.2016.01.012

Xu, C., Liu, K., Ahmed, H., Loppnau, P., Schapira, M., and Min, J. (2015). Structural Basis for the Discriminative Recognition of N^6-Methyladenosine RNA by the Human YT521-B Homology Domain Family of Proteins. *J. Biol. Chem.* 290, 24902–24913. doi:10.1074/jbc.M115.680389

Yamashita, T., Wada, R., Sasaki, T., Deng, C., Bierfreund, U., Sandhoff, K., et al. (1999). A Vital Role for Glycosphingolipid Synthesis During Development and Differentiation. *Proc. Natl. Acad. Sci. U.S.A.* 96, 9142–9147. doi:10.1073/pnas.96.16.9142

Yankova, E., Blackaby, W., Albertella, M., Rak, J., De Braekeleer, E., Tsagkogeorga, G., et al. (2021). Small-Molecule Inhibition of METTL3 as a Strategy Against Myeloid Leukaemia. *Nature* 593, 597–601. doi:10.1038/s41586-021-03536-w

Zhang, C., Chen, Y., Sun, B., Wang, L., Yang, Y., Ma, D., et al. (2017). M6A Modulates Haematopoietic Stem and Progenitor Cell Specification. *Nature* 549, 273–276. doi:10.1038/nature23883

Zhang, X., Wu, Z., Bu, M., Hu, R., Zhang, X., Li, W., et al. (2021). The CCAAT/Enhancer Binding Protein Beta (Cebpb) Is Essential for the Development of Enveloping Layer (EVL) in Zebrafish. *Aquac. Fish.* 9 (5), e95087. doi:10.1016/j.aaf.2021

Zhang, Z., Xing, X., Hensley, G., Chang, L.-W., Liao, W., Abu-Amer, Y., et al. (2010). Resistin Induces Expression of Pro-Inflammatory Cytokines and Chemokines in Human Articular Chondrocytes via Transcription and mRNA Stabilization. *Arthritis Rheum.* 62 (7), 1993–2003. doi:10.1002/art.27473

Zheng, G., Dahl, J. A., Niu, Y., Fedorcsak, P., Huang, C.-M., Li, C. J., et al. (2013). ALKBH5 is a Mammalian RNA Demethylase that Impacts RNA Metabolism and Mouse Fertility. *Mol. Cell* 49, 18–29. doi:10.1016/j.molcel.2012.10.015

Conflict of Interest: The authors declare that the research was conducted in the absence of any commercial or financial relationships that could be construed as a potential conflict of interest.

Publisher's Note: All claims expressed in this article are solely those of the authors and do not necessarily represent those of their affiliated organizations, or those of the publisher, the editors and the reviewers. Any product that may be evaluated in this article, or claim that may be made by its manufacturer, is not guaranteed or endorsed by the publisher.

frontiers | Frontiers in Genetics

TYPE Original Research
PUBLISHED 13 October 2022
DOI 10.3389/fgene.2022.1030275

OPEN ACCESS

EDITED BY
Kunqi Chen,
Fujian Medical University, China

REVIEWED BY
Bowen Song,
University of Liverpool, United Kingdom
Songyao Zhang,
National University of Singapore, Singapore

*CORRESPONDENCE
Hong Liu,
liuhongzhang0101@163.com

†These authors contributed equally to this work and share the first authorship

SPECIALTY SECTION
This article was submitted to Epigenomics and Epigenetics, a section of the journal Frontiers in Genetics

RECEIVED 28 August 2022
ACCEPTED 03 October 2022
PUBLISHED 13 October 2022

CITATION
Huang Z, Lou K and Liu H (2022), A novel prognostic signature based on N7-methylguanosine-related long non-coding RNAs in breast cancer. *Front. Genet.* 13:1030275. doi: 10.3389/fgene.2022.1030275

A novel prognostic signature based on N7-methylguanosine-related long non-coding RNAs in breast cancer

Zhidong Huang†, Kaixin Lou† and Hong Liu*

The Second Surgical Department of Breast Cancer, Tianjin Medical University Cancer Institute and Hospital, National Clinical Research Center for Cancer, Key Laboratory of Cancer Prevention and Therapy, Tianjin's Clinical Research Center for Cancer, Tianjin, China

Long non-coding RNA (lncRNA) are closely associated with the occurrence and progression of tumors. However, research on N7-methylguanosine (m7G)-related lncRNA in breast cancer is lacking. Therefore, the present study explored the prognostic value, gene expression characteristics, and effects of m7G-related lncRNA on tumor immune cell infiltration and tumor mutational burden (TMB) in breast cancer. lncRNA expression matrices and clinical follow-up data of patients with breast cancer were obtained from The Cancer Genome Atlas, revealing eight significantly differentially expressed and prognostically relevant m7G-related lncRNAs in breast cancer tissues: *BAIAP2-DT*, *COL4A2-AS1*, *FARP1-AS1*, *RERE-AS1*, *NDUFA6-DT*, *TFAP2A-AS1*, *LINC00115*, and *MIR302CHG*. A breast cancer prognostic signature was created based on these m7G-related lncRNAs according to least absolute shrinkage and selection operator Cox regression. The prognostic signature combined with potential prognostic factors showed independent prognostic value, reliability, and specificity. Meanwhile, we constructed a risk score-based nomogram to assist clinical decision-making. Gene set enrichment analysis revealed that low- and high-risk group were associated with metabolism-related pathways. Our study demonstrated the association between tumor immune cell infiltration based on analyses with the CIBERSORT algorithm and prognostic signature. We also assessed the correlation between prognostic signature and TMB. Lastly, quantitative real-time polymerase chain reaction analysis was performed to validate differentially expressed lncRNAs. The effective prognostic signature based on m7G-related lncRNAs has the potential to predict the survival prognosis of patients with breast cancer. The eight m7G-related lncRNAs identified in this study might represent potential biomarkers and therapeutic targets of breast cancer.

KEYWORDS

breast cancer, m7G-related lncRNA, prognostic signature, tumor immune cell infiltration, tumor mutational burden

1 Introduction

Breast cancer (BC) is the most common malignancy worldwide (Winters et al., 2017), and its mortality rate is increasing every year. Among all malignant diseases, representing approximately 23% of cancer-related deaths, BC is considered a leading cause of death in postmenopausal women (Akram et al., 2017). The World Health Organization emphasizes that early diagnosis remains the most critical approach for improving the outcomes and survival rate of patients with BC (Bray et al., 2018). Therefore, it is indispensable to explore novel prognostic biomarkers and develop further measures for the diagnosis and treatment of BC.

Multiple mechanisms intertwine to ensure the correct and timely expression of each gene, with several of these mechanisms targeting the life cycle of RNA molecules, from transcription to translation (Batista, 2017; Zhang et al., 2019a). The modification of RNA have been reportedly demonstrated a crucial link with the development of cancer, as well as cardiovascular, metabolic, neurological, and other diseases, because of their reversibility, dynamics, and involvement in important biological processes (Jonkhout et al., 2017). The rapid development of RNA methylation profiling technologies and high-throughput sequencing (Qiang et al., 2018; Zou et al., 2019; Hasan et al., 2020; Tang et al., 2021) has revealed that N7-methylguanosine (m7G) modification is a considerable portion of RNA modifications.

As one of the most prevalent RNA modifications, m7G modifications are usually located in the 5′ cap and inner position of eukaryotic mRNAs or within rRNA and tRNA (Zhang et al., 2019b; Song et al., 2020). To date, studies on m7G primary focused on methylases of m7G, including the Trm8p/Trm82p heterodimer complex in yeast and the corresponding homologous methyltransferase-like protein-1 (METTL1) and WD repeat domain 4 (WDR4) proteins in humans. It has been reported that the METTL1/WDR4 complex could stabilize the tertiary structure of tRNA through the installation of m7G modifications at site G46 of diverse tRNA variable loops (Shaheen et al., 2015). In addition, the METTL1/WDR4 complex promotes miRNA biogenesis by modifying primary miRNA transcripts with m7G (Pandolfini et al., 2019). In addition, research has confirmed that the m7G modification is tightly correlated to tumor development and progression. In intrahepatic cholangiocarcinoma, the methylase METTL1 mediates m7G tRNA modification, selectively regulating the translation of oncogenic transcripts, including genes involved with the cell cycle and epidermal growth factor receptor (EGFR) pathways (Chen Z. et al., 2021). In hepatocellular carcinoma, c-Myc (MYC) activates WDR4 transcription and facilitates the stability and translation of CCNB1 mRNA through m7G modification, affecting the phosphorylation of PI3K and AKT and promoting P53 ubiquitination, ultimately fueling the progression of hepatocellular carcinoma (Chen Z. et al., 2021). In BC, the proliferative activity of BC cells is approximately 35% higher in patients with *PIK3CA* mutations, which are dependent on the m7G regulator mRNA cap methyltransferase (RNMT). As such, RNMT-targeted therapies in patients with *PIK3CA* mutations have better developmental prospects (Dunn et al., 2019). However, further m7G RNA methylation studies are needed to explore the mechanisms underlying cancer development.

Advances in genome sequencing technology have revealed that most of the genome does not encode proteins; nevertheless, non-coding genetic material is of great importance to various biological processes, like DNA methylation and RNA modification. Non-coding RNAs can be divided into two major categories based on their length: short non-coding RNAs (e.g., miRNAs and snRNAs) and long non-coding RNAs (lncRNAs). lncRNAs, a large group of structurally complex RNA genes, could regulate gene expression by interacting with DNA, RNA, or protein molecules and play cellular roles through various mechanisms. lncRNAs have been proposed as biomarkers of cancer (Lai et al., 2020; Li et al., 2021). For instance, *CAT104*, *LINC01234*, and *STXBP5-AS1* have been confirmed to predict the prognosis of patients with BC (Fernandes et al., 2019). Compared with the healthy controls, plasma lncRNA *HULC* concentrations are higher in patients with hepatocellular carcinoma (Parasramka et al., 2016). Likewise, overexpressed in prostate cancer, *PCA3* is considered as a diagnostic biomarker and therapeutic target, which is a prostate-specific lncRNA (Lee et al., 2011). Identifying the differential expression of lncRNAs in tumors, which play roles in promoting both tumorigenesis and tumor suppression, provides an opportunity to develop new cancer therapies based on targeting lncRNAs.

Currently, studies on the interaction between m7G modification and lncRNAs in BC are lacking. Thus, the purpose of present study is to explore the prognostic ability, gene expression features, clinical value, and predictive value on tumor immune cell infiltration and TMB of m7G-related lncRNAs in BC. To this end, we identified prognostic m7G-related lncRNAs in BC, created a prognostic risk signature, and further developed a nomogram according to the risk score, presenting a tool with promising prognostic value for BC (Figure 1).

2 Materials and methods

2.1 Data collection and processing

The lncRNA expression and clinical follow-up data shown in this research were collected from The Cancer Genome Atlas (TCGA) database (http://cancergenome.nih.gov/). Data from 1,222 breast tissues, including 1109 BC and 113 normal tissues, were analyzed. Table 1 presents the clinicopathological characteristics of the patients.

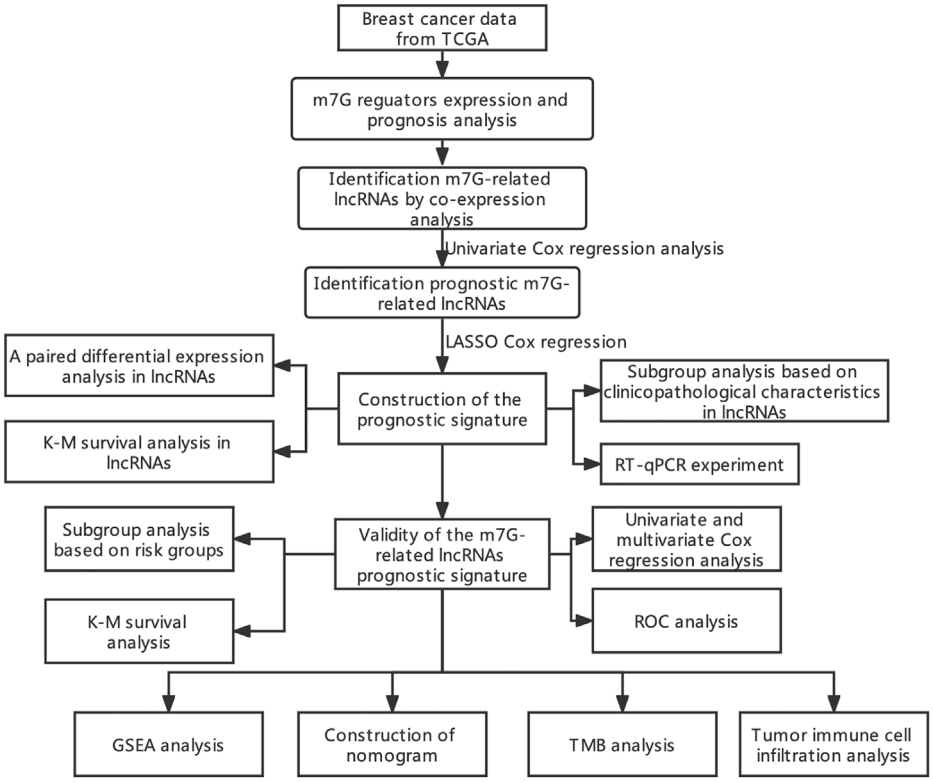

FIGURE 1
Flow chart of the study.

2.2 Identification of m7G-related lncRNAs

From previously published studies, we extracted 40 m7G regulators; gene sets were selected from the GSEA (https://www.gsea-msigdb.org) database ("GOMF_M7G_5_PPPN_DIPHOSPHATASE_ACTIVITY", "GOMF_RNA_7_METHYLGUANOSINE_CAP_BINDING", and "GOMF_RNA_CAP_BINDING"). Pearson correlation analysis was performed using the "limma" R package to select m7G-lncRNA. The m7G-lncRNA pairs with a correlation coefficient >0.4 and $p < 0.001$ were kept. A total of 429 m7G-related lncRNAs were identified. The "dplyr," "ggalluvial," and "ggplot2" R packages were used to visualize the results of the m7G-lncRNA co-expression network as Sankey diagrams.

2.3 Selection of prognostic m7G-lncRNAs

First, we conducted a univariate Cox proportional hazards analysis with a $p < 0.01$ to select m7G-related lncRNAs that has association with the survival of patients with BC. Subsequently, using the least absolute shrinkage and selection operator (LASSO) Cox regression analysis, the best prognostically relevant lncRNAs were selected to build the prognostic signature. Gene interaction networks and Sankey plots were generated using Cytoscape 3.8, "dplyr," "ggalluvial," and "ggplot2" R packages.

2.4 Development and validation of the m7G-lncRNA prognostic signature (m7G-LPS) and nomogram

We used the "glmnet" R package to develop a lasso signature, which optimizes the L1 regularization parameter lambda through a built-in cross-validation function. With the help of the following formula, we calculated the risk score for each patient:

$$Risk\ score = \sum_{i=1}^{n} Coef\,i * xi$$

where $Coef_i$ and x_i represent the survival-related regression coefficient and expression of each m7G-lncRNA, respectively.

Thereafter, based on the median of the prognostic risk score, the patient was assigned to either low- or high-risk groups. The heat map and scatter plots were generated using the heatmap

TABLE 1 Clinical characteristics of breast cancer patients in the training cohort.

Variables	No. of patients	Percentage (%)
Age (years)		
≤55	471	42.9
>55	626	57.1
Unknown	19	1.7
Gender		
Female	1,085	98.9
Male	12	1.1
Pathological stage		
I	183	16.7
II	621	56.6
III	249	22.7
IV	20	1.8
Unknown	24	2.2
T stage		
T1	281	25.6
T2	635	57.9
T3	138	12.6
T4	40	3.6
Unknown	3	0.3
N stage		
N0	516	47.0
N1	364	33.2
N2	120	10.9
N3	77	7.0
Unknown	20	1.8
M stage		
M0	912	83.1
M1	22	2.0
Unknown	163	14.9

function in R. The survival curves were plotted with the Kaplan-Meier method and adopted to analyze the discrepancy in overall survival (OS) between patients in the low- and high-risk groups. Univariate and multivariate Cox regression analyses were implemented to evaluate the independence of the risk score in predicting prognosis compared to other clinical variables. With the aid of the R package "ROCR," the performance of the prognostic signature was evaluated by receiver operating characteristic (ROC) curve analysis. We then developed a nomogram using the R library "rms" package based on the independent prognostic factors for the clinical quantitative prediction of survival in patients with BC. Nomogram calibration was assessed using calibration plots. The genomes, which contains m7G genomes, m7G-lncRNA genomes, and m7G-LPS group expression profiles were implemented for effective dimensionality reduction, pattern recognition, and exploratory visual analysis through principal component analysis (PCA).

2.5 Gene set enrichment analysis (GSEA) analysis

GSEA analysis was performed to identify potential biological signaling pathways involved in low- and high-risk groups. When the |normalized enrichment score| > 1, nominal p-value < 0.05, and false-discovery rate q-value < 0.25, the pathways were defined as significantly enriched.

2.6 Correlation between the prognostic signature and tumor immune cell infiltration

The CIBERSORT with the LM22 gene set that we obtained from the CIBERSORT website was utilized to estimate the total immune infiltration in each BC sample and immune cell subsets (http://cibersort.stanford.edu/). Defining 22 human immune cell subtypes, LM22 is an annotated gene signature matrix containing 547 marker genes (e.g., dendritic cells, T cells, and B cells). With the aim of improving the accuracy of the deconvolution algorithm, 100 permutations of the default signature matrix to calculate the CIBERSORT p-values and root mean square errors for each sample file were implemented. Subsequently, regarding the differences in immune cell infiltration between the low- and high-risk groups, we utilized a threshold of $p < 0.05$ to analyze the differences by screening BC data. Spearman's test was performed to assess correlations among different tumor immune cell types.

2.7 Analysis of tumor mutational burden

We obtained the somatic mutation data of BC from the TCGA database and calculated the tumor mutational burden (TMB) of each BC sample. We investigated the difference in TMB between the high-risk and low-risk groups and visualized it using "maftool," "limma," and "ggpubr" R packages. We obtained the optimal TMB cut-off value according to the algorithm in the "survminer" R package, and divided all samples into the high-TMB and low-TMB groups. We drew the Kaplan–Meier survival curve of high-TMB and low-TMB groups and analyzed the difference in the OS using the "survival" R package. The high- and low-TMB groups were further divided based on the prognostic signature into four groups: high-TMB and high-risk, low-TMB and high-risk, low-TMB and low-risk, and low-TMB and high-risk.

2.8 Cell culture

Breast cancer cell lines MCF7 were cultured in Dulbecco's Modified Eagle Medium (DMEM, Gibco) supplemented with 10% FBS and 100 U/mL Penicillin/Streptomycin in a 5%

TABLE 2 Primer sequences used for RT-qPCR.

Primer	Sequence 5′ to 3′
BAIAP2-DT- F	CATCCAGAGATCGCCCTGAC
BAIAP2-DT- R	GTCAGGTTCCACAGCTACCC
COL4A2-AS1-F	TGTGGGATGGAGACATCCTGA
COL4A2-AS1-R	CAGAGCTGTTCCAAAATGCCA
FARP1-AS1-F	CAGGTGGATGGAAAGAGG
FARP1-AS1-R	AGATCACGGAGATGGTGG
RERE-AS1-F	CCCAGGAAGGCAGACAGATAA
RERE-AS1-R	CTCGGGGGAGCTGTAGTTTG
NDUFA6-DT-F	CTGCCGTCTTATCCCAGGAG
NDUFA6-DT-R	GAGACGTTCAGTCGAAGCCC
TFAP2A-AS1-F	ATTGCTCGCCAGTACCACAA
TFAP2A-AS1-R	GTGGCGGAATTGGGGTAAGA
LINC00115-F	GCTTTTTGTGGCCAAACCCA
LINC00115-R	CTCAGTGACGGAACCGGAC
MIR302CHG-F	TGTTCCTGCTTGTGGTGCAT
MIR302CHG-R	AAAGTTGAAGGGAGCCCACC
GAPDH-F	GGTGTGAACCATGAGAAGTATGA
GAPDH-R	GAGTCCTTCCACGATACCAAAG

CO2 incubator. Human normal breast cell lines MCF-10A were cultured in DMEM-F12 medium supplemented with 10% fetal bovine serum, 100 μg mL^{-1} epidermal growth factor (EGF), 1 mg mL^{-1} hydrocortisone, 10 mg mL^{-1} insulin, 100 U mL^{-1} penicillin G and 100 μg mL^{-1} streptomycin. Cells were collected at 90% confluence, and the medium was changed every 24–48 h.

2.9 RNA extraction and reverse transcription-quantitative polymerase chain reaction (RT-qPCR)

Gene expression for eight m7G-related lncRNA was measured by RT-qPCR. Total RNA was obtained from MCF-10A and MCF-7 cells using TRIzol reagent (TAKARA, Japan). The cDNA was synthesized with RNA Transcription Kit (TAKARA, Japan) and RT-qPCR was performed using SYBR Premix Ex Taq II (TAKARA, Japan). Expression was measured using CT values, normalized to that of GAPDH (ΔΔCT = ((CT (target, test) –CT (reference, test)) – (CT (target, calibrator) – CT (reference, calibrator)), and then expressed as 2-ΔΔCT. All RT-qPCR primers are listed in Table 2.

2.10 Statistical analysis

Kruskal–Wallis or Wilcoxon tests were used for intergroup comparisons of the differences in the expression of m7G regulators and m7G-related lncRNAs, the clinicopathological parameter, the proportion of the 21 tumor-infiltrating immune cell subtypes, and TMB in high- and low-risk groups. Two-sided log-rank tests were performed to compare Kaplan–Meier OS curves. All statistical analyses were carried out using software R (version 4.2.1). p-values < 0.05 were regarded as indicating statistically significant differences.

3 Results

3.1 Identification of m7G-related lncRNAs and construction of the prognostic signature

To explore the role of m7G regulators in BC, we analysis the expression of m7G-related genes in breast cancer. Supplementary Figure S1 shown that 31 genes are differentially expressed in breast cancer. In addition, patients with different m7G-related gene expression levels have different prognosis in breast cancer, despite the lack of statistical significance which needs to be further improved in the future work (Supplementary Figure S2). But we can still see the significance of m7G in breast cancer. On the basis of the co-expression analysis in TCGA database, the lncRNAs of 387 genes were identified as co-expressed with m7G (Figure 2A). Further, the prognosis of BC was tightly associated with 11 m7G-related lncRNAs using univariate Cox regression analysis (p < 0.001): *BAIAP2-DT*, *COL4A2-AS1*, *RNF213-AS1*, *FARP1-AS1*, *RERE-AS1*, *SH3BP5-AS1*, *NDUFA6-DT*, *TFAP2A-AS1*, *SEMA3F-AS1*, *LINC00115*, and *MIR302CHG* (Figure 2B). Among them, eight m7G-related lncRNAs were further selected to construct a prognostic indicator based on the LASSO Cox regression algorithm, namely, *BAIAP2-DT*, *COL4A2-AS1*, *FARP1-AS1*, *RERE-AS1*, *NDUFA6-DT*, *TFAP2A-AS1*, *LINC00115*, and *MIR302CHG* (Figure 2C). The coefficients of the eight selected genes calculated by LASSO regression analysis are shown in Table 3. The m7G-associated lncRNA–mRNA interaction network consisted of four m7G regulators and eight lncRNAs, as shown in Figure 2D, demonstrating that the m7G regulator EIF4A1 is a key node co-expressed with seven lncRNAs and the prognostic role of all lncRNAs in BC are protective factors.

3.2 Validation of the clinical significance of eight m7G-lncRNAs

To support the clinical significance of these lncRNAs, a paired differential expression analysis was performed, revealing significant group differences in all lncRNAs.

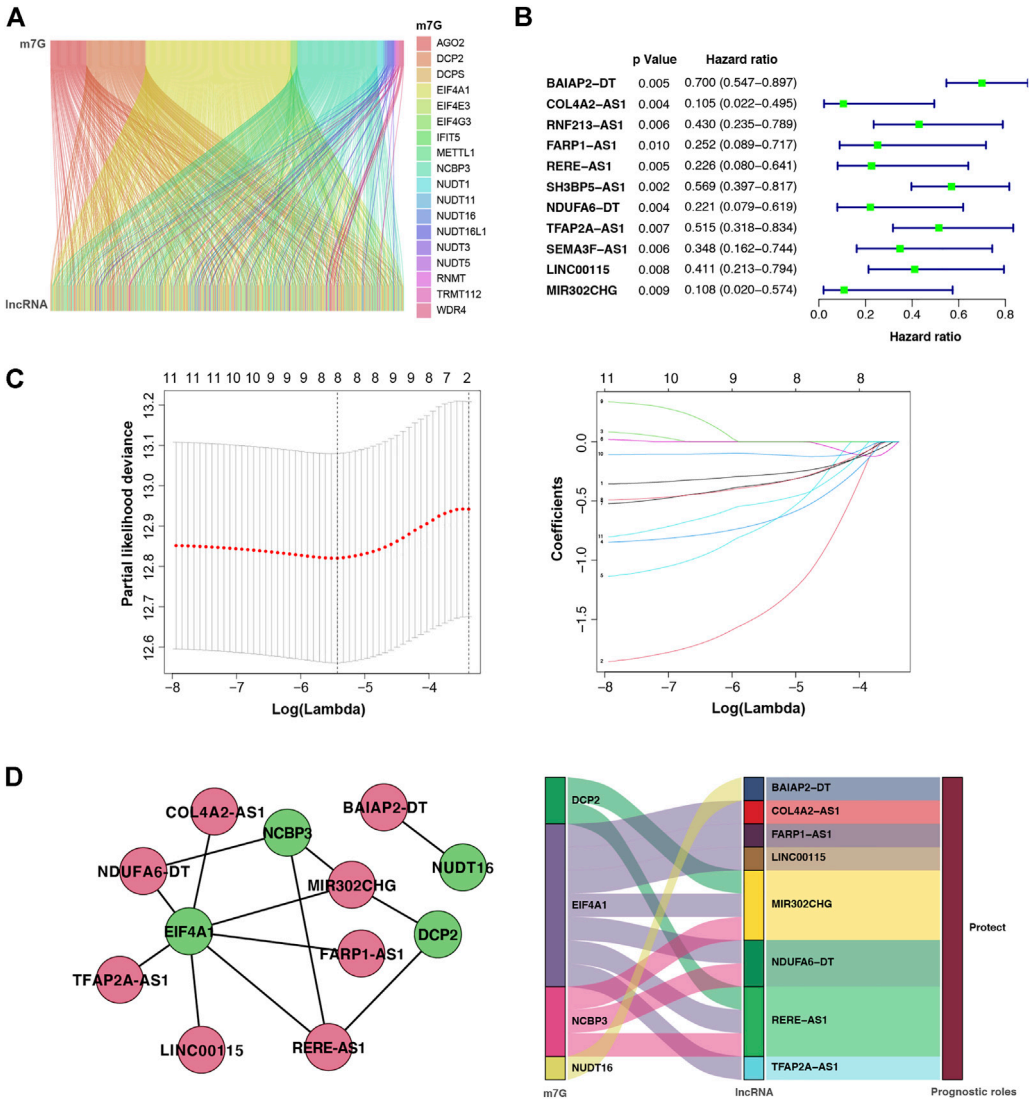

FIGURE 2
m7G-associated lncRNAs (m7G-lncRNAs) and their co-expression networks with significant prognostic value in breast cancer. **(A)** Sankey plot showing the relationship between m7G and m7G-lncRNAs. **(B)** Forest diagram of univariate Cox regression analysis of m7G-lncRNAs. **(C)** A LASSO Cox regression was used to select independent factors and construct a prognostic signature. **(D)** Network and Sankey plot showing the connection of m7G and eight m7G-lncRNAs with independent prognostic value.

Specifically, *COL4A2-AS1* and *MIR302CHG* expression was high in normal tissues (Figure 3A). In addition, we conducted the Kaplan–Meier survival analysis, Supplementary Figure S3 revealed that *BAIAP2-DT*, *COL4A2-AS1*, *RERE-AS1*, *NDUFA6-DT*, *TFAP2A-AS1*, and *LINC00115* were associated with good prognosis. Last, we examined the relationship between m7G-lncRNA expression and clinicopathological characteristics, demonstrating significant differences between different molecular subtypes of BC ($p < 0.001$). Moreover, the expression levels of *RERE-AS1* ($p < 0.05$), *TFAP2A-AS1* ($p < 0.01$), and *MIR302CHG* ($p < 0.05$) varied according to tumor stage (stage I, II, III, and IV), *COL4A2-AS1*, *RERE-AS1*, *NDUFA6-DT*, and *MIR302CHG* varied according to T stage (T1, T2, T3, and T4). However, in the subgroup analyses based on the N stage (N0, N1, N2, and N3), only *BAIAP2-DT* and *FARP1-AS1* were differentially expressed in different N stages (Figure 3B).

3.3 Validity of the m7G-LPS

Using the m7G-LPS, patients were classified into two subgroups based on whether the risk score was more than (high-risk) or less than (low-risk) the median of all patient

TABLE 3 m7G-lncRNAs selected to build m7G-LPS and the corresponding coefficients.

lncRNAs	Coefficients
BAIAP2-DT	−0.27758412746579
COL4A2-AS1	−1.41967228671049
FARP1-AS1	−0.671077622897499
RERE-AS1	−0.69129846535715
NDUFA6-DT	−0.352552610278439
TFAP2A-AS1	−0.360410426066037
LINC00115	−0.107203641246423
MIR302CHG	−0.508621483491941

risk scores. The heat map in Figure 4A showed that eight m7G-related lncRNAs are significantly differentially expressed between low- and high-risk groups. Besides, T stage, age, and survival status of patients with BC are related to risk subgroups. The risk curve and scatter plot showed an increased mortality rate with an increasing risk score (Figure 4B). Further, we investigated if m7G-LPS could predict survival by performing the survival analysis of Kaplan–Meier. The high-risk group exhibited remarkably worse OS compared to the low-risk group ($p < 0.001$; Figure 4C). These findings support that the m7G-LPS has prognostic value for patients with BC.

Furthermore, we verified the prognostic value of the m7G-LPS and patient clinicopathological characteristics. The univariate and multivariate hazard ratio (HR) values of the risk score were 693 and 576, respectively, and all p-values were <0.001. This indicated that the risk score calculated through the m7G-LPS could serve as an independent predictor of prognosis in BC. In addition, univariate analysis showed that age, T, N, and M stages, but not gender, had significant prognostic value ($p < 0.001$). However, only age played an independent role in multivariate analysis (HR = 1.034, $p < 0.001$; Table 4). Based on ROC curve analyses, we found that the risk score yielded an area under the ROC curve (AUC) value of 0.686, which was the largest value among all clinicopathological factors. In addition, the 3-, 5-, and 10-year ROC curves showed corresponding AUC of the risk score of 0.693, 0.630, and 0.686, respectively (Figure 5A). These findings confirm that the signature can reliably predict the outcome of patients with BC. The prediction accuracy of the m7G-LPS was further validated. Thus, age and risk scores were included in the nomogram to better predict the 3-, 5-, and 10-year survival of patients with BC (Figure 5B). The calibration plots for the nomogram shown that the model calibration line is very close to the ideal calibration line, depicting good calibration (Figure 5C).

3.4 Differences in the m7G status of low- and high-risk groups and biological pathways of the m7G-LPS

PCA in four groups revealed that compared with the other three groups, BC samples in the m7G-LPS group could be better divided into two different groups (Figure 6A), further demonstrating the sensitivity and specificity of the m7G-LPS. To identify the potential biological signaling pathways underlying the molecular differences between high- and low-risk groups, we applied GSEA analysis. The result revealed that KEGG pathways, such as citrate cycle, TCA cycle, oxidative phosphorylation, pentose phosphate pathway, steroid biosynthesis, and terpenoid backbone biosynthesis, were remarkably enriched in high-risk samples, and alpha linolenic acid metabolism, ether lipid metabolism, glycerospholipid metabolism, inositol phosphate metabolism, and linoleic acid metabolism in low-risk samples (Figure 6B). The results indicated that m7G-related lncRNAs may involve in metabolism-related signaling pathway.

3.5 Correlation between m7G-LPS and tumor immune cell infiltration

Tumor immune cell infiltration is closely related to tumor occurrence, invasion, and metastasis. Therefore, further investigation was conducted to explore whether the m7G-LPS risk score correlates with the expression of 21 tumor-infiltrating immune cell types. As shown in Figure 7A, naive B cells ($p < 0.001$), CD8 T cells ($p < 0.001$), resting CD4 memory T cells ($p = 0.007$), activated CD4 memory T cells ($p = 0.0016$), M0 macrophages ($p < 0.001$), M2 macrophages ($p < 0.001$), and neutrophils ($p < 0.001$) showed significantly different levels of infiltration between the low- and high-risk groups. Correlations between tumor-infiltrating immune cells in BC tissues are shown in Figure 7B. Both resting CD4 T memory and CD8 T cells showed a moderately negative correlation with M0 macrophages (r = –0.51 and –0.51, respectively).

3.6 TMB analysis and correlation with m7G-LPS

TMB is associated with immunotherapy efficacy and is emerging as a potential biomarker. To examine the underlying value of TMB in BC, we performed TMB analysis through single nucleotide variation BC data in TCGA database to assess cancer-associated gene mutation frequency. Figure 7C shows a high TMB (85.03%) in the high-risk group. Gene mutations were more frequent in TP53 (39%). In the low-risk group, the proportion of samples with mutations was 82.2%, slightly lower than that in the high-risk group, and PIK3CA was the most frequently mutated gene (38%). In addition, our risk subgroup-based analysis, shown in

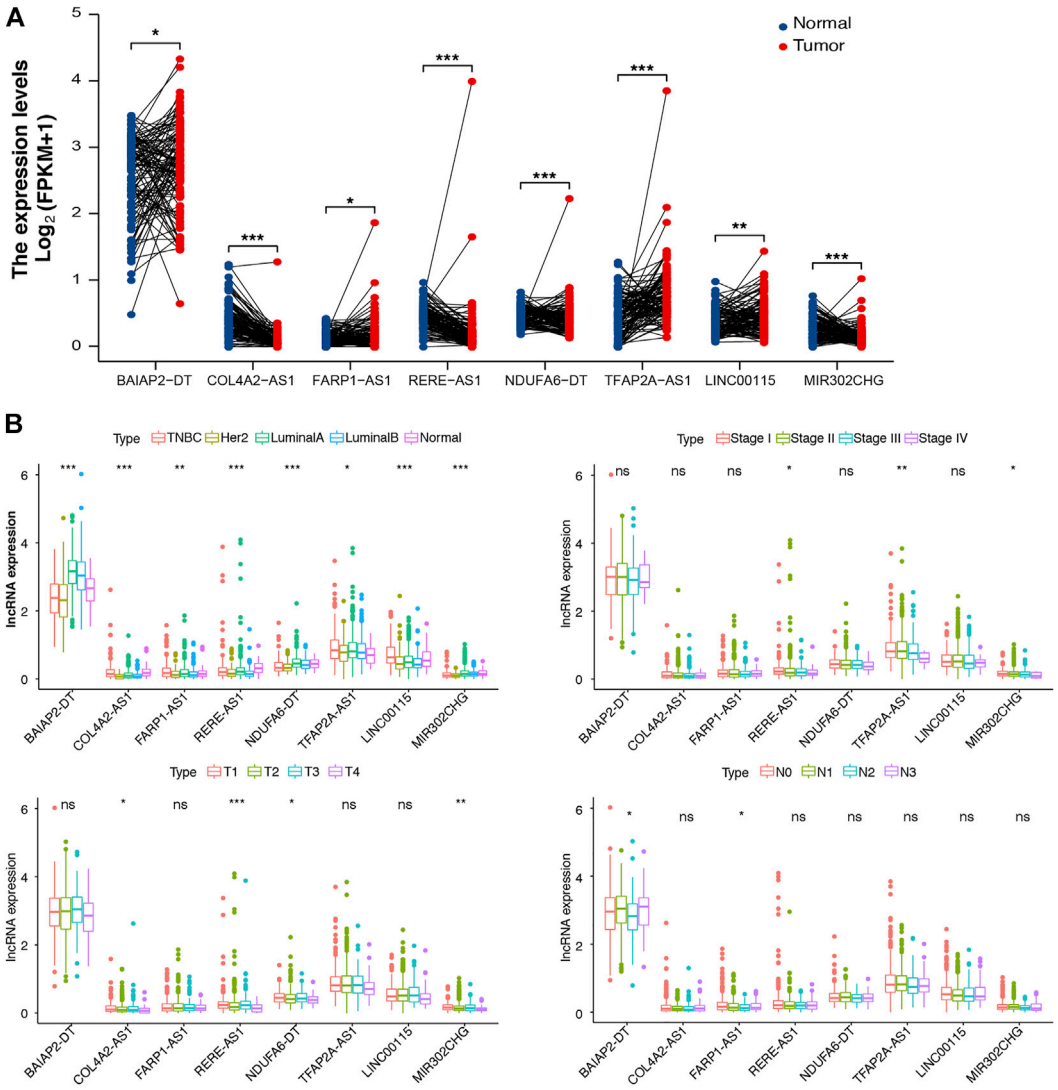

FIGURE 3
Differential expression analysis of m7G-associated lncRNAs (m7G-lncRNAs). **(A)** A paired differential expression analysis of the eight prognosis-related m7G-lncRNAs in normal and breast cancer (BC) tissues. **(B)** Differential expression analysis of m7G-lncRNAs in BC tissues according to molecular subtype, histological stage, T stage, and N stage (ns: not significant; *$p < 0.05$; * *$p < 0.01$; * * *$p < 0.001$).

Figure 7D, manifested that the TMB of high-risk patients was higher than that of low-risk patients. Subsequently, according to the TMB score, we classified all patients into low- and high-TMB groups. We further analyzed the value of the prognosis of TMB in patients with BC by Kaplan–Meier survival analysis. Our findings indicated worse OS for high-TMB patients by contrast with low-TMB patients. In combination with the prognostic signature, we found that patients with BC with both high-TMB and high-risk scores had the worst prognosis. The above data indicate that TMB has prognostic value in BC, and combined with the risk model, it can better predict the outcome of patients with BC (Figure 7E).

3.7 RT-qPCR validation of differentially expressed m7G-related lncRNAs

Univariate Cox regression and lasso Cox regression analysis was used to screen prognostic m7G-related lncRNAs, which were used to construct m7G-LPS. Further studies are required to validate the findings of lncRNAs, so we conducted the RT-qPCR test *in vitro*. Supplementary Figure S4 shows *BAIAP2-DT*, *FARP1-AS1*, *NDUFA6-DT*, *MIR302CHG*, *and TFAP2A-AS1* high expression in MCF-7, and *LINC00115* low expression in MCF-7.

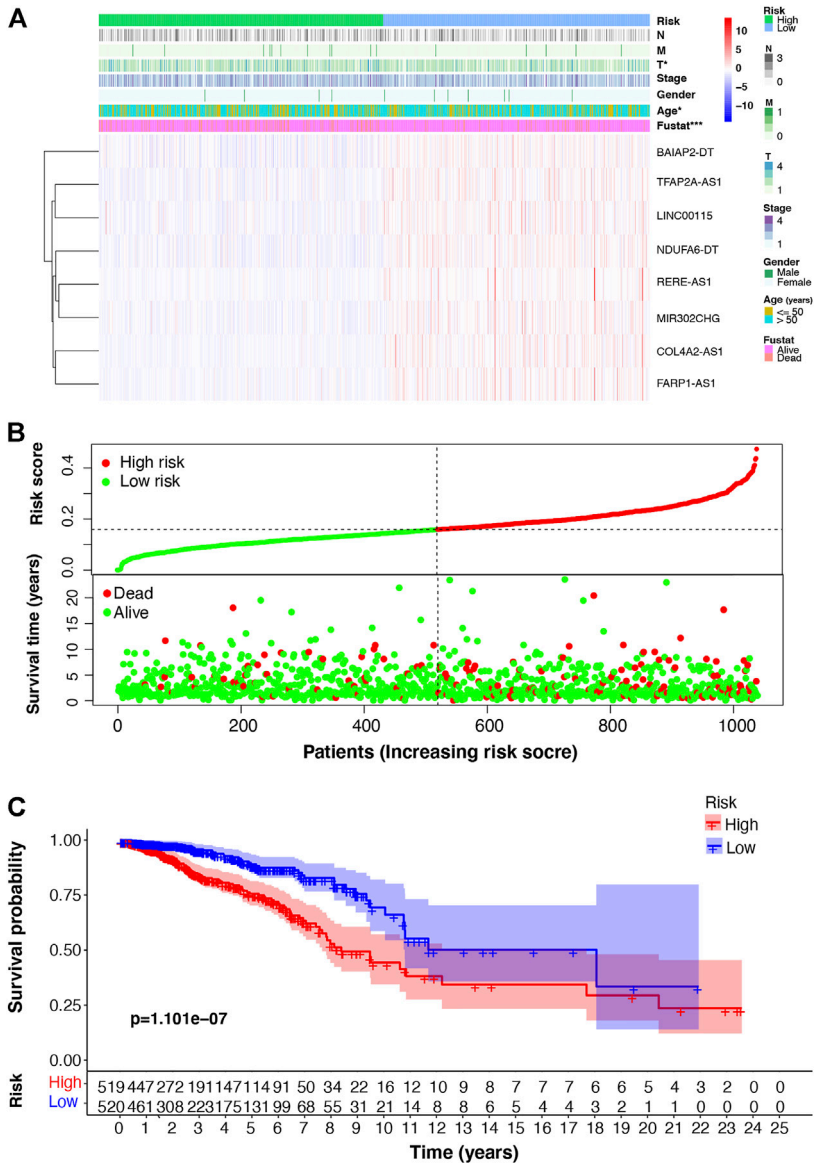

FIGURE 4
m7G-associated lncRNA (m7G-lncRNA) prognostic signature based on the eight prognosis-related m7G-lncRNAs. **(A)** Heat map of the difference in expression of the m7G-lncRNAs and clinicopathologic factors between the high- and low-risk groups **(B)** Distribution of the relationship between the risk score and patient survival status. **(C)** Kaplan–Meier survival analysis in the high- and low-risk groups (*$p < 0.05$; * * *$p < 0.001$).

4 Discussion

Worldwide, BC is the most common malignant tumor in women (Momenimovahed and Salehiniya, 2019). Despite continuing advancements in the multidisciplinary approach to its treatment (Waks and Winer, 2019), BC remains the primary killer of women with cancer. In recent years, with the development of bioinformatics and the application of high-throughput sequencing, m7G modification has been recognized as playing a key role in RNA splicing, stability, and efficient translation (Malbec et al., 2019; Chen K. et al., 2021, 0; Zhang et al., 2021). However, functional studies of the m7G modification-related lncRNAs remain limited. Therefore, in this study, we selected and validated eight differentially expressed m7G-related lncRNAs with prognostic values in BC, namely, *BAIAP2-DT*, *COL4A2-AS1*, *FARP1-AS1*, *RERE-AS1*, *NDUFA6-DT*, *TFAP2A-AS1*, *LINC00115*, and *MIR302CHG*, created m7G-LPS, and conducted a combined analysis of the clinicopathological characteristics, tumor immune cell infiltration, and TMB to

TABLE 4 Univariate and Multivariate analysis of m7G-LPS and clinicopathological factors.

Characteristics	Univariate analysis		Multivariate analysis	
	Hazard ratio (95% CI)	*p* value	Hazard ratio (95% CI)	*p* value
Age	1.033 (1.019–1.048)	<0.001	1.034 (1.019–1.049)	<0.001
Gender	0.866 (0.121–6.212)	0.886	0.555 (0.077–4.008)	0.559
Stage	2.149 (1.698–2.720)	<0.001	1.680 (0.999–2.826)	0.050
T	1.510 (1.216–1.876)	<0.001	0.945 (0.698–1.280)	0.715
M	6.481 (3.633–11.561)	<0.001	1.716 (0.750–3.926)	0.201
N	1.688 (1.401–2.035)	<0.001	1.165 (0.864–1.572)	0.316
Risk score	693.158 (71.684–6702.607)	<0.001	575.749 (57.656–5749.424)	<0.001

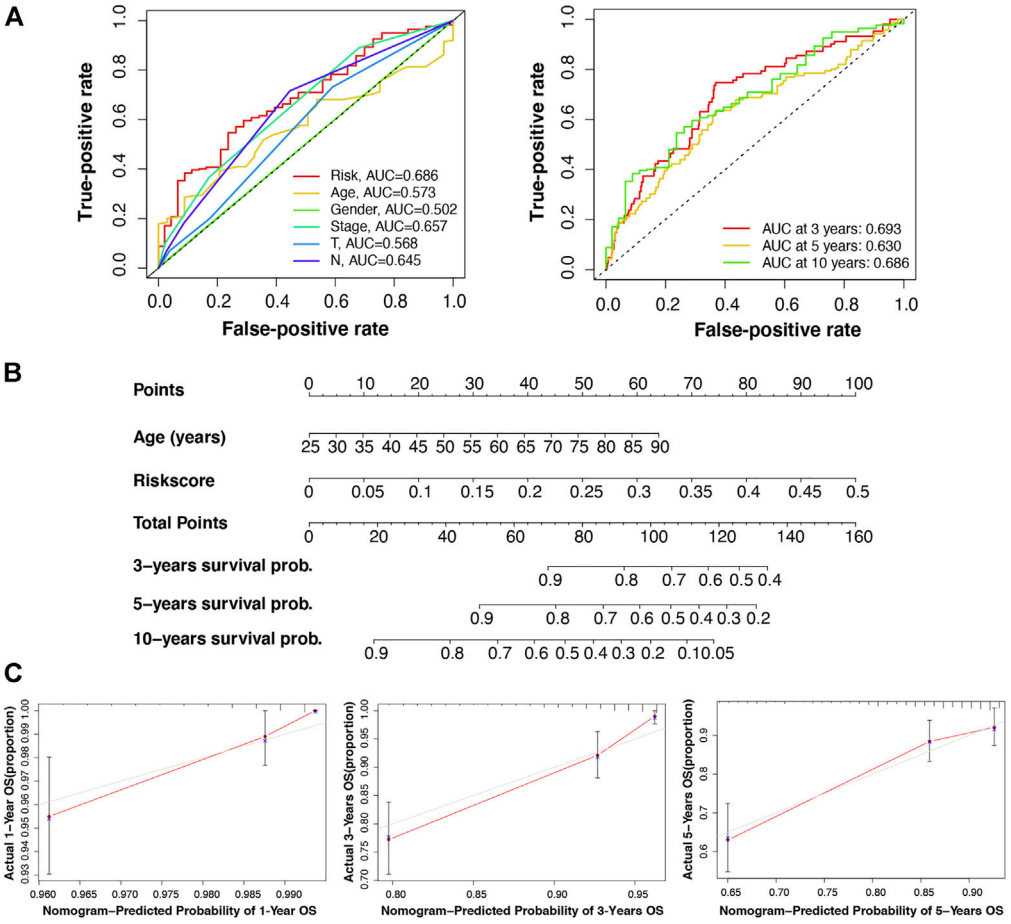

FIGURE 5
Validation of the reliability of the m7G-LPS and development of the nomogram. **(A)** Receiver operating characteristic curve of m7G-LPS and clinicopathological factors. **(B)** The nomogram developed based on the independent prognostic factors of age and risk score to predict the 3-, 5-, and 10-year survival rates. **(C)** The calibration plots of the nomogram were measured to evaluate the predicted probabilities of the nomogram.

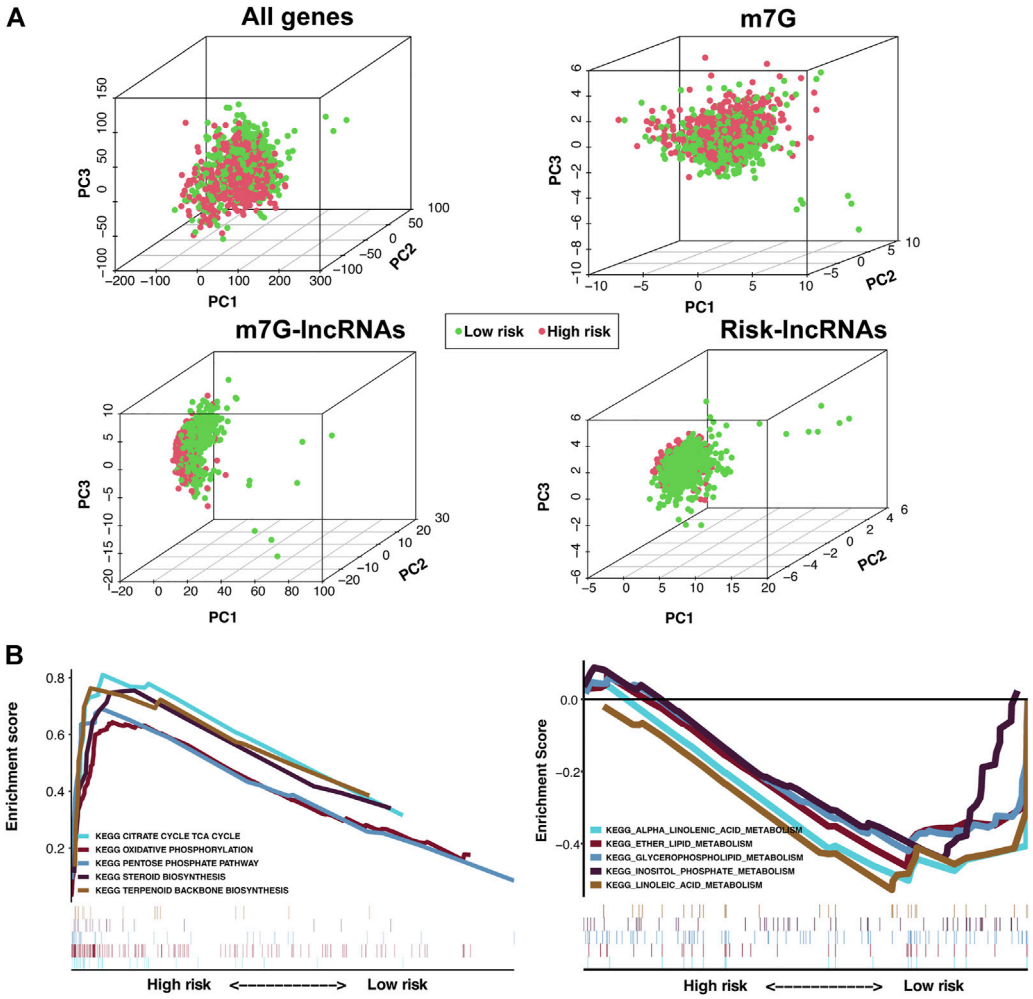

FIGURE 6
Principal component analysis (PCA) and GSEA analysis of the m7G-LPS. **(A)** PCA on the expression patterns of grouped samples based on the whole genome, m7G RNA modification-related genes, m7G-related lncRNAs, and the m7G-LPS expression profiles. **(B)** KEGG analysis of the m7G-LPS using GSEA.

examine the role of m7G-related lncRNAs in BC. We found that the m7G-LPS can predict the clinical outcome of patients with BC and evaluate the immune cell infiltration of tumors and TMB in BC. Model-lncRNAs can be used as diagnostic lncRNA biomarkers and may serve as potential therapeutic targets. Overall, the m7G-LPS discovered in this study extends the concept of post-transcriptional modifications of lncRNA, paving a path toward the exploitation of new measures for disease prevention, early detection, and therapy, ultimately contributing to improving patient prognoses.

Currently, many studies have constructed prognostic models of m7G-related lncRNAs by analyzing transcriptomic data from open databases, which can be used to estimate the prognosis of cancer patients (Song et al., 2021, 2022; Liu et al., 2022). For instance, in esophageal squamous cell carcinoma, a prognostic model constructed using seven prognostic m7G-related lncRNAs could predict the prognosis of patients, and the risk score calculated through risk signature was strongly associated with the level of immune cell infiltration (Zhao et al., 2022). In clear cell renal cell carcinoma, 12 prognostic m7G-related lncRNAs were screened, and the constructed model proved to have good accuracy and reliability in predicting OS (Ming and Wang, 2022). In hepatocellular carcinoma, m7G-LPS showed clinical value in predicting outcomes, immunotherapy effects, and drug sensitivity in patients with hepatocellular carcinoma (Wei et al., 2022). Collectively, these findings and those of previous studies support that m7G-related lncRNAs could serve as prognostic and diagnostic biomarkers for cancer, helping treatment selection and disease monitoring. In addition, these m7G-related lncRNAs could be therapeutic targets for BC. In this study, we created an m7G-LPS based on eight prognostic m7G-related lncRNAs and confirmed its

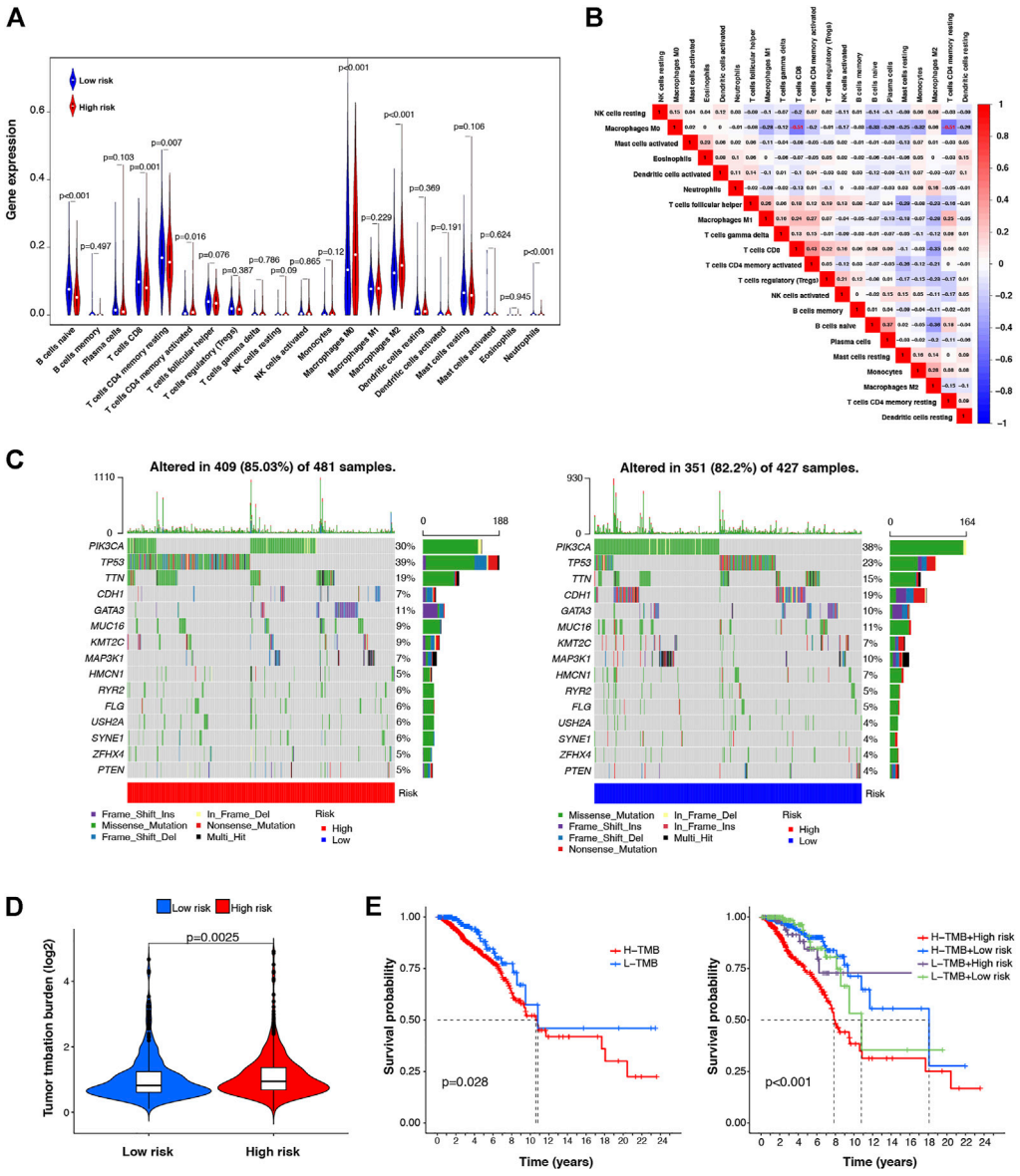

FIGURE 7
Correlation between the m7G-LPS and infiltrating level of immune cells and TMB. **(A)** Violin plots of the infiltrating level of 21 types of tumor-infiltrating immune cells between high- and low-risk groups. **(B)** Spearman correlation analysis of 21 types of tumor-infiltrating immune cells. **(C)** TMB analysis in low- and high-risk groups. **(D)** Difference analysis of TMB between low- and high-risk group **(E)** Kaplan–Meier curve analysis of OS is shown for patients classified according to the TMB and risk score.

prognostic value. The risk score, combined with age, is an independent prognostic factor for patients with BC, according to univariate and multivariate Cox regression analyses. Further, the AUC value of the ROC curve also showed that the prognostic signature has high prediction accuracy. Thus, for a more objective prediction of the 3-, 5-, and 10-year survival rates of patients with BC, we created a nomogram on the basis of age and the risk score. Results of PCA showed that compared with the whole-genome, m7G-related genes, and m7G-related lncRNAs, the expression profiles in the m7G-LPS group could better distinguish between low-risk and high-risk patients. Thus, the m7G-LPS has independent value and extremely high reliability and specificity for predicting BC prognosis. To the best of our knowledge, this is the first predictive signature of BC prognosis based on m7G-related lncRNAs and will likely be further refined by incorporating accumulating data.

m7G modification is indispensable for RNA metabolism, processing, and function. It is involved in tumor development,

progression, and response to therapy. METTL1 methyltransferase mediates m7G methylation in Let-7e-5p miRNA and modulates the malignant phenotype of cell migration through its catalytic activity (Pandolfini et al., 2019). In addition, METTL1 also mediates Arg-TCT-4-1 tRNA modification, driving oncogenic transformation by remodeling the mRNA "translatome" (Orellana et al., 2021). In lung cancer, m7G methylase also regulated the m7G modification level of tRNA, promoting lung cancer growth and invasion. In this research, we also attempted to analyze the potential biological functions of the m7G-LPS using GSEA. The Kyoto Encyclopedia of Genes and Genomes pathway enrichment analysis showed that metabolism-related pathways were the most enriched in the high- and low-risk group. Diseases are often caused by deregulated metabolic signaling (Beckwith et al., 2018, 80), including BC (Akella et al., 2019). On the one hand, emerging evidence suggests that oncogenes and tumor suppressor genes in cancer, which usually include MYC, HIF, P53, and RAS, regulate the metabolic phenotype of tumor cells and inhibit the TCA cycle, diverting glutamine to fuel the TCA cycle (Anderson et al., 2018). In contrast, previous studies confirmed that the stability of the pentose phosphate pathway is crucial for the cell cycle, proliferation, and metastases (Lin et al., 2018; Leal et al., 2019). Thus, through enrichment analysis, we can surmise that the m7G-LPS may promote BC by regulating metabolic pathways.

Tumor-infiltrating immune cells, key components of the tumor microenvironment, are reportedly useful in predicting cancer prognosis, including that of BC (Bense et al., 2017). Thus, immune cells have emerged as a novel therapeutic target for cancer (Lazăr et al., 2018). For instance, $CD8^+$ T cells are associated with tumor size, lymph node status, Ki-67 index, and molecular subtypes of BC. In addition, infiltration of CXCL13-expressing $CD4^+$ follicular helper cells is predictive of BC prognosis (Zhu et al., 2016). B cells that are acutely activated may be involved in eliminating early tumor cells or tumor clearance through classical immunoglobulin-mediated mechanisms (DeNardo and Coussens, 2007). Here, we used TCGA data to investigate the correlation between the m7G-LPS and the tumor immune cell infiltration levels. We found significantly different levels of infiltrating naive B cells, CD8 T cells, resting CD4 memory T cells, activated CD4 memory T cells, M0 macrophages, M2 macrophages, and neutrophils between the low- and high-risk groups, with higher infiltration levels in the low-risk group, compared to the high-risk group. Our work indicates that the m7G-LPS have the ability to predict the infiltration levels of tumor immune cells in BC, thus, more accurately predicting the prognosis of BC.

The TMB conceptually represents the total number of mutations in a tumor sample. Tumor mutations cause the presence of immunogenic neoantigens on the surface of carcinoma cells. In general, the more mutations (i.e., the higher the TMB), the greater the likelihood that neoantigens presented by MHC proteins will be immunogenic, which aids T cells in recognizing and eliminating carcinoma cells (Rooney et al., 2015; Chabanon et al., 2016). However, 5% of patients with BC have high TMB, primarily patients with metastatic BC. A study has shown that TMB is a novel biomarker of immune checkpoint inhibitor sensitivity. Compared with the immunohistochemistry detection of PD-1 and PD-L1 expression, TMB is more effective in predicting the immunotherapy of patients with tumors, treated with PD-1 and PD-L1 inhibitors. Therefore, patients with high TMB may benefit from immune checkpoint inhibitors (Barroso-Sousa et al., 2020). In this work, we also preliminarily examined the correlation between M7G-LPS and TMB. We found that *TP53* gene mutation was mainly found in patients with a high-risk score, and TMB was higher in patients with low-risk scores. In the prognostic analysis, we found that patients with high TMB had poor prognoses. The survival outcome of patients with high TMB and high-risk scores was the worst in the entire cohort. The above results indicate that M7G-LPS is helpful in predicting the TMB of patients with BC, and the combination of TMB and prognostic m7G-related lncRNAs as biomarkers may help predict the patient outcome and guide the selection of immunological treatment.

There are limitations in our study. First, we constructed a m7G-LSP based on prognostic and differentially expressed m7G-related lncRNAs, however we have not yet found other data sets that included expression of eight lncRNAs, clinicopathological characteristics, and follow-up data. Thus, the m7G-LSP could not be verified further. In addition, we verified the expression levels of all eight m7G-related lncRNAs *in vitro*, but further functional experiments are needed in future. We leave further verifications as future work.

In conclusion, we identified a novel and reliable prognostic signature based on eight m7G-related lncRNAs. *BAIAP2-DT*, *COL4A2-AS1*, *FARP1-AS1*, *RERE-AS1*, *NDUFA6-DT*, *TFAP2A-AS1*, *LINC00115*, and *MIR302CHG* were screened as diagnostic biomarkers. Further improvement and validation to refine the predictive signature, nomogram, and diagnostic biomarkers might provide the necessary evidence for its adoption into clinical practice, drive the relentless improvement in prognostic information, and provide new prognostic biological targets for patients with BC.

Data availability statement

The original contributions presented in the study are included in the article/Supplementary Material, further inquiries can be directed to the corresponding author.

Author contributions

HL designed the study and reviewed the manuscript. ZH analyzed the data, performed RT-qPCR experiment, and edited the manuscript. KL wrote the manuscript and prepared figures

and tables. Contributions from all authors were reviewed and approved before the article was submitted.

Acknowledgments

We acknowledge the high-quality data provided by the TCGA Network.

Conflict of interest

The authors declare that the research was conducted in the absence of any commercial or financial relationships that could be construed as a potential conflict of interest.

Publisher's note

Supplementary material

The Supplementary Material for this article can be found online at: https://www.frontiersin.org/articles/10.3389/fgene.2022.1030275/full#supplementary-material

References

Akella, N. M., Ciraku, L., and Reginato, M. J. (2019). Fueling the fire: Emerging role of the hexosamine biosynthetic pathway in cancer. *BMC Biol.* 17, 52. doi:10.1186/s12915-019-0671-3

Akram, M., Iqbal, M., Daniyal, M., and Khan, A. U. (2017). Awareness and current knowledge of breast cancer. *Biol. Res.* 50, 33. doi:10.1186/s40659-017-0140-9

Anderson, N. M., Mucka, P., Kern, J. G., and Feng, H. (2018). The emerging role and targetability of the TCA cycle in cancer metabolism. *Protein Cell* 9, 216–237. doi:10.1007/s13238-017-0451-1

Barroso-Sousa, R., Jain, E., Cohen, O., Kim, D., Buendia-Buendia, J., Winer, E., et al. (2020). Prevalence and mutational determinants of high tumor mutation burden in breast cancer. *Ann. Oncol.* 31, 387–394. doi:10.1016/j.annonc.2019.11.010

Batista, P. J. (2017). The RNA modification N6-methyladenosine and its implications in human disease. *Genomics Proteomics Bioinforma.* 15, 154–163. doi:10.1016/j.gpb.2017.03.002

Beckwith, S. L., Schwartz, E. K., García-Nieto, P. E., King, D. A., Gowans, G. J., Wong, K. M., et al. (2018). The INO80 chromatin remodeler sustains metabolic stability by promoting TOR signaling and regulating histone acetylation. *PLoS Genet.* 14, e1007216. doi:10.1371/journal.pgen.1007216

Bense, R. D., Sotiriou, C., Piccart-Gebhart, M. J., Haanen, J. B. A. G., van Vugt, M. A. T. M., de Vries, E. G. E., et al. (2017). Relevance of tumor-infiltrating immune cell composition and functionality for disease outcome in breast cancer. *J. Natl. Cancer Inst.* 109, djw192. doi:10.1093/jnci/djw192

Bray, F., Ferlay, J., Soerjomataram, I., Siegel, R. L., Torre, L. A., and Jemal, A. (2018). Global cancer statistics 2018: GLOBOCAN estimates of incidence and mortality worldwide for 36 cancers in 185 countries. *Ca. Cancer J. Clin.* 68, 394–424. doi:10.3322/caac.21492

Chabanon, R. M., Pedrero, M., Lefebvre, C., Marabelle, A., Soria, J.-C., and Postel-Vinay, S. (2016). Mutational landscape and sensitivity to immune checkpoint blockers. *Clin. Cancer Res.* 22, 4309–4321. doi:10.1158/1078-0432.CCR-16-0903

Chen, K., Song, B., Tang, Y., Wei, Z., Xu, Q., Su, J., et al. (2021a). RMDisease: A database of genetic variants that affect RNA modifications, with implications for epitranscriptome pathogenesis. *Nucleic Acids Res.* 49, D1396–D1404. doi:10.1093/nar/gkaa790

Chen, Z., Zhu, W., Zhu, S., Sun, K., Liao, J., Liu, H., et al. (2021b). METTL1 promotes hepatocarcinogenesis via m7 G tRNA modification-dependent translation control. *Clin. Transl. Med.* 11, e661. doi:10.1002/ctm2.661

DeNardo, D. G., and Coussens, L. M. (2007). Inflammation and breast cancer. Balancing immune response: Crosstalk between adaptive and innate immune cells during breast cancer progression. *Breast Cancer Res.* 9, 212. doi:10.1186/bcr1746

Dunn, S., Lombardi, O., Lukoszek, R., and Cowling, V. H. (2019). Oncogenic PIK3CA mutations increase dependency on the mRNA cap methyltransferase, RNMT, in breast cancer cells. *Open Biol.* 9, 190052. doi:10.1098/rsob.190052

Fernandes, J. C. R., Acuña, S. M., Aoki, J. I., Floeter-Winter, L. M., and Muxel, S. M. (2019). Long non-coding RNAs in the regulation of gene expression: Physiology and disease. *Noncoding. RNA* 5, 17. doi:10.3390/ncrna5010017

Hasan, M. M., Basith, S., Khatun, M. S., Lee, G., Manavalan, B., and Kurata, H. (2020). Meta-i6mA: An interspecies predictor for identifying DNA N6-methyladenine sites of plant genomes by exploiting informative features in an integrative machine-learning framework. *Brief. Bioinform.* 22, bbaa202. doi:10.1093/bib/bbaa202

Jonkhout, N., Tran, J., Smith, M. A., Schonrock, N., Mattick, J. S., and Novoa, E. M. (2017). The RNA modification landscape in human disease. *RNA* 23, 1754–1769. doi:10.1261/rna.063503.117

Lai, J., Chen, B., Zhang, G., Li, X., Mok, H., and Liao, N. (2020). Molecular characterization of breast cancer: A potential novel immune-related lncRNAs signature. *J. Transl. Med.* 18, 416. doi:10.1186/s12967-020-02578-4

Lazăr, D. C., Avram, M. F., Romoşan, I., Cornianu, M., Tăban, S., and Goldiş, A. (2018). Prognostic significance of tumor immune microenvironment and immunotherapy: Novel insights and future perspectives in gastric cancer. *World J. Gastroenterol.* 24, 3583–3616. doi:10.3748/wjg.v24.i32.3583

Leal, A. R., Ortiz-Lazareno, P. C., Jave-Suárez, L. F., De Arellano, A. R., Aguilar-Lemarroy, A., Ortiz-García, Y. M., et al. (2019). 17β-estradiol-induced mitochondrial dysfunction and Warburg effect in cervical cancer cells allow cell survival under metabolic stress. *Int. J. Oncol.* 56, 33–46. doi:10.3892/ijo.2019.4912

Lee, G. L., Dobi, A., and Srivastava, S. (2011). Prostate cancer: Diagnostic performance of the PCA3 urine test. *Nat. Rev. Urol.* 8, 123–124. doi:10.1038/nrurol.2011.10

Li, X., Jin, F., and Li, Y. (2021). A novel autophagy-related lncRNA prognostic risk model for breast cancer. *J. Cell. Mol. Med.* 25, 4–14. doi:10.1111/jcmm.15980

Lin, P., He, R., Ma, F., Liang, L., He, Y., Yang, H., et al. (2018). Systematic analysis of survival-associated alternative splicing signatures in gastrointestinal pan-adenocarcinomas. *EBioMedicine* 34, 46–60. doi:10.1016/j.ebiom.2018.07.040

Liu, L., Song, B., Chen, K., Zhang, Y., de Magalhães, J. P., Rigden, D. J., et al. (2022). WHISTLE server: A high-accuracy genomic coordinate-based machine learning platform for RNA modification prediction. *Methods* 203, 378–382. doi:10.1016/j.ymeth.2021.07.003

Malbec, L., Zhang, T., Chen, Y.-S., Zhang, Y., Sun, B.-F., Shi, B.-Y., et al. (2019). Dynamic methylome of internal mRNA N7-methylguanosine and its regulatory role in translation. *Cell Res.* 29, 927–941. doi:10.1038/s41422-019-0230-z

Ming, J., and Wang, C. (2022). N7-Methylguanosine-Related lncRNAs: Integrated analysis associated with prognosis and progression in clear cell renal cell carcinoma. *Front. Genet.* 13, 871899. doi:10.3389/fgene.2022.871899

Momenimovahed, Z., and Salehiniya, H. (2019). Epidemiological characteristics of and risk factors for breast cancer in the world. *Breast Cancer*. 11. Auckland: Dove Med Press, 151–164. doi:10.2147/BCTT.S176070

Orellana, E. A., Liu, Q., Yankova, E., Pirouz, M., De Braekeleer, E., Zhang, W., et al. (2021). METTL1-mediated m7G modification of Arg-TCT tRNA drives oncogenic transformation. *Mol. Cell* 81, 3323–3338.e14. e14. doi:10.1016/j.molcel.2021.06.031

Pandolfini, L., Barbieri, I., Bannister, A. J., Hendrick, A., Andrews, B., Webster, N., et al. (2019). METTL1 promotes let-7 MicroRNA processing via m7G methylation. *Mol. Cell* 74, 1278–1290. e9. doi:10.1016/j.molcel.2019.03.040

Parasramka, M. A., Maji, S., Matsuda, A., Yan, I. K., and Patel, T. (2016). Long non-coding RNAs as novel targets for therapy in hepatocellular carcinoma. *Pharmacol. Ther.* 161, 67–78. doi:10.1016/j.pharmthera.2016.03.004

Qiang, X., Chen, H., Ye, X., Su, R., and Wei, L. (2018). M6AMRFS: Robust prediction of N6-methyladenosine sites with sequence-based features in multiple species. *Front. Genet.* 9, 495. doi:10.3389/fgene.2018.00495

Rooney, M. S., Shukla, S. A., Wu, C. J., Getz, G., and Hacohen, N. (2015). Molecular and genetic properties of tumors associated with local immune cytolytic activity. *Cell* 160, 48–61. doi:10.1016/j.cell.2014.12.033

Shaheen, R., Abdel-Salam, G. M. H., Guy, M. P., Alomar, R., Abdel-Hamid, M. S., Afifi, H. H., et al. (2015). Mutation in WDR4 impairs tRNA m7G46 methylation and causes a distinct form of microcephalic primordial dwarfism. *Genome Biol.* 16, 210. doi:10.1186/s13059-015-0779-x

Song, B., Chen, K., Tang, Y., Wei, Z., Su, J., de Magalhães, J. P., et al. (2021). ConsRM: Collection and large-scale prediction of the evolutionarily conserved RNA methylation sites, with implications for the functional epitranscriptome. *Brief. Bioinform.* 22, bbab088. bbab088. doi:10.1093/bib/bbab088

Song, B., Huang, D., Zhang, Y., Wei, Z., Su, J., Pedro de Magalhães, J., et al. (2022). m6A-TSHub: Unveiling the context-specific m6A methylation and m6A-affecting mutations in 23 human tissues. *Genomics Proteomics Bioinforma.* S1672-0229 (22), 00114. –0. doi:10.1016/j.gpb.2022.09.001

Song, B., Tang, Y., Chen, K., Wei, Z., Rong, R., Lu, Z., et al. (2020). m7GHub: deciphering the location, regulation and pathogenesis of internal mRNA N7-methylguanosine (m7G) sites in human. *Bioinformatics* 36, 3528–3536. doi:10.1093/bioinformatics/btaa178

Tang, Y., Chen, K., Song, B., Ma, J., Wu, X., Xu, Q., et al. (2021). m6A-Atlas: a comprehensive knowledgebase for unraveling the N6-methyladenosine (m6A) epitranscriptome. *Nucleic Acids Res.* 49, D134–D143. doi:10.1093/nar/gkaa692

Waks, A. G., and Winer, E. P. (2019). Breast cancer treatment: A review. *JAMA* 321, 288–300. doi:10.1001/jama.2018.19323

Wei, W., Liu, C., Wang, M., Jiang, W., Wang, C., and Zhang, S. (2022). Prognostic signature and tumor immune landscape of N7-methylguanosine-related lncRNAs in hepatocellular carcinoma. *Front. Genet.* 13, 906496. doi:10.3389/fgene.2022.906496

Winters, S., Martin, C., Murphy, D., and Shokar, N. K. (2017). "Breast cancer epidemiology, prevention, and screening," in *Progress in molecular biology and translational science* (Elsevier), 1–32. doi:10.1016/bs.pmbts.2017.07.002

Zhang, S.-Y., Zhang, S.-W., Fan, X.-N., Meng, J., Chen, Y., Gao, S.-J., et al. (2019a). Global analysis of N6-methyladenosine functions and its disease association using deep learning and network-based methods. *PLoS Comput. Biol.* 15, e1006663. doi:10.1371/journal.pcbi.1006663

Zhang, S.-Y., Zhang, S.-W., Fan, X.-N., Zhang, T., Meng, J., and Huang, Y. (2019b). FunDMDeep-m6A: Identification and prioritization of functional differential m6A methylation genes. *Bioinformatics* 35, i90–i98. doi:10.1093/bioinformatics/btz316

Zhang, S.-Y., Zhang, S.-W., Tang, Y., Fan, X.-N., Meng, J., and Huang, Y. (2021). FunDMDeep-m6A: Identification and prioritization of functional differential m6A methylation genes. *Bioinformatics* 35, i90–i98. btab362. doi:10.1093/bioinformatics/btz316

Zhao, F., Dong, Z., Li, Y., Liu, S., Guo, P., Zhang, D., et al. (2022). Comprehensive analysis of molecular clusters and prognostic signature based on m7G-related LncRNAs in esophageal squamous cell carcinoma. *Front. Oncol.* 12, 893186. doi:10.3389/fonc.2022.893186

Zhu, S., Lin, J., Qiao, G., Wang, X., and Xu, Y. (2016). Tim-3 identifies exhausted follicular helper T cells in breast cancer patients. *Immunobiology* 221, 986–993. doi:10.1016/j.imbio.2016.04.005

Zou, Q., Xing, P., Wei, L., and Liu, B. (2019). Gene2vec: Gene subsequence embedding for prediction of mammalian N6-methyladenosine sites from mRNA. *RNA* 25, 205–218. doi:10.1261/rna.069112.118

frontiers | Frontiers in Cell and Developmental Biology

TYPE Original Research
PUBLISHED 18 October 2022
DOI 10.3389/fcell.2022.945202

OPEN ACCESS

EDITED BY
Xiao Han,
Fuzhou University, China

REVIEWED BY
Xiaolong Wang,
Northwest A&F University, China
Hui Wang,
Southwest Minzu University, China

*CORRESPONDENCE
Zhibin Ji,
zbji916@sdau.edu.cn

SPECIALTY SECTION
This article was submitted to Epigenomics and Epigenetics, a section of the journal Frontiers in Cell and Developmental Biology

RECEIVED 16 May 2022
ACCEPTED 04 October 2022
PUBLISHED 18 October 2022

CITATION
Wang S, Zhang L, Xuan R, Li Q, Ji Z, Chao T, Wang J and Zhang C (2022), Identification and functional analysis of m^{6}A in the mammary gland tissues of dairy goats at the early and peak lactation stages.
Front. Cell Dev. Biol. 10:945202.
doi: 10.3389/fcell.2022.945202

Identification and functional analysis of m^{6}A in the mammary gland tissues of dairy goats at the early and peak lactation stages

Shujun Wang[1], Lu Zhang[1], Rong Xuan[1], Qing Li[1], Zhibin Ji[1]*, Tianle Chao[1], Jianmin Wang[1] and Chunlan Zhang[2]

[1]College of Animal Science and Technology, Shandong Agricultural University, Taian, China, [2]College of Biological and Agricultural Engineering, Weifang University, Weifang, China

N6-methyladenosine (m^{6}A) is the most common reversible epigenetic RNA modification in the mRNA of all higher eukaryotic organisms and plays an important role in the regulation of gene expression and cell function. In this study, m^{6}A-modified methylated RNA immunoprecipitation sequencing (MeRIP-seq) and transcriptome sequencing (RNA-seq) were used to identify the key genes with m^{6}A modification during mammary gland development and lactation in dairy goats. The results showed that m^{6}A methylation occurred at 3,927 loci, which were significantly enriched in the 3′ untranslated region (3′UTR) and the termination codon region. In the early stage and peak stage of lactation, m^{6}A methylation occurred extensively in mammary tissues, and a total of 725 differentially expressed m^{6}A-modified genes were obtained, all negatively correlated with mRNA expression. In addition, Gene Ontology (GO) enrichment and Kyoto Encyclopedia of Genes and Genomes (KEGG) pathway analysis showed that different methylated genes were mainly involved in the growth and apoptosis of mammary epithelial cells through signaling pathways, such as the mitogen-activated protein kinase (MAPK) and phospholipase D pathways, and then affected the development and lactation of mammary gland. All in all, we identified and analyzed the methylation events related to the development and lactation regulation of mammary gland at the early and peak lactation stages, and provided a theoretical basis to reveal the physiological regulatory system of mammary gland development and lactation in dairy goats.

KEYWORDS

dairy goats, mammary gland, lactation, MeRIP-seq, m^{6}A

Introduction

In the 1970s, scientists discovered that m^{6}A modification can occur on RNA adenine (A). Subsequent studies showed that m^{6}A methylation is not the only modification that exists in the mRNA of prokaryotes, eukaryotes, and viruses; more than 150 posttranscriptional modifications have been revealed in the RNA of all organisms (Dubin and Stollar, 1975; Boccaletto et al., 2018). The molecular functions of m^{6}A are

diverse but ultimately affect mRNA transcription by regulating splicing, half-life, stability, and translation (Nachtergaele and He, 2018). m^{6}A derivatives mediate the posttranscriptional regulation of gene expression to ensure the precise control of multiple biological processes. Currently, studies on m^{6}A have been conducted in humans, plants, and yeast (Bodi et al., 2015; Wang M et al., 2020; Hu et al., 2021). In mammals, m^{6}A has been investigated in swine, cattle, and cashmere goats (Cao et al., 2020; Wang T et al., 2020; Li et al., 2021). It is mainly involved in the regulation of spermatogenesis, oogenesis, embryonic development, and stem cell pluripotency (Lin et al., 2017; Fan et al., 2019; Ji and Zhang, 2021; Xu et al., 2021).

The mammary gland is one of the unique organs of mammals, which function is to produce and secrete milk to feed offspring (Macias and Hinck, 2012). Its development can be divided into five stages, i.e., embryonic stage, puberty, gestation, lactation, and degeneration, and the developmental process is mainly regulated by hormones, growth factors, and cytokines (Brisken and Ataca, 2015). There are many physiological differences in the mammary gland at different stages of development and lactation. From the early stage to the peak stage of lactation, mammary epithelial cells continue to differentiate, the number of lactating cells increases, lactation activity increases, and the lactation volume gradually increases, reaching a maximum at the peak stage of lactation (Stefanon et al., 2002). Studies on mammary gland development and lactation in dairy goats mostly focus on mRNA (Ji et al., 2019), long noncoding RNAs (lncRNAs) (Ji et al., 2020), and microRNA (Xuan et al., 2020), not on m^{6}A. Therefore, in-depth studies of the key genes, signaling pathways, and their regulatory mechanisms in the development of mammary glands in dairy goats are of great value.

The aim of this study was to explore differentially expressed m^{6}A-methylated genes in the mammary gland tissues of Laoshan dairy goats during the early and peak lactation stages through methylated RNA immunoprecipitation sequencing (MeRIP-Seq) and to analyze the mechanism of regulation of the development and lactation of mammary gland tissue in the early and peak lactation stages in dairy goats. This study is expected to provide a theoretical basis for the molecular breeding of Laoshan dairy goats.

Materials and methods

Animals

The three Laoshan dairy goats used in this study were all from the Qingdao Laoshan dairy goat breeding farm. Mammary gland tissue was collected by surgical procedure after general anesthesia during the early lactation period (postpartum 20 days) and the peak lactation period (postpartum 90 days),respectively. The dairy goats used in the experiment were randomly selected from the group, all healthy, non-inbred individuals, 2 years old, first parity, and similar birth date, weight, and lambing, they were uniformly managed and fed. All experimental animal/procedures were treated/performed in accordance with the guidelines of the Experimental Animal Management Committee of Shandong Agricultural University. Every effort was made to reduce animal suffering during the experiments.

RNA extraction and quality control

Total RNA was extracted using a Trizol kit (Invitrogen, United States). The integrity of the RNA samples was evaluated using an Agilent 2100 B bioanalyzer (Agilent Technologies, United States). A Nano Photometer spectrophotometer was used to analyze DNA contamination. A Qubit 2.0 fluorometer was used to accurately quantify the RNA concentration used to construct the sequencing library. RNase-free agarose gel electrophoresis was used for visualization.

Library construction and sequencing

Eukaryotic mRNA from the extracted total RNA was enriched using Oligo (dT) beads, and a Ribo-Zero™ Magnetic Kit (Epicentre, United States) was used to remove rRNA and enrich prokaryotic mRNA. Then, the enriched mRNA fragments were broken into short fragments using fragment buffer, and the RNA was broken into two samples, one of which was used as the input control. The transcriptome sequencing library was constructed to eliminate noise during the capture of methylated fragments. 10 ug total RNA from each sample was enriched respectively with an m^{6}A-specific antibody for the library construction; after the m^{6}A-modified RNA was captured, the antibody was eluted with magnetic beads to reduce the background noise from nonspecific binding, and the ligation product was subjected to agarose gel electrophoresis, PCR amplification and Illumina Novaseq6000 sequencing. All sequencing work was performed by Gene Denovo Biotechnology Co. Ltd. (Guangzhou, China).

RNA-seq data analysis

The raw reads obtained from the sequencing included adaptors and low-quality reads. fastp (version 0.18.0) was used to obtain high-quality pure reads (Chen et al., 2018). The specific procedure was as follows: 1) reads containing adaptors were removed; 2) reads containing more than 10% unknown nucleotides (N) were removed; and 3) reads containing

more than 50% of low-quality bases (q value ≤20) were removed. HISAT 2.2.4 (Kim et al., 2015) was used to compare the clean data with the reference genome. The matched reads were assembled into transcripts using StringTie v1.3.1 (Pertea et al., 2015; Pertea et al., 2016). For each transcript, RSEM (Li and Dewey, 2011) was used to calculate the FPKM value (fragments per kilobase of transcript per million mapped reads) to quantify expression abundance and change.

m^{6}A-seq data analysis

The raw image data obtained by sequencing were converted into sequence data *via* base calling, which is called raw data and stored in FASTQ file format. To ensure data quality, quality control was performed on the original data to reduce the noise through data filtering and obtain high-quality clean reads for subsequent analysis. HISAT was used to align the clean reads with the reference genome of Capra hircus (version: GCF_001704415.1_ARS1) with default parameters for subsequent analysis. ExomePeak2 (version: 1.0.0) (Meng et al., 2014) was used to perform peak calling in the whole genome, and the threshold was $p < 0.05$. The position information for peaks (RNA regions and sites where m^{6}A modification occurs) in the genome, and sequence information for peak regions, were analyzed to screen out peak-related genes. RNA methylation rate = RPM (MeRIP)/RPM (input) was used to calculate the relative methylation rate of each peak, and then exomePeak2 (Meng et al., 2014) was used for differential analysis of the RNA methylation rate for all peaks in the IP group. FDR<0.05 and |log2FC|>1 (Wang Y et al., 2020) were used to screen differential peaks and perform Gene Ontology (GO) enrichment and Kyoto Encyclopedia of Genes and Genomes (KEGG) functional enrichment analysis of differentially expressed peak-related genes.

Correlation analysis of m^{6}A-seq and RNA-seq data

To comprehensively compare the relationship between m^{6}A methylation level and gene expression abundance, correlation analysis was performed for m^{6}A-seq and RNA-seq data. The peak-related genes were sorted on the basis of their expression levels and divided into 20 equal parts, and the proportion of peak in each part was analyzed. The correlation between expression level and peak enrichment fold change was analyzed using the basic functions of the R package to create a scatter plot of the gene expression-peak enrichment fold change, and the number of genes shared between differentially expressed genes (DEGs) in the transcriptome and differentially methylated genes (DMGs) identified *via* MeRIP-seq were analyzed to find potential inter-omics linked genes. The fold difference was used as the dividing standard to draw a nine-quadrant map to analyze the coregulatory relationship among common DEGs. The default threshold for screening DEGs was |log2FC|>1 (Wang Y et al., 2020). The coregulated genes obtained from the nine-quadrant map were used for subsequent GO and KEGG enrichment analysis to investigate the function of m^{6}A-modified mRNA.

GO and KEGG enrichment analyses

GO (Ashburner et al., 2000) is an internationally standardized gene function classification system that maps DEGs to various terms in the GO database (http://www.geneontology.org/). The number of genes for each term was calculated, and the number of genes with a certain GO function (molecular function, cellular composition, and biological process) were counted. The hypergeometric test was used to find the GO entries that were significantly enriched in the DEGs against the entire reference gene. The p value is calculated using the following formula:

$$\mathbf{P} = \mathbf{1} - \sum_{i=0}^{m-1} \frac{\left(\frac{M}{i}\right)\left(\frac{N-M}{n-i}\right)}{\frac{N}{n}}$$

Where N is the number of genes with a GO annotation; n is the number of DEGs in N; M is the number of genes annotated as a specific GO term; and m is the number of DEGs annotated to a specific GO term. After the calculated p value underwent Bonferroni correction, the corrected-p ≤ 0.05 was used as the threshold to obtain GO terms that were significantly enriched in the DEGs. The main biological functions of DEGs were determined by GO functional significance enrichment analysis.

KEGG (Kanehisa and Goto, 2000) is the main public database for pathways. Pathway significance enrichment analysis was performed using KEGG pathways as the unit, and a hypergeometric test was used to identify pathways that were significantly enriched in DEGs. The calculation formula for the p value is the same as that for the p value of the GO functional significance enrichment analysis, where N is the number of genes with a pathway annotation; n is the number of DEGs in N; M is the number of genes annotated as a specific pathway; and m is the number of DEGs annotated as a specific pathway. Pathways with a Q ≤ 0.05 were defined as pathways that were significantly enriched in differentially expressed proteins.

Construction of regulatory networks

Genes related to mammary gland development and lactation were selected based on the GO and KEGG annotation results, and

TABLE 1 Comparison of the quality of sequencing data and the reference genome between the two libraries.

Sample	Raw data	Clean reads	Q20%	Q30%	GC%	Unique mapped reads	Multiple mapped reads	Total mapped
E1-IN	49336232	48723832 (99.01%)	6989937247 (97.26%)	6613256954 (92.02%)	3645518978 (50.72%)	41781542 (85.75%)	3549962 (7.29%)	45331504 (93.04%)
E1-IP	47274568	45934328 (97.25%)	2021227037 (92.21%)	1871690851 (85.39%)	1137970055 (51.92%)	25455216 (55.42%)	9434574 (20.54%)	34889790 (75.96%)
E2-IN	52823280	52215686 (99.02%)	7497513916 (97.32%)	7095665407 (92.10%)	3798320528 (49.30%)	45085065 (86.34%)	4680842 (8.96%)	49765907 (95.31%)
E2-IP	50759632	49339766 (97.25%)	2216090699 (92.50%)	2054835901 (85.77%)	1241473438 (51.82%)	30472303 (61.76%)	8603775 (17.44%)	39076078 (79.20%)
E3-IN	64813138	64356886 (99.58%)	9254754450 (97.39%)	8792123099 (92.53%)	4696932492 (49.43%)	55296223 (85.92%)	6533475 (10.15%)	61829698 (96.07%)
E3-IP	58311116	56966536 (97.76%)	2373500143 (93.15%)	2216974301 (87.00%)	1291671026 (50.69%)	36019943 (63.23%)	10062207 (17.66%)	46082150 (80.89%)
P1-IN	50993434	50524106 (99.25%)	7295972140 (97.32%)	6901424197 (92.06%)	3711262517 (49.50%)	43640296 (86.38%)	4544886 (9.00%)	48185182 (95.37%)
P1-IP	44199300	43141986 (97.65%)	1688812739 (93.05%)	1577322072 (86.91%)	935110181 (51.52%)	27756879 (64.34%)	6412478 (14.86%)	34169357 (79.20%)
P2-IN	49823380	49215396 (99.11%)	7017856509 (97.28%)	6651148714 (92.20%)	3724866910 (51.63%)	43060635 (87.49%)	3391325 (6.89%)	46451960 (94.39%)
P2-IP	49680806	48636994 (97.97%)	2206924336 (93.49%)	2056514036 (87.12%)	1238363897 (52.46%)	29752521 (61.17%)	9099850 (18.71%)	38852371 (79.88%)
P3-IN	59977268	59418754 (99.24%)	8522800666 (97.60%)	8108542674 (92.85%)	4263050443 (48.82%)	50915336 (85.69%)	6397019 (10.77%)	57312355 (96.45%)
P3-IP	46226638	45314946 (98.07%)	2087434412 (93.51%)	1947410259 (87.24%)	1164951525 (52.19%)	31992607 (70.60%)	5985301 (13.21%)	37977908 (83.81%)

IN, input; IP, m^{6}A; E repsents the early stage, E1, E2 and E3 repsents the different libraries.
The P repsents the peak stage, P1, P2 and P3 repsents the different libraries.

gene regulatory networks were constructed using Scytoscape v3.9.1 software (Shannon et al., 2003) and the STRING database (Version 11.5).

Results

Comparison of the quality of the sequencing data and the reference genome

In this study, MeRIP-seq was used to identify the m^{6}A data (IP) and corresponding mRNA data (input, IN) for m^{6}A methylation in dairy goats at the early stage (E-stage, postpartum 20 days) and peak stage (P-stage, postpartum 90 days) of lactation. In the RNA-seq library, 166,972,650 and 160,794,082 raw reads were obtained from the three mammary gland samples in the early and peak stages, of which 165,695,678 and 159,511,700 were clean reads, accounting for 99.24% and 99.2% of the reads, respectively. The Q20% values for the early and peak stages were 97.32% and 97.40% respectively, and the Q30% values were 92.22% and 92.37%, respectively. In the MeRIP-seq library, 15,634,516 and 140,106,744 raw reads were obtained for mammary gland samples from the early and peak stages, of which 152,341,796 and 137,170,868 were clean reads, accounting for 97.44% and 97.9% of the reads, respectively. The Q20% values for the early and peak stages were 92.62% and 93.35%, respectively, and the Q30% values were 86.05% and 87.09%, respectively (Table 1).

After comparing the reads with the reference sequences, the alignment rate of valid reads for replicated samples of dairy goat mammary gland tissue in the early stage in the RNA-seq library was 93.04%–96.08%, of which the single alignment rate was 85.75%–86.34% and the multiple alignment rate was 7.29%–10.15%. The alignment rate of valid reads for the replicated samples of dairy goat mammary gland tissue in the peak stage was 94.39%–96.46%, of which the single alignment rate was 85.69%–87.49% and the multiple alignment rate was 6.89%–10.77%. In the MeRIP-seq library, the alignment rate of the valid reads for the replicated samples of dairy goat mammary gland tissue in the early stage was 75.96%–80.89%, of which the single alignment rate was 55.42%–63.23% and the multiple alignment rate was 17.44%–20.54%. The alignment rate of valid reads in the replicated samples of dairy goat mammary

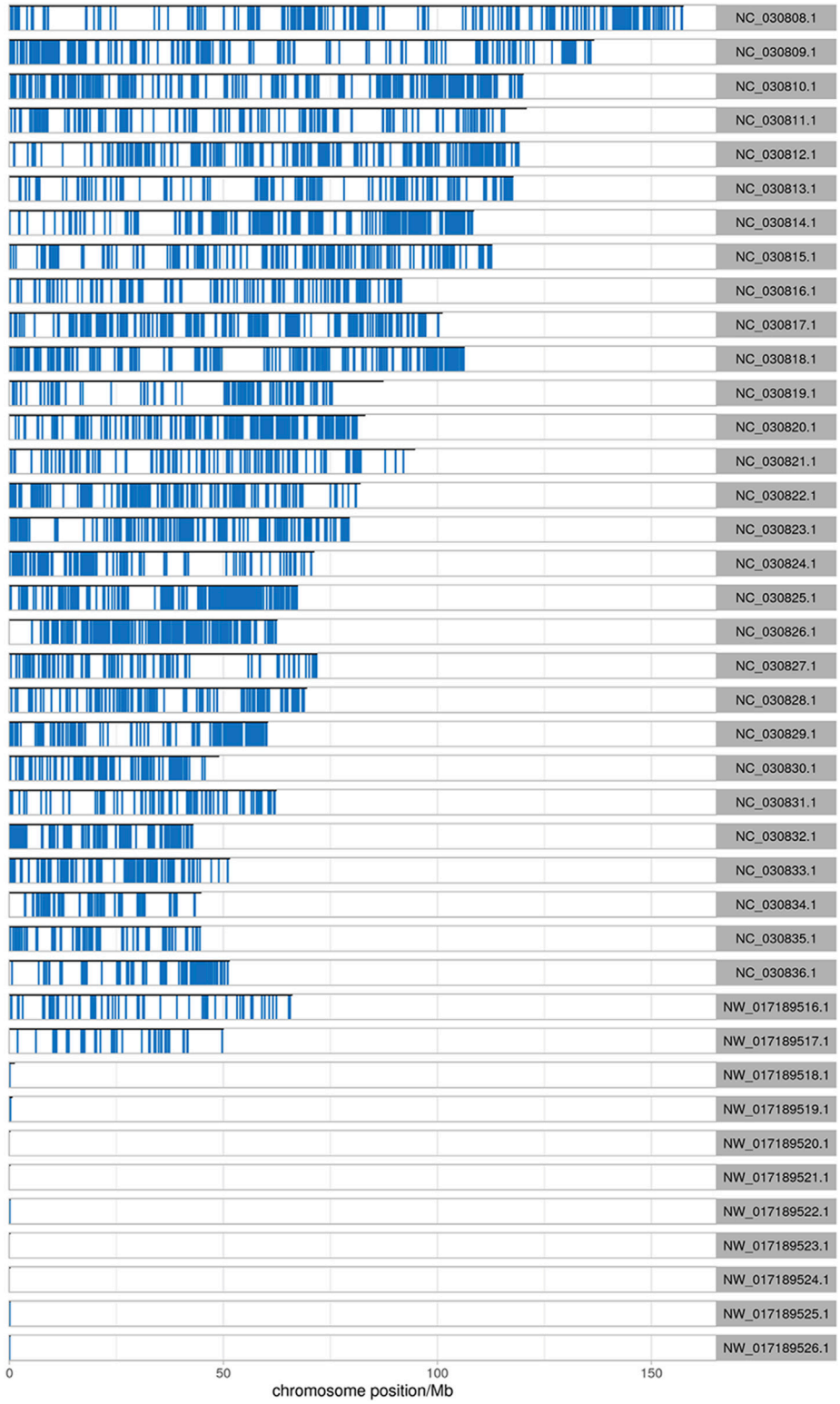

FIGURE 1
Distribution of reads on chromosomes. The abscissa is the chromosome locus (Mb), and the ordinate is the chromosome ID.

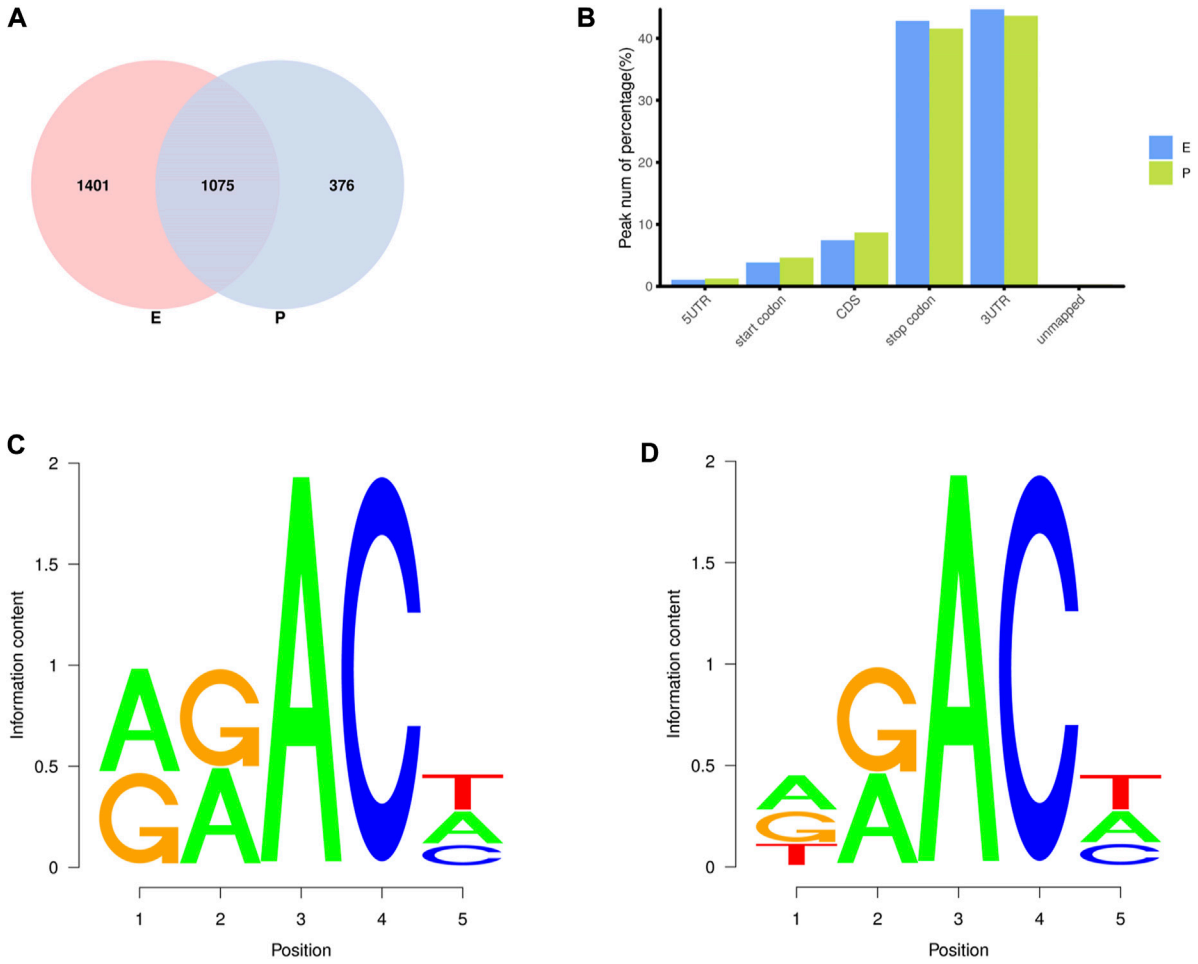

FIGURE 2
Regional distribution and motif sequence of m^{6}A modifications on transcripts. **(A)** Peak distribution of m^{6}A modifications in early and peak lactation. **(B)** The distribution of m^{6}A in transcripts **(C)** and **(D)** Two common motifs with the highest m^{6}A abundance. E represents the early lactation, P represents the peak lactation, the following are the same.

gland tissue in the peak stage was 79.2%–83.81%, of which the single alignment rate was 61.17%–70.60% and the multiple alignment rate was 13.21%–18.71% (Table 1). The most reads for different samples were distributed on the NC_030808.1 chromosome (Figure 1).

Identification of m^{6}A modification sites and motif analysis

In the two lactation periods, 2,476 peaks were identified during the early stage of lactation, and 1,451 peaks were identified at the peak stage (Figure 2A). To understand the degree of m^{6}A modification in genes and to compare the changes in m^{6}A gene modification in the two periods, the priority regions of peak gene distribution were analyzed.

The results showed that peaks were significantly enriched in the 3′ untranslated region (3′UTR, 44.67%) and the termination codon region (42.81%), followed by the coding DNA sequence (CDS, 7.43%) and initiation codon region (3.84%) (Figure 2B), these findings are consistent with the results of previous studies on m^{6}A modification such as pigs and goose (Cao et al., 2020; Xu et al., 2021). These results indicate that m^{6}A modification presents different distribution patterns on different gene functional elements, which indicates that m^{6}A is involved in the regulation of gene function, which may have unique functions related to mammary gland development and lactation. In previous studies, researchers found that the m^{6}A modification site was often accompanied by motif sequences, e.g., 5′-DRACH-3′ and 5′-RRACH-3’ (D = G/A/U, R = G/A, H = A/U/C) (Dominissini et al., 2012; Meyer et al., 2012). This study found that 96.36% sequences contained target motifs (Table 2). The motif sequences with the highest frequency were GGACT (10.55%) (Figure 2C) and AAACA (10.13%) (Figure 2D).

TABLE 2 The motif sequences of m^{6}A peaks and their proportions in the two lactation stages.

	Motif	*p*-value	% Of target	% Of background
E-IP vs. E-input	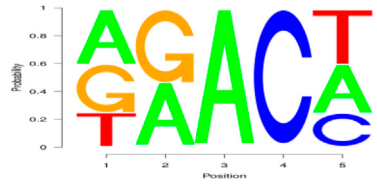	1e-7	97.94	95.76%
	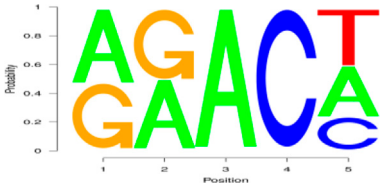	1e-10	95.56	91.77%
P-IP vs. P-input	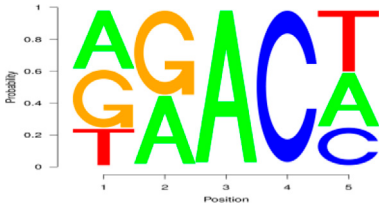	1e-4	97.11	94.70%
	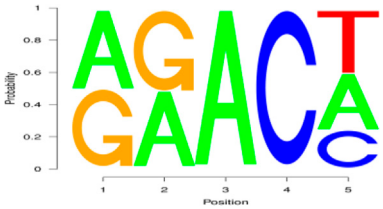	1e-9	94.83	89.83%

Note: Count the frequency (RRACH, DRACH) distribution of specific motifs in all peaks in two periods, and use homer to construct an averaged base frequency matrix for each motif for enrichment analysis.

RNA-seq gene identification and functional analysis

From the early to peak stages of lactation, a total of 21,518 genes were identified, including 20,606 known genes and 912 new genes. Among the 758 DEGs screened using FDR<0.05 and |log2FC|>1, 228 genes were upregulated, and 530 genes were downregulated during the peak stage of lactation (Figure 3A).

GO enrichment analysis indicated that 553 DEGs were annotated into 54 GO terms, including 150 upregulated DEGs and 394 downregulated DEGs. Among them, 444 DEGs were annotated to 17 cell components, which were mainly distributed in cells, cell parts, organs, and organelles. 471 DEGs were annotated to 23 biological processes, mainly involved in biological regulation, cellular processes, metabolic processes, and single organs. A total of 385 DEGs were annotated to 10 molecular functions, mainly related to binding, catalytic activity, and transport activity (Figure 3C). In the KEGG enrichment analysis, 758 DEGs were involved in four major KEGG pathways, which mainly involved cellular processes (162 genes), environmental information processes (202 genes), genetic information processes (44 genes), and metabolism (180 genes), and were involved in 40 secondary KEGG pathways, including cell growth and apoptosis, cell viability, signal transduction, transport, and catalysis (Figure 3B).

Identification and functional analysis of the MeRIP-seq peaks

To analyze m^{6}A modification in different stages of lactation, MeRIP-seq was used to identify the m^{6}A peaks during the early and peak stages of lactation. In the early stage, there were 1,401 unique peaks, and in the peak stage, there were

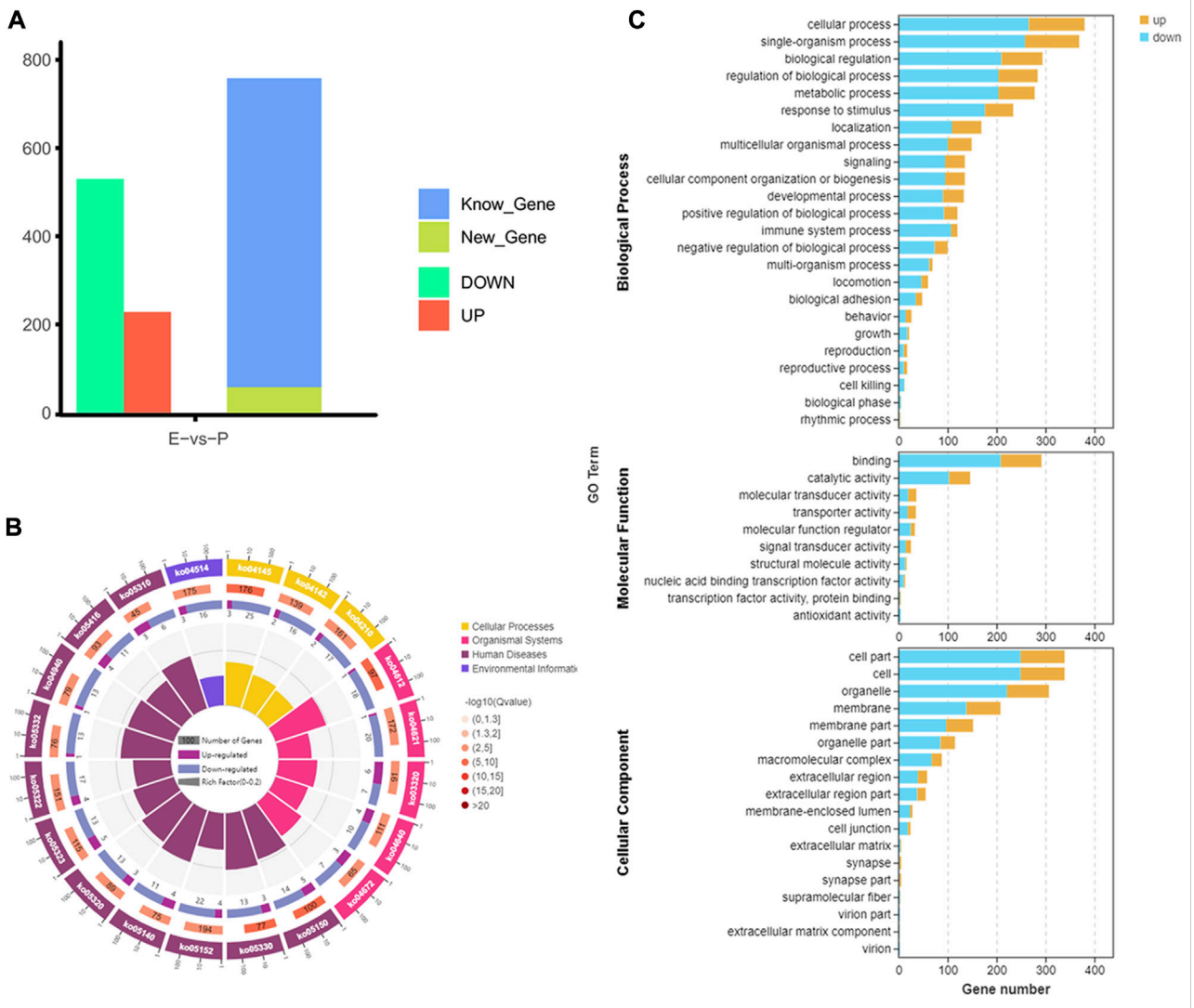

FIGURE 3
Analysis of gene expression and function in dairy goats during early and peak lactation. **(A)** Analysis results of gene identification at different lactation stages. **(B)** KEGG pathway analysis of DEGs. From inside to outside: the first circle—the top 20 KEGG terms enriched, the coordinates of gene number in the outside circle, and different colors represent different A class; the second circle—the number of genes, different colors represent different Q value, the smaller Q value, the more red color; the third circle—bar graph of gene numbers, dark purple represents the number of upregulated genes, and light purple represents thenumber of downregulated genes; the fourth circle—the rich factor value of each pathway. **(C)** GO annotation analysis results of DEGs.

376 unique peaks; the common peaks in the two stages were 1,075 (Figure 2A). After screening, 725 differential peaks were obtained, of which 112 were upregulation events and 613 were downregulation events during the peak stage of lactation (Figure 4A), which distributed in 720 DMGs (Supplementary Table S1).

GO enrichment analysis of the DMGs indicated that in the three libraries, 553 DMGs were annotated into 54 GO terms: 455 DMGs were annotated to 19 cell components, distributed in cells, cell membranes, cell parts, organs, and organelles; 460 DMGs were annotated to 26 biological processes, involving biological regulation, cellular processes, single biological processes, multicellular biological processes, and reproductive processes; and 429 DMGs were annotated to nine molecular functions, involving binding, catalytic activity, transport activity, molecular function regulation, molecular structure activity, and molecular sensor activity (Figure 4C, Supplementary Table S2.

The functional classification of DMGs was obtained by KEGG pathway analysis. Among the DMGs, 349 were involved in six major KEGG pathways, involving cellular processes (94 genes), environmental information processes

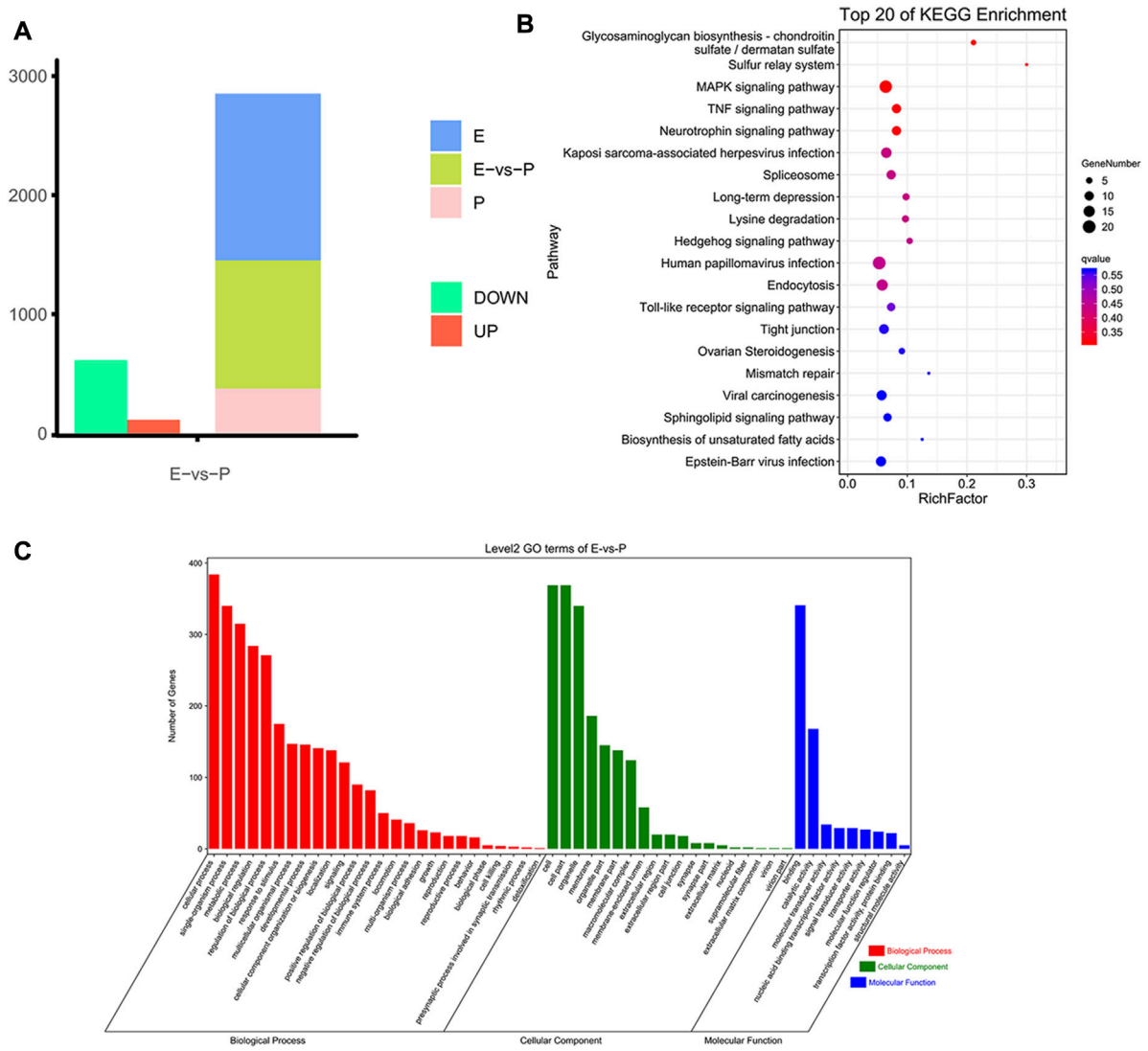

FIGURE 4
Identification and functional analysis of m^{6}A peaks. **(A)** Peak identification during different lactation stages. **(B)** Enrichment results for the top 20 DMGs pathways. **(C)** GO annotation enrichment results for DMGs.

(96 genes), genetic information processes (73 genes), human diseases (121 genes), organic systems (105 genes), and metabolism (82 genes). Thirty-nine secondary KEGG pathways were involved, including cell growth and apoptosis, cell viability, membrane transport, signal transduction, signal molecule interaction, transport, and decomposition. Among the 284 pathways analyzed, 24 significantly enriched pathways were identified, including the MAPK signaling pathway, spliceosome signaling pathway, Hedgehog signaling pathway, tight junction signaling pathway, and NF-kappa B signaling pathway et al. The pathways were mainly involved in biological processes such as mammary epithelial cell proliferation and apoptosis (Figure 4B, Supplementary Table S3).

Correlation analysis of MeRIP-seq and RNA-seq data

In the intragroup association analysis, 2,240 genes were modified by m^{6}A methylation during the early stage, and 1,343 genes were modified by m^{6}A methylation in the peak stage. According to the cumulative curve, the expression level of genes modified *via* methylation was low under the same cumulative frequency of m^{6}A methylation (Figure 5A). Based on the scatter plot of gene expression-peak enrichment fold change, the m^{6}A methylation level was negatively correlated with gene expression abundance, i.e., the peak enrichment of relatively highly expressed genes was relatively low (Figure 5B). Through the analysis of the proportion of peaks in

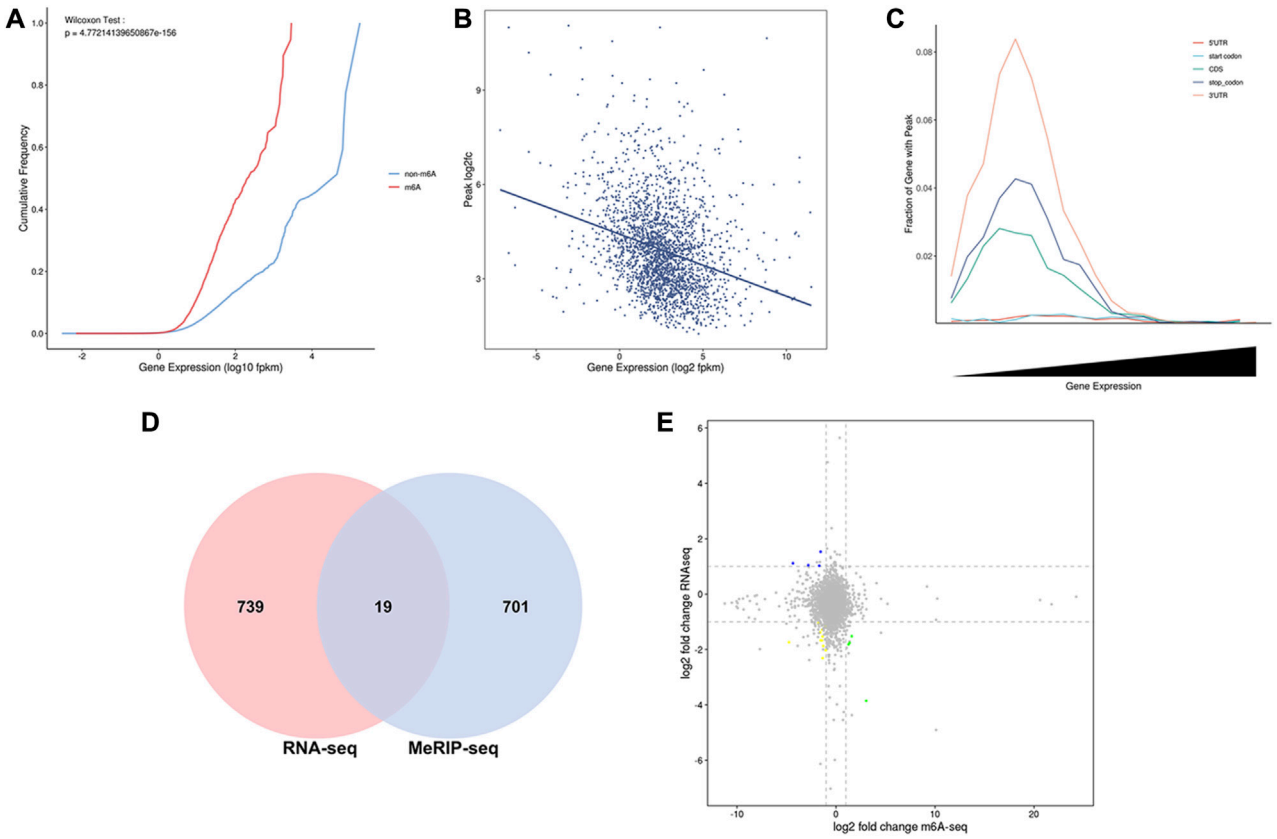

FIGURE 5
Combined MeRIP-seq and RNA-seq analysis. **(A)** Cumulative curve for gene expression with/without m^{6}A modification. The red line represents the gene set with m^{6}A peak signal, and the blue line represents the gene set without m^{6}A peak signal. **(B)** Relation of gene expression and peak enrichment fold change **(C)** Peak distribution in different gene elements and expression abundance. **(D)** Venn diagram of differential gene distribution in methylomics and transcriptomics **(E)** Nine-quadrant plot of DEGs with differential peaks. The horizontal axis is the fold difference (log_2) in m^{6}A peak abundance, and the vertical axis is the fold difference (log_2) of gene expression abundance in the transcriptome. Blue dots represent upregulated genes and downregulated m^{6}A genes, yellow dots represent downregulated genes and downregulated m^{6}A genes, and green dots represent downregulated genes and upregulated m^{6}A genes.

different gene elements, it was found that each element exhibited a nonmonotonic functional relationship pattern. When gene expression abundance reached a certain level, the proportion of peaks showed a downward trend as gene expression continued to increase (Figure 5C). In the combined analysis of DEGs and DMGs, 720 DMGs were identified, of which 19 genes were present in the transcriptome (Figure 5D, Supplementary Table S4).

To visually represent the coexpression of genes and m^{6}A, we analyzed the nine-quadrant plots and found that 79% of the genes (15 of 19) were downregulated in the differentially expressed m^{6}A-modifying genes (Figure 5E). Among them, seven genes are related to mammary gland development and lactation, including three hypomethylated and upregulated genes (*COLGALT2*, *IL20RA*, *PRKG1*), two hypermethylated and downregulated genes (*LOC102185917*, *GPR132*), two hypomethylated and down regulated genes (*GADD45G*, *RGS10*).

Functional analysis of differential genes enriched peak in two lactation stages

To more accurately analyze the relationship between the transcriptome and m^{6}A methylation, this study combined analysis of DEMs enriched peaks and the DEGs in the early and peak stages (Figure 6A), found that the peaks in early stage was distributed among 70 DEGs, and in the peak stage the peaks was distributed in 46 DEGs, 36 DEGs were existed uniquely in the early stage, and 12 DEGs were for peak stage uniquely.

In addition, through analysis, it was found that there were 34 genes in common between the differential peak-related genes and the differential transcriptome genes in the two periods, and GO and KEGG enrichment analyses were performed (Supplementary Table S5). The top 20 GO terms were enriched in biological processes and molecular functions, which were mainly concentrated in the regulation of biological processes, cell apoptosis, cell growth

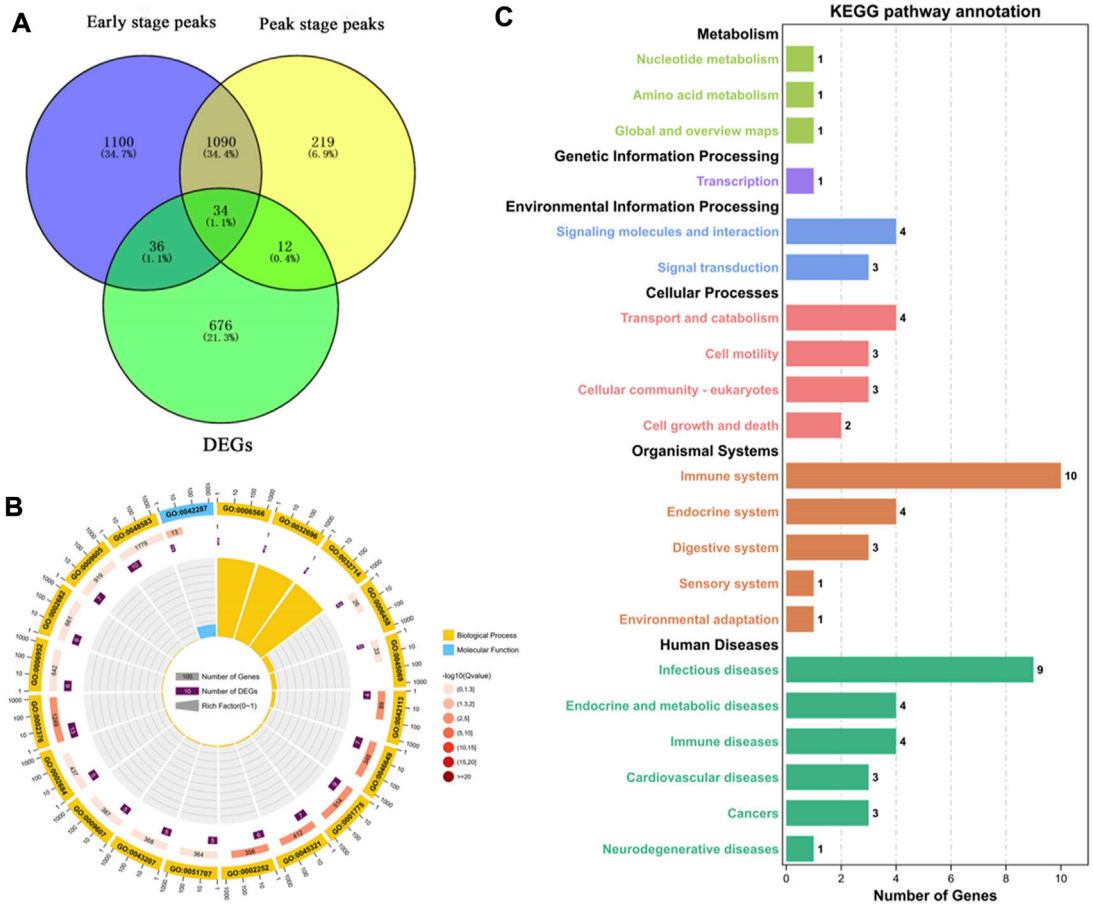

FIGURE 6
Functional analysis of peak enriched DEGs during early and peak lactation stages. **(A)** Venn diagram of peak distribution in differential expression genes between early and peak lactation stages. **(B)** GO enrichment analysis of the 34 common peak DEGs. **(C)** KEGG enrichment analysis of the 34 common peak DEGs.

processes, cellular components or biogenesis, signal transduction, etc., involving 22 genes (*ISG15*, *ISG20*, *TBX21*, *MALT1*, *SLC27A1*, *ACTB*, *TNFRSF21*, TNFAIP8L2, *VEGFC*, *PLTP*, *ANP32A*, *SLA2*, *TBC1D10C*, *CD8B*, *ITM2C*, *FGD3*, *TMSB4X*, *TUBB*, *RGS1*, *LOC102174841*, *PTMA*, and *PFDN4*) (Figure 6B). In the KEGG enrichment analysis, the relevant pathways were mainly enriched in cellular processes, environmental information processes, gene information processes, and organ systems, including cell transport and catabolism, cell viability, and interactions of signaling molecules, involving phagosomes (*TUBB*, *ACTB*, *LOC102180664*, and *LOC102185917*), cell adhesion molecules (*LOC102180664*, *CD8B*, *LOC102185917*), the PPAR signaling pathway (*SLC27A1* and *PLTP*), glycine, serine, and threonine metabolism (*LOC102174841*), insulin resistance (*SLC27A1*), apoptosis (*ACTB* and *LOC102185917*), the MAPK signaling pathway (*VEGFC*), and the PI3K-Akt signaling pathway (*VEGFC*) (Figure 6C).

Mammary gland development and lactation regulatory network

Using the GO and KEGG annotation results, 150 genes that directly annotated mammary gland development and lactation were selected from the 2,468 common genes obtained from the two groups (Figure 7A). These genes are mainly involved in mammary gland formation (GO: 0060592), mammary epithelial cell proliferation (GO: 0033599), mammary gland epithelial cell differentiation (GO: 0060644), and biological processes involved in mammary gland development (GO: 0003006). They are involved in KEGG pathways, such as cancer (ko05200), the MAPK signaling pathway (ko04013), cell apoptosis (ko04210), and the PI3K-Akt signaling pathway (ko04151). Based on the interaction analysis of coexpressed genes in STRING database, consisting of 89 nodes and 378 edges, the core genes that showed the most interactions were *HRAS*, *JUN*, and *EGFR* (Figure 7B).

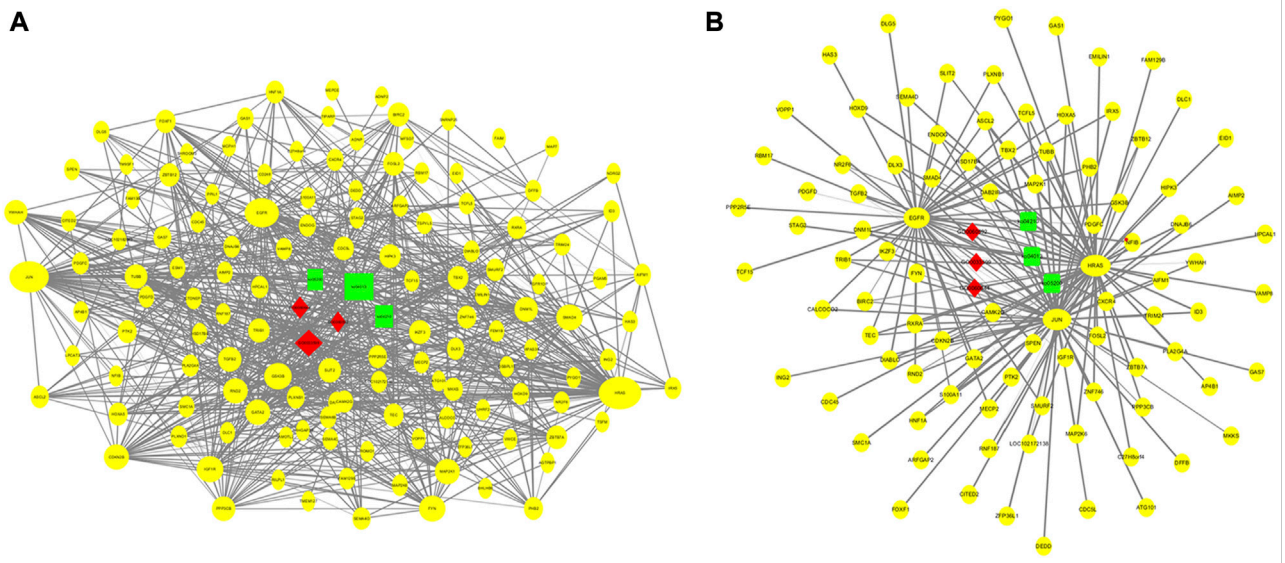

FIGURE 7
Regulation networks related to mammary gland development and lactation of dairy goats. **(A)** Interaction networks of 150 coexpressed genes. **(B)** Regulation networks of core gene module.

Discussion

Methylation modification is an important means of regulating gene expression in epigenetics and also the earliest epigenetic modification discovered. m^{6}A methylation is the most conserved and extensive RNA modification in living organisms (Rengaraj et al., 2021). Studies on m^{6}A have been conducted in humans, viruses, fruit flies, plants, and yeast. (Bodi et al., 2015; Wang M et al., 2020; Hu et al., 2021). In mammals, only swine, cattle, and cashmere goats have been studied. (Cao et al., 2020; Wang T et al., 2020; Li et al., 2021). However, there have no studies on m^{6}A methylation in dairy goats to date, therefore, m^{6}A methylation and its mechanism during mammary gland development and lactation in dairy goats are still unknown. At present, numerous studies have shown that m^{6}A widely involved in spermatogenesis, oogenesis, skin hair follicle morphogenesis, embryonic development, stem cell pluripotency, and myoepithelial cell differentiation, etc. (Luo et al., 2014; Dai et al., 2018; Hui et al., 2022). m^{6}A may also play a crucial role in mammary gland development and lactation of dairy goats.

In this study, coimmunoprecipitation sequencing and general transcription sequencing data were combined to analyze the correlation between m^{6}A modification and the expression of mammary gland development and lactation-related genes based on mRNA in the mammary gland tissue of dairy goats. Previous studies have found that m^{6}A modification characteristics and patterns are highly consistent in the same species but different in various species (Dominissini et al., 2012; Meyer et al., 2012; Wang A et al., 2021). Based on this technology, we investigated the characteristics and patterns of m^{6}A modification, including the degree of m^{6}A modification, the distribution position of m^{6}A in the transcript, and the m^{6}A methylation sequence motif, in the mRNA transcriptome of dairy goats. During mammary gland development and lactation, there were a large number of m^{6}A methylation modifications in mammary gland tissue, including 2,476 peaks identified during the early lactation stage and 1,451 peaks identified during the peak lactation stage. In addition, the abundance of m^{6}A in the 3′UTR was higher, a finding that is consistent with the abundance pattern of m^{6}A in the skin tissue of Liaoning cashmere goats (Wang Y et al., 2021). It was reported that m^{6}A peaks are significantly enriched in the CDS and initiation codons (Xu et al., 2021); however, the distribution pattern of m^{6}A in the goat methylation group was different from that in goose (Xu et al., 2021), *Bombyx mori* (Li et al., 2019), *mice* (Meyer et al., 2012), and *Arabidopsis* (Luo et al., 2014; Duan et al., 2017), indicating that the distribution pattern of m^{6}A is species specific.

Based on the combined analysis of DEGs in transcriptomes and differential peaks, 24 DEGs with m^{6}A methylation modifications were identified in this study, all of which were associated with mammary gland development and lactation in goats. These data indicate that there are dynamic changes in the regulation of important processes by m^{6}A during mammary gland development and lactation. Similarly, dynamic changes in the m^{6}A modification in the follicular selection process of chickens (Fan et al., 2019), different skin tissues of Liaoning cashmere goats (Wang T et al., 2020), and different stages of porcine follicular development in swine (Cao et al., 2020) have also been observed. Among the hypermethylated and downregulated genes in the

differentially coexpressed DEGs and DMGs in the combined analysis, the proton-sensing G protein-coupled receptor *GPR132* activate signals and transduce signals into cells by lowering pH (Weiß et al., 2017), and its homolog, *GPR68*, promotes apoptosis and inhibits the proliferation of goat mammary epithelial cells (Zhu et al., 2021). In addition, *PRKG1*, the hypomethylated and upregulated protein kinase, was negatively correlated with the expression of placental-associated miR-517a-3p before and after delivery (Kambe et al., 2014), indirectly regulating mammary gland development and lactation.

m^{6}A is a chemical marker associated with transcript degradation (He et al., 2017). High levels of m^{6}A modification may endow transcripts with higher stability at lower transcription levels or provide stronger signals for reader proteins, thereby more effectively exerting biological functions (Niu et al., 2013; Wang et al., 2014). In this study, approximately 15% of m^{6}A-modified genes had 2 m^{6}A modification sites, and approximately 3% of m^{6}A-modified genes had 3 m^{6}A modification sites, which may also increase RNA stability or the probability of being recognized by reader proteins. These results all indicate that m^{6}A modification plays a posttranscriptional regulatory role in the mammary gland transcriptome of dairy goats. To elucidate the possible mechanisms underlying the involvement of differentially coexpressed genes in mammary gland development and lactation regulation, GO and KEGG enrichment analyses were performed. Cells, organelles, and cellular parts were annotated as cellular components; cellular processes, signal transduction, metabolic processes, and biological regulation were annotated as molecular functions; and binding and catalytic activation were annotated as biological processes. For the KEGG pathway analysis, the cancer pathway, the PI3K-Akt signaling pathway, and the MAPK signaling pathway were the main enriched metabolic pathways.

Based on the GO and KEGG pathway analysis results, 150 genes related to mammary gland development and lactation were subjected to an interaction analysis of coexpressed genes. The core genes that showed the most interactions in the network were *HRAS*, *JUN*, and *EGFR*. The p21 protein encoded by the *HRAS* proto-oncogene induces the invasive phenotype of human mammary epithelial cells and plays an important role in the development of breast cancer (Moon et al., 2000). Curcumin can inhibit the signal transduction of HRAS-transformed mammary epithelial cells (HRAS MCF10A) to reduce the incidence of breast cancer (Hahn et al., 2018), thereby promoting mammary gland development and lactation. *JUN* (AP-1 transcription factor subunit) proto-oncogenes include *c-Jun*, *JunB*, and *JunD*. AP-1 is involved in the proliferation and differentiation of lymphocytes, osteoblasts, and keratinocytes (Elkeles et al., 1999; Hess et al., 2004). *JunB* inhibits cell proliferation by activating the expression of p16 (*INK4a*). Furthermore, *JunB* is a negative regulator of cell proliferation (Passegue and Wagner, 2000). Therefore, the *JUN* gene may regulate mammary gland cell apoptosis. Studies have found that c-Jun N-terminal kinase (*JNK*) can regulate the proliferation of mammary gland cells and lactoprotein synthesis in dairy cows by activating Tudor-SN (Ao et al., 2021). *EGFR* is a member of the epidermal growth factor receptor (*HER*) family. Studies have found that *EGFR* promotes adhesion between mammary gland cells and regulates the growth and differentiation of human mammary epithelial cells (Mukhopadhyay et al., 2013). *EGFR*, at concentrations ranging from 12.5 to 50 ng/ml, facilitates the proliferation of mammary epithelial cells in dairy goats, and activation of the EGFR-mediated signaling pathway promotes the survival of mammary epithelial cells in dairy goats (Huang et al., 2020). Therefore, the data obtained in this study provide a basis for future studies on the role of m^{6}A methylation in the development of mammary glands in dairy goats.

Conclusion

In summary, this study revealed the differences in the transcription and methylation levels of genes in mammary gland tissue between the early and peak stage of lactation and explored their regulation in mammary gland development and lactation function. The proportion, distribution and motif of m^{6}A gene modification in the mRNA transcriptome of mammary gland tissue from dairy goats were consistent with the pattern of m^{6}A modification in the same species; the level of m^{6}A modification in mammary gland tissue was highly negatively correlated with the abundance of modified transcripts. The genes that were modified by m^{6}A at both stages were mainly involved in the regulation of the proliferation and differentiation of mammary gland epithelial cells and the development of mammary gland tissue. Among 150 genes closely related to mammary gland development and lactation, *HRAS*, *JUN*, and *EGFR* were most likely to play a key role in regulating mammary gland development and lactation. This study can provide a theoretical basis for the molecular mechanism of mammary gland development and lactation regulation in dairy goats.

Data availability statement

The datasets presented in this study can be found in online repositories. The names of the repository/repositories and accession number(s) can be found below: GEO database. The accession number is GSE210386.

Ethics statement

The animal study was reviewed and approved by Experimental Animal Management Committee of Shandong Agricultural

University. Written informed consent was obtained from the owners for the participation of their animals in this study.

Author contributions

ZJ designed the experiments and applied for the funds for this study, SW and ZJ wrote the manuscript, SW, LZ, RX, and QL analyzed the data of MeRIP-seq, SW, TC, and CZ analyzed the data of RNA-seq, JW performed a correction for this article.

Funding

This work was supported by the National Natural Science Foundation of China (31672401) and the Shandong Provincial Modern Agriculture Industry Technology System (SDAIT-10).

Acknowledgments

We will give thanks to the members of the Animal Conservation Biology Laboratory of Shandong Agricultural University for their help in collecting data. We are grateful to Guangzhou Genedenovo Biotechnology Co., Ltd. for assisting in sequencing and bioinformatics analysis. We also thank all editors and reviewers for their helps to our paper.

Conflict of interest

The authors declare that the research was conducted in the absence of any commercial or financial relationships that could be construed as a potential conflict of interest.

Publisher's note

Supplementary material

The Supplementary Material for this article can be found online at: https://www.frontiersin.org/articles/10.3389/fcell.2022.945202/full#supplementary-material

References

Ao, J., Ma, Z., Li, R., Zhang, S., Gao, X., and Zhang, M. (2021). Phospho-Tudor-SN coordinates with STAT5 to regulate prolactin-stimulated milk protein synthesis and proliferation of bovine mammary epithelial cells. *Anim. Biotechnol.* 13, 1–11. doi:10.1080/10495398.2021.1879824

Ashburner, M., Ball, C. A., Blake, J. A., Botstein, D., Butler, H., Cherry, J. M., et al. (2000). Gene ontology: tool for the unification of biology. The gene Ontology consortium. *Nat. Genet.* 25 (1), 25–29. doi:10.1038/75556

Boccaletto, P., Machnicka, M. A., Purta, E., Piatkowski, P., Baginski, B., Wirecki, T. K., et al. (2018). MODOMICS: a database of RNA modification pathways. 2017 update. *Nucleic Acids Res.* 46, D303–D307. doi:10.1093/nar/gkx1030

Bodi, Z., Bottley, A., Archer, N., May, S., and Fray, R. (2015). Yeast m6A methylated mRNAs are enriched on translating ribosomes during meiosis, and under rapamycin treatment. *PLOS One* 10 (7), e0132090. doi:10.1371/journal.pone.0132090

Brisken, C., and Ataca, D. (2015). Endocrine hormones and local signals during the development of the mouse mammary gland. *Wiley Interdiscip. Rev. Dev. Biol.* 4 (3), 181–195. doi:10.1002/wdev.172

Cao, Z., Zhang, D., Wang, Y., Tong, X., Avalos, L. F. C., Khan, L. M., et al. (2020). Identification and functional annotation of m6A methylation modification in granulosa cells during antral follicle development in pigs. *Anim. Reprod. Sci.* 219, 106510. doi:10.1016/j.anireprosci.2020.106510

Chen, S., Zhou, Y., Chen, Y., and Gu, J. (2018). Fastp: an ultra-fast all-in-one FASTQ preprocessor. *Bioinformatics* 34 (17), i884–i890. doi:10.1093/bioinformatics/bty560

Dai, W., Zou, Y., White, R., Liu, J., and Liu, H. (2018). Transcriptomic profiles of the bovine mammary gland during lactation and the dry period. *Funct. Integr. Genomics* 18 (2), 125–140. doi:10.1007/s10142-017-0580-x

Dominissini, D., Moshitch-Moshkovitz, S., Schwartz, S., Salmon-Divon, M., Ungar, L., Cesarkas, S. O. K., et al. (2012). Topology of the human and mouse m6A RNA methylomes revealed by m6A-seq. *Nature* 485 (7397), 201–206. doi:10.1038/nature11112

Duan, H.-C., Wei, L.-H., Zhang, C., Wang, Y., Chen, L., Lu, Z., et al. (2017). ALKBH10B is an RNA N6-methyladenosine demethylase affecting Arabidopsis floral transition. *Plant Cell* 29 (12), 2995–3011. doi:10.1105/tpc.16.00912

Dubin, D. T., and Stollar, V. (1975). Methylation of Sindbis virus "26S" messenger RNA. *Biochem. Biophys. Res. Commun.* 66 (4), 1373–1379. doi:10.1016/0006-291x(75)90511-2

Elkeles, A., Juven-Gershon, T., Israeli, D., Wilder, S., Zalcenstein, A., and Oren, M. (1999). The c-fos proto-oncogene is a target for transactivation by the p53 tumor suppressor. *Mol. Cell. Biol.* 19 (4), 2594–2600. doi:10.1128/MCB.19.4.2594

Fan, Y., Zhang, C., and Zhu, G. (2019). Profiling of RNA N6-methyladenosine methylation during follicle selection in chicken ovary. *Poult. Sci.* 98 (11), 6117–6124. doi:10.3382/ps/pez277

Hahn, Y., Kim, S., Chio, B., Cho, K., Bandu, R., Kim, K., et al. (2018). Curcumin interacts directly with the Cysteine 259 residue of STAT3 and induces apoptosis in H-Ras transformed human mammary epithelial cells. *Sci. Rep.* 8 (1), 6409. doi:10.1038/s41598-018-23840-2

He, S., Wang, H., Liu, R., He, M., Che, T., Jin, L., et al. (2017). mRNA N6-methyladenosine methylation of postnatal liver development in pig. *PLoS one* 12 (3), e0173421. doi:10.1371/journal.pone.0173421

Hess, J., Angel, P., and Schorpp-Kistner, M. (2004). AP-1 subunits: quarrel and harmony among siblings. *J. Cell Sci.* 117 (25), 5965–5973. doi:10.1242/jcs.01589

Hu, J., Cai, J., Park, S., Lee, K., Li, Y., Chen, Y., et al. (2021). N6 -Methyladenosine mRNA methylation is important for salt stress tolerance in Arabidopsis. *Plant J.* 106 (6), 1759–1775. doi:10.1111/tpj.15270

Huang, J., Dai, B., Qu, H., Zhong, Y., Ma, Y., Luo, J., et al. (2020). Epidermal growth factor stimulates fatty acid synthesis mainly via PLC-γ1/akt signaling pathway in dairy goat mammary epithelial cells. *Animals.* 10 (6), 930. doi:10.3390/ani10060930

Hui, T., Zhu, Y., Shen, J., Bai, M., Fan, Y., Feng, S., et al. (2022). Identification and molecular analysis of m^{6}A-circRNAs from cashmere goat reveal their integrated

regulatory network and putative functions in secondary hair follicle during anagen stage. *Animals*. 12 (6), 694. doi:10.3390/ani12060694

Ji, R., and Zhang, X. (2021). The roles of RNA N6-methyladenosine in regulating stem cell fate. *Front. Cell Dev. Biol.* 9, 765635. doi:10.3389/fcell.2021.765635

Ji, Z., Chao, T., Zhang, C., Liu, Z., Hou, L., Wang, J., et al. (2019). Transcriptome analysis of dairy goat mammary gland tissues from different lactation stages. *DNA Cell Biol.* 38 (2), 129–143. doi:10.1089/dna.2018.4349

Ji, Z., Chao, T., Liu, Z., Hou, L., Wang, J., Wang, A., et al. (2020). Genome-wide integrated analysis demonstrates widespread functions of lncRNAs in mammary gland development and lactation in dairy goats. *BMC Genomics* 21 (1), 254. doi:10.1186/s12864-020-6656-3

Kambe, S., Yoshitake, H., Yuge, K., Ishida, Y., Ali, M. M., Takizawa, T., et al. (2014). Human exosomal placenta-associated miR-517a-3p modulates the expression of PRKG1 mRNA in Jurkat cells. *Biol. Reprod.* 91 (5), 129. doi:10.1095/biolreprod.114.121616

Kanehisa, M., and Goto, S. (2000). KEGG: kyoto encyclopedia of genes and genomes. *Nucleic Acids Res.* 28 (1), 27–30. doi:10.1093/nar/28.1.27

Kim, D., Langmead, B., and Salzberg, S. L. (2015). HISAT: a fast spliced aligner with low memory requirements. *Nat. Methods* 12 (4), 357–360. doi:10.1038/nmeth.3317

Li, B., and Dewey, C. N. (2011). RSEM: accurate transcript quantification from RNA-seq data with or without a reference genome. *BMC Bioinforma.* 12, 323. doi:10.1186/1471-2105-12-323

Li, B., Wang, X., Li, Z., Lu, C., Zhang, Q., Chang, L., et al. (2019). Transcriptome-wide analysis of N6-methyladenosine uncovers its regulatory role in gene expression in the lepidopteran *Bombyx mori*. *Insect Mol. Biol.* 28 (5), 703–715. doi:10.1111/imb.12584

Li, T., Lin, C., Zhu, Y., Xu, H., Yin, Y., Wang, C., et al. (2021). Transcriptome profiling of m6A mRNA modification in bovine mammary epithelial cells treated with *Escherichia coli*. *Int. J. Mol. Sci.* 22 (12), 6254. doi:10.3390/ijms22126254

Lin, Z., Hsu, P., Xing, X., Fang, J., Lu, Z., Zou, Q., et al. (2017). Mettl3-/Mettl14-mediated mRNA N 6-methyladenosine modulates murine spermatogenesis. *Cell Res.* 27 (10), 1216–1230. doi:10.1038/cr.2017.117

Luo, G.-Z., MacQueen, A., Zheng, G., Duan, H., Dore, L. C., Lu, Z., et al. (2014). Unique features of the m6A methylome in *Arabidopsis thaliana*. *Nat. Commun.* 5, 5630. doi:10.1038/ncomms6630

Macias, H., and Hinck, L. (2012). Mammary gland development. *Wiley Interdiscip. Rev. Dev. Biol.* 1 (4), 533–557. doi:10.1002/wdev.35

Meng, J., Lu, Z., Liu, H., Zhang, L., Zhang, S., Chen, Y., et al. (2014). A protocol for RNA methylation differential analysis with MeRIP-Seq data and exomePeak R/Bioconductor package. *Methods* 69 (3), 274–281. doi:10.1016/j.ymeth.2014.06.008

Meyer, K., Saletore, Y., Zumbo, P., Elemento, O., Mason, C., and Jaffrey, S. (2012). Comprehensive analysis of mRNA methylation reveals enrichment in 3' UTRs and near stop codons. *Cell* 149 (7), 1635–1646. doi:10.1016/j.cell.2012.05.003

Moon, A., Kim, M., Kim, T., Kim, S., Kim, H., Chen, Y., et al. (2000). H-ras, but not N-ras, induces an invasive phenotype in human breast epithelial cells: a role for MMP-2 in the H-ras-induced invasive phenotype. *Int. J. Cancer* 85 (2), 176–181. doi:10.1002/(sici)1097-0215(20000115)85:2<176:aid-ijc5>3.0.co;2-e

Mukhopadhyay, C., Zhao, X., Maroni, D., Band, V., and Naramura, M. (2013). Distinct effects of EGFR ligands on human mammary epithelial cell differentiation. *PLoS one* 8 (10), e75907. doi:10.1371/journal.pone.0075907

Nachtergaele, S., and He, C. (2018). Chemical modifications in the life of an mRNA transcript. *Annu. Rev. Genet.* 52, 349–372. doi:10.1146/annurev-genet-120417-031522

Niu, Y., Zhao, X., Wu, Y.-S., Li, M.-M., Wang, X.-J., and Yang, Y.-G. (2013). N6-methyl-adenosine (m^6A) in RNA: an old modification with a novel epigenetic function. *Genomics Proteomics Bioinforma.* 11 (1), 8–17. doi:10.1016/j.gpb.2012.12.002

Passegue, E., and Wagner, E. F. (2000). JunB suppresses cell proliferation by transcriptional activation of p16(INK-4a) expression. *EMBO J.* 19 (12), 2969–2979. doi:10.1093/emboj/19.12.2969

Pertea, M., Pertea, G. M., Antonescu, C. M., Chang, T. C., Mendell, J. T., and Salzberg, S. L. (2015). StringTie enables improved reconstruction of a transcriptome from RNA-seq reads. *Nat. Biotechnol.* 33 (3), 290–295. doi:10.1038/nbt.3122

Pertea, M., Kim, D., Pertea, G. M., Leek, J. T., and Salzberg, S. L. (2016). Transcript-level expression analysis of RNA-seq experiments with HISAT, StringTie and Ballgown. *Nat. Protoc.* 11 (9), 1650–1667. doi:10.1038/nprot.2016.095

Rengaraj, P., Obrdlík, A., Vukić, D., Varadarajan, N. M., Keegan, L. P., Vaňáčová, S., et al. (2021). Interplays of different types of epitranscriptomic mRNA modifications. *RNA Biol.* 18, 19–30. doi:10.1080/15476286.2021.1969113

Shannon, P., Markiel, A., Ozier, O., Baliga, N. S., Wang, J. T., Ramage, D., et al. (2003). Cytoscape: a software environment for integrated models of biomolecular interaction networks. *Genome Res.* 13 (11), 2498–2504. doi:10.1101/gr.1239303

Stefanon, B., Colitti, M., Gabai, G., Knight, C. H., and Wilde, C. J. (2002). Mammary apoptosis and lactation persistency in dairy animals. *J. Dairy Res.* 69 (1), 37–52. doi:10.1017/s0022029901005246

Wang, A., Ji, Z., Xuan, R., Zhao, X., Hou, L., Li, Q., et al. (2021). Differentially expressed MiRNAs of goat submandibular glands among three developmental stages are involved in immune functions. *Front. Genet.* 12, 678194. doi:10.3389/fgene.2021.678194

Wang, X., Lu, Z., Gomez, A., Hon, G. C., Yue, Y., Han, D., et al. (2014). N6-methyladenosine-dependent regulation of messenger RNA stability. *Nature* 505 (7481), 117–120. doi:10.1038/nature12730

Wang, M., Liang, Y., Ibeagha-Awemu, E., Li, M., Zhang, H., Chen, Z., et al. (2020). Genome-wide DNA methylation analysis of mammary gland tissues from chinese holstein cows with staphylococcus aureus induced mastitis. *Front. Genet.* 11, 550515. doi:10.3389/fgene.2020.550515

Wang, T., Kong, S., Tao, M., and Ju, S. (2020). The potential role of RNA N6-methyladenosine in Cancer progression. *Mol. Cancer* 19 (1), 88. doi:10.1186/s12943-020-01204-7

Wang, Y., Zheng, Y., Guo, D., Zhang, X., Guo, S., Hui, T., et al. (2020). m^6A methylation analysis of differentially expressed genes in skin tissues of coarse and fine type liaoning cashmere goats. *Front. Genet.* 10, 1318. doi:10.3389/fgene.2019.01318

Wang, Y., Li, G., Zhang, X., Guo, S., Guo, D., Zhang, X., et al. (2021). Analysis of m^6A methylation in skin tissues of different sex Liaoning cashmere goats. *Anim. Biotechnol.* 25, 1–11. doi:10.1080/10495398.2021.1962897

Weiß, K. T., Fante, M., Köhl, G., Schreml, J., Haubner, F., Kreutz, M., et al. (2017). Proton-sensing G protein-coupled receptors as regulators of cell proliferation and migration during tumor growth and wound healing. *Exp. Dermatol.* 26 (2), 127–132. doi:10.1111/exd.13209

Xu, T., Xu, Z., Liu, L., Zeng, T., Gu, L., Huang, Y., et al. (2021). Transcriptome-wide study revealed m6A regulation of embryonic muscle development in Dingan goose (*Anser cygnoides* orientalis). *BMC Genomics* 22 (1), 270. doi:10.1186/s12864-021-07556-8

Xuan, R., Chao, T., Wang, A., Zhang, F., Sun, P., Liu, S., et al. (2020). Characterization of microRNA profiles in the mammary gland tissue of dairy goats at the late lactation, dry period and late gestation stages. *PLOS One* 15 (6), e0234427. doi:10.1371/journal.pone.0234427

Zhu, C., Wang, L., Zhu, J., Jiang, Y., Du, X., Duan, Q., et al. (2021). OGR1 negatively regulates β-casein and triglyceride synthesis and cell proliferation via the PI3K/AKT/mTOR signaling pathway in goat mammary epithelial cells. *Anim. Biotechnol.* 32 (5), 627–636. doi:10.1080/10495398.2020.1737099

frontiers | Frontiers in Genetics

TYPE Original Research
PUBLISHED 20 October 2022
DOI 10.3389/fgene.2022.990594

OPEN ACCESS

EDITED BY
Kunqi Chen,
Fujian Medical University, China

REVIEWED BY
Qingjia Chi,
Wuhan University of Technology, China
Wenxiong Zhang,
Second Affiliated Hospital of Nanchang University, China

*CORRESPONDENCE
Li Li,
lily9711214@126.com
Qi Zhang,
zhangqi4116@126.com

†These authors have contributed equally to this work

SPECIALTY SECTION
This article was submitted to RNA, a section of the journal Frontiers in Genetics

RECEIVED 10 July 2022
ACCEPTED 03 October 2022
PUBLISHED 20 October 2022

CITATION
Lu Q, Liu L, Wang S, Zhang Q and Li L (2022), Comprehensive analysis of m5C-Related lncRNAs in the prognosis and immune landscape of hepatocellular carcinoma.
Front. Genet. 13:990594.
doi: 10.3389/fgene.2022.990594

Comprehensive analysis of m5C-Related lncRNAs in the prognosis and immune landscape of hepatocellular carcinoma

Qian Lu[1,2†], Lianyu Liu[3,2†], Shuai Wang[4], Qi Zhang[1,2*] and Li Li[1,2*]

[1]Department of Gastroenterology, The Affiliated Hospital of Xuzhou Medical University, Xuzhou, China, [2]Institute of Digestive Diseases, Xuzhou Medical University, Xuzhou, China, [3]Department of General Surgery, The Affiliated Hospital of Xuzhou Medical University, Xuzhou, China, [4]The Graduate School, Xuzhou Medical University, Xuzhou, China

5-Methyladenosine (m5C) is a type of epigenetic modification involved in the progression of various cancers. To investigate the role of m5C-related long non-coding RNAs (lncRNAs) in the prognosis and immune cell infiltration in hepatocellular carcinoma (HCC), we obtained patients' clinical information and transcriptome data of HCC from the Cancer Genome Atlas (TCGA) database. We applied Pearson correlation analysis to construct an m5C-related lncRNA–messenger RNA (mRNA) co-expression network. Univariate Cox analysis, least absolute shrinkage and selection operator (LASSO), and multivariate Cox analysis were employed to establish an m5C-related lncRNA prognostic risk model. We then verified the model using Kaplan–Meier analysis, principal component analysis, as well as univariate and multivariate Cox analyses. The expression of m5C-related lncRNAs was validated in HCC tissues and different cell lines. Combining the risk score and clinicopathological features, a nomogram was established for predicting the overall survival (OS) of HCC patients. Furthermore, gene set enrichment analysis (GSEA) revealed that some tumor-associated pathways were significantly enriched in the high-risk group. Immune cell infiltration analysis demonstrated that the levels of Treg cells, neutrophils, and M2 macrophages were higher in the high-risk group. In addition, patients with high tumor mutation burden (TMB) had worse OS than those with low TMB. We also assessed the immune checkpoint level and chemotherapeutic agent sensibility. Then *in vitro* experiments were performed to examine the biological function of MKLN1-AS in HCC cells and found that knockdown of MKLN1-AS suppressed the proliferation, migration, and invasion. In conclusion, m5C-related lncRNAs played a critical role in predicting the prognosis of patients with HCC and may serve as new therapeutic targets for HCC patients.

KEYWORDS

m5C, lncRNA, hepatocellular carcinoma, prognosis, immune landscape

Introduction

Hepatocellular carcinoma (HCC) is one of the most common malignancies and the fourth leading cause of cancer-related deaths worldwide (Ma et al., 2016; Xu et al., 2022). Many types of pharmaceutical therapies have been approved to treat HCC, including targeted tyrosine kinase inhibitors, immune-based therapies, and combination of chemotherapy. However, due to chemoresistance and immunosuppressive elements, current therapies have not effectively improved the outcome for HCC patients (Foerster et al., 2022). Therefore, there is an urgent need for novel accurate prognostic biomarkers that could lead to more effective diagnostic and treatment strategies.

RNA modification could regulate genetic expression in a dynamic and reversible way. It is primarily modulated by three types of effector proteins: writers, readers, and erasers (Biswas and Rao, 2018). N6-Methylcytosine (m6A) is the main type of modification in eukaryotic cellular RNAs and plays a vital role in biological progress, including embryonic stem cell self-renewal, metabolism, immunity, and apoptosis (Meyer and Jaffrey, 2017). 5-Methylcytosine (m5C) is another common RNA modification. Similar to m6A methylation, m5C methylation is involved in RNA metabolism, structural stability, and stress response (Zhao et al., 2017). Furthermore, increasing evidence has shown that m5C modification can affect the progression of multiple malignant tumors, including HCC. Sun et al. reported that NSUN2-mediated m5C modification of long non-coding RNA (lncRNA) H19 was positively associated with poor differentiation of HCC (Sun et al., 2020). Cui et al. reported that NSUN4 was conspicuously upregulated in HCC and could work as an independent prognostic factor (Cui et al., 2022).

LncRNA is a type of non-coding RNA molecule with a length greater than 200 nt. It modulates gene expression mainly at epigenetic, transcriptional, and post-transcriptional levels (Bridges et al., 2021). Numerous lncRNAs have been reported to be closely correlated with carcinogenesis, metastasis, prognosis, and diagnosis of various cancers (Abbastabar et al., 2018). Previous studies have found that some methylation regulators could affect tumor progression by regulating the level of relevant lncRNAs. Dai et al. (2020) reported that METTL3 could upregulate the expression level of LINC00958 by increasing its stability, and LINC00958 sponged miR-3619-5p to upregulate hepatoma-derived growth factor, thereby promoting HCC progression. Hu et al. reported that IGF2BP2 could serve as a member of m6A readers and increase the stability of lncRNA DANCR, thus promoting cell proliferation and carcinogenesis of pancreatic cancer (Hu et al., 2020). In addition, Cui et al. reported that RNA m6A demethylase FTO could epigenetically upregulate the expression of LINC00022, thereby promoting tumorigenesis of esophageal squamous cell carcinoma (Cui et al., 2021). So far, few studies have reported the relationship between m5C regulators and lncRNAs in HCC progression and immune cell infiltration. Therefore, further understanding of how m5C modification interacts with lncRNAs in HCC may be favorable for exploring effective biomarkers and novel therapeutic targets.

Accumulating studies have shown that immune cells in the tumor microenvironment (TME) play a determinative role in tumor progression (Hinshaw and Shevde, 2019). A series of immunotherapy approaches have been successfully applied in clinical practices, such as the adoptive cell transfer, modulation of immune checkpoints, and dendritic cell-based vaccination (Lei et al., 2020). LncRNAs were key regulators in the immune system, which could regulate tumor invasion and evade immune surveillance by regulating tumor immune cell activation, proliferation, and cytokine secretion. In HCC, lncRNA FENDRR sponged miR-423-5p to suppress the inhibitory function of Tregs within TME, therefore weakening the immune evasion capability (Yu et al., 2019). Xue et al. (2019) reported that M2 macrophages were the predominant tumor-infiltrating immune cells in bladder cancer and associated with the prognosis of patients. However, the relationship between m5C-related lncRNAs and tumor-associated immune cells in HCC remains unknown.

This study aimed to explore the prognostic significance and immune landscape of the m5C-related lncRNAs in HCC. Based on the Cancer Genome Atlas (TCGA) database and bioinformatic analyses, we constructed an m5C-related lncRNA prognostic model and subsequently validated the accuracy and efficiency of the model. We utilized a nomogram to predict patients' survival rates. Furthermore, the association between immune cell infiltration and the risk model was analyzed. More importantly, the responses of HCC patients to chemotherapy and immunotherapy were predicted to provide guidance for clinical treatment. Finally, we conducted experiments *in vitro* to identify the biological function of MKLN1-AS identified with the highest contribution in the risk model.

Materials and methods

Data and m5C regulator acquisition

The clinical and transcriptome data of 374 HCC tissues and 50 normal tissues were obtained from TCGA data website (http://portal.gdc.cancer.gov/). After excluding four samples without complete survival time and status, 370 HCC samples were included for further study. The clinical characteristics of these patients with HCC are shown in Supplementary Table S1. We also downloaded the annotation file of GRCH38 from the Ensemble official website (http://asia.ensembl.org) to distinguish mRNAs and lncRNAs. A total of 16 m5C regulators (NOP2, DNMT1, DNMT3A, DNMT3B, NSUN2, NSUN3, NSUN4, NSUN5, NSUN6, NSUN7, TRDMT1, ALYREF, YBX1, TET1, TET2, and TET3) were selected according to previous publications. The differential expression

of 16 m5C regulators between tumor and normal tissues was analyzed using the limma package in R software ($p < 0.05$, | log2 (folding change) | > 1). We also used survival and survminer packages to perform survival analysis.

Construction and validation of m5C-Related lncRNA prognostic risk model

Pearson correlation analysis was implemented to identify m5C-related lncRNAs with |Pearson R| > 0.4 and $p < 0.001$. We then used the limma package to perform differential m5C-related lncRNA expression analysis between HCC tissues and normal tissues and thus acquired 633 differentially expressed lncRNAs ($p < 0.05$). HCC cases were randomly divided into a training cohort and a testing cohort in a 1:1 ratio. In the training cohort, we conducted the univariate Cox regression analysis to screen out prognostic lncRNAs. Based on screened 17 lncRNAs with prognostic value, we performed the least absolute shrinkage and selection operator (LASSO) Cox regression and multivariate Cox regression to construct the prognostic prediction model. Five lncRNAs were extracted and used for further analysis. The risk score of each patient was calculated using the following formula:

Risk score = $\sum_{i=1}^{n} Coef_i \times X_i$ ($Coef_i$ represents the coefficients, and X_i represents the expression value of each m5C-related lncRNA).

Next, we graded each HCC patient. All patients were divided into high- and low-risk groups based on the median risk score calculated from the training cohort. We used the survival R package to implement Kaplan–Meier (KM) survival curve analysis. Receiver operating characteristic (ROC) curves was also constructed to evaluate the prognostic capability of the risk model. Moreover, we used principal component analysis (PCA) to visualize whether the risk score could well distinguish the high-risk group from the low-risk group.

Evaluation of m5C-Related lncRNA risk model as independent prognostic indicator

We performed subgroup stratification survival analysis in clinicopathological features using KM plot to confirm the prediction performance of the model. Univariate and multivariate Cox regression analyses were conducted to assess whether the risk model was an independent factor. In addition, we constructed a heatmap based on clinical characteristics and differential expression of the five prognostic lncRNAs in different risk groups. Furthermore, combining the risk score and TNM stage, we established a nomogram to improve clinical diagnosis and application. Moreover, the nomogram's predictive value was evaluated using ROC curve.

Cell culture and quantitative real-time PCR assay

Human HCC cell lines (Huh7, HepG2, Hep3B, and SNU-387) and one normal liver cell line (L-02) were obtained from the Cell Bank of the Chinese Academy of Sciences (Shanghai, China). The cell lines were cultured in medium containing 10% fetal bovine serum (FBS) with 5% CO_2 at 37°C. We also collected 20 pairs of HCC and para-carcinoma tissue samples from the Department of Hepatobiliary Surgery, the Affiliated Hospital of Xuzhou Medical University, from March 2021 to May 2022. To evaluate the expression level of m5C-related lncRNAs, we used RNA Isolater Total RNA Extraction Reagent (Vazyme, Nanjing, China) to isolate total RNAs from the tissue samples and cell lines. Reverse transcription was performed using HiScript II Q RT SuperMix (Vazyme, Nanjing, China), and quantitative real-time PCR was then conducted using ChamQ SYBR qPCR Master Mix (Vazyme, Nanjing, China). The relative expression of the five lncRNAs was calculated using the $2^{-\Delta\Delta CT}$ method, and GAPDH served as an internal control. The primer sequences used in our study are listed in Supplementary Table S2.

Prediction of m5C sites on five lncRNAs

RNAm5Cfinder (Ban et al., 2020), m5C-Atlas (Ma et al., 2022), and iRNA-m5C (Chen et al., 2021) databases were used to predict the m5C site of the lncRNAs.

Function and signaling pathways enrichment analysis

The limma package was implemented to screen genes that were differentially expressed between the high- and low-risk groups. Subsequently, we performed gene ontology (GO) and Kyoto encyclopedia of genes and genomes (KEGG) analysis to explore the potential function and pathway between the differentially expressed genes (DEGs). Finally, GSEA software (GSEA_4.2.2) was used to identify potential signaling pathways in the high- and low-risk groups.

Tumor immune analysis and somatic variant analysis

We calculated the correlation coefficient between the risk score and the immune infiltrated cells based on currently acknowledged software, including TIMER, XCELL, QUANTISEQ, MCPcounter, EPIC, CIBERSORT-ABS, and CIBERSORT. We used Wilcoxon signed-rank test to analyze the difference in immune infiltrating cell abundance between high- and low-risk groups. We also measured Spearman

correlation coefficients between the risk score and the immune infiltrated cells, and the results are displayed herein in a lollipop diagram. The activities of 13 immune-related pathways between two groups were quantified using the "GSVA" package by ssGSEA. Next, we performed a two-way analysis of variance (ANOVA) to explore the association of the immune infiltration subtype with a risk score. R package maftools were used to analyze the gene somatic mutation data downloaded from the Genomic Data Commons (GDC) database.

Immunotherapy response and drug sensitivity analysis

The TIDE algorithm was applied to predict the immunotherapeutic response. We also analyzed the differential expression level of 34 immune checkpoints between different risk groups. Furthermore, we used R package pRRophetic to predict the half-maximal inhibitory concentration (IC_{50}) of drugs for HCC samples from different risk groups. In addition, the association between the expression level of prognostic lncRNAs and drug sensitivity was determined using relevant data obtained from CellMiner database.

Cell transfection

SiRNAs targeting MKLN1-AS (si-MKLN1-AS#1, si-MKLN1-AS#2) and the negative control (si-NC) were designed and synthesized by Gene Pharma Technology (Shanghai, China). HepG2 cells were transfected with siRNAs by siLentFect Lipid Reagent (Bio-Rad, CA, United States). After 48 h, the cells were collected for further experiments. The siRNAs sequences against MKLN1-AS are listed in Supplementary Table S3.

Cell counting Kit-8 (CCK-8) assay

Transfected cells (2000 cells/pore) were seeded into 96-well plates for CCK-8 assay. Then, 10 μl of CCK-8 reagent (APExBIO, USA) and 100 μl of serum-free MEM medium were introduced into cells and incubated for 2 h. Subsequently, the absorbance was measured at 450 nm at 0, 24, 48, 72, and 96 h.

Transwell assay

In invasion assay, the top chamber was treated with Matrigel (BD Biosciences, Mississauga, Canada) while in the migration assay was not. Transfected cells (5×10^5 cells/pore) were seeded into the upper layer of the transwell. A total of 700 μl chamber MEM medium with 20% FBS was added to the lower chamber, and the chamber was cultured at 37°C for 24–48 h. The invaded cells were fixed by 4% paraformaldehyde and stained with 0.1% crystal violet. A light microscope was used to observe cell migration and invasion.

Wound healing assay

Transfected HepG2 cells were seeded in six-well plates and cultured to 80% confluence. Then, 200 μL pipette tips were used to create clear scratches in each well. Thereafter, the cells were cultured in a serum-free MEM medium. The scratches were imaged by a light microscopy at 0 and 24 h.

Statistical analysis

One-way ANOVA was used to compare the differential expression level of 16 m5C regulators between HCC tissues and normal tissues. Cytoscape was used to plot the co-expression network of five m5C-related lncRNA–mRNA. The KM method and log-rank test were employed to compare the survival curves between various subgroups. Univariate and multivariate Cox regression analyses were used to identify independent prognostic factors. The nomogram was evaluated for predictable performance by calibration curve, and ROC curve was used to measure the prognostic efficiency of the nomogram for 1-, 3-, and 5-year overall survival (OS). Statistical analysis was carried out using R version 4.1.1, and $p < 0.05$ was considered statistically significant.

Results

The Landscape of Expression and Prognosis of 16 m5C Regulators in HCC Tissues.

The workflow of this study is shown in Figure 1. We first explored the differential expression of 16 m5C regulators between HCC tissues and normal tissues in TCGA dataset. We found that all 16 m5C regulators except TET2 and TRDMT1 were differentially expressed. NSUN6 expression was significantly downregulated in HCC than in normal tissues, whereas that of the other 13 m5C regulators was significantly upregulated in HCC (Figure 2A). To evaluate the interaction among 16 m5C regulators, the correlation analysis showed that most m5C regulators were positively correlated with other regulators. We found a weak correlation between NSUN6 and other regulators and a strong correlation between DNMT3A and TET3 (Figure 2B). The m5C regulator network was depicted to indicate the interactions, connection, and prognostic value of m5C regulators for HCC patients. The

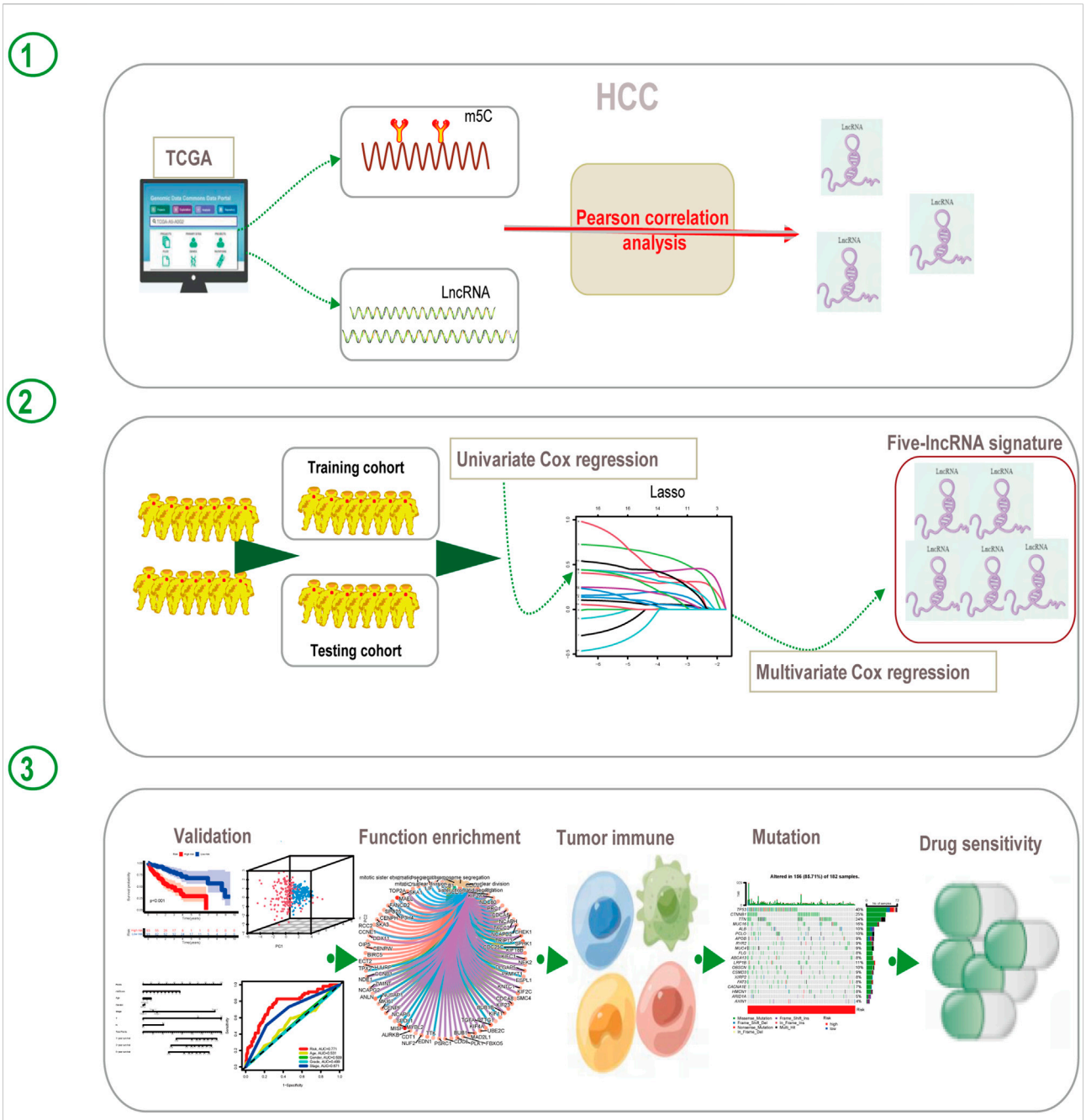

FIGURE 1
Flow diagram of this study.

most common positive correlation was found not only in the same category but also between different types of regulators. Negative correlations occurred between NSUN6 and NSUN5, NSUN6, and YBX1, and NSUN6 and ALYREF (Figure 2C). KM survival analysis showed significant differences among 15 m5C regulators in OS of HCC patients (Figures 2D–F and Supplementary Figure S1).

Construction and verification of the m5C-Related lncRNA risk model

Pearson correlation analysis was conducted to identify the m5C-related lncRNAs based on the expression of m5C regulators and lncRNAs in HCC patients. Then 633 m5C-related lncRNAs were screened out using differential expression analysis. We

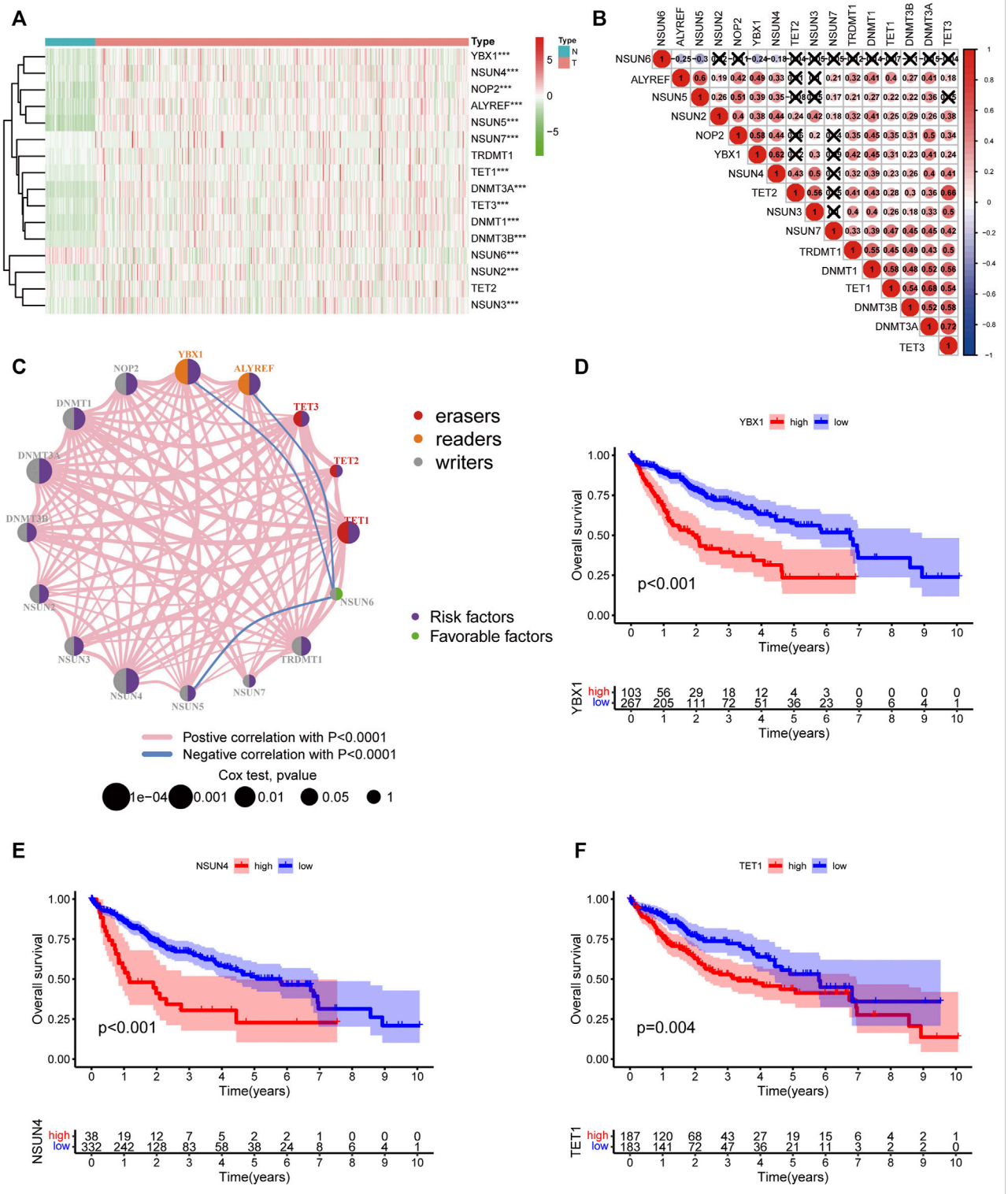

FIGURE 2
The landscape of expression and prognosis of m5C regulators in HCC patients. **(A)** Heatmap displaying different expressions of m5C regulators in HCC. **(B)** Spearman correlation analysis of 16 m5C regulators. **(C)** The interaction between m5C regulators in HCC. The size of the circle represented the influence of each regulator on prognosis, and the range of values calculated by log-rank test was $p < 0.0001$, $p < 0.001$, $p < 0.01$, $p < 0.05$, and $p < 1$. Purple in the right part of the circle indicates risk survival factors and green in the right part of the circle indicates favorable survival factors. The types of m5C regulators are labeled as different colors in the left part of the circle. The thickness of lines shows correlation strength. Positive correlation is shown in pink and negative correlation in blue. **(D–F)** Overall survival analysis based on three m5C regulators' expression in HCC.

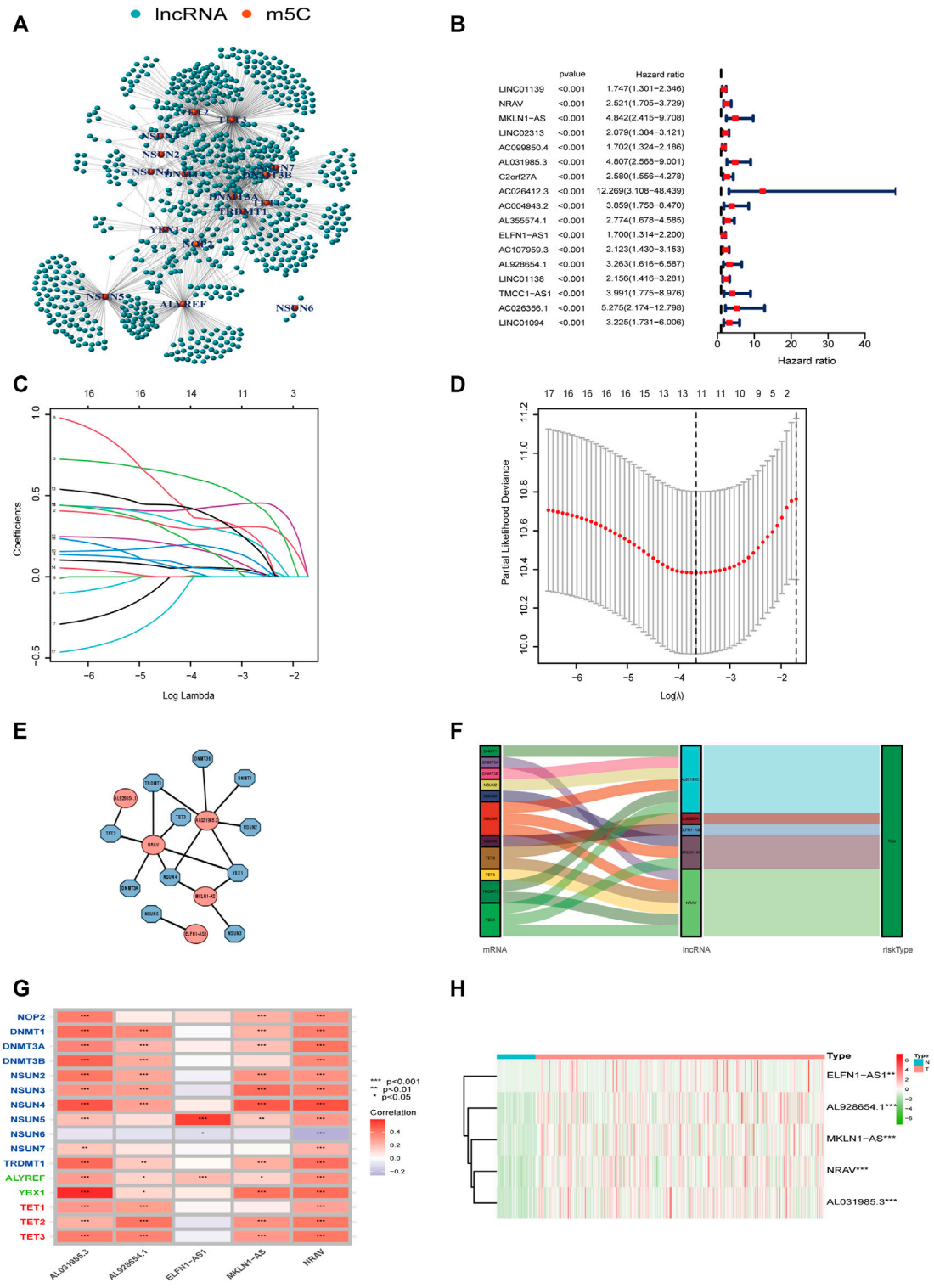

FIGURE 3
Construction of the m5C-lncRNA risk model. **(A)** The co-expression network of m5C regulators and their related lncRNAs. **(B)** Forest plot showing the hazard ratio of 17 lncRNAs with prognostic value using univariate Cox regression analysis. **(C,D)** LASSO regression is performed, and cross-validation for optimal parameter. **(E)** Co-expression network of the five m5C-related lncRNAs and m5C regulators. **(F)** Sankey diagram showing the relationship between m5C regulators and m5C-related lncRNAs. **(G)** The correlations between 16 m5C regulators and five m5C-related lncRNAs. **(H)** Heatmap of the differential expression of five lncRNAs in tumor-and normal tissues.

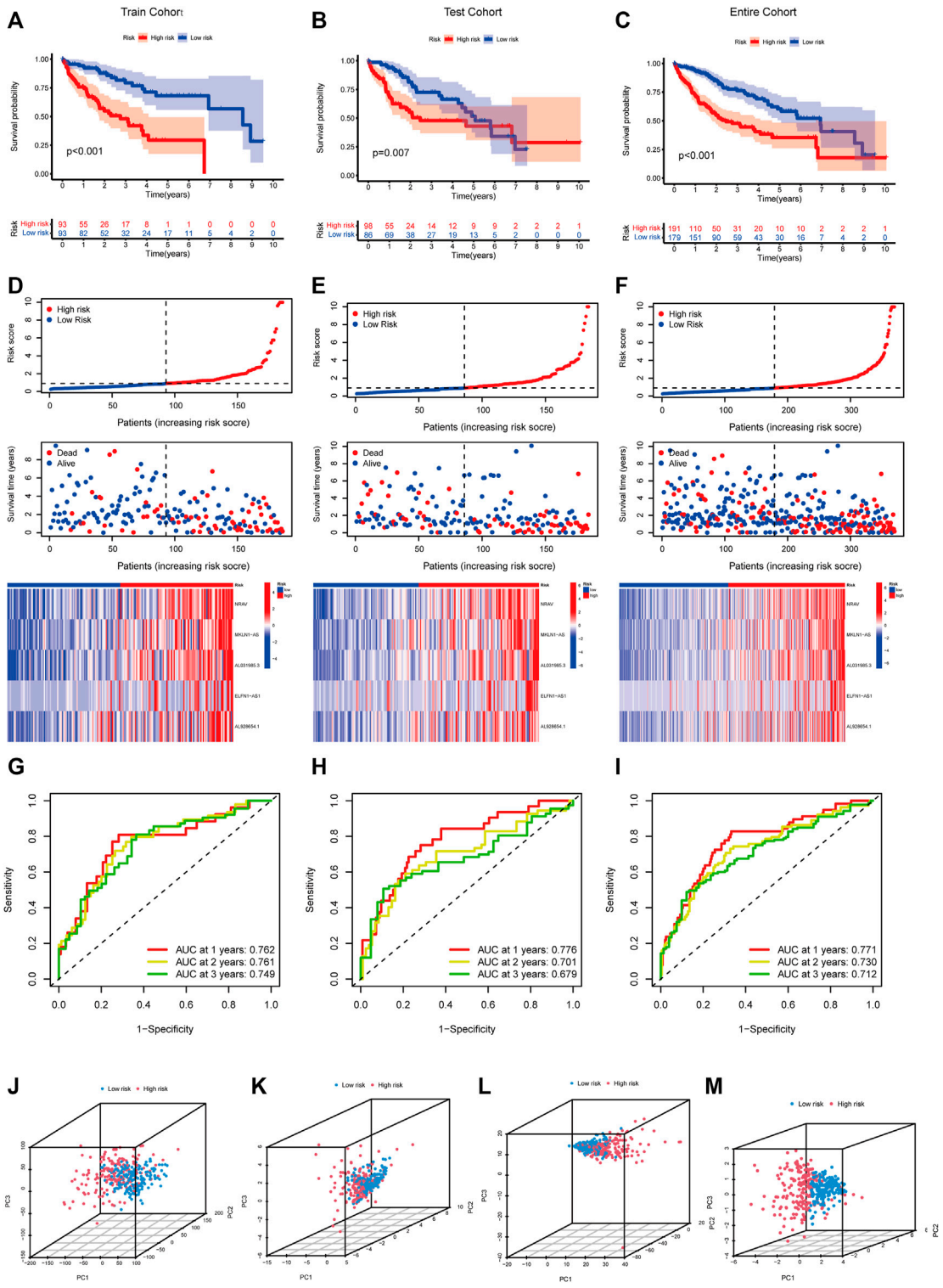

FIGURE 4
Verification of the m5C-lncRNA risk model. Kaplan-Meier curves of overall survival of high-risk and low-risk groups in the training cohort **(A)**, testing cohort **(B)**, and entire cohort **(C)**. The distribution of risk scores, survival status and expression matrix of five-lncRNA signature in the training cohort **(D)**, testing cohort **(E)**, and entire cohort **(F)**. ROC curves of the model for OS prediction including 1, 2, and 3 years in the training cohort **(G)**, testing cohort **(H)**, and entire cohort **(I)**. PCA analysis between the high-risk and low-risk groups based on all genes **(J)**, m5C genes **(K)**, m5C-lncRNAs **(L)**, and risk lncRNAs **(M)**.

constructed a co-expression network of m5C regulators and their related lncRNAs (Figure 3A). In addition, we randomly divided 370 HCC cases into a training cohort (50%, n = 186 cases) and a testing cohort (50%, n = 184 cases). Next, univariate Cox regression analysis was conducted to screen the prognostic m5C-related lncRNAs in the training cohort. The result showed that 17 lncRNAs with increased risk (hazard ration, HR > 1) were deemed to have important prognostic value (Figure 3B). Subsequently, we performed LASSO Cox regression to analyze the 17 prognostic m5C-related lncRNAs, followed by multivariate Cox regression analysis to build a prognostic risk model for HCC (Figures 3C,D). Finally, we obtained five lncRNAs with a prognostic significance to construct the prognostic model (Supplementary Table S4). A co-expression network for the visualization of the five m5C-related lncRNAs and 16 m5C regulators was established (Figures 3E,F). We also observed that NRAV and AL031985.3 had the strongest correlation with m5C regulators, whereas ELFN1-AS1 had the weakest correlation. Moreover, correlations among m5C regulators and lncRNAs were mostly positive (Figure 3G). As displayed in Figure 3H, the expression levels of the five m5C-related lncRNAs were significantly different between HCC and normal tissues. The risk score of each HCC patient was calculated as follows: Risk score = 0.4635* NRAV expression level +0.8199* MKLN1-AS expression level +0.6452* AL031985.3 expression level + 0.3553* ELFN1-AS1 expression level +0.7350* AL928654.1 expression level. Notably, the positive coefficients of the five lncRNAs revealed that they were all risk survival factors. We then divided the patients of the training cohort into high- and low-risk groups based on the median risk score. KM survival curves showed that patients with high-risk scores had poor prognoses (Figure 4A). Risk score and survival status distributions showed that more and more patients died as the risk score increased. Additionally, our analysis showed that all the five lncRNAs had higher expression levels in the high-risk group (Figure 4D). Then, we used the same score formula to calculate the risk score of each patient in the testing cohort and the entire cohort, which were employed to validate the signature. The results were similar to those displayed in the training cohort (Figures 4B,C,E,F). Furthermore, we analyzed the prognostic accuracy of risk score using the ROC analysis (in the training cohort: 1-, 2-, and 3-year AUC = 0.762, 0.761, and 0.749, respectively; in the testing cohort: 1-, 2-, and 3-year AUC = 0.776, 0.701, and 0.679, respectively; in the entire cohort: 1-, 2-, and 3-year AUC = 0.771, 0.730, and 0.712, respectively) (Figures 4G–I). We used PCA to visualize the different distribution patterns between the two groups based on all genes, m5C genes, m5C-lncRNAs, and risk lncRNAs. Based on risk lncRNAs, patients were distributed in obviously different directions, so that the m5C-related lncRNA risk model may well differentiate between the high- and low-risk groups (Figures 4J–M).

Validation of the suitability of the model using stratified survival analysis

We conducted stratified analysis by dividing the HCC patients into various subgroups and comparing the OS between high- and low-risk groups to evaluate the prognostic value of this model under different HCC clinicopathological subgroups. The survival analysis revealed that patients with high-risk scores had shorter OS in various subgroups (age >65 years *versus* age ≤65 years, female *versus* male, G1–2 *versus* G3–4, T stage1–2 *versus* T stage3–4, M0 stage, N0 stage, TNM stage I–II *versus* TNM stage III–IV) (Supplementary Figure S2).

The m5C-Related lncRNA risk model was an independent prognostic factor for HCC patients

According to the expression level of each lncRNA, we divided HCC patients into high- and low-expression groups and then performed KM survival analysis on them. The survival curves showed that patients in the high-expression group of AL031985.3, AL928654.1, MKLN1-AS, and NRAV had shorter OS and worse prognoses. Nevertheless, OS of ELFN1-AS1 in the high- and low-expression groups had no statistical differences (Figures 5A–E). According to the heatmap, TNM and T stages ($p < 0.01$) were statistically significantly different between the high- and low-risk groups, but other clinicopathological features had no statistical differences (Figure 5F). Furthermore, we conducted univariate and multivariate Cox regression analyses to confirm whether the risk score calculated using the m5C-related lncRNA risk model could be used as an independent prognostic factor. The univariate analysis showed that TNM stage ($p < 0.001$), T stage ($p < 0.001$), M stage ($p = 0.021$), and risk score ($p < 0.001$) were prognostic factors, whereas the multivariate Cox regression analysis revealed that TNM stage ($p < 0.001$) and risk score ($p < 0.001$) could serve as independent prognostic factors for patients with HCC (Figures 5G,H). In clinical practices, to provide an accurate quantitative tool for evaluating the individual OS of HCC patients, we formulated a nomogram based on risk score and TNM stage screened by multivariate Cox regression analysis to predict 1-, 3-, and 5-year OS probability (Figure 6A). As shown in the calibration curve, the actual and predicted 1-, 3-, and 5-year OS were almost in perfect concordance (Figures 6B–D). The time-dependent ROC curves were used to evaluate the specificity and sensitivity of the nomogram for predicting the prognosis of HCC patients. Our results revealed that AUC values of nomogram were 0.778, 0.806, and 0.786 at 1-, 3-, and 5-year OS, respectively (Figure 6E). Besides, we compared AUC values of risk score, age, gender, grade, and stage and noted that the risk score was superior to

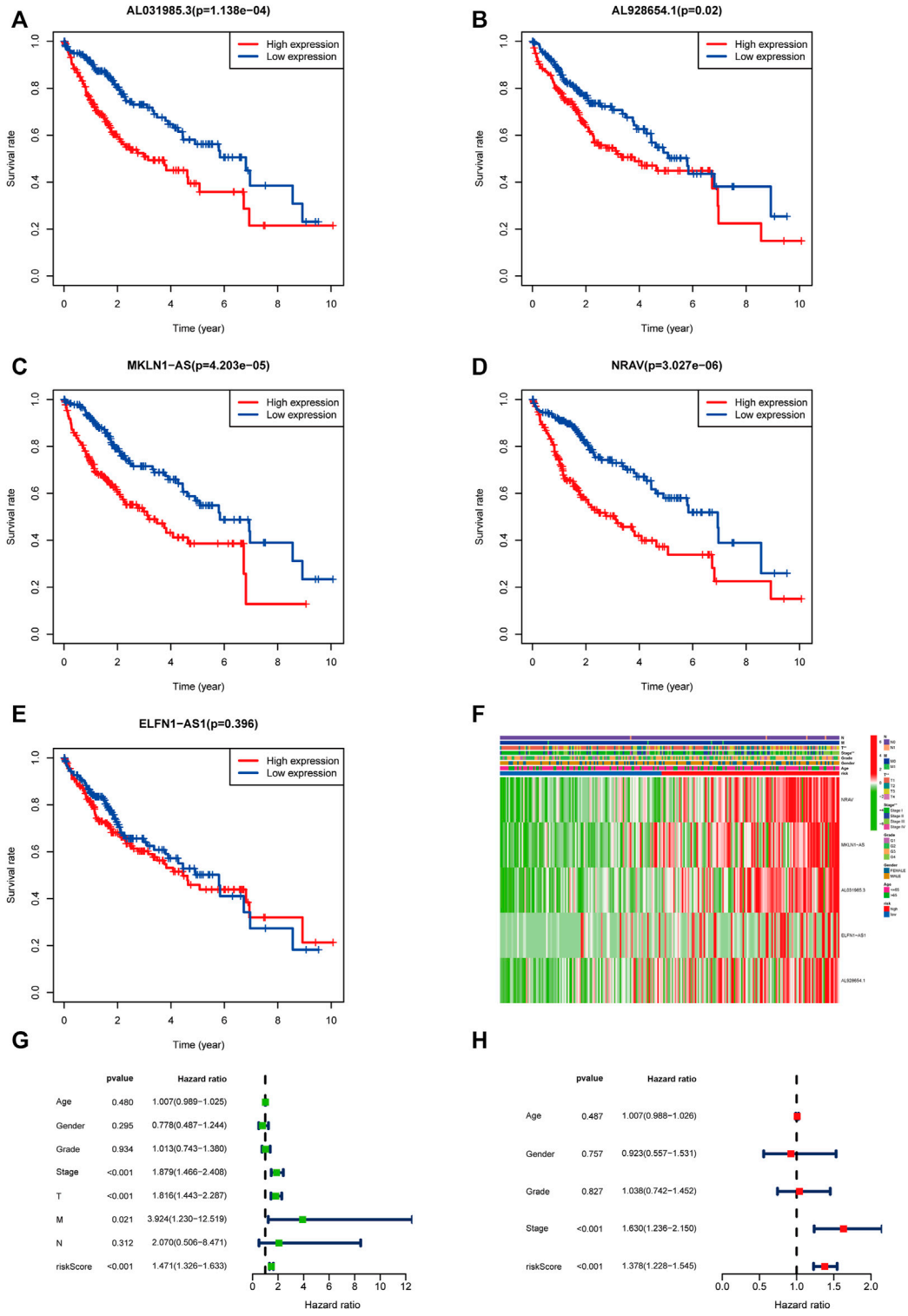

FIGURE 5
Validation of the m5C-related lncRNAs risk score as an independent prognostic factor in HCC patients. **(A–E)** KM survival curves indicated the relationship of the five lncRNAs with prognosis in HCC patients. **(F)** Heatmap showing the correlation between expression levels of the five m5C-lncRNAs and clinicopathological features. **(G,H)** Univariate and multivariate Cox regression analysis of risk score and clinicopathological parameters.

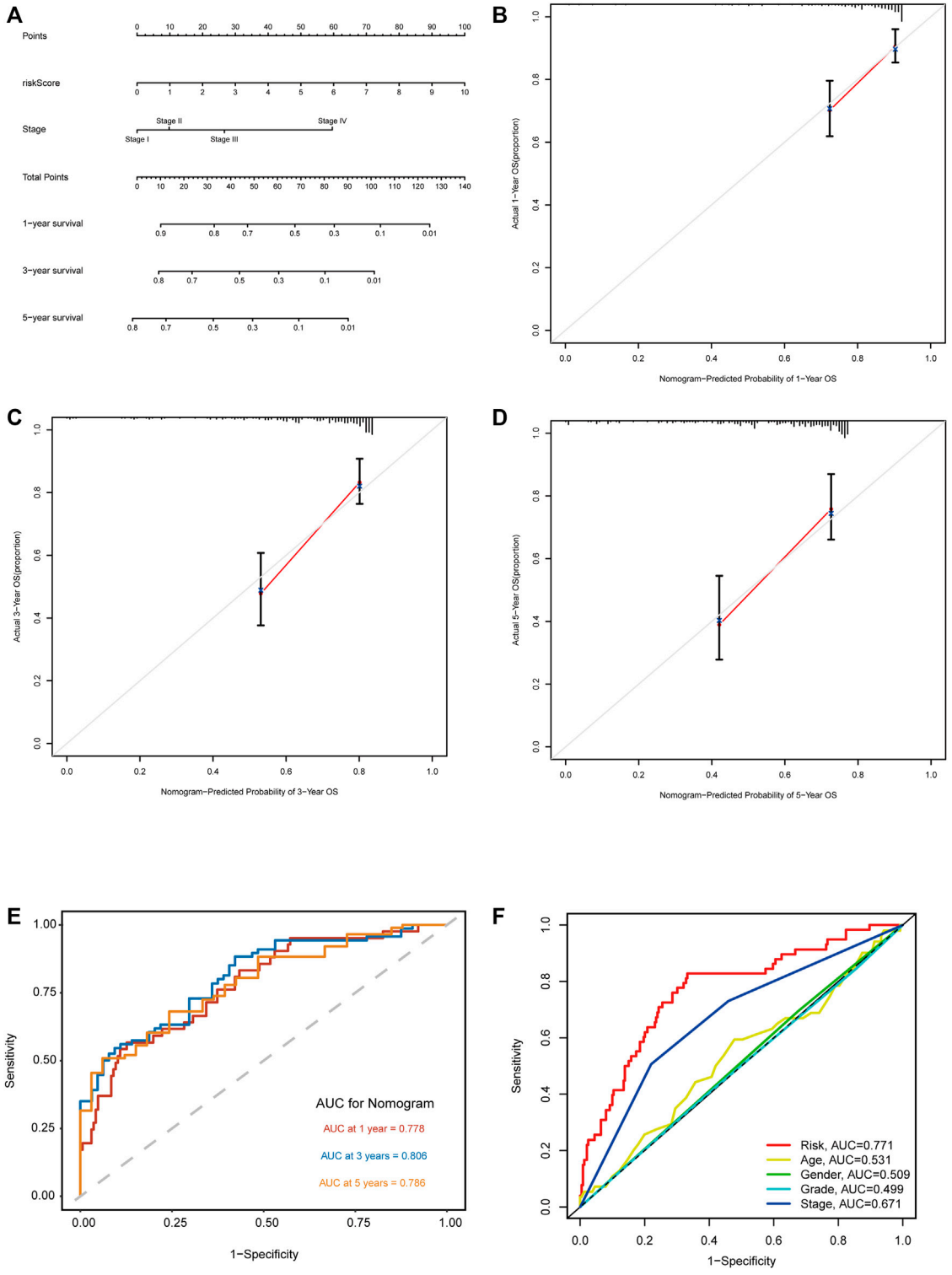

FIGURE 6
Construction and validation of the nomogram based on m5C-related lncRNA risk model. **(A)** Nomogram with risk score and TNM stage for predicting 1-, 3-, and 5-year survival for HCC patients. **(B–D)** The calibration curves showing the consistency of nomogram-predicted and actual 1-, 3-, and 5-year OS. **(E)** ROC analysis evaluating the predictability of the nomogram for 1, 3, and 5 years OS. **(F)** A comparison of AUC of risk score and clinical factors at 1-year showed the optimal prognostic value of the risk score.

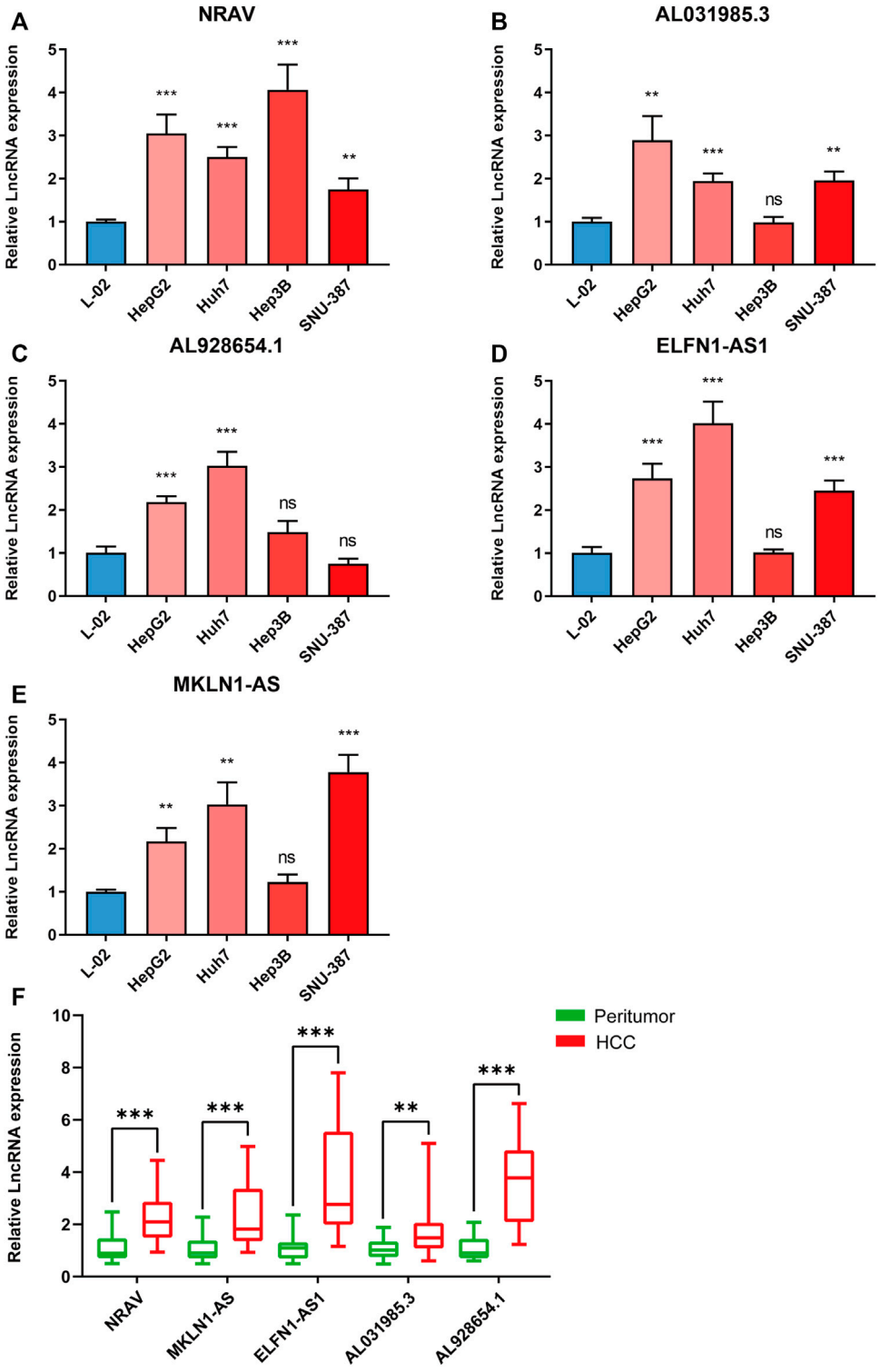

FIGURE 7
Validating the expression levels of five m5C-related lncRNAs. The expression levels of m5C-related lncRNAs in **(A–E)** 5 cell lines and **(F)** 20 pairs HCC tissues and paracancerous tissues. *$p < 0.05$, **$p < 0.01$, and ***$p < 0.001$.

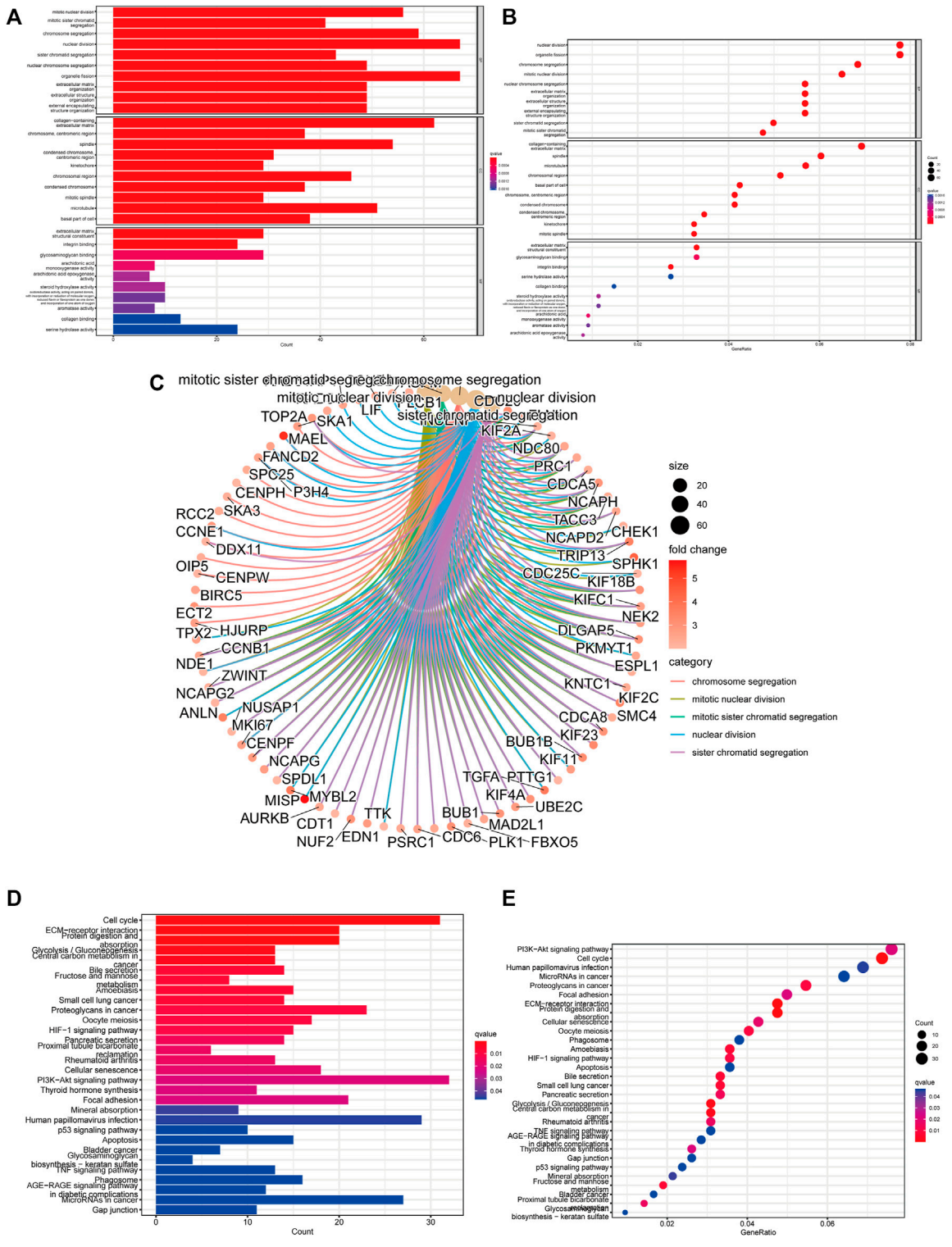

FIGURE 8
Function and pathways enrichment analysis of m5C-related lncRNAs. **(A–C)** Visualization of the enriched biological processes by GO analysis. **(D,E)** KEGG analysis displaying the enriched signaling pathways related to risk model.

other clinical factors (Figure 6F). In summary, the m5C-related lncRNA risk model had the optimal ability to predict the prognosis of HCC patients.

Validation of the five m5C-Related lncRNA expression in hepatocellular carcinoma cell lines and tissues, and analysis of m5C modification sites

We further validated the five m5C-related lncRNA expression levels in HCC cell lines and tissue samples by RT-qPCR assay. The expression levels of these five lncRNAs were examined in Huh7, HepG2, Hep3B, SNU-387, and L-02 cell lines. Our results showed that NRAV expression level was upregulated in HCC cell lines compared with the liver cell line (Figure 7A). AL031985.3, AL928654.1, ELFN1-AS1, and MKLN1-AS expressions were upregulated in part of HCC cell lines (Figures 7B–E). We then performed the differential expression analysis of the five lncRNAs in 20 pairs of HCC and para-carcinoma tissue samples. The results revealed that MKLN1-AS, NRAV, ELFN1-AS1, AL928654.1, and AL031985.3 expression levels were upregulated in HCC tissues (Figure 7F). After scanning the m5C-Atlas, we found two m5C modification sites on NRAV and eleven m5C modification sites on MKLN1-AS. We also utilized RNAm5Cfinder and iRNA-m5C databases to predict potential m5C modification sites on our five lncRNAs, and eventually obtained m5C modification sites on all five lncRNAs (Supplementary Table S5).

The functional and pathway enrichment analysis

We conducted GO and KEGG analysis based on the differential genes between the high- and low-risk groups to better identify the potential biological mechanisms. The top five GO terms were sister chromatid segregation, nuclear division, mitotic sister chromatid segregation, mitotic nuclear division, and chromosome segregation (Figures 8A–C). KEGG analysis showed that these signaling pathways were mainly enriched in cell cycle, PI3K-Akt signaling pathway, proteoglycans in cancer, glycolysis/gluconeogenesis, and ECM–receptor interaction (Figures 8D,E). Furthermore, the activated pathways enriched in the high- and low-risk groups were identified through gene set enrichment analysis (GSEA). We found that Notch signaling pathway, cell cycle, regulation of autophagy, and pathways in cancer were activated in the high-risk group, whereas fatty acid metabolism, tryptophan metabolism, PPAR signaling pathway, and beta alanine metabolism were activated in the low-risk group (Supplementary Figure S3). These results revealed the association of m5C-related lncRNAs with biological function in HCC.

Association of m5C-Related lncRNAs with immune cell infiltration

We conducted a Spearman correlation analysis to illustrate the relationship between the m5C-related lncRNAs and immune cell infiltration. As shown in the lollipop diagram, the risk score was positively correlated with Treg cells, CD4 + T cells, neutrophils, M1 macrophages, and M2 macrophages and negatively correlated with hematopoietic stem cells and endothelial cells (Figure 9A and Supplementary Table S6). The heatmap indicated the difference in the infiltrating levels of immune cells between the high- and low-risk groups based on the TIMER, XCELL, QUANTISEQ, MCPcounter, EPIC, CIBERSORT-ABS, and CIBERSORT software (Figure 9B). Comparative analysis of immune-related functions or pathways by ssGSEA showed that the scores of APC co-stimulation, MHC class I and para-inflammation were higher in the high-risk group, while the cytolytic activity and type II IFN response scores were the opposite (Figure 9C). Furthermore, we compared the risk score in different immune infiltration subtypes and found that the high-risk score was strikingly correlated with C1, while the low-risk score was strikingly correlated with C4 (Figure 9D). The above results suggested that the m5C-related lncRNA risk model of HCC was related to immune status.

Tumor mutation burden based on m5C-Related lncRNA risk model

We analyzed the association between the risk score and tumor mutation burden (TMB) using somatic mutation information downloaded from TCGA-HCC cohort. Figures 9E,F show the top 20 mutated genes with a high mutation frequency. We found that patients in the high-risk group had more mutation event compared with those in the low-risk group (Figure 9G), and TP53 presented the highest mutation frequency in both groups. Besides, patients with high TMB suffered shorter survival time than those with low TMB (Figure 9H). Next, we divided HCC patients into four groups to conduct a combined analysis of TMB and risk score: high TMB + high risk, high TMB + low risk, low TMB + high risk, and low TMB + low risk. As shown in Figure 9I, patients in the low TMB + low-risk group were found with a better survival probability than those in the other three groups.

Evaluation of responses to immunotherapy and chemotherapy based on m5C-Related lncRNA risk model

The TIDE algorithm was used to predict immunotherapy response in the high- and low-risk groups. As demonstrated in Figure 10A, the patients in the high-risk group were found with

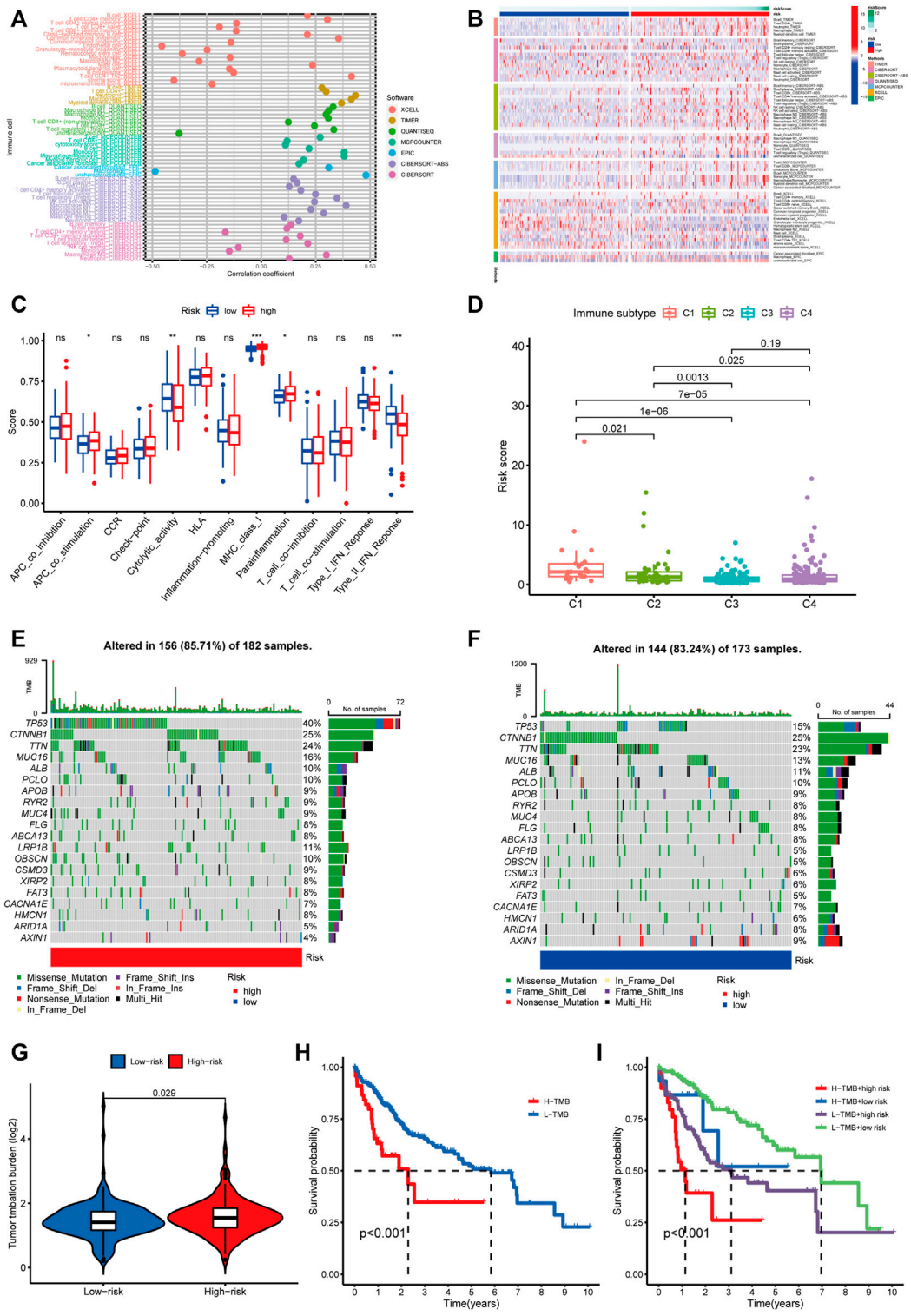

FIGURE 9
Estimating the correlation between m5C-related lncRNAs and immune infiltration and mutation analysis. **(A)** The correlation analysis of risk score and tumor-infiltrating immune cells by TIMER, XCELL, QUANTISEQ, MCPcounter, EPIC, CIBERSORT-ABS, and CIBERSORT software. **(B)** A heatmap indicating the differential immune responses between the high- and low-risk groups based on the above seven software. **(C)** The differential scores of 13 immune-related functions in high- and low-risk groups. **(D)** Comparison of the risk score in different immune infiltration subtypes. *$p < 0.05$, **$p < 0.01$, and ***$p < 0.001$; ns, non-significant. **(E,F)** Waterfall plot of the 20 top mutated genes with high mutation frequency in the high-risk group **(E)** and low-risk group. **(F,G)** The different mutation event between two groups. **(H)** KM analysis between high/low TMB groups. **(I)** Comparative analysis of prognosis combining risk score and TMB.

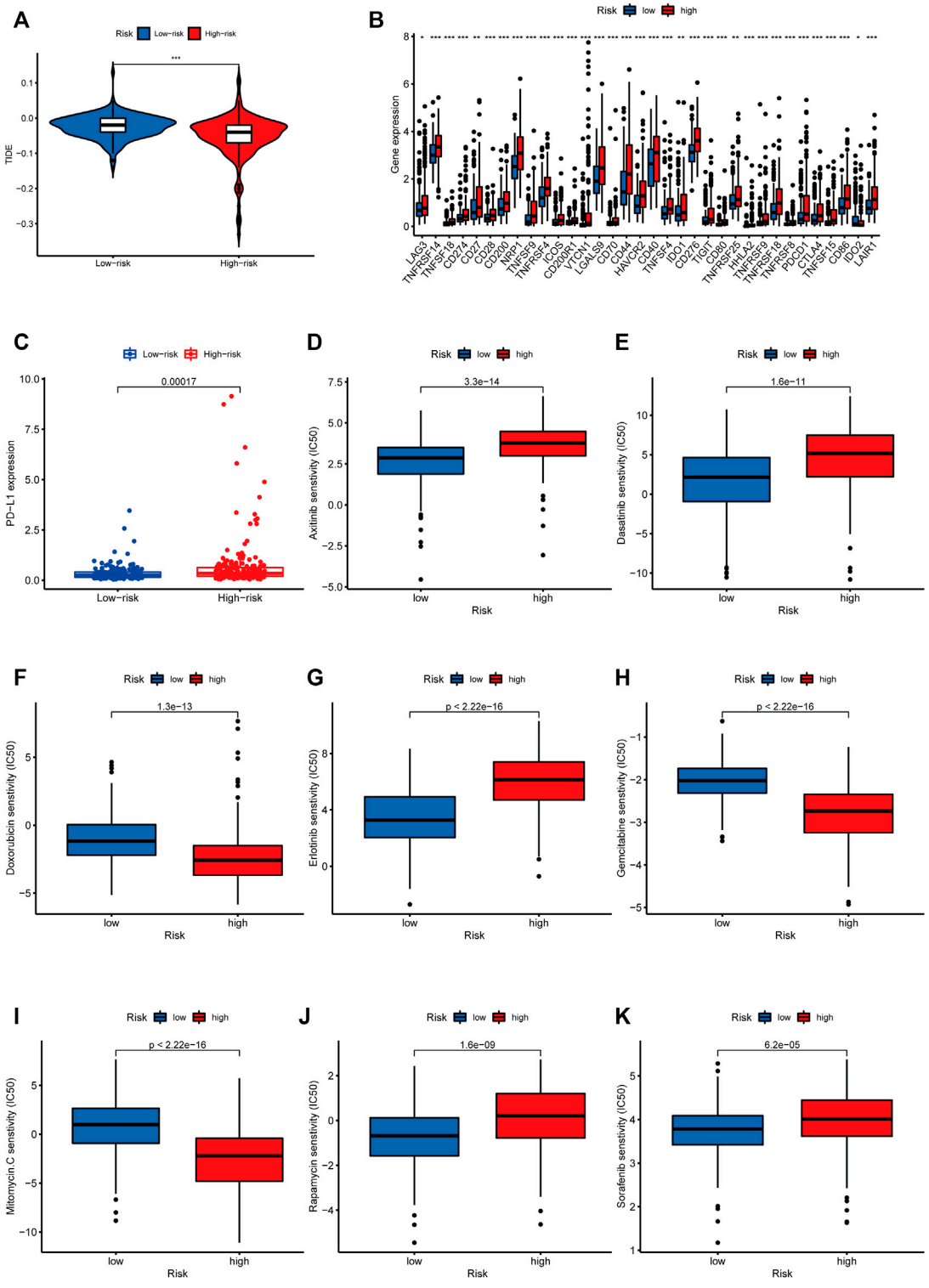

FIGURE 10
Analysis of immunotherapy and chemotherapy responses based on m5C-related lncRNAs risk model. **(A)** Comparison of TIDE scores between the high-risk and low-risk groups. **(B)** The difference of 34 immune checkpoints expression level between high- and low-risk groups shown in the box plot. **(C)** Differences in PD-L1 expression between high- and low-risk groups. IC_{50} of axitinib **(D)**, dasatinib **(E)**, doxorubicin **(F)**, erlotinib **(G)**, gemcitabine **(H)**, mitomycin.C **(I)**, rapamycin **(J)**, and sorafenib **(K)** in high- and low-risk groups.

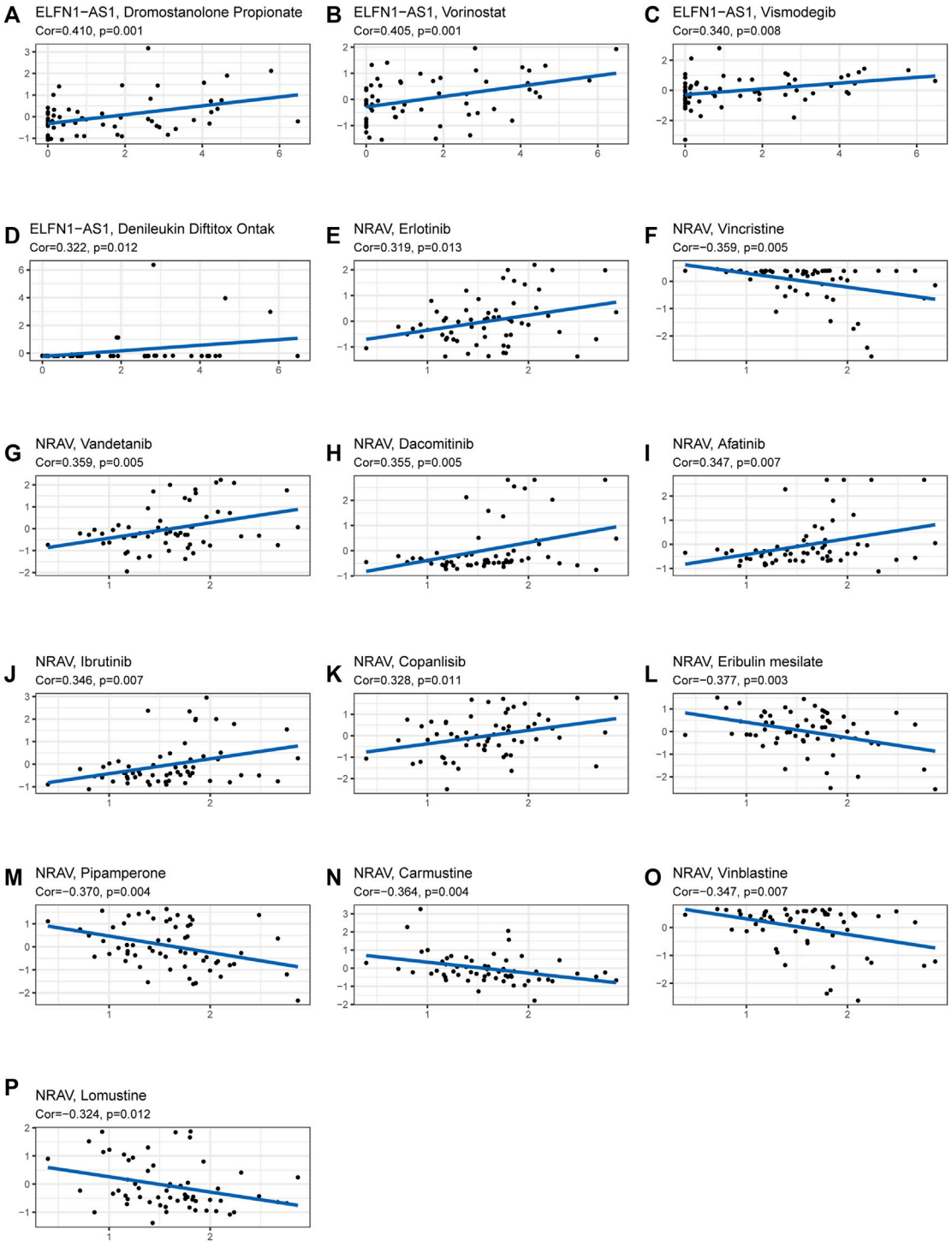

FIGURE 11
Analysis of correlation between the prognostic lncRNAs expression and drug sensitivity. **(A–P)** The scatter plot showed the top 16 associations between prognostic lncRNAs expression and drug sensitivity.

higher TIDE scores than those in the low-risk group, suggesting that the high-risk group was more likely to react to immunotherapy. To investigate the relationship between the risk group and the expression of immune checkpoints, we compared the expression levels of 34 immune checkpoints and found higher expression level in the high-risk group than

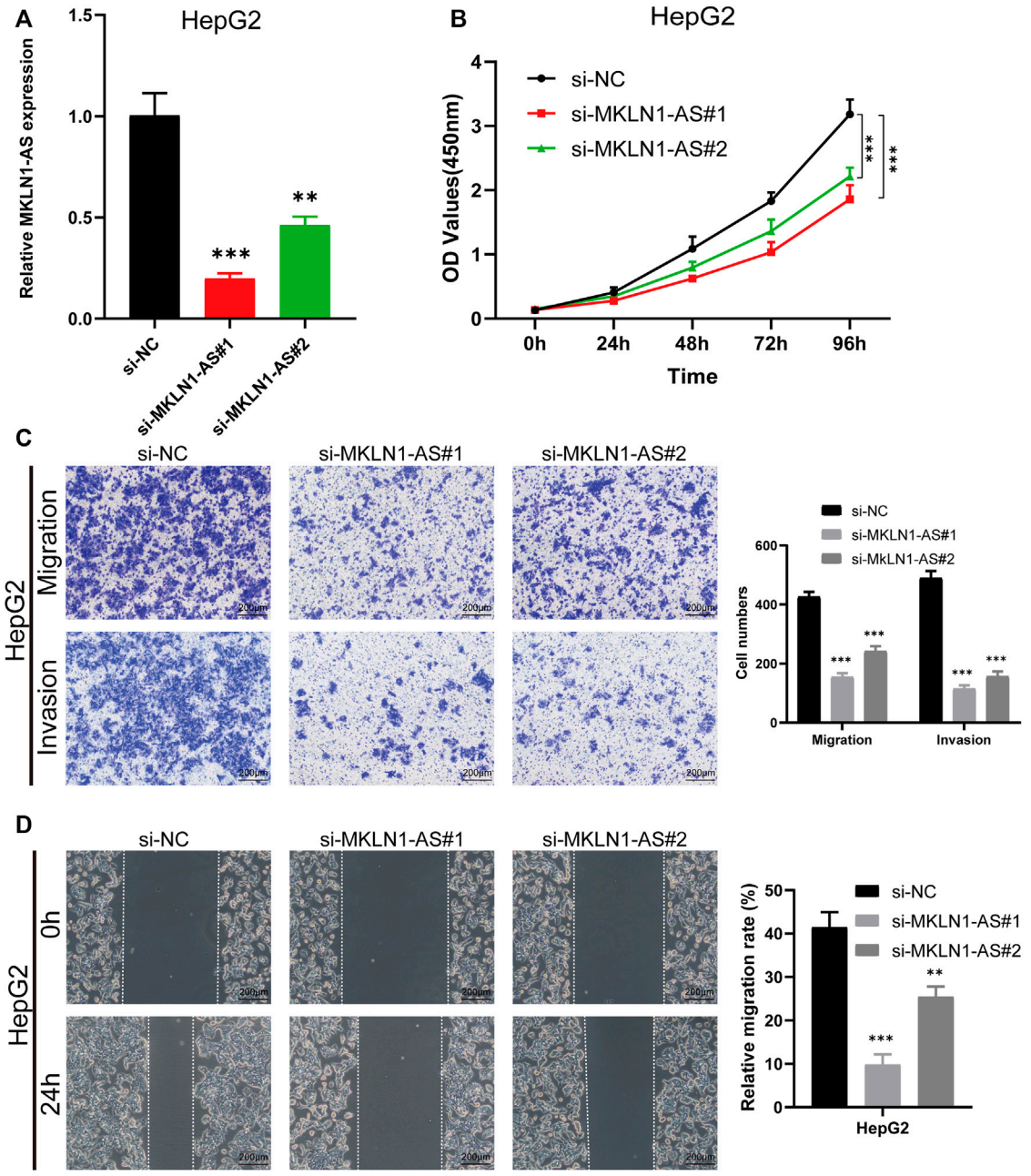

FIGURE 12
MKLN1-AS facilitated the proliferation, migration, and invasion of HCC cells *in vitro*. **(A)** qRT-PCR validation of MKLN1-AS expression in HepG2 cells transfected with siRNAs. **(B)** The viability of HepG2 detected by the CCK-8 assay. **(C)** Transwell assay performed to evaluate the migration and invasion abilities of HepG2 cell transfected with indicated siRNAs. **(D)** Cell migration ability detected *via* wound healing assay. All data are presented as the mean ± standard deviation (SD). * $p < 0.05$, ** $p < 0.01$, *** $p < 0.001$.

in the low-risk group (Figure 10B). Recently, immune checkpoint inhibitors (ICIs) have been conducted in the field of HCC therapy. Programmed cell death 1 ligand 1 (PD-L1), one of the key indicators in cancer immune evasion, has already been used to predict the potential response to immune checkpoint blockade (ICB) therapy. In our study, we discovered that PD-L1 expression level was significantly higher in the high-risk group than in the low-risk group, indicating that high-risk patients were more sensitive to PD-L1 blockade immunotherapy (Figure 10C). Furthermore, we identified the relationship between risk score

and common chemotherapeutic drug sensitivity. The results showed that IC_{50} values of axitinib, rapamycin, dasatinib, sorafenib, and erlotinib were higher in the high-risk group, suggesting that patients from the low-risk group had higher sensitivity to these five drugs. Besides, IC_{50} values of gemcitabine, doxorubicin, and mitomycin C was higher in the low-risk group, which indicated higher sensitivity to these three drugs in the high-risk group (Figures 10D–K). Finally, we investigated the prognostic lncRNAs from the CellMiner database NCI 60 RNA seq and compound activity: DTP NCI-60. As revealed in Figure 11, ELFN1-AS1 and NRAV were correlative to the sensitivity of some chemotherapy drugs, and the correlativity between ELFN1-AS1 expression level and the sensitivity of drug dromostanolone propionate was the strongest (correlation = 0.410, $p = 0.001$).

Functional validation analysis

We then selected MKLN1-AS with the highest contribution in the risk model (Coef = 0.8) for further biological function verification in HCC cells. HepG2 cell was chosen for MKLN1-AS knockdown *via* transfection with siRNAs. qRT-PCR assays were performed to detect the transfection efficiency, and both siRNA fragments downregulated the expression level of MKLN1-AS (Figure 12A). CCK-8 assay indicated that MKLN1-AS knockdown markedly repressed the proliferation of HepG2 cells (Figure 12B). Then, we observed that the knockdown of MKLN1-AS remarkably suppressed migration and invasion abilities of HepG2 cells *via* transwell assay (Figure 12C). Furthermore, wound healing assay showed that after culture for 24 h, scratches of knock-down groups healed slowly and the area of cell migration decreased, indicating that downregulation of MKLN1-AS expression could inhibite the migratory ability of HepG2 cells (Figure 12D). Collectively, these findings confirmed that MKLN1-AS promotes HCC cell proliferation, migration, and invasion *in vitro*.

Discussion

RNA post-transcriptional modifications (such as m6A, m5C, m1A, and m7G), as well-explored events, have been proved to be involved in the carcinogenesis and progression of various cancers. M5C modification, already observed in various RNAs, can promote the proliferation, migration, invasion, and angiogenesis of cancers (Li et al., 2022). LncRNAs, which are widely used as a target or biomarker for disease and treatment, can regulate tumor growth through various mechanisms, including chromatin remodeling, natural antisense transcripts, and chromatin interactions (Fang and Fullwood, 2016). A growing body of evidence has indicated that m6A modification can modulate lncRNAs to affect the pathological processes of cancer development. However, few studies have systematically reported the function of m5C-related lncRNAs in HCC. Taken together, gaining more insight into the relationship between lncRNAs and m5C has a meaningful likelihood of predicting the prognosis and guiding therapy for HCC. In this study, we constructed a prognostic risk model of five m5C-related lncRNAs and analyzed their role in the prognosis and immune cell infiltration. Moreover, cell experiments for one of the five m5C-related lncRNAs, MKLN1-AS, were conducted to confirm the accuracy of the prognostic risk model. So far, no study has been conducted to analyze the prognostic value of m5C-related lncRNAs in HCC. Our findings may be used as novel biomarkers or therapeutic targets for more accurate diagnosis, prognosis, and treatment.

Recently, ferroptosis-related gene signature, pyroptosis-related lncRNA signature, inflammatory response-related gene signature, immune-related gene signature, and m6A-related gene signature have been constructed to predict OS for HCC. In this study, we explored m5C-related lncRNAs by analyzing HCC data downloaded from TCGA database, and five m5C-related lncRNAs capable of prognostic value were finally selected to construct a prognostic risk model. PCA analysis showed that high-risk group patients could be clearly differentiated from the low-risk group patients by using the model. Besides, the model can serve as an independent prognostic factor for HCC patients based on univariate and multivariate Cox regression analyses. In addition, our nomogram could figuratively predict 1-, 3-, and 5-year survival according to the comprehensive score. The results above suggested that the prognostic risk model constructed by five lncRNAs had a potential predictive effect. The five m5C-related lncRNAs, which were NRAV, AL031985.3, MKLN1-AS, ELFN1-AS1, and AL928654.1, were highly expressed in tumor tissues by bioinformatics analysis. We subsequently validated the expressions of the five lncRNAs in HCC cell lines and tissues by RT-qPCR assay. The results were consistent with results from bioinformatics analysis. Besides, four of these lncRNAs were associated with prognosis based on survival analysis. A recent study has revealed that NRAV could negatively regulate antiviral responses by repressing the expression of interferon-stimulated genes (Ouyang et al., 2014). MKLN1-AS has been proven to be one of lncRNAs in hepatocellular carcinoma-related competing endogenous RNA networks and affected HCC progression (Gao et al., 2020). Our results showed that the knockdown of MKLN1-AS could suppress proliferation, migration, and invasion in the HepG2 cell line. Bioinformatic analysis showed that AL031895.3, as inflammatory response-related lncRNA and immune-related gene, was also overexpressed in HCC cell lines, which indicated that AL031985.3 could be an adverse prognostic indicator for HCC (Li et al., 2022). ELFN1-AS1 affects the proliferation, invasion, and metastasis of esophageal cancer and colorectal cancer by regulating miRNAs (Zhang et al., 2020; Zhai et al., 2021). AL928654.1 has not been reported yet; hence, further studies are needed to clarify the effects of these five lncRNAs in the tumorigenesis and development of HCC.

Using GSEA, we explored the molecular mechanism underlying m5C-related lncRNAs. Notch signaling pathway, cell cycle, regulation of autophagy, and pathways in cancer were significantly enriched in the high-risk group. Previous studies have shown that Notch signaling pathway was related to the pathogenesis of liver fibrosis, and EGFL8 regulated HCC cell migration, invasion, and apoptosis *via* the activation of Notch signaling pathway (Wu et al., 2021; Zhu et al., 2021). The cell cycle regulates the duplication and transmission of genetic information; however, the dysregulated cell cycle progression is common in the pathogenesis of cancer (Wiman and Zhivotovsky, 2017). Autophagy plays a key role in cellular homeostasis maintenance and tumorigenesis. A relevant study has indicated that in the progress of affecting lipid metabolism in hypoxic environments, autophagy could maintain the proliferation of HCC cells and promote cancer cell survival (Toshima et al., 2014). It is worth noting that the metabolism-related pathways were closely linked with patients in the low-risk groups. Many studies illustrate the role of metabolic-related pathways in HCC progression; for instance, CD147, which is overexpressed in many cancers, influences tumor progression by promoting the reprogramming of fatty acid metabolism (Li et al., 2015). These results suggested that m5C-related lncRNAs may participate in the genesis and development of HCC by the pathways mentioned above, but further experimentation verification is needed. LncRNAs are known to be expressed in various immune cells and play a vital role in controlling the development and differentiation of these immune cells (Atianand et al., 2017). Tumor infiltration of immune cells in TME, which influences the prognosis of many tumor patients, is attracting much attention. In this study, we made an in-depth analysis of the relationship between risk scores and tumor-infiltrating immune cells using seven common methods. We found higher infiltrating levels of Treg cells, CD4 + T cells, neutrophils, M1 macrophages, and M2 macrophages in the high-risk group than in the low-risk group. Alternatively, endothelial cells and hematopoietic stem cells had a higher expression level in the low-risk group. Based on previous studies, the increased expression of tumor-associated neutrophils, M2 macrophages, and Treg cells are correlated with adverse clinical outcomes in HCC patients (Zhou et al., 2016; Wu et al., 2021). Our results were consistent with previous results. Moreover, the increased activities of type II IFN response meant that tumor immune surveillance and elimination play a role in the high-risk group (Kaplan et al., 1998; Liang et al., 2022). Immunotherapy has received much attention and is expected to become a promising therapeutic method in HCC. We used TIDE algorithm to evaluate the immunotherapeutic response. The result indicated that HCC patients in the high-risk group had a better response to immunotherapy.

ICB therapy, such as anti-PD-L1 antibodies, has shown good prospects in a variety of malignancies. In HCC, the anti-PD-1 antibodies and the anti-Cytotoxic T-Lymphocyte Antigen 4 (CTLA-4) antibodies have been approved for second-line treatment (Pinter et al., 2021). However, immune-related adverse events occur during therapy. Thus, predictive biomarkers for ICB response are urgently needed to maximize the efficacy and keep more patients from adverse effects and heavy economic burden of immunotherapy. Therefore, we compared the expression level of 34 immune checkpoint genes and found a higher expression in the high-risk group. The results above prove that the risk model could predict the expression level of immune checkpoints and is expected to provide important insights into the enhancement of immunotherapy efficacy. Recent studies have found that tumor mutation burden was related to the production of antitumor neoantigens and was identified as a useful biomarker to predict the response to immunotherapy, especially PD-L1 therapy (Chan et al., 2019). As shown in our result, TMB was higher in the high-risk group than the low-risk group, indicating better sensitivity to immunotherapy in the high-risk group. Furthermore, survival analysis suggested that patients with a high burden of tumor mutations had poor prognoses than patients with a low burden. Besides, we combined TMB and risk score and analyzed their survival. The prognosis of patients with high tumor mutation loads in the high-risk subgroup was the worst. Taken together, our research is the first study to explore the relationship between m5C-related lncRNA prognostic risk model and immune cell infiltration, especially immunotherapy.

Tumor resistance to chemotherapeutic drugs often makes chemotherapy unsatisfactory, and thus, efficient and individualized drugs and targets are needed to benefit more HCC patients (Wu et al., 2021). Drug sensitivity analysis suggested that doxorubicin, gemcitabine, and mitomycin are ideal choices for HCC patients in the high-risk group, while axitinib, dasatinib, erlotinib, sorafenib, and rapamycin are suitable for patients in the low-risk group. We also explored the therapeutic potential of five m5C-related lncRNAs by analyzing their association with drug sensitivity of some small-molecule drugs. Our results showed that ELFN1-AS1 was sensitive to dromostanolone propionate, vorinostat, denileukin diftitox ontak, and vismodegib. NRAV was sensitive to vandetanib, dacomitinib, afatinib, lbrutinib, copanlisib, and erlotinib. Ibrutinib is a first-in-class oral irreversible inhibitor of BTK (Bruton's tyrosine kinase) and has been demonstrated to be an effective treatment for chronic lymphocytic leukemia and other B-cell lymphomas (Ahn and Brown, 2021). Erlotinib, an epidermal growth factor receptor tyrosine kinase inhibitor, is used to treat some types of non-small cell lung cancer and advanced pancreatic cancer (Carter et al., 2022). Vorinostat (Lin et al., 2021), dacomitinib (Ji et al., 2021), vandetanib (Carvalho et al., 2022), afatinib (Wu et al., 2021), and vismodegib (Duplaine et al., 2021) also have anticancer effects in malignancies. In the future, further experiments are required to confirm their therapeutic potential for the targeted therapy of HCC.

However, there are some shortcomings and limitations in our study. For example, we constructed and validated our m5C-related lncRNA risk model using TCGA database, lacking external validation from ICGC or GEO databases for lack of expression data of some selected m5C-related lncRNAs. In addition, we validated the five m5C-lncRNA expression levels using RT-qPCR, but further underlying molecular mechanisms studies are required to make the prediction results more reliable. Moreover, partial clinical information, such as M stage and N stage, was unavailable. Hence, in the future, more clinical and experimental studies are warranted to confirm the accuracy of the prognostic risk model.

Conclusion

We constructed a new prognostic risk model consisting of five m5C-related lncRNAs. Our risk model proved to be meaningful in functional analysis, immune cell infiltration, tumor mutation load, and drug sensitivity, indicating the prospect of targeting these lncRNAs for improving the responsiveness to immunotherapy and chemotherapy in HCC. To a certain degree, our study provides new insights to support further research on the role of m5C-related lncRNAs in HCC occurrence and development.

Data availability statement

The original contributions presented in the study are included in the article/Supplementary Material, further inquiries can be directed to the corresponding authors.

Ethics statement

The studies involving human participants were reviewed and approved by the Medical Ethics Committee of Affiliated Hospital of Xuzhou Medical University. The patients/participants provided their written informed consent to participate in this study.

Author contributions

LL and QZ designed and monitored the research. QL and LL drafted the manuscript. QL and SW analyzed the data. All authors contributed to the article and approved the submitted version.

Funding

This study was supported by the Science and Technology Agency of Xuzhou (KC21185).

Acknowledgments

We thank TCGA dataset for providing high quality data.

Conflict of interest

The authors declare that the research was conducted in the absence of any commercial or financial relationships that could be construed as a potential conflict of interest.

Publisher's note

Supplementary material

The Supplementary Material for this article can be found online at: https://www.frontiersin.org/articles/10.3389/fgene.2022.990594/full#supplementary-material

References

Abbastabar, M., Sarfi, M., Golestani, A., and Khalili, E. (2018). lncRNA involvement in hepatocellular carcinoma metastasis and prognosis. *EXCLI J.* 17, 900–913. doi:10.17179/excli2018-1541

Ahn, I. E., and Brown, J. R. (2021). Targeting bruton's tyrosine kinase in CLL. *Front. Immunol.* 12, 687458. doi:10.3389/fimmu.2021.687458

Atianand, M. K., Caffrey, D. R., and Fitzgerald, K. A. (2017). Immunobiology of long noncoding RNAs. *Annu. Rev. Immunol.* 35, 177–198. doi:10.1146/annurev-immunol-041015-055459

Ban, Y., Tan, P., Cai, J., Li, J., Hu, M., Zhou, Y., et al. (2020). LNCAROD is stabilized by m6A methylation and promotes cancer progression via forming a ternary complex with HSPA1A and YBX1 in head and neck squamous cell carcinoma. *Mol. Oncol.* 14, 1282–1296. doi:10.1002/1878-0261.12676

Biswas, S., and Rao, C. M. (2018). Epigenetic tools (The Writers, the Readers and the Erasers) and their implications in cancer therapy. *Eur. J. Pharmacol.* 837, 8–24. doi:10.1016/j.ejphar.2018.08.021

Bridges, M. C., Daulagala, A. C., and Kourtidis, A. (2021). LNCcation: lncRNA localization and function. *J. Cell Biol.* 220, e202009045. doi:10.1083/jcb.202009045

Carter, J., and Tadi, P.Erlotinib, StatPearls (2022). StatPearls publishing. *Copyright © 2022.* Treasure Island (FL): StatPearls Publishing LLC.

Carvalho, D. M., Richardson, P. J., Olaciregui, N., Stankunaite, R., Lavarino, C., Molinari, V., et al. (2022). Repurposing vandetanib plus everolimus for the treatment of ACVR1-mutant diffuse intrinsic pontine glioma. *Cancer Discov.* 12, 416–431. doi:10.1158/2159-8290.Cd-20-1201

Chan, T. A., Yarchoan, M., Jaffee, E., Swanton, C., Quezada, S. A., Stenzinger, A., et al. (2019). Development of tumor mutation burden as an immunotherapy biomarker: Utility for the oncology clinic. *Ann. Oncol.* 30, 44–56. doi:10.1093/annonc/mdy495

Chen, H., Yao, J., Bao, R., Dong, Y., Zhang, T., Du, Y., et al. (2021). Cross-talk of four types of RNA modification writers defines tumor microenvironment and pharmacogenomic landscape in colorectal cancer. *Mol. Cancer* 20, 29. doi:10.1186/s12943-021-01322-w

Cui, M., Qu, F., Wang, L., Liu, X., Yu, J., Tang, Z., et al. (2022). m5C RNA methyltransferase-related gene NSUN4 stimulates malignant progression of hepatocellular carcinoma and can be a prognostic marker. *Cancer Biomark.* 33, 389–400. doi:10.3233/CBM-210154

Cui, Y., Zhang, C., Ma, S., Li, Z., Wang, W., Li, Y., et al. (2021). RNA m6A demethylase FTO-mediated epigenetic up-regulation of LINC00022 promotes tumorigenesis in esophageal squamous cell carcinoma. *J. Exp. Clin. Cancer Res.* 40, 294. doi:10.1186/s13046-021-02096-1

Dai, F., Wu, Y., Lu, Y., An, C., Zheng, X., Dai, L., et al. (2020). Crosstalk between RNA m(6)A modification and non-coding RNA contributes to cancer growth and progression. *Mol. Ther. Nucleic Acids* 22, 62–71. doi:10.1016/j.omtn.2020.08.004

Duplaine, A., Beylot-Barry, M., Mansard, S., Arnault, J. P., Grob, J. J., Maillard, H., et al. (2021). Vismodegib efficacy in unresectable trichoblastic carcinoma: A multicenter study of 16 cases. *J. Am. Acad. Dermatol.* 86, 1365–1366. doi:10.1016/j.jaad.2021.05.024

Fang, Y., and Fullwood, M. J. (2016). Roles, functions, and mechanisms of long non-coding RNAs in cancer. *Genomics Proteomics Bioinforma.* 14, 42–54. doi:10.1016/j.gpb.2015.09.006

Foerster, F., Gairing, S. J., Ilyas, S. I., and Galle, P. R. (2022). Emerging immunotherapy for hepatocellular carcinoma: A guide for hepatologists. Baltimore, Md: Hepatology. doi:10.1002/hep.32447

Gao, W., Chen, X., Chi, W., and Xue, M. (2020). Long non-coding RNA MKLN1-AS aggravates hepatocellular carcinoma progression by functioning as a molecular sponge for miR-654-3p, thereby promoting hepatoma-derived growth factor expression. *Int. J. Mol. Med.* 46, 1743–1754. doi:10.3892/ijmm.2020.4722

Hinshaw, D. C., and Shevde, L. A. (2019). The tumor microenvironment innately modulates cancer progression. *Cancer Res.* 79, 4557–4566. doi:10.1158/0008-5472.Can-18-3962

Hu, X., Peng, W. X., Zhou, H., Jiang, J., Zhou, X., Huang, D., et al. (2020). IGF2BP2 regulates DANCR by serving as an N6-methyladenosine reader. *Cell Death Differ.* 27, 1782–1794. doi:10.1038/s41418-019-0461-z

Ji, W., Shen, J., Wang, B., Chen, F., Meng, D., Wang, S., et al. (2021). Effects of dacomitinib on the pharmacokinetics of poziotinib *in vivo* and *in vitro*. *Pharm. Biol.* 59, 457–464. doi:10.1080/13880209.2021.1914114

Kaplan, D. H., Shankaran, V., Dighe, A. S., Stockert, E., Aguet, M., Old, L. J., et al. (1998). Demonstration of an interferon gamma-dependent tumor surveillance system in immunocompetent mice. *Proc. Natl. Acad. Sci. U. S. A.* 95, 7556–7561. doi:10.1073/pnas.95.13.7556

Lei, X., Lei, Y., Li, J. K., Du, W. X., Li, R. G., Yang, J., et al. (2020). Immune cells within the tumor microenvironment: Biological functions and roles in cancer immunotherapy. *Cancer Lett.* 470, 126–133. doi:10.1016/j.canlet.2019.11.009

Li, J., Huang, Q., Long, X., Zhang, J., Huang, X., Aa, J., et al. (2015). CD147 reprograms fatty acid metabolism in hepatocellular carcinoma cells through Akt/mTOR/SREBP1c and P38/PPARα pathways. *J. Hepatol.* 63, 1378–1389. doi:10.1016/j.jhep.2015.07.039

Li, M., Tao, Z., Zhao, Y., Li, L., Zheng, J., Li, Z., et al. (2022). 5-methylcytosine RNA methyltransferases and their potential roles in cancer. *J. Transl. Med.* 20, 214. doi:10.1186/s12967-022-03427-2

Li, X., Zhang, S., Zhang, S., Kuang, W., and Tang, C. (2022). Inflammatory response-related long non-coding RNA signature predicts the prognosis of hepatocellular carcinoma. *J. Oncol.* 2022, 9917244. doi:10.1155/2022/9917244

Liang, W., Luo, Q., Zhang, Z., Yang, K., Yang, A., Chi, Q., et al. (2022). An integrated bioinformatics analysis and experimental study identified key biomarkers CD300A or CXCL1, pathways and immune infiltration in diabetic nephropathy mice. *Biocell* 46, 1989–2002. doi:10.32604/biocell.2022.019300

Lin, C. Y., Huang, K. Y., Lin, Y. C., Yang, S. C., Chung, W. C., Chang, Y. L., et al. (2021). Vorinostat combined with brigatinib overcomes acquired resistance in EGFR-C797S-mutated lung cancer. *Cancer Lett.* 508, 76–91. doi:10.1016/j.canlet.2021.03.022

Ma, C., Kesarwala, A. H., Eggert, T., Medina-Echeverz, J., Kleiner, D. E., Jin, P., et al. (2016). NAFLD causes selective CD4(+) T lymphocyte loss and promotes hepatocarcinogenesis. *Nature* 531, 253–257. doi:10.1038/nature16969

Ma, J., Song, B., Wei, Z., Huang, D., Zhang, Y., Su, J., et al. (2022). m5C-Atlas: a comprehensive database for decoding and annotating the 5-methylcytosine (m5C) epitranscriptome. *Nucleic Acids Res.* 50, D196–d203. doi:10.1093/nar/gkab1075

Meyer, K. D., and Jaffrey, S. R. (2017). Rethinking m(6)A readers, writers, and erasers. *Annu. Rev. Cell Dev. Biol.* 33, 319–342. doi:10.1146/annurev-cellbio-100616-060758

Ouyang, J., Zhu, X., Chen, Y., Wei, H., Chen, Q., Chi, X., et al. (2014). NRAV, a long noncoding RNA, modulates antiviral responses through suppression of interferon-stimulated gene transcription. *Cell Host Microbe* 16, 616–626. doi:10.1016/j.chom.2014.10.001

Pinter, M., Jain, R. K., and Duda, D. G. (2021). The current landscape of immune checkpoint blockade in hepatocellular carcinoma: A review. *JAMA Oncol.* 7, 113–123. doi:10.1001/jamaoncol.2020.3381

Sun, Z., Xue, S., Zhang, M., Xu, H., Hu, X., Chen, S., et al. (2020). Aberrant NSUN2-mediated m(5)C modification of H19 lncRNA is associated with poor differentiation of hepatocellular carcinoma. *Oncogene* 39, 6906–6919. doi:10.1038/s41388-020-01475-w

Toshima, T., Shirabe, K., Matsumoto, Y., Yoshiya, S., Ikegami, T., Yoshizumi, T., et al. (2014). Autophagy enhances hepatocellular carcinoma progression by activation of mitochondrial β-oxidation. *J. Gastroenterol.* 49, 907–916. doi:10.1007/s00535-013-0835-9

Wiman, K. G., and Zhivotovsky, B. (2017). Understanding cell cycle and cell death regulation provides novel weapons against human diseases. *J. Intern. Med.* 281, 483–495. doi:10.1111/joim.12609

Wu, C. E., Chang, C. F., Huang, C. Y., Yang, C. T., Kuo, C. S., Hsu, P. C., et al. (2021). Feasibility and effectiveness of afatinib for poor performance status patients with EGFR-mutation-positive non-small-cell lung cancer: A retrospective cohort study. *BMC cancer* 21, 859. doi:10.1186/s12885-021-08587-w

Wu, F., Zhang, F. Y., Tan, G. Q., Chen, W. J., Huang, B., Yan, L., et al. (2021). Down-regulation of EGFL8 regulates migration, invasion and apoptosis of hepatocellular carcinoma through activating Notch signaling pathway. *BMC cancer* 21, 704. doi:10.1186/s12885-021-08327-0

Wu, J., Gao, W., Tang, Q., Yu, Y., You, W., Wu, Z., et al. (2021). M2 macrophage-derived exosomes facilitate HCC metastasis by transferring $\alpha_M \beta_2$ integrin to tumor cells. *Hepatology* 73, 1365–1380. doi:10.1002/hep.31432

Wu, Y., Zhang, J., and Li, Q. (2021). Autophagy, an accomplice or antagonist of drug resistance in HCC? *Cell Death Dis.* 12, 266. doi:10.1038/s41419-021-03553-7

Xu, R., Wu, Q., Gong, Y., Wu, Y., Chi, Q., and Sun, D. (2022) A novel prognostic target-gene signature and nomogram based on an integrated bioinformatics analysis in hepatocellular carcinoma. 46, 1261–1288. doi:10.32604/biocell.2022.018427

Xue, Y., Tong, L., LiuAnwei Liu, F., Liu, A., Zeng, S., Xiong, Q., et al. (2019). Tumor-infiltrating M2 macrophages driven by specific genomic alterations are associated with prognosis in bladder cancer. *Oncol. Rep.* 42, 581–594. doi:10.3892/or.2019.7196

Yu, Z., Zhao, H., Feng, X., Li, H., Qiu, C., Yi, X., et al. (2019). Long non-coding RNA FENDRR acts as a miR-423-5p sponge to suppress the treg-mediated immune escape of hepatocellular carcinoma cells. *Mol. Ther. Nucleic Acids* 17, 516–529. doi:10.1016/j.omtn.2019.05.027

Zhai, L. Q., Wang, X. X., Qu, C. X., Yang, L. Z., Jia, C. M., and Shi, X. C. (2021). A long non-coding RNA, ELFN1-AS1, sponges miR-1250 to upregulate MTA1 to promote cell proliferation, migration and invasion, and induce apoptosis in colorectal cancer. *Eur. Rev. Med. Pharmacol. Sci.* 25, 4655–4667. doi:10.26355/eurrev_202107_26376

Zhang, C., Lian, H., Xie, L., Yin, N., and Cui, Y. (2020). LncRNA ELFN1-AS1 promotes esophageal cancer progression by up-regulating GFPT1 via sponging miR-183-3p. *Biol. Chem.* 401, 1053–1061. doi:10.1515/hsz-2019-0430

Zhao, B. S., Roundtree, I. A., and He, C. (2017). Post-transcriptional gene regulation by mRNA modifications. *Nat. Rev. Mol. Cell Biol.* 18, 31–42. doi:10.1038/nrm.2016.132

Zhou, S. L., Zhou, Z. J., Hu, Z. Q., Huang, X. W., Wang, Z., Chen, E. B., et al. (2016). Tumor-associated neutrophils recruit macrophages and T-regulatory cells to promote progression of hepatocellular carcinoma and resistance to sorafenib. *Gastroenterology* 150, 1646–1658. e1617. doi:10.1053/j.gastro.2016.02.040

Zhu, C., Ho, Y. J., Salomao, M. A., Dapito, D. H., Bartolome, A., Schwabe, R. F., et al. (2021). Notch activity characterizes a common hepatocellular carcinoma subtype with unique molecular and clinicopathologic features. *J. Hepatol.* 74, 613–626. doi:10.1016/j.jhep.2020.09.032

frontiers | Frontiers in Genetics

TYPE Original Research
PUBLISHED 24 October 2022
DOI 10.3389/fgene.2022.1051800

OPEN ACCESS

EDITED BY
Kunqi Chen,
Fujian Medical University, China

REVIEWED BY
Fuyi Li,
The University of Melbourne, Australia
Haoran Shi,
University of Giessen, Germany

*CORRESPONDENCE
Wei Chen,
greatchen@ncst.edu.cn

SPECIALTY SECTION
This article was submitted to Epigenomics and Epigenetics, a section of the journal Frontiers in Genetics

RECEIVED 23 September 2022
ACCEPTED 10 October 2022
PUBLISHED 24 October 2022

CITATION
Li M, Zhang T and Chen W (2022), Development of necroptosis-related gene signature to predict the prognosis of colon adenocarcinoma.
Front. Genet. 13:1051800.
doi: 10.3389/fgene.2022.1051800

Development of necroptosis-related gene signature to predict the prognosis of colon adenocarcinoma

Miaomiao Li[1], Tianyang Zhang[1] and Wei Chen[1,2]*

[1]School of Life Sciences, North China University of Science and Technology, Tangshan, China, [2]Innovative Institute of Chinese Medicine and Pharmacy, Chengdu University of Traditional Chinese Medicine, Chengdu, China

Colon adenocarcinoma (COAD) is a common malignancy and has a high mortality rate. However, the current tumor node metastasis (TNM) staging system is inadequate for prognostic assessment of COAD patients. Therefore, there is an urgent need to identify reliable biomarkers for the prognosis COAD patients. The aberrant expression of necroptosis-related genes (NRGs) is reported to be associated with tumorigenesis and metastasis. In the present work, we compared the expression profiles of NRGs between COAD patients and normal individuals. Based on seven differentially expressed NRGs, a risk score was defined to predict the prognosis of COAD patients. The validation results from both training and independent external cohorts demonstrated that the risk score is able to distinguish the high and low risk COAD patients with higher accuracies, and is independent of the other clinical factors. To facilitate its clinical use, by integrating the proposed risk score, a nomogram was built to predict the risk of individual COAD patients. The C-index of the nomogram is 0.75, indicating the reliability of the nomogram in predicting survival rates. Furthermore, two candidate drugs, namely dapsone and xanthohumol, were screed out and validated by molecular docking, which hold the potential for the treatment of COAD. These results will provide novel clues for the diagnosis and treatment of COAD.

KEYWORDS

colon adenocarcinoma, necroptosis, gene signature, survival analysis, nomogram, molecular docking

Abbreviations: AUC, area under the ROC curve; COAD, colon adenocarcinoma; Cmap, connectivity map; DEGs, differentially expressed genes; FC, fold change; GEO, gene expression omni molecular docking bus; GSEA, gene set enrichment Analysis; HR, hazard ratio; LASSO, least absolute shrinkage and selection operator; M, metastasis; N, node; NRGs, necroptosis-related genes; OS, overall survival; PDB, protein data bank; ROC, receiver operating characteristic; RCSB, Research Collaboratory for Structural Bioinformatics; T, tumor; TCGA, the cancer genome atlas; TPM, transcripts per million.

1 Introduction

Colon adenocarcinoma (COAD) is one of the most common cancers worldwide and the second leading cause of cancer death (Bray et al., 2018). Surgery and chemotherapy remain the mainstay of colon cancer treatment (Miller et al., 2019). At present, the prognostic assessment and treatment planning of COAD patients depend largely on the TNM staging system (Kehoe and Khatri, 2006). Even at the same tumor stage, however, due to tumor heterogeneity, there are still significant disparities in disease progression and clinical outcomes. Hence, TNM staging system is not fully capable of predicting the prognosis of colon cancer patients. Accordingly, more reliable prognostic biomarkers are needed for the diagnose of colon cancer. The occurrence of tumors is inseparable from the abnormal gene expressions, and which have been used as biomarkers to predict the prognosis of diseases (Liu et al., 2018; Gao et al., 2020). Most recently, it was reported that the aberrant expression of necroptosis-related genes (NRGs) is closely associated with the tumorigenesis and metastasis (Ding et al., 2022; Qi et al., 2022).

Necroptosis is a double-edged sword in the carcinogenesis and progression of cancer. The tumor cell necrosis can lead to tumor necrosis and promoted tumor metastasis (Lebrec et al., 2015). For example, the pro-necrosis proteins, such as RIPK1, RIPK3, and MLKL, play key roles in promoting tumor growth (Liu et al., 2016). Conversely, necroptosis also exhibits tumor suppressive effects. Results from two independent groups showed that overexpression of the cell necroptosis factor RIP3 inhibited the proliferation of colon cancer cells (Feng et al., 2015; Krysko et al., 2017). These findings show that cellular necrosis has a multifaceted biological role in carcinogenesis and invasion. Therefore, NRGs have gained attentions of researchers and have been proposed for risk classification and survival prediction of COAD patients. For example, Huang *et al.* found that a necroptosis-related miRNA risk signature consisting of seven miRNAs could be used to predict the prognosis of colon cancer patients (Huang et al., 2021). Subsequently, Yang et al. constructed a necroptosis-related miRNA signature for predicting colon cancer prognosis (Yang et al., 2022). Later on, Liu *et al.* proposed another model to predict the prognosis of colon cancer patients based on necroptosis-related lncRNAs(Liu et al., 2022). However, these studies only used the TCGA dataset for internal validation, and did not test their results on the external validation dataset. Moreover, their accuracies for predicting the prognosis of colon cancer patients are not satisfactory. Therefore, new reliable signatures are needed to predict survival in COAD patients.

In this study, based on the seven differently expressed NRGs, we proposed a new NRGs-based model to predict the prognosis of COAD patients. The proposed model is able to distinguish the high and low risk patients in both internal training and external testing dataset with higher accuracies. In order to facilitate its clinical use, a prognostic nomogram was built to quantify the death risk of individual patients. Moreover, on the basis of Connectivity Map (Cmap) database (Subramanian et al., 2017), the candidate drugs for the treatment of high risk patients were screened out and validated by molecular docking analysis. The workflow of this work was shown in Figure 1.

2 Materials and methods

2.1 Data collection

The TCGA public database (https://portal.gdc.cancer.gov/) was used to gather COAD RNA-sequencing (RNA-seq) data and clinical follow-up information. After excluding the samples with a follow-up period of less than 30 days and samples with duplicate patients, we obtained 417 tumor tissue samples and 41 non-tumor tissue samples. The RNA-seq data were then converted to transcripts per million (TPM). The 556 independent validation samples were fetched from the GEO dataset (https://www.ncbi.nlm.nih.gov/geo/) with the accession number GSE39582.

2.2 Acquisition of differentially expressed NRGs

159 NRGs involved in the necroptosis signaling pathway were obtained from the KEGG database (https://www.genome.jp/kegg/, Supplementary Table S1). The limma package (version 3.42.2) in R software (version 3.6.1) was used to perform the differential expression analysis of NRGs in tumor and non-tumor tissue with $p < 0.05$, false discovery rate (FDR) < 0.05 and |log2FoldChange|>0. The pheatmap (version 1.0.12) and EnhancedVolcano (version 1.4.0) packages were used for the visualization of differentially expressed genes (DEGs). The R package clusterProfiler (Yu et al., 2012) (version 3.14.3) was used for GO and KEGG enrichment analysis, and enrichplot (version 1.6.1) was used for visualization studies.

2.3 Definition of the NRGs based risk score

Univariate Cox regression analysis was used to screen NRGs that were significantly ($p < 0.05$) associated with COAD survival rates. And then, a LASSO-Cox regression analysis was used to select the NRGs signature. The genes thus obtained were used to define a risk score defined as following,

$$Risk\ score = \sum_{i=1}^{n} Coef_i * Exp_i$$

where i stands for one of the n NRGs, Exp_i is the expression level of gene i, and $Coef_i$ is the corresponding coefficient determined

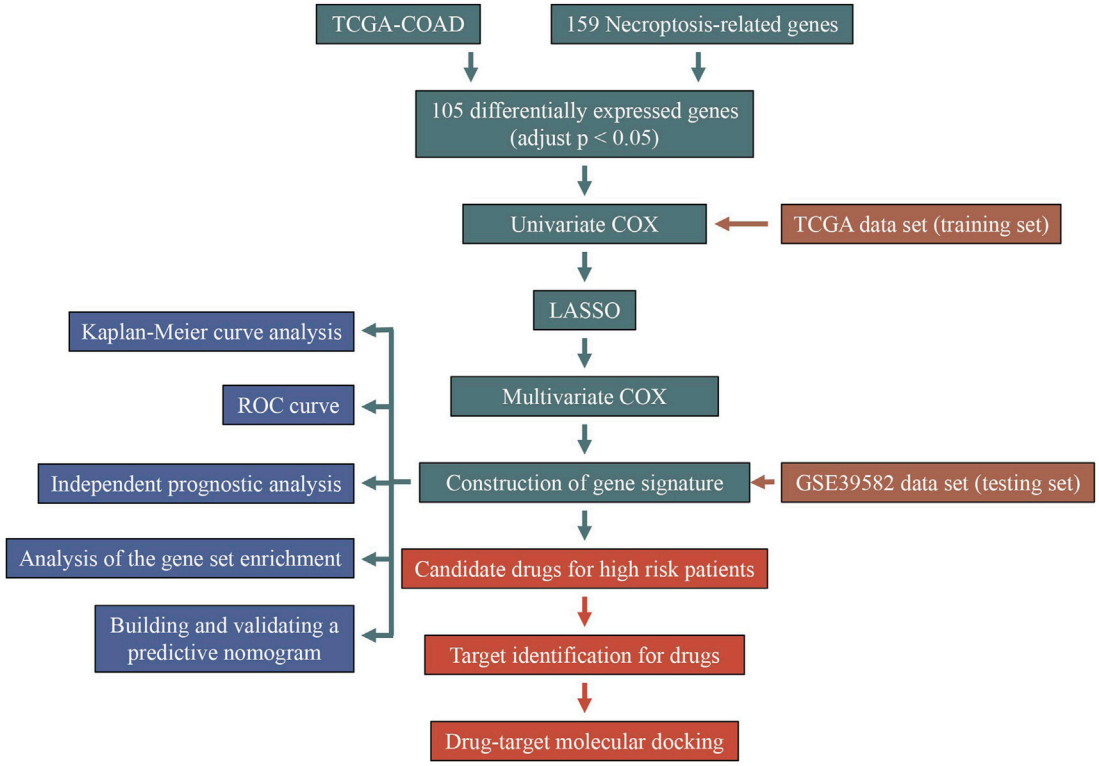

FIGURE 1
The flow chart of this study.

by LASSO-Cox regression analysis. Patients were then split into two subgroups, namely low risk group and high risk group, based on the median of risk score. The survival (version: 3.2–7) and glmnet (version: 4.1–1) (Friedman et al., 2010) packages in R were used for the analysis.

2.4 Prognostic performance analysis of risk signature

Kaplan-Meier survival analysis was used to assess the survival differences between the two risk groups. The receiver operating characteristic (ROC) curve was used to evaluate the accuracy for predicting the overall survival (OS) of COAD patients. The univariate and multivariate Cox regression analysis were used to test whether the risk score is independent of the other clinical traits (age, sex, stage, TNM grade).

2.5 Gene set enrichment analysis

The org. Hs.eg.db (version 3.10.0), clusterProfiler (version 3.14.3), and ggplot2 (version 3.3.3) packages in R were used to perform gene set enrichment analysis (adjust $p < 0.05$).

2.6 Construction and verification of nomogram

For facilitating clinical use, the nomogram was built by using the rms (version 6.1–1) and survival (version 3.2–7) packages in R. The discriminative ability of the nomogram was assessed by using AUC smoothing curve and C-index. Calibration curves were used to evaluate the relationship between actual results (45-degree diagonal) and predictive probabilities. The accuracy was obtained after 1,000 times of bootstraps (Huang et al., 2016).

2.7 Candidate drug identification

The Cmap database was used to identify the drugs for the treatment of patients in the high risk group. The DEGs between high and low risk groups in the TCGA-COAD cohort were identified by using differential expression analysis ($|\log_2 FC| \geq 1.5$, $p < 0.05$, and FDR<0.05). By inputting the DEGs of the high risk group into Cmap, the potential drug candidates were obtained and sorted based on their scores ranging from -100 to 100. The positive scores indicate the synergistic effects of the drugs on diseases, while negative scores indicate antagonistic effects of the drugs on diseases (Subramanian et al., 2017). Hence, the drugs

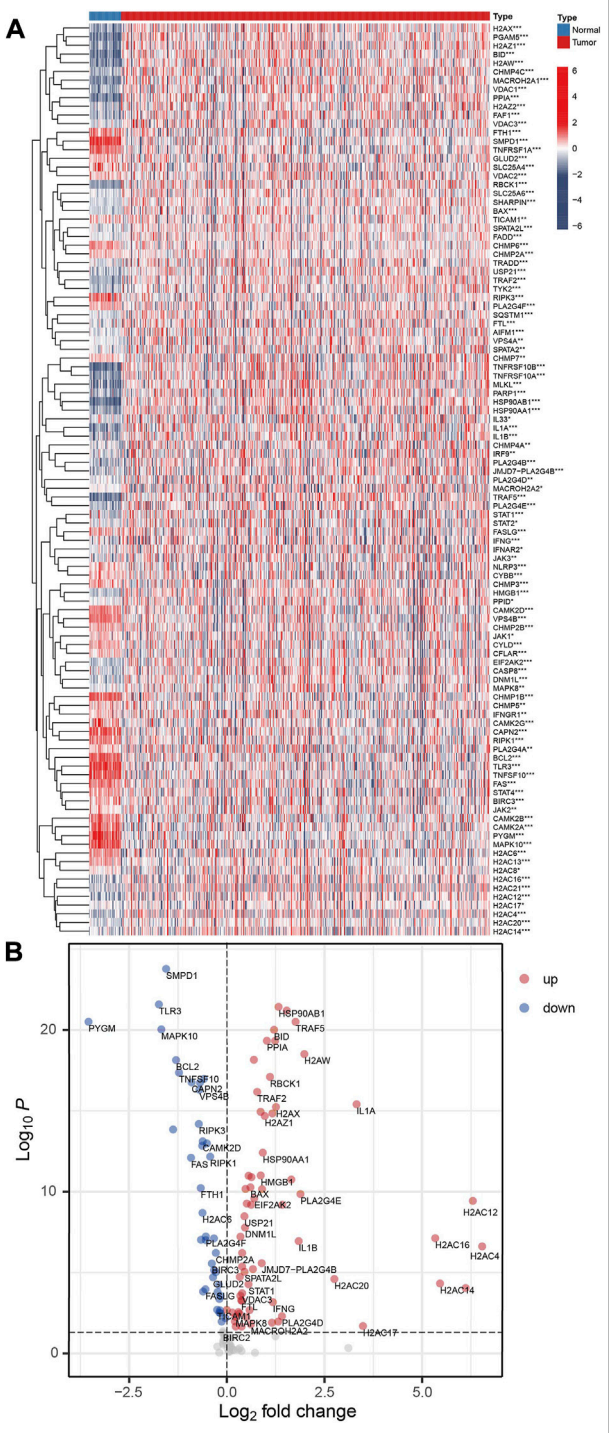

FIGURE 2
The differentially expressed NRGs. **(A)** Heatmap for the 105 differentially expressed NRGs. Red is tumor tissue samples, and blue is normal samples (*$p < 0.05$; **$p < 0.01$; ***$p < 0.001$). **(B)** A volcano plot of NRGs. Up-regulated and down-regulated genes are indicated by red and blue, respectively.

with negative scores hold the potential for the treatment of diseases. In the present work, drugs with score less than -80 were selected out for further analysis.

2.8 Drug targets identification and validation

The targets of the candidate drugs were predicted by using the STITCH database (http://stitch.embl.de/) with the confidence score greater than 0.8 (Szklarczyk et al., 2016). Only the targets that differentially expressed between high and low risk groups and significantly correlated with patient OS were screened out. The 2D structures of candidate drugs were taken from the PubChem database (https://pubchem.ncbi.nlm.nih.gov/), and their 3D chemical structures were drawn using ChemOffice 2019. The protein structures of the targets were obtained from the RCSB PDB database (PDB, http://www.pdb.org/). The AutoDockTools-1.5.6 and Autodock Vina-1.1.2 were used to perform molecular docking between candidate drugs and the targets (Morris et al., 2009; Trott and Olson, 2010). A docking free energy less than -5.0 kcal/mol was regarded as a stable binding (Li et al., 2022). PyMOL-2.4.0 and Discovery studio 4.5 were used to visualize the molecular docking results.

2.9 Statistical analysis

All statistical analysis and result visualization were performed by using R (version 3.6.1). The Wilcoxon test was utilized to determine the difference between the two groups. The Pearson correlation coefficient was calculated to assess the associations between clinicopathological characteristics and risk scores. $p < 0.05$ was regarded as statistically significant for two-sided tests.

3 Results

3.1 Differentially expression of NRGs

Among the 159 NRGs, 105 were differentially expressed ($p <$ 0.05 and FDR<0.05) between normal and COAD samples, Figure 2A. Further analysis demonstrated that 40 NRGs were significantly under-expressed in tumor tissues, and 65 were significantly over-expressed, Figure 2B and Supplementary Table S2. The results from KEGG analysis demonstrated that the most significantly enriched pathway of the differentially expressed NRGs is necroptosis (Supplementary Figures

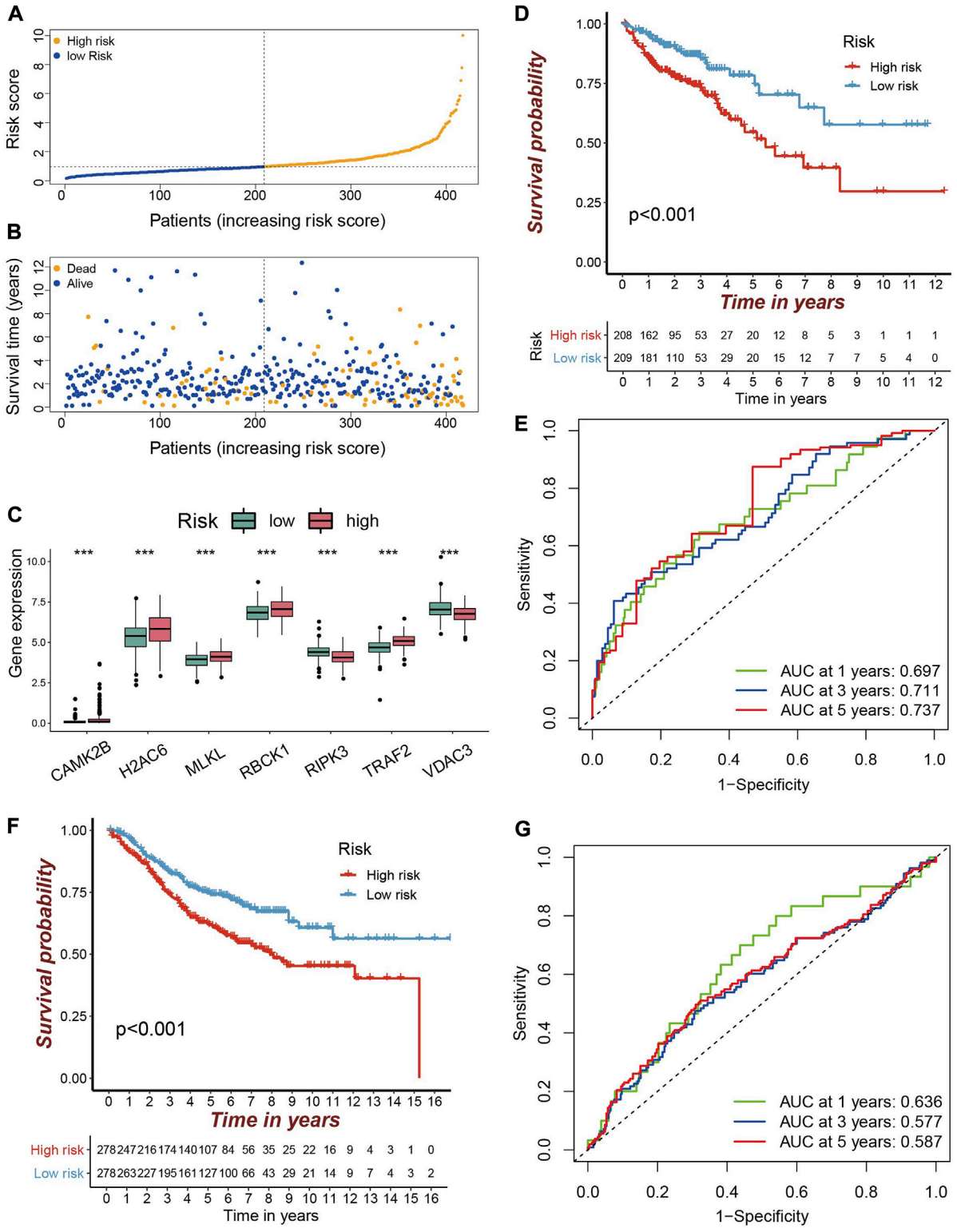

FIGURE 3
Validation of the prognostic NRGs signature in COAD patients **(A–B)** The TCGA-COAD samples were divided into high and low risk groups according to the median risk score. The larger the risk score, the more the samples of deaths. **(C)** Differentially expression of prognostic genes in high and low risk groups are depicted in a boxplot. Red is the high risk group and green is the low risk group (***$p < 0.001$). **(D)** Kaplan-Meier curve for predicting OS in the TCGA cohort. Red is the high risk group and blue is the low risk group. **(E)** ROC curve in the TCGA cohort. **(F)** Kaplan–Meier curve for predicting OS in the GEO cohort. **(G)** ROC curve in the GEO cohort.

S1A,B). However, the GO enrichment analysis demonstrated that the under-expressed and over-expressed NRGs were enriched in different entries (Supplementary Figure S1C and S1D). For the biological process (BP), the up-regulated genes were most significantly enriched in regulation of apoptotic signaling pathway, while down-regulated genes were in necroptotic process. In terms of cellular component (CC), the up-regulated genes were in nuclear chromatin, while down-regulated genes were in endosome membrane. The most significantly enriched molecular function of up-regulated genes is cytokine receptor binding, while that of down-regulated genes is protein serine/threonine kinase activity. These results demonstrated that the differentially expressed NRGs were associated distinct biological functions.

3.2 Establishment and validation of the prognostic NRGs signature in COAD patients

Univariate Cox regression analysis showed that eight NRGs were significantly associated with the survival status of COAD patients (Supplementary Table S3). We further employed the LASSO-Cox regression analysis to assess the survival rates of COAD patients, and obtained seven NRGs (Supplementary Figures S2A,B, Supplementary Table S4). It was found that five of them (CAMK2B, H2AC6, MLKL, RBCK1, and TRAF2) were risk factors and two (RIPK3 and VDAC3) were protective factors (Supplementary Figure S2C). Then, they were used to build the prognostic-related NRG signature (also called risk score, see section 2.3).

On the basis of the prognostic-related NRG signature, each sample was assigned a risk score. With the median risk score as a cut-off value, the samples in the dataset were divided into high risk group (n = 208) and low risk (n = 209) group, respectively. With the increasement of risk score, the number of deaths increased progressively (Figures 3A,B). In the high risk group, the risk factors were significantly overexpressed, while the protective factors were significantly under expressed (Figure 3C). The Kaplan-Meier survival curve based on the risk score shows that the high and low risk groups have significantly different survival rates. Patients in the high risk group having a lower OS than those in the low risk group (Figure 3D).

The performance of the risk score for predicting the patient's OS was evaluated by using the ROC curve. Its area under the ROC curve (AUC) for 1-year, 3-year and 5-year OS were 0.697, 0.711, and 0.737 (Figure 3E), respectively. The AUC for predicting 5-year OS is better than those reported by Huang et al. (AUC = 0.724) (Huang et al., 2021), Yang *et al.* (AUC = 0.656) (Yang et al., 2022), and Liu *et al.* (AUC = 0.639) (Liu et al., 2022). The 7-NRGs based risk score model was further validated in the independent GEO dataset (GSE39582). Compared with low risk patients, patients in the high risk group also had a worse OS (Figure 3F). The AUCs for 1-, 3-, and 5-year OS were 0.636, 0.577, and 0.587 (Figure 3G). These results indicate that the developed prognostic model is reliable, and the seven NRGs holds the potential to be efficient biomarkers for the prognosis of COAD.

3.3 NRGs signature is an independent prognostic factor

The univariate and multivariate Cox regression analysis were further performed to test whether the risk score is independent of the other clinical factors. The result of univariate Cox regression analysis demonstrated that risk score, age, stage, T, N, and M stages were all associated with patient survivals (Figure 4A). The multivariate Cox regression analysis demonstrated that the risk score is independent of the above mentioned clinical factors (Figure 4B), and can satisfactorily classify the survival status, tumor stage, N and M grades of COAD patients (Figures 4C–F). With the increase of the risk score, the pathological degree of tumor become worse. These findings imply that the risk score is effective in predicting the survival and prognosis of COAD patients.

3.4 Gene set enrichment analysis

The results of GSEA demonstrated that the focal adhesion, ECM-receptor interaction and glycosaminoglycan biosynthesis pathways were enriched in the high risk group (Figures 5A–C, Supplementary Table S5), indicating that the tumor metastasis and invasion were the characteristics of high risk group. Chemical carcinogenesis-DNA adducts, ferroptosis and chemical carcinogenesis-reactive oxygen species were the enriched pathways of the low risk group (Figures 5D–F), demonstrating that tumor formation and progression are the characteristics of the low risk group. These results were consistent with the progression of COAD.

3.5 Construction and evaluation of a prognostic nomogram for individual COAD patients

In order to facilitate personalized survival prediction of COAD patients, the nomogram was built based on risk score, T and age (Figure 6A). The C-index and AUC were used to evaluate the performance of the nomogram, and the calibration curve is used to see how well the prediction matches the actual. The C-index of the

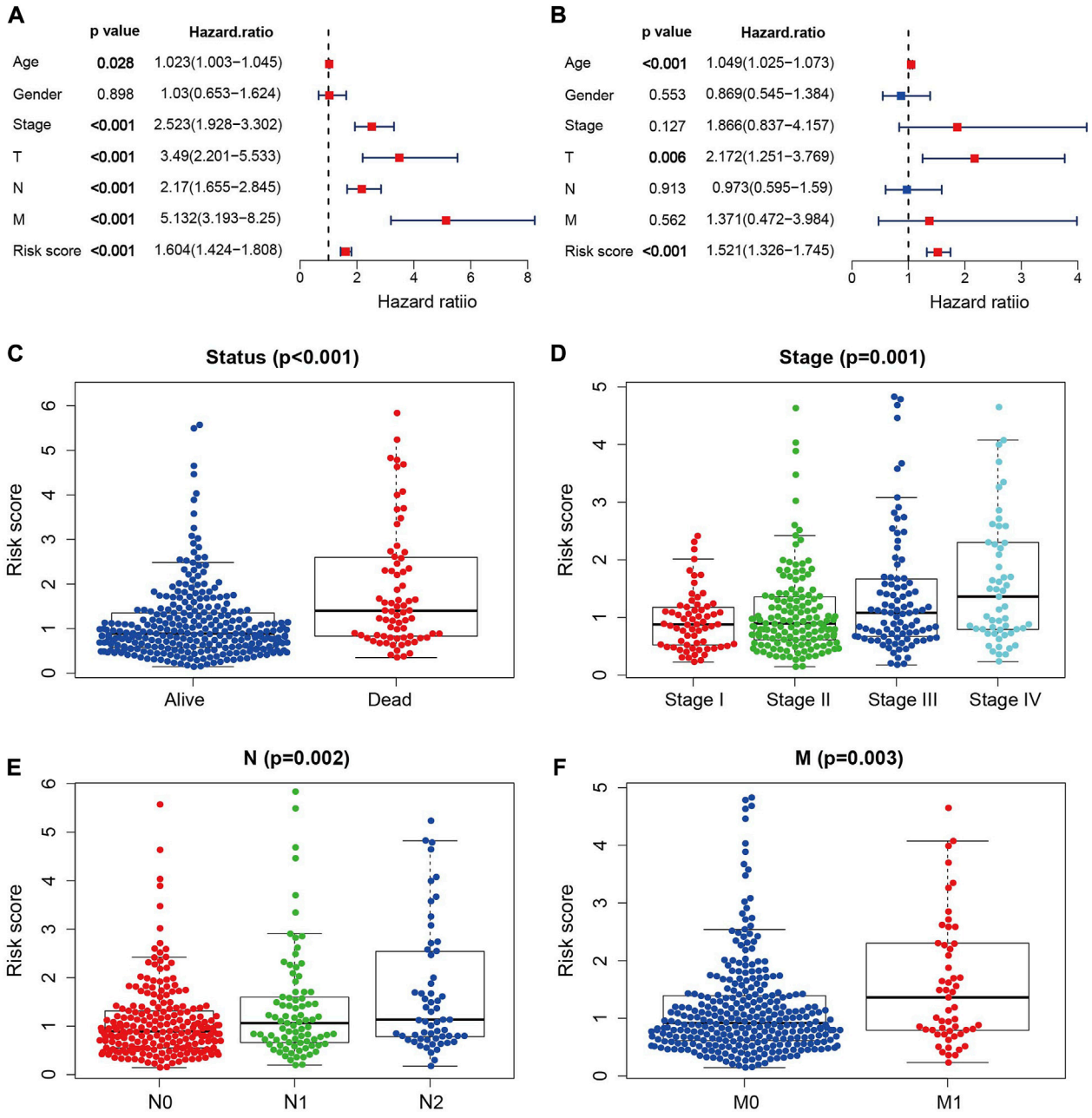

FIGURE 4
Independent prognostic analysis. **(A)** Univariate independent prognostic analysis in the TCGA cohort. **(B)** Multivariate independent prognostic analysis in the TCGA cohort. **(C–F)** NRGs signature based outcome stratification of different clinicopathological features (Status, Stage, N, M).

model is 0.75 and the 1-, 3-, and 5-year survival probabilities are quite close to ideal performance (45-degree line), indicating satisfactory performance of the nomogram in predicting OS (Figure 6B). When compared with a single kind of prognostic feature, the nomogram outperforms risk score, T and age for predicting the survivals of COAD patients, suggesting the better performance of nomogram (Figure 6C).

3.6 Candidate drugs identification for high risk COAD patients

To identify potential drugs for the treatment of high risk COAD patients, a total of 237 DEGs (Supplementary Table S6) were used as the inputs of the Cmap database, among which, 210 DEGs were significantly up-regulated and 27 were

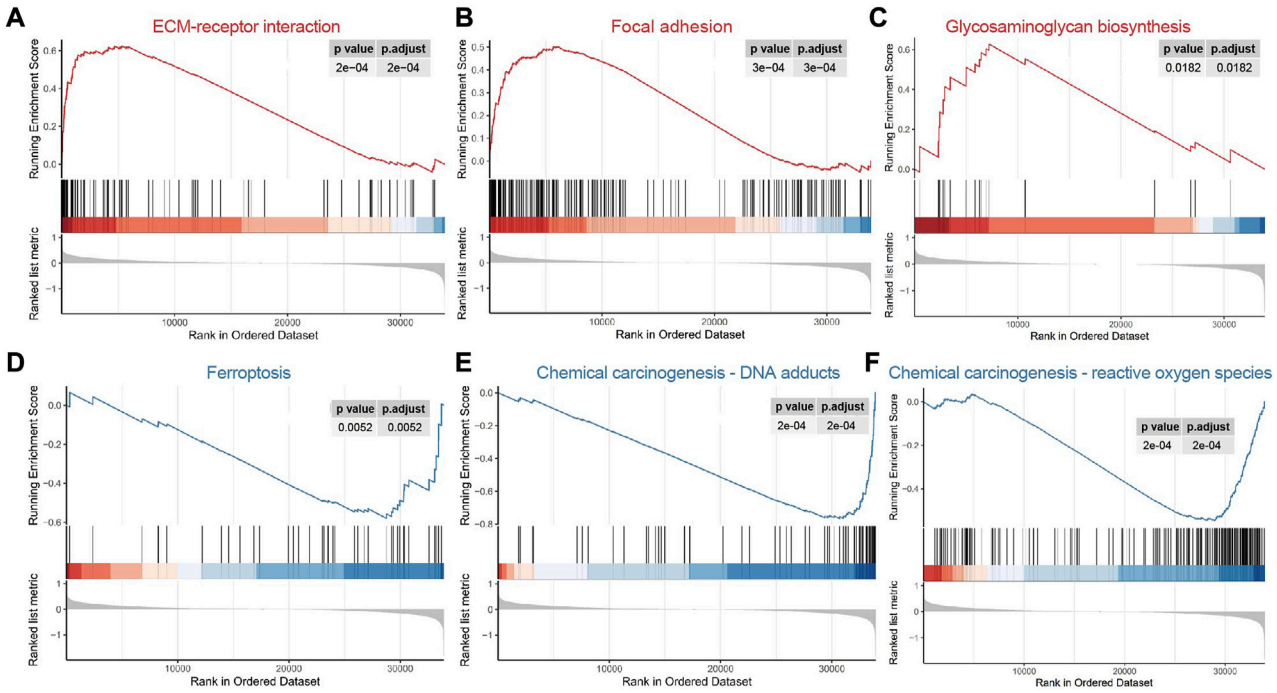

FIGURE 5
Functional gene set enrichment analysis. **(A–C)** The pathways enriched in high risk group; **(D–F)** The pathways enriched in low risk group.

significantly down-regulated in the high risk group. It was found that five drugs, namely MST-312, flucytosine, ganglioside, xanthohumol and dapsone, were with the scores less than -80 and held the potential for the treatment of high risk patients (Table 1).

3.7 Targets screening and molecular docking

Based on the STITCH database, we obtained 17 targets for the five candicate drugs, including seven for dapsone, three for flucytosine, and seven for xanthohumol, respectively (Figures 7A–C). Eight of the 17 genes were differentially expressed in high risk group. NOTCH1, DNMT1, LCAT were over-expressed, while CYP3A4, NAT2, DGAT1, CYP3A5, CYP3A7 were under-expressed (Figure 7D). Further analysis demonstrated that only two of the eight differentially expressed genes were significantly associated with the survival of COAD patients (Figures 7E,F and Supplementary Figure S3). The patients with a high expression of NAT2 and a low expression of LCAT exhibit the higher survival rate (Figures 7E,F). Therefore, it is speculated that the drugs xanthohumol and dapsone may affect tumor progression by affecting the abnormally expression of LCAT and NAT2, respectively.

To validate whether the xanthohumol and dapsone could interact with target genes, the molecular docking was performed between the drugs and target genes, i.e. dapsone and NAT2, xanthohumol and LCAT, respectively. The dapsone and NAT2 (PDB ID: 2 P FR) had a docking affinity score of -6.4 kcal/mol (Figure 8A). Dapsone binds to NAT2 through interacting with amino acid residues, such as glu261, leu275, ser274, gly276, glu264, leu267, asn278, leu279, val263 and glu260. The docking affinity score between xanthohumol and LCAT (PDB ID: 4X96) was -7.1 kcal/mol (Figure 8B). Xanthohumol binds to LCAT through interacting with amino acid residues, such as asp56, phe58, glu55, thr54, lys53, thr123, arg52, asn379, his122, phe382, gly199 and tyr51. These results demonstrate that dapsone and xanthohumol possess good combination with their targets, and hold the potential to be the drugs for the treatment of COAD.

4 Discussion

The development of biomarkers and therapeutic targets at the molecular level is crucial for the prognosis and treatment of COAD. Tumorigenesis and metastasis are both aided by necroptosis (Stoll et al., 2017; Seehawer et al., 2018; Yan et al., 2022). Dysregulated expression of necroptosis genes can lead to chronic colonic inflammation which promotes colon cancer growth (Wang et al.,

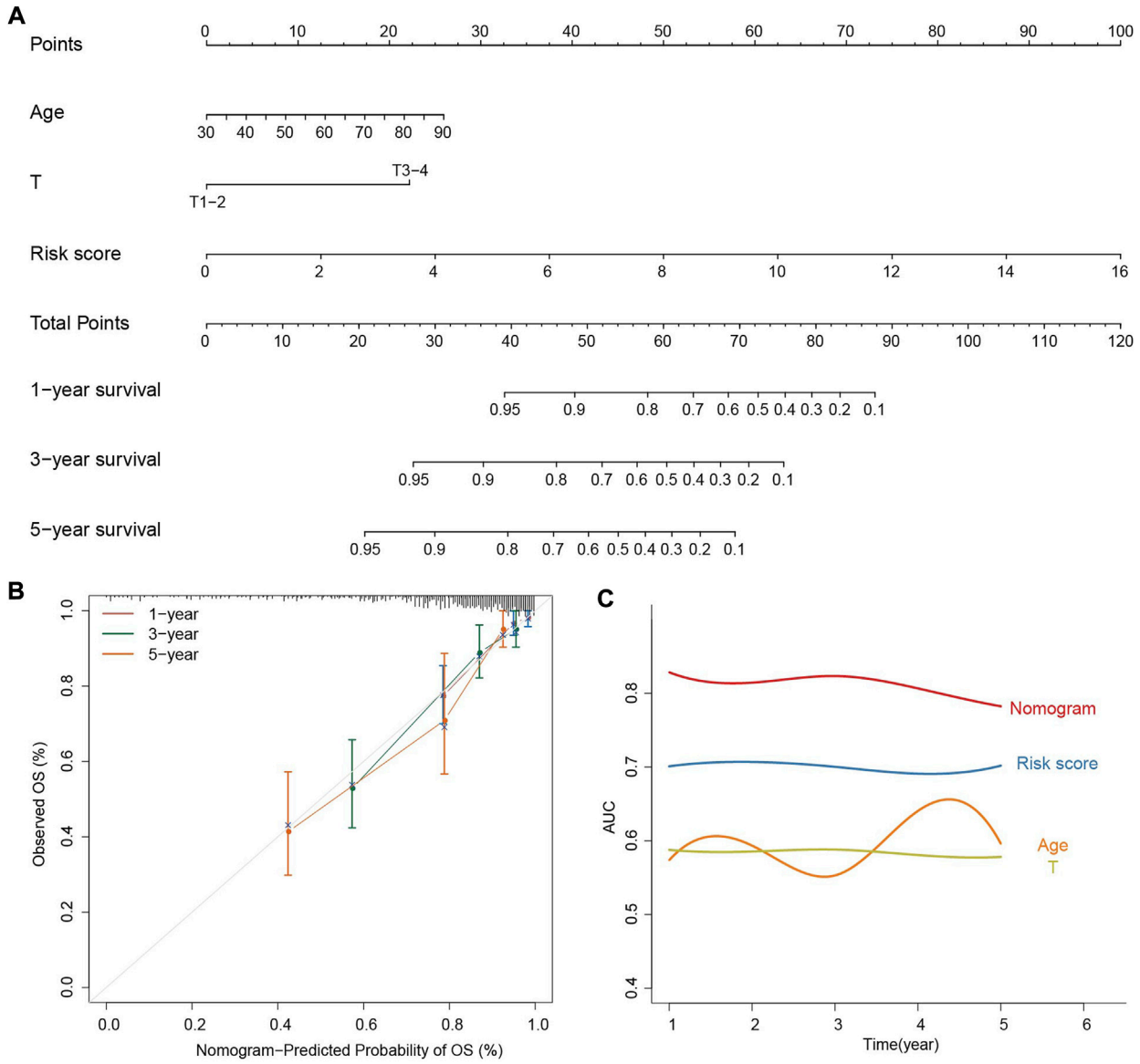

FIGURE 6
Construction and evaluation of the prognostic nomogram. **(A)** The nomogram predicts the probability of the 1-, 3-, and 5-year OS. **(B)** The calibration plot of the nomogram for predicting the probability of the 1-, 3-, and 5-year OS. **(C)** AUC smooth curve for evaluating the accuracy of nomogram predictions.

TABLE 1 Summary of connectivity map prediction results.

Drugs	Score	Description
MST-312	-93.38	Telomerase inhibitor
Flucytosine	-87.35	Antifungal
Ganglioside	-85.85	SRC activator
Xanthohumol	-82.18	ATPase inhibitor
Dapsone	-80.21	Bacterial antifolate

2020), suggesting that necroptosis is important for the development of COAD. At the meantime, it was also reported that medicines and substances that can interact with necroptosis genes have anticancer potentials (Su et al., 2015; Gong et al., 2019). In the present work, we therefore developed a NRGs based model for predicting the prognosis of COAD patients and identified the candidate drugs for the treatment COAD.

The proposed risk score model was built by using seven differentially expressed NRGs, namely CAMK2B, H2AC6,

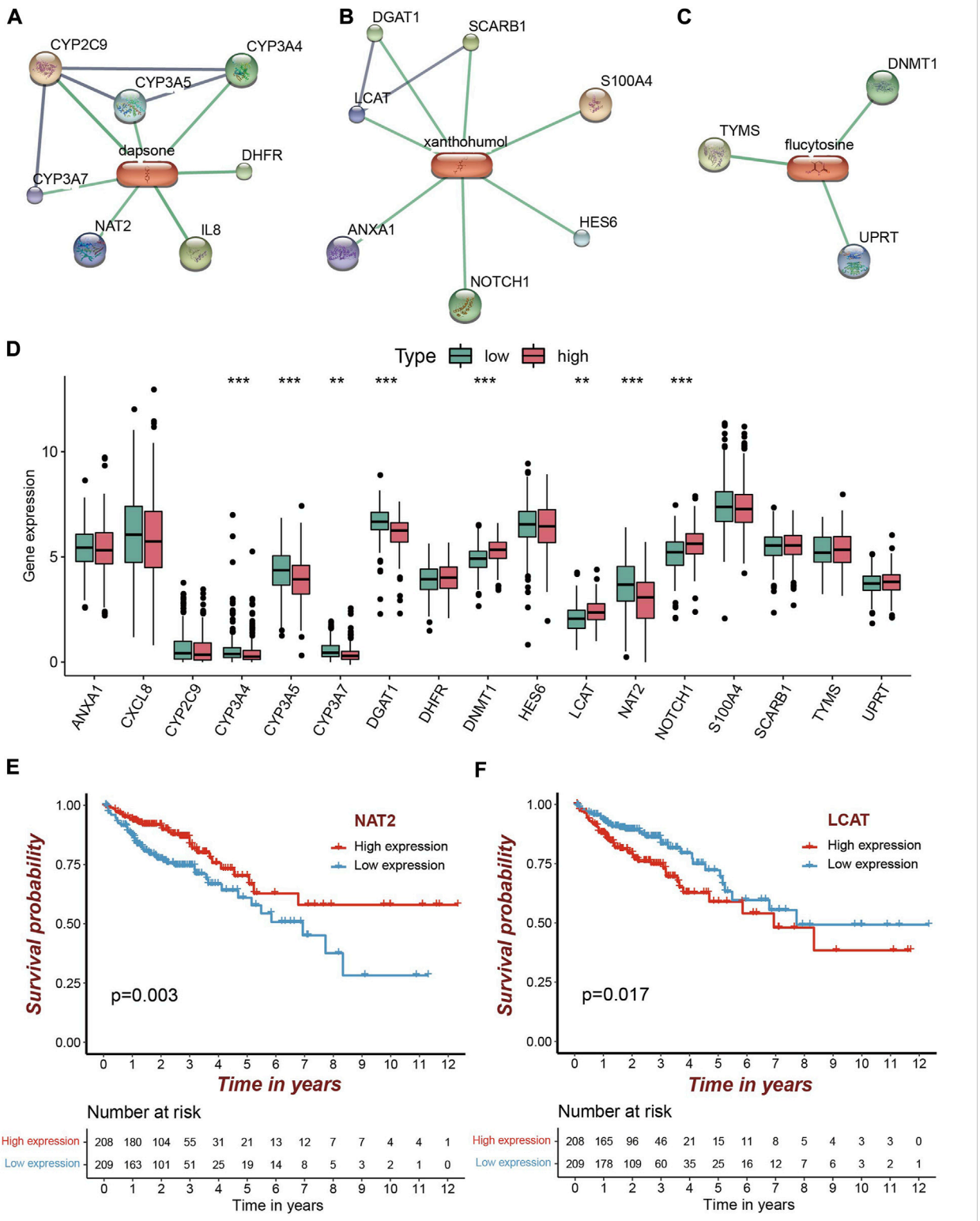

FIGURE 7
Candidate drugs screening for high risk patients and target identification. **(A–C)** The identified targets (confidence score>0.8) from STRING for dapsone, xanthohumol and flucytosine, respectively. **(D)** Eight of the 17 targets were significantly differentially expressed, of which five were significantly under-expressed in the high risk group and three were significantly over-expressed (**$p < 0.01$; ***$p < 0.001$). **(E,F)** Patients with a high NAT2 expression and patients with a low LCAT expression had a higher survival rate.

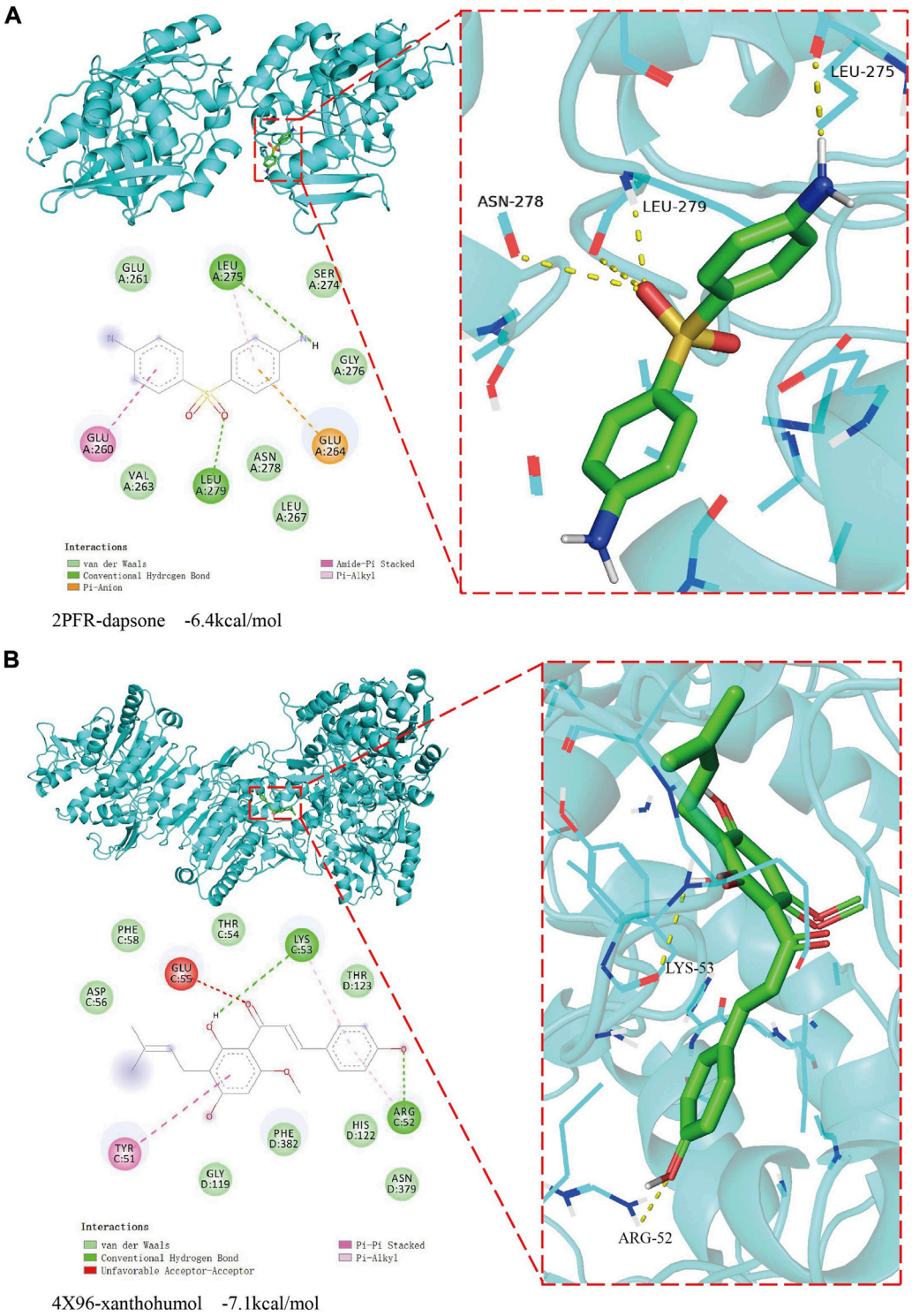

FIGURE 8
The result of molecular docking between candidate drugs and targets. **(A)** The molecular docking results between dapsone and its target NAT2. **(B)** The molecular docking results between xanthohumol and its target LCAT.

MLKL, RBCK1, VDAC3, RIPK3, and TRAF2. CAMK2B regulates the microenvironmental remodeling of renal papillary cell carcinoma, which has an anti-tumor effect (Jia et al., 2022). H2AC6, which belongs to the H2A family of histones, is a replication-dependent histone. Histone H2A has been linked to diabetic nephropathy, atherosclerosis, cardiovascular disease, and hypertensive kidney injury (Gao et al., 2013; Jiang et al., 2018; Yerra and Advani, 2018; Pei et al., 2021). MLKL may serve as a promising target to block tumor regeneration and participate in the regulation of necroptosis pathway, thereby improving the efficacy of radiation therapy for colorectal cancer (Wang et al., 2019). Overexpression of RBCK1 was reported to be associated with a poor prognosis in colorectal cancer patients (Liu et al., 2019). VDAC3 has been linked to cancer and pathology as a potential marker of mitochondrial status (Reina et al., 2016). Up-regulation of RIPK3 can prevent the development of liver cancer (Wu et al., 2020). TRAF2 is a tumor suppressor gene in colon cancer (Moon et al., 2021). Considering that RNA modifications were associated with the development of cancers, we performed the conservation analysis of N^6-methyladenosine (m^6A) modification for the seven genes by using ConsRM(Song et al., 2021). The conserved m^6A sites were identified in TRAF2 and RBCK1, suggesting that m^6A modification may be also associated with the pathogenesis of COAD.

Based on the proposed model, the patients in the TCGA cohort were clustered into low and high risk groups. In the high risk group, patients have a considerably shorter OS than those in the low risk group. The ROC curves obtained from the TCGA training data and the independent GEO data indicated that the proposed model has a relative high accuracy for predicting the OS of COAD patients and could be utilized as an independent predictor to predict patients' risk of death.

The results from GSEA enrichment analysis demonstrated that the tumor metastasis and invasion associated signaling pathways were enriched in the high risk group (Figure 5). For example, the focal adhesion signaling pathway is closely related to tumor invasion (Golubovskaya and Cance, 2010). ECM-receptor interaction is an important pathway for colorectal cancer cell metastasis (Nersisyan et al., 2021). Glycosaminoglycan can promote cancer angiogenesis and metastasis (Wei et al., 2020). Signaling pathways related to tumor formation and progression were enhanced in the low risk group. Ferroptosis and chemical carcinogenesis promote the occurrence and development of cancer (de Bono et al., 2020; Chaudhary et al., 2021).

In order to provide insights for the treatment of COAD, we identified two candidate drugs, namely dapsone and xanthohumol, from the Cmap database. The dapsone improves the overall survival of colon cancer patients by inhibiting the expression level of tumor growth-driving elements IL-8 (Fisher et al., 2019; Kast et al., 2022). Xanthohumol acts as a carcinogenic inhibitor, low dose xanthohumol treatment blocks the proliferation and spread of primary colon cancer cells (Torrens-Mas et al., 2022). The results of molecular docking analysis demonstrated that dapsone and xanthohumol can interact with NAT2 and LCAT, respectively. Thus, dapsone and xanthohumol may alter the tumor progression of high risk COAD patients by acting on NAT2 and LCAT, respectively. Further experimental analysis was needed to illustrate the detail mechanisms.

Taken together, we developed a NRGs signature that can be used to predict the prognosis of COAD patients and screened out two candidate drugs for the treatment of high risk COAD patients. Inevitably, the following limitations should be considered in the future works. First, the robustness of the proposed model should be validated by large-scale prospective trials or cell experiments. Second, experiments are needed to validate the interactions between candidate drugs and targets and to demonstrate their treatment mechanisms on COAD. In addition, the data from the RNA modification databases, such as m6A-atlas (Tang et al., 2021), m5C-atlas (Ma et al., 2022), and m7Ghub (Song et al., 2020), should be integrated to further examine whether RNA modifications are associated with COAD as well.

Data availability statement

The datasets presented in this study can be found in online repositories. The names of the repository/repositories and accession number(s) can be found in the article/Supplementary Material.

Author contributions

ML collected the data, performed data analysis, and wrote the manuscript; ML and TZ provided help in data collection and result analysis; WC designed and supervised the project, and wrote the manuscript.

Acknowledgments

Thanks to TCGA and the GEO database for their selfless dedication.

Conflict of interest

The authors declare that the research was conducted in the absence of any commercial or financial relationships that could be construed as a potential conflict of interest.

Publisher's note

All claims expressed in this article are solely those of the authors and do not necessarily represent those of their

affiliated organizations, or those of the publisher, the editors and the reviewers. Any product that may be evaluated in this article, or claim that may be made by its manufacturer, is not guaranteed or endorsed by the publisher.

Supplementary material

The Supplementary Material for this article can be found online at: https://www.frontiersin.org/articles/10.3389/fgene.2022.1051800/full#supplementary-material

References

Bray, F., Ferlay, J., Soerjomataram, I., Siegel, R. L., Torre, L. A., and Jemal, A. (2018). Global cancer statistics 2018: GLOBOCAN estimates of incidence and mortality worldwide for 36 cancers in 185 countries. *Ca. Cancer J. Clin.* 68 (6), 394–424. doi:10.3322/caac.21492

Chaudhary, N., Choudhary, B. S., Shah, S. G., Khapare, N., Dwivedi, N., Gaikwad, A., et al. (2021). Lipocalin 2 expression promotes tumor progression and therapy resistance by inhibiting ferroptosis in colorectal cancer. *Int. J. Cancer* 149 (7), 1495–1511. doi:10.1002/ijc.33711

de Bono, J. S., Guo, C., Gurel, B., De Marzo, A. M., Sfanos, K. S., Mani, R. S., et al. (2020). Prostate carcinogenesis: Inflammatory storms. *Nat. Rev. Cancer* 20 (8), 455–469. doi:10.1038/s41568-020-0267-9

Ding, C., Yu, Z., Zhu, J., Li, X., Dai, M., and Qiang, H. (2022). Construction and validation of a necroptosis-related gene signature for predicting prognosis and tumor microenvironment of pancreatic cancer. *Dis. Markers* 2022, 9737587. doi:10.1155/2022/9737587

Feng, X., Song, Q., Yu, A., Tang, H., Peng, Z., and Wang, X. (2015). Receptor-interacting protein kinase 3 is a predictor of survival and plays a tumor suppressive role in colorectal cancer. *Neoplasma* 62 (4), 592–601. doi:10.4149/neo_2015_071

Fisher, R. C., Bellamkonda, K., Alex Molina, L., Xiang, S., Liska, D., Sarvestani, S. K., et al. (2019). Disrupting inflammation-associated CXCL8-CXCR1 signaling inhibits tumorigenicity initiated by sporadic- and colitis-colon cancer stem cells. *Neoplasia* 21 (3), 269–281. doi:10.1016/j.neo.2018.12.007

Friedman, J., Hastie, T., and Tibshirani, R. (2010). Regularization paths for generalized linear models via coordinate descent. *J. Stat. Softw.* 33 (1), 1–22. doi:10.18637/jss.v033.i01

Gao, C., Chen, G., Liu, L., Li, X., He, J., Jiang, L., et al. (2013). Impact of high glucose and proteasome inhibitor MG132 on histone H2A and H2B ubiquitination in rat glomerular mesangial cells. *J. Diabetes Res.* 2013, 589474. doi:10.1155/2013/589474

Gao, T., Du, T., Hu, X., Dong, X., Li, L., Wang, Y., et al. (2020). Cosmc overexpression enhances malignancies in human colon cancer. *J. Cell. Mol. Med.* 24 (1), 362–370. doi:10.1111/jcmm.14740

Golubovskaya, V. M., and Cance, W. (2010). Focal adhesion kinase and p53 signal transduction pathways in cancer. *Front. Biosci.* 15 (3), 901–912. doi:10.2741/3653

Gong, Y., Fan, Z., Luo, G., Yang, C., Huang, Q., Fan, K., et al. (2019). The role of necroptosis in cancer biology and therapy. *Mol. Cancer* 18 (1), 100. doi:10.1186/s12943-019-1029-8

Huang, Y. Q., Liang, C. H., He, L., Tian, J., Liang, C. S., Chen, X., et al. (2016). Development and validation of a radiomics nomogram for preoperative prediction of lymph node metastasis in colorectal cancer. *J. Clin. Oncol.* 34 (18), 2157–2164. doi:10.1200/jco.2015.65.9128

Huang, Y., Zou, Y., Xiong, Q., Zhang, C., Sayagués, J. M., Shelat, V. G., et al. (2021). Development of a novel necroptosis-associated miRNA risk signature to evaluate the prognosis of colon cancer patients. *Ann. Transl. Med.* 9 (24), 1800. doi:10.21037/atm-21-6576

Jia, Q., Liao, X., Zhang, Y., Xu, B., Song, Y., Bian, G., et al. (2022). Anti-tumor role of CAMK2B in remodeling the stromal microenvironment and inhibiting proliferation in papillary renal cell carcinoma. *Front. Oncol.* 12, 740051. doi:10.3389/fonc.2022.740051

Jiang, W., Agrawal, D. K., and Boosani, C. S. (2018). Cell-specific histone modifications in atherosclerosis (Review). *Mol. Med. Rep.* 18 (2), 1215–1224. doi:10.3892/mmr.2018.9142

Kast, R. E., Alfieri, A., Assi, H. I., Burns, T. C., Elyamany, A. M., Gonzalez-Cao, M., et al. (2022). Mdact: A new principle of adjunctive cancer treatment using combinations of multiple repurposed drugs, with an example regimen. *Cancers (Basel)* 14 (10), 2563. doi:10.3390/cancers14102563

Kehoe, J., and Khatri, V. P. (2006). Staging and prognosis of colon cancer. *Surg. Oncol. Clin. N. Am.* 15 (1), 129–146. doi:10.1016/j.soc.2005.08.006

Krysko, O., Aaes, T. L., Kagan, V. E., D'Herde, K., Bachert, C., Leybaert, L., et al. (2017). Necroptotic cell death in anti-cancer therapy. *Immunol. Rev.* 280 (1), 207–219. doi:10.1111/imr.12583

Lebrec, H., Ponce, R., Preston, B. D., Iles, J., Born, T. L., and Hooper, M. (2015). Tumor necrosis factor, tumor necrosis factor inhibition, and cancer risk. *Curr. Med. Res. Opin.* 31 (3), 557–574. doi:10.1185/03007995.2015.1011778

Li, X., Xiang, L., Lin, Y., Tang, Q., Meng, F., and Chen, W. (2022). Computational analysis illustrates the mechanism of qingfei paidu decoction in blocking the transition of COVID-19 patients from mild to severe stage. *Curr. Gene Ther.* 22 (3), 277–289. doi:10.2174/1566523221666210907162005

Liu, L., Huang, L., Chen, W., Zhang, G., Li, Y., Wu, Y., et al. (2022). Comprehensive analysis of necroptosis-related long noncoding RNA immune infiltration and prediction of prognosis in patients with colon cancer. *Front. Mol. Biosci.* 9, 811269. doi:10.3389/fmolb.2022.811269

Liu, M. L., Zang, F., and Zhang, S. J. (2019). RBCK1 contributes to chemoresistance and stemness in colorectal cancer (CRC). *Biomed. Pharmacother.* 118, 109250. doi:10.1016/j.biopha.2019.109250

Liu, X., Zhou, M., Mei, L., Ruan, J., Hu, Q., Peng, J., et al. (2016). Key roles of necroptotic factors in promoting tumor growth. *Oncotarget* 7 (16), 22219–22233. doi:10.18632/oncotarget.7924

Liu, Z., Guan, C., Lu, C., Liu, Y., Ni, R., Xiao, M., et al. (2018). High NUSAP1 expression predicts poor prognosis in colon cancer. *Pathol. Res. Pract.* 214 (7), 968–973. doi:10.1016/j.prp.2018.05.017

Ma, J., Song, B., Wei, Z., Huang, D., Zhang, Y., Su, J., et al. (2022). m5C-Atlas: a comprehensive database for decoding and annotating the 5-methylcytosine (m5C) epitranscriptome. *Nucleic Acids Res.* 50 (D1), D196–d203. doi:10.1093/nar/gkab1075

Miller, K. D., Nogueira, L., Mariotto, A. B., Rowland, J. H., Yabroff, K. R., Alfano, C. M., et al. (2019). Cancer treatment and survivorship statistics, 2019. *Ca. Cancer J. Clin.* 69 (5), 363–385. doi:10.3322/caac.21565

Moon, S. W., Son, H. J., Choi, E. J., Yoo, N. J., and Lee, S. H. (2021). Brief research report regional difference in TRAF2 and TRAF3 gene mutations in colon cancers. *Pathol. Oncol. Res.* 27, 625438. doi:10.3389/pore.2021.625438

Morris, G. M., Huey, R., Lindstrom, W., Sanner, M. F., Belew, R. K., Goodsell, D. S., et al. (2009). AutoDock4 and AutoDockTools4: Automated docking with selective receptor flexibility. *J. Comput. Chem.* 30 (16), 2785–2791. doi:10.1002/jcc.21256

Nersisyan, S., Novosad, V., Engibaryan, N., Ushkaryov, Y., Nikulin, S., and Tonevitsky, A. (2021). ECM-receptor regulatory network and its prognostic role in colorectal cancer. *Front. Genet.* 12, 782699. doi:10.3389/fgene.2021.782699

Pei, H. J., Yang, J., Hu, F. X., Chen, Y. Z., and Yang, C. H. (2021). Tribulus terrestris L. protects glomerular endothelial cells via the miR155-H2AC6 interaction network in hypertensive renal injury. *Ann. Transl. Med.* 9 (21), 1626. doi:10.21037/atm-21-5641

Qi, L., Xu, R., Ren, X., Zhang, W., Yang, Z., Tu, C., et al. (2022). Comprehensive profiling reveals prognostic and immunogenic characteristics of necroptosis in soft tissue sarcomas. *Front. Immunol.* 13, 877815. doi:10.3389/fimmu.2022.877815

Reina, S., Guarino, F., Magrì, A., and De Pinto, V. (2016). VDAC3 as a potential marker of mitochondrial status is involved in cancer and pathology. *Front. Oncol.* 6, 264. doi:10.3389/fonc.2016.00264

Seehawer, M., Heinzmann, F., D'Artista, L., Harbig, J., Roux, P. F., Hoenicke, L., et al. (2018). Necroptosis microenvironment directs lineage commitment in liver cancer. *Nature* 562 (7725), 69–75. doi:10.1038/s41586-018-0519-y

Song, B., Chen, K., Tang, Y., Wei, Z., Su, J., de Magalhães, J. P., et al. (2021). ConsRM: Collection and large-scale prediction of the evolutionarily conserved RNA methylation sites, with implications for the functional epitranscriptome. *Brief. Bioinform.* 22 (6), bbab088. doi:10.1093/bib/bbab088

Song, B., Tang, Y., Chen, K., Wei, Z., Rong, R., Lu, Z., et al. (2020). m7GHub: deciphering the location, regulation and pathogenesis of internal mRNA N7-methylguanosine (m7G) sites in human. *Bioinformatics* 36 (11), 3528–3536. doi:10.1093/bioinformatics/btaa178

Stoll, G., Ma, Y., Yang, H., Kepp, O., Zitvogel, L., and Kroemer, G. (2017). Pro-necrotic molecules impact local immunosurveillance in human breast cancer. *Oncoimmunology* 6 (4), e1299302. doi:10.1080/2162402x.2017.1299302

Su, Z., Yang, Z., Xu, Y., Chen, Y., and Yu, Q. (2015). Apoptosis, autophagy, necroptosis, and cancer metastasis. *Mol. Cancer* 14, 48. doi:10.1186/s12943-015-0321-5

Subramanian, A., Narayan, R., Corsello, S. M., Peck, D. D., Natoli, T. E., Lu, X., et al. (2017). A next generation connectivity map: L1000 platform and the first 1, 000, 000 profiles. *Cell* 171 (6), 1437–1452. doi:10.1016/j.cell.2017.10.049

Szklarczyk, D., Santos, A., von Mering, C., Jensen, L. J., Bork, P., and Kuhn, M. (2016). Stitch 5: Augmenting protein-chemical interaction networks with tissue and affinity data. *Nucleic Acids Res.* 44 (D1), D380–D384. doi:10.1093/nar/gkv1277

Tang, Y., Chen, K., Song, B., Ma, J., Wu, X., Xu, Q., et al. (2021). m6A-Atlas: a comprehensive knowledgebase for unraveling the N6-methyladenosine (m6A) epitranscriptome. *Nucleic Acids Res.* 49 (D1), D134–d143. doi:10.1093/nar/gkaa692

Torrens-Mas, M., Alorda-Clara, M., Martínez-Vigara, M., Roca, P., Sastre-Serra, J., Oliver, J., et al. (2022). Xanthohumol reduces inflammation and cell metabolism in HT29 primary colon cancer cells. *Int. J. Food Sci. Nutr.* 73 (4), 471–479. doi:10.1080/09637486.2021.2012561

Trott, O., and Olson, A. J. (2010). AutoDock Vina: Improving the speed and accuracy of docking with a new scoring function, efficient optimization, and multithreading. *J. Comput. Chem.* 31 (2), 455–461. doi:10.1002/jcc.21334

Wang, R., Li, H., Wu, J., Cai, Z. Y., Li, B., Ni, H., et al. (2020). Gut stem cell necroptosis by genome instability triggers bowel inflammation. *Nature* 580 (7803), 386–390. doi:10.1038/s41586-020-2127-x

Wang, Y., Zhao, M., He, S., Luo, Y., Zhao, Y., Cheng, J., et al. (2019). Necroptosis regulates tumor repopulation after radiotherapy via RIP1/RIP3/MLKL/JNK/IL8 pathway. *J. Exp. Clin. Cancer Res.* 38 (1), 461. doi:10.1186/s13046-019-1423-5

Wei, J., Hu, M., Huang, K., Lin, S., and Du, H. (2020). Roles of proteoglycans and glycosaminoglycans in cancer development and progression. *Int. J. Mol. Sci.* 21 (17), E5983. doi:10.3390/ijms21175983

Wu, L., Zhang, X., Zheng, L., Zhao, H., Yan, G., Zhang, Q., et al. (2020). RIPK3 orchestrates fatty acid metabolism in tumor-associated macrophages and hepatocarcinogenesis. *Cancer Immunol. Res.* 8 (5), 710–721. doi:10.1158/2326-6066.cir-19-0261

Yan, J., Wan, P., Choksi, S., and Liu, Z. G. (2022). Necroptosis and tumor progression. *Trends Cancer* 8 (1), 21–27. doi:10.1016/j.trecan.2021.09.003

Yang, Z., Lu, S., Wang, Y., Tang, H., Wang, B., Sun, X., et al. (2022). A novel defined necroptosis-related miRNAs signature for predicting the prognosis of colon cancer. *Int. J. Gen. Med.* 15, 555–565. doi:10.2147/ijgm.s349624

Yerra, V. G., and Advani, A. (2018). Histones and heart failure in diabetes. *Cell. Mol. Life Sci.* 75 (17), 3193–3213. doi:10.1007/s00018-018-2857-1

Yu, G., Wang, L. G., Han, Y., and He, Q. Y. (2012). clusterProfiler: an R package for comparing biological themes among gene clusters. *Omics* 16 (5), 284–287. doi:10.1089/omi.2011.0118

frontiers | Frontiers in Genetics

TYPE Original Research
PUBLISHED 31 October 2022
DOI 10.3389/fgene.2022.1045395

OPEN ACCESS

EDITED BY
Kunqi Chen,
Fujian Medical University, China

REVIEWED BY
Qing Long,
Kunming Medical University, China
Haolong Li,
Peking Union Medical College Hospital, China
Ahmed Hammad,
Egyptian Atomic Energy Authority, Egypt
Malihe Rastegarpanah,
Breast Cancer Research Center, Motamed Cancer Institute, Iran
Haoran Shi,
University of Giessen, Germany

*CORRESPONDENCE
Hanwang Zhang,
hwzhang605@126.com
Fang Ren,
fccrenf@zzu.edu.cn

SPECIALTY SECTION
This article was submitted to Epigenomics and Epigenetics, a section of the journal Frontiers in Genetics

RECEIVED 15 September 2022
ACCEPTED 14 October 2022
PUBLISHED 31 October 2022

CITATION
Cai L, Liao Z, Li S, Wu R, Li J, Ren F and Zhang H (2022), PLP1 may serve as a potential diagnostic biomarker of uterine fibroids.
Front. Genet. 13:1045395.
doi: 10.3389/fgene.2022.1045395

PLP1 may serve as a potential diagnostic biomarker of uterine fibroids

Lei Cai[1], Zhiqi Liao[1], Shiyu Li[2], Ruxing Wu[1], Jie Li[1], Fang Ren[3]* and Hanwang Zhang[1]*

[1]Reproductive Medicine Center, Tongji Hospital, Tongji Medical College, Huazhong University of Science and Technology, Wuhan, China, [2]Institute of Digestive Disease and Department of Medicine and Therapeutics, State Key Laboratory of Digestive Diseases, Li Ka Shing Institute of Health Sciences, The Chinese University of Hong Kong, Hong Kong, China, [3]Department of Gynecology, First Affiliated Hospital of Zhengzhou University, Zhengzhou, China

Objective: We aim to identify the crucial genes or potential biomarkers associated with uterine fibroids (UFs), which may provide clinicians with evidence about the diagnostic biomarker of UFs and reveal the mechanism of its progression.

Methods: The gene expression and genome-wide DNA methylation profiles were obtained from Gene Expression Omnibus database (GEO). GSE45189, GSE31699, and GSE593 datasets were included. GEO2R and Venn diagrams were used to analyze the differentially expressed genes (DEGs) and extract the hub genes. Gene Ontology (GO) analysis was performed by the online tool Database for Annotation, Visualization, and Integrated Discovery (DAVID). The mRNA and protein expression of hub genes were validated by RT-qPCR, western blot, and immunohistochemistry. The receiver operating characteristic (ROC) curve was used to evaluate the diagnostic value.

Results: We detected 22 DEGs between UFs and normal myometrium, which were enriched in cell maturation, apoptotic process, hypoxia, protein binding, and cytoplasm for cell composition. By finding the intersection of the data between differentially expressed mRNA and DNA methylation profiles, 3 hub genes were identified, including transmembrane 4 L six family member 1 (TM4SF1), TNF superfamily member 10 (TNFSF10), and proteolipid protein 1 (PLP1). PLP1 was validated to be up-regulated significantly in UFs both at mRNA and protein levels. The area under the ROC curve (AUC) of PLP1 was 0.956, with a sensitivity of 79.2% and a specificity of 100%. Conclusion: Overall, our results indicate that PLP1 may be a potential diagnostic biomarker for uterine fibroids.

KEYWORDS

uterine fibroids, bioinformatics analysis, DNA methylation, PLP1, biomarker

1 Introduction

Uterine fibroids (UFs) are one of the most common uterine benign neoplasms in women of reproductive age, with a morbidity of 77% (Stewart, 2005), and symptomatic lesions occur in 20%–40% of UFs patients (Leyland et al., 2022). The main clinical symptom includes menorrhagia, abnormal uterine bleeding, infertility, recurrent spontaneous abortion, and other pelvic disorder (Styer and Rueda, 2016; Dolmans et al., 2021). Moreover, UFs are the primary incidents of hysterectomy (Ciarmela et al., 2022) with a quantifiable economic and social burden (Cardozo et al., 2012). Ultrasound is the first-line imaging technique in the evaluation of UFs (Russo et al., 2022). It can provide information about some characteristics of morphology, such as cystic area, echogenicity, borders, and vascularization of the lesion. Nevertheless, it is difficult for clinicians to differentiate the benign myoma in the uterine from malignant leiomyosarcoma accurately. Recently, a novel diagnosis strategy has emerged that integrates the histological features and molecular biomarkers to provide a comprehensive assessment of UFs and determine whether a complete hysterectomy is required (Levy et al., 2013; Trovik et al., 2014; Croce and Chibon, 2021; Machado-Lopez et al., 2021). However, these potential biomarkers still lack reliable clinical utility (Levy et al., 2013), as the sensitivity or specificity of them is less than 75% or 99.6%, respectively (Anderson et al., 2010). Thus, more valuable biomarkers validated for the diagnosis of UFs are desperately required. It may also enable us better understand the mechanism of progression and some important features of UFs.

DNA methylation, one of the epigenetic modifications of DNA in mammalians, refers to the transfer of a methyl group to the fifth carbon of a cytosine residue on the DNA sequence to form 5-methylcytosine (Reik et al., 2001). It occurs in CpG dinucleotides that are clustered frequently in regions of about 1–2 kb in length, called CpG islands, in or near the promoter and first exon regions of genes (Jones, 2012; Schübeler, 2015; Dor and Cedar, 2018). The frequency of CpG in gene regulatory regions is different. It was demonstrated that in leiomyomas, CpG sites were hypomethylated in the distal region of the estrogen receptor-alpha (ER-alpha) promoter combined with the higher ER-alpha mRNA levels (Asada et al., 2008). Besides, the aberrant expression of methyltransferases (Li et al., 2003) and other existence of differently methylated genomic locus in fibroids were also reported to separate the UFs from myometrium (Croce and Chibon, 2015; Braný et al., 2019; Liu et al., 2019; Sato et al., 2019; Maekawa et al., 2022). Based on the specific hypomethylated/hypermethylated genes (Islam et al., 2013; Sato et al., 2016) and the genome-wide DNA methylation profiles of UFs (Navarro et al., 2012; Maekawa et al., 2013), DNA methylation is considered to be the mainstay epigenetic mechanism of UFs. It is involved in the developmental processes of UFs by silencing, switching, and stabilizing genes. Hence, genes associated with DNA methylation may offer us some useful clinical diagnostic biomarkers for UFs. Nevertheless, the hub gene is still unclear.

In the present study, three Gene Expression Omnibus (GEO) datasets were utilized for analyzing the key gene relevant to DNA methylation in UFs. The hub gene was further validated by RT-qPCR, western blot, and immunohistochemistry. Finally, the receiver operating characteristic (ROC) curve was used to evaluate the performance of this biomarker for diagnosing UFs.

2 Methods

2.1 Obtaining the gene expression profiles in UFs

All three gene expression profiles in leiomyoma and normal myometrium tissue (GSE45189, GSE31699, and GSE593) were obtained from the National Center of Biotechnology Information (NCBI) Gene Expression Omnibus (GEO). The retrieval strategy was present with several keywords: leiomyoma, myometrium, gene expression profiling, and DNA methylation genome-wide association study. The inclusion was as follows: 1) a case-control research design; 2) includes UFs and normal myometrium tissue; 3) The original profiles should contain a genome-wide assessment. The exclusion criteria were the following: 1) non-case–control research design; 2) Other tissue. The analysis of the GSE45189 data set was based on 3 frozen UFs and 3 normal myometrium tissue obtained from the uterus with leiomyoma. The GSE31699 data set includes the gene expression profile of 68 UFs and paired normal myometrium tissue. The GSE593 data set included 6 tissue samples for DEGs analysis only. All details of sample information and experiment type are shown in Table 1.

2.2 Identification of DEGs between uterine fibroids and normal myometrium

We analyzed the DEGs between UFs and normal myometrium tissue from the gene expression profiles of GSE45189, GSE593, and GSE31699 datasets respectively. The differential DNA methylation genes were analyzed from the genome-wide DNA methylation profiles in GSE45189 and GSE31699 datasets respectively. All differential genes were identified using the online analysis tool GEO2R (https://www.ncbi.nlm.nih.gov/geo/geo2r/). Benjamin-Hochberg was applied for the control of false discovery rate (FDR), and $p < 0.05$ was utilized as the database's cut-off criteria. We draw the Venn diagram by the online tool (http://bioinformatics.psb.ugent.be/webtools/Venn/).

2.3 Gene Ontology analysis

In this study, Gene Ontology (GO) analysis was performed by the online tool, Database for Annotation, Visualization, and Integrated Discovery (DAVID version 2021, https://david.

TABLE 1 Gene Expression Omnibus (GEO) data set.

GEO accession	Platform	UFs	Normal myometrium	Experiment type
GSE593	GPL96	5	5	Affymetrix Human Genome U133A Array
GSE45189	GPL6244	3	3	Affymetrix Human Gene 1.0 ST Array
	GPL13534	3	3	HumanMethylation450 BeadChip
GSE31699	GPL6947	68	68	Illumina HumanHT-12 V3.0 expression Beadchip
	GPL8490	68	68	Illumina HumanMethylation27 BeadChip

Note: UFs, uterine fibroids.

ncifcrf.gov/home.jsp) (Han et al., 2022). The 22 DEGs distracted from all 3 datasets were uploaded to DAVID, and $p < 0.05$ was identified as the critical threshold for significant enrichment. The GO term included the following three criteria: molecular function (MF), cell composition (CC), and biological process (BP).

2.4 PLP1 methylation analysis

The CpG islands around the PLP1 gene promoter were profiled by the UCSC Genome online tool (https://genome.ucsc.edu/). The DNA methylation data of the PLP1 gene was retrieved from the DiseaseMeth version 2.0 database (http://bio-bigdata.hrbmu.edu.cn/diseasemeth/) (Song et al., 2022). The RNA modification type of PLP1 was identified by m6A-atlas (Tang et al., 2021) (http://rnamd.org/m6a) and m5C-atlas (Ma et al., 2022) (http://rnamd.org/m5c-atlas/index.html). The possible m6a regulator of PLP1 was analyzed by the online tools m6a target (http://m6a2target.canceromics.org/).

2.5 Clinical data

A total of 48 patients of UFs were recruited for this study who underwent myomectomy or hysterectomy with a final histological diagnosis of uterine fibroids in Tongji Hospital from 2018–2020. 14 UFs-free individuals were considered a control group. The slices of normal myometrium tissue were difficult to obtain, especially for UFs patients who underwent myomectomy. We included the patients with single uterine prolapse (8/14) who underwent hysterectomy, or patients with cesarean section scar diverticulum (CDS) who were treated by hysteroscopy (6/14) as a comparable control. The normal myometrium tissue from the slices of the CDS patients was identified by pathologists and only the section of myometrium tissue was included for further IHC analysis. Exclusion criteria for all participants consisted of fibroid degeneration, leiomyosarcoma, adenomyosis, and other gynecologic or pelvic malignant disorders. Any women with complicated diseases, for example, metabolic disorders, hypertension, autoimmune diseases, and treated with hormones before surgery were excluded. The information of all patients was collected from electronic medical records in Tongji Hospital which contains age, myoma location (FIGO), the maximum diameter of fibroids, and previous history of pregnancies and surgery. All procedures of this study were approved by the Ethics Committee of Tongji Medical College, Huazhong University of Science and Technology (2022S068).

2.6 RT-qPCR

Total RNA was extracted from leiomyoma and normal myometrium tissue using RNA-easy Isolation Reagent (Vazyme, R701). Synthesis of cDNA was performed using the PrimeScript™ RT Master Mix (Takara, RR036A). Then, real-time PCR analyses (Vazyme, Q712-02) were carried out in triplicate for each sample. All gene expression was normalized to GAPDH. The expression levels were calculated using the 2-ΔΔ Cq method (Livak and Schmittgen, 2001). The PCR primers were listed at supplemental Tabel1.

2.7 Western blot

All leiomyoma and normal myometrium tissue was lysed by RIPA buffer contended with 1% PMSG. Standard western blotting procedures were used (Liu C. et al., 2021). The primary antibody used PLP1 (Abcam, ab254363, 1:2000). Equal loading was confirmed using the glyceraldehyde-3-phosphate dehydrogenase (GAPDH) antibody (CST, 5174S, 1:2000). The appropriate anti-Rabbit HRP-linked secondary antibody (CST, 7074, 1:3000) was used.

2.8 Immunohistochemistry and hematoxylin and eosin stain

The section (4-μm thick) of paraffin-embedded leiomyoma and normal myometrium were deparaffinized and rehydrated using a series of graded xylene and alcohol. All slices used EDTA

for antigen retrieval. After 1 h cooled, 10% H_2O_2 was used to quench endogenous peroxidase activity. Blocking was performed using goat serum for 30 min, RT. The primary antibody used PLP1 (Abcam, ab254363, 1:2000). The HRP labeled anti-Rabbit secondary antibody was used the following day. Finally, the slices were mounted with the coverslips using Permount TM Mounting Medium. And all adjacent slices were stained with hematoxylin and eosin (H&E) based on the basic protocol. The percentage of positive stained was conculcated as follows (Karpathiou et al., 2021): 0 = 0%, 1 = 0–25%, 2 = 26–50%, 3 = 51–75%, 4 = 76–100%. The intensity scoring was conducted as follows: 0 = no staining, 1 = weak, 2 = moderate, 3 = strong. The final scores of all sections were based on multiplying the percentage by intensity. [0] = negative expression; [1–3] = low expression; [4–12] = high expression.

2.9 Statistical analysis

All data were presented as the mean ± SD, and data generated *in vitro* were compared using Student's t-tests. We performed χ2 test to explore the relationship between UFs and normal myometrium for categorical data. Receiver operating characteristic (ROC) analysis based on the IHC score of all cases was performed to evaluate the diagnostic value of PLP1. The optimal cutoff value in the ROC curve was set to the value that maximizes the Youden index. Youden's index was defined as sensitivity + specificity—1. The statistical significance threshold was set at a p-value of <0.05. SPSS v21.0 (IBM, United States) and GraphPad Prism 8.0 (GraphPad, United States) were used for statistical analysis and figures preparation.

3 Results

3.1 Identification of differentially expressed genes between uterine fibroids and normal myometrium

A total of 163 DEGs were identified between UFs and normal myometrium in GSE593 data set by GEO2R analysis, including 58 upregulating genes and 105 downregulating genes. DEGs were analyzed from the gene expression profiles in GSE45189 and GSE31699 datasets respectively. Thereinto, 189 upregulated and 309 downregulated genes were identified by GEO2R analysis in GSE45189 dataset. As for GSE31699 dataset, 2060 DEGs were identified, which included 1129 upregulating genes and 931 downregulated genes. The DEGs of UFs and normal myometrium for each dataset was visualized in the corresponding volcano plots (Figures 1A–C). The DEGs from all datasets were identified by the Venn diagram (Figure 1 D), 22 DEGs were shown in Table 2.

3.2 Analysis of Gene Ontology Enrichment

The GO enriched terms were analyzed by DAVID database. The results showed that DEGs between UFs and normal myometrium of all 3 datasets were mainly enriched in cell maturation, regulation of the apoptotic process, cellular response to hypoxia, and response to testosterone in the biological process. Protein binding was the most enrichment term in the molecular function criterion. Considering the cell composition criterion, the results showed that DEGs mainly concentrated on the cytoplasm. All terms of GO analysis are presented in Figure 1E.

3.3 Identify the hub gene

Epigenomic aberrations, especially DNA methylation have been identified as one of the main mechanisms for UFs pathogenesis (Mlodawska et al., 2022). Over the years, literature has reported that aberrant DNA methylation occurs throughout the genome in UFs (Islam et al., 2013; Sato et al., 2014; Sato et al., 2016; Sato et al., 2019; Maekawa et al., 2022), accompanied by mRNA expression discrepancy, demonstrating that aberrant gene expression caused by aberrant DNA methylation plays a key role in the pathogenesis of UFs. The datasets included in this study, GSE31699 and GSE45189, provided data about genome-wide DNA methylation of UFs (Navarro et al., 2012; Maekawa et al., 2013). The differential DNA methylation genes were analyzed by GEO2R. The volcano plots of the hypermethylation/hypomethylation genes were presented in the supplemental figure. To investigate the accurate genes with aberrantly DNA promoter methylation, we drew the Venn diagram as followed (Figure 2A). The differential DNA methylation genes in both GSE31699 and GSE45189 datasets and the 22 DEGs extracted from all 3 datasets were analyzed, and three hub genes were found (TM4SF1, TNFSF10, PLP1). The RT-qPCR was implemented to verify the gene expression. Among them, PLP1 was overexpressed in UFs tissue (Figures 2B–D).

3.4 The expression of PLP1 might be regulated by both DNA methylation and RNA modification

Multiple CpG islands were present in Supplemental Figure S2. Then, we found that the PLP1 transcripts were methylated to varying degrees in uterine carcinosarcoma and uterine corpus endometrial carcinoma (Supplemental Figure S2). Interestingly, we discovered that PLP1 was linked to N6-methyladenosine (m6A) modification. Metagene analysis of m6A indicating modification of PLP1 in 3′UTR gene region in the human embryonic stem cells (ESC). The RNA binding protein and

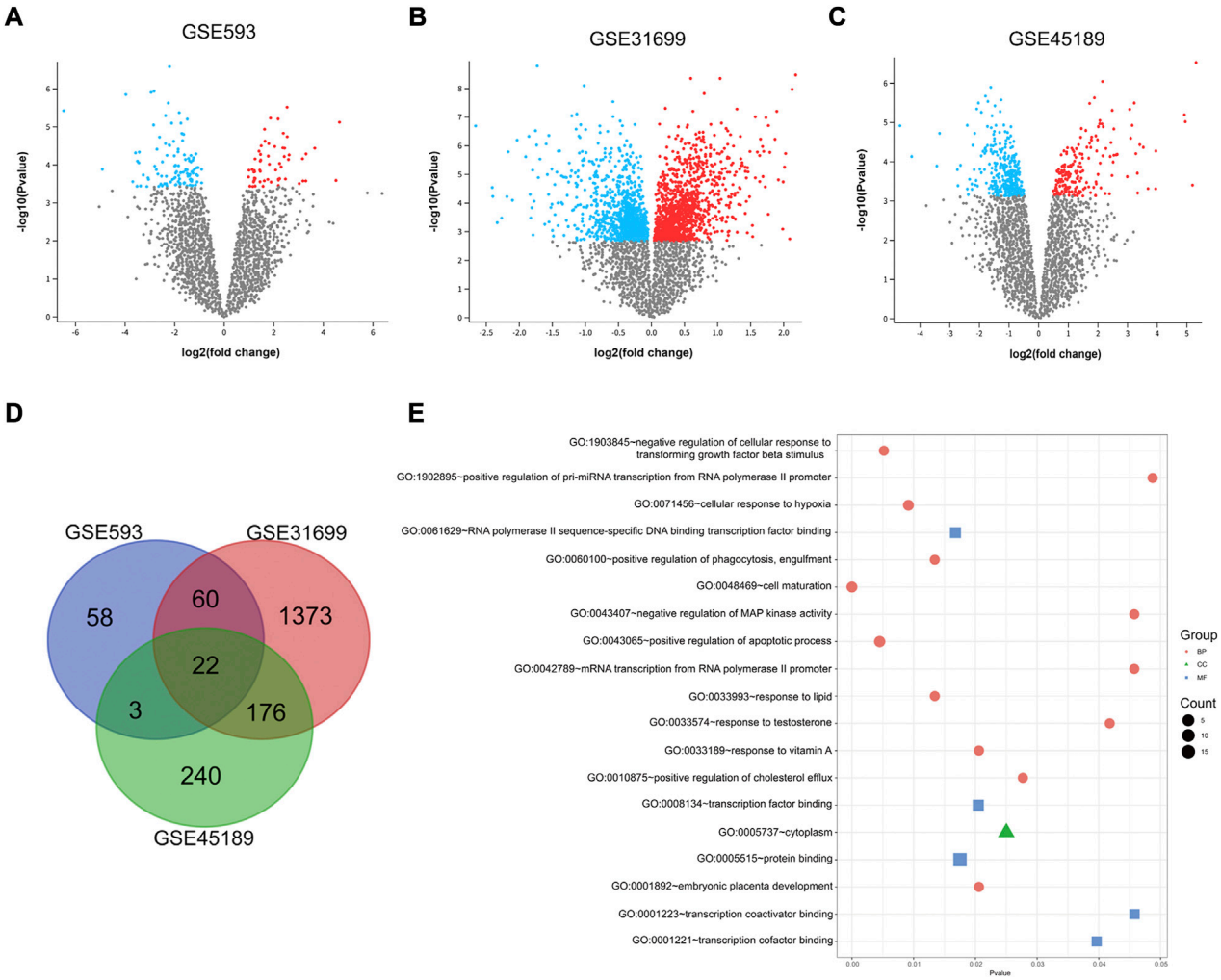

FIGURE 1
DEGs identified by GEO2R. Volcano plot of differentially expressed genes in GSE593 **(A)**, GSE31699 **(B)**, and GSE45189 **(C)** datasets. Up-regulation and down-regulation genes are marked with red and blue respectively. The criteria for a DEG are |log2FC|>1 and adjusted *p*-value < 0.05. **(D)** Venn diagram based on the DEGs from all 3 datasets, 22 genes were extracted. **(E)** Gene Ontology Enrichment analysis of 22 DEGs. *P* < 0.05 was identified as the critical threshold for significant enrichment. MF, molecular function, CC, cell composition, BP, and biological process.

binding region were present in Supplemental Table S2. We curated and analyzed a set of 5 acknowledged m6A regulators of PLP1 (4 readers and 1 writer). The detailed descriptions of m6A regulators were present in Supplemental Table S3.

3.5 Baseline characteristics of the patients

To verify the expression of PLP1 in UFs tissue, we collected tissue samples from UFs patients. A total of 48 UFs patients from Tongji Hospital who underwent abdominal surgery caused by uterine fibroids (UFs) and 14 UFs-free individuals were included in this study. The mean age of all participants enrolled in this study is approximately 45, of which the age of UFs patients is 42 and UFs-free participants is 44. There was no statistical difference in age, number of pregnancies, and whether previous abdominal surgery was performed between these two groups. The basic characteristics of all participants were shown in Table 3. The additional fibroid characteristics of UFs patients were summarized in Table 4. The mean maximum diameter of leiomyoma in this study is 6.4 cm. The mean size of UFs in this study was relatively large because all those fibroids were detected for surgical reasons. Myomectomy was operated on in 79.2% (38/48) of patients while the rest of the patients (20.8%, 10/48) underwent a hysterectomy. Notably, 12.5% (6/48) of patients had a previous myomectomy.

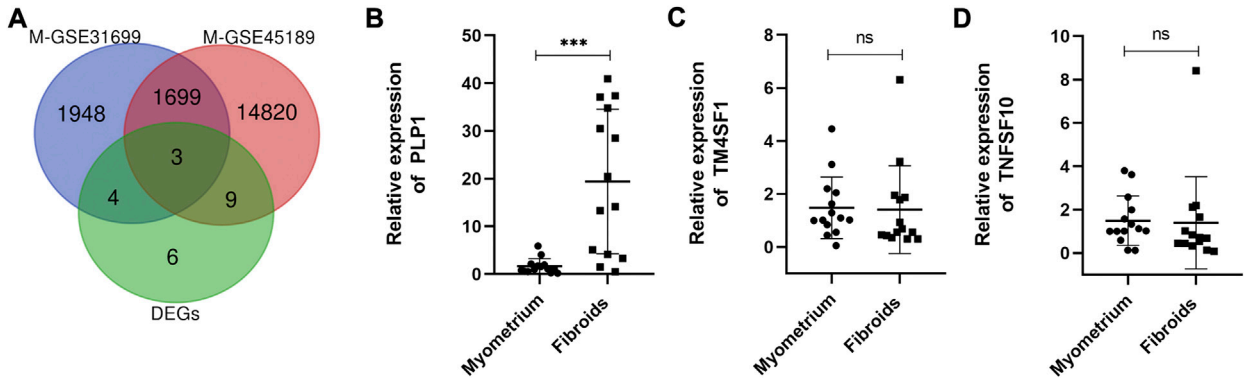

FIGURE 2
Identification of the hub gene. **(A)** The co-expressive differentially expressed genes in differently mRNA expression profiles (from GSE593, GSE31699, and GSE45189 datasets) and genome-wide DNA methylation genes (from GSE31699, GSE45189 datasets) by Venn diagram. M-GSE31699, M-GSE45189 indicated the differential DNA methylation genes. **(B–D)** The relative mRNA expression of TM4SF1, TNFSF10, and PLP1 by RT-qPCR. n = 14/groups. ***$p < 0.001$. ns no statistical significance.

TABLE 2 Gene symbol of 22 differentially expressed genes.

Gene symbol	Gene full name	FDR
KIF5C	kinesin family member 5C	4.652
PLP1	proteolipid protein 1	3.158
RAD51B	RAD51 paralog B	2.189
ZMAT3	zinc finger matrin-type 3	1.867
TYMS	thymidylate synthetase	1.795
NAV2	neuron navigator 2	1.403
CFLAR	CASP8 and FADD like apoptosis regulator	-0.91
PRKCH	protein kinase C eta	-1.07
ITGB4	integrin subunit beta 4	-1.351
MPP5	membrane palmitoylated protein 5	-1.379
GPC4	glypican 4	-1.408
TNFSF10	tumor necrosis factor superfamily member 10	-1.505
ADIRF	adipogenesis regulatory factor	-1.608
EPAS1	endothelial PAS domain protein 1	-1.634
GATA2	GATA binding protein 2	-1.709
CALCRL	calcitonin receptor like receptor	-1.947
ABLIM1	actin binding LIM protein 1	-2.04
ABCA8	ATP binding cassette subfamily A member 8	-2.644
PPARG	peroxisome proliferator activated receptor gamma	-2.74
SPTBN1	spectrin beta, non-erythrocytic 1	-3.376
TM4SF1	transmembrane 4 L six family member 1	-3.498
DUSP1	dual specificity phosphatase 1	-4.915

3.6 Elevated PLP1 expression in UFs tissue

The qRT-PCR and Western blot results showed PLP1 was overexpressed in UFs compared with that in normal myometrium (Figure 2B, Figures 3A,B). In addition, IHC staining of PLP1 was performed in UFs and paired normal myometrium (Figure 3C). The corresponding H&E-stained sections were also shown in Figure 3C to illustrate the histological characteristics of UFs. PLP1 was upregulated in UFs compared with that in normal myometrium tissue. The relative IHC score based on all cases demonstrated the expression of PLP1 significantly increased in UFs (Figure 3D).

3.7 ROC curve analysis

The diagnostic value of PLP1 of uterine fibroids was determined by the ROC curve which was constructed by the IHC score (Figure 4). The area under the ROC curve (AUC) was 0.956 with $p < 0.005$. The results showed the cutoff value was 2.069 with a sensitivity of 79.2% and a specificity of 100%, suggesting PLP1 presented high diagnostic accuracy of UFs.

4 Discussion

Uterine fibroids, formed by the proliferation of smooth muscle cells, are one of the most common benign tumors in women of reproductive age (Styer and Rueda, 2016). Numerous studies have demonstrated the potential biomarker for the diagnosis and surveillance of UFs, but the efficacies were still unclear (Levy et al., 2013). In this study, comprehensive bioinformatics methods were used to verify the biomarker as well as to investigate the possible molecular mechanism underlying the development of UFs.

We analyzed the DEGs of 3 datasets, including GSE593, GSE45189, and GSE31699 datasets, under the same criteria using GEO2R. 22 DEGs were found between UFs and normal

TABLE 3 Baseline characteristics of all participants.

Characteristic		UFs (n = 48)	UFs-free (n = 14)	*p*-value
Age (mean ± SD; range)		42.10 ± 7.23; 27–53	44.07 ± 11.22; 29–61	0.435
No. of pregnancies (mean ± SD; range)		2.17 ± 1.49; 0–5	2.85 ± 1.28; 0–5	0.127
Previous abdominal surgery				
	yes	23	9	0.281
	no	25	5	

Note: SD, standard deviation; UFs, uterine fibroids.

TABLE 4 Fibroid characteristics in participants with fibroids (n = 48).

Parameters		No. cases	%
Location			
	Anterior	16	33.3
	Posterior	12	25.0
	Lateral	6	12.5
	Fundal	10	20.8
	others (broad ligament, cervix *etc.*)	4	8.3
Maximum diameter			
	mean		
	<5	6	12.5
	5–8	37	77.1
	>8	5	10.4
Surgery type			
	myomectomy	38	79.2
	hysterectomy	10	20.8
Previous myomectomy			
	Yes	6	12.5
	No	42	87.5

myometrium tissue samples. The DEGs were mainly enriched in cell maturation and regulator of apoptotic. It is well known that apoptosis is one of the key regulators of fibroid growth, and the dysregulation of apoptotic pathways may contribute to the development of UFs (Okolo, 2008). Another main enrichment in the biological process was the cellular response to hypoxia. Leiomyoma grows in the hypoxia microenvironment, and such environment may lead to the formation of UFs (Zhou et al., 2011; Tal and Segars, 2014). The hypoxia-inducible factor-1protein was also overexpressed in UFs tissue compared with myometrium (Miyashita-Ishiwata et al., 2022a; b). Response to testosterone was also enriched in our analysis. Fujimoto *et al.* reported that testosterone increased after treatment with estradiol dipropionate in leiomyoma, while it not occurred in the myometrium, which indicated that testosterone might participate in the biological process of UFs (Fujimoto et al., 1994). Nonetheless, Ke LQ *et al.* failed to find reliable evidence to prove the effectiveness of danazol, a synthetic isoxazole derivative chemically related to 17-ethinyl testosterone, in UFs in clinical trials (Ke et al., 2009). Although there is still an uncertain conclusion on the response of testosterone in UFs, the aberrant activities of this process might impact the development of UFs, which is consistent with our enrichment analysis. Most of the DEGs were enriched in protein binding for molecular function (19/22) based on our results.

As one of the well-studied epigenomic processes in mammals (Bestor, 2000), DNA methylation was considered as a potential mechanism in the pathology of UFs. Many aberrantly hypermethylation/hypomethylation genes were detected in by genome-wide DNA methylation assays (Li et al., 2003; Yamagata et al., 2009; Navarro et al., 2012; Islam et al., 2013; Maekawa et al., 2013; Carbajo-García et al., 2022), and numerous genes were validated to participate in the developmental progress of the UFs *in vitro* experiments. SATB homeobox 2 and neuregulin 1 were proved to be the upregulated hypermethylated genes involved in the pathogenesis of uterine leiomyoma by activating the WNT/β-

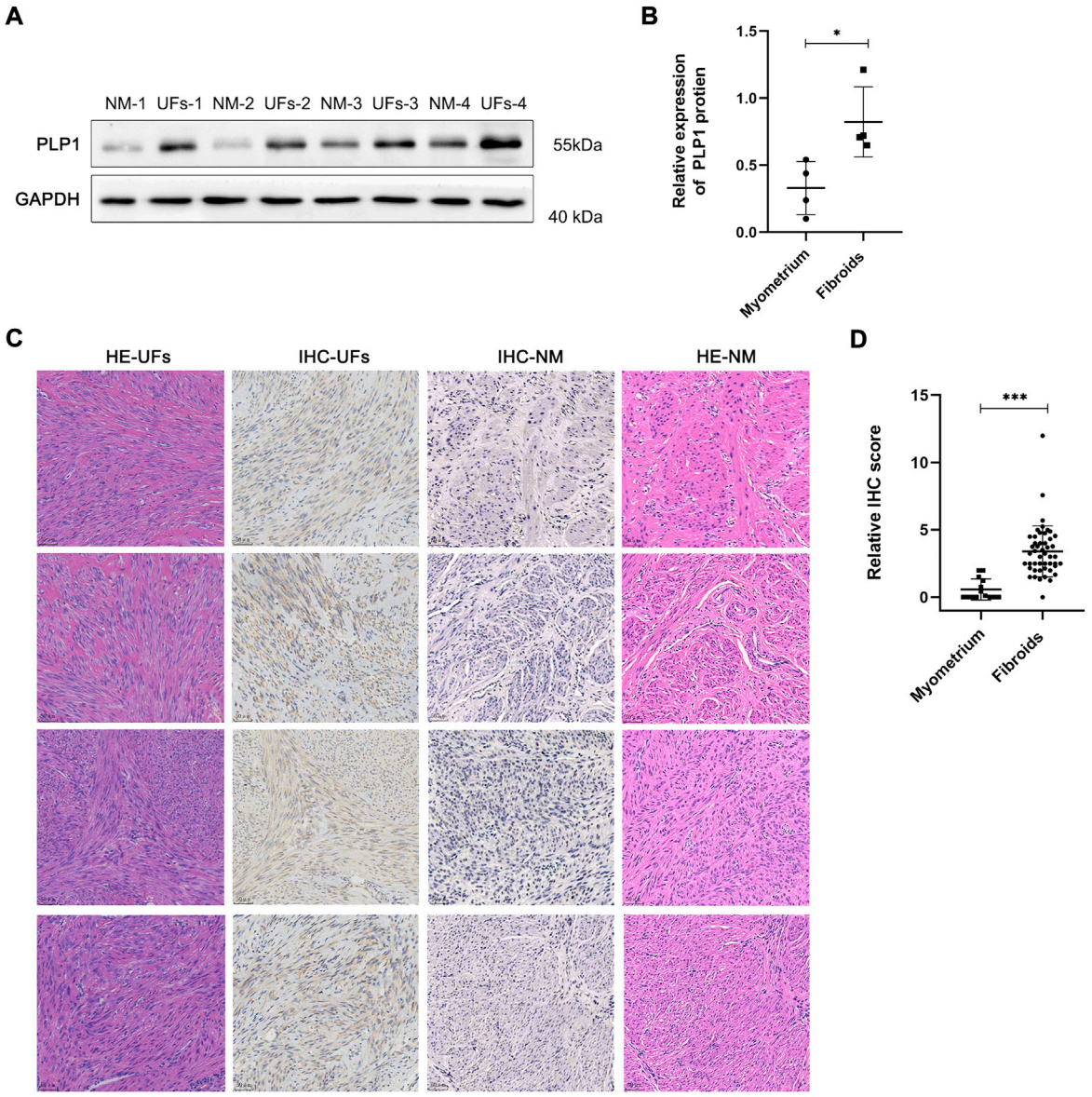

FIGURE 3
PLP1 expression in UFs tissue **(A)** The PLP1 protein expression of tissue from fibroids and normal myometrium was assessed by Western blot. **(B)** The relative expression of PLP1 is based on the gray value of Western blot. N = 4/groups. *$p < 0.05$. **(C)** Immunohistochemical and corresponding hematoxylin and eosin stains results of fibroids and normal myometrium tissue (magnification 200). IHC, immunohistochemical, HE, hematoxylin and eosin stains, UFs, Uterine Fibroids, NM, Normal Myometrium. **(D)** Relative IHC score. UFs, n = 48. NM, n = 14. ***$p < 0.001$.

catenin and TGF-β pathways (Sato et al., 2019). Shimeng Liu *et al.* sorted cells from UFs tissue into stem cell-like cells and revealed that most of the stem cells in UFs were hypermethylated. Meanwhile, tumor growth was suppressed when administered the hypomethylating drug, 5′-Aza (Liu et al., 2020; Liu S. et al., 2021). The methylation condition of mediator complex subunit 12 (MED12), one of the most widely reported somatic mutation genes in UFs (Mäkinen et al., 2011), also could separate the UFs from myometrium on account of the aberrantly clustering molecular pathways based on the MED12 methylation-induced DEGs (Maekawa et al., 2022). All these facts combined with the genome-wide DNA methylation profile of UFs suggested that methylation was the vital epigenetic mechanism in UFs and the significant DEGs between UFs

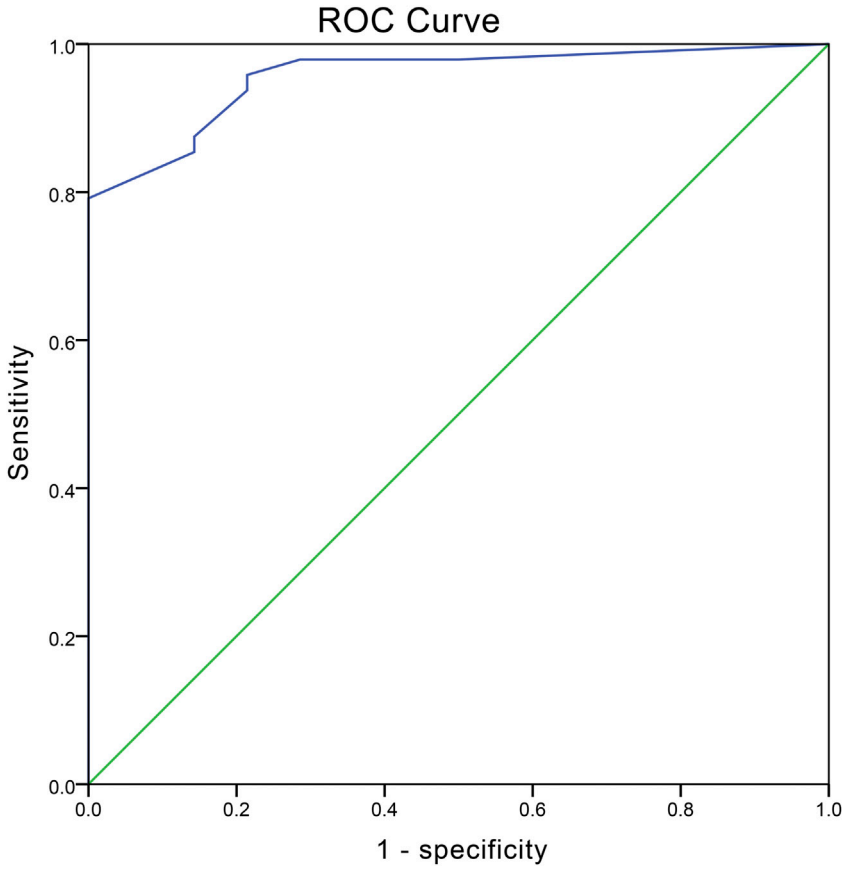

FIGURE 4
ROC curve depicting the diagnostic value of PLP1. The values of AUC, optimum cutoff, sensitivity, and specificity are 0.956 ($p < 0.001$), 2.069, 79.2% and 100%, respectively.

and myometrium might be induced by the local changes of DNA methylation at genome loci. To identify the key genes in this progress, we next combined the DEGs extracted above with the different DNA methylation conditions genes in both GSE45189 and GSE31699 datasets. Consequently, TM4SF1, TNFSF10, and PLP1 were identified, in which only PLP1 was significantly upregulated as verified by RT-qPCR.

PLP1 is the most abundant protein of myelination (Eng et al., 1968; Norton and Poduslo, 1973; Wight, 2017), and the mutation of PLP1 can lead to the X-chromosome-linked leukodystrophy Pelizaeus–Merzbacher disease (Elitt et al., 2020). PLP1 has been widely reported in the formation of the central nervous system while the aberrant expression of PLP1 in various malignant tumors was identified by the bioinformatic analysis (Li et al., 2017). Remarkably, the high level of PLP1 in primary colorectal cancer patients presents poorer overall survival times than those with low expression levels (Han et al., 2020). Although the underlying mechanism is unclear, PLP1 was still considered a potential biomarker in other diseases other than only in nervous system lesions (Khalaf et al., 2022). PLP1 was considered as the hypomethylation and transcriptionally upregulated genes in leiomyoma based on the genome-wide DNA methylation and mRNA expression analysis (Navarro et al., 2012). The results of this present study showed that the PLP1 was over-expressed in UFs tissue based on the comprehensive analysis of irregular methylation genes and DEGs in fibroids. Then the validation was conducted at both mRNA and protein levels based on the tissue samples from leiomyoma patients. To the best of our knowledge, it is the first time to validate the dysregulation of PLP1 in benign tumors. Our result suggested that the hypomethylation of PLP1 might be involved in the pathophysiology of UFs, but further experiments still need to implement. Moreover, overexpressed PLP1 exhibited major oxidative phosphorylation deficits (Wight, 2017) and the down-regulation of oxidative phosphorylation aggravates therapeutically adverse tumor hypoxia (Ashton et al., 2018). According to our result that the 22 DEGs including PLP1 were

enriched in hypoxia, we constructed the posits that PLP1 might participate in the hypoxia program to onset the fibroids. However, the underlying mechanisms were speculated through different tissue types, which should be further investigated in UFs.

To evaluate the diagnostic meaning of PLP1 expression in UFs, we drew the ROC curve based on the calculation of the IHC score, indicating that PLP1 expression can be a convincing biomarker for UFs with the AUC, sensitivity, and specificity of 0.956, 79.2%, and 100%, respectively. However, the limitation of this ROC analysis is based on IHC score only, lacking clinical utility. The specificity analysis was limited by the fact that PLP1 expression tissue samples were derived only from UFs and normal myometrium, although it was credible.

5 Conclusion

In summary, we obtained 22 DEGs in UFs *via* bioinformatical analysis and identified PLP1 as the core gene by the combined analysis of genome-wide DNA methylation profiles and 22 DEGs. The over-expression of PLP1 in UFs tissue was validated in both mRNA and protein levels for the first time. Our findings indicated that PLP1 is a potential diagnostic biomarker of the UFs.

Data availability statement

The original contributions presented in the study are included in the article/Supplementary Material, further inquiries can be directed to the corresponding authors.

Ethics statement

The studies involving human participants were reviewed and approved by the Ethics Committee of Tongji Medical College, Huazhong University of Science and Technology (No. 2022S068). The patients/participants provided their written informed consent to participate in this study.

Author contributions

LC collected data, organized the structure, prepared the figures, and drafted the manuscript. ZL and JL prepared the figures. ZL and SL checked the manuscript. RW and FR collected data. HZ, ZL, and SL participated in the discussion. All authors approved the final version to be published.

Funding

This work was supported by the Foundation of Tongji Hospital (No. 2020JZKT469) and Excellent Youth Funding of Henan Provincial Foundation Committee (No. 222300420091).

Acknowledgments

We appreciate Shitong Lin for his suggestions on the article.

Conflict of interest

The authors declare that the research was conducted in the absence of any commercial or financial relationships that could be construed as a potential conflict of interest.

Publisher's note

Supplementary materials

The Supplementary Material for this article can be found online at: https://www.frontiersin.org/articles/10.3389/fgene.2022.1045395/full#supplementary-material

References

Anderson, G. L., Mcintosh, M., Wu, L., Barnett, M., Goodman, G., Thorpe, J. D., et al. (2010). Assessing lead time of selected ovarian cancer biomarkers: A nested case-control study. *J. Natl. Cancer Inst.* 102, 26–38. doi:10.1093/jnci/djp438

Asada, H., Yamagata, Y., Taketani, T., Matsuoka, A., Tamura, H., Hattori, N., et al. (2008). Potential link between estrogen receptor-alpha gene hypomethylation and uterine fibroid formation. *Mol. Hum. Reprod.* 14, 539–545. doi:10.1093/molehr/gan045

Ashton, T. M., Mckenna, W. G., Kunz-Schughart, L. A., and Higgins, G. S. (2018). Oxidative phosphorylation as an emerging target in cancer therapy. *Clin. Cancer Res.* 24, 2482–2490. doi:10.1158/1078-0432.CCR-17-3070

Bestor, T. H. (2000). The DNA methyltransferases of mammals. *Hum. Mol. Genet.* 9, 2395–2402. doi:10.1093/hmg/9.16.2395

Braný, D., Dvorská, D., Grendár, M., Ňachajová, M., Szépe, P., Lasabová, Z., et al. (2019). Different methylation levels in the KLF4, ATF3 and DLEC1 genes in the myometrium and in corpus uteri mesenchymal tumours as assessed by MS-HRM. *Pathol. Res. Pract.* 215, 152465. doi:10.1016/j.prp.2019.152465

Carbajo-García, M. C., Corachán, A., Juárez-Barber, E., Monleón, J., Payá, V., Trelis, A., et al. (2022). Integrative analysis of the DNA methylome and transcriptome in uterine leiomyoma shows altered regulation of genes involved

in metabolism, proliferation, extracellular matrix, and vesicles. *J. Pathol.* 257, 663–673. doi:10.1002/path.5920

Cardozo, E. R., Clark, A. D., Banks, N. K., Henne, M. B., Stegmann, B. J., and Segars, J. H. (2012). The estimated annual cost of uterine leiomyomata in the United States. *Am. J. Obstet. Gynecol.* 206, 211.e211–e9. doi:10.1016/j.ajog.2011.12.002

Ciarmela, P., Delli Carpini, G., Greco, S., Zannotti, A., Montik, N., Giannella, L., et al. (2022). Uterine fibroid vascularization: From morphological evidence to clinical implications. *Reprod. Biomed. Online* 44, 281–294. doi:10.1016/j.rbmo.2021.09.005

Croce, S., and Chibon, F. (2015). MED12 and uterine smooth muscle oncogenesis: State of the art and perspectives. *Eur. J. Cancer* 51, 1603–1610. doi:10.1016/j.ejca.2015.04.023

Croce, S., and Chibon, F. (2021). Molecular prognostication of uterine smooth muscle neoplasms: From CGH array to CINSARC signature and beyond. *Genes Chromosom. Cancer* 60, 129–137. doi:10.1002/gcc.22906

Dolmans, M. M., Cacciottola, L., Donnez, J., and Poirot, C. (2021). Fertility preservation: How to preserve ovarian function in children, adolescents and adults. *J. Clin. Med.* 10, 5247. doi:10.3390/jcm10225247

Dor, Y., and Cedar, H. (2018). Principles of DNA methylation and their implications for biology and medicine. *Lancet* 392, 777–786. doi:10.1016/S0140-6736(18)31268-6

Elitt, M. S., Barbar, L., Shick, H. E., Powers, B. E., Maeno-Hikichi, Y., Madhavan, M., et al. (2020). Suppression of proteolipid protein rescues Pelizaeus-Merzbacher disease. *Nature* 585, 397–403. doi:10.1038/s41586-020-2494-3

Eng, L. F., Chao, F. C., Gerstl, B., Pratt, D., and Tavaststjerna, M. G. (1968). The maturation of human white matter myelin. Fractionation of the myelin membrane proteins. *Biochemistry* 7, 4455–4465. doi:10.1021/bi00852a042

Fujimoto, J., Nishigaki, M., Hori, M., Ichigo, S., Itoh, T., and Tamaya, T. (1994). The effect of estrogen and androgen on androgen receptors and mRNA levels in uterine leiomyoma, myometrium and endometrium of human subjects. *J. Steroid Biochem. Mol. Biol.* 50, 137–143. doi:10.1016/0960-0760(94)90020-5

Han, J., Zhang, X., Liu, Y., Jing, L., Liu, Y. B., and Feng, L. (2020). CLCA4 and MS4A12 as the significant gene biomarkers of primary colorectal cancer. *Biosci. Rep.* 40, BSR20200963. doi:10.1042/BSR20200963

Han, X., Yang, Y., Qi, J., Zhang, M., Xue, Y., Chu, X., et al. (2022). Protective effects and possible mechanism of 6-gingerol against arsenic trioxide-induced nephrotoxicity based on network pharmacological analysis and experimental validation. *Int. Immunopharmacol.* 110, 108926. doi:10.1016/j.intimp.2022.108926

Islam, M. S., Protic, O., Stortoni, P., Grechi, G., Lamanna, P., Petraglia, F., et al. (2013). Complex networks of multiple factors in the pathogenesis of uterine leiomyoma. *Fertil. Steril.* 100, 178–193. doi:10.1016/j.fertnstert.2013.03.007

Jones, P. A. (2012). Functions of DNA methylation: Islands, start sites, gene bodies and beyond. *Nat. Rev. Genet.* 13, 484–492. doi:10.1038/nrg3230

Karpathiou, G., Chauleur, C., Papoudou-Bai, A., Dagher, S., and Peoc'h, M. (2021). CD56 is expressed in uterine smooth muscle tumors. *Int. J. Gynecol. Pathol.* 40, 315–323. doi:10.1097/PGP.0000000000000696

Ke, L. Q., Yang, K., Li, J., and Li, C. M. (2009). Danazol for uterine fibroids. *Cochrane Database Syst. Rev.* 2009, CD007692. doi:10.1002/14651858.CD007692.pub2

Khalaf, G., Mattern, C., Begou, M., Boespflug-Tanguy, O., Massaad, C., and Massaad-Massade, L. (2022). Mutation of proteolipid protein 1 gene: From severe hypomyelinating leukodystrophy to inherited spastic paraplegia. *Biomedicines* 10, 1709. doi:10.3390/biomedicines10071709

Levy, G., Hill, M. J., Plowden, T. C., Catherino, W. H., and Armstrong, A. Y. (2013). Biomarkers in uterine leiomyoma. *Fertil. Steril.* 99, 1146–1152. doi:10.1016/j.fertnstert.2012.10.048

Leyland, N., Leonardi, M., Murji, A., Singh, S. S., Al-Hendy, A., and Bradley, L. (2022). A call-to-action for clinicians to implement evidence-based best practices when caring for women with uterine fibroids. *Reprod. Sci.* 29, 1188–1196. doi:10.1007/s43032-022-00877-3

Li, M., Sun, Q., and Wang, X. (2017). Transcriptional landscape of human cancers. *Oncotarget* 8, 34534–34551. doi:10.18632/oncotarget.15837

Li, S., Chiang, T. C., Richard-Davis, G., Barrett, J. C., and Mclachlan, J. A. (2003). DNA hypomethylation and imbalanced expression of DNA methyltransferases (DNMT1, 3A, and 3B) in human uterine leiomyoma. *Gynecol. Oncol.* 90, 123–130. doi:10.1016/s0090-8258(03)00194-x

Liu, C., Wang, M., Zhang, H., and Sui, C. (2021). Altered microRNA profiles of extracellular vesicles secreted by endometrial cells from women with recurrent implantation failure. *Reprod. Sci.* 28, 1945–1955. doi:10.1007/s43032-020-00440-y

Liu, S., Yin, P., Kujawa, S. A., Coon, J. S. T., Okeigwe, I., and Bulun, S. E. (2019). Progesterone receptor integrates the effects of mutated MED12 and altered DNA methylation to stimulate RANKL expression and stem cell proliferation in uterine leiomyoma. *Oncogene* 38, 2722–2735. doi:10.1038/s41388-018-0612-6

Liu, S., Yin, P., Xu, J., Dotts, A. J., Kujawa, S. A., Coon, V. J., et al. (2021). Progesterone receptor-DNA methylation crosstalk regulates depletion of uterine leiomyoma stem cells: A potential therapeutic target. *Stem Cell Rep.* 16, 2099–2106. doi:10.1016/j.stemcr.2021.07.013

Liu, S., Yin, P., Xu, J., Dotts, A. J., Kujawa, S. A., Coon, V. J., et al. (2020). Targeting DNA methylation depletes uterine leiomyoma stem cell-enriched population by stimulating their differentiation. *Endocrinology* 161, bqaa143. doi:10.1210/endocr/bqaa143

Livak, K. J., and Schmittgen, T. D. (2001). Analysis of relative gene expression data using real-time quantitative PCR and the 2(-Delta Delta C(T)) Method. *Methods* 25, 402–408. doi:10.1006/meth.2001.1262

Ma, J., Song, B., Wei, Z., Huang, D., Zhang, Y., Su, J., et al. (2022). m5C-Atlas: a comprehensive database for decoding and annotating the 5-methylcytosine (m5C) epitranscriptome. *Nucleic Acids Res.* 50, D196–D203. doi:10.1093/nar/gkab1075

Machado-Lopez, A., Simon, C., and Mas, A. (2021). Molecular and cellular insights into the development of uterine fibroids. *Int. J. Mol. Sci.* 22, 8483. doi:10.3390/ijms22168483

Maekawa, R., Sato, S., Tamehisa, T., Sakai, T., Kajimura, T., Sueoka, K., et al. (2022). Different DNA methylome, transcriptome and histological features in uterine fibroids with and without MED12 mutations. *Sci. Rep.* 12, 8912. doi:10.1038/s41598-022-12899-7

Maekawa, R., Sato, S., Yamagata, Y., Asada, H., Tamura, I., Lee, L., et al. (2013). Genome-wide DNA methylation analysis reveals a potential mechanism for the pathogenesis and development of uterine leiomyomas. *PLoS One* 8, e66632. doi:10.1371/journal.pone.0066632

Mäkinen, N., Mehine, M., Tolvanen, J., Kaasinen, E., Li, Y., Lehtonen, H. J., et al. (2011). MED12, the mediator complex subunit 12 gene, is mutated at high frequency in uterine leiomyomas. *Science* 334, 252–255. doi:10.1126/science.1208930

Miyashita-Ishiwata, M., El Sabeh, M., Reschke, L. D., Afrin, S., and Borahay, M. A. (2022a). Differential response to hypoxia in leiomyoma and myometrial cells. *Life Sci.* 290, 120238. doi:10.1016/j.lfs.2021.120238

Miyashita-Ishiwata, M., El Sabeh, M., Reschke, L. D., Afrin, S., and Borahay, M. A. (2022b). Hypoxia induces proliferation via NOX4-Mediated oxidative stress and TGF-β3 signaling in uterine leiomyoma cells. *Free Radic. Res.* 56, 163–172. doi:10.1080/10715762.2022.2061967

Mlodawska, O. W., Saini, P., Parker, J. B., Wei, J. J., Bulun, S. E., Simon, M. A., et al. (2022). Epigenomic and enhancer dysregulation in uterine leiomyomas. *Hum. Reprod. Update* 28, 518–547. doi:10.1093/humupd/dmac008

Navarro, A., Yin, P., Monsivais, D., Lin, S. M., Du, P., Wei, J. J., et al. (2012). Genome-wide DNA methylation indicates silencing of tumor suppressor genes in uterine leiomyoma. *PLoS One* 7, e33284. doi:10.1371/journal.pone.0033284

Norton, W. T., and Poduslo, S. E. (1973). Myelination in rat brain: Changes in myelin composition during brain maturation. *J. Neurochem.* 21, 759–773. doi:10.1111/j.1471-4159.1973.tb07520.x

Okolo, S. (2008). Incidence, aetiology and epidemiology of uterine fibroids. *Best. Pract. Res. Clin. Obstet. Gynaecol.* 22, 571–588. doi:10.1016/j.bpobgyn.2008.04.002

Reik, W., Dean, W., and Walter, J. (2001). Epigenetic reprogramming in mammalian development. *Science* 293, 1089–1093. doi:10.1126/science.1063443

Russo, C., Camilli, S., Martire, F. G., Di Giovanni, A., Lazzeri, L., Malzoni, M., et al. (2022). Ultrasound features of highly vascularized uterine myomas (uterine smooth muscle tumors) and correlation with histopathology. *Ultrasound Obstet. Gynecol.* 60, 269–276. doi:10.1002/uog.24855

Sato, S., Maekawa, R., Tamura, I., Shirafuta, Y., Shinagawa, M., Asada, H., et al. (2019). SATB2 and NGR1: Potential upstream regulatory factors in uterine leiomyomas. *J. Assist. Reprod. Genet.* 36, 2385–2397. doi:10.1007/s10815-019-01582-y

Sato, S., Maekawa, R., Yamagata, Y., Asada, H., Tamura, I., Lee, L., et al. (2014). Potential mechanisms of aberrant DNA hypomethylation on the x chromosome in uterine leiomyomas. *J. Reprod. Dev.* 60, 47–54. doi:10.1262/jrd.2013-095

Sato, S., Maekawa, R., Yamagata, Y., Tamura, I., Lee, L., Okada, M., et al. (2016). Identification of uterine leiomyoma-specific marker genes based on DNA methylation and their clinical application. *Sci. Rep.* 6, 30652. doi:10.1038/srep30652

Schübeler, D. (2015). Function and information content of DNA methylation. *Nature* 517, 321–326. doi:10.1038/nature14192

Song, B., Wang, X., Liang, Z., Ma, J., Huang, D., Wang, Y., et al. (2022). RMDisease V2.0: An updated database of genetic variants that affect RNA modifications with disease and trait implication. *Nucleic Acids Res.* 50, 10290–10310. doi:10.1093/nar/gkac830

Stewart, C. L. W. E. A., and Stewart, E. A. (2005). Uterine fibroids: The elephant in the room. *science* 308, 1589–1592. doi:10.1126/science.1112063

Styer, A. K., and Rueda, B. R. (2016). The epidemiology and Genetics of uterine leiomyoma. *Best. Pract. Res. Clin. Obstet. Gynaecol.* 34, 3–12. doi:10.1016/j.bpobgyn.2015.11.018

Tal, R., and Segars, J. H. (2014). The role of angiogenic factors in fibroid pathogenesis: Potential implications for future therapy. *Hum. Reprod. Update* 20, 194–216. doi:10.1093/humupd/dmt042

Tang, Y., Chen, K., Song, B., Ma, J., Wu, X., Xu, Q., et al. (2021). m6A-Atlas: a comprehensive knowledgebase for unraveling the N6-methyladenosine (m6A) epitranscriptome. *Nucleic Acids Res.* 49, D134–D143. doi:10.1093/nar/gkaa692

Trovik, J., Salvesen, H. B., Cuppens, T., Amant, F., and Staff, A. C. (2014). Growth differentiation factor-15 as biomarker in uterine sarcomas. *Int. J. Gynecol. Cancer* 24, 252–259. doi:10.1097/IGC.0000000000000037

Wight, P. A. (2017). Effects of intron 1 sequences on human PLP1 expression: Implications for PLP1-related disorders. *ASN Neuro* 9, 1759091417720583. doi:10.1177/1759091417720583

Yamagata, Y., Maekawa, R., Asada, H., Taketani, T., Tamura, I., Tamura, H., et al. (2009). Aberrant DNA methylation status in human uterine leiomyoma. *Mol. Hum. Reprod.* 15, 259–267. doi:10.1093/molehr/gap010

Zhou, S., Yi, T., Shen, K., Zhang, B., Huang, F., and Zhao, X. (2011). Hypoxia: The driving force of uterine myometrial stem cells differentiation into leiomyoma cells. *Med. Hypotheses* 77, 985–986. doi:10.1016/j.mehy.2011.08.026

frontiers | Frontiers in Genetics

TYPE Original Research
PUBLISHED 04 November 2022
DOI 10.3389/fgene.2022.996245

OPEN ACCESS

EDITED BY
Xiao Han,
Fuzhou University, China

REVIEWED BY
Lili Xu,
Beijing Children's Hospital, Capital Medical University, China
Xianlin Han,
Peking Union Medical College Hospital (CAMS), China

*CORRESPONDENCE
Dongliang Li,
dongliangli93@163.com
Minghua Lin,
drlmh543@126.com

†These authors have contributed equally to this work

SPECIALTY SECTION
This article was submitted to RNA, a section of the journal Frontiers in Genetics

RECEIVED 17 July 2022
ACCEPTED 19 October 2022
PUBLISHED 04 November 2022

CITATION
Gao H, Wang X, Ma H, Lin S, Zhang D, Wu W, Liao Z, Chen M, Li Q, Lin M and Li D (2022), METTL16 regulates m^{6}A methylation on chronic hepatitis B associated gene HLA-DPB1 involved in liver fibrosis.
Front. Genet. 13:996245.
doi: 10.3389/fgene.2022.996245

METTL16 regulates m^{6}A methylation on chronic hepatitis B associated gene HLA-DPB1 involved in liver fibrosis

Haibing Gao[1,2†], Xiangmei Wang[1†], Huaxi Ma[1†], Shenglong Lin[1], Dongqing Zhang[1], Wenjun Wu[1], Ziyuan Liao[1], Mengyun Chen[1,2], Qin Li[1], Minghua Lin[1*] and Dongliang Li[2,3*]

[1]Mengchao Hepatobiliary Hospital of Fujian Medical University, Fujian, China, [2]Fuzong Clinical Medical College of Fujian Medical University, Fujian, China, [3]900th Hospital of Joint Logistics Support Forces of the Chinese PLA, Fujian, China

The role of genetic factors in the occurrence and progression of CHB (CHB) is still not fully explored. In recent years, genome-wide association studies on CHB patients have demonstrated that a large number of CHB-associated single nucleotide polymorphisms exist in the gene intron, which may regulate expression at the transcriptional level. Modification of RNA m^{6}A methylation is one of the key mechanisms regulating gene expression. Here we show that *METTL16*, an m^{6}A regulator involved in mRNA intron splicing, is differentially expressed in CHB the tissue of patients who has definite diagnosis of mild and severe fibrosis. At the same time, there are also significant differences in the expression of CHB-associated genes such as *HLA-DPA1* and *HLA-DPB1*. The expression of *HLA-DPB1* is related to *METTL16*. Furthermore, analyses of RNA binding of METTL16 and *HLA-DPB1* show that the silencing of *METTL16* in astrocytes downregulates m^{6}A and expression of HLA-DPB1. In conclusion, *METTL16* participates in the progression of CHB fibrosis by regulating the m^{6}A level and expression of HLA-DPB1.

KEYWORDS

M6A, METTL16, CHB (chronic hepatitis B), HBV-hepatitis B virus, GWAS

Introduction

Chronic hepatitis B (CHB) is a chronic inflammatory disease in patients with hepatitis B virus (HBV) infection. The incidence of CHB ranks first among all kinds of infectious diseases (Lok, 2002). More than 1.3 billion people in global are infected with HBV, about 260 million are with CHB, which causes about 1 million deaths every year (Perz et al., 2006; Schweitzer et al., 2015). CHB has become a very serious health and social problem.

Heredity, the virus, and the environment are important factors in the pathogenesis of CHB, which leads to high heterogeneity in clinic. From the perspective of population susceptibility to CHB and disease progression, genetic variation can lead to differences in clinical manifestations among individuals. Since the publication of the first genome-wide

association study (GWAS) of CHB in 2009, genetic studies on patients with CHB have revealed many single nucleotide polymorphisms (SNPs) associated with susceptibility to CHB (Raza et al., 2007). Several studies have confirmed that these SNPs are mainly concentrated in a series of human leukocyte antigen (HLA) loci, including *HLA-DP*, *HLA-DQ*, *HLA-C*, and *HLA-DOA* (Lau et al., 2011; Yamada et al., 2014; Akcay et al., 2018). Among them, Mbared et al. found that the SNP rs9277535 with the most significant association with CHB in a Japanese population was located in the 3′ untranslated region of *HLA-DPB1*. The SNP was also identified in Korean, Thai, and Han populations with different significance. Moreover, rs3077, a representative CHB-associated SNP in different populations, is located in the 3′ untranslated region of HLA-DPA1. In addition, SNPs located in *EHMT2*, *TCF19*, *UBE2l3*, *CFB*, *FDX1*, and other gene regions are also associated with susceptibility to CHB in different regions. However, CHB progresses to liver cirrhosis and liver cancer. GWAS shows that variation in the SNP of *HLA* gene closely related to the progression of CHB to liver cirrhosis and participates in the occurrence of liver cancer. Previous studies have shown that the cytotoxicity of HLA class I and class II play an critical role in the spontaneous clearance of HBV. However, the clinical heterogeneity of CHB cannot be fully analyzed from only the level of genetic variation. The associated SNPs vary in different populations, and some findings are difficult to replicate, or even show the opposite results. In the results of GWAS, the genes that play an important role in CHB is not statistically significant. Most SNPs located at *HLA* loci are located in the untranslated region. The functional mechanism is not clear, which may be related to mRNA expression of the gene. SNP loci associated with hepatitis are distributed in the intron region of the gene. From the perspective of SNP–amino acid protein function, the mechanism of action of these SNPs cannot be deeply analyzed. Although it is believed that these SNPs can affect the pathogenesis of CHB by altering gene expression, their key mechanism of action has not been revealed.

Recent studies have found that modification of N6 methyl adenosine (m^6A) is an important way of controlling gene expression by eukaryotic mRNA. m^6A modification is mainly distributed in introns and the 3′ untranslated region, especially in region near the stop codon and splice site, which is involved in RNA processing and metabolic function (Liu and Zhang, 2018). m^6A modification takes part in different stages of development of mRNA (Imam et al., 2018), including RNA folding, stability, splicing, nuclear output, translation regulation, and degradation, to regulate RNA biological function, protein translation, and life activity (Zhao et al., 2021; Tong et al., 2022). m^6A modification of precursor mRNA mainly takes place in the untranslated region, and m^6A methylase and reader proteins located in the nucleus. Thus, it can be inferred that m^6A modification mainly occurs in the nucleus and affects mRNA splicing (Meyer et al., 2012; Zhao et al., 2014; Xu et al., 2017). Knockout of *METTL3* results in the downregulation of introns. In addition, m^6A demethylase FTO preferentially binds to the RNA intron region, downregulates m^6A modification on the one hand, but prevents RNA from binding to splicing protein *SRSF2* on the other hand, resulting in abnormal splicing (Dominissini et al., 2012). These studies show that m^6A modification of RNA in untranslated regions could affects gene expression by regulating RNA processing and metabolism. This phenomenon provides clues for analyzing the role of SNPs in the untranslated region in the pathogenesis of CHB. We speculate that SNPs in the untranslated region impact the occurrence and development of CHB by affecting m^6A modification and regulating gene expression.

In addition, many studies have shown that m^6A modification can change expression of important viral genes. Researchers have proven that modification of m^6A methylation is widely involved in replication of the HBV virus, inflammatory response, immune regulation, and fibrosis and plays a role in liver injury, tumors, and organ failure (Kostyusheva et al., 2021). Imam h et al. mapped the m^6A site in HBV RNA (Qu et al., 2021; Cheng et al., 2022; Kim et al., 2022; Kim and Siddiqui, 2022; Zhao et al., 2022). m^6A modification is necessary for efficient reverse transcription of the viral genome and can also regulate the stability of HBV RNA (Kim and Siddiqui, 2021a). Chronic infection with HBV and hepatitis C virus is the main cause of hepatocellular carcinoma (Xiao et al., 2016; Xu et al., 2017). There is increasing evidence that hepatocellular carcinoma oncoproteins induced by both virus are controlled by m^6A modification. Recent works found that m^6A modification involves the regulation of hepatocellular carcinoma through METTL3 and METTL14. First, Chen et al. (2018) observed the expression of *METTL3* increased abnormally in liver cancer and increased cell proliferation *in vitro*, resulting in promoted tumorigenicity *in vivo* (Xu et al., 2017). METTL3 is significantly upregulated in hepatocellular carcinoma and promotes tumor progression. It inhibits SOCS2 expression and promotes cancer cell proliferation and metastasis through the m^6A-YTHDF2 mechanism. Chen et al. (2018) found interference with METTL3 reduce the expression of SOCS2 mRNA. Second, it was reported that METTL14 is downregulated in liver cancer, and thereby regulates the development of liver cancer (Bartosovic et al., 2017; Ma et al., 2017). Together these evidences suggest that m^6A modification has a key role in liver-related diseases through various m^6A-related proteins (Wu et al., 2019; Wu et al., 2020; Kim and Siddiqui, 2021b; Wang and Zhou, 2022). Modification of m^6A methylation is involved in the pathogenesis of liver injury, organ failure, and fibrosis. However, it is unclear whether it is involved in the development of CHB.

Here, we investigated the expression of m^6A regulator in different stages of CHB, examined the relationship between m^6A and CHB-associated genes, and checked the change in m^6A and expression of gene loci with CHB-associated SNPs.

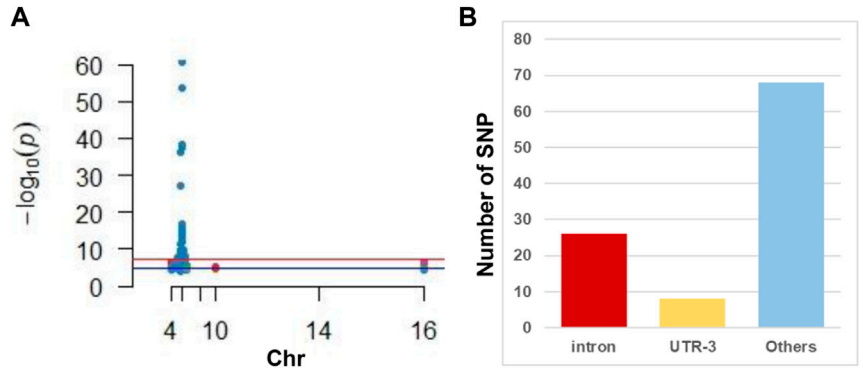

FIGURE 1
Illustration of GWAS studies in CHB. **(A)** Manhattan plot of CHB associated SNP reviewed from published literature. Note that most SNPs located in the chromosome 6. **(B)** Distribution of SNP in gene different regions. Note that intron is hot regions where CHB associated SNP frequently located.

Materials and methods

Patients

The ethical approval was approved by the ethics committee of Mengchao Hepatobiliary Hospital of Fujian Medical University and all study participants obtained informed consent. Clinical data were collected from patients with CHB diagnosed by liver biopsy in our hospital in 2019 or 2020. The diagnostic criteria were in accordance with the guidelines for the prevention and treatment of CHB (2019 Edition), and study subjects provided informed consent before enrollment. Inclusion criteria were 1) being HBsAg positive for more than 6 months and HBsAb negative and 2) being between 18 and 60 years old. Exclusion criteria were 1) the presence of acute hepatitis B, liver failure, or primary liver cancer, in combination with drug liver, alcoholic liver, or fatty liver, in combination with any other viral infection and other serious disease; 2) use of antiviral drugs up to 3 months before enrollment; 3) receipt of immunosuppressant and immunomodulator treatment up to 6 months before enrollment; 4) autoimmune liver disease and systemic autoimmune disease; and 5) pregnancy.

Specimens

A BARD puncture biopsy gun (with a sampling length of 2.2 cm) and 16 g disposable cutting biopsy needle were used for the liver puncture biopsy. One tissue specimen was stained with he, Masson, and reticular fibers, and a single pathologist read the film uniformly according to the pathological diagnostic criteria. The other specimen was kept in the refrigerator at −80°C.

Tandem mass spectrometry (LC/MS)

After total RNA is extracted with Trizol, mRNA can be enriched with Oligo (dT) magnetic beads. RNA was digested from a single strand into a single base with nuclease P1. Alkaline phosphatase and ammonium bicarbonate were added, the sample was allowed to incubate for several hours, and then the sample was injected into a liquid chromatograph. Finally, the overall degree of m^6A methylation on mRNA was calculated according to the ratio of m^6A to total adenine.

Real-time fluorescence quantitative PCR

Tissues or cells were digested and lysed by Trizol reagent. After Trizol was added to cells or tissues, total RNA was extracted with chloroform isopropanol extraction. cDNA was synthesized by reverse transcription with a one-step PrimeScript cDNA synthesis kit. Quantitative PCR was performed with a one-step SYBR PrimeScript RT-PCR kit. GAPDH was used as the internal reference gene, and the quantitative results were $2^{-\Delta\Delta CT}$ indicates. The primer information was in (Supplemental Table S1).

meIP-PCR

The combination of immunoprecipitation (ChIP) and PCR technology can be utilized to efficiently determine the interaction *in vivo*. RNA was isolated and broken into small fragments by ultrasounication. An specific antibody was added, and the antibody formed an immune binding complex with the target protein. De crosslinking, RNA purification and qPCR were further processed.

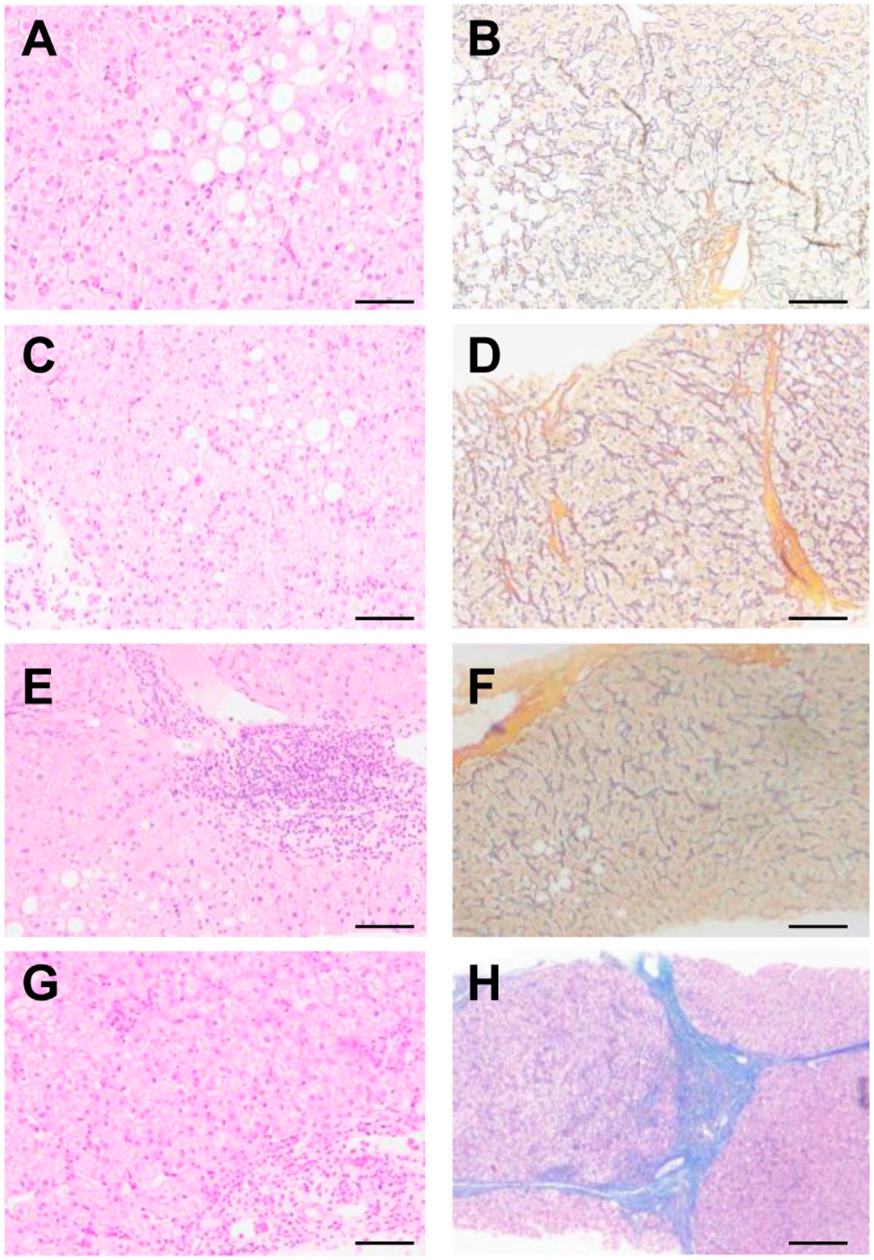

FIGURE 2
Pathological analysis of patients with different levels of liver fibrosis. According to Ishak scoring **(A,B)** s1, **(C,D)** s2, **(E,F)** s4, **(G,H)** s5. **(A,C,E,G)** HE, **(B,D,F,H)** Masson.

Statistical analysis

SPSS 20.0 was used for statistical the analysis. The measurement data conforming to normal distribution adopts mean ± standard deviation (±s). *t* tests were used for pairwise comparisons of normally distributed data. Single-factor analysis of variance was used for multigroup comparisons. Spearman correlation analysis was used to analyze correlations between various factors and the occurrence and degree of liver fibrosis in patients with CHB.

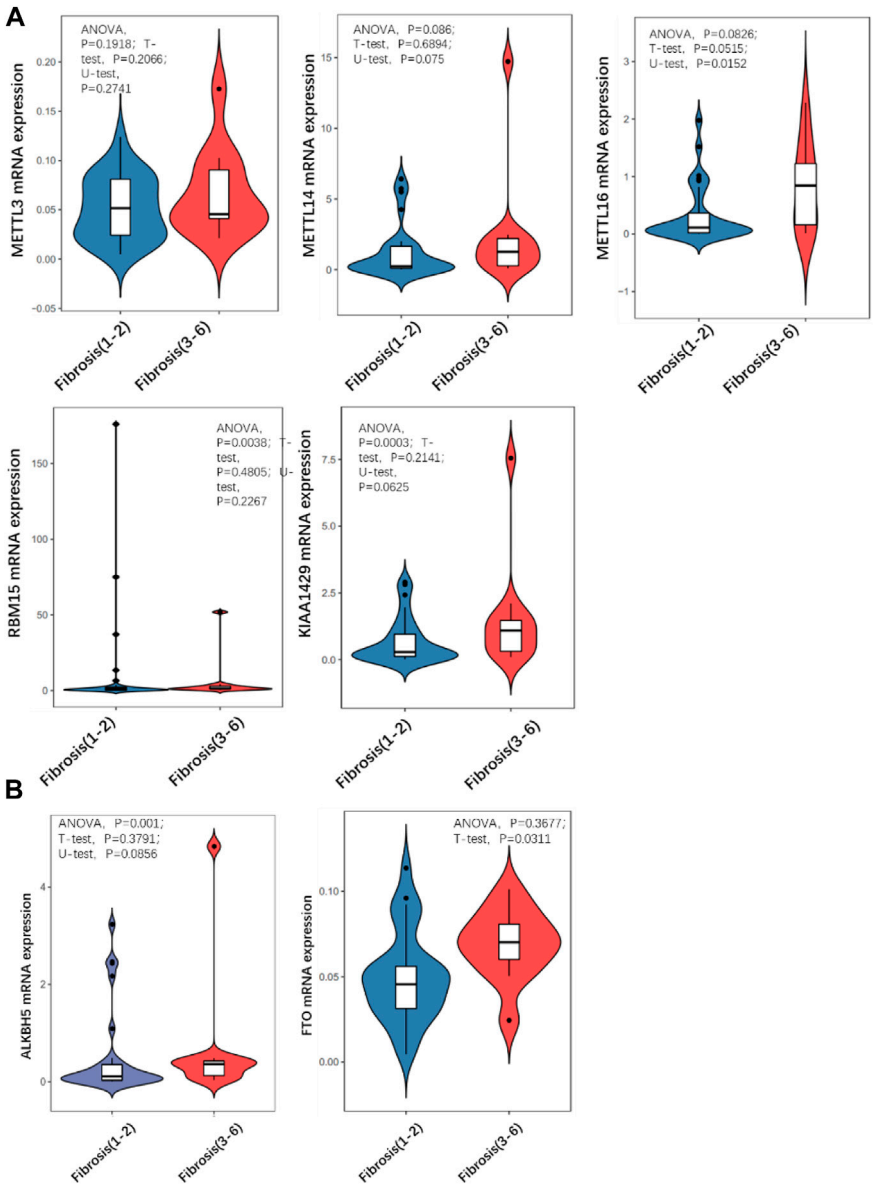

FIGURE 3
Comparison of expression level of m^{6}A regulator in mild and severe fibrosis groups. **(A)** writers, **(B)** erasers. Note that METTL16 is significantly up-regulated in severe fibrosis group.

Results

SNPs associated with susceptibility to CHB are located in different genes

GWAS has identified 102 SNP sites related to susceptibility to or progression of CHB (Figure 1A and Supplemental Table S2). We discovered that only three SNPs were distributed in the exon region of the gene, nearly 26 were distributed in the intron region of the gene, and the rest were distributed in the 3′ and 5′ untranslated regions (Figure 1B).

Patients show different levels of liver fibrosis

A BARD puncture biopsy gun (with a sampling length of 2.2 cm) and 16 g disposable cutting biopsy needle were used for

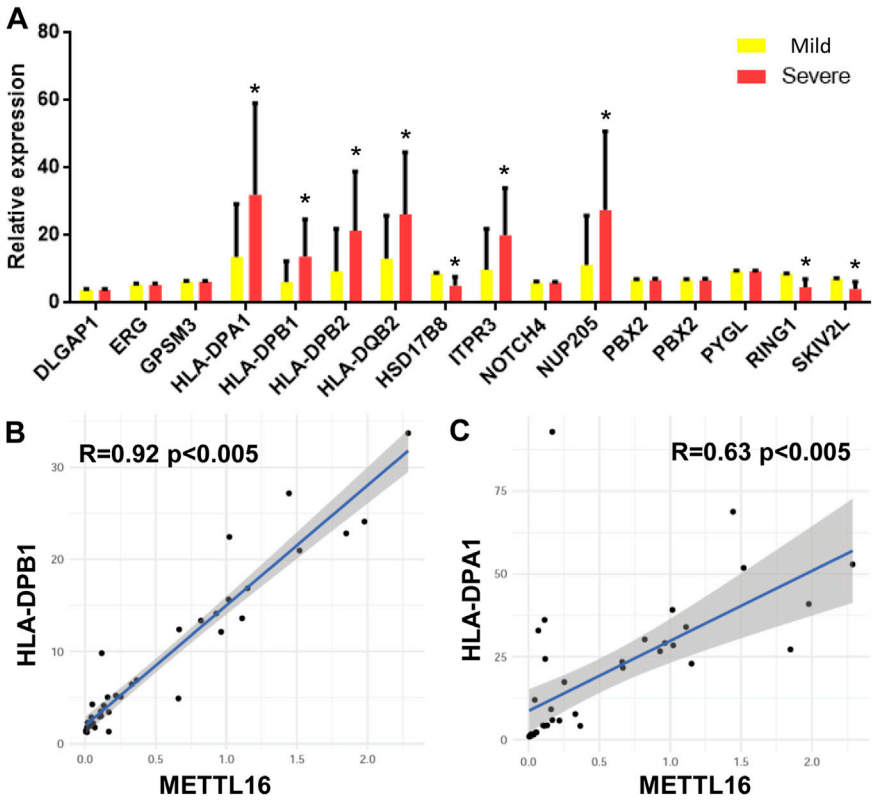

FIGURE 4
CHB GWAS genes differentially expressed between mild and severe fibrosis groups. **(A)** expression level of CHB GWAS genes. Note that HLA-DPB1 is up-regulated in severe fibrosis group. **(B,C)** METTL16 is co-expressed with HLA-DPB1 and HLA-DPA1.

the liver puncture biopsy. Two complete liver tissues with a length of about 1.5–2.0 cm were taken. One tissue sample was sectioned consecutively into five pieces; and stained with conventional HE staining, Masson staining, and reticular fibers. A single pathologist read the film uniformly according to the pathological diagnostic criteria and divided the films into a mild fibrosis group (s1–s2) and a severe fibrosis group (s4–s5) according to Ishak scoring criteria (Figure 2).

METTL16 is differentially expressed in the mild and severe fibrosis groups

Quantitative PCR was carried out to detect the expression level of a series of m^{6}A methyltransferase regulator genes. *METTL16* expression was significantly higher in the severe group than in the mild group (Figure 3A). The expression of other m^{6}A demethyl regulators were also checked, and there was no statistically significant differences. Then we detected the m^{6}A modification level of total RNA in the two groups by LC/MS and found that it was significantly (more than 2 times) higher in the severe group than in the mild group (Figure 3B).

HLA-DPB1 is differentially expressed in fibrosis groups

As mentioned earlier, SNPs related to CHB are located in different genes in the genome according to GWAS. The expression of 15 genes was detected in each sample by quantitative RT-PCR. A total of eight genes were significantly differentially expressed in the two groups of samples. That is, HLA-DPA1, HLA-DPB1, HLA-DPB2, HLA-DQB2, ITPR3, and NUP205 were upregulated in the severe group. In contrast, HSD17B8, RING1, and SKIV2L were downregulated in the severe group (Figure 4A).

The relationships between these differentially expressed genes and the expression of m^{6}A regulators were analyzed by Pearson correlation analysis. mettl16 was significantly positively correlated with HLA-DPB1 and HLA-DPA1 (Figures 4B,C).

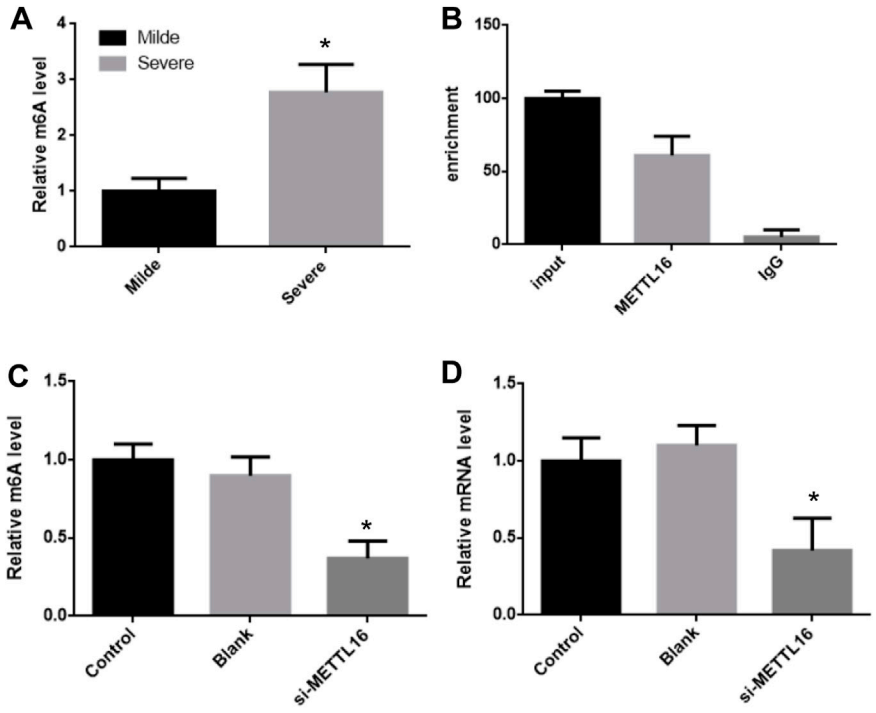

FIGURE 5
METTL16 control HLA-DPB1 expression through regulating m^{6}A level. **(A)** m^{6}A level of HLA-DPB1 mRNA between mild and severe fibrosis groups. **(B)** METTL16 interact with HLA-DPB1 mRNA. **(C,D)** knock-down METTL16 reduced m^{6}A and mRNA of HLA-DPB1 in hepatic stellate cells.

There are different levels of m^{6}A on HLA-DPB1 in the mild and severe fibrosis groups

It was suggesting that the expression of HLA-DPB1 is related to the level of RNA m^{6}A. The m^{6}A level of HLA-DPB1 in each sample was detected by MeIP qPCR. The level of m^{6}A on HLA-DPB1 mRNA was significantly increased in the severe group than in the mild group (Figure 5A).

METTL16 interacts with HLA-DPB1 mRNA

The m^{6}A level of *HLA-DPB1* mRNA was consistent with its expression in each group and was also related to the expression of mettl16. This implies that mettl16 may be one of the causes of the difference in m^{6}A level and expression of *HLA-DPB1*. First RNAip experiments showed that mettl16 could bind to HLA-DPB1 mRNA (Figure 5B).

Then we silenced the expression of METTL16 in hepatic stellate cells and detected the expression of HLA-DPB1 and the degree of m^{6}A modification. In the METTL16 silencing group, the m^{6}A level of HLA-DPB1 mRNA was significantly downregulated by more than 2 times (Figures 5C,D).

Discussion

Molecular genetics research on CHB has revealed a large amount of genetic information that is of great value for obtaining a complete understanding of the pathogenesis of CHB and the development of innovative treatments. Especially in the past 2 decades of population genetics research, a large number of SNPs related to susceptibility to and progression of CHB have been found through GWAS. Most of these studies have been conducted in Asian populations, and their conclusions are well targeted. The high prevalence of CHB in Asia can be further understood from these research results. The SNPs found in these GWASs are mainly concentrated in HLA loci, including HLA-DPA1, -DPB1, -DQB2, and -DPB2. As an important gene group that regulates the body's immune response, the HLA complex participates in the anti-HBV immune response, affects the chronicity of HBV infection and the strength of the immune response, and participates in the progression of CHB to cirrhosis and liver cancer. Therefore, the expression of these genes is likely closely related to CHB. In our study, we found that HLA-DPA1 and HLA-DPB1 differed significantly in groups with different degrees of liver fibrosis. This result suggests that the expression of these two genes may be involved in

mediating the progression of CHB. In addition, we found that other CHB-related loci, such as HSD17b8, ITPR3, NUP205, RING1, and SKIV2l, were upregulated or downregulated in different ways in the groups with different degrees of liver fibrosis. This shows that controlling the expression of CHB-related genes at the transcriptional level is of great significance for regulating the progression of CHB. However, we found a large number of CHB-associated SNPs found in GWAS were located in the noncoding region of the locus, which suggests that these genes may be involved in regulating CHB at the transcriptional level rather than the function of the encoded protein. In conclusion, our data show that genes with CHB-associated SNPs can participate in the mechanism of CHB through transcriptional regulation.

m^6A modification plays an vital role in transcriptional regulation in eukaryotes. The stability, transportation, splicing, and translation efficiency of mRNA are closely related to the degree of m^6A modification. This modification is regulated by the complex. METTL3, METTL14, WTAP, and KIAA1429 form the "writer," whereas alkbh4 and FTO form the "eraser." These usually regulate the modification of mRNA in the coding region and the 3′ or 5′ end. Recent studies have found that RNA has m^6A modifications in the intron region, which affects the splicing of mRNA. Mettl16 is a key methyltransferase whose precursor mrnam^{6}a modification affects intron cleavage. In our study, key regulatory factors of m^6A, especially mettl16, were differentially expressed in tissues with different degrees of liver fibrosis, although other m^6A regulators did not differ significantly. This shows that m^6A participates in the regulation of CHB mainly through mett16. However, the GWASs summarized above found that SNPs associated with CHB are mainly located in the noncoding region of the gene. This is consistent with the function of mettl16. We further found that mettl16 could bind to HLA-DPB1 mRNA and change its m^6A modification level and expression. In clinical samples, the expression of METTL16 was also correlated with HLA-DPB1. All these findings suggest that mettl16 may affect CHB by regulating the expression of these CHB-associated loci, a new mechanism in the process of CHB that needs to be analyzed further.

Data availability statement

The original contributions presented in the study are included in the article/Supplementary Material, further inquiries can be directed to the corresponding authors.

Ethics statement

The studies involving human participants were reviewed and approved by the ethics committee of Mengchao Hepatobiliary Hospital of Fujian Medical University. The patients/participants provided their written informed consent to participate in this study.

Author contributions

HG, ML, and DL designed the project and wrote the manuscript. HG, XW, and HM did almost molecular experiments. SL, DZ, WW, ZL, MC, and QL helped data analysis and revised manuscript.

Funding

Fujian Medical Innovation Project (2020CXB038); Fujian Natural Science Foundation (2021J011289); Fuzhou Science and technology plan project (2021-S-099; 2021-S-114; 2020-WS-130).

Conflict of interest

The authors declare that the research was conducted in the absence of any commercial or financial relationships that could be construed as a potential conflict of interest.

Publisher's note

Supplementary material

The Supplementary Material for this article can be found online at: https://www.frontiersin.org/articles/10.3389/fgene.2022.996245/full#supplementary-material

References

Akcay, I. M., Katrinli, S., Ozdil, K., Doganay, G. D., and Doganay, L. (2018). Host genetic factors affecting Hepatitis B infection outcomes: Insights from genome-wide association studies. *World J. Gastroenterol.* 24 (30), 3347–3360. doi:10.3748/wjg.v24.i30.3347

Bartosovic, M., Molares, H. C., Gregorova, P., Hrossova, D., Kudla, G., and Vanacova, S. (2017). N6-methyladenosine demethylase FTO targets pre-mRNAs and regulates alternative splicing and 3'-end processing. *Nucleic Acids Res.* 45 (19), 11356–11370. doi:10.1093/nar/gkx778

Chen, M., Wei, L., Law, C. T., Tsang, F. H., Shen, J., Cheng, C. L., et al. (2018). RNA N6-methyladenosine methyltransferase-like 3 promotes liver cancer progression through YTHDF2-dependent posttranscriptional silencing of SOCS2. *Hepatol. Baltim. Md)* 67 (6), 2254–2270. doi:10.1002/hep.29683

Cheng, D., Wu, C., Li, Y., Liu, Y., Mo, J., Fu, L., et al. (2022). METTL3 inhibition ameliorates liver damage in mouse with Hepatitis B virus-associated acute-on-chronic liver failure by regulating miR-146a-5p maturation. *Biochim. Biophys. Acta. Gene Regul. Mech.* 1865 (3), 194782. doi:10.1016/j.bbagrm.2021.194782

Dominissini, D., Moshitch-Moshkovitz, S., Schwartz, S., Salmon-Divon, M., Ungar, L., Osenberg, S., et al. (2012). Topology of the human and mouse m6A RNA methylomes revealed by m6A-seq. *Nature* 485 (7397), 201–206. doi:10.1038/nature11112

Imam, H., Khan, M., Gokhale, N. S., McIntyre, A. B. R., Kim, G. W., Jang, J. Y., et al. (2018). N6-methyladenosine modification of Hepatitis B virus RNA differentially regulates the viral life cycle. *Proc. Natl. Acad. Sci. U. S. A.* 115 (35), 8829–8834. doi:10.1073/pnas.1808319115

Kim, G. W., Moon, J. S., and Siddiqui, A. (2022). N6-methyladenosine modification of the 5' epsilon structure of the HBV pregenome RNA regulates its encapsidation by the viral core protein. *Proc. Natl. Acad. Sci. U. S. A.* 119 (7), e2120485119. doi:10.1073/pnas.2120485119

Kim, G. W., and Siddiqui, A. (2022). Hepatitis B virus X protein expression is tightly regulated by N6-methyladenosine modification of its mRNA. *J. Virol.* 96 (4), e0165521. doi:10.1128/JVI.01655-21

Kim, G. W., and Siddiqui, A. (2021). Hepatitis B virus X protein recruits methyltransferases to affect cotranscriptional N6-methyladenosine modification of viral/host RNAs. *Proc. Natl. Acad. Sci. U. S. A.* 118 (3), e2019455118. doi:10.1073/pnas.2019455118

Kim, G. W., and Siddiqui, A. (2021). The role of N6-methyladenosine modification in the life cycle and disease pathogenesis of Hepatitis B and C viruses. *Exp. Mol. Med.* 53 (3), 339–345. doi:10.1038/s12276-021-00581-3

Kostyusheva, A., Brezgin, S., Glebe, D., Kostyushev, D., and Chulanov, V. (2021). Host-cell interactions in HBV infection and pathogenesis: The emerging role of m6A modification. *Emerg. Microbes Infect.* 10 (1), 2264–2275. doi:10.1080/22221751.2021.2006580

Lau, K. C., Lam, C. W., Law, C. Y., Lai, S. T., Tsang, T. Y., Siu, C. W., et al. (2011). Non-invasive screening of HLA-DPA1 and HLA-DPB1 alleles for persistent Hepatitis B virus infection: Susceptibility for vertical transmission and toward a personalized approach for vaccination and treatment. *Clin. Chim. Acta.* 412 (11-12), 952–957. doi:10.1016/j.cca.2011.01.030

Liu, Z., and Zhang, J. (2018). Human C-to-U coding RNA editing is largely nonadaptive. *Mol. Biol. Evol.* 35 (4), 963–969. doi:10.1093/molbev/msy011

Lok, A. S. (2002). Chronic Hepatitis B. *N. Engl. J. Med.* 346 (22), 1682–1683. doi:10.1056/NEJM200205303462202

Ma, J. Z., Yang, F., Zhou, C. C., Liu, F., Yuan, J. H., Wang, F., et al. (2017). METTL14 suppresses the metastatic potential of hepatocellular carcinoma by modulating N(6) -methyladenosine-dependent primary MicroRNA processing. *Hepatol. Baltim. Md)* 65 (2), 529–543. doi:10.1002/hep.28885

Meyer, K. D., Saletore, Y., Zumbo, P., Elemento, O., Mason, C. E., and Jaffrey, S. R. (2012). Comprehensive analysis of mRNA methylation reveals enrichment in 3' UTRs and near stop codons. *Cell* 149 (7), 1635–1646. doi:10.1016/j.cell.2012.05.003

Perz, J. F., Armstrong, G. L., Farrington, L. A., Hutin, Y. J., and Bell, B. P. (2006). The contributions of Hepatitis B virus and hepatitis C virus infections to cirrhosis and primary liver cancer worldwide. *J. Hepatol.* 45 (4), 529–538. doi:10.1016/j.jhep.2006.05.013

Qu, S., Jin, L., Huang, H., Lin, J., Gao, W., and Zeng, Z. (2021). A positive-feedback loop between HBx and ALKBH5 promotes hepatocellular carcinogenesis. *BMC Cancer* 21 (1), 686. doi:10.1186/s12885-021-08449-5

Raza, S. A., Clifford, G. M., and Franceschi, S. (2007). Worldwide variation in the relative importance of Hepatitis B and hepatitis C viruses in hepatocellular carcinoma: A systematic review. *Br. J. Cancer* 96 (7), 1127–1134. doi:10.1038/sj.bjc.6603649

Schweitzer, A., Horn, J., Mikolajczyk, R. T., Krause, G., and Ott, J. J. (2015). Estimations of worldwide prevalence of chronic Hepatitis B virus infection: A systematic review of data published between 1965 and 2013. *Lancet (London, Engl.* 386 (10003), 1546–1555. doi:10.1016/S0140-6736(15)61412-X

Tong, J., Zhang, W., Chen, Y., Yuan, Q., Qin, N. N., and Qu, G. (2022). The emerging role of RNA modifications in the regulation of antiviral innate immunity. *Front. Microbiol.* 13, 845625. doi:10.3389/fmicb.2022.845625

Wang, Y., and Zhou, X. (2022). N(6)-methyladenosine and its implications in viruses. *Genomics Proteomics Bioinforma*. S1672-0229(22), 00083–3. doi:10.1016/j.gpb.2022.04.009

Wu, F., Cheng, W., Zhao, F., Tang, M., Diao, Y., and Xu, R. (2019). Association of N6-methyladenosine with viruses and related diseases. *Virol. J.* 16 (1), 133. doi:10.1186/s12985-019-1236-3

Wu, F., Cheng, W., Zhao, F., Tang, M., Diao, Y., and Xu, R. (2020). Association of N6-methyladenosine with viruses and virally induced diseases. *Front. Biosci.* 25 (6), 1184–1201. doi:10.2741/4852

Xiao, W., Adhikari, S., Dahal, U., Chen, Y. S., Hao, Y. J., Sun, B. F., et al. (2016). Nuclear m(6)A reader YTHDC1 regulates mRNA splicing. *Mol. Cell* 61 (4), 507–519. doi:10.1016/j.molcel.2016.01.012

Xu, K., Yang, Y., Feng, G. H., Sun, B. F., Chen, J. Q., Li, Y. F., et al. (2017). Mettl3-mediated m(6)A regulates spermatogonial differentiation and meiosis initiation. *Cell Res.* 27 (9), 1100–1114. doi:10.1038/cr.2017.100

Yamada, N., Shigefuku, R., Sugiyama, R., Kobayashi, M., Ikeda, H., Takahashi, H., et al. (2014). Acute Hepatitis B of genotype H resulting in persistent infection. *World J. Gastroenterol.* 20 (11), 3044–3049. doi:10.3748/wjg.v20.i11.3044

Zhao, B., Wang, W., Zhao, Y., Qiao, H., Gao, Z., and Chuai, X. (2021). Regulation of antiviral immune response by N (6)-methyladenosine of mRNA. *Front. Microbiol.* 12, 789605. doi:10.3389/fmicb.2021.789605

Zhao, T., Qi, J., Liu, T., Wu, H., and Zhu, Q. (2022). N6-Methyladenosine modification participates in the progression of hepatitis B virus-related liver fibrosis by regulating immune cell infiltration. *Front. Med.* 9, 821710. doi:10.3389/fmed.2022.821710

Zhao, X., Yang, Y., Sun, B. F., Shi, Y., Yang, X., Xiao, W., et al. (2014). FTO-dependent demethylation of N6-methyladenosine regulates mRNA splicing and is required for adipogenesis. *Cell Res.* 24 (12), 1403–1419. doi:10.1038/cr.2014.151

frontiers | Frontiers in Genetics

TYPE Original Research
PUBLISHED 29 November 2022
DOI 10.3389/fgene.2022.1059325

OPEN ACCESS

EDITED BY
Kunqi Chen,
Fujian Medical University, China

REVIEWED BY
Jia Meng,
Xi'an Jiaotong-Liverpool University, China
Shaofeng Lin,
Huazhong University of Science and Technology, China
Ying Ye,
Huazhong University of Science and Technology, China

*CORRESPONDENCE
Xiumin Zhou,
alice-xm@163.com

†These authors have contributed equally to this work and share first authorship

SPECIALTY SECTION
This article was submitted to RNA, a section of the journal Frontiers in Genetics

RECEIVED 01 October 2022
ACCEPTED 07 November 2022
PUBLISHED 29 November 2022

CITATION
Wang Z, Shen L, Wang J, Huang J, Tao H and Zhou X (2022), Prognostic analysis of m6A-related genes as potential biomarkers in idiopathic pulmonary fibrosis.
Front. Genet. 13:1059325.
doi: 10.3389/fgene.2022.1059325

Prognostic analysis of m6A-related genes as potential biomarkers in idiopathic pulmonary fibrosis

Zhiqiang Wang[1,2†], Lanyu Shen[1†], Junjie Wang[2], Jiaqian Huang[2], Huimin Tao[1] and Xiumin Zhou[1*]

[1]Department of Oncology, The First Affiliated Hospital of Soochow University, Suzhou, China, [2]Department of Biochemistry and Molecular Biology, Medical College, Soochow University, Suzhou, China

Idiopathic pulmonary fibrosis (IPF) is a progressive, fatal lung disease with limited treatment options. N6-methyladenosine (m6A) is a reversible RNA modification and has been implicated in various biological processes. However, there are few studies on m6A in IPF. This project mainly explores the prognostic value of m6A-related genes as potential biomarkers in IPF, in order to establish a set of accurate prognostic prediction model. In this study, we used GSE28042 dataset in GEO database to screen out 218 m6A-related candidate genes with high IPF correlation and high differential expression through differentially expressed gene analysis, WGCNA and m6A correlation analysis. The genes associated with the prognosis of IPF were screened out by univariate Cox regression analysis, LASSO analysis, and multivariate Cox regression analysis, and the multivariate Cox model of prognostic risk of related genes was constructed. We found that RBM11, RBM47, RIC3, TRAF5 and ZNF14 were key genes in our model. Finally, the prognostic prediction ability and independent prognostic characteristics of the risk model were evaluated by survival analysis and independent prognostic analysis, and verified by the GSE93606 dataset, which proved that the prognostic risk model we constructed has a strong and stable prediction efficiency.

KEYWORDS

N6-methyladenosine (m6A), WGCNA, m6A-related genes, prognosis risk model, IPF

1 Introduction

Pulmonary fibrosis (PF) is a chronic, progressive tissue repair response, which leading to irreversible scarring and lung remodeling (King et al., 2011). PF can occur secondary to certain predisposing factors or diseases, such as radiation (He et al., 2019), asbestos (Pira et al., 2018), silica (Cao et al., 2020), drugs (Della Latta et al., 2015), autoimmune diseases (Fischer and Distler, 2019), etc. However, some patients with PF without a clear cause, which is called idiopathic pulmonary fibrosis (IPF). IPF is a chronic, age-related

interstitial lung disease (ILD) characterized by excessively deposition of extracellular matrix (ECM) protein and irreversible loss of lung function, causing progressive respiratory failure (Richeldi et al., 2017; Barratt et al., 2018). The pathogeny of IPF is still unknown, but it likely related to heredity and environment. There are large regional differences in the incidence of IPF, ranging from 0.35 to 1.30 per 100,000 individuals in Asia–Pacific countries, 0.09 to 0.49 per 100,000 individuals in Europe, and 0.75 to 0.93 per 100,000 individuals in North America (Maher et al., 2021). IPF tends to occur in men between 40 and 50 years of age and has a poor prognosis. The average life expectancy of untreated IPF patients is only 3–5 years, and most patients die of acute exacerbations of IPF or respiratory failure. Actually, acute exacerbations of IPF can occur at any time during the course of the disease and are associated with extremely high mortality (Spagnolo and Wuyts, 2017). Although two antifibrotic drugs, nintedanib and pirfenidone, have been shown to delay the progression of IPF, there is currently no drug that can cure IPF (Raghu et al., 2015).

Epigenetics usually refers to the heritable modification of genetic material without changing gene sequence, including DNA methylation, RNA methylation, histone modification, chromosome remodeling, etc., which plays an important role in various diseases and tumors (Berger et al., 2009). At present, more than 100 kinds of RNA (mRNA, lncRNA, snRNA, etc.) have been found post-transcriptional modifications, among which N6-methyladenosine (m6A) is the most common (Yue et al., 2015; Boccaletto et al., 2018). M6A RNA modification is a dynamic and reversible post-transcriptional modification process mediated by m6A WER proteins (methyltransferase "writers", demethylase "erasers", binding proteins "readers"), which plays a crucial regulatory role in RNA metabolism, splicing, translation and other processes (Wang et al., 2020). Previous studies have shown that m6A is widely involved in the development of various diseases, such as pneumonia, lung cancer, colorectal cancer, breast cancer, nasopharyngeal cancer, systemic lupus erythematosus, etc. (Li et al., 2018; Chang et al., 2020; Yue et al., 2020; Maher et al., 2021; Meng et al., 2021; Li et al., 2022). For example, Li et al. (2021) found that SNHG4 promoted LPS-induced inflammation by inhibiting METTL3-mediated m6A level of STAT2 mRNA. And research pointed out that overexpressed FTO enhanced the expression of MZF1 by reducing the m6A modification level and stability of MZF1 mRNA, thereby promoting the development of lung cancer (Liu et al., 2018). Similarly, enhanced activity of methyltransferase METTL3 increased the m6A modification level of JUNB mRNA and accelerated the progression of TGF-β-induced lung adenocarcinoma (LUAD) (Wanna-Udom et al., 2020). These studies indicated that RNA methylation regulators could affect the development of the above diseases by regulating the m6A modification of RNA. M6A-related genes can also be used as diagnostic and prognostic markers for lung diseases. For example, studies found that m6A-related genes (EGFR, RFXAP, KHDRBS2, ADAMTS6, etc.) were determined to be associated with overall survival (OS) in patients with LUAD, in which RFXAP and KHDRBS2 exhibited independent prognostic value (Sun et al., 2021). Additionally, Jia et al. (2022) showed that three m6A-related genes (FAM71F1, MT1E, and MYEOV) were identified as prognostic genes in Lung Squamous Carcinoma (LUSC). However, there are few reports on m6A methylation modification in the occurrence and development of IPF. Therefore, it is of great significance to explore m6A-related genes and construct IPF-related prognostic risk model to assist in judging the progression and prognosis of IPF.

Weighted gene co-expression network analysis (WGCNA) is a comprehensive analysis technique based on biological network, which can identify a class of genes (or proteins) that are co-expressed, and cluster genes with similar expression patterns through algorithms into different modules, analyze the association between modules and characteristic traits or phenotypes, use clustering modules to associate with phenotypes to build a co-expression network, and explore the core genes (or proteins) in the modules, so as to provide ideas for exploring the molecular mechanism of diseases (Presson et al., 2008; Yin et al., 2018). Compared with microarray and high-throughput sequencing analysis, WGCNA is suitable for multiple statistical tests to analyze the correlation between genes and avoid losing the trend information of genes according to a fixed threshold screening.

The Cox proportional hazards model is essentially a regression model commonly used in medical research statistics to study the association between a patient's survival time and one or more predictor variables (Cox, 1972). It is applicable to quantitative predictor variables and categorical variables. It mainly includes univariate and multivariate Cox regression analysis. Univariate Cox analysis is usually used to remove collinearity, but may lead to synergistic effects caused by other variables, so multivariate Cox regression is performed to correct other factors, which is often used for data modeling in survival analysis (Huang and Liu, 2006; Li et al., 2016).

In this paper, the microarray data GSE28042 was downloaded from the Gene Expression Omnibus (GEO) database, and the gene expression profiles of peripheral blood mononuclear cell (PBMC) and the corresponding clinical data of 75 IPF samples and 19 normal samples were obtained. Through the analysis of differentially expressed genes, WGCNA and m6A correlation analysis method, a group of m6A-related candidate genes with high IPF correlation and differential expression were screened. The genes associated with the prognosis of IPF were screened out by univariate Cox regression analysis, LASSO analysis, and multivariate Cox regression analysis, and the multivariate Cox model of prognostic risk of related genes was constructed. Finally, the prognostic predictive ability and independent prognostic characteristics of the risk model were

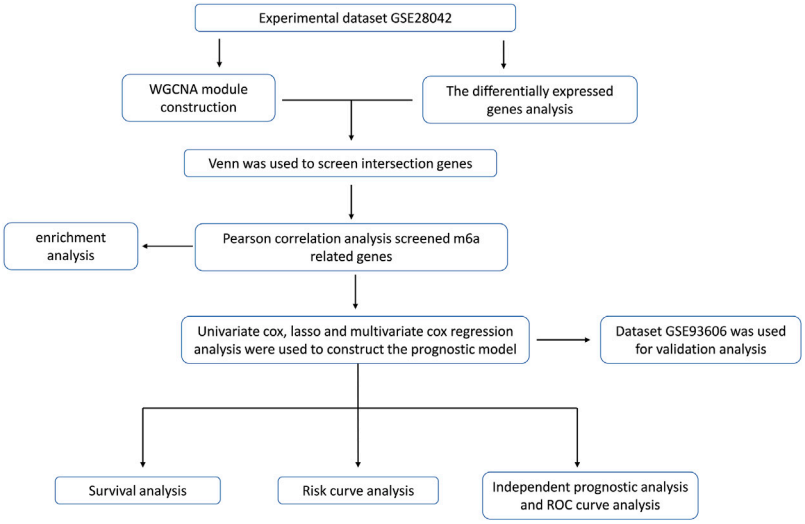

FIGURE 1
The workflow for prognostic analysis of m6A-related genes as potential biomarkers for idiopathic pulmonary fibrosis.

evaluated by survival analysis and independent prognostic analysis, and verified by GSE93606 dataset, which is intended to provide a basis for prognostic prediction of IPF patients (Figure 1).

2 Materials and methods

2.1 Data collection and processing

First, we searched the GEO database (https://www.ncbi.nlm.nih.gov/geo/) for keywords such as "idiopathic pulmonary fibrosis", "survival", "blood", etc. Then, by combining samples for survival information, we eventually included the GSE28042 and GSE93606 datasets into the study. GSE28042 was used as the experimental dataset and GSE93606 was used as the validation dataset. The GSE28042 dataset contains the gene expression profiles of peripheral blood mononuclear cell (PBMC) and their corresponding clinical data of 75 IPF patients and 19 healthy people. The probes were converted to corresponding gene symbols by referring to the annotation information of the GPL6480 [Agilent-014850 Whole Human Genome Microarray 4 × 44K G4112F (Probe Name version)] platform. The GSE93606 dataset contains peripheral whole blood gene expression profiles and corresponding clinical data of 60 IPF patients and 20 healthy subjects. The probes were converted to the corresponding gene symbols by referring to the annotation information of GPL11532 [Hugene-11-ST] Affymetrix Human Gene 1.1 ST Array [transcript (Gene) version] platform.

2.2 Construction of weighted gene co-expression network analysis

In order to explore the modules and genes related to the clinical characteristics of healthy people and IPF patients, the data of GSE28042 were analyzed by using the WGCNA package of R language, and the samples were clustered. In order to ensure the reliability of the results, we analyzed the samples and removed the samples that were not clustered, that is, the outlier samples. In order to ensure that the network conforms to the scale-free network distribution, the "pickSoftTreshold" function in the WGCNA package is used to calculate the correlation coefficient of β value and the mean of gene connectivity, and the appropriate soft threshold β is selected to make the network conform to the standard of scale-free network. Then, the modules were clustered with a minimum cluster of 100 genes and a cut height of 0.25. Finally, the gene significance (GS) and module membership (MM) were calculated and correlated with clinical traits. The two modules with the highest correlation with IPF were selected, and the genes in the modules were further analyzed. Genes in the co-expression module have high connectivity and genes in the same module may have similar biological functions.

2.3 DEG analysis

Using R language (R) 4.0.3 limma package to analyze the gene differences between the gene expression matrix of peripheral blood monocytes of healthy people and IPF patients. Set the screening criteria as $|\log_2 FC| > 0.5$, $p < 0.05$

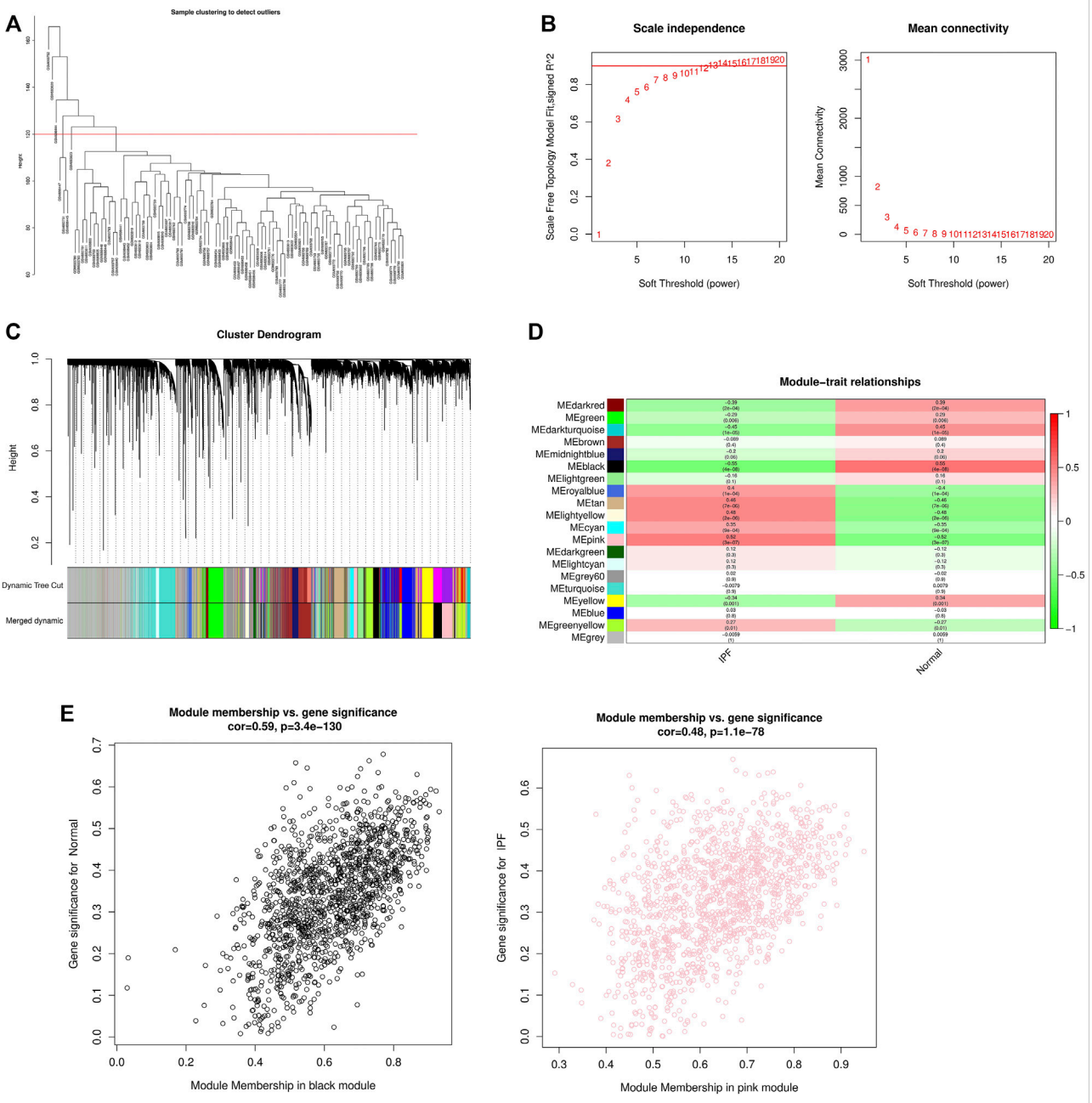

FIGURE 2
WGCNA module construction and selection of modules with high correlation with IPF. **(A)** Sample clustering diagram (delete 7 outlier samples by setting the height to 120); **(B)** Determination of the optimal soft threshold (in the process of module selection, the adjacency matrix is converted into a topology matrix, and the optimal soft threshold β = 10 is determined); **(C)** Cluster tree of co-expressed gene modules (similar genes are grouped into the same module through dynamic splicing and cluster analysis); **(D)** The correlation between gene modules and clinical information (The redder the color, the higher the positive correlation; the greener the color, the higher the negative correlation. Numbers in the figure are Pearson's correlation coefficient, and corresponding *p*-values are in parentheses); **(E)** The correlation between Black and Pink modules and IPF is represented by scatter plot.

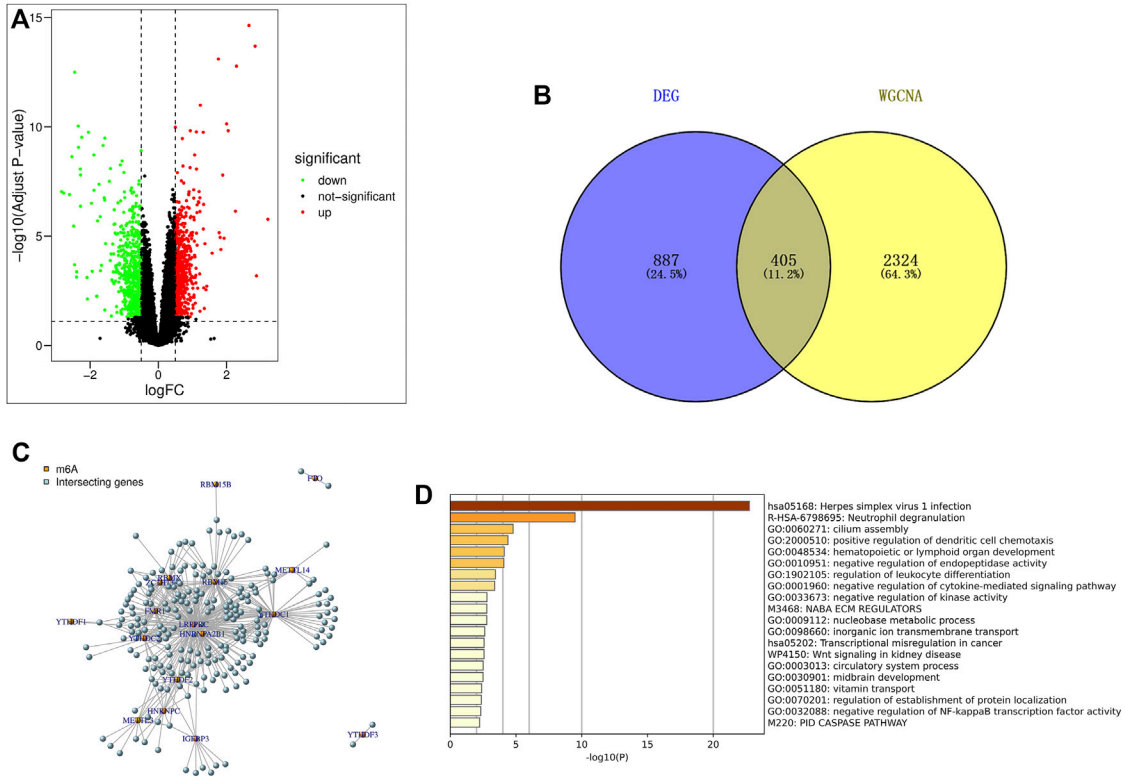

FIGURE 3
Screening and enrichment analysis of m6A related candidate genes. **(A)** Volcano map of differentially expressed genes (red are up-regulated genes, green are down-regulated genes, black are non-differentially expressed genes); **(B)** The genes screened by DEG and WGCNA were intersected by Venn diagram, and IPF highly correlated differentially expressed genes were obtained; **(C)** Pearson correlation analysis was used to screen out m6A-related candidate genes in IPF; **(D)** GO and KEGG enrichment analysis were performed for m6A related candidate genes.

(correction method is FDR). The up-and down-regulated genes were represented by mapping volcanoes.

2.4 Screening of differentially expressed genes associated highly with idiopathic pulmonary fibrosis

The common genes obtained by WGCNA analysis and DEG analysis were defined as IPF highly correlated differential genes. Use the Venn diagram (https://bioinfogp.cnb.csic.es/tools/venny/index.html) to show all the differentially expressed genes associated highly with IPF.

2.5 Identification of m6A-related candidate genes

The cor () and cor. test () functions of R language were used to calculate the correlation between the expression levels of 23 m6A regulators (METTL3, METTL14, METTL16, WTAPI, VIRMA, ZC3H13, RBM15, RBM15B, YTHDC1, YTHDC2, YTHDF1, YTHDF2, YTHDF3, HNRNPC, FMR1, LRPPRC, HNRNPA2B1, IGFBP1, IGFBP2, IGFBP3, RBMX, FTO, ALKBH5) and the expression levels of IPF highly correlated differential genes and calculate the p value (Deng et al., 2018; Chen et al., 2019). The genes significantly associated with either m6A regulator (| Pearson R | > 0.5 and $p < 0.05$) was defined as candidate genes related to m6A.

2.6 Gene function and pathway enrichment analysis

The online website Metascap (https://metascape.org/gp/index.html) was used to analyze the module function and pathway enrichment of m6A-related candidate genes to further explore the biological functions of these genes. GO analysis was used to annotate the functions of genes and their products in three aspects, including biological process (BP), molecular function (MF) and cellular component (CC). KEGG database is a collection of information about genes, proteins,

chemical components and their interactions, reactions and relationship networks to annotate gene functions and metabolic pathways.

2.7 Construction of prognostic risk model and independent prognostic analysis

A series of m6A-related prognostic genes were screened by univariate Cox regression analysis (KM < 0.05, $p < 0.05$), and further screened by LASSO regression method. Then, the prognosis model was constructed by multivariate Cox regression analysis, and the forest map was drawn. The Kaplan-Meier method of the "survival" function package was used to analyze the survival of the screened genes, and the survival curve was drawn.

The median prognostic risk value was set as a threshold. According to this threshold, samples from patients with IPF patients were divided into low-risk and high-risk groups. The distribution of risk grades between the low-risk group and the high-risk group was plotted as a scatter plot. The survival status and survival time of patients in the two different risk groups were also plotted as a scatter plot. Then the Kaplan-Meier method was used to draw survival curves for the risk models.

Clinical traits and risk values were compared with survival time and survival status. Independent prognostic analysis was conducted to test the prognostic ability of the prognostic risk model, and to observe whether the prognostic model can be independent of other clinical traits and whether it has independent prognostic characteristics of IPF. The R package "timeROC" was used to draw time-dependent ROC curves and "survivalROC" was used to verify the accuracy of the prognostic risk model. The ROC curve was drawn to predict the accuracy of the model, and the accuracy was judged by the area under the curve.

2.8 Statistical analysis

In this study, the R (version 4.2.0) and RStudio software were utilized to carry out the statistical analysis and figure preparation. *p*-values less than 0.05 were defined as statistically significant.

3 Results

3.1 WGCNA module construction and selection of modules with high correlation with idiopathic pulmonary fibrosis

WGCNA analysis was performed using gene expression matrix. After setting the high degree to 120, 7 outlier samples (GSM693752, GSM693820, GSM698444, GSM698447, GSM698445, GSM693751, GSM693823) were removed. Finally, 71 IPF samples and 16 normal samples were analyzed later (Figure 2A). When the scale-free topological fitting index R2 reaches 0.9, the appropriate β value is chosen as 10 (Figure 2B). The dynamic clipping tree algorithm was provided to segment the modules and construct the network diagram. Cluster analysis was performed on the modules and the modules with similarity greater than 0.75 were merged into new modules, in which the minimum module had 100 genes and the clipping height was 0.25 (Figure 2C). On this basis, the WGCNA method based on sequence free network was used to modularize genes, and the topological overlap matrix between all genes was described by heat map, and the relationship between sample features and modules was analyzed. The colors corresponding to the modules are darkred, green, darkturquoise, brown, midnightblue, black, lightgreen, royalblue, tan, lightyellow, cyan, pink, darkgreen, lightcyan, grey60, turquoise, yellow, blue, greenyellow, grey. Among them, the grey module is the gene that cannot be clustered to other modules, so it will not be analyzed in the subsequent analysis (Figure 2D). Key modules were identified according to the correlation coefficient between module features and traits, in which the black module had the highest positive correlation (cor = 0.59, $p < 3.4e\text{-}130$), and the pink module had the highest negative correlation (cor = 0.48, $p < 1.1e\text{-}78$), and finally determined that the black module and the pink module were the two modules with the highest degree of IPF correlation. A scatter plot was used to represent the correlation between black or pink modules and IPF, and a total of 2729 genes were found (Figure 2E).

3.2 The differentially expressed genes between idiopathic pulmonary fibrosis samples and normal samples were screened

Using the limma package in R language to screen differentially expressed genes, based on $|\log_2 FC|>0.5$ and $p < 0.05$ (correction method is FDR) as the threshold, the differential genes in the IPF patients and healthy population samples in the GSE28042 dataset were screened. A total of 1292 differentially expressed genes were found, of which 606 genes were up-regulated and 686 were down-regulated. The results of differentially expressed genes were used to construct a volcano plot, where red represents up-regulated genes, green represents down-regulated genes, and black represents genes defined as non-differential (Figure 3A).

3.3 Screening of IPF highly correlated differentially expressed genes

The 2729 genes in Black and Pink modules obtained by WGCNA analysis were highly correlated with IPF, and the

TABLE 1 The univariate Cox regression analysis demonstrating 30 genes associated with IPF prognosis.

ID	HR	*p* value
ACPP	2.819365	0.007666706
ADAP2	3.162390	0.010084724
BEST1	2.767257	0.004894885
BIRC3	0.380656	0.001404292
C19orf59	2.313709	0.003886102
CLEC2D	0.330340	0.002016299
CLK1	0.274811	0.005419468
CLK4	0.201311	0.00567289
DOCK5	3.361948	0.00399794
EFHA2	0.556492	0.007436865
FAM161A	0.571926	0.045819138
FRAT1	2.398299	0.009385627
JDP2	2.102222	0.005909982
KIAA1147	0.418338	0.02874775
KLF12	0.438746	0.007658451
LRBA	0.432600	0.048624944
MIDN	2.336528	0.03280022
RBM11	0.465034	0.0003472
RBM47	3.284265	0.001557636
RIC3	0.410807	0.00061674
SACS	0.520899	0.04322521
SLC38A1	0.327794	0.002712488
SLC8A1	2.434524	0.012780222
TIMP2	2.492529	0.030980637
TRAF5	0.257449	0.000397483
TTC18	0.314697	0.001033081
ZNF14	0.295492	0.000512298
ZNF30	0.380889	0.007052629
ZNF529	0.298259	0.000842414
ZNF573	0.258771	0.001805436

1292 genes obtained by DEG analysis were significantly different. Therefore, a total of 405 genes were obtained by taking the intersection of the two genes through Venn diagram, and these genes were defined as IPF highly correlated differentially expressed genes (Figure 3B).

3.4 Screening and enrichment analysis of m6A-related candidate genes

Pearson correlation analysis was used to screen out 218 candidate genes related to m6A from IPF highly correlated differentially expressed genes (|Pearson R|>0.5, $p < 0.05$) (Figure 3C). At the same time, the online website Metascap (https://metascape.org/gp/index.html) was used to analyze the candidate genes related to m6A. The results showed that the candidate genes mainly focused on the pathways of herpes simplex virus type I infection, neutrophil degranulation, cilia assembly and so on (Figure 3D).

3.5 Construction of prognostic risk model

30 genes associated with IPF prognosis were screened out from 218 m6A-related candidate genes by univariate Cox method (Table 1), and 5 genes associated with IPF prognosis were further screened by LASSO method (Figure 4A). On this basis, further multivariate Cox regression analysis showed that RBM11, RBM47, RIC3, TRAF5 and ZNF14 candidate genes had significant impact on the prognosis of IPF patients (Figure 4B). These five genes were used to construct a multivariate Cox model of prognostic risk in IPF patients, riskscore= (−0.44084*RBM11)+ (0.631579*RBM47) + (−0.01935*RIC3) + (−0.58291*TRAF5) + (−0.00528*ZNF14) (Table 2). The expression heat map and survival analysis of these five genes were displayed (Figures 4C,D). Among them, the survival rate was low when RBM47 was highly expressed, while the survival rate was high when RBM11, RIC3, TRAF5, and ZNF14 were highly expressed. The protein-protein interactions between 5 genes and 23 m6A regulators were analyzed by the STRING database (https://cn.string-db.org/), and it was found that there were obvious protein-protein interactions between RBM11, RBM47 and m6A regulators (Figure 4E). In addition, m6A-Atlas (http://rnamd.org/m6a/) also showed that the five key genes had m6A sites, which increased the credibility of the research content.

3.6 Survival analysis and independent prognostic analysis

To further verify the predictive ability of the model for prognosis, we took the median risk value of patients as the threshold, divided patients into high risk group and low risk group, and analyzed the survival status and survival time of patients in two different risk groups (Figure 5A). And through the survival curve, it was found that the survival rate of high-risk patients was low, while the survival rate of low-risk patients was high, which preliminarily demonstrated the correctness of the model (Figure 5B).

To further assess whether the risk model for these 5 key genes has independent prognostic features of IPF, we performed an independent prognostic analysis. We performed univariate and multivariate independent prognostic analyses for the above five key genes, respectively, indicating that the risk model of the five key genes was independent of other clinicopathological parameters (gender, age) (Figures 5C,D).

By analyzing the prognostic risk model and drawing the ROC curve, it was found that compared with other factors, the AUC

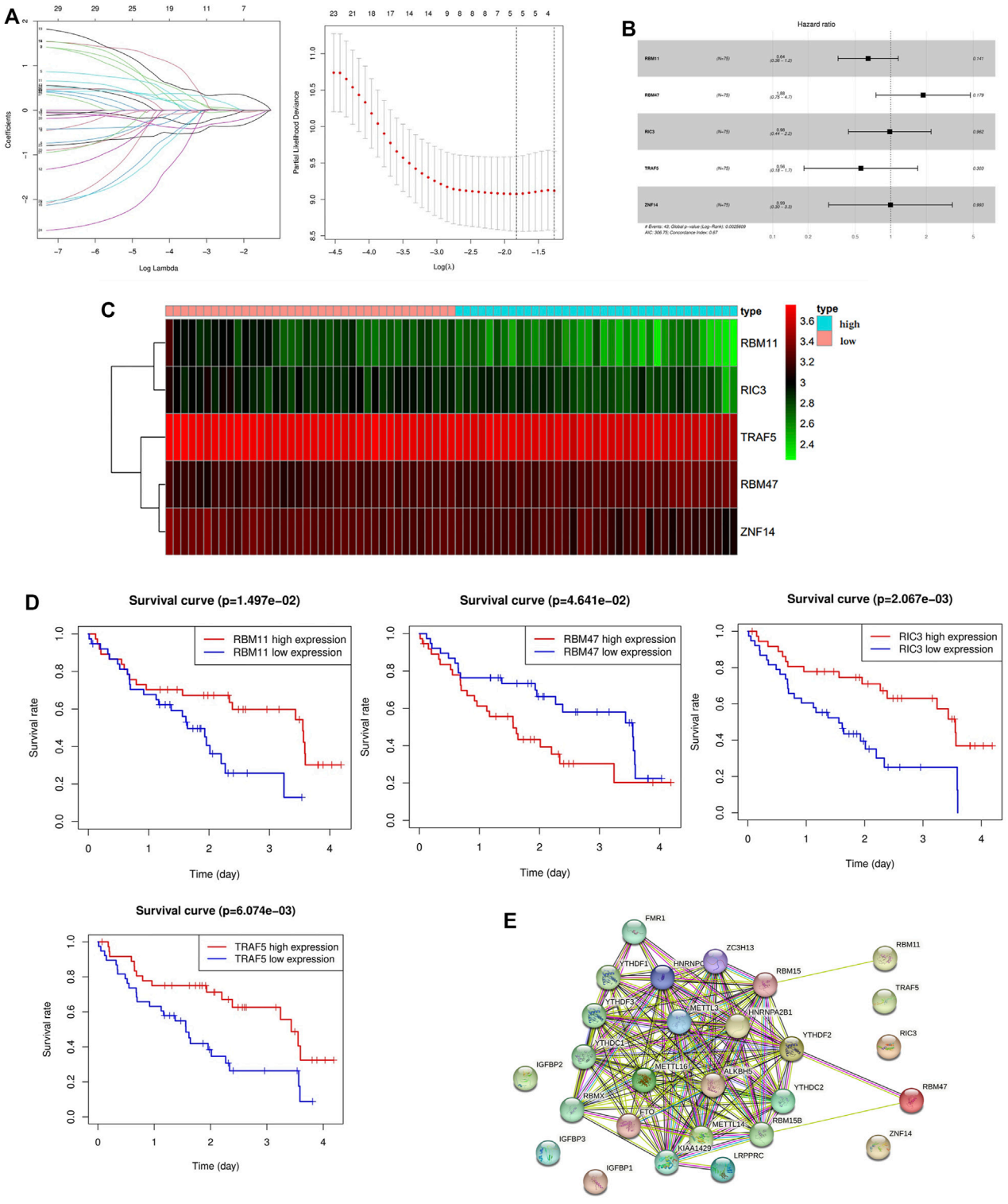

FIGURE 4
Screening of key genes associated with IPF prognosis. **(A)** LASSO regression analysis screened 5 genes associated with prognosis; **(B)** Multivariate Cox regression analysis of the effect of five key genes RBM11, RBM47, RIC3, TRAF5, ZNF14 on the prognosis of patients with IPF; **(C)** Expression levels of key candidate genes in different IPF samples; **(D)** Kaplan-Meier survival analysis of key genes; **(E)** Protein interactions between five key genes and 23 m6A regulators.

TABLE 2 The result of multivariate COX regression analysis.

ID	COEF	HR	HR.95L	HR.95H	*p* value
RBM11	−0.44084	0.643493	0.357941	1.156848	0.140723
RBM47	0.631579	1.880578	0.748600	4.724255	0.178993
RIC3	−0.01935	0.980836	0.438145	2.195713	0.962464
TRAF5	−0.58291	0.558274	0.184302	1.691076	0.302605
ZNF14	−0.00528	0.994734	0.297910	3.321466	0.993152

value of riskscore was greater than that of other factors (age and gender) (Figure 5E). By plotting the time-dependent ROC curve of the prognostic risk model, it can be found that although the AUC value in the first year was low (AUC at 1 year = 0.63), the AUC value gradually increased with time (AUC at 2 years = 0.77, AUC at 3 years = 0.85, AUC at 4 years = 0.95) (Figure 5F). This indicates that the accuracy of our prognostic model is good.

3.7 Validation of prognostic risk model

The GSE93606 dataset was used as the validation dataset to validate our prognostic risk model by survival analysis and independent prognostic analysis. In the validation dataset, survival analysis verified that high-risk patients had a low survival rate, while low-risk patients had a high survival rate (Figures 6A,B). Multivariate prognostic analysis verified that the prognostic risk model was independent of other clinicopathological parameters (gender and age) (Figure 6C). ROC curve verified the accuracy of the prognostic risk model (Figures 6D,E). These results indicate that the prognostic risk model has strong and stable predictive efficiency.

4 Discussion

The etiology of IPF is still not fully understood, but some studies have shown that its pathogenesis may be related to the abnormal damage and repair of alveolar epithelial cells, epithelial-to-mesenchymal transition (EMT), fibroblast-to-myofibroblast transformation (FMT), and inflammatory response (King et al., 2011). Worldwide, the incidence and mortality of IPF are on the rise. Lung transplantation is the only treatment for IPF that can prolong life expectancy (Kumar et al., 2018). Unfortunately, IPF patients without lung transplantation have a short median survival time. M6A is the most abundant post-transcriptional modification in mRNA and long non-coding RNA (lncRNA) in most eukaryotes. In addition, studies have reported that m6A is involved in post-transcriptional modification, cell differentiation, cell recoding, cell stress and other processes, and plays an important role in lung diseases such as lung cancer, pulmonary hypertension and chronic obstructive pulmonary disease through various mechanisms. However, there are few studies on m6A in IPF. Therefore, it is necessary to explore the prognostic value of m6A-related genes in IPF and establish a set of prediction models for evaluating the survival time of IPF and improving the prognosis of patients.

In this study, we downloaded GSE28042 dataset from GEO database, which included peripheral blood monocyte cell gene expression profiles and their corresponding clinical information of 75 IPF samples and 19 normal samples, and analyzed the obtained data. The gene expression matrix was used for differential gene analysis, and 606 up-regulated genes and 686 down-regulated genes were screened. The correlation between each module and the trait was obtained by WGCNA analysis combined with correlation heat map. The black and pink modules with the highest positive and negative correlations were selected, and 405 intersection genes were obtained by intersection of the DEG and the module genes with the highest correlation in the selected WGCNA. Then, 218 m6A-related candidate genes were screened out from the 405 IPF highly correlated differentially expressed genes by Pearson correlation analysis, and the enrichment analysis of these genes showed that the above genes were mainly enriched in herpes simplex virus type I(HSV-1) infection, neutrophil degranulation, ciliary assembly and other pathways. Studies have shown that chronic viral infections, mainly herpes virus infections, may contribute to the development of IPF. And HSV-1 is a kind of herpes virus, it can enter the alveoli through the respiratory tract and spread with the blood, resulting in focal necrotizing pneumonia, followed by diffuse pulmonary fibrosis (Luyt, 2020). Neutrophil degranulation is one of the important links that neutrophils participate in the inflammatory response. As inflammatory cells, neutrophils participate in the progression of PF by promoting the proliferation of fibroblasts and enhancing the differentiation of myofibroblasts (Gregory et al., 2015; Klopf et al., 2021). Cilia is an organelle protruding from the cell surface. The abnormal structure and function of cilia can cause various diseases, such as bronchiectasis and reproductive infertility (Jain et al., 2012; Girardet et al., 2019). Moreover, studies have shown that pulmonary fibrosis is associated with bronchiectasis (Fitzgerald et al., 2017). The above relevant findings suggest that the m6A-related candidate genes screened were closely related to the occurrence and development of PF. Therefore, we hypothesized that the m6A-related candidate genes were associated with IPF.

In order to explore the role of m6A-related candidate genes in the prognosis of IPF, we screened out 30 genes associated with patient prognosis by univariate Cox analysis, and then screened out 5 key genes (RBM11, RBM47, RIC3, TRAF5, ZNF14) by LASSO analysis and multivariate Cox analysis. The above studies indicate that the five key genes and 23 m6A regulators are significantly correlated and modified by their regulation. This regulation can be direct or indirect, but its specific mechanism is

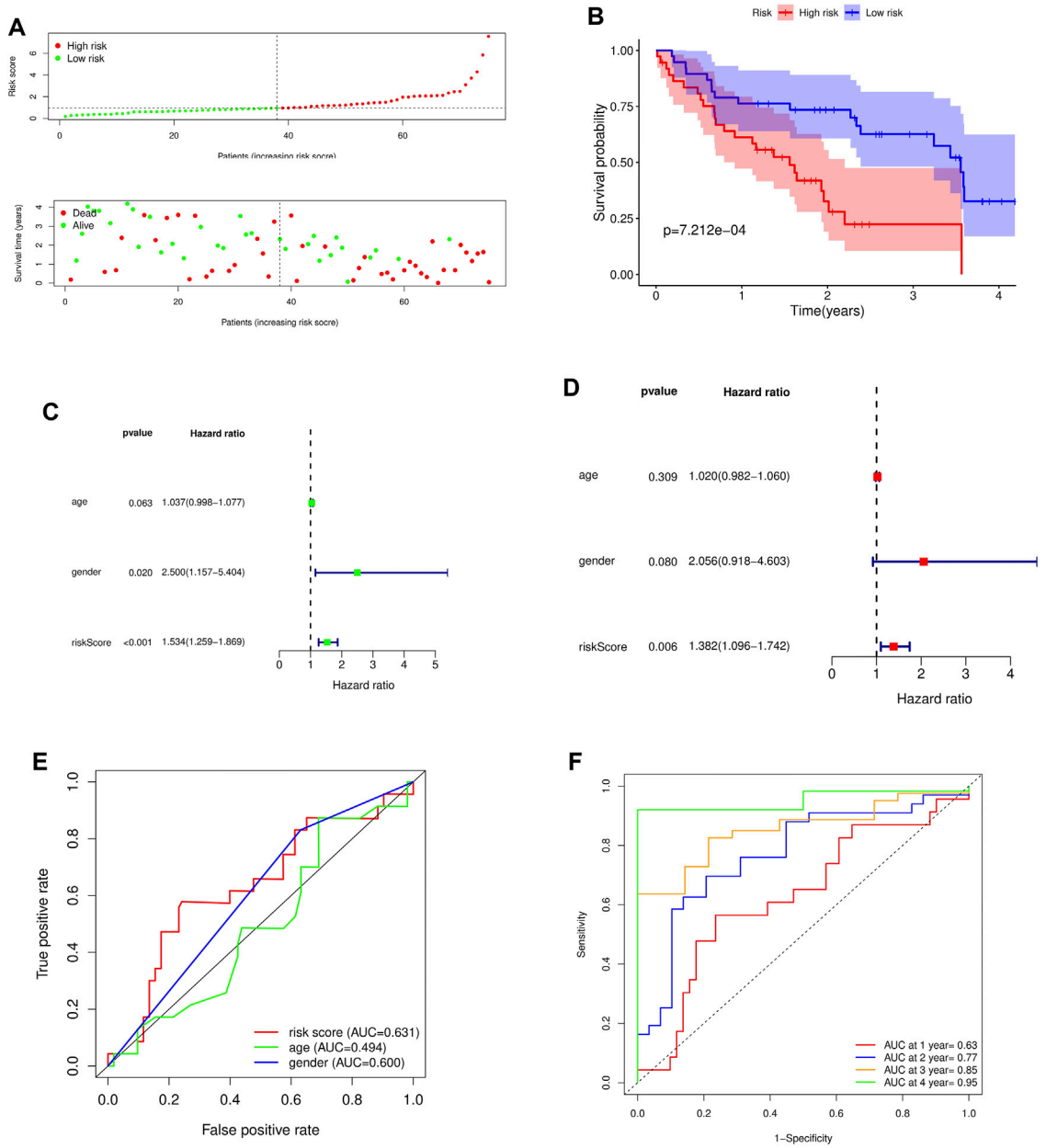

FIGURE 5
Survival analysis and independent prognostic analysis of the prognostic risk model. **(A)** Distribution of patients in different risk groups and risk levels; **(B)** Overall survival curve of the model; **(C)** Univariate independent prognostic analysis; **(D)** Multivariate independent prognostic analysis; **(E)** ROC curve of different factors (riskscore, age, gender); **(F)** ROC curve of different years (1, 2, 3 and 4 years).

still unknown. The results of protein-protein interaction analysis also showed that RBM11 and RBM47 had protein-protein interactions with m6A regulators, and the m6A-Atlas analysis showed that all five key genes had m6A sites (Tang et al., 2021), which added confidence to our results. We construct a riskscore model as an indicator to predict the prognosis of IPF [riskscore = (−0.44084*RBM11) + (0.631579*RBM47) + (−0.01935*RIC3) + (−0.58291*TRAF5) + (−0.00528*ZNF14)], and then survival analysis was performed to assess the effect of the above genes on the prognosis of IPF patients. The results of single-gene survival analysis showed that high expression of RBM11, RIC3, TRAF5, ZNF14 was associated with good prognosis of IPF, while high expression of RBM47 was associated with poor prognosis; overall survival analysis of the risk prognostic model showed that high-risk patients had poor survival, while low-risk patients had higher survival, which preliminarily indicated the

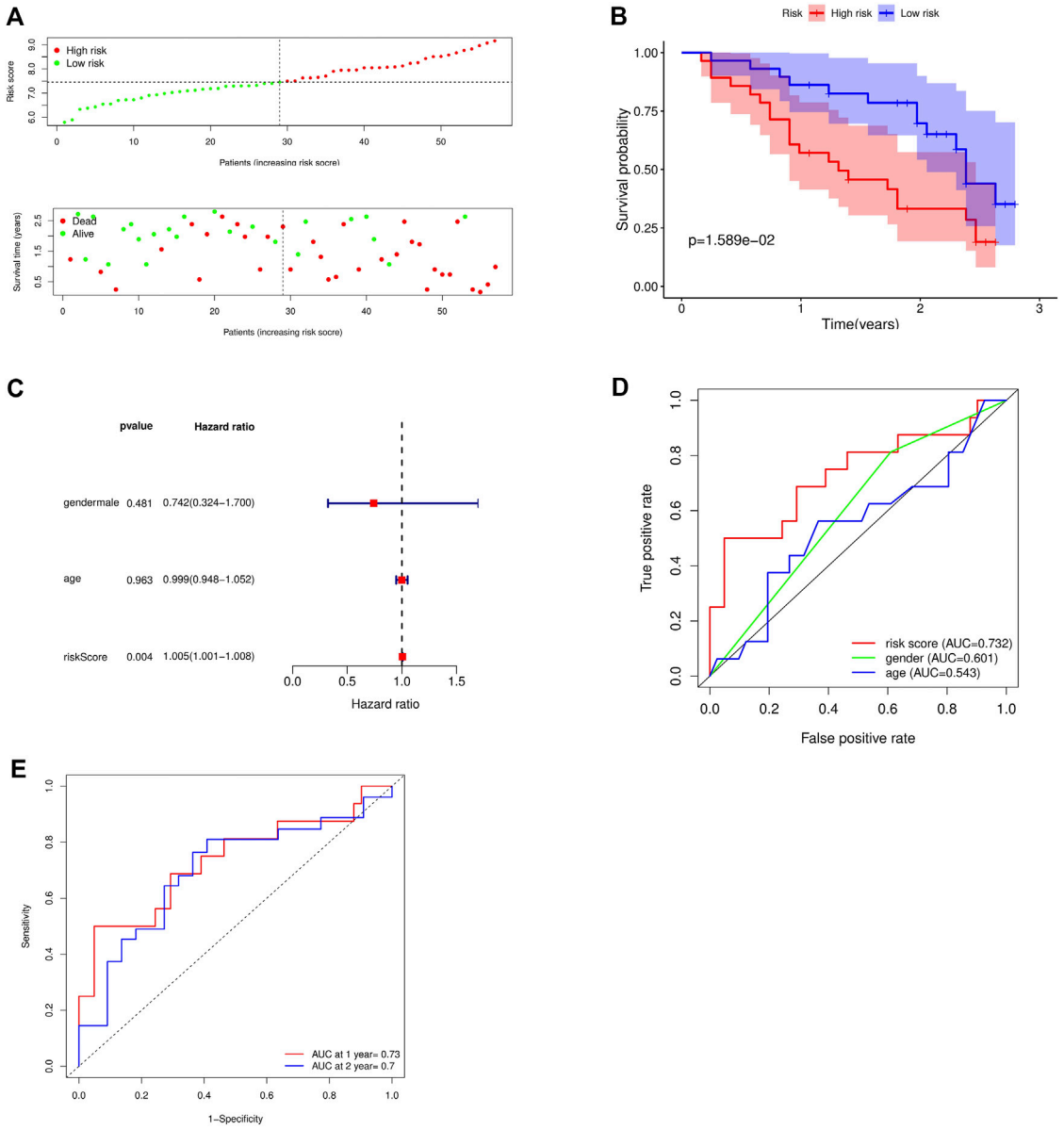

FIGURE 6
Validation of the accuracy of the prognostic model using the GSE93606 dataset. **(A)** Distribution of patients and risk levels in different risk groups; **(B)** Overall survival curve of the model; **(C)** Multivariate independent prognostic analysis; **(D)** ROC curve of different factors (age and riskscore); **(E)** ROC curve of different years (1, 2 years).

correctness of the model. Simultaneous univariate and multivariate independent prognostic analyses indicated that the risk model for these five key genes was independent of other clinicopathological parameters (gender, age). TRAF5 is an important signal transducer for a wide range of TNF receptor superfamily members, and it mainly mediates the activation of NF-κB pathway (Au and Yeh, 2007). Indeed, study has shown that overactivation of NF-κB pathway is associated with apoptosis of alveolar epithelial type II cells (AEC2) and the development of PF (Yang et al., 2018). Besides, Ben-David et al. (2016) demonstrated that inflammatory signals regulate the expression and splicing of RIC3, thereby influencing the α7 nA-ChR mediated cholinergic anti-inflammatory pathway. Although the role of inflammation in fibrosis is controversial, it is still considered to be an important component of IPF. Recently, Kim et al. (2019) pointed out that RBM47 promotes the EMT of cells by promoting TJP1-mediated alternative splicing. Globally, EMT is considered to be one of the key mechanisms of PF. When

tissues are subjected to various injuries, a series of immune signals are generated, leading to inflammation and promoting EMT. In this process, macrophages, neutrophils and other immune cells are recruited and release proinflammatory cytokines to maintain inflammation and pulmonary fibrosis (Salton et al., 2019). In conclusion, we speculate that the above three genes are closely related to the progression of pulmonary fibrosis. However, studies on RBM11 and ZNF14 in lung diseases are rare.

These results indicated that the key genes screened by bioinformatics methods were highly correlated with the occurrence and development of IPF, and had a significant correlation with the prognosis of IPF patients. Therefore, the above five key genes can provide reference for the diagnosis and treatment of IPF. We also analyzed the risk model. By drawing the time-dependent ROC curve of the prognostic model, we found that the AUC value gradually increased with the increase of time, indicating that the accuracy of our prognostic model was good. Finally, the prognostic model was verified by the GSE93606 dataset. It can be seen that the prognostic model is also applicable to this dataset, which further confirms that the prognostic risk model has a strong and stable prediction efficiency.

However, the study also has certain limitations. First, our results are based on data from existing public databases. Therefore, a large-scale, prospective, multicenter study is needed to further validate our results. Secondly, our study population is mainly from European and American populations. Therefore, our findings may not be optimal for patients from other countries and ethnicities. Finally, the correlation between some key genes and the development and progression of IPF has not been confirmed by biological experiments. In follow-up studies, experimental validation will be performed to reveal the relationship between key genes and IPF. In this way, we can determine their suitability as new diagnostic and therapeutic targets to provide a rationale for the clinical diagnosis and treatment of IPF.

Data availability statement

Publicly available datasets were analyzed in this study. This data can be found here: https://www.ncbi.nlm.nih.gov/geo/query/acc.cgi?acc=GSE28042 https://www.ncbi.nlm.nih.gov/geo/query/acc.cgi

Author contributions

Conceptualization, ZW; Data curation, ZW and HT; Formal analysis, JH and HT; Funding acquisition, XZ; Investigation, JW; Methodology, LS and JW; Software, ZW and LS; Validation, JW and JH; Writing—original draft, ZW and LS; Writing—review and editing, ZW, LS, and XZ.

Funding

This research was supported by grants from The National Natural Science Foundation of China (81301906); Horizontal Scientific Research Project of Soochow University (H201033).

Conflict of interest

The authors declare that the research was conducted in the absence of any commercial or financial relationships that could be construed as a potential conflict of interest.

Publisher's note

All claims expressed in this article are solely those of the authors and do not necessarily represent those of their affiliated organizations, or those of the publisher, the editors and the reviewers. Any product that may be evaluated in this article, or claim that may be made by its manufacturer, is not guaranteed or endorsed by the publisher.

Supplementary material

The Supplementary Material for this article can be found online at: https://www.frontiersin.org/articles/10.3389/fgene.2022.1059325/full#supplementary-material

References

Au, P. Y., and Yeh, W. C. (2007). Physiological roles and mechanisms of signaling by TRAF2 and TRAF5. *Adv. Exp. Med. Biol.* 597, 32–47. doi:10.1007/978-0-387-70630-6_3

Barratt, S. L., Creamer, A., Hayton, C., and Chaudhuri, N. (2018). Idiopathic pulmonary fibrosis (IPF): An overview. *J. Clin. Med.* 7, E201. doi:10.3390/jcm7080201

Ben-David, Y., Mizrachi, T., Kagan, S., Krisher, T., Cohen, E., Brenner, T., et al. (2016). RIC-3 expression and splicing regulate nAChR functional expression. *Mol. Brain* 9, 47. doi:10.1186/s13041-016-0231-5

Berger, S. L., Kouzarides, T., Shiekhattar, R., and Shilatifard, A. (2009). An operational definition of epigenetics. *Genes Dev.* 23, 781–783. doi:10.1101/gad.1787609

Boccaletto, P., Machnicka, M. A., Purta, E., Piatkowski, P., Baginski, B., Wirecki, T. K., et al. (2018). Modomics: A database of RNA modification pathways. 2017 update. *Nucleic Acids Res.* 46, D303–D307. doi:10.1093/nar/gkx1030

Cao, Z., Song, M., Liu, Y., Pang, J., Li, Z., Qi, X., et al. (2020). A novel pathophysiological classification of silicosis models provides some new insights into the progression of the disease. *Ecotoxicol. Environ. Saf.* 202, 110834. doi:10.1016/j.ecoenv.2020.110834

Chang, G., Shi, L., Ye, Y., Shi, H., Zeng, L., Tiwary, S., et al. (2020). YTHDF3 induces the translation of m(6)a-enriched gene transcripts to promote breast cancer brain metastasis. *Cancer Cell* 38, 857–871. e7. doi:10.1016/j.ccell.2020.10.004

Chen, X. Y., Zhang, J., and Zhu, J. S. (2019). The role of m(6)A RNA methylation in human cancer. *Mol. Cancer* 18, 103. doi:10.1186/s12943-019-1033-z

Cox, D. R. (1972). "Regression models and life-tables," in *Breakthroughs in statistics*. Editors S. Kotz and N. L. Johnson (Berlin, Germany: Springer Science & Business Media), 34.

Della Latta, V., Cecchettini, A., Del Ry, S., and Morales, M. A. (2015). Bleomycin in the setting of lung fibrosis induction: From biological mechanisms to counteractions. *Pharmacol. Res.* 97, 122–130. doi:10.1016/j.phrs.2015.04.012

Deng, X., Su, R., Weng, H., Huang, H., Li, Z., and Chen, J. (2018). RNA N(6)-methyladenosine modification in cancers: Current status and perspectives. *Cell Res.* 28, 507–517. doi:10.1038/s41422-018-0034-6

Fischer, A., and Distler, J. (2019). Progressive fibrosing interstitial lung disease associated with systemic autoimmune diseases. *Clin. Rheumatol.* 38, 2673–2681. doi:10.1007/s10067-019-04720-0

Fitzgerald, E., Priestnall, S. L., and Lamb, C. R. (2017). Imaging diagnosis-computed tomography of traction bronchiectasis secondary to pulmonary fibrosis in A patterdale terrier. *Vet. Radiol. Ultrasound* 58, E42–E44. doi:10.1111/vru.12403

Girardet, L., AugièRE, C., Asselin, M. P., and BelleannéE, C. (2019). Primary cilia: Biosensors of the male reproductive tract. *Andrology* 7, 588–602. doi:10.1111/andr.12650

Gregory, A. D., Kliment, C. R., Metz, H. E., Kim, K. H., Kargl, J., Agostini, B. A., et al. (2015). Neutrophil elastase promotes myofibroblast differentiation in lung fibrosis. *J. Leukoc. Biol.* 98, 143–152. doi:10.1189/jlb.3HI1014-493R

He, Y., Thummuri, D., Zheng, G., Okunieff, P., Citrin, D. E., Vujaskovic, Z., et al. (2019). Cellular senescence and radiation-induced pulmonary fibrosis. *Transl. Res.* 209, 14–21. doi:10.1016/j.trsl.2019.03.006

Huang, J. Z., and Liu, L. (2006). Polynomial spline estimation and inference of proportional hazards regression models with flexible relative risk form. *Biometrics* 62, 793–802. doi:10.1111/j.1541-0420.2005.00519.x

Jain, R., Javidan-Nejad, C., Alexander-Brett, J., Horani, A., Cabellon, M. C., Walter, M. J., et al. (2012). Sensory functions of motile cilia and implication for bronchiectasis. *Front. Biosci.* 4, 1088–1098. doi:10.2741/s320

Jia, E., Ren, N., Guo, B., Cui, Z., Zhang, B., and Xue, J. (2022). Construction and validation of a novel prognostic model for lung squamous cell cancer based on N6-methyladenosine-related genes. *World J. Surg. Oncol.* 20, 59. doi:10.1186/s12957-022-02509-1

Kim, Y. E., Won, M., Lee, S. G., Park, C., Song, C. H., and Kim, K. K. (2019). RBM47-regulated alternative splicing of TJP1 promotes actin stress fiber assembly during epithelial-to-mesenchymal transition. *Oncogene* 38, 6521–6536. doi:10.1038/s41388-019-0892-5

King, T. E., Pardo, A., and Selman, M. (2011). Idiopathic pulmonary fibrosis. *Lancet* 378, 1949–1961. doi:10.1016/S0140-6736(11)60052-4

Klopf, J., Brostjan, C., Eilenberg, W., and Neumayer, C. (2021). Neutrophil extracellular traps and their implications in cardiovascular and inflammatory disease. *Int. J. Mol. Sci.* 22, E559. doi:10.3390/ijms22020559

Kumar, A., Kapnadak, S. G., Girgis, R. E., and Raghu, G. (2018). Lung transplantation in idiopathic pulmonary fibrosis. *Expert Rev. Respir. Med.* 12, 375–385. doi:10.1080/17476348.2018.1462704

Li, B., Cairns, J. A., Robb, M. L., Johnson, R. J., Watson, C. J., Forsythe, J. L., et al. (2016). Predicting patient survival after deceased donor kidney transplantation using flexible parametric modelling. *BMC Nephrol.* 17, 51. doi:10.1186/s12882-016-0264-0

Li, L. J., Fan, Y. G., Leng, R. X., Pan, H. F., and Ye, D. Q. (2018). Potential link between m(6)A modification and systemic lupus erythematosus. *Mol. Immunol.* 93, 55–63. doi:10.1016/j.molimm.2017.11.009

Li, S. X., Yan, W., Liu, J. P., Zhao, Y. J., and Chen, L. (2021). Long noncoding RNA SNHG4 remits lipopolysaccharide-engendered inflammatory lung damage by inhibiting METTL3 - mediated m(6)A level of STAT2 mRNA. *Mol. Immunol.* 139, 10–22. doi:10.1016/j.molimm.2021.08.008

Li, Z. X., Zheng, Z. Q., Yang, P. Y., Lin, L., Zhou, G. Q., Lv, J. W., et al. (2022). WTAP-mediated m(6)A modification of lncRNA DIAPH1-AS1 enhances its stability to facilitate nasopharyngeal carcinoma growth and metastasis. *Cell Death Differ.* 29, 1137–1151. doi:10.1038/s41418-021-00905-w

Liu, J., Ren, D., Du, Z., Wang, H., Zhang, H., and Jin, Y. (2018). m(6)A demethylase FTO facilitates tumor progression in lung squamous cell carcinoma by regulating MZF1 expression. *Biochem. Biophys. Res. Commun.* 502, 456–464. doi:10.1016/j.bbrc.2018.05.175

Luyt, C. E. (2020). Herpes simplex virus pneumonia. *Virol. (Montrouge)* 24, 307–313. doi:10.1684/vir.2020.0860

Maher, T. M., Bendstrup, E., Dron, L., Langley, J., Smith, G., Khalid, J. M., et al. (2021). Global incidence and prevalence of idiopathic pulmonary fibrosis. *Respir. Res.* 22, 197. doi:10.1186/s12931-021-01791-z

Meng, Y., Zhang, Q., Wang, K., Zhang, X., Yang, R., Bi, K., et al. (2021). RBM15-mediated N6-methyladenosine modification affects COVID-19 severity by regulating the expression of multitarget genes. *Cell Death Dis.* 12, 732. doi:10.1038/s41419-021-04012-z

Pira, E., Donato, F., Maida, L., and Discalzi, G. (2018). Exposure to asbestos: Past, present and future. *J. Thorac. Dis.* 10, S237–S245. doi:10.21037/jtd.2017.10.126

Presson, A. P., Sobel, E. M., Papp, J. C., Suarez, C. J., Whistler, T., Rajeevan, M. S., et al. (2008). Integrated weighted gene co-expression network analysis with an application to chronic fatigue syndrome. *BMC Syst. Biol.* 2, 95. doi:10.1186/1752-0509-2-95

Raghu, G., Rochwerg, B., Zhang, Y., Garcia, C. A., Azuma, A., Behr, J., et al. (2015). An official ATS/ERS/JRS/ALAT clinical practice guideline: Treatment of idiopathic pulmonary fibrosis. An update of the 2011 clinical practice guideline. *Am. J. Respir. Crit. Care Med.* 192, e3–e19. doi:10.1164/rccm.201506-1063ST

Richeldi, L., Collard, H. R., and Jones, M. G. (2017). Idiopathic pulmonary fibrosis. *Lancet* 389, 1941–1952. doi:10.1016/S0140-6736(17)30866-8

Salton, F., Volpe, M. C., and Confalonieri, M. (2019). Epithelial¯Mesenchymal transition in the pathogenesis of idiopathic pulmonary fibrosis. *Med. Kaunas.* 55, E83. doi:10.3390/medicina55040083

Spagnolo, P., and Wuyts, W. (2017). Acute exacerbations of interstitial lung disease: Lessons from idiopathic pulmonary fibrosis. *Curr. Opin. Pulm. Med.* 23, 411–417. doi:10.1097/MCP.0000000000000405

Sun, J., Ping, Y., Huang, J., Zeng, B., Ji, P., and Li, D. (2021). N6-Methyladenosine-Regulated mRNAs: Potential prognostic biomarkers for patients with lung adenocarcinoma. *Front. Cell Dev. Biol.* 9, 705962. doi:10.3389/fcell.2021.705962

Tang, Y., Chen, K., Song, B., Ma, J., Wu, X., Xu, Q., et al. (2021). m6A-Atlas: a comprehensive knowledgebase for unraveling the N6-methyladenosine (m6A) epitranscriptome. *Nucleic Acids Res.* 49, D134–d143. doi:10.1093/nar/gkaa692

Wang, T., Kong, S., Tao, M., and Ju, S. (2020). The potential role of RNA N6-methyladenosine in Cancer progression. *Mol. Cancer* 19, 88. doi:10.1186/s12943-020-01204-7

Wanna-Udom, S., Terashima, M., Lyu, H., Ishimura, A., Takino, T., Sakari, M., et al. (2020). The m6A methyltransferase METTL3 contributes to Transforming Growth Factor-beta-induced epithelial-mesenchymal transition of lung cancer cells through the regulation of JUNB. *Biochem. Biophys. Res. Commun.* 524, 150–155. doi:10.1016/j.bbrc.2020.01.042

Yang, L., Wang, Y., Pan, Z., Gao, S., Zou, B., Lin, Z., et al. (2018). Tetraspanin 1 inhibits TNFα-induced apoptosis via NF-κB signaling pathway in alveolar epithelial cells. *Inflamm. Res.* 67, 951–964. doi:10.1007/s00011-018-1189-9

Yin, L., Cai, Z., Zhu, B., and Xu, C. (2018). Identification of key pathways and genes in the dynamic progression of HCC based on WGCNA. *Genes (Basel)* 9, E92. doi:10.3390/genes9020092

Yue, C., Chen, J., Li, Z., Li, L., Chen, J., and Guo, Y. (2020). microRNA-96 promotes occurrence and progression of colorectal cancer via regulation of the AMPKα2-FTO-m6A/MYC axis. *J. Exp. Clin. Cancer Res.* 39, 240. doi:10.1186/s13046-020-01731-7

Yue, Y., Liu, J., and He, C. (2015). RNA N6-methyladenosine methylation in post-transcriptional gene expression regulation. *Genes Dev.* 29, 1343–1355. doi:10.1101/gad.262766.115

frontiers | Frontiers in Cell and Developmental Biology

TYPE Original Research
PUBLISHED 06 January 2023
DOI 10.3389/fcell.2022.1080626

OPEN ACCESS

EDITED BY
James V. Dunne,
Providence Health Care, Canada

REVIEWED BY
Michael Tellier,
University of Oxford, United Kingdom
Nathan Archer,
University of Nottingham,
United Kingdom
Shifeng Xue,
National University of Singapore,
Singapore

*CORRESPONDENCE
Riccardo Pecori,
r.pecori@dkfz-heidelberg.de
Fotini Nina Papavasiliou,
n.papavasiliou@dkfz-heidelberg.de

†PRESENT ADDRESS
Isabel Chillón, Institut de Génétique Moléculaire de Montpellier, Centre National de la Recherche Scientifique, University of Montpellier, CNRS-UMR 5535, Montpellier, France

SPECIALTY SECTION
This article was submitted to Epigenomics and Epigenetics, a section of the journal Frontiers in Cell and Developmental Biology

RECEIVED 26 October 2022
ACCEPTED 12 December 2022
PUBLISHED 06 January 2023

CITATION
Pecori R, Chillón I, Lo Giudice C, Arnold A, Wüst S, Binder M, Marcia M, Picardi E and Papavasiliou FN (2023), ADAR RNA editing on antisense RNAs results in apparent U-to-C base changes on overlapping sense transcripts.
Front. Cell Dev. Biol. 10:1080626.
doi: 10.3389/fcell.2022.1080626

ADAR RNA editing on antisense RNAs results in apparent U-to-C base changes on overlapping sense transcripts

Riccardo Pecori[1,2]*, Isabel Chillón[3†], Claudio Lo Giudice[4], Annette Arnold[1], Sandra Wüst[5], Marco Binder[5], Marco Marcia[3], Ernesto Picardi[4] and Fotini Nina Papavasiliou[1]*

[1]Division of Immune Diversity, German Cancer Research Centre (DKFZ), Research Program Immunology and Cancer, Heidelberg, Germany, [2]Helmholtz Institute for Translational Oncology (HI-TRON), Mainz, Germany, [3]European Molecular Biology Laboratory (EMBL) Grenoble, Grenoble, France, [4]Department of Biosciences, Biotechnologies and Biopharmaceutics, University of Bari "Aldo Moro", Bari, Italy, [5]Research Group "Dynamics of Early Viral Infection and the Innate Antiviral Response," German Cancer Research Centre (DKFZ), Research Program Infection, Inflammation and Cancer, Division Virus Associated Carcinogenesis (F170), Heidelberg, Germany

Despite hundreds of RNA modifications described to date, only RNA editing results in a change in the nucleotide sequence of RNA molecules compared to the genome. In mammals, two kinds of RNA editing have been described so far, adenosine to inosine (A-to-I) and cytidine to uridine (C-to-U) editing. Recent improvements in RNA sequencing technologies have led to the discovery of a continuously growing number of editing sites. These methods are powerful but not error-free, making routine validation of newly-described editing sites necessary. During one of these validations on *DDX58* mRNA, along with A-to-I RNA editing sites, we encountered putative U-to-C editing. These U-to-C edits were present in several cell lines and appeared regulated in response to specific environmental stimuli. The same findings were also observed for the human long intergenic non-coding RNA p21 (hLincRNA-p21). A more in-depth analysis revealed that putative U-to-C edits result from A-to-I editing on overlapping antisense RNAs that are transcribed from the same loci. Such editing events, occurring on overlapping genes transcribed in opposite directions, have recently been demonstrated to be immunogenic and have been linked with autoimmune and immune-related diseases. Our findings, also confirmed by deep transcriptome data, demonstrate that such loci can be recognized simply through the presence of A-to-I and U-to-C mismatches within the same locus, reflective A-to-I editing both in the sense-oriented transcript and in the cis-natural antisense transcript (cis-NAT), implying that such clusters could be a mark of functionally relevant ADAR1 editing events.

KEYWORDS

ADAR, RNA editing, U-to-C, MultiEditR, DDX58/RIG-I, LINC-P21

1 Introduction

Recent years have seen an exponential increase in RNA sequencing (RNA-seq) technologies providing scientists with an incredible amount of transcriptomic data. Once compared to genomic data (DNA-seq), RNA-seq reveals information about several post-transcriptional processes that RNA molecules can undergo. For example, RNA editing is a mechanism that alters the RNA sequence itself. In mammals, two distinct kinds of RNA editing have been described so far, adenosine to inosine (A-to-I) and cytidine to uridine (C-to-U). These edits are the result of the deamination activity by proteins belonging to the adenosine deaminase acting on RNA (ADAR) (Bass, 2002; Nishikura, 2010; Savva et al., 2012) and the apolipoprotein B mRNA editing enzyme catalytic subunit (APOBEC) (Blanc and Davidson, 2010; Sharma et al., 2015, 2019; Lerner et al., 2018; Pecori et al., 2022) families, respectively. Reverse transcriptase incorporates guanosines (G) and thymidines (T) into cDNA at positions where inosines and uridines are present in the RNA, leading to base changes not present in the genomic DNA. For this reason, editing sites can be detected by directly comparing RNA-seq to DNA-seq data or a reference genome (Levanon et al., 2004; Picardi and Pesole, 2013; Wang et al., 2016; John et al., 2017; Piechotta et al., 2017).

Several bioinformatics pipelines have been developed for the analysis of next-generation sequencing (NGS) data to detect RNA editing sites (Ramaswami and Li, 2016; Eisenberg and Levanon, 2018; Diroma et al., 2019), leading to a constant increase of entries in their catalogs and the generation of new databases (Kiran and Baranov, 2010; Ramaswami and Li, 2014; Picardi et al., 2017; Mansi et al., 2021). Despite these improvements, RNA editing detection in NGS datasets remains challenging due to the many sources of DNA-RNA sequence mismatches, leading to the necessity of routine validation by reverse transcription-polymerase chain reaction (RT-PCR). RT-PCR is a two-step method in which the RNA is first retrotranscribed into cDNA, and then cDNA is amplified at specific locations *via* PCR. This method has some variations; for example, cDNA can be produced from oligo-dT, random hexamers, or specific primers for a particular transcript. In this latter case, and when a Hot Start DNA Polymerase is used, the reverse transcription and PCR amplification of a specific target take place one after the other in the same tube, in a so-called one-step RT-PCR reaction. This method allows a fast and easy RT-PCR setup, optimal for RNA editing detection validation. Additionally, one-step RT-PCRs exclusively generate cDNA from the transcript of interest leading to higher sensitivity in RNA editing detection when the transcript of interest is poorly expressed or edited (Wacker and Godard, 2005; Kluesner et al., 2021).

In this study, we report the observation of a putative U-to-C RNA editing while validating some A-to-I ADAR1 editing sites. U-to-C edits were observed on an mRNA (*DDX58*) and a long intergenic non-coding RNA (*hLincRNA-p21*) nearby A-to-I editing sites. In both cases, U-to-C editing appeared to be regulated upon specific stimulations a feature characteristic of RNA modifications. After looking for an RNA modification that could lead to this base change, we realized that U-to-C edits result from A-to-I editing on overlapping antisense RNAs that had not been previously described. We have also confirmed this finding by the analysis of known sense–antisense transcripts through deep transcriptome data from human tissues.

2 Materials and methods

2.1 Cell lines, treatments, and transfections

RCK8 cells (DSMZ, Cat# ACC-561, RRID: CVCL_1883) and U2932 (DSMZ, Cat# ACC-633, RRID: CVCL_1896) were cultured at 37°C, 5% CO_2, in RPMI-1640 medium (Sigma-Aldrich, Cat# R8758), supplemented with 15% fetal bovine serum (PAN Biotech, Cat# P40-37100) and 1% of Penicillin/Streptomycin (Sigma-Aldrich, Cat# P4333). A549 cells (DSMZ, Cat# ACC-107, RRID: CVCL_0023) were cultured at 37°C, 5% CO_2 in high-glucose DMEM (Sigma-Aldrich, Cat# D6429) supplemented with 10% fetal bovine serum (PAN Biotech, Cat# P40-37100) and 1% penicillin/streptomycin (Sigma-Aldrich, Cat# P4333). HEK293T cells (obtained from DKFZ, ATCC, Cat# CRL-3216, RRID: CVCL_0063) were cultured at 37°C, 5% CO_2 in high-glucose DMEM (Sigma-Aldrich, Cat# D6429) supplemented with 5% FBS (PAN Biotech, Cat# P40-37100) and 1% penicillin/streptomycin (Sigma-Aldrich, Cat# P4333). Cell lines were authenticated using Multiplex Cell Authentication by Multiplexion (Heidelberg, Germany) as described recently (Castro et al., 2013). Additionally, the purity of cell lines was validated using the Multiplex cell Contamination Test by Multiplexion (Heidelberg, Germany) as described recently (Schmitt and Pawlita, 2009). No Mycoplasma, SMRV or interspecies contamination was detected.

For interferon-alpha (IFNα) stimulation, 2.5×10^5 HEK293T cells were seeded in 12-well plates in a total volume of 1 ml media containing 200 U/ml of IFN-α (PBL Assay Science, Cat# 11100–1). After 16 h, cells were collected, and RNA was extracted using a Qiagen RNeasy Plus kit (Qiagen, Cat# 74134).

For doxorubicin treatment, 10^5 HEK293T cells were seeded in 24-well plates to have around 30%–50% confluency the day after. The following day the cells were transfected with pcDNA3-hLincRNAp21-MS2 (Chillón and Pyle, 2016) using a mix of plasmid DNA and polyethyleneimine (PEI, Polysciences, Cat# 23966) in an approximately 1:1 ratio (2.5 μg DNA:2 μg of PEI). 6 h post-transfection, the media was replaced with new complete media and 2 μM doxorubicin hydrochloride (Sigma-Aldrich, Cat# D1515) or DMSO only as control (Sigma-Aldrich, Cat# D2650) were added 10–12 h post-transfection, for 12 h. RNA was

then extracted using a Qiagen RNeasy Plus kit (Qiagen, Cat# 74134).

2.2 Plasmids

pcDNA3-hLincRNAp21-MS2 contains the 3898 nt-long LIsoE2 isoform of the human lincRNA-p21 (GenBank: KU881768.1) tagged with 24 copies of MS2 RNA hairpins, as previously described (Chillón and Pyle, 2016).

LentiCRISPRv2 was a gift from Feng Zhang (Addgene, plasmid #52961; https://addgene.org/52961; RRID: Addgene_52961) (Sanjana et al., 2014). DNA oligos #12–13 were cloned into this plasmid following the instructions of "lenti-CRISPRv2 and lentiGuide oligo cloning protocol" (Addgene plasmid #52961) to generate lenti-CRISPR-ADAR1 exon 4 [from Pestal et al. (2015); Supplementary Figure S7A]. As a control, lenti-CRISPR-NT (Lenti-NT) was cloned accordingly using oligos #14–15 based on control 800 from the GeCKO v2 library (Sanjana et al., 2014). pCMVDR8.91 (coding for HIV gag-pol) and pMD2.G (encoding the VSV-G glycoprotein) were a kind gift from Prof. Didier Trono (Lausanne, Switzerland).

pSpCas9(BB)-2A-GFP (PX458) was a gift from Feng Zhang (Addgene plasmid # 48138; https://n2t.net/addgene:48138; RRID:Addgene_48138) (Ran et al., 2013). DNA oligos #16–19 were cloned into this plasmid linearized by restriction digestion (BbsI) using NEBuilder® HiFi DNA Assembly Master Mix (NEB, Cat# E2621). We, therefore, obtained three plasmids for knocking out human DTWD1, DTWD2, or TSR3 as previously described (Takakura et al., 2019; Babaian et al., 2020) and an additional non-targeting control (NT-ctrl) based on control 800 from the GeCKO v2 library (Sanjana et al., 2014).

2.3 Genome-wide A-to-I sense-antisense RNA editing analysis

Ribo-depleted RNA-seq experiments from seven human tissues (Supplementary Material S1) were selected from the "RNA Atlas" project (Lorenzi et al., 2021) and downloaded from GEO under the accession GSE138734. Known annotations for antisense and protein-coding genes were obtained from Gencode (v38), downloaded in gtf format, and converted into bed format. Antisense and protein-coding annotations were intersected by means of the "intersect" function embedded in the Bedtools package (Quinlan, 2014), discarding overlapping intervals less than 300 bp. The resulting genomic coordinates of overlapping sense-antisense genes were used as input in a modified version of REDItools (Picardi and Pesole, 2013), able to split reads according to their orientation. Only editing candidates supported by more than five reads and organized in non-redundant clusters (represented by A-to-G or T-to-C mismatches according to gene strandness) were retained. All the editing sites considered in this analysis are described in Supplementary Material S1.

Circular heatmaps were generated using the R package circlize (Gu et al., 2014) and the cytoband representation of the human genome assembly hg38. Heatmaps color scale represents an RPKM-like normalization of editing events.

The entire pipeline and scripts are available at https://github.com/BioinfoUNIBA/antisenseEditing.

2.4 A-to-I and U-to-C editing sites validation and quantification

For editing site validation, PCRs were performed on genomic DNA (gDNA) and RNA. gDNA was extracted using the High Pure PCR Template Preparation kit (Roche, Cat# 11796828001) following manufacturer instructions. PCR amplification was performed using Q5® High-Fidelity DNA Polymerase (NEB, Cat# M0491). RNA was extracted using the RNeasy Plus Mini kit (Qiagen, Cat# 74134) and treated with DNase (Invitrogen, Cat# AM 1907). Following RNA extraction, RT-PCRs were performed with gene-specific primers (Supplementary Table S1) and a One-step RT-PCR kit (Qiagen, Cat# 210212). All the PCR products were purified (Macherey-Nagel, Cat# 740609) and analyzed by Sanger sequencing. Quantification of editing was performed directly from the Sanger traces using MultiEditR (Kluesner et al., 2021). Alternatively, the PCR products were cloned using a CloneJET PCR cloning kit (Thermo Scientific, Cat# K1232) according to the manufacturer's instructions and transformed into DH5a bacteria (NEB, Cat# C2987). Ten to twenty resultant bacteria colonies were sent for sequencing to determine edits and their frequency in the targeted region. All the primers used in this study were designed using Primer-BLAST (Ye et al., 2012), AmplifX 2.0.7 (by Nicolas Jullien; Aix-Marseille Univ, CNRS, INP, Inst Neurophysiopathol, Marseille, France—https://inp.univ-amu.fr/en/amplifx-manage-test-and-design-your-primers-for-pcr) or ApE (by M. Wayne Davis, https://jorgensen.biology.utah.edu/wayned/ape/). The chromosomal locations of all the editing sites analyzed in this study are listed in Supplementary Table S2.

2.5 RT-qPCR

RNA was extracted using the RNeasy Plus Mini kit (Qiagen, Cat# 74134). Before qPCR, RNA was additionally treated with DNase (Invitrogen, Cat# AM 1907). cDNA synthesis was then performed using ProtoScript M-MuLV First-Strand Synthesis Kit (NEB, Cat# E6300) using 1 μg of RNA DNAse digested. cDNA was synthesized using oligo-dT or random primers to detect *DDX58* or *hLincRNA-p21*, respectively. Two microliters of

a 1:2 diluted cDNA were used to set up a 10 µl qPCR reaction using SsoAdvanced Universal SYBR Green Supermix (Bio-rad, Cat# 1725270). Finally, fold change expression was calculated using the comparative CT method (ΔΔCT) (Livak and Schmittgen, 2001). Supplementary Table S1 lists all the primers used in this study.

2.6 Generation of a HEK293T ADAR1 knockout cell line

Lenti-CRISPR-ADAR1 or lenti-CRISPR-NT, in combination with pCMV-DR8.91 and pMD2.G, were calcium-phosphate transfected into HEK293T cells for lentiviral particle production (ratio 3:1:3). After 48–72 h, cell-free supernatant was collected and used for transduction of HEK293T cells. The transduced cells were selected with puromycin (1 µg/ml). As soon as non-transduced cells died (~2 days), ADAR1 knockout cells were seeded in 96-well plates in a limiting dilution (0.5 cells/well). Upon expansion of single clones, ADAR1 KO clones were validated by Western blot (Cell Signaling Technology, Cat# 14175, RRID: AB_2722520) following IFN-α stimulation using β-Actin as a loading control (Sigma-Aldrich, Cat# A5441, RRID: AB_476744). Lenti-NT control cells were kept polyclonal. After screening, clones three and four were shown to completely abolish ADAR1 (p110 and p150) expression (Supplementary Figure S7B). Therefore, clone three was used for the experiments conducted in this work.

2.7 Generation of HEK293T DTWD1, DTWD2 or TSR3 knockout cell lines

pSpCas9(BB)-2A-GFP carrying the sgRNAs for DTWD1, DTWD2 or TSR3 were transfected into HEK293T cells using Lipofectamine 2000 (ThermoFisher, Cat# 11668019) following manufacturer instructions. 48 h after transfection, GFP-positive cells were sorted and plated (one cell per well) in 96-well plates. The clonality was validated by visual inspection with a microscope, and positive clones were screened by Sanger sequencing.

2.8 Statistical analysis and data visualization

Data were analyzed and plotted using GraphPad Prism (version 9.3.1). Specific information about data presentation is provided in each figure caption throughout the manuscript. Statistical significance was calculated by unpaired, two-tailed Student's t-test: $^{*}p < 0.05$, $^{**}p < 0.01$, $^{***}p < 0.001$, $^{****}p < 0.0001$, ns: not significant.

3 Results

3.1 Observation of a persistent U-to-C base change in *DDX58*

RNA-seq data analysis represents a powerful method to detect new RNA editing sites. Unfortunately, these technologies are not error-free; thus, validation of these newly discovered RNA editing sites is still necessary. This validation is performed *via* PCR amplification of a specific region containing the editing sites to be validated from either DNA or cDNA (the latter represents the RNA). In a recent work from our lab, we identified RNA editing sites comparing RNA- and DNA-seq data in a cohort of Diffuse large B cell lymphoma (DLBCL) patients (Pecori et al., 2021). We used a one-step RT-PCR reaction to validate some of those sites due to its higher sensitivity in RNA editing detection for low edited or expressed transcripts (Wacker and Godard, 2005; Kluesner et al., 2021). While validating some A-to-I editing sites within the transcript *DDX58* in RCK8, a B cell lymphoma-derived cell line, we also observed the presence of numerous putative U-to-C edits. In a short region (~600 nucleotides) of the 3′ untranslated region (3′UTR) of *DDX58* we could detect 11 A-to-I sites and 11 U-to-C sites (Figure 1A, upper). A-to-I and U-to-C RNA editing events are observed as A-to-G and T-to-C in cDNA. Despite all the detections and quantifications being done on cDNA, throughout this manuscript, we refer to them as A-to-I and U-to-C base changes.

All those edits are visible in Sanger sequencing following amplification of cDNA but not genomic DNA (gDNA), validating them as real RNA editing sites (Figure 1A, lower). While U-to-C editing is well described in plants (Yoshinaga et al., 1996; Knie et al., 2016; Ruchika et al., 2021), it has been rarely described in Metazoans (Villegas et al., 2002; Liu et al., 2004); thus, we decided to investigate further this preliminary observation. We then performed the same validation on another three cell lines, namely U2932, HEK293T, and A549. Except for A549, we confirmed the observation of putative U-to-C base changes at the same precise sites identified in RCK8 (Figure 1B). To check a possible functional connection between the A-to-I and U-to-C editing, we quantified the frequency of U-to-C and A-to-I at all sites for all the cell lines (Figures 1C, D). No specific trend was observed, with different cell lines showing variations in the level of both editing types. Altogether these findings demonstrate the presence of an apparent and persistent U-to-C RNA editing in *DDX58* mRNA. This editing can be found at the exact locations in different cell lines, and it seems independent of A-to-I editing. Indeed, the A549 cell line shows high A-to-I editing within *DDX58* but no U-to-C editing.

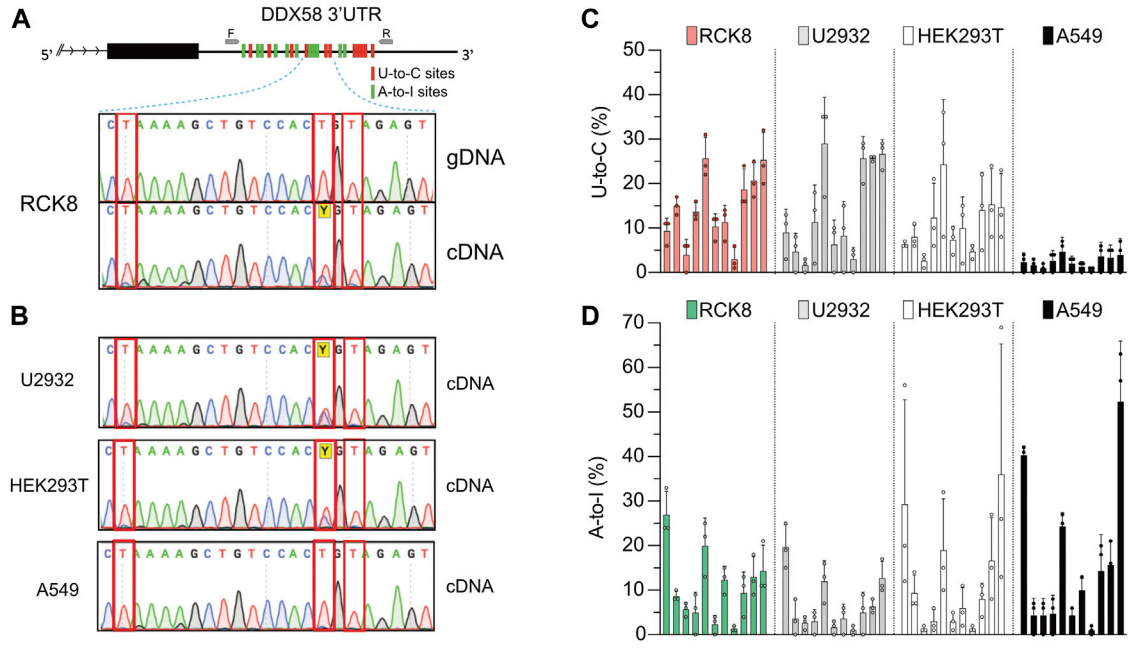

FIGURE 1
A persistent U-to-C base change in *DDX58* cDNA. **(A)** Upper: schematic representing the identification of 11 U-to-C (red bars) and 11 A-to-I (green bars) base changes within the 3′UTR of *DDX58* in the B cell line RCK8. Primers used for PCR amplification are indicated as small grey arrows. Lower: representative image of Sanger traces showing that U-to-C base changes (inside the red rectangles) are only present in cDNA and not in genomic DNA (gDNA). **(B)** These RNA base changes are present at the same in other cell lines. **(C,D)** Quantification of the 11 U-to-C **(C)** and 11 A-to-I **(D)** sites within different cell lines. Quantification was performed directly from Sanger traces using MultiEditR (Kluesner et al., 2021). Center = mean and error bars = standard deviation, N = 3.

3.2 U-to-C editing in *DDX58* mRNA is dynamic

It is known that RNA modification in general and RNA editing specifically are crucial during the cellular response to environmental stimuli or stress (Roundtree et al., 2017; Tan et al., 2017). To test if the U-to-C editing observed in *DDX58* would change after specific stimulation, we decided to treat HEK293T cells with interferon-alpha (IFNα). IFNα treatment has two relevant consequences for this experiment: first, it induces ADAR1 p150 expression (Patterson et al., 1995), which leads to an increase in A-to-I RNA editing (Hartwig et al., 2004, 2006); second, it leads to the overexpression of *DDX58*, which is an interferon-stimulated gene (ISG) itself (Matsumiya and Stafforini, 2010). HEK293T cells were chosen for this experiment because of the high level of U-to-C editing observed within *DDX58* and because they are responsive to IFNα stimulation (Figures 1B, C and Supplementary Figure S1). Following stimulation, RNA extraction and one-step RT-PCR were performed. PCR products were introduced into bacteria, and single bacterial colonies were sequenced using Sanger sequencing. Alignment to the unedited reference genome allowed us to easily count the editing sites in the presence or absence of stimulation to assess the frequency of A-to-I and U-to-C editing for each site in the two conditions (Figure 2A and Supplementary Figure S2). Not surprisingly, IFNα stimulation leads to a significant increase in A-to-I editing (~4-fold increase of the mean, Figures 2B, D) which is expected due to the induction of ADAR1 p150 expression (Patterson et al., 1995; Hartwig et al., 2004, 2006). However, the opposite effect was observed for U-to-C editing, for which the treatment led to a significant decrease (~5-fold decrease of the mean, Figures 2B, C). These data suggest that putative U-to-C base changes are differently regulated compared to ADAR-induced A-to-I editing.

3.3 U-to-C editing within the long intergenic non-coding RNA *hLincRNA-p21*

After characterizing the U-to-C editing within *DDX58* mRNA, we asked if this editing was also present in other RNA species, such as long non-coding RNAs (lncRNAs). *LincRNA-p21* is a crucial molecule during the response to cellular stress driven by p53 (Huarte et al., 2010). While initially discovered in mice, *LincRNA-p21* is also present in humans (*hLincRNA-p21*, formally known as *TP53COR1*). Recent work has shown that hLincRNA-p21 contains

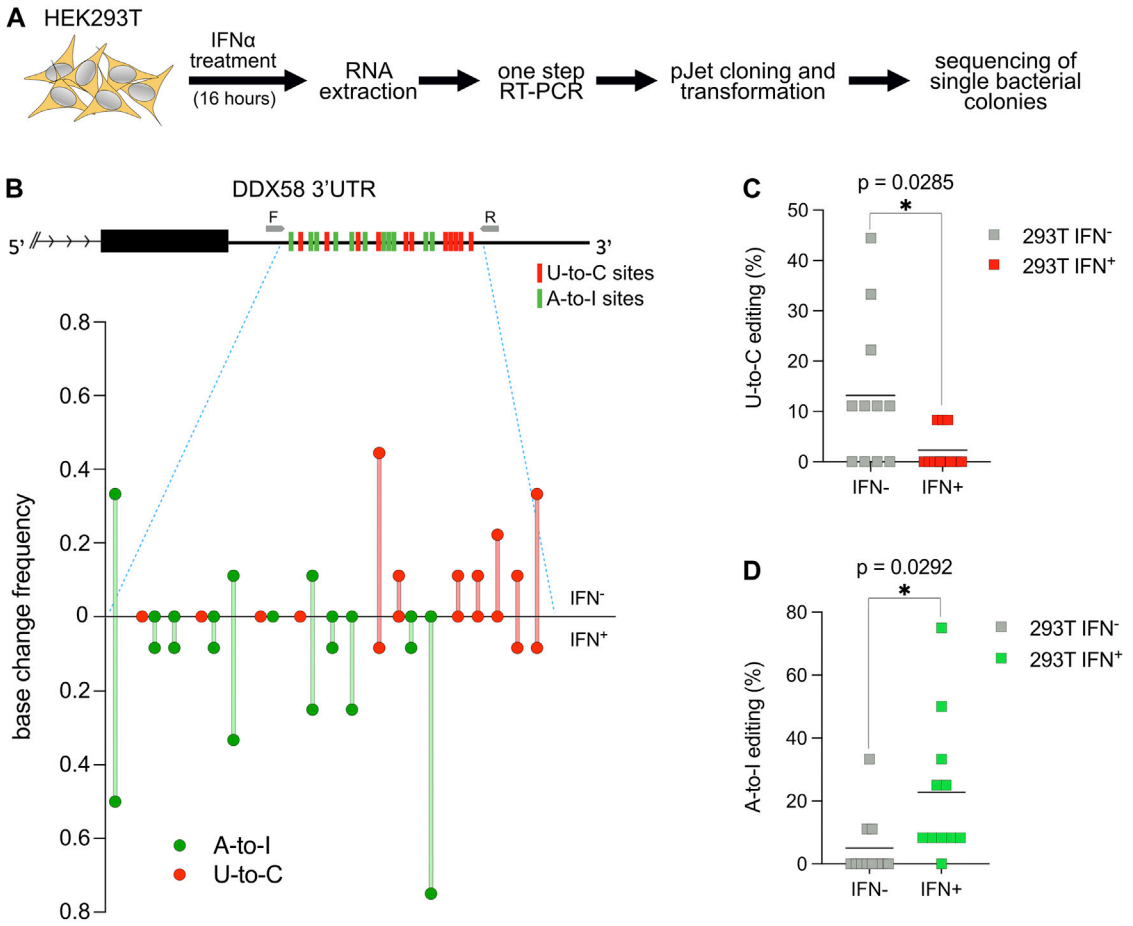

FIGURE 2
U-to-C base changes within DDX58 are dynamic. **(A)** Flowchart of the experiment. **(B)** Upper: schematic representing the 11 U-to-C (red bars) and 11 A-to-I (green bars) base changes within the 3′UTR of *DDX58*. Primers used for cDNA synthesis and PCR amplification are indicated as small grey arrows. Lower: Quantification of base changes within *DDX58* 3′UTR with and without interferon (IFN) treatment based on sequences from bacterial colonies (Supplementary Figure S2). U-to-Cs and A-to-Is are shown in red and green, respectively. **(C,D)** Dot plots showing the decrease in U-to-Cs and the increase A-to-Is upon IFN treatment. Each dot = one single site; line = mean. A two-tailed unpaired *t*-test was used to compare the differences (*$p < .05$).

inverted-repeat *Alu* elements, which can fold as independent domains (Chillón and Pyle, 2016). Interestingly, putative U-to-C editing events were identified in both sense and antisense *Alu* elements (Chillón and Pyle, 2016).

For this reason, we decided to first transfect in HEK293T a plasmid encoding *hLincRNA-p21* and then treat the transfected cells with doxorubicin, a chemotherapeutic drug that induces DNA damage. We then performed RNA extraction and one-step RT-PCR to amplify the sense *Alu*. Detection and quantification of editing were performed as described above for *DDX58* mRNA (Figure 3A). While doxorubicin treatment was shown to upregulate *hLincRNA-p21* in some cell lines (Chillón and Pyle, 2016), we did not observe any significant changes in the expression of the endogenous, or in the stability of the exogenous, *hLincRNA-p21* in HEK293T upon treatment (Supplementary Figure S3). In the absence of treatment, we observed only nine U-to-C and four A-to-I edits with editing frequency lower than 0.2 within the sense *Alu* (Figures 3B–D and Supplementary Figure S4). However, induction of DNA damage by doxorubicin leads to a significant increase in both editing types (~2.5- and ~16-fold increase of the mean for U-to-C and A-to-I, respectively; Figures 3B–D). Notably, we observed a substantial increase in the number of low-frequency (<0.1) edits that were not visible in the absence of stimulation (Figure 3B and Supplementary Figure S4). The increase of A-to-I editing upon DNA damage may be explained by recent findings showing an overall change in ADAR editing in response to DNA breaks (Jimeno et al., 2021). These data confirm the previous observation that putative U-to-C editing can also be identified in lncRNAs.

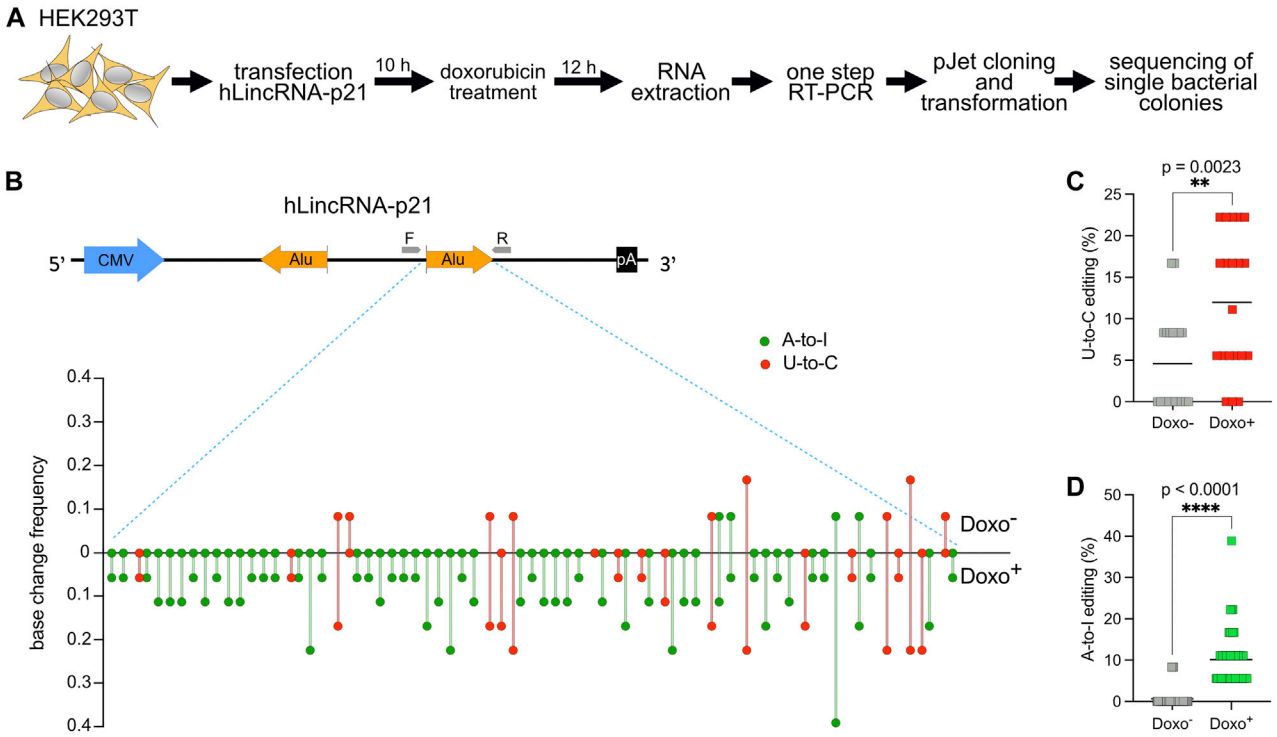

FIGURE 3
U-to-C base changes are present and dynamic also in the long intergenic non-coding RNA *hLincRNA-p21*. **(A)** Flowchart of the experiment. **(B)** Upper: schematic representing the plasmid used for overexpression of *hLincRNA-p21*. This long non-coding RNA contains two inverted Alu elements (big orange arrows). Primers used for cDNA synthesis and PCR amplification are represented as small grey arrows. Lower: Quantification of base changes within hLincRNA-p21 sense Alu element with and without doxorubicin (doxo) treatment based on sequences from bacterial colonies (Supplementary Figure S3). U-to-Cs and A-to-Is are shown in red and green, respectively. **(C,D)** Dot plots showing the increase of both U-to-Cs and A-to-Is upon doxorubicin treatment. Each dot = one single site; line = mean. A two-tailed unpaired *t*-test was used to compare the differences (**$p < 0.01$; ****$p < 0.0001$).

3.4 Apparent U-to-C base changes result from A-to-I antisense RNA editing

We then decided to look for the enzyme responsible for generating this U-to-C RNA editing. Few RNA modifications of uridines have been described to lead to a U-to-C base change. 4-thiouridine (s4U) itself leads to low levels of U-to-C transitions after reverse transcription (Hafner et al., 2010), and this level can be increased by chemical treatments of the RNA [reviewed in (Duffy et al., 2019)]. Indeed, s4U is often used in methods to study RNA metabolism because its presence can be easily detected *via* sequencing (Herzog et al., 2017; Schofield et al., 2018). Unfortunately, while s4U is present in bacterial and archaeal tRNAs, it has not been described in human tRNA (Boccaletto et al., 2018). It thus is very unlikely to be related to the U-to-C editing described here. In contrast, the 3-amino-3-carboxypropylation of uridine has been recently described in humans (Takakura et al., 2019). This modification leads to the formation of a 3-(3-amino-3-carboxypropyl) uridine (acp3U), which can be observed as an apparent U-to-C conversion caused by misincorporation during cDNA synthesis (Takakura et al., 2019; Kimura et al., 2020). Additionally, amino-carboxypropylation of methylated pseudouridine (ψ) has been described in rRNA in humans (Meyer et al., 2016). This m1acp3ψ modification perturbs standard base pairing during cDNA synthesis leading to U-to-C conversion (Babaian et al., 2020). Therefore, we decided to knock out the writers of these modifications, namely DTWD1, DTWD2, and TSR3, in HEK293T cells, as previously described (Takakura et al., 2019; Babaian et al., 2020). We successfully obtained knockout cell lines for those proteins. However, we did not observe any changes in U-to-C editing within *DDX58* (Supplementary Figure S5).

A-to-I RNA editing has also been reported on antisense RNA, with some studies proposing that 15% of editing originated from transcripts expressed from the antisense strand (Porath et al., 2014). Widespread antisense transcription has been reported in humans, with 5%–10% of all genomic loci expressing overlapping sense and antisense

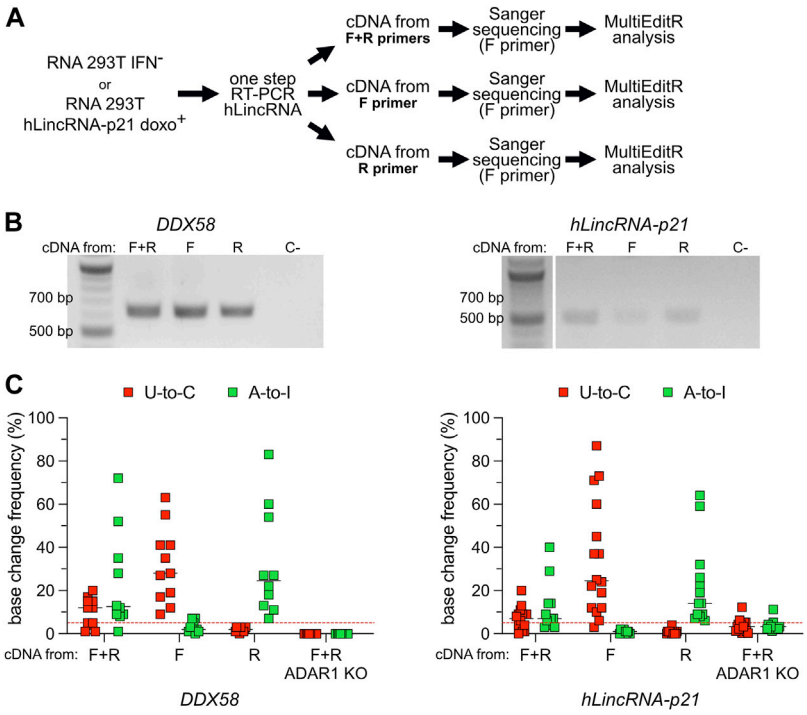

FIGURE 4
U-to-C base changes originate from A-to-I RNA editing on antisense RNA. **(A)** Flowchart of the experiment. **(B)** Representative agarose gel of the amplification products of *DDX58* and *hLincRNA-p21* upon one-step PCR using different primers for cDNA synthesis. C- = negative control. **(C)** Dot plots showing the editing frequency in U-to-Cs and A-to-Is measured from Sanger sequencing dependent on the primer used for cDNA synthesis. Only sites with editing higher than 5% in at least one condition are plotted. Each dot = one single site; line = median; red dashed line represents the limit of detection of MultiEditR (Kluesner et al., 2021). U-to-Cs and A-to-Is are shown in red and green, respectively.

RNAs (Lehner et al., 2002; Shendure and Church, 2002; Yelin et al., 2003). Overlapping sense and antisense RNAs often form structured motifs characterized by the presence of double-stranded hairpins that can act as substrates for ADAR (Supplementary Figure S6A). Using one-step RT-PCR methods with target-specific primers, the cDNA will be synthesized from both the sense and the antisense RNA. Following Sanger sequencing, A-to-I antisense RNA editing may result in an apparent U-to-C base (Supplementary Figure S6B). Therefore, we explored the possibility that previously-uncharacterized transcripts are expressed in antisense orientation to *DDX58* and *hLincRNA-p21* and modified by ADAR through A-to-I editing. To answer this question, we selected RNA samples from the two experimental conditions, which showed the majority of putative U-to-C editing in *DDX58* and *hLincRNA-p21*, namely IFN$^-$ and doxorubicin$^+$, respectively (Figures 2, 3). On these samples, we performed in parallel three different one-step RT-PCR, providing both forward (F) and reverse (R) primers, or only the F or only the R primer, during the cDNA synthesis step (Figure 4). In this way, we obtained strand-specific amplification, with F and R primers generating cDNA specifically from the antisense and sense RNA, respectively (Supplementary Figure S6B). Both, *DDX58* and *hLincRNA-p21* showed abundant amplification from the antisense RNA on an agarose gel (Figure 4B). Strikingly, antisense-specific amplification resulted in high detection of putative U-to-C and no detection of A-to-I. The opposite was observed following amplification of the sense RNA for both *DDX58* and *hLincRNA-p21* (Figure 4C). Additionally, standard one-step RT-PCR from a HEK293T ADAR1 KO cell line (Supplementary Figure S7) resulted in no U-to-C or A-to-I editing detected in *DDX58* and only a very low residual editing in *hLincRNA-p21* (Figure 4C). Our data demonstrate that the putative U-to-C editing results from A-to-I editing on the antisense RNA indicating high editing activity by ADAR1 on both sense and antisense *DDX58* and *hLincRNA-21*.

3.5 A-to-I antisense RNA editing in NGS

After observing antisense A-to-I RNA editing in both an mRNA and a lincRNA, we asked what the impact of this process

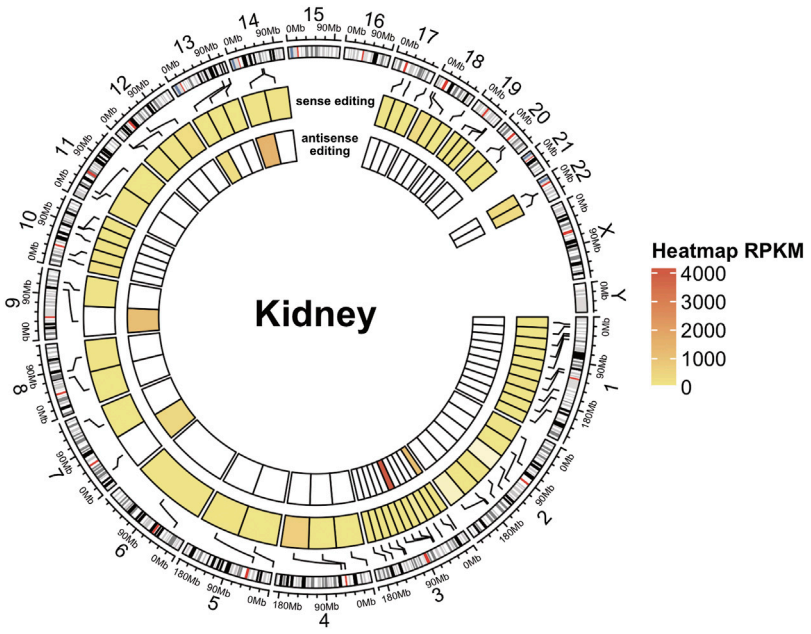

FIGURE 5
A-to-I antisense RNA editing in NGS data. Circular heatmap for a kidney RNA-seq sample. The external circle represents the chromosomes, and the two inner circles represent sense (intermediate circle) and antisense (internal circle) editing. A-to-I RNA editing locations are indicated with black lines connecting the heatmap to the cytoband context of the chromosomes (human genome assembly hg38). Editing levels are depicted in circular heatmaps using a color scale based on RPKM-like values.

at the transcriptome level in different tissues is. To elucidate this point, we investigated antisense A-to-I RNA editing genome-wide by using seven ribo-depleted strand-oriented RNA-seq experiments from various human tissues of the "RNA Atlas" project (Lorenzi et al., 2021). We created a catalog of sense-antisense gene overlaps based on Gencode annotations to provide an unbiased overview of antisense editing. Known antisense transcripts were initially selected from Gencode, then overlapping regions of at least 300 bp with sense transcripts were collected to a total number of 1677 suitable overlaps. For each one of these, corresponding to a well-defined genomic interval, we called RNA editing using pre-aligned RNA-seq reads and a modified version of the REDItools software (Picardi and Pesole, 2013) able to split reads according to their orientation. A-to-I RNA editing events supported by at least five reads and organized in clusters of A-to-G or T-to-C mismatches were selected for downstream analyses.

On the whole, we observed that the number of A-to-I editing changes, normalized by the overlap length, was higher in the sense strands of overlaps than in antisense strands, and this trend was common to all analyzed samples and tissues, supporting the previous notion that antisense editing is low Figure 5 and Supplementary Figure S8; and (Neeman et al., 2005). On average, only 199 out of 1677 potential overlaps showed evidence of A-to-I RNA editing. Of these, 21 displayed obvious sense and antisense editing, 164 sense editing, and 35 antisense editing only.

However, DDX58 was not among the transcripts identified by our approach, suggesting its limitations. Namely, antisense transcripts might be less abundant, leading to lower read depth (and problems in detecting editing); alternatively, naturally poor editing on some transcripts might be reported as "no editing" (depending on cut-offs). Both of these are limitations to our approach. These limitations could be cell type-specific or disease-specific. Overall though, our work suggests that clusters of A-to-I (and U-to-C) editing might specify dually edited, convergently transcribed regions, offering a potentially simple way to identify loci that may be of disease relevance (Li et al., 2022).

4 Discussion

Recent improvements in RNA-seq and DNA-seq data have provided scientists with a considerable amount of data from which several new RNA editing sites were discovered. However, these technologies are also affected by other sources of DNA-RNA sequence mismatches. Thus, RNA editing detection from NGS data remains a challenging task (Ramaswami and Li, 2016; Eisenberg and Levanon, 2018; Diroma et al., 2019), and validation of newly discovered editing sites is necessary. Here, we report the observation of U-to-C base changes and A-to-I

editing within *DDX58* mRNA and the lncRNA *hLincRNA-p21*. U-to-C edits show typical features of a *bona fide* RNA modification. Indeed, they can be identified in multiple cell systems and respond to environmental stimulation differently from other co-existing modifications. However, careful evaluation demonstrated that putative U-to-C corresponds to A-to-I editing introduced by ADAR on overlapping antisense transcripts (Figure 4). Antisense transcription is a frequent process within the human transcriptome (Lehner et al., 2002; Shendure and Church, 2002; Yelin et al., 2003). Overlapping sense and antisense RNAs result in a high sequence complementarity. Thus, these two molecules could potentially anneal to each other, creating a dsRNA that can function as a perfect substrate for ADAR [and in the absence of ADAR, for MDA5, which can sense such structures and ignite an interferon response (Li et al., 2022)]. Despite several studies proposing such a mechanism (Kumar and Carmichael, 1998; Wang et al., 2000; Carmichael, 2003), only a few cases of editing in sense–antisense pairs have been reported to date (Kimelman and Kirschner, 1989; Peters et al., 2003; Athanasiadis et al., 2004; Li et al., 2022).

On the other hand, sense and antisense transcripts folding co-transcriptionally as independent domains can also generate distinct dsRNA without needing to pair with each other (Heilman-Miller and Woodson, 2003; Lai et al., 2013). dsRNA structures formed by local intramolecular interactions are in line with other reports on ADAR editing, showing that the majority of A-to-I antisense editing events are observed within *Alu* regions and only rarely within regions that could result from inter-molecular sense-antisense RNAs interactions (Athanasiadis et al., 2004; Neeman et al., 2005; Kawahara and Nishikura, 2006). Our observations with regard to *hLincRNA-p21*, where no modifications were observed outside the *Alu* regions, are in line with the hypothesis of dsRNA formed by the intramolecular interaction (Kawahara and Nishikura, 2006; Chillón and Pyle, 2016).

For the transcripts whose analysis motivated the work we report herein (*DDX58* and *hLincRNA-p21*), the antisense editing was catalyzed by ADAR1 (Figure 4). ADAR1-mediated editing represents most A-to-I editing in humans and occurs in non-coding regions of the transcriptome (Eisenberg and Levanon, 2018). The primary function of this editing is to discriminate between harmless endogenous (or "self") and harmful exogenous viral dsRNAs, preventing activation of the cytosolic innate immune system in the absence of infection. Indeed, ADAR1-mediated editing of self dsRNA is required to avoid recognition of these structures by the dsRNA sensor melanoma differentiation-associated protein 5 (MDA5), which otherwise would bind self dsRNA and, upon interaction with the mitochondrial antiviral signaling protein (MAVS), would lead to an interferon response (Mannion et al., 2014; Liddicoat et al., 2015; Pestal et al., 2015). It is still not completely understood if specific self dsRNAs must be deaminated by ADAR1 to avoid the cytosolic innate immune reaction through MDA5. Recent work performed by JB Li and colleagues has shown that DNA mutations (SNPs) that culminate in a reduction of A-to-I editing within specific immunogenic dsRNAs underlie the risk for autoimmune and immune-related diseases. Notably, the authors identified two kinds of immunogenic dsRNAs, the ones that originated from an intramolecular pairing of inverted *Alu* repeats and, surprisingly, from an intermolecular pairing of antisense transcripts (Li et al., 2022).

Spurred by this finding, we performed a transcriptome-wide analysis looking for (annotated) antisense transcripts and matching them with reported editing events. Like others before us, we find that such events are rare overall. However, when convergent transcription overlaps with editing, at least a quarter (56 out of 199, ~28%) of such transcripts are edited in the antisense orientation (thus generating apparent "U-to-C" RNA modification events). Around half of these are edited in both orientations, suggesting that these events, though rare, are not insignificant. It is important to note that antisense transcripts are frequently degraded by the nuclear RNA exosome limiting their detection in RNA-seq data. Using alternative NGS methods such as chromatin RNA-seq may improve the detection of antisense transcripts and, therefore, antisense editing. Finally, our analysis was limited to known antisense transcripts. Defining the antisense signal directly from the RNA-seq, despite being more challenging, may lead to the discovery of non-annotated antisense transcript and, thus, more antisense RNA editing.

Whether the antisense editing is derived from intra- or intermolecular interactions of RNAs, the fact that ADAR1 edits overlapping sense and antisense RNAs may suggest those transcripts as particularly relevant in activating MDA5 and, therefore, could be highly immunogenic. In such a scenario, the identification of clusters of apparent U-to-C and A-to-I modifications could simplify the prediction of potentially strongly immunogenic self-dsRNAs [which are thought to be functionally relevant (Li et al., 2022)].

It is also interesting to notice that changes in sense and antisense RNA editing upon treatments may happen for different reasons. For example, the decrease in antisense editing within *DDX58* upon IFN treatment is probably due to the ~20-fold increase in expression of its sense-transcript together with a 2-fold increase in ADAR1 expression (Supplementary Figure S1). Intriguingly, upon doxorubicin treatment, we observed an increase in both sense and antisense editing without any increase in ADAR1 expression (Figure 3 and Supplementary Figure S3B). These results are in agreement with recent findings by Huertas and others, which describe an increase of A-to-I editing upon treatment with DSBs-inducing agents, despite no changes in ADAR protein expression levels (Jimeno et al., 2021).

Regarding *DDX58*, it is interesting to note that although the locus is not annotated as a source of cis-NATs, we can functionally identify antisense transcripts in some cell lines (RCK8, U2932, HEK293T) but not in others (e.g., A549). Indeed, A549 shows abundant A-to-I but no U-to-C editing indicating the absence of antisense transcription (Figure 1). Considering that *DDX58* is an ISG and its transcription is

highly regulated (Matsumiya and Stafforini, 2010), it is tempting to speculate that antisense transcription from the *DDX58* locus could have regulatory functions.

Overall, our study demonstrates that antisense A-to-I editing can result in instances of apparent U-to-C RNA modification, which may be misinterpreted as novel modification events. At the same time, we note that clusters of A-to-I and "U-to-C" modification events could be simple markers of ADAR activity on functionally important loci (a characteristic that will aid in their identification).

Data availability statement

Publicly available datasets were analyzed in this study. This data can be found here: The RNA datasets analyzed in this study can be downloaded from Gene Expression Omnibus at NCBI under the accessions GSM4118041, GSM4118068, GSM4118074, GSM4118077, GSM4118080, GSM4118083, GSM4118086, respectively for samples RNAAtlas285, RNAAtlas294, RNAAtlas296, RNAAtlas297, RNAAtlas298, RNAAtlas299 and RNAAtlas300. Computer code used for the A-to-I sense-antisense RNA editing analysis can be found at https://github.com/BioinfoUNIBA/antisenseEditing.

Author contributions

RP and FP designed the experiments. RP and AA performed all the experiments. IC and MM contributed to designing, performing, and analyzing the hLincRNA-p21 data. CLG and EP designed and performed NGS analysis to identify antisense editing. MB and SW developed the ADAR1 KO cell line. RP and FP analyzed the data and wrote the manuscript with input from all other authors. RP and FP conceived the study and supervised the research. All authors have read and approved the manuscript.

Funding

This work was supported by the European Research Council (ERC) under the European Union's Horizon 2020 research and innovation program (grant agreement no. 649019), the DFG German Research Foundation (TRR319-RMaP and SPP1784) awarded to FP and the HI-TRON Kick-Start Seed Funding Program 2021 awarded to RP. Work in the Marcia lab has partly been funded by the Agence Nationale de la Recherche (ANR-15-CE11-0003-01), by ITMO Cancer (18CN047-00), and by the Fondation ARC pour la recherche sur le cancer (PJA-20191209284).

Acknowledgments

We thank the Flow Cytometry unit of the Imaging and Cytometry Core Facility, German Cancer Research Center (DKFZ), for providing excellent sorting service. We thank Qiang Pan Hammarström (Karolinska Institutet, Sweden) and Ralf Bartenschlager (University Hospital of Heidelberg) for the generous gift of RCK8, U2932 cells, and A549, respectively. We also thank Bruno Fosso (University of Bari, Italy) for realizing figures related to sense and antisense editing in NGS data.

Conflict of interest

The authors declare that the research was conducted in the absence of any commercial or financial relationships that could be construed as a potential conflict of interest.

Publisher's note

All claims expressed in this article are solely those of the authors and do not necessarily represent those of their affiliated organizations, or those of the publisher, the editors and the reviewers. Any product that may be evaluated in this article, or claim that may be made by its manufacturer, is not guaranteed or endorsed by the publisher.

Supplementary material

The Supplementary Material for this article can be found online at: https://www.frontiersin.org/articles/10.3389/fcell.2022.1080626/full#supplementary-material

Supplementary Material and information about editing sites in the NGS data can be found in Data Presentation 1 and Table 1, respectively.

References

Athanasiadis, A., Rich, A., and Maas, S. (2004). Widespread A-to-I RNA editing of alu-containing mRNAs in the human transcriptome. *PLOS Biol.* 2, e391. doi:10.1371/journal.pbio.0020391

Babaian, A., Rothe, K., Girodat, D., Minia, I., Djondovic, S., Milek, M., et al. (2020). Loss of m1acp3Ψ ribosomal RNA modification is a major feature of cancer. *Cell Rep.* 31, 107611. doi:10.1016/j.celrep.2020.107611

Bass, B. L. (2002). RNA editing by adenosine deaminases that act on RNA. *Annu. Rev. Biochem.* 71, 817–846. doi:10.1146/annurev.biochem.71.110601.135501

Blanc, V., and Davidson, N. O. (2010). APOBEC-1 mediated RNA editing. *Wiley Interdiscip. Rev. Syst. Biol. Med.* 2, 594–602. doi:10.1002/wsbm.82

Boccaletto, P., MacHnicka, M. A., Purta, E., Pitkowski, P., Baginski, B., Wirecki, T. K., et al. (2018). Modomics: A database of RNA modification

pathways. 2017 update. *Nucleic Acids Res.* 46, D303–D307. doi:10.1093/nar/gkx1030

Carmichael, G. G. (2003). Antisense starts making more sense. *Nat. Biotechnol.* 21, 371–372. doi:10.1038/nbt0403-371

Castro, F., Dirks, W. G., Fähnrich, S., Hotz-Wagenblatt, A., Pawlita, M., and Schmitt, M. (2013). High-throughput SNP-based authentication of human cell lines. *Int. J. Cancer* 132, 308–314. doi:10.1002/ijc.27675

Chillón, I., and Pyle, A. M. (2016). Inverted repeat Alu elements in the human lincRNA-p21 adopt a conserved secondary structure that regulates RNA function. *Nucleic Acids Res.* 44, 9462–9471. doi:10.1093/nar/gkw599

Diroma, M. A., Ciaccia, L., Pesole, G., and Picardi, E. (2019). Elucidating the editome: Bioinformatics approaches for RNA editing detection. *Briefings Bioinforma.* 20, 436–447. doi:10.1093/bib/bbx129

Duffy, E. E., Schofield, J. A., and Simon, M. D. (2019). Gaining insight into transcriptome-wide RNA population dynamics through the chemistry of 4-thiouridine. *Wiley Interdiscip. Rev. RNA* 10, e1513. doi:10.1002/wrna.1513

Eisenberg, E., and Levanon, E. Y. (2018). A-to-I RNA editing — Immune protector and transcriptome diversifier. *Nat. Rev. Genet.* 19, 473–490. doi:10.1038/s41576-018-0006-1

Gu, Z., Gu, L., Eils, R., Schlesner, M., and Brors, B. (2014). Circlize Implements and enhances circular visualization in R. *Bioinformatics* 30, 2811–2812. doi:10.1093/bioinformatics/btu393

Hafner, M., Landthaler, M., Burger, L., Khorshid, M., Hausser, J., Berninger, P., et al. (2010). Transcriptome-wide identification of RNA-binding protein and MicroRNA target sites by PAR-CLIP. *Cell* 141, 129–141. doi:10.1016/J.CELL.2010.03.009

Hartwig, D., Schoeneich, L., Greeve, J., Schütte, C., Dorn, I., Kirchner, H., et al. (2004). Interferon-alpha stimulation of liver cells enhances hepatitis delta virus RNA editing in early infection. *J. Hepatol.* 41, 667–672. doi:10.1016/j.jhep.2004.06.025

Hartwig, D., Schütte, C., Warnecke, J., Dorn, I., Hennig, H., Kirchner, H., et al. (2006). The large form of ADAR 1 is responsible for enhanced hepatitis delta virus RNA editing in interferon-alpha-stimulated host cells. *J. Viral Hepat.* 13, 150–157. doi:10.1111/j.1365-2893.2005.00663.x

Heilman-Miller, S. L., and Woodson, S. A. (2003). Effect of transcription on folding of the Tetrahymena ribozyme. *RNA* 9, 722–733. doi:10.1261/rna.5200903

Herzog, V. A., Reichholf, B., Neumann, T., Rescheneder, P., Bhat, P., Burkard, T. R., et al. (2017). Thiol-linked alkylation of RNA to assess expression dynamics. *Nat. Methods* 14, 1198–1204. doi:10.1038/nmeth.4435

Huarte, M., Guttman, M., Feldser, D., Garber, M., Koziol, M. J., Kenzelmann-Broz, D., et al. (2010). A large intergenic noncoding RNA induced by p53 mediates global gene repression in the p53 response. *Cell* 142, 409–419. doi:10.1016/j.cell.2010.06.040

Jimeno, S., Prados-Carvajal, R., Fernández-Ávila, M. J., Silva, S., Silvestris, D. A., Endara-Coll, M., et al. (2021). ADAR-mediated RNA editing of DNA:RNA hybrids is required for DNA double strand break repair. *Nat. Commun.* 12, 5512. doi:10.1038/s41467-021-25790-2

John, D., Weirick, T., Dimmeler, S., and Uchida, S. (2017). RNAEditor: Easy detection of RNA editing events and the introduction of editing islands. *Brief. Bioinform* 18, 993–1001. doi:10.1093/bib/bbw087

Kawahara, Y., and Nishikura, K. (2006). Extensive adenosine-to-inosine editing detected in Alu repeats of antisense RNAs reveals scarcity of sense-antisense duplex formation. *FEBS Lett.* 580, 2301–2305. doi:10.1016/j.febslet.2006.03.042

Kimelman, D., and Kirschner, M. W. (1989). An antisense mRNA directs the covalent modification of the transcript encoding fibroblast growth factor in Xenopus oocytes. *Cell* 59, 687–696. doi:10.1016/0092-8674(89)90015-9

Kimura, S., Dedon, P. C., and Waldor, M. K. (2020). Comparative tRNA sequencing and RNA mass spectrometry for surveying tRNA modifications. *Nat. Chem. Biol.* 16, 964–972. doi:10.1038/s41589-020-0558-1

Kiran, A., and Baranov, P. V. (2010). Darned: A DAtabase of RNa EDiting in humans. *Bioinformatics* 26, 1772–1776. doi:10.1093/bioinformatics/btq285

Kluesner, M., Tasakis, R. N., Lerner, T., Arnold, A., Wüst, S., Binder, M., et al. (2021). MultiEditR: The first tool for the detection and quantification of RNA editing from Sanger sequencing demonstrates comparable fidelity to RNA-seq. *Mol. Ther. - Nucleic Acids* 1, 515–523. doi:10.1016/j.omtn.2021.07.008

Knie, N., Grewe, F., Fischer, S., and Knoop, V. (2016). Reverse U-to-C editing exceeds C-to-U RNA editing in some ferns – A monilophyte-wide comparison of chloroplast and mitochondrial RNA editing suggests independent evolution of the two processes in both organelles. *BMC Evol. Biol.* 16, 134. doi:10.1186/s12862-016-0707-z

Kumar, M., and Carmichael, G. G. (1998). Antisense RNA: Function and fate of duplex RNA in cells of higher eukaryotes. *Microbiol. Mol. Biol. Rev.* 62, 1415–1434. doi:10.1128/MMBR.62.4.1415-1434.1998

Lai, D., Proctor, J. R., and Meyer, I. M. (2013). On the importance of cotranscriptional RNA structure formation. *RNA* 19, 1461–1473. doi:10.1261/rna.037390.112

Lehner, B., Williams, G., Campbell, R. D., and Sanderson, C. M. (2002). Antisense transcripts in the human genome. *Trends Genet.* 18, 63–65. doi:10.1016/S0168-9525(02)02598-2

Lerner, T., Papavasiliou, F. N., and Pecori, R. (2018). RNA editors, cofactors, and mRNA targets: An overview of the C-to-U RNA editing machinery and its implication in human disease. *Genes (Basel)* 10, 13. doi:10.3390/genes10010013

Levanon, E. Y., Eisenberg, E., Yelin, R., Nemzer, S., Hallegger, M., Shemesh, R., et al. (2004). Systematic identification of abundant A-to-I editing sites in the human transcriptome. *Nat. Biotechnol.* 22, 1001–1005. doi:10.1038/nbt996

Li, Q., Gloudemans, M. J., Geisinger, J. M., Fan, B., Aguet, F., Sun, T., et al. (2022). RNA editing underlies genetic risk of common inflammatory diseases. *Nature* 608, 569–577. doi:10.1038/s41586-022-05052-x

Liddicoat, B. J., Piskol, R., Chalk, A. M., Ramaswami, G., Higuchi, M., Hartner, J. C., et al. (2015). RNA editing by ADAR1 prevents MDA5 sensing of endogenous dsRNA as nonself. *Science* 1, 1115–1120. doi:10.1126/science.aac7049

Liu, Z., Song, W., and Dong, K. (2004). Persistent tetrodotoxin-sensitive sodium current resulting from U-to-C RNA editing of an insect sodium channel. *Proc. Natl. Acad. Sci.* 101, 11862–11867. doi:10.1073/pnas.0307695101

Livak, K. J., and Schmittgen, T. D. (2001). Analysis of relative gene expression data using real-time quantitative PCR and the 2(-Delta Delta C(T)) Method. *Methods* 25, 402–408. doi:10.1006/meth.2001.1262

Lorenzi, L., Chiu, H.-S., Avila Cobos, F., Gross, S., Volders, P.-J., Cannoodt, R., et al. (2021). The RNA Atlas expands the catalog of human non-coding RNAs. *Nat. Biotechnol.* 39, 1453–1465. doi:10.1038/s41587-021-00936-1

Mannion, N. M., Greenwood, S. M., Young, R., Cox, S., Brindle, J., Read, D., et al. (2014). The RNA-editing enzyme ADAR1 controls innate immune responses to RNA. *Cell Rep.* 1, 1482–1494. doi:10.1016/j.celrep.2014.10.041

Mansi, L., Tangaro, M. A., Lo Giudice, C., Flati, T., Kopel, E., Schaffer, A. A., et al. (2021). REDIportal: Millions of novel A-to-I RNA editing events from thousands of RNAseq experiments. *Nucleic Acids Res.* 49, D1012–D1019. doi:10.1093/nar/gkaa916

Matsumiya, T., and Stafforini, D. M. (2010). Function and regulation of retinoic acid-inducible gene-I. *Crit. Rev. Immunol.* 30, 489–513. doi:10.1615/critrevimmunol.v30.i6.10

Meyer, B., Wurm, J. P., Sharma, S., Immer, C., Pogoryelov, D., Kötter, P., et al. (2016). Ribosome biogenesis factor Tsr3 is the aminocarboxypropyl transferase responsible for 18S rRNA hypermodification in yeast and humans. *Nucleic Acids Res.* 44, 4304–4316. doi:10.1093/nar/gkw244

Neeman, Y., Dahary, D., Levanon, E. Y., Sorek, R., and Eisenberg, E. (2005). Is there any sense in antisense editing? *Trends Genet.* 21, 544–547. doi:10.1016/j.tig.2005.08.005

Nishikura, K. (2010). Functions and regulation of RNA editing by ADAR deaminases. *Annu. Rev. Biochem.* 79, 321–349. doi:10.1146/annurev-biochem-060208-105251

Patterson, J. B., Thomis, D. C., Hans, S. L., and Samuel, C. E. (1995). Mechanism of interferon action: Double-stranded RNA-specific adenosine deaminase from human cells is inducible by alpha and gamma interferons. *Virology* 210, 508–511. doi:10.1006/viro.1995.1370

Pecori, R., Di Giorgio, S., Paulo Lorenzo, J., and Nina Papavasiliou, F. (2022). Functions and consequences of AID/APOBEC-mediated DNA and RNA deamination. *Nat. Rev. Genet.* 23, 505–518. doi:10.1038/s41576-022-00459-8

Pecori, R., Ren, W., Wang, X., Berglund, M., Li, W., Tasakis, R. N., et al. (2021). *RNA-Editing-Initiated MAVS signaling is a key epitranscriptomic alteration in human B cell lymphoma*. Rochester, NY: Social Science Research Network. doi:10.2139/ssrn.3927430

Pestal, K., Funk, C. C., Snyder, J. M., Price, N. D., Treuting, P. M., and Stetson, D. B. (2015). Isoforms of RNA-editing enzyme ADAR1 independently control nucleic acid sensor MDA5-driven autoimmunity and multi-organ development. *Immunity* 43, 933–944. doi:10.1016/j.immuni.2015.11.001

Peters, N. T., Rohrbach, J. A., Zalewski, B. A., Byrkett, C. M., and Vaughn, J. C. (2003). RNA editing and regulation of Drosophila 4f-rnp expression by sas-10 antisense readthrough mRNA transcripts. *RNA* 9, 698–710. doi:10.1261/rna.2120703

Picardi, E., D'Erchia, A. M., Giudice, C. L., and Pesole, G. (2017). REDIportal: A comprehensive database of A-to-I RNA editing events in humans. *Nucleic acids Res.* 45, D750–D757. doi:10.1093/nar/gkw767

Picardi, E., and Pesole, G. (2013). REDItools: High-throughput RNA editing detection made easy. *Bioinformatics* 29, 1813–1814. doi:10.1093/bioinformatics/btt287

Piechotta, M., Wyler, E., Ohler, U., Landthaler, M., and Dieterich, C. (2017). Jacusa: Site-specific identification of RNA editing events from replicate sequencing data. *BMC Bioinforma.* 18, 7. doi:10.1186/s12859-016-1432-8

Porath, H. T., Carmi, S., and Levanon, E. Y. (2014). A genome-wide map of hyper-edited RNA reveals numerous new sites. *Nat. Commun.* 5, 4726. doi:10.1038/ncomms5726

Quinlan, A. R. (2014). BEDTools: The Swiss-army tool for genome feature analysis. *Curr. Protoc. Bioinforma.* 47, 111–1234. doi:10.1002/0471250953.bi1112s47

Ramaswami, G., and Li, J. B. (2016). Identification of human RNA editing sites: A historical perspective. *Methods* 107, 42–47. doi:10.1016/j.ymeth.2016.05.011

Ramaswami, G., and Li, J. B. (2014). Radar: A rigorously annotated database of A-to-I RNA editing. *Nucleic Acids Res.* 42, D109–D113. doi:10.1093/nar/gkt996

Ran, F. A., Hsu, P. D., Wright, J., Agarwala, V., Scott, D. A., and Zhang, F. (2013). Genome engineering using the CRISPR-Cas9 system. *Nat. Protoc.* 8, 2281–2308. doi:10.1038/nprot.2013.143

Roundtree, I. A., Evans, M. E., Pan, T., and He, C. (2017). Dynamic RNA modifications in gene expression regulation. *Cell* 169, 1187–1200. doi:10.1016/j.cell.2017.05.045

Ruchika, N., Okudaira, C., Sakari, M., and Tsukahara, T. (2021). Genome-wide identification of U-to-C RNA editing events for nuclear genes in *Arabidopsis thaliana*. *Cells* 10, 635. doi:10.3390/cells10030635

Sanjana, N. E., Shalem, O., and Zhang, F. (2014). Improved vectors and genome-wide libraries for CRISPR screening. *Nat. Methods* 11, 783–784. doi:10.1038/nmeth.3047

Savva, Y. A., Rieder, L. E., and Reenan, R. A. (2012). The ADAR protein family. *Genome Biol.* 13, 252. doi:10.1186/gb-2012-13-12-252

Schmitt, M., and Pawlita, M. (2009). High-throughput detection and multiplex identification of cell contaminations. *Nucleic Acids Res.* 37, e119. doi:10.1093/nar/gkp581

Schofield, J. A., Duffy, E. E., Kiefer, L., Sullivan, M. C., and Simon, M. D. (2018). TimeLapse-seq: Adding a temporal dimension to RNA sequencing through nucleoside recoding. *Nat. Methods* 1, 221–225. doi:10.1038/nmeth.4582

Sharma, S., Patnaik, S. K., Taggart, R. T., Kannisto, E. D., Enriquez, S. M., Gollnick, P., et al. (2015). APOBEC3A cytidine deaminase induces RNA editing in monocytes and macrophages. *Nat. Commun.* 1, 6881. doi:10.1038/ncomms7881

Sharma, S., Wang, J., Alqassim, E., Portwood, S., Gomez, E. C., Maguire, O., et al. (2019). Mitochondrial hypoxic stress induces widespread RNA editing by APOBEC3G in natural killer cells. *Genome Biol.* 20, 37. doi:10.1186/s13059-019-1651-1

Shendure, J., and Church, G. M. (2002). Computational discovery of sense-antisense transcription in the human and mouse genomes. *Genome Biol.* 3, RESEARCH0044. research0044. doi:10.1186/gb-2002-3-9-research0044

Takakura, M., Ishiguro, K., Akichika, S., Miyauchi, K., and Suzuki, T. (2019). Biogenesis and functions of aminocarboxypropyluridine in tRNA. *Nat. Commun.* 10, 5542. doi:10.1038/s41467-019-13525-3

Tan, M. H., Li, Q., Shanmugam, R., Piskol, R., Kohler, J., Young, A. N., et al. (2017). Dynamic landscape and regulation of RNA editing in mammals. *Nature* 550, 249–254. doi:10.1038/nature24041

Villegas, J., Müller, I., Arredondo, J., Pinto, R., and Burzio, L. O. (2002). A putative RNA editing from U to C in a mouse mitochondrial transcript. *Nucleic Acids Res.* 30, 1895–1901. doi:10.1093/nar/30.9.1895

Wacker, M. J., and Godard, M. P. (2005). Analysis of one-step and two-step real-time RT-PCR using SuperScript III. *J. Biomol. Tech.* 16, 266–271.

Wang, Q., Khillan, J., Gadue, P., and Nishikura, K. (2000). Requirement of the RNA editing deaminase ADAR1 gene for embryonic erythropoiesis. *Science* 290, 1765–1768. doi:10.1126/science.290.5497.1765

Wang, Z., Lian, J., Li, Q., Zhang, P., Zhou, Y., Zhan, X., et al. (2016). RES-scanner: A software package for genome-wide identification of RNA-editing sites. *Gigascience* 5, 37. doi:10.1186/s13742-016-0143-4

Ye, J., Coulouris, G., Zaretskaya, I., Cutcutache, I., Rozen, S., and Madden, T. L. (2012). Primer-BLAST: A tool to design target-specific primers for polymerase chain reaction. *BMC Bioinforma.* 13, 134. doi:10.1186/1471-2105-13-134

Yelin, R., Dahary, D., Sorek, R., Levanon, E. Y., Goldstein, O., Shoshan, A., et al. (2003). Widespread occurrence of antisense transcription in the human genome. *Nat. Biotechnol.* 21, 379–386. doi:10.1038/nbt808

Yoshinaga, K., Iinuma, H., Masuzawa, T., and Uedal, K. (1996). Extensive RNA editing of U to C in addition to C to U substitution in the rbcL transcripts of hornwort chloroplasts and the origin of RNA editing in green plants. *Nucleic Acids Res.* 24, 1008–1014. doi:10.1093/nar/24.6.1008

frontiers | Frontiers in Genetics

TYPE Original Research
PUBLISHED 06 January 2023
DOI 10.3389/fgene.2022.1072948

OPEN ACCESS

EDITED BY
Kunqi Chen,
Fujian Medical University, China

REVIEWED BY
Domitilla Mandatori,
University of Studies G. d'Annunzio Chieti and Pescara, Italy
Jianlin Shen,
Southern Medical University, China
Kong Lingsuo,
The First Affiliated Hospital of University of Science and Technology of China Anhui Provincial Hospital, China

*CORRESPONDENCE
Yang Liu,
liuyang0369@126.com
Shuguo Zheng,
kqzsg86@bjmu.edu.cn

SPECIALTY SECTION
This article was submitted to Epigenomics and Epigenetics, a section of the journal Frontiers in Genetics

RECEIVED 18 October 2022
ACCEPTED 29 November 2022
PUBLISHED 06 January 2023

CITATION
Qiao Y, Li J, Liu D, Zhang C, Liu Y and Zheng S (2023), Identification and experimental validation of key m6A modification regulators as potential biomarkers of osteoporosis.
Front. Genet. 13:1072948.
doi: 10.3389/fgene.2022.1072948

Identification and experimental validation of key m6A modification regulators as potential biomarkers of osteoporosis

Yanchun Qiao, Jie Li, Dandan Liu, Chenying Zhang, Yang Liu* and Shuguo Zheng*

Department of Preventive Dentistry, Peking University School and Hospital of Stomatology & National Center of Stomatology & National Clinical Research Center for Oral Diseases & National Engineering Laboratory for Digital and Material Technology of Stomatology & Beijing Key Laboratory of Digital Stomatology & Research Center of Engineering and Technology for Computerized Dentistry Ministry of Health & NMPA Key Laboratory for Dental Materials, Beijing, China

Osteoporosis (OP) is a severe systemic bone metabolic disease that occurs worldwide. During the coronavirus pandemic, prioritization of urgent services and delay of elective care attenuated routine screening and monitoring of OP patients. There is an urgent need for novel and effective screening diagnostic biomarkers that require minimal technical and time investments. Several studies have indicated that N6-methyladenosine (m6A) regulators play essential roles in metabolic diseases, including OP. The aim of this study was to identify key m6A regulators as biomarkers of OP through gene expression data analysis and experimental verification. GSE56815 dataset was served as the training dataset for 40 women with high bone mineral density (BMD) and 40 women with low BMD. The expression levels of 14 major m6A regulators were analyzed to screen for differentially expressed m6A regulators in the two groups. The impact of m6A modification on bone metabolism microenvironment characteristics was explored, including osteoblast-related and osteoclast-related gene sets. Most m6A regulators and bone metabolism-related gene sets were dysregulated in the low-BMD samples, and their relationship was also tightly linked. In addition, consensus cluster analysis was performed, and two distinct m6A modification patterns were identified in the low-BMD samples. Subsequently, by univariate and multivariate logistic regression analyses, we identified four key m6A regulators, namely, *METTL16*, *CBLL1*, *FTO*, and *YTHDF2*. We built a diagnostic model based on the four m6A regulators. *CBLL1* and *YTHDF2* were protective factors, whereas *METTL16* and *FTO* were risk factors, and the ROC curve and test dataset validated that this model had moderate accuracy in distinguishing high- and low-BMD samples. Furthermore, a regulatory network was constructed of the four hub m6A regulators and 26 m6A target bone metabolism-related genes, which enhanced our understanding of the regulatory mechanisms of m6A modification in OP. Finally, the expression of the four key m6A regulators was validated *in vivo* and *in vitro*, which is consistent with the bioinformatic analysis results. Our findings identified four key m6A regulators that are essential for bone

metabolism and have specific diagnostic value in OP. These modules could be used as biomarkers of OP in the future.

KEYWORDS

osteoporosis, bone metabolism, M6A, RNA modification, biomarker, osteoclast

1 Introduction

Osteoporosis (OP) is a systemic skeletal disease characterized by increased fracture risk and decreased bone density or bone strength that occurs widely in postmenopausal women (Miller, 2016). The prevalence of OP increases with age, from 19.57% in women aged 50–59 years to 56.10% in women aged 80 years and older, and it will continue to rise with the aging of the population in China (Chen et al., 2016). Traditionally, bone mineral density (BMD) measured by dual X-ray absorptiometry (DXA) is used to diagnose OP, assess fracture risk, and monitor changes in BMD over time (Chun, 2011). However, DXA presents some disadvantages, namely, that accessibility to DXA is limited in many locations (Curtis et al., 2017). The rapid spread of the COVID-19 pandemic makes it more difficult to monitor BMD frequently during OP therapy, as medical resources are diverted from chronic disease care to combat the pandemic. In addition, errors in DXA scans/reports are common due to difficulties in the maintenance of high-quality instrument calibration, data acquisition/analysis, interpretation, and reporting of results (Licata et al., 2018). Therefore, exploring novel and effective screening diagnostic biomarkers that require minimal technical investment is crucial for the early screening and timely treatment of OP.

Maintenance of normal bone mass relies on a dynamic balance between bone resorption and formation. Emerging evidence has demonstrated that disruption of the balance, especially overactive osteoclast-induced bone resorption, predominates the progression of OP(Yao et al., 2017; Chen et al., 2020). N6-methyladenosine (m6A) modification is the most abundant internal modification in eukaryotic cells, affecting mRNA metabolism and various biological processes, including bone metabolic processes (Wei et al., 2017). m6A modification can be catalyzed by methyltransferase complexes, including METTL3, METTL14, WTAP, METTL16, RBM15, RBM15B, CBLL1, and ZC3H13, which can be removed by the demethylases ALKBH5 and FTO. Simultaneously, a variety of proteins that specifically recognize m6A sites have been found, including YTH family proteins (YTHDF1-3, YTHDC1-2) and ribonucleoproteins (HNRNPC), which can recognize m6A modification to regulate mRNA fates (Wu et al., 2018b). Increasing evidence has demonstrated the roles of m6A modification in diverse cancers by influencing their proliferation, migration, and invasion (An and Duan, 2022). Recently, the association between m6A modification and OP has also attracted the attention of some researchers. METTL3 is the most studied molecule and has different effects in different cell lines. In BMSCs, METTL3 functions as an inhibitor in OP to promote osteogenic differentiation and enhance bone formation by activating the PI3K-Akt signaling pathway or the PTH/Pth1r signaling axis (Wu et al., 2018a; Tian et al., 2019). However, another study reported that METTL3 could regulate osteoclast differentiation by increasing the bone resorption ability in RAW 264.7 cells, which may contribute to OP (Li D. et al., 2020). In addition, several studies have reported that FTO might be a new candidate for OP, which acts as an activator in OP, and its single nucleotide polymorphisms (SNPs) have a close relationship with BMD variation (DR, 1997; Guo et al., 2011; Li et al., 2019). Furthermore, YTHDF2 disrupts bone homeostasis by regulating osteoclast differentiation and inflammatory processes (Yu et al., 2019). The above findings demonstrate that m6A modification plays a vital role in OP. Nevertheless, gene signatures with diagnostic value for m6A modification in OP remain largely unstudied.

Various skeletal disorders have been found to be related to abnormalities in peripheral blood monocytes (PBMCs), which are widely accepted as the *in vivo* working cell model to study mechanisms in relation to OP(Zhou et al., 2015). PBMCs can migrate to the bone surface, differentiate into osteoclasts, and act as precursor cells of osteoclasts. Moreover, PBMCs produce essential cytokines for osteoclast differentiation, activation, and apoptosis (Kylmaoja et al., 2018). Recent advances in high-throughput technologies enable researchers to determine the molecular mechanisms and potential biomarkers of OP by isolating and analyzing the gene expression of PBMs. However, no such reports have systematically investigated the molecular mechanisms of m6A modification in OP using high-throughput data analysis.

In this study, we systematically analyzed the expression of m6A regulators mainly in PBMCs from different BMD samples, and the impact of m6A modification on bone metabolism microenvironment characteristics was also explored. Then, we performed consensus cluster analysis and identified two m6A modification patterns in low-BMD samples. In addition, we built a diagnostic model based on four key m6A regulators for distinguishing high- and low-BMD samples, and a regulatory network was then constructed to explore the possible regulatory mechanisms of m6A regulators in OP. Furthermore, we validated the altered m6A pattern of the four key regulators during RANKL- and/or MCSF induced osteoclast formation *in vitro*. Finally, an ovariectomized (OVX) mouse OP model was constructed to further validate

TABLE 1 The description of 14 m6A RNA methylation regulators from the Ensembl database.

Gene	Ensembl	Type	Gene	Ensembl	Type
METTL3	ENSG00000165819	Writers	FTO	ENSG00000140718	Erasers
METTL16	ENSG00000127804	Writers	YTHDF1	ENSG00000149658	Readers
WTAP	ENSG00000146457	Writers	YTHDF2	ENSG00000198492	Readers
RBM15	ENSG00000162775	Writers	YTHDF3	ENSG00000185728	Readers
RBM15B	ENSG00000259956	Writers	YTHDC1	ENSG00000083896	Readers
CBLL1	ENSG00000105879	Writers	YTHDC2	ENSG00000047188	Readers
ZC3H13	ENSG00000123200	Writers	HNRNPC	ENSG00000092199	Readers

the role of m6A modification in OP. Altogether, the present findings demonstrate that m6A regulators have a crucial impact on bone metabolism in OP, suggesting their future potential as diagnostic biomarkers of OP.

2 Materials and methods

2.1 Data collection and processing

We searched "osteoporosis" in the GEO and Array Express databases and retrieved datasets with a sample size greater than or equal to 80. Finally, two datasets were obtained, GSE56815 (https://www.ncbi.nlm.nih.gov/geo/query/acc.cgi?acc=GSE56815) and E-MEXP-1618 (https://www.ebi.ac.uk/arrayexpress/experiments/E-MEXP-1618/?query=osteoporosis&page=3&) The GSE56815 dataset contains the gene expression data of PBMCs from 80 Caucasian females, including 40 patients with high hip BMD (20 pre- and 20 postmenopausal) and 40 patients with low hip BMD (20 pre- and 20 postmenopausal), and this dataset served as the training dataset in the present study. The sample characteristics and RNA extraction protocol were well described in a previous study (Zhou et al., 2018). Moreover, the E-MEXP-1618 dataset served as the test dataset in this study, including 84 transiliac bone biopsies of postmenopausal females (50–86 years) with different BMDs. The detailed characteristics of the samples were presented in an early study (Reppe et al., 2010).

After downloading the two datasets, the probes were converted to gene symbols based on the corresponding annotation files. We only kept the probe with the largest numerical value when encountering probes corresponding to the same molecule. Then, we used the normalizeBetweenArrays function of the limma package to standardize the data, which was visualized with a box plot. Clustering of the samples was assessed through the principal component analysis (PCA) chart and the uniform manifold approximation and projection (UMAP) chart using the ggplot2 and umap packages.

2.2 Selection and expression analysis of m6A regulators

Sixteen widely recognized m6A regulators were selected from published literature, but the expression of two genes, METTL14 and ALKBH5, was not detected in the selected datasets, so the two genes were not included in this study. Therefore, 14 m6A regulators were involved in this study, namely, seven m6A writers, one m6A eraser, and six m6A readers (Table 1). The protein–protein interaction (PPI) network of these regulators was constructed using the STRING database (https://cn.string-db.org), and the expression correlations among the 14 m6A regulators in all samples were calculated by Spearman correlation analysis. To compare the expression differences of these m6A regulators between the high- and low-BMD samples, we used the limma package, and the results were visualized with a heatmap and box plot. Because the sample size was limited (although still among the largest of such studies in this field), we used a p-value <0.05 as the threshold for nominally significant differential expression.

2.3 Analysis of the characteristics of the bone metabolic microenvironment

The bone metabolism-related gene sets were obtained from the GSEA database (http://www.gsea-msigbd.org/gsea/index.jsp) and were related to bone formation and bone resorption, such as bone remodeling, ossification, and multiple cellular processes of osteoclasts and osteoblasts (Supplementary Table S1). Single-sample gene set enrichment analysis (ssGSEA) was then used to calculate an enrichment score for each gene set in every sample, and we finally obtained the enrichment score matrix using the R package GSVA. The limma package was used to assess the changes in the abundance and activity of these gene sets in the high- and low-BMD samples, and the results are shown in a box plot. In addition, the relationship between the m6A regulators and these gene sets was evaluated by Spearman correlation analysis.

2.4 Identification of m6A modification patterns

To further explore the diverse m6A modification patterns in OP, unsupervised clustering analysis was employed to classify the low-BMD samples into different subtypes based on the expression of the 14 m6A regulators using the ConsensusClusterPlus package. Different modification patterns were verified by PCA using the ggplot2 package. Then, the distribution characteristics of m6A regulators and bone metabolism-related gene sets among the different subgroups were also compared using the limma package.

2.5 Construction of a diagnostic model based on the key m6A regulators

All 14 m6A regulators were used to perform univariate logistic regression, and the differentially expressed m6A regulators were included in multivariate logistic regression to further identify the key m6A regulators in OP. Then, these key genes serving as variables were used to construct the diagnostic model and calculate the risk score of each sample. Next, the median risk score was used as the cutoff, and the samples with a risk score higher than the median score were divided into the high-risk subgroup, whereas the samples with a risk score lower than the median were divided into the low-risk subgroup. The result was visualized with the risk factor graph using the ggplot2 package. Furthermore, the sensitivity and specificity of the model in the training and test datasets were determined by the ROC curve using the pROC package.

2.6 Creation of a network of m6A regulators-m6A target genes

All the targets of these key m6A regulators were screened from M6A2Target (http://m6a2target. canceromics.org), a comprehensive database for target genes of m6A modification, including validated targets reported in the articles and potential targets based on high-throughput sequencing data analysis. Then, a Venn diagram was generated to reveal the common and unique target genes of these m6A regulators. The common target genes coregulated by these key m6A regulators were further analyzed. Their biological functions in Gene Ontology (GO) and KEGG pathway enrichment were annotated using the clusterProfiler package. Finally, the regulatory network of these key m6A regulator-m6A target genes was built using Cytoscape software (version 3.9.1).

2.7 Cell culture and osteoclast differentiation

RAW264.7 cells (a murine macrophage cell line) were cultured in growth medium containing Dulbecco's modified Eagle's medium (DMEM; Gibco, Paisley, United Kingdom) and 10% fetal bovine serum (FBS; Gibco) in a humidified 5% CO2 incubator at 37°C. For gene expression analysis and TRAP staining, RAW264.7 cells were seeded at 1.5×10^4 cells/well in 24-well plates in differentiation medium consisting of growth medium and 10 ng/ml nuclear factor (NF)-κB (RANKL; R&D Systems, Minnesota, United States). The osteoclast differentiation medium was changed every 2 days to induce differentiation, and the cells were cultured for 4 days.

Bone marrow-derived macrophages (BMMs) were isolated from the tibiae and femurs of 6- to 8-week-old C57BL/6 mice (Vital River Laboratory, Beijing, China) by flushing the bone marrow cavity with α-MEM. Then, the cells were cultured in α-MEM containing 10% FBS overnight to separate the suspended cells. The suspended cells were then collected and cultured in α-MEM containing 10% FBS with 10 ng/ml RANKL and 30 ng/ml mouse macrophage colony-stimulating factor (MCSF; R&D Systems). The medium was changed every 2 days to induce differentiation, and the cells were incubated at 37°C with 5% CO2 for 4 days. The experiment was approved by the Biomedical Ethics Committee of Peking University (issue number: LA2020199).

2.8 OVX model construction

Ten healthy female C57BL/6 mice aged 8 weeks (25–30 g) were randomly divided into two groups (n = 5 per group): the sham operation group and the OVX group. Ovaries were surgically removed on both sides after anesthesia, and then the wound was sutured. Eight weeks after surgery, blood samples were collected by eyeball plucking, and then PBMCs were isolated from blood samples using a mouse peripheral blood monocyte isolation kit according to the manufacturer's protocols (Solarbio, Beijing, China). Briefly, 0.75–1 ml peripheral blood samples were collected from a 16-week-old mouse and diluted with an equal volume of phosphate buffered saline (PBS). Then, the white mononuclear cell layer was collected after density gradient centrifugation and washed with PBS three times followed by centrifugation at 250 g at room temperature for 10 min to obtain the mononuclear cell precipitate. Finally, we purified the cells by the differential adherent method. Cell precipitation was resuspended in 10% FBS DMEM and seed on a 24-well plate. Two to 4 hours after incubation, the inadherent cells were washed away, and the remaining monocytes were used for RNA extraction.

TABLE 2 Primer pairs used in the real-time PCR

Genes	Forward primer	Reverse primer
METTL16	GACAAACCACCTGACTTCGCA	TCTGACTGCTTCGGGGTCTT
FTO	TTCATGCTGGATGACCTCAATG	GCCAACTGACAGCGTTCTAAG
CBLL1	GCGAGCCGAATCATGGATCA	CTTCTTCATCACCTTGCGGG
YTHDF2	GAGCAGAGACCAAAAGGTCAAG	CTGTGGGCTCAAGTAAGGTTC
RPS18	TTCCAGCACATTTTGCGAGTA	CACGCCCTTAATGGCAGTGAT

2.9 Tartrate-resistant acid phosphatase staining and osteoclasts counting

All culture media were pipetted out, and samples were washed with PBS three times and then fixed with 4% paraformaldehyde for 15 min at room temperature. Next, the cells were stained with a TRAP Kit (Sigma–Aldrich Merck, Darmstadt, Germany) according to the manufacturer's protocol for 40 min at 37°C in the dark. The cells were imaged using light microscopy (BX51, Olympus, Japan), and TRAP-positive cells were quantified as osteoclasts. This experiment was independently repeated three times.

2.10 Hematoxylin and eosin staining

HE staining of mouse femurs was used to detect bone destruction in OVX and sham mice. Femurs were dissected and fixed in 4% paraformaldehyde for 24 h, decalcified in 14% ethylene diamine tetraacetic acid (EDTA) at 37°C for 20 days, and then embedded into paraffin for sectioning. Bone sections were stained with HE (Beyotime Biotechnology, Shanghai, China) according to a standard protocol to quantify the surface area of bone and adipose tissues.

2.11 m6A quantification

Total m6A content was detected by a m6A RNA methylation assay kit (Abcam, Cambridge, United Kingdom) following the manufacture's protocol. Briefly, total RNA samples of 200 ng for each group were administered with the solution containing the anti-m6A antibody. The m6A levels were quantified by using the colorimetric analysis *via* absorbance at 450 nm.

2.12 Real-time PCR

Total RNA was extracted with TRIzol reagent (Invitrogen, CA, United States) and obtained through chloroform isolation and isopropanol precipitation. Then, cDNA was generated *via* reverse transcription using a reverse transcription kit (Thermo Scientific, MA, United States). Next, the cDNA was amplified by a SYBR Kit (Roche Applied Science, IN, United States) on the ABI 7500 Sequencing Detection System (Applied Biosystems, CA, United States). RPS18 was used as a housekeeping gene, and the primer sequences used in this process are shown in Table 2.

2.13 Western blotting

The total protein was extracted using a RIPA kit (Huaxing Bio, Beijing, China), and then the protein concentration was quantified using a bicinchoninic acid (BCA) kit (Thermo Fisher). Protein samples (25 ug) were separated on electrophoresed in polyacrylamide gels and transferred onto polyvinylidene difluoride membranes (Millipore, MA, United States). After blocking in 5% skimmed milk at room temperature for 1 h, membranes were incubated with primary antibodies against FTO (Proteintech, Wuhan, China), METTL16 (Proteintech), YTHDF2 (Abcam), CBLL1 (Proteintech), and GAPDH (Huaxing bio) at 4°C overnight. The membranes were incubated with HRP-conjugated secondary antibodies (Huaxing Bio) for 1 h and visualized by an enhanced chemiluminescence blotting kit (Cwbiotech, Jiangsu, China). The intensities of the bands were quantified using Quantity One software (Bio-Rad, CA, United States). GAPDH was used as the internal control.

2.14 Statistical analysis

All the gene expression data from public datasets used in this study were processed using R software (version 3.6.3). For the gene expression data from public datasets, correlation analysis between these m6A regulators and the bone metabolism-related gene sets was conducted using the Spearman method. The limma R package was used to analyze these parameters between different groups. The m6A modification patterns were identified by unsupervised clustering analysis using the ConsensusClusterPlus package. Univariate and multivariate logistic regression analyses were applied to reduce the non-significant regulators, and the results were visualized using the

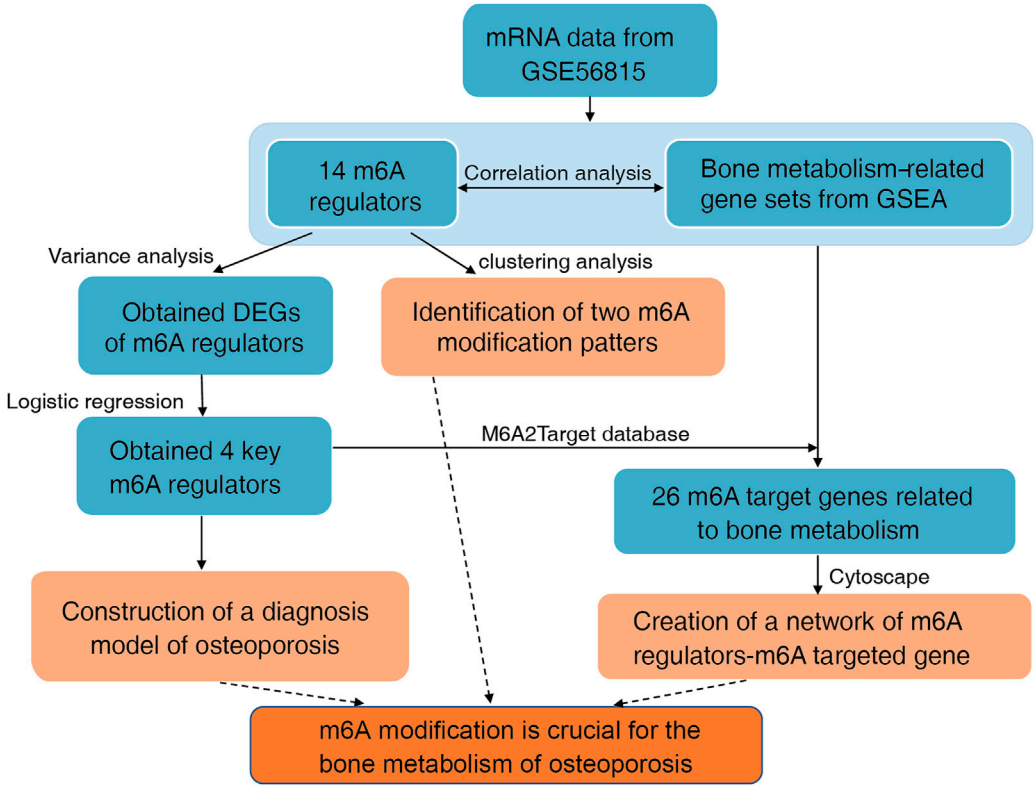

FIGURE 1
Flowchart and analysis strategy used in this study.

forestplot package. The prediction efficiency of the diagnostic model was assessed by the ROC curve using the pROC package. The data from the experimental verification are presented as the mean ± standard deviation, and the comparison between two groups was performed using the two-tailed Student's t test. All comparisons are presented as p values, and a p-value < 0.05 was considered statistically significant. Significant differences were considered at $p < 0.05$ *, $p < 0.01$ **, and $p < 0.001$ ***.

3 Results

3.1 Expression of m6A regulators in the high- and low-BMD groups

The flowchart and analysis strategy used in the present study are shown in Figure 1. Before further analysis, the RNA expression data of GSE56815 were normalized (Figure 2A). UMAP and PCA plots were generated to reduce the dimensionality of the data and show the diverse gene expression patterns between the high- and low-BMD samples (Figures 2B,C). To explore the m6A modification patterns between the two groups, we thoroughly screened the complete gene expression profiles. There were 14 vital m6A regulators involved in the study, and their correlations were assessed at the protein and transcriptome levels. The PPI network was built on the STRING database and showed close direct physical interactions and indirect functional correlations between these m6A regulators (Figure 3A). Then, the correlation analysis revealed their strong relationship at the RNA level; notably, *YTHDF3* and *RBM15* were the most correlated genes, suggesting that they might work as a unit to act on OP (Figure 3B, Supplementary Table S2). Further variation analysis was performed to examine the expression differences in the 14 m6A regulators in the different groups (Figures 3C,D, Supplementary Table S3). Among these differentially expressed genes, four m6A regulators (*METTL3*, *METTL16*, *HNRNPC*, and *FTO*) were upregulated, and two m6A regulators (*CBLL1* and *YTHDF2*) were downregulated.

3.2 Correlations between m6A regulators and the bone metabolism microenvironment

As mentioned above, metabolic alterations in bone tissues contribute to BMD changes and OP occurrence. To probe

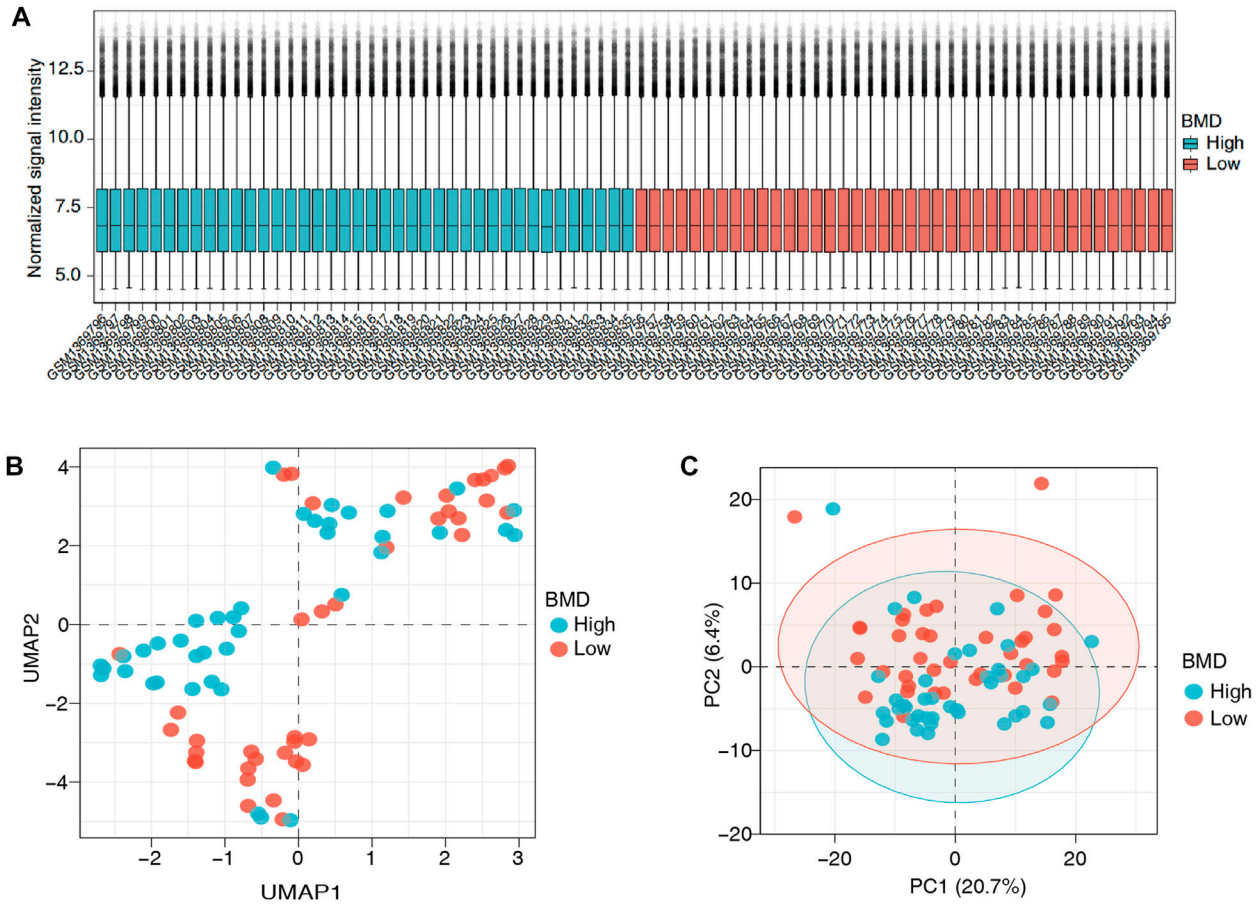

FIGURE 2
Standardization of gene expression. **(A)** Box plots of the gene expression data after normalization. **(B)** The uniform manifold approximation and projection (UMAP) plot and **(C)** principal component analysis (PCA) plot show the differences in gene expression between the two groups. The blue points represent the high bone mineral density (BMD) data, and the red points represent the low BMD data.

their association with m6A regulators and the bone metabolism microenvironment, 13 bone metabolism-related gene sets were obtained from the GSEA database, and ssGSEA was used to calculate the relative enrichment score of each bone metabolism-related gene set in every sample. The results of the variation analysis are shown in Figure 4A; eight of the 13 bone metabolism-related gene sets were significantly dysregulated in low-BMD samples compared to high-BMD samples, illustrating the disturbance of the bone metabolic microenvironment in OP (Supplementary Table S4). Then, the correlations of m6A regulators with bone metabolism-related gene sets were explored. The results showed that they had a very close relationship, in which the *RBM15*-module pair was most negatively correlated (r = -0.735), while the *RBM15B*-multinuclear osteoclast pair was most positively correlated (r = 0.565) (Figure 4B, Supplementary Table S5).

3.3 Identification of two distinct m6A methylation patterns

To further understand the role of m6A regulators in low BMD, unsupervised clustering analysis based on the 14 m6A regulators was performed and divided the low-BMD samples into two distinct m6A modification patterns, including 22 samples in cluster 1 and 18 samples in cluster 2 (Figures 5A–C, Supplementary Table S6). The PCA results confirmed that these m6A regulators could differentiate the two clusters in low-BMD samples (Figure 5D). Subsequently, we explored the expression of m6A regulators and bone metabolism-related gene sets between the two clusters. The variance analysis revealed that eight of 14 m6A regulators had a significant expression difference, validating the existence of diverse expression patterns mediated by m6A methylation modification in low-BMD samples (Figure 6A, Supplementary Table S7). Likewise,

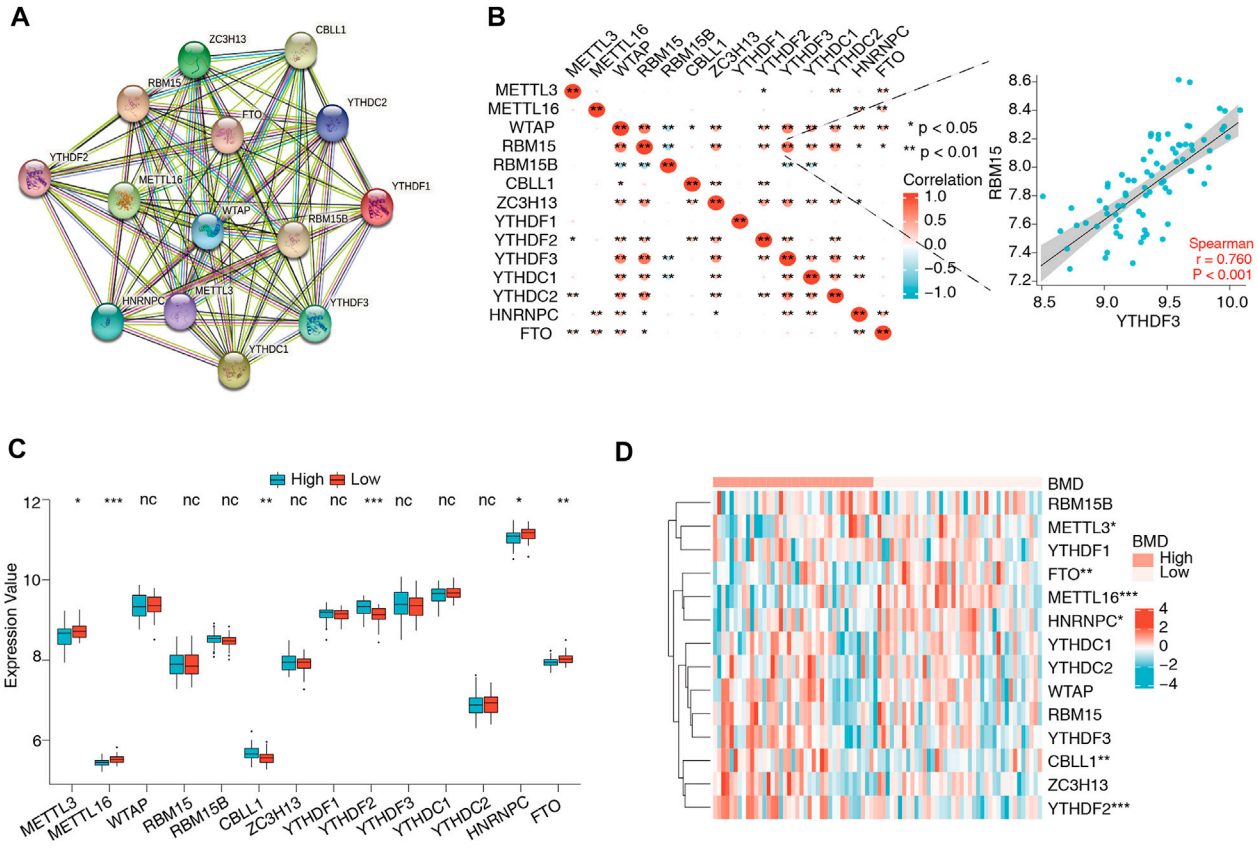

FIGURE 3
Expression and correlation of 14 m6A regulators in osteoporosis. **(A)** Protein–protein interactions of 14 m6A regulators. **(B)** Expression correlations of the 14 m6A regulators in all samples. The depth of the color block represents the level of the correlation coefficient, and * denotes the significance of the statistical analysis. The most correlated gene pair was *YTHDF2* and *RBM15*, the expression status of which is presented in the scatter plot in the right panel. **(C,D)** The box plot and heatmap plot show the summary of 14 m6A regulators between the high- and low-BMD groups, and six m6A regulators (*METTL3*, *METTL16*, *CBLL1*, *FTO*, *YTHDF2*, and *HNRNPC*) were significantly dysregulated.

eight of 13 bone metabolism-related gene sets showed significant changes between the two clusters, and interestingly, we found that all these dysregulated gene sets were upregulated in cluster 2 compared to cluster 1, suggesting that cluster 2 might have more active bone metabolism characteristics (Figure 6B, Supplementary Table S8).

3.4 Construction and validation of a diagnostic model of OP

The above findings indicated that m6A regulators were closely associated with bone metabolism-related gene sets and played an essential role in BMD and OP. Univariate logistic regression analysis was conducted to determine the differentially expressed genes, and five m6A regulators were found to be significantly correlated with BMD (Figure 7A, Supplementary Table S9). Then, we employed multivariate logistic regression to further reduce the unimportant regulators, and four key regulators were identified, namely, *METTL16*, *CBLL1*, *YTHDF2*, and *FTO* (Figure 7B, Supplementary Table S10). Next, these four key m6A regulators serving as variables were used to calculate the risk score of each sample and construct a diagnostic model of OP. The risk scores of the samples were determined (Supplementary Table S11), and the median risk score (-0.366) was used as the cutoff point to divide all the samples into two groups, namely, the high-risk group and the low-risk group. The high-risk and low-risk groups corresponded well to the low- and high-BMD groups, respectively (Figure 7C). In the diagnostic model, *CBLL1* and *YTHDF2* were protective factors, and their expression showed a downward trend with increasing risk score. *METTL16* and *FTO* were risk factors, and their expression showed an upward trend with increasing risk score. Furthermore, the ROC curve demonstrated that the expression values of the four key m6A regulators had moderate diagnostic accuracy (Figure 7D). The same result was also obtained for the test dataset (Figure 7E).

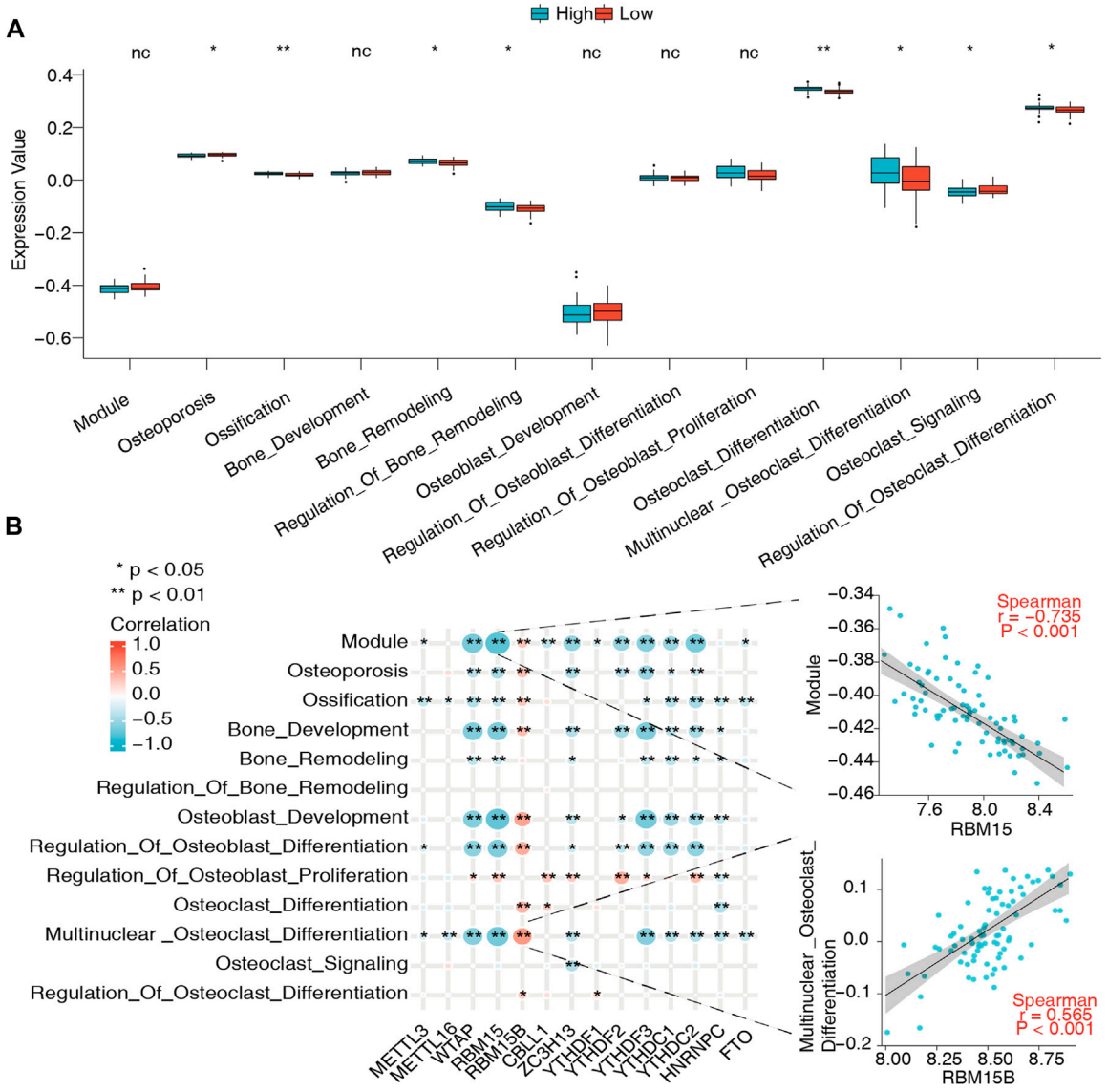

FIGURE 4
Relationship between bone metabolism-related gene sets and m6A regulators. **(A)** Differences in abundance and activity of bone metabolism-related gene sets in the high- and low-BMD groups. **(B)** Expression correlations of these bone metabolism-related gene sets and m6A regulators in all samples. Significantly, the *RBM15*-module pair was the most negatively correlated, the expression status of which is presented in the scatter plot in the upper right panel, while the *RBM15B*-multinuclear osteoclast differentiation pair was the most positively correlated with expression status presented in the scatter plot in the lower right panel.

3.5 Creation of a BMD-related m6A regulator-m6A target gene regulatory network

We obtained 4,868 METTL16 targets, 7,727 CBLL1 targets, 5,207 FTO targets, and 9979 YTHDF2 targets from M6A2Target, of which 306 genes were potentially coregulated with the four key m6A regulators (Figure 8A, Supplementary Table S12). Furthermore, these 306 targets were intersected with genes in the bone metabolism-related gene sets, and 26 target genes were finally obtained (Figure 8B, Supplementary Table S13). The KEGG pathway analysis showed that these genes were mainly enriched in parathyroid hormone synthesis, secretion, action, human papillomavirus infection, and the P13K-AKT signaling pathway, suggesting that these pathways might be closely related to BMD and OP (Figure 8C). The GO analysis indicated that the biological processes of these genes were mainly enriched in ossification, regulation of ossification, connective tissue development, and osteoblast differentiation, which were primarily related to bone metabolism (Figure 8D,

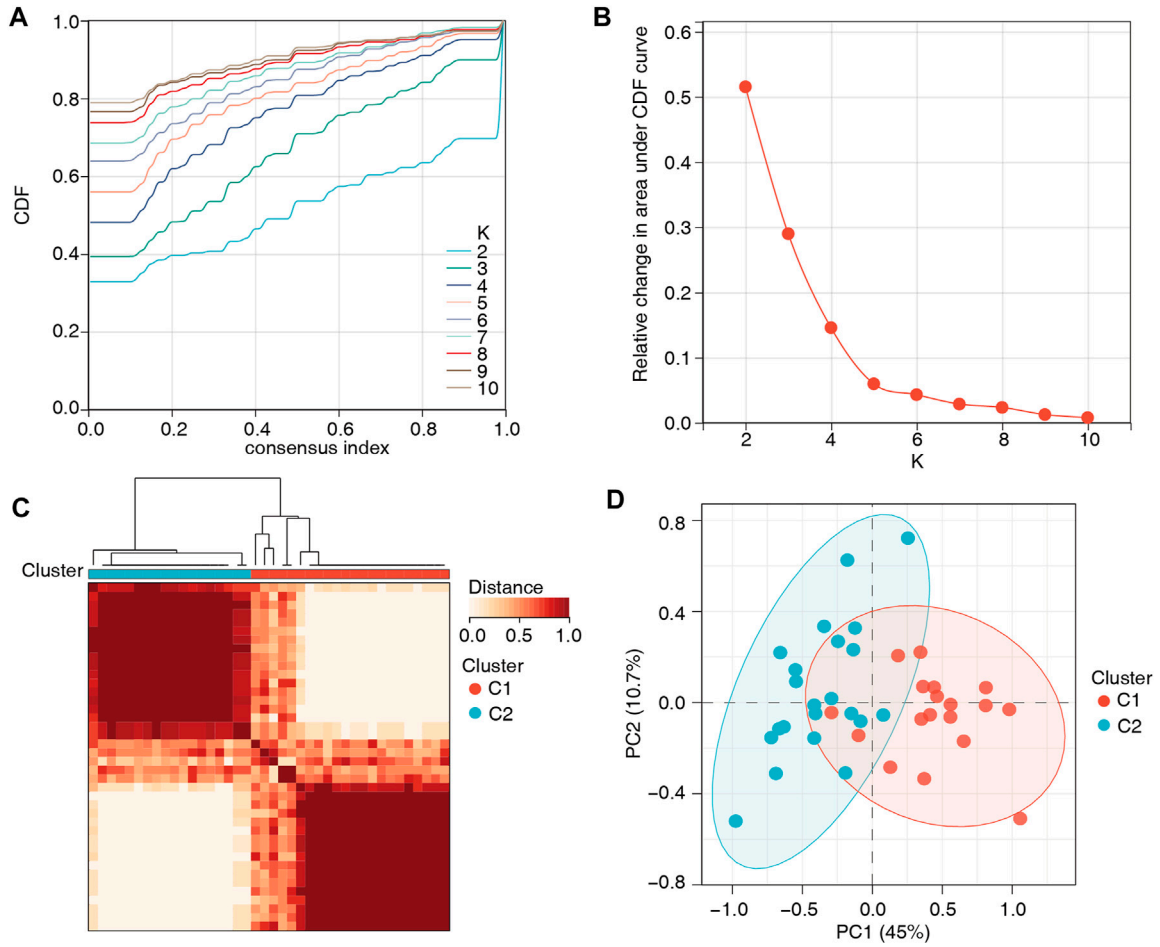

FIGURE 5
Unsupervised clustering analysis based on the 14 m6A regulators. **(A,B)** Consensus clustering cumulative distribution function (CDF) and the relative area under the CDF curve for k = 2–10. According to the recommendations for selecting the number of clusters, the number of clusters with the highest average consistency was k = 2. **(C)** The heatmap shows the consensus matrix for the optimal k = 2. **(D)** The PCA plot confirmed the striking difference between the two m6A modification patterns.

Supplementary Table S14). Then, we used Cytoscape software and created a regulatory network composed of the four hub m6A regulators and the 26 m6A target bone metabolism-related genes (Figure 8E).

3.6 Validation of the expression of the key m6A regulators *in vitro* and *in vivo*

To identify the reliability of the results based on bioinformatics analysis, we examined the expression of the four key m6A regulators (METTL16, CBLL1, YTHDF2, and FTO) *in vitro* and *in vivo*. RAW 264.7 cells, which are a classic cell line model for osteoclast and OP studies *in vitro*, were used in this study. RANKL treatment induced intense osteoclast differentiation of RAW264.7 cells (Figure 9A, Supplementary Figure S1A). Compared to control cells, a significantly elevated number of TRAP$^+$ multinuclear osteoclasts formed upon RANKL stimulation for 4 days, indicating that the osteoclast induction model *in vitro* was successfully constructed (Figure 9B). We quantified the m6A content in total RNA by ELISA assays, and the m6A content was significantly decreased during osteoclast differentiation (Figure 9C). The expression patterns of METTL16, FTO, CBLL1, and YTHDF2 at the RNA and protein levels were examined in RAW264.7 cells, and the results showed downregulated expression of CBLL1 and YTHDF2 and upregulated expression of METTL16 and FTO during osteoclast differentiation (Figures 9D–F). Likewise, osteoclast differentiation induced from mouse BMMs were used for further validation. The number of TRAP$^+$ multinuclear osteoclasts significantly increased upon RANKL- and MCSF

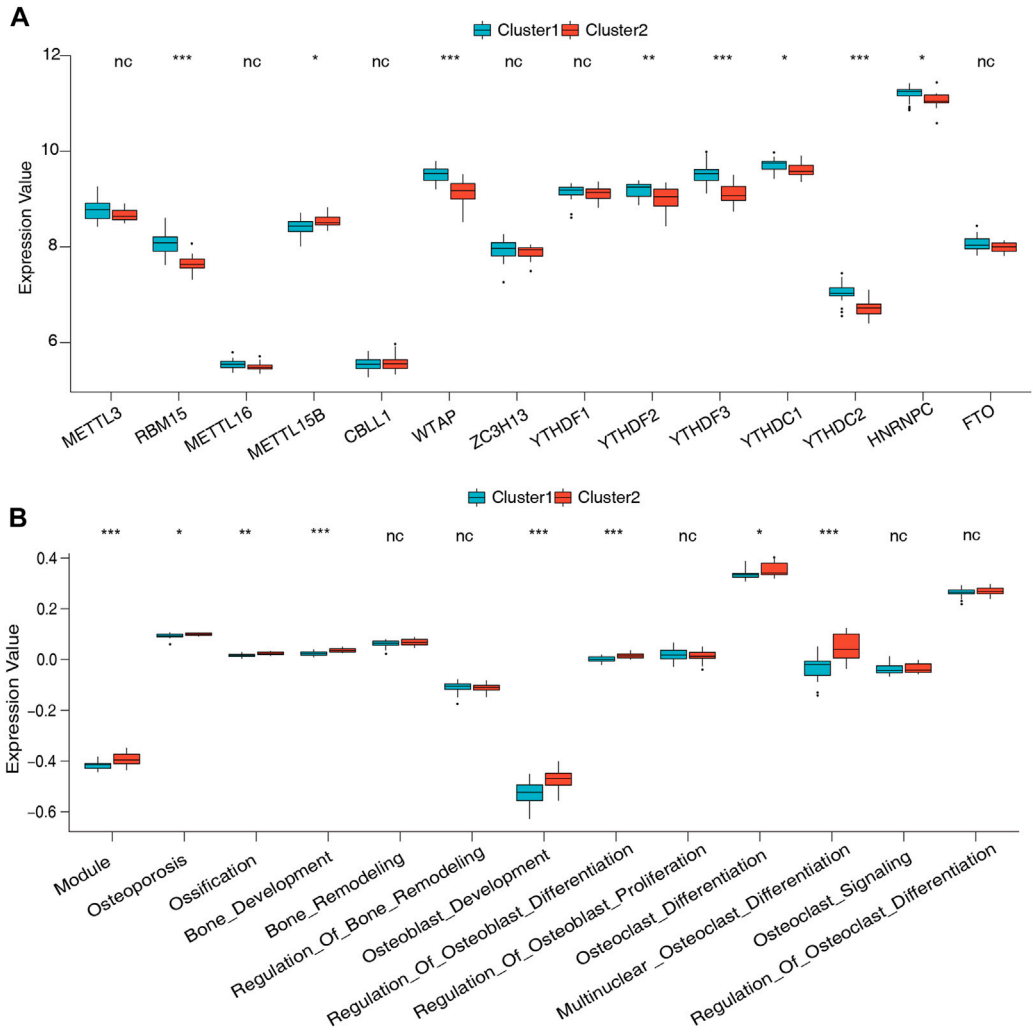

FIGURE 6
Expression of the m6A regulators and bone metabolism characteristics between the two m6A modification patterns. **(A)** Expression differences of 14 m6A regulators in the two m6A modification patterns. **(B)** Differences in the abundance and activity of bone metabolism-related gene sets in the two m6A modification patterns.

stimulation. (Figures 9G,H, Supplementary Figure S1B). Next, we examined the total m6A level and the expression of four key genes in BMMs during osteoclast differentiation. The results were the same as those in RAW264.7 cells, except METTL16 at the protein level (Figures 9I–L). Finally, an OVX mouse model was constructed to represent the OP patients, and a schematic diagram was drawn to show how we obtained the PBMCs from mice (Figure 9M). Bone destruction was indicated by HE staining, and the bone mass was significantly decreased in OVX mice, which suggested that OP model was successfully constructed. (Figure 9N). We obtained the same total m6A level and mRNA expression data of these four key m6A regulators in PBMCs from the OVX model (Figures 9O, P). These results were consistent with our integrated analysis, indicating that the four key m6A regulators might be used as biomarkers of OP. However, the exact regulatory mechanism requires further study.

4 Discussion

OP, characterized by reduced BMD, is a widespread disease with a high prevalence in older women (Camacho et al., 2020). Abnormal bone metabolism, including enhanced bone resorption and diminished bone formation related to low sex hormones, is the primary pathological mechanism of OP in older adults (Awasthi et al., 2018). m6A RNA methylation is the most common epigenetic modification and is confirmed to be involved in almost every aspect of metabolism (Wei et al., 2017; Wu et al.,

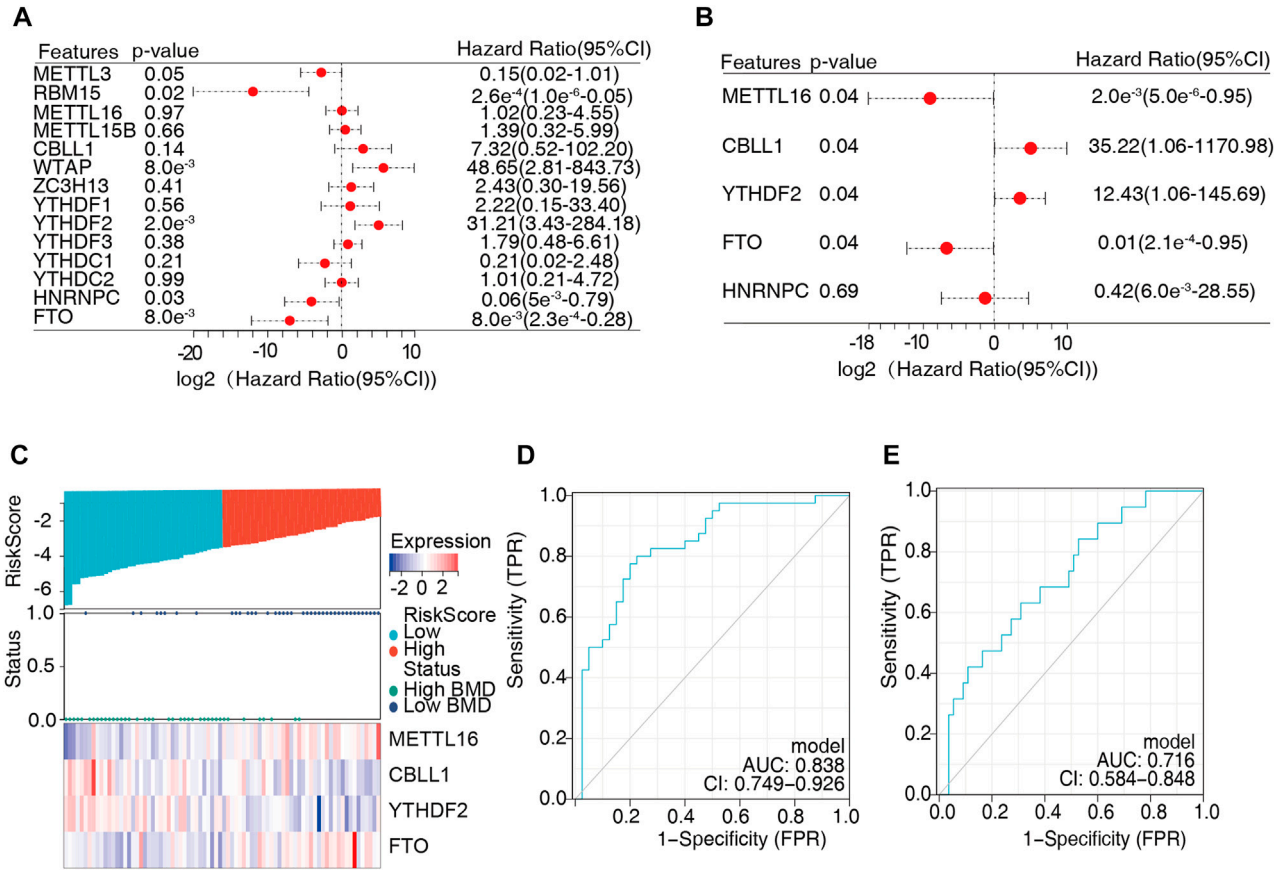

FIGURE 7
Construction of a diagnostic model of osteoporosis. **(A)** Univariate logistic regression analysis was conducted to identify the critical m6A regulators, indicating that five m6A regulators were significant for osteoporosis (*METTL16*, *CBLL1*, *YTHDF2*, *HNRNPC*, and *FTO*). **(B)** Multivariate logistic regression was employed to identify the independent modules, and four vital m6A regulators were obtained for the diagnostic model (*METTL16*, *CBLL1*, *YTHDF2*, and *FTO*). **(C)** The risk score was calculated based on the expression of the four vital m6A regulators, and the median risk score (−0.366) was used as the cutoff point. All samples were divided into two groups: the high-risk group and the low-risk group. **(D,E)** The sensitivity and specificity of the diagnostic model in the training dataset **(D)** and test dataset **(E)** were determined by receiver operating characteristic (ROC) curves, and the area under the curve was calculated.

2018b). Studies have found that some m6A regulators, such as METTL3, FTO, and YTHDF2, play an essential role in bone metabolism by affecting the differentiation and proliferation of bone-related cells (Wu et al., 2018a; Li et al., 2019; Yu et al., 2019). However, an integrated bioinformatics analysis of various m6A regulators and bone metabolism characteristics in OP has not been systematically researched, which may increase understanding of the molecular mechanisms of m6A-mediated OP and provide some evidence for subsequent treatment.

We first searched GEO datasets and downloaded GSE56815 data concerning the gene expression of PBMCs in pre- and postmenopausal females, including 40 high-BMD and 40 low-BMD samples. First, we found that many m6A regulators have strong protein interactions or expression correlations, suggesting that they may function as complexes. The expression of most m6A regulators was altered between the high-BMD and low-BMD samples, illustrating that m6A regulators may be involve in OP development. Next, to investigate the relationship between m6A regulators and bone metabolism, we obtained 13 bone metabolism-related gene sets from the GESA database. Osteoporosis and osteoclast signaling gene sets were upregulated in the low-BMD group, while ossification, bone remodeling, and osteoclast differentiation, among other gene sets, were downregulated, implying the disturbance of the bone metabolic microenvironment in OP. In addition, we found that these bone metabolism-related gene sets were closely associated with m6A regulators. *RBM15* was most negatively connected with Module. The module pathway represents the degree of bone mineralization, which determines BMD (Roschger et al., 2014). A previous study demonstrated that circ-CTNNB1 interacted with RBM15 and subsequently promoted the aerobic glycolysis process (Yang et al., 2022).

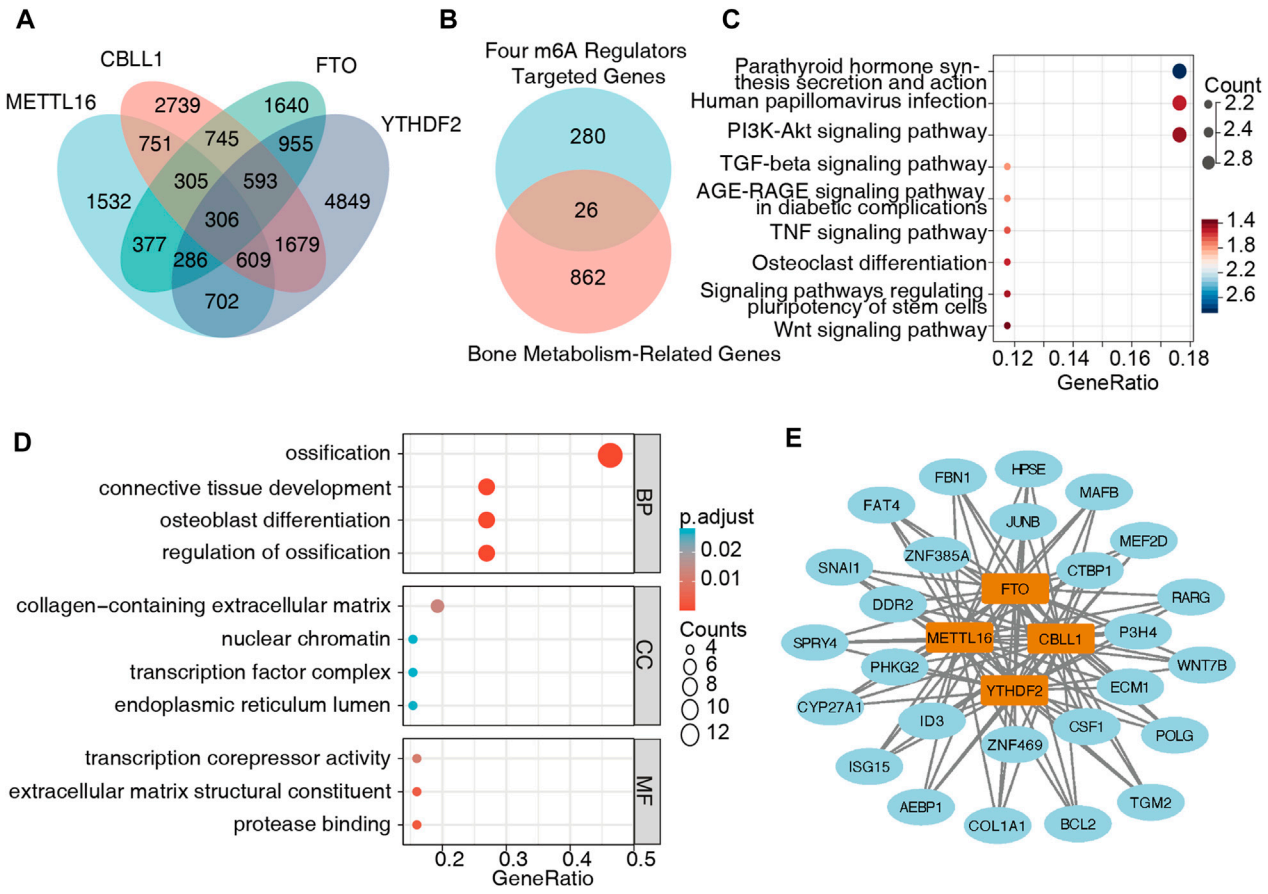

FIGURE 8
Creation of a regulatory network of m6A regulators-m6A target genes. **(A)** m6A target genes were obtained from M6A2Target, and 306 genes were potentially coregulated with the four m6A regulators. **(B)** Twenty-six m6A target genes were also closely related to bone metabolism. **(C)** KEGG pathway analysis showed that these 26 genes were mainly enriched in parathyroid hormone synthesis, secretion, action, human papillomavirus infection, and the P13K-AKT signaling pathway. **(D)** The GO analysis indicated that the biological processes of these genes were mainly enriched in ossification, regulation of ossification, connective tissue development, and osteoblast differentiation. **(E)** A regulatory network was built with four hub m6A regulators and 26 m6A target genes.

Meanwhile, aerobic glycolysis is critical for osteoclastogenesis, and increased aerobic glycolysis may induce excessive bone resorption and lead to osteoporotic fractures (Li B. et al., 2020). *RBM15B* was most positively connected with multinuclear osteoclast differentiation, which accelerates bone absorption and then promotes the occurrence and development of OP, while no relevant studies have explored the role of RBM15B in multinuclear osteoclast differentiation, which needs to be further studied in the future. However, it has been reported that METTL3 can modulate Atp6v0d2 mRNA degradation and Traf6 mRNA nuclear export to regulate osteoclast differentiation and function (Li D. et al., 2020). These results suggested that m6A modification had an essential regulatory role in shaping different bone metabolic microenvironments in OP.

Unsupervised clustering analyses have been used in several studies based on gene signatures to help elucidate the underlying mechanism of the studied disease (Zhang et al., 2020; Shen et al., 2021a; Liu et al., 2021). A recent study employed this method to comprehensively evaluate the m6A modification patterns among 9,804 pancancer samples and identified three distinct m6A modification subtypes, which enhanced our understanding of the dysregulation of RNA methylation in tumor microenvironments (Shen et al., 2021b). We used 14 m6A signatures and developed two distinct m6A modification subgroups with different bone metabolism microenvironments in the low-BMD group. Compared with cluster 1, cluster 2 had more active bone metabolic activities. The unique characteristics of bone metabolism between the two clusters verified the feasibility of classifying the bone metabolic microenvironment by m6A regulators. Simultaneously, our findings aid a deeper understanding of the molecular mechanisms of OP and may be used as a basis for individualized choice of drug therapy (Marozik et al.,

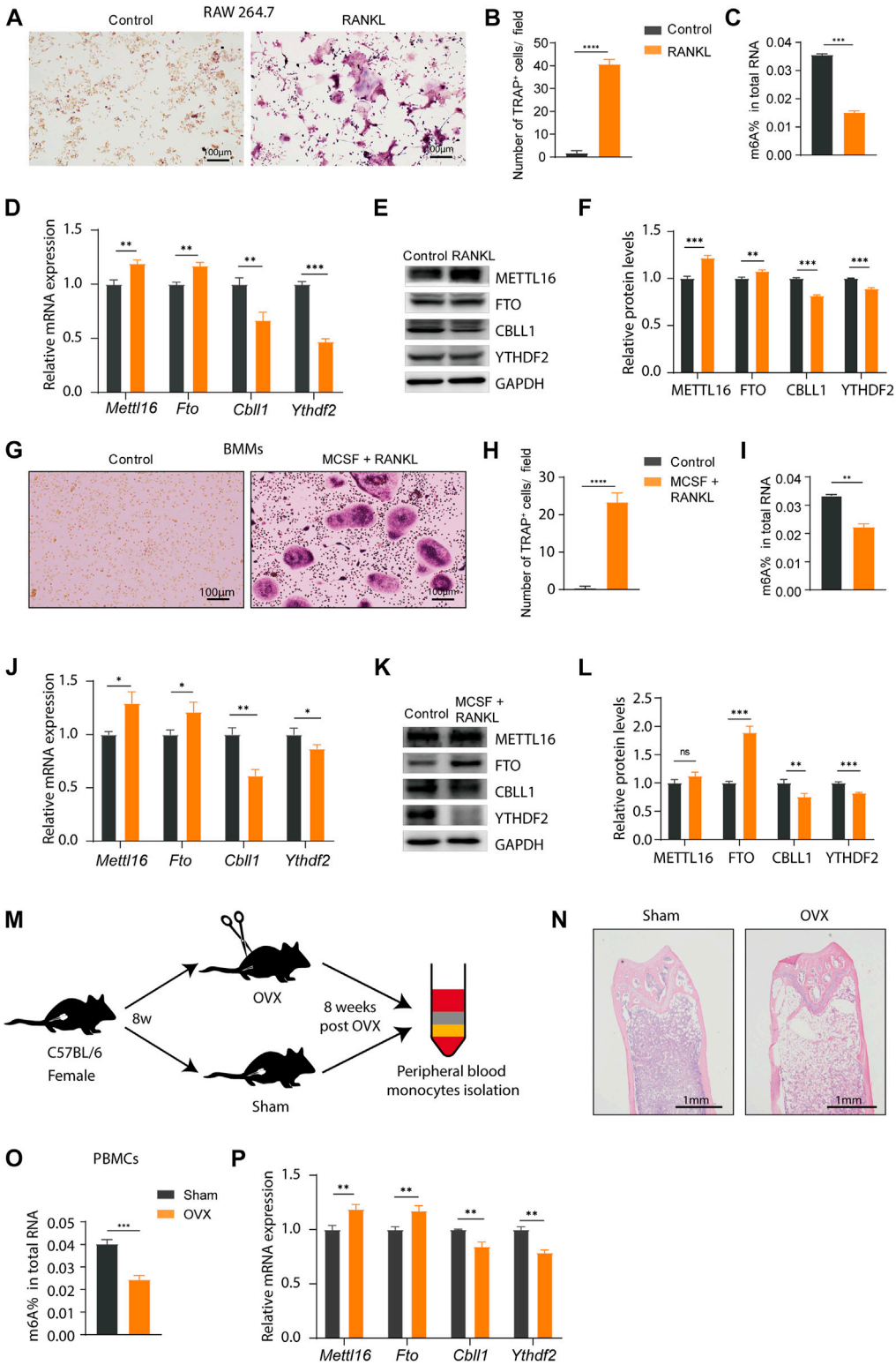

FIGURE 9
Validation of the expression of the key m6A regulators *in vitro* and *in vivo*. **(A,B)** Tartrate-resistant acid phosphatase (TRAP) staining and TRAP$^+$ multinuclear cells counting of RAW 264.7 cells with or without nuclear factor (NF)-κB (RANKL) stimulation. Scale bar, 100 μm. **(C)** The m6A level in total RNA isolated from RAW264.7 cells during the osteoclast differentiation. **(D)** The expression of *Mettl16*, *Fto*, *Cbll1*, and *Ythdf2* in RAW264.7 cells was detected by real-time PCR after cultured with RANKL for 4 days **(E,F)** Western blotting and quantification of METTL16, FTO, CBLL1 and
(*Continued*)

FIGURE 9 (Continued)
YTHDF2 in RAW264.7 cells after cultured in RANKL. **(G,H)** TRAP staining and TRAP^{+} multinuclear cells counting of bone marrow-derived macrophages (BMMs) with or without RANKL and macrophage colony-stimulating factor (MCSF) stimulation. Scale bar, 100 μm. **(I)** The m6A level in total RNA isolated from BMMs during the osteoclast differentiation. **(J)** The expression of *Mettl16*, *Fto*, *Cbll1*, and *Ythdf2* in BMMs was detected by real-time PCR after cultured with RANKL and MCSF for 4 days **(K,L)** Western blotting and quantification of METTL16, FTO, CBLL1, and YTHDF2 in BMMs after cultured in RANKL and MCSF. **(M)** A schematic diagram shows how peripheral blood monocytes (PBMCs) were obtained from the ovariectomized (OVX) and sham mice. **(N)** Representative images of Hematoxylin and eosin (HE) staining of mouse femurs showing the reduction of bone formation in the OVX mice relative to the sham-control counterparts. **(O)** The m6A level in total RNA isolated from PBMCs of the OVX and sham mice. **(P)** The mRNA expression level of *Mettl16*, *Fto*, *Cbll1*, and *Ythdf2* in PBMCs of the OVX and sham groups. Compared with the sham group.

2019). Unsupervised clustering analyses have also been used in some clinical studies of OP. A study divided patients into nine subgroups with significant differences in clinical features, BMD distribution, and medical care costs. It quantified patients into three different fracture risk levels, which showed a better understanding of fracture risk phenotypes (Kruse et al., 2017).

We evaluated the role of m6A regulators in diagnosing OP or the BMD phenotype using univariate and multivariate logistic regression analyses, which are widely applied in diagnosing diseases such as periodontitis and appendicitis (Eddama et al., 2019; Zhang et al., 2021). Four key m6A regulators significantly associated with the BMD phenotype were chosen for the diagnostic model. In this model, patients with high *CBLL1* and *YTHDF2* expression had a low likelihood of decreased bone density. In contrast, patients with high expression of *METTL16* and *FTO* had an increased risk of OP. Subsequently, the risk score of all the samples was evaluated. The results showed that patients with low BMD had a higher risk score, suggesting their potential clinical value for the diagnosis of OP. Furthermore, the model's predictive power was assessed by ROC analysis, which showed moderate accuracy. The same result was also obtained in the test dataset, which further verified the extrapolation of the results. The roles of FTO and YTHDF2 have been studied in OP. FTO promotes OP through demethylating Runx2 mRNA and inhibiting osteogenic differentiation (Wang et al., 2021). YTHDF2 might be involved in regulation of the lipopolysaccharide (LPS)-stimulated inflammatory reactions *via* regulating the stability of MAP2K4 and MAP4K4 mRNAs in RAW 264.7 cells (Yu et al., 2019). However, CBLL1 and METTL16 have mainly been studied in cancers and act as oncogenic markers to promote the development and progression of tumors (Hui et al., 2019; Su et al., 2022). Their role in OP has not been reviewed, which guides us to further explore their relevant roles in the OP field.

A gene regulatory network containing the four hub m6A regulators and 26 m6A target genes related to bone metabolism was constructed to further understand the role of m6A regulators in OP. The biological processes of these target genes were mainly enriched in ossification, implying their essential role in OP or BMD. In addition, KEGG analysis revealed that these genes primarily focused on parathyroid hormone synthesis, secretion, action, human papillomavirus infection, and the P13K-AKT signaling pathway. Parathyroid hormone has been reported to augment bone formation, particularly in trabecular and cortical bone, and has a central role in regulating extracellular fluid Ca^{++} and phosphate (Pi) homeostasis (Goltzman, 2018). One study has showed that METTL3 reduces the translation efficiency of the bone marrow stem cell (BMSC) lineage allocator parathyroid hormone receptor 1 and disrupts parathyroid hormone-induced osteogenic and adipogenic responses to promote OP (Wu et al., 2018a). There is no related research on HPV infection and OP, but one study found higher mean alveolar bone loss in patients with HPV-positive tumors (Mine Tezal et al., 2009). The PI3K-AKT signaling pathway has been reported to be involved in various cellular processes, including BMSCs proliferation and osteoclast differentiation (Shen G. Y. et al., 2018). Conditional knockdown of METTL3 in BMSC suppressed PI3K-Akt signaling and limited the expression of bone formation-related genes to regulate osteogenic differentiation and alternative splicing of Vegfa in BMSC(Tian et al., 2019). These findings may provide a foundation for m6A modification in OP and imply a direction for the relationship between m6A regulators and bone metabolism-related genes in OP.

Finally, we verified the expression of the key m6A regulators *in vivo* and *in vitro* models of OP. Excessive osteoclast activity results in reduced bone mass and decreased bone strength in OP, hence, osteoclasts are considered therapeutic targets for bone-related diseases including OP. In the present study, we established RANKL- and/or MCSF-induced BMMs and RAW264.7 cells as osteoclast differentiation cell models (Kim et al., 2020). In addition, we constructed animal models of OP to further investigate our results, and the OVX model is the most utilized approach in such studies (Fu et al., 2020). We first quantified m6A contents and found that the total m6A levels were significantly decreased in osteoclast differentiation cells and OVX mice, which was consistent with the related research in OP (Yan et al., 2020). The expression of METTL16, CBLL1, YTHDF2, and FTO at the RNA and protein levels was consistent with our bioinformatics analysis results. However, interestingly, METTL16 and FTO, which exhibit opposing m6A catalytic abilities, were significantly

upregulated in RAW264.7 cells, BMMs and PBMCs. The upregulation trend of FTO, the most important demethylase, was consistent with the decreasing m6A level and downregulated expression of CBLL1 and YTHDF2, while METTL16 exhibited a negative correlation with that. One possible explanation for the increased METTL16 might be that METTL16 could be compensating for the feedback of descending m6A modification induced by FTO, CBLL1 and YTHDF2 in RAW264.7 cells, BMMs and PBMCs. The phenomenon that these enzymes with opposite functions have the same expression trend is common in other m6A-related studies (Ma et al., 2017). The OVX mouse model is an excellent preclinical model. However, because a small amount of peripheral blood, approximately 0.75–1 ml for each mouse, can be obtained, the number of PMBCs is limited. These PMBCs could obtain approximately 1 ug of RNA, which met the experimental verification at the RNA level. However, those PMBCs were not enough for protein level verification, and the relevant validation needs to be carried out in other large animals or clinical trials in the future.

These findings further illustrated the impact of m6A regulators on the bone metabolic microenvironment of OP. However, there are still some limitations to our study. First, collecting blood samples from human patients is an invasive operation. Considering that our study is a preliminary exploratory study, it cannot benefit patients for the time being. Especially during the COVID-19 pandemic, due to the requirements of ethics and social management, we were unable to collect human samples, which are more credible than cell lines and mouse samples. Of course, if we can collect some blood samples during the operation of OP patients in the future, we will carry out corresponding experiments for further verification. In addition, the datasets on OP presently lack a more extensive sample study, so extrapolation of the above results may be limited due to the small sample size of our study. Finally, our study mainly focused on exploring the role of m6A modification in the diagnosis of OP, and we did not investigate the specific regulatory mechanism of m6A regulators in OP. Relevant studies have shown that FTO can regulate the occurrence and development of OP through the GDF11-FTO-Pparg axis, which can be used as a potential therapeutic target (Shen G. S. et al., 2018). Moreover, only a limited number of FTO inhibitors have been identified, yet their efficacy and safety are inconclusive. Notably, there are currently no m6A-based drugs developed for OP. Therefore, to address these limitations, we still have a long way to go.

5 Conclusion

In conclusion, we preliminarily explored the implications of m6A regulators in OP by identifying two m6A modification patterns and constructing a regulatory network of the m6A regulator-m6A target genes. In addition, we successfully identified four m6A regulators, namely, *METTL16*, *CBLL1*, *YTHDF2*, and *FTO*, as potential biomarkers for diagnosing OP and the expression of the four key m6A regulators was validated *in vitro* and *in vivo*. Taken together, our results revealed that m6A modification has essential roles in OP, which may imply a direction for us to further explore the specific mechanism of these m6A regulators in OP.

Data availability statement

The original contributions presented in the study are included in the article/Supplementary Material, further inquiries can be directed to the corresponding authors.

Ethics statement

The animal study was reviewed and approved by Biomedical Ethics Committee of Peking University (issue number: LA2020199).

Author contributions

Study design and conception: YQ, YL, and SZ. Data acquisition: YQ, JL, DL, and CZ. Data analysis, interpretation, and experimental validation: YQ and JL. Drafting the work: YQ, JL, DL, CZ, YL, and SZ. Critical revision of the work for important intellectual content: YQ, YL, and SZ. All authors have read and approved the final manuscript.

Funding

This work was supported by the National Natural Science Foundation of China (Grant number 81771053), National Natural Science Foundation of China Youth Fund Project (Grant number 82001029). The authors have no other relevant affiliations or financial involvement with any organization or entity with a financial interest in or financial conflict with the subject matter or materials discussed in the manuscript apart from those disclosed.

Acknowledgments

Special thanks for Dear Prof. Yao Zhong Liu from Tulane University to share the gene expression data of samples in GSE56815 and Dear Prof. Sjur Reppe from Oslo University to share the gene expression data in E-MEXP-1618.

Conflict of interest

The authors declare that the research was conducted in the absence of any commercial or financial relationships that could be construed as a potential conflict of interest.

Publisher's note

All claims expressed in this article are solely those of the authors and do not necessarily represent those of their affiliated organizations, or those of the publisher, the editors and the reviewers. Any product that may be evaluated in this article, or claim that may be made by its manufacturer, is not guaranteed or endorsed by the publisher.

Supplementary material

The Supplementary Material for this article can be found online at: https://www.frontiersin.org/articles/10.3389/fgene.2022.1072948/full#supplementary-material

References

An, Y., and Duan, H. (2022). The role of m6A RNA methylation in cancer metabolism. *Mol. Cancer* 21 (1), 14. doi:10.1186/s12943-022-01500-4

Awasthi, H., Mani, D., Singh, D., and Gupta, A. (2018). The underlying pathophysiology and therapeutic approaches for osteoporosis. *Med. Res. Rev.* 38 (6), 2024–2057. doi:10.1002/med.21504

Camacho, P. M., Petak, S. M., Binkley, N., Diab, D. L., Eldeiry, L. S., Farooki, A., et al. (2020). American association of clinical endocrinologists/American college of endocrinology clinical practice guidelines for the diagnosis and treatment of postmenopausal osteoporosis-2020 update. *Endocr. Pract.* 26, 1–46. doi:10.4158/GL-2020-0524SUPPL

Chen, P., Li, Z., and Hu, Y. (2016). Prevalence of osteoporosis in China: A meta-analysis and systematic review. *BMC Public Health* 16 (1), 1039. doi:10.1186/s12889-016-3712-7

Chen, Y., Xie, Z., Zhang, Y., Xia, C., Yang, M., and Hu, X. (2020). Shikonin relieves osteoporosis of ovariectomized mice by inhibiting RANKL-induced NF-κB and NFAT pathways. *Exp. Cell. Res.* 394 (1), 112115. doi:10.1016/j.yexcr.2020.112115

Chun, K. J. (2011). Bone densitometry. *Semin. Nucl. Med.* 41 (3), 220–228. doi:10.1053/j.semnuclmed.2010.12.002

Curtis, E. M., Moon, R. J., Harvey, N. C., and Cooper, C. (2017). The impact of fragility fracture and approaches to osteoporosis risk assessment worldwide. *Bone* 104, 29–38. doi:10.1016/j.bone.2017.01.024

Dr, E. (1997). Bone biomarkers as tools in osteoporosis management. *Spine* 22 (24S), 17S–24S. doi:10.1097/00007632-199712151-00004

Eddama, M., Fragkos, K. C., Renshaw, S., Aldridge, M., Bough, G., Bonthala, L., et al. (2019). Logistic regression model to predict acute uncomplicated and complicated appendicitis. *Ann. R. Coll. Surg. Engl.* 101 (2), 107–118. doi:10.1308/rcsann.2018.0152

Fu, L., Wu, W., Sun, X., and Zhang, P. (2020). Glucocorticoids enhanced osteoclast autophagy through the PI3K/Akt/mTOR signaling pathway. *Calcif. Tissue Int.* 107 (1), 60–71. doi:10.1007/s00223-020-00687-2

Goltzman, D. (2018). Physiology of parathyroid hormone. *Endocrinol. Metab. Clin. North Am.* 47 (4), 743–758. doi:10.1016/j.ecl.2018.07.003

Guo, Y., Liu, H., Yang, T. L., Li, S. M., Li, S. K., Tian, Q., et al. (2011). The fat mass and obesity associated gene, FTO, is also associated with osteoporosis phenotypes. *Plos One* 6 (11), e27312. doi:10.1371/journal.pone.0027312

Hui, L., Zhang, S., Wudu, M., Ren, H., Xu, Y., Zhang, Q., et al. (2019). CBLL1 is highly expressed in non-small cell lung cancer and promotes cell proliferation and invasion. *Thorac. Cancer* 10 (6), 1479–1488. doi:10.1111/1759-7714.13097

Kim, E. N., Kwon, J., Lee, H. S., Lee, S., Lee, D., and Jeong, G. S. (2020). Inhibitory effect of cudratrixanthone U on RANKL-induced osteoclast differentiation and function in macrophages and BMM cells. *Front. Pharmacol.* 11, 1048. doi:10.3389/fphar.2020.01048

Kruse, C., Eiken, P., and Vestergaard, P. (2017). Clinical fracture risk evaluated by hierarchical agglomerative clustering. *Osteoporos. Int.* 28 (3), 819–832. doi:10.1007/s00198-016-3828-8

Kylmaoja, E., Nakamura, M., Turunen, S., Patlaka, C., Andersson, G., Lehenkari, P., et al. (2018). Peripheral blood monocytes show increased osteoclast differentiation potential compared to bone marrow monocytes. *Heliyon* 4 (9), e00780. doi:10.1016/j.heliyon.2018.e00780

Li, B., Lee, W. C., Song, C., Ye, L., Abel, E. D., and Long, F. (2020a). Both aerobic glycolysis and mitochondrial respiration are required for osteoclast differentiation. *FASEB J.* 34 (8), 11058–11067. doi:10.1096/fj.202000771R

Li, D., Cai, L., Meng, R., Feng, Z., and Xu, Q. (2020b). METTL3 modulates osteoclast differentiation and function by controlling RNA stability and nuclear export. *Int. J. Mol. Sci.* 21 (5), 1660. doi:10.3390/ijms21051660

Li, Y., Yang, F., Gao, M., Gong, R., Jin, M., Liu, T., et al. (2019). miR-149-3p regulates the switch between adipogenic and osteogenic differentiation of BMSCs by targeting FTO. *Mol. Ther. Nucleic Acids* 17, 590–600. doi:10.1016/j.omtn.2019.06.023

Licata, A. A., Binkley, N., Petak, S. M., and Camacho, P. M. (2018). Consensus statement by the American association of clinical endocrinologists and American college of endocrinology on the quality of dxa scans and reports. *Endocr. Pract.* 24 (2), 220–229. doi:10.4158/CS-2017-0081

Liu, F., Yu, X., and He, G. (2021). m6A-mediated tumor invasion and methylation modification in breast cancer microenvironment. *J. Oncol.* 2021, 9987376. doi:10.1155/2021/9987376

Ma, J. Z., Yang, F., Zhou, C. C., Liu, F., Yuan, J. H., Wang, F., et al. (2017). METTL14 suppresses the metastatic potential of hepatocellular carcinoma by modulating N(6) -methyladenosine-dependent primary MicroRNA processing. *Hepatology* 65 (2), 529–543. doi:10.1002/hep.28885

Marozik, P., Alekna, V., Rudenko, E., Tamulaitiene, M., Rudenka, A., Mastaviciute, A., et al. (2019). Bone metabolism genes variation and response to bisphosphonate treatment in women with postmenopausal osteoporosis. *Plos One* 14 (8), e0221511. doi:10.1371/journal.pone.0221511

Miller, P. D. (2016). Management of severe osteoporosis. *Expert Opin. Pharmacother.* 17 (4), 473–488. doi:10.1517/14656566.2016.1124856

Reppe, S., Refvem, H., Gautvik, V. T., Olstad, O. K., Hovring, P. I., Reinholt, F. P., et al. (2010). Eight genes are highly associated with BMD variation in postmenopausal Caucasian women. *Bone* 46 (3), 604–612. doi:10.1016/j.bone.2009.11.007

Roschger, P., Misof, B., Paschalis, E., Fratzl, P., and Klaushofer, K. (2014). Changes in the degree of mineralization with osteoporosis and its treatment. *Curr. Osteoporos. Rep.* 12 (3), 338–350. doi:10.1007/s11914-014-0218-z

Shen, G. S., Zhou, H. B., Zhang, H., Chen, B., Liu, Z. P., Yuan, Y., et al. (2018a). The GDF11-FTO-PPARγ axis controls the shift of osteoporotic MSC fate to adipocyte and inhibits bone formation during osteoporosis. *Biochim. Biophys. Acta. Mol. Basis Dis.* 1864 (12), 3644–3654. doi:10.1016/j.bbadis.2018.09.015

Shen, G. Y., Ren, H., Huang, J. J., Zhang, Z. D., Zhao, W. H., Yu, X., et al. (2018b). Plastrum testudinis extracts promote BMSC proliferation and osteogenic differentiation by regulating Let-7f-5p and the TNFR2/PI3K/AKT signaling pathway. *Cell. Physiol. biochem.* 47 (6), 2307–2318. doi:10.1159/000491541

Shen, S., Yan, J., Zhang, Y., Dong, Z., Xing, J., and He, Y. (2021a). N6-methyladenosine (m6A)-mediated messenger RNA signatures and the tumor immune microenvironment can predict the prognosis of hepatocellular carcinoma. *Ann. Transl. Med.* 9 (1), 59. doi:10.21037/atm-20-7396

Shen, S., Zhang, R., Jiang, Y., Li, Y., Lin, L., Liu, Z., et al. (2021b). Comprehensive analyses of m6A regulators and interactive coding and non-coding RNAs across 32 cancer types. *Mol. Cancer* 20 (1), 67. doi:10.1186/s12943-021-01362-2

Su, R., Dong, L., Li, Y., Gao, M., He, P. C., Liu, W., et al. (2022). METTL16 exerts an m(6)A-independent function to facilitate translation and tumorigenesis. *Nat. Cell. Biol.* 24 (2), 205–216. doi:10.1038/s41556-021-00835-2

Tezal, M., Nasca, M. S., Stoler, D. L., Melendy, T., Hyland, A., Smaldino, P. J., et al. (2009). Chronic periodontitis–human papillomavirus synergy in base of tongue

cancers. *Arch. Otolaryngol. Head. Neck Surg.* 135 (4), 391–396. doi:10.1001/archoto.2009.6

Tian, C., Huang, Y., Li, Q., Feng, Z., and Xu, Q. (2019). Mettl3 regulates osteogenic differentiation and alternative splicing of vegfa in bone marrow mesenchymal stem cells. *Int. J. Mol. Sci.* 20 (3), 551. doi:10.3390/ijms20030551

Wang, J., Fu, Q., Yang, J., Liu, J. L., Hou, S. M., Huang, X., et al. (2021). RNA N6-methyladenosine demethylase FTO promotes osteoporosis through demethylating Runx2 mRNA and inhibiting osteogenic differentiation. *Aging* 13 (17), 21134–21141. doi:10.18632/aging.203377

Wei, W., Ji, X., Guo, X., and Ji, S. (2017). Regulatory role of N(6) -methyladenosine (m6A) methylation in RNA processing and human diseases. *J. Cell. Biochem.* 118 (9), 2534–2543. doi:10.1002/jcb.25967

Wu, Y., Xie, L., Wang, M., Xiong, Q., Guo, Y., Liang, Y., et al. (2018a). Mettl3-mediated m(6)A RNA methylation regulates the fate of bone marrow mesenchymal stem cells and osteoporosis. *Nat. Commun.* 9 (1), 4772. doi:10.1038/s41467-018-06898-4

Wu, Y., Zhou, C., and Quan, Y. (2018b). Role of DNA and RNA N6-adenine methylation in regulating stem cell fate. *Curr. Stem Cell. Res. Ther.* 13 (1), 31–38. doi:10.2174/1574888X12666170621125457

Yan, G., Yuan, Y., He, M., Gong, R., Lei, H., Zhou, H., et al. (2020). m(6)A methylation of precursor-miR-320/RUNX2 controls osteogenic potential of bone marrow-derived mesenchymal stem cells. *Mol. Ther. Nucleic Acids* 19, 421–436. doi:10.1016/j.omtn.2019.12.001

Yang, F., Liu, Y., Xiao, J., Li, B., Chen, Y., Hu, A., et al. (2022). Circ-CTNNB1 drives aerobic glycolysis and osteosarcoma progression via m6A modification through interacting with RBM15. *Cell. Prolif.* 2022, e13344. doi:10.1111/cpr.13344

Yao, G. Q., Troiano, N., Simpson, C. A., and Insogna, K. L. (2017). Selective deletion of the soluble Colony-Stimulating Factor 1 isoform *in vivo* prevents estrogen-deficiency bone loss in mice. *Bone Res.* 5, 17022. doi:10.1038/boneres.2017.22

Yu, R., Li, Q., Feng, Z., Cai, L., and Xu, Q. (2019). m6A reader YTHDF2 regulates LPS-induced inflammatory response. *Int. J. Mol. Sci.* 20 (6), 1323. doi:10.3390/ijms20061323

Zhang, S., Liu, F., Wu, Z., Xie, J., Yang, Y., and Qiu, H. (2020). Contribution of m6A subtype classification on heterogeneity of sepsis. *Ann. Transl. Med.* 8 (6), 306. doi:10.21037/atm.2020.03.07

Zhang, X., Zhang, S., Yan, X., Shan, Y., Liu, L., Zhou, J., et al. (2021). m6A regulator-mediated RNA methylation modification patterns are involved in immune microenvironment regulation of periodontitis. *J. Cell. Mol. Med.* 25 (7), 3634–3645. doi:10.1111/jcmm.16469

Zhou, Y., Deng, H. W., and Shen, H. (2015). Circulating monocytes: An appropriate model for bone-related study. *Osteoporos. Int.* 26 (11), 2561–2572. doi:10.1007/s00198-015-3250-7

Zhou, Y., Gao, Y., Xu, C., Shen, H., Tian, Q., and Deng, H. W. (2018). A novel approach for correction of crosstalk effects in pathway analysis and its application in osteoporosis research. *Sci. Rep.* 8 (1), 668. doi:10.1038/s41598-018-19196-2

frontiers | Frontiers in Genetics

TYPE Original Research
PUBLISHED 09 March 2023
DOI 10.3389/fgene.2023.985764

OPEN ACCESS

EDITED BY
Ernesto Picardi,
University of Bari Aldo Moro, Italy

REVIEWED BY
Ian James Martins,
University of Western Australia, Australia
Igor Jurak,
University of Rijeka, Croatia
Zhuanjian Li,
Henan Agricultural University, China

*CORRESPONDENCE
Caihong Wei,
weicaihong@caas.cn
Yuqin Wang,
Wangyq6836@163.com

SPECIALTY SECTION
This article was submitted to RNA, a section of the journal Frontiers in Genetics

RECEIVED 04 July 2022
ACCEPTED 27 February 2023
PUBLISHED 09 March 2023

CITATION
Fei X, Jin M, Yuan Z, Li T, Lu Z, Wang H, Lu J, Quan K, Yang J, He M, Wang T, Wang Y and Wei C (2023), MiRNA-Seq reveals key MicroRNAs involved in fat metabolism of sheep liver.
Front. Genet. 14:985764.
doi: 10.3389/fgene.2023.985764

MiRNA-Seq reveals key MicroRNAs involved in fat metabolism of sheep liver

Xiaojuan Fei[1], Meilin Jin[1], Zehu Yuan[2], Taotao Li[1], Zengkui Lu[3], Huihua Wang[1], Jian Lu[4], Kai Quan[5], Junxiang Yang[6], Maochang He[6], Tingpu Wang[7], Yuqin Wang[8]* and Caihong Wei[1]*

[1]Institute of Animal Science, Chinese Academy of Agricultural Sciences, Beijing, China, [2]Joint International Research Laboratory of Agriculture and Agri-Product Safety of Ministry of Education, Yangzhou University, Yangzhou, China, [3]Lanzhou Institute of Husbandry and Pharmaceutical Sciences, Chinese Academy of Agricultural Sciences, Lanzhou, China, [4]National Animal Husbandry Service, Beijing, China, [5]College of Animals Science and Technology, Henan University of Animal Husbandry and Economy, Zhengzhou, China, [6]Gansu Institute of Animal Husbandry and Veterinary Medicine, Pingliang, China, [7]College of Bioengineering and Biotechnology, TianShui Normal University, Tianshui, China, [8]College of Animals Science and Technology, Henan University of Science and Technology, Luoyang, China

There is a genetic difference between Hu sheep (short/fat-tailed sheep) and Tibetan sheep (short/thin-tailed sheep) in tail type, because of fat metabolism. Previous studies have mainly focused directly on sheep tail fat, which is not the main organ of fat metabolism. The function of miRNAs in sheep liver fat metabolism has not been thoroughly elucidated. In this study, miRNA-Seq was used to identify miRNAs in the liver tissue of three Hu sheep (short/fat-tailed sheep) and three Tibetan sheep (short/thin-tailed sheep) to characterize the differences in fat metabolism of sheep. In our study, Hu sheep was in a control group, we identified 11 differentially expressed miRNAs (DE miRNAs), including six up-regulated miRNAs and five down-regulated miRNAs. Miranda and RNAhybrid were used to predict the target genes of DE miRNAs, obtaining 3,404 target genes. A total of 115 and 67 GO terms as well as 54 and 5 KEGG pathways were significantly (padj < 0.05) enriched for predicted 3,109 target genes of up-regulated and 295 target genes of down-regulated miRNAs, respectively. oar-miR-432 was one of the most up-regulated miRNAs between Hu sheep and Tibetan sheep. And SIRT1 is one of the potential target genes of oar-miR-432. Furthermore, functional validation using the dual-luciferase reporter assay indicated that the up-regulated miRNA; oar-miR-432 potentially targeted sirtuin 1 (SIRT1) expression. Then, the oar-miR-432 mimic transfected into preadipocytes resulted in inhibited expression of SIRT1. This is the first time reported that the expression of SIRT1 gene was regulated by oar-miR-432 in fat metabolism of sheep liver. These results could provide a meaningful theoretical basis for studying the fat metabolism of sheep.

KEYWORDS

miRNA, liver, fat metabolism, Hu sheep, Tibetan sheep

1 Introduction

MicroRNAs (miRNAs) are a kind of small RNA, whose length is about 22 nt (nucleotide). Previous studies revealed that miRNAs have distinctive biological characteristics in proliferation, differentiation, metabolism, and disease (Lin et al., 2020). In animals and plants, miRNAs are involved in the regulation of post-transcriptional gene

expression. miRNAs usually bind to the 3'UTR region of mRNA to inhibit the post-transcriptional translation of target genes and enhance the degradation or repress the translation of mRNAs (Rouleau et al., 2017). In Chinese indigenous sheep, sheep can be divided into short/thin-tailed sheep, long/thin-tailed sheep, short/fat-tailed sheep, long/fat-tailed sheep, and fat-buttock sheep, because of the degree of fat deposition along the tail vertebra and the length of the tail vertebra (Lu et al., 2020). Hu sheep (short/fat-tailed sheep) and Tibetan sheep (short/thin-tailed sheep) are two Chinese indigenous sheep breeds with different tail types. Tail fat is the main energy source for sheep migration, drought, and food deprivation (Luo et al., 2021). However, studies mainly focus directly on tail fat to study fat metabolism, which is not the main organ of fat metabolism (Zhou et al., 2017; Li et al., 2020). The liver is a primary organ of fat metabolism, fat metabolization in the liver is equally important to its metabolism in fat tissue. Triglyceride is one of the lipids mostly formed in the liver, whose metabolism is mainly controlled through liver parenchyma cells. And the degree of fat deposition in fat tissue depends on the fat flow in the liver for fat synthesis. (Carotti et al., 2020). There are differences in the liver of sheep with different tail types that can reflect the underlying mechanism of sheep fat metabolism.

With the development of high-throughput sequencing technology, miRNA-Seq has been widely used in the omics analysis of humans (Zheng et al., 2016), mice (Peng et al., 2013), chickens (Sikorska et al., 2021) and cows (Zhang et al., 2019; Chen et al., 2020) species. And researchers showed that miRNA has an important function in fat metabolism (Deng et al., 2020). Many studies have explored the role of miRNA in liver fat metabolism disease models to clarify the process of disease occurrence. In a non-alcoholic fatty liver disease (NAFLD) mouse model, Lin et al. identified that miR-29a not only made body weight gain decrease, but also the subcutaneous, visceral, and intestinal fat accumulation and hepatocellular steatosis (Jeon and Carr., 2020). In the non-alcoholic steatohepatitis (NASH) mouse model, inhibiting the expression of miR-21 decreased liver injury, inflammation, and fibrosis (SOARES et al., 2016). In a high-fat-induced mouse model, miR-378 targeted *AMPK* to promote the occurrence of liver fibrosis and inflammation (Lin et al., 2019). Meanwhile, researchers have analyzed the expression patterns of miRNA in the liver of pigs (Li et al., 2021) and cows (Liang et al., 2017) across periods. These studies represented a foundation for further understanding the molecular regulatory mechanisms of liver tissue fat metabolism.

Because there is a genetic difference between Hu sheep (short/fat-tailed sheep) and Tibetan sheep (short/thin-tailed sheep) in tail type, comparing their livers' miRNA features may find miRNAs affecting the fat metabolism of Hu sheep (short/fat-tailed sheep) and Tibetan sheep (short/thin-tailed sheep). Our results could provide a theoretical basis for further study of the fat metabolism between different sheep breeds.

2 Matericals and methods

2.1 Tissue collection and sequencing

All animal experiments were approved by the Science Research Department of the Institute of Animal Sciences, Chinese Academy of Agriculture Sciences (IAS-CAAS). Ethical approval complied with the Animal Ethics Committee of the IAS-CAAS (No. IAS 2019-49). Samples of liver tissues were collected from three Hu sheep (short/fat-tailed sheep, Yongdeng, Gansu, China) and three Tibetan sheep (short/thin-tailed sheep, Yushu, Qinghai, China). Samples from Hu sheep are named HG1, HG2, and HG3, respectively. Samples from Tibetan sheep are named ZG1, ZG2, and ZG3, respectively. All sheep were males and slaughtered at age 1.5. All samples were frozen in liquid nitrogen in 1.5 mL RNase-free freezing tubes and stored at −80°C for use. Trizol (Invitrogen, Carlsbad, CA, United States) was used to extract total RNA. A NanoDrop2000 spectrophotometer (Thermo Fisher Scientific, Wilmington, MA, United States) was used to quantify RNA purity at 260 and 280 nm. Six libraries were constructed with a commercial sequencing provider: BGI (Mortazavi et al., 2008; Wang et al., 2009). An Agilent 2,100 Bioanalyzer (Agilent Technologies, Palo Alto, CA, United States) was used to examine the integrity of the library. All FASTQ sequencing files have been stored in the Sequence Read Archive (accession numbers PRJNA785102).

2.2 Sequence analysis

The cleaning of the raw data was performed based on: 1) poor quality sequencing reads, 2) reads with 5′ adaptors and without 3' adaptors; 3) reads without insert segments; and 5) reads containing poly A; and 6) reads longer than 18 nucleotides. To ensure that each small RNA had a unique label, according to the order of possible ribosomal RNA, small conditional RNA, small nucleolar RNA, small nuclear RNA (snRNA), and transfer RNA sequences to annotate (Balaskas et al., 2020). The sheep reference genome Oar_v3.1 (https://www.ebi.ac.uk/ena/browser/view/GCA_000298735.1, accessed on 20 February 2021) and miRbase21.0 (http://www.mirbase.org, accessed on 20 February 2021) was used to map clean reads with Bowtie2 (Langmead et al., 2009).

2.3 MiRNA identification and differential expression analysis

MiRDeep2 software was used to predict novel miRNAs (Kern et al., 2020). The expression of miRNA was calculated by absolute numbers counting of molecules using unique molecular identifiers (Pflug and Haeseler., 2018). Moreover, the lengths of small RNAs (sRNAs) and the proportion of miRNAs were calculated. The "oar-miR-" and "novel_mir" terms identify known miRNAs and novel miRNAs, respectively. Hu sheep is set as a control, DESeq2 software was used to perform the differential expression analysis, in which the statistical significance was set at a fold discover rate (FDR) adjusted p-value (padj ≤0.05) by Benjamini-Hochberg and |Log2Foldchange| > 0.5.

2.4 Target gene prediction of miRNAs and gene function enrichment analysis

Miranda (John et al., 2004) and RNAhybrid (Lin et al., 2022) were used to find more accurate targets of differentially expressed

miRNA (DE miRNA). g: Profiler was used for genes function enrichment analysis, in which the statistical significance was set at a fold discover rate (FDR) adjusted *p*-value (padj ≤0.05) by Benjamini–Hochberg (Raudvere et al., 2019). There are 3,109 target genes of upregulated and 295 target genes of downregulated DE miRNAs were annotated with Gene Ontology (GO) (http://www.geneontology.org/, accessed on 19 January 2022) and the Kyoto Encyclopedia of Genes and Genomes (KEGG) (http://www.genome.jp, accessed on 19 January 2022), respectively.

2.5 Quantitative real-Time PCR

Steam-loop real-time qPCR was used to validate miRNA sequencing data from seven randomly selected miRNAs (oar-miR-432, novel_mir70, novel_mir21, nov-el_mir64, novel_mir58, oar-miR-19b, and oar-miR-29b). The total RNA of each sample was reversed transcribed with a miRNA 1st Strand cDNA Synthesis Kit. RT-qPCR was performed on a LightCycler® 480II qPCR system using miRNA universal SYBR qPCR Master Mix (Vazyme, Nanjing, China). U6 was used as the reference gene. To detect the expression of *SIRT1*, HiScript III 1st Strand cDNA Synthesis Kit (+gDNA wiper) and ChamQ universal SYBR qPCR Master Mix (Vazyme, Nanjing, China) were used. And *beta-actin* was used as the reference gene. The reverse transcription and PCR primer sequences are listed in Supplementary Table S1. The relative expression levels of miRNA and mRNA were calculated using $2^{-\Delta\Delta CT}$ (Rao et al., 2013).

2.6 Dual -Luciferase reporter assay

To verify the target relationship of *SIRT1* and oar-miR-432, Xho I and NotI restriction enzyme cutting sites were amplified with the wild-type 3'UTR of the *SIRT1*. The primers are listed in Supplementary Table S1. The wild-type 3'UTR of the *SIRT1* was ligated to vectors and named psiCHECK2-*SIRT1*-3'UTR-WT.

Using a Site-Directed Mutagenesis Kit (Thermo Fisher Scientific, MA, United States), the mutant-type 3'UTR of *SIRT1* was obtained and named psiCHECK2-*SIRT1*-3'UTR-MT. PsiCHECK2-*SIRT1*-3'UTR-WT, psiCHECK2-*SIRT1*-3'UTR-MT, or pure vectors were co-transfected with oar-miR-432 mimics; pure vectors were co-transfected with negative control (NC) or oar-miR-432 mimics into 293T (Pan et al., 2018). After incubation for 6 h, the culture medium was changed. After 48 h of incubation, the relative luciferase activity in the cells was measured using a Dual-Luciferase Reporter Assay System (Promega, Promega, WI, United States). Each treatment was performed 4 times for each group. All plasmid, oar-miR-432 mimics, and negative control were synthesized by GenePharma (Shanghai, China).

2.7 Sheep preadipocytes culture and transfection

Sheep preadipocytes were isolated from the tail fat of a 70-day-old Hu sheep fetus by collagenase digestion. Preadipocyte transfection and culture were according to our previous method (Jin et al., 2022). When the cell showed contact inhibition, we collected cells and extracted protein.

2.8 Western blot

Proteins from cell were extracted with RIPA buffer and separated on SDS-PAGE gel including 4% concentrated glue and 12% separation gel. After transfer, the PVDF blot membranes were blocked and then probed with rabbit polyclonal antibody against SIRT1 (1: 1,000, Proteintech, Chicago, IL, United States) at 4°C overnight. Alpha-tubulin poly-clonal antibody (1:3,000, Abclonal, Beijing, China) was used as an internal reference. These blots were further conjugated with a goat anti-rabbit IgG secondary antibody (1:1,000, Proteintech, Chicago, IL, United States) labeled with HRP *via* incubation and revealed with an ECL kit (Engreen, Beijing, China), and exposed to X-ray films. Blot intensity quantification was performed using ImageJ software (1.51j8) (Rha and Gyeol Yoo, 2015).

2.9 Statistical analysis

The data were processed by SPSS 20.0 two-tailed Student's t-test (Singh et al., 2019). All the results are presented as means ± standard deviation. Furthermore, * indicates statistically significant ($p < 0.05$). ** indicates statistically significant ($p < 0.01$).

3 Result

3.1 Quality control

The results of the miRNA-Seq data after quality control are displayed in Table 1. The clean tag count of each sample ranged from 27 to 28 million, and the Q20 of clean tags ranged from 98.20% to 98.50%. About 88.63%–92.75% of the clean reads were mapped to the sheep reference genome.

3.2 Identification of miRNAs

In this study, 134 known miRNAs and 275 novel miRNAs were identified from HG1; 132 known miRNAs and 291 novel miRNAs were identified from HG2; 137 known miRNAs and 298 novel miRNAs were identified from HG3; 132 known miRNAs and 295 novel miRNAs were identified from ZG1; 133 known miRNAs and 198 novel miRNAs were identified from ZG2; and 129 known miRNAs and 273 novel miRNAs were identified from ZG3 (Supplementary Table S2).

3.3 Analysis of differentially expressed miRNAs

We found 379 novel miRNAs and 139 known miRNAs. Hu sheep is set as a control, based on the padj ≤0.05, we detected 11 DE

TABLE 1 Summary of sequencing data for each library.

Sample name	Sequence type	Raw tag count	Clean tag count	Percentage of clean tag (%)	Q20* of clean tag (%)	Percentage of mapped tag (%)
HG1 (short/fat-tailed sheep)	SE50	28,376,193	27,508,714	96.94	98.50	92.75
HG2 (short/fat-tailed sheep)	SE50	28,289,347	27,054,271	95.63	98.40	91.58
HG3 (short/fat-tailed sheep)	SE50	29,793,809	28,483305	95.60	98.40	90.48
ZG1 (short/thin-tailed sheep)	SE50	30,184,839	28,487,066	94.35	98.30	88.63
ZG2 (short/thin-tailed sheep)	SE50	28,886,721	27,154,416	94.70	98.20	89.46
ZG3 (short/thin-tailed sheep)	SE50	29,008,123	27,666,601	95.38	98.50	89.77

miRNAs in ZG compared with HG (Figure 1 and Supplementary Table S3). There are six upregulated miRNAs, including novel_mir471, oar-miR-432, novel_mir21, novel_mir59, novel_mir394 and, novel_mir70. There are five downregulated miRNAs, including oar-miR-29b, novel_mir58, novel_mir54, oar-miR-19b, and novel_mir64. Three miRNAs were reported that were associated with fat metabolism.

3.4 DE miRNAs target prediction and functional analysis

Miranda and RNAhybrid software were used to predict the target genes of DE miRNAs, resulting in 3,404 predicted target genes (Supplementary Table S4). GO annotation enrichment was used to describe the functions of the target genes of upregulated and downregulated DE miRNAs. These were involved in cellular components (CCs), molecular function (MF), and biological processes (BP), including animal organ development, intracellular organelle lumen, ATP binding, intracellular vesicles, and kinesin and calcium ion binding (Figures 2A,B and Supplementary Table S5). A total of 115 GO terms were significantly enriched by target genes of the upregulated DE miRNAs, and 54 terms were significantly enriched by target genes of the downregulated DE miRNAs. DE miRNAs were used in a KEGG pathway enrichment analysis. Based on all the target genes of upregulated and downregulated miRNAs, 67 and 5 KEGG pathways were significantly enriched, respectively (Supplementary Table S6). As shown in Figures 2C,D, the ECM–receptor interaction signaling pathway, KEGG root term signaling pathway, transcriptional regulation in the cancer signaling pathway, the focal adhesion signaling pathway, and the breast cancer signaling pathway were simultaneously enriched. Other signaling pathways related to fat metabolism were enriched, including the PI3K-Akt signaling pathway, calcium signaling pathway, AMPK signaling pathway, and MAPK signaling pathway, which are related to fat metabolism.

3.5 Verified the DE miRNA and the expression of miRNA by RT-qPCR

The RT-qPCR technique was used to validate the sequencing results. Seven miRNAs were randomly selected for RT-qPCR verification. The validation results are displayed in Figure 3A and Supplementary Table S7.

3.6 Plasmid identification

Eight randomly selected monoclonals and vector universal primers were used to identify the wild-type psiCHECK2 plasmid by polymerase chain reaction (PCR) (Supplementary Figure S1) and sequencing. The sequencing primers are shown in Supplementary Table S1. Site-directed mutation was used to obtain the mutant-type psiCHECK2 plasmid. The sequencing results of wild-type psiCHECK2 plasmid and mutant-type psiCHECK2 are in Supplementary Table S8 and Supplementary Table S9. Eventually, the plasmids were constructed successfully.

3.7 Validation of the target relationship between oar-miR-432 and *SIRT1*

A dual-luciferase reporter assay indicated that oar-miR-432 significantly suppressed the luciferase activities for co-transfection with *SIRT1* 3'UTR wild-types, although did not affect the mutant types of SIRT1 3'UTR or blank vectors (Figure 4B and Supplementary Table S10). These results initially confirmed the direct interactions between oar-miR-432 and *SIRT1*.

3.8 Expression of *SIRT1* in Liver tissue

The RT-qPCR results showed that the expression trends in oar-miR-432 and *SIRT1* were contrasting. oar-miR-432 was highly expressed in the liver tissue of Hu sheep, while the *SIRT1* was highly expressed in the liver tissue of Tibetan sheep (Figure 3B, Supplementary Table S7).

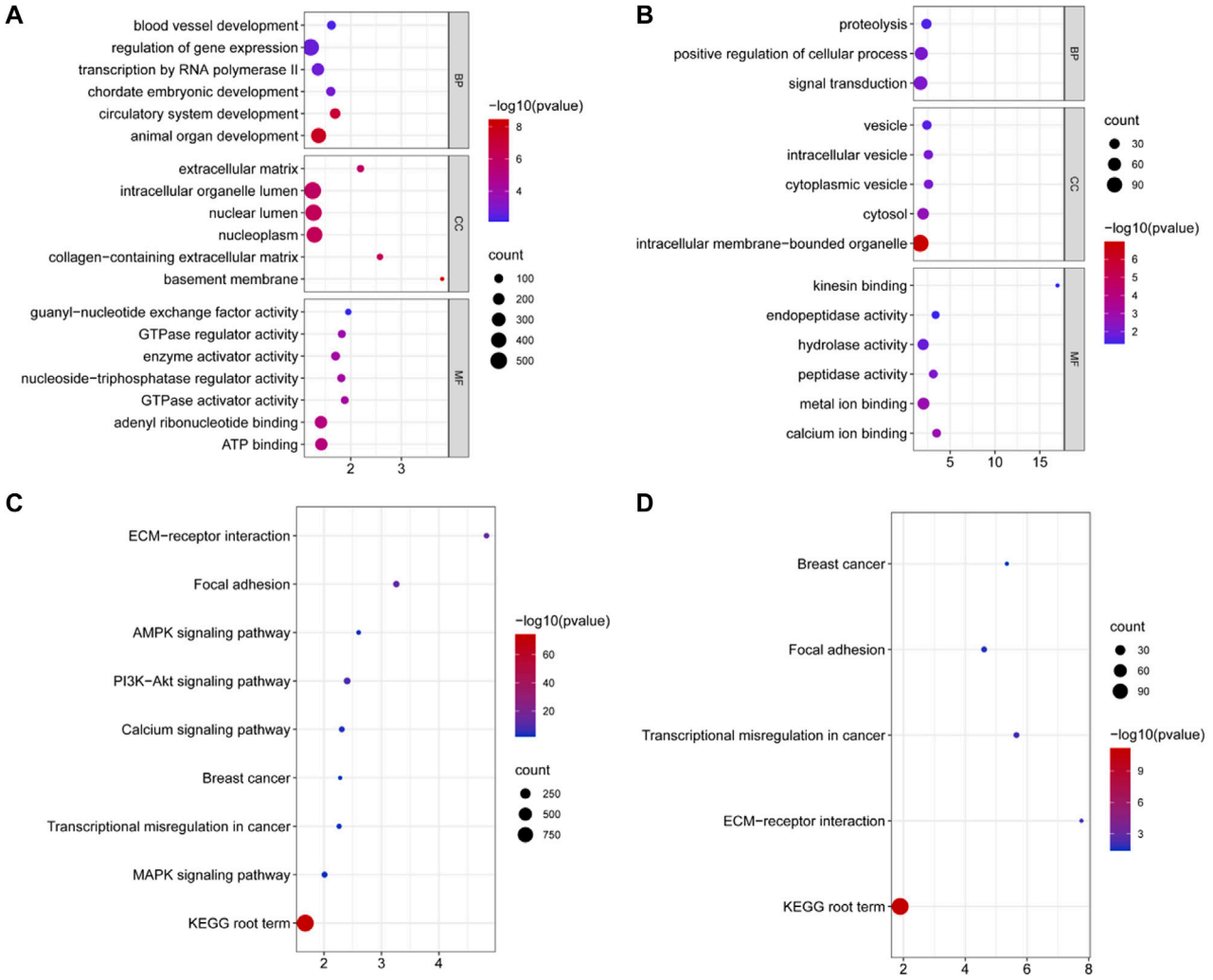

FIGURE 1
The volcano plots of all expressed miRNAs in the livers of Hu sheep (short/fat-tailed sheep) and Tibetan sheep (short/thin-tailed sheep). The *x*-axis denotes the values of log2 (fold-change), whereas the *y*-axis denotes the −log10 (padj). The colored dots represent the expressed miRNAs, with blue indicating downregulated miRNAs and red indicating upregulated miRNAs (padj ≤0.05). The black dots indicate that the miRNAs are not statistically significant (padj >0.05).

3.9 Expression of *SIRT1* in preadipocytes

Oar-miR-432 mimics and negative control were transfected into preadipocytes. Then we detected the expression of oar-miR-432 and SIRT1. The expression of oar-miR-432 was increased by oar-miR-432 mimics (Jin et al., 2022). The result of the Western blot showed the expression of SIRT1 was inhibited by oar-miR-432 mimics (Figures 3C,D, Supplementary Table S11, Supplementary Figure S2, Supplementary Figure S3).

4 Discussion

Thus far, miRNA expression has been studied in the liver tissues of buffalos (Rha and Gyeol Yoo, 2015), dairy cows (Bu et al., 2017), mice (Seclaman et al., 2019), rats (Wang et al., 2017), pigeons (Wang et al., 2020), pigs (Kai et al., 2019), chickens (Xu et al., 2019), and geese (Zheng et al., 2015). RNA-Seq was used to construct 41 pairs of ceRNA networks on liver tissue from three Holstein cows, which provide new insight into resolving bovine lipid metabolism (Liang et al., 2017). In bovine hepatocytes, miR-27a-5p inhibited calcium sensing receptor (*CASR*) expression, triacylglycerol (*TAG*) accumulation was significantly suppressed, and low very density lipoprotein (*VLDL*) secretion was reduced (Yang et al., 2018). established miRNA-mRNA regulatory networks related to lipid deposition and metabolism in the livers of Landrace pigs with the extreme backfat thickness (Kai et al., 2019). RNA-Seq was used to construct miRNA-mRNA networks between Jinhua and Landrace pigs (Huang et al., 2019). These studies provided new insights into the molecular mechanisms to explore fat metabolism in pigs. Also, the study found there was a lncRNA-FNIP2/miR-24-3p/FNIP2 axis, which can regulate lipid metabolism in Sanghuang chicken liver (Guo et al., 2021).

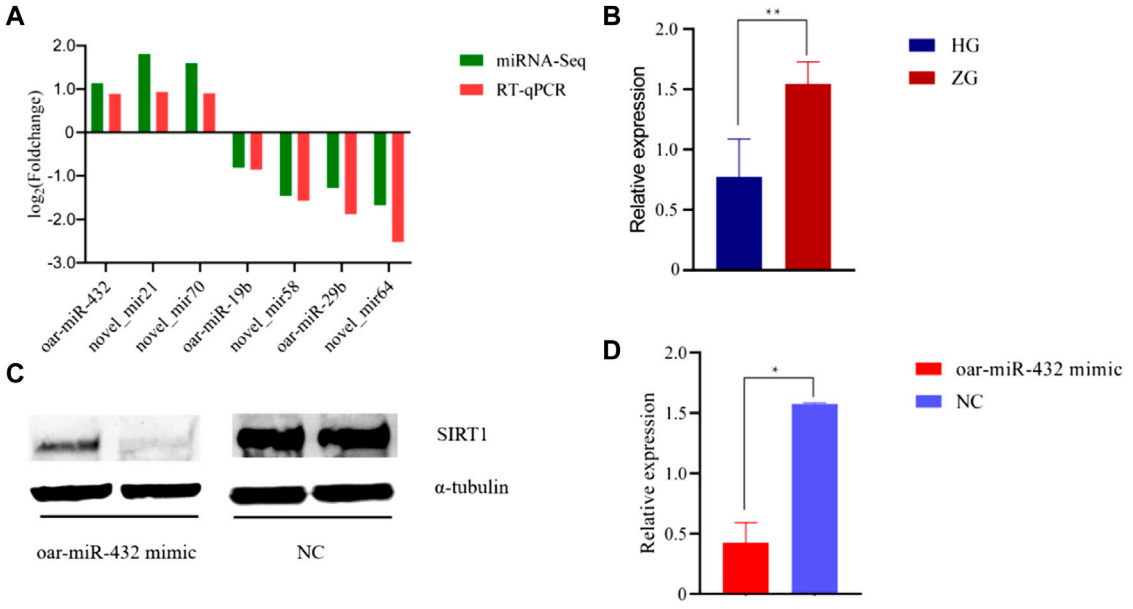

FIGURE 2
Significantly enriched Gene Ontology and KEGG for the target genes of DE miRNAs. **(A)** Some GO terms of target genes of upregulated DE miRNAs for BP, CC, and MF in two groups. **(B)** GO terms of target genes of downregulated DE miRNAs for BP, CC, and MF in two groups. The *x*-axis displays enrichment, and the *y*-axis rep-resents the GO terms. The filled colored circles display each statistically significant GO term. The size of the circles represents the gene number. **(C)** Signal pathway of the target genes of upregulated DE miRNAs in two groups. **(D)** Some signal pathways of the target genes of upregulated DE miRNAs in two groups. The *x*-axis displays the enrich-ment factor of the target genes, and the *y*-axis represents the KEGG pathway. The filled colored circles represent each statistically significant KEGG pathway. The size of the circles represents the number of genes.

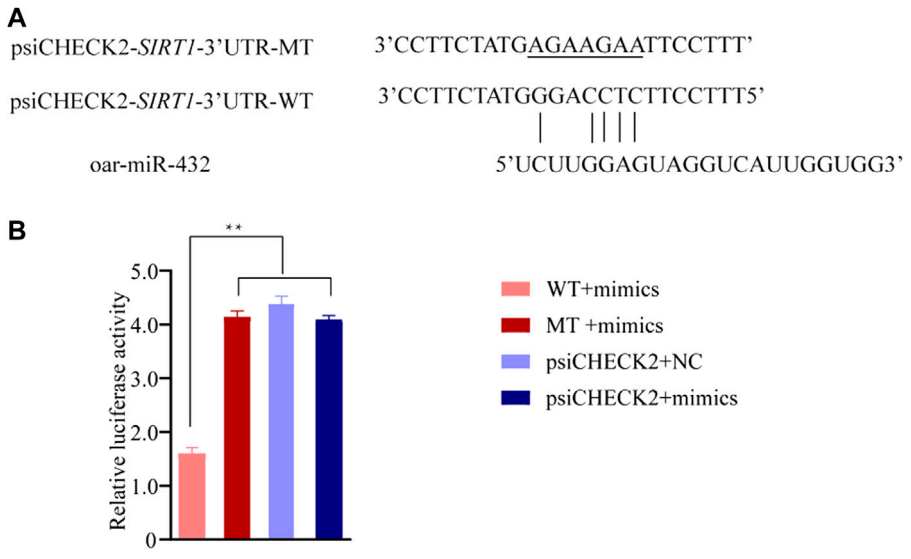

FIGURE 3
The results of RT-qPCR and Western blot. **(A)** RNA-Seq and RT-qPCR results of seven differentially expressed miRNAs in ZG compared with HG. **(B)** RT-qPCR results of SIRT1 in HG and ZG. **(C)** **(D)** Western blot results of SIRT1 in preadipocytes. NC exhibits negative control.

In this study, we used high-throughput sequencing to identify the expression of miRNA in the livers of Hu sheep and Tibetan sheep. This study complements the current understanding of miRNA expression patterns in sheep livers and will help future research on the specific role of miRNA in regulating fat metabolism. In our study, we identified 11 differential miRNAs. miR-432, miR-19b, and miR-29b are associated with fat metabolism, and a previous study showed that miR-432 inhibits milk fat synthesis by targeting stearoyl CoA desaturase (*SCD*) and *LPL* in ovine mammary epithelial cells. Additionally, miR-432 inhibits the proliferation of ovine mammary

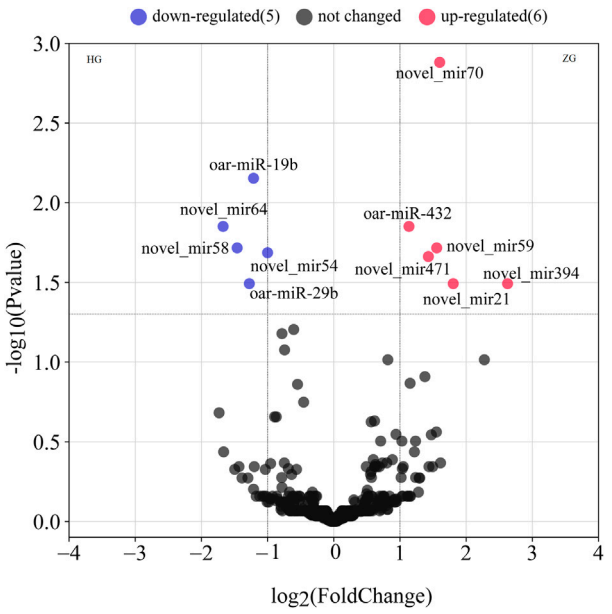

FIGURE 4
Result of the luciferase reporter assay. **(A)** Potential binding site between oar-miR-432 and SIRT13′UTR. The underlined sequences represent the mutant sites. **(B)** WT exhibits the psiCHECK2-SIRT1-3′UTR-WT. MT exhibits psiCHECK2-SIRT1-3′UTR-MT. psiCHECK2 exhibits psiCHECK2 pure vectors. Mimics exhibits oar-miR-432 mimics. NC exhibits negative control. **: indicates statistically significant ($p < 0.01$).

epithelial cells (Hao et al., 2021). Transcriptome analysis revealed that miR-432 was differentially expressed in the backfat of cattle; the protein kinase AMP-activated catalytic subunit alpha 1/2 (*PRKAA1/2*) and peroxisome proliferator-activated receptor alpha (*PPARA*) were regulation targets to modulate lipid and fatty acid metabolism (Sun et al., 2014). Interestingly, miR-432 was differentially expressed in tail fat between Hu sheep and Tibetan sheep, which could have an important function in sheep fat metabolism (Fei et al., 2022). In mice SVF cells, miR-19b had an inhibitory effect on the browning process of adipose tissue (Lv et al., 2018). Researchers found that miR-29b can regulate blood sugar in adult mice, representing a target for treating metabolism disease (Hung et al., 2019). Additionally, miR-29b inhibits the differentiation of pig muscle and subcutaneous preadipocytes through targeted regulation complement component 1 (*C1q*) and TNF-related protein 6 (*CTRP6*) (Wu et al., 2021). Ma et al. found that lncRNAs, including TCONS_00372,767 and TCONS_00171,926, were related to fat metabolism among Lanzhou fat-tailed sheep, small-tailed Han sheep, and Tibetan sheep, and constructed two co-expression networks of differentially expressed mRNA and lncRNA (Ma et al., 2018). The research conducted by Cheng et al. showed that there were differences in the livers of Mongolian and Lanzhou fat-tailed sheep through RNA-Seq, which provided a reference for researching the sheep genome (Cheng et a., 2016).

Hu sheep set as a control to identify DE miRNAs. The extracellular matrix (ECM)–receptor interaction signaling pathway was significantly enriched by the target genes of upregulated DE miRNAs and downregulated DE miRNAs. The main constituents of the ECM–receptor interaction signaling pathway in adipose tissue include collagen (type I, IV, and VI), fibronectin (FN), laminin (LN1,8), hyaluronan, and proteoglycan (Lee et al., 2013). The functional analysis showed differently expressed genes in the subcutaneous and intramuscular fat of cattle were enriched in ECM–receptor interaction signaling pathway. In the study of San et al., some genes which affected intramuscular fat (IMF) deposition was significantly enriched in the ECM–receptor interaction signaling pathway (San et al., 2021). In our study, the target genes of upregulated DE miRNAs were enriched in the PI3K-Akt signaling pathway, calcium signaling pathway, the AMPK signaling pathway, and MAPK signaling pathway, which are associated with fat metabolism (Fu et al., 2022). In our study, forkhead boxO3 (*FoxO3*) was enriched in the PI3K/AKT signaling pathway and AMPK signal pathway. In mice fed high-glucose and high-sucrose diets, FoxO3 promoted hepatic triglyceride synthesis and hepatic triglyceride accumulation in the liver by positively regulating the sterol regulatory element binding transcription factor 1 (*SREBP1c*) (Wang et al., 2019). Additionally, *SIRT1* was enriched in the AMPK signal pathway. SIRT1 plays an important biological role in regulating liver lipid metabolism, oxidative stress, and inflammation, and can be used as a therapeutic target for the treatment of alcoholic and non-alcoholic fatty liver diseases (Ding et al., 2017). It has been shown that vitamin D can activate the AMPK/SIRT1 pathway to inhibit the accumulation of fat in C2C12 skeletal muscle cells (Chang and Kim., 2019). miR-29 can regulate SIRT1 to inhibit fat deposits in mouse livers (Kurtz et al., 2015). Additionally, Liang et al. that dietary cholesterol can promote the occurrence of steatohepatitis through the calcium signaling pathway (Liang et al., 2018). In a diabetic mouse model, the ginsenoside metabolite compound K inhibits the activation of the NLR family pyrin domain containing 3 (*NLRP3*) through the NF-κB/p38 signaling pathway (Song et al., 2018). Previous studies have shown that in human liver fat cells, transforming growth factor-beta 1 (*TGF-β1*) regulates the platelet-derived growth factor receptor beta (*PDGFD-β*) subunit to maintain the activation and proliferation of fat cells (Pinzani et al., 1995). In our previous study, these pathways were enriched significantly, including ECM–receptor interaction signaling pathway, PI3K-Akt signaling pathway, calcium signaling pathway, AMPK signaling pathway, and MAPK signaling pathway (Fei et al., 2022). All of the results showed that these pathways could have a vital function in sheep fat metabolism.

In this research, our goal was to preliminarily determine how oar-miR-432 and *SIRT1* regulate fat metabolism. In our current study, we use dual-luciferase reporter assays to verify the binding relationship between miR-432 and the target gene *SIRT1*. The expression of *SIRT1* was detected in the liver tissues of Hu sheep and Tibetan sheep. RT-qPCR results showed that the expression of SIRT1 in Tibetan sheep was significantly higher than that in Hu sheep. We transfected oar-miR-432 in preadipocytes, and we found oar-miR-432 can inhibit the expression of SIRT1 at the protein level. This is the first time reported that the expression of *SIRT1* gene was regulated by oar-miR-432 in fat metabolism of sheep liver. The regulation of the process leading from mRNA to protein is generally very complex. Studies have shown that gene repression could be changed due to the post-transcriptional regulation of miRNA (Pasquier and Gardès., 2016). Our study showed that oar-miR-432 downregulated the expression of *SIRT1* at the transcriptional level in sheep liver tissue. Meanwhile, the result of Western blot showed that oar-miR-432 can downregulated the expression of

SIRT1 protein in preadipocytes. Our study indicated that p53 is independent of the oar-miR-432 *SIRT1* gene regulation.

5 Conclusion

In summary, our results provide a comprehensive expression profile of miRNA in the livers between two different sheep breeds. The DE miRNAs reported in this article may play an important role in sheep fat metabolism. We have verified that oar-miR-432 can target the regulation gene *SIRT1* in sheep. This study provides a reference for further research addressing the modulation of fat metabolism in different sheep breeds.

Data availability statement

The datasets presented in this study can be found in online repositories. The sequencing files have been stored in the Sequence Read Archive (accession numbers PRJNA785102).

Ethics statement

The animal study was reviewed and approved by Ethical approval was in compliance with the Animal Ethics Committee of the Institute of Animal Sciences, Chinese Academy of Agriculture Sciences(IAS-CAAS).

Author contributions

Conceptualization, CW and YW; methodology, ZL, ZY, and HW; software, JL, KQ, MH, and ZL; validation, XF, MJ, and TL; formal analysis, JY and TW; writing—original draft preparation, XF; writing—review and editing, ZY.

Funding

This research was supported by China Agriculture Research System of MOF and MARA (CARS-38). National Natural Science Foundation of China (32272851).

Conflict of interest

The authors declare that the research was conducted in the absence of any commercial or financial relationships that could be construed as a potential conflict of interest.

Publisher's note

All claims expressed in this article are solely those of the authors and do not necessarily represent those of their affiliated organizations, or those of the publisher, the editors and the reviewers. Any product that may be evaluated in this article, or claim that may be made by its manufacturer, is not guaranteed or endorsed by the publisher.

Supplementary material

The Supplementary Material for this article can be found online at: https://www.frontiersin.org/articles/10.3389/fgene.2023.985764/full#supplementary-material

References

Balaskas, P., Green, J., Haqqi, T., Dyer, P., Kharaz, Y. A., Fang, Y., et al. (2020). Small non-coding RNAome of ageing chondrocytes. *Int. J. Mol. Sci.* 21 (16), 5675. doi:10.3390/ijms21165675

Bu, D., Bionaz, M., Wang, M., Nan, X., Ma, L., and Wang, J. (2017). Transcriptome difference and potential crosstalk be-tween liver and mammary tissue in mid-lactation primiparous dairy cows. *PLoS. One.* 12 (3), e0173082. doi:10.1371/journal.pone.0173082

Carotti, S., Aquilano, K., Valentini, F., Ruggiero, S., Alletto, F., Morini, S., et al. (2020). An overview of deregulated lipid metabolism in nonalcoholic fatty liver disease with special focus on lysosomal acid lipase. *Am. J. Physiol. Gastrointest. Liver. Physiol.* 319 (4), G469–G480. doi:10.1152/ajpgi.00049.2020

Chang, E., and Kim, Y. (2019). Vitamin D ameliorates fat accumulation with AMPK/SIRT1 activity in C2C12 skeletal muscle cells. *Nutrients* 11 (11), 2806. doi:10.3390/nu11112806

Chen, X., Raza, S. H. A., Cheng, G., Ma, X., Wang, J., and Zan, L. (2020). Bta-miR-376a targeting KLF15 interferes with adipogenesis signaling pathway to promote differentiation of qinchuan beef cattle preadipocytes. *Anim. (Basel)* 10 (12), 2362. doi:10.3390/ani10122362

Cheng, X., Zhao, S., Yue, Y., Liu, Z., Li, H., and Wu, J. (2016). Comparative analysis of the liver tissue transcriptomes of Mongolian and Lanzhou fat-tailed sheep. *Genet. Mol. Res.* 15 (2), gmr8572. doi:10.4238/gmr.15028572

Deng, K., Ren, C., Fan, Y., Liu, Z., Zhang, G., Zhang, Y., et al. (2020). miR-27a is an important adipogenesis reg-ulator associated with differential lipid accumulation between intramuscular and subcutaneous adipose tissues of sheep. *Domest. Anim. Endocrinol.* 71, 106393. doi:10.1016/j.domaniend.2019.106393

Ding, R., Bao, J., and Deng, C. (2017). Emerging roles of SIRT1 in fatty liver diseases. *Int. J. Biol. Sci.* 13 (7), 852–867. doi:10.7150/ijbs.19370

Fu, Y., Jia, R., Xu, L., Su, D., Li, Y., Liu, L., et al. (2022). Fatty acid desaturase 2 affects the milk-production traits in Chinese Holsteins. *Anim. Genet.* 53 (3), 422–426. doi:10.1111/age.13192

Fei, X., Jin, M., Wang, Y., Li, T. T., Lu, Z., Yuan, Z., et al. (2022). Tran-scriptome reveals key microRNAs involved in fat deposition between different tail sheep breeds. *PLoS One* 17 (3), e0264804. doi:10.1371/journal.pone.0264804

Guo, L., Chao, X., Huang, W., Li, Z., Luan, K., Ye, M., et al. (2021). Whole transcriptome analysis reveals a potential regulatory mechanism of LncRNA-FNIP2/miR-24-3p/FNIP2 Axis in chicken adipogenesis. *Front. Cell. Dev. Biol.* 9, 653798. doi:10.3389/fcell.2021.653798

Hao, Z., Luo, Y., Wang, J., Hickford, J. G. H., Zhou, H., Hu, J., et al. (2021). MicroRNA-432 inhibits milk fat synthesis by targeting SCD and LPL in ovine mammary epithelial cells. *Food. Funct.* 12 (19), 9432–9442. doi:10.1039/d1fo01260f

Hu, F., Wang, M., Xiao, T., Yin, B., He, L., Meng, W., et al. (2015). miR-30 promotes thermogenesis and the development of beige fat by targeting RIP140. *Diabetes* 64 (6), 2056–2068. doi:10.2337/db14-1117

Huang, M., Chen, L., Shen, Y., Chen, J., Guo, X., and Xu, N. (2019). Integrated mRNA and miRNA profile ex-pression in livers of Jinhua and Landrace pigs. *Asian-Australas. J. Anim. Sci.* 32 (10), 1483–1490. doi:10.5713/ajas.18.0807

Hung, Y., Kanke, M., Kurtz, C., Cubit, T., Bunaciu, R., Miao, J., et al. (2019). Acute suppression of insulin resistance-associated hepatic miR-29 *in vivo* improves glycemic control in adult mice. *Physiol. Genomics.* 51 (8), 379–389. doi:10.1152/physiolgenomics.00037.2019

Jeon, S., and Carr, R. (2020). Alcohol effects on hepatic lipid metabolism. *J. Lipid. Res.* 61 (4), 470–479. doi:10.1194/jlr.R119000547

Jin, M., Fei, X., Li, T., Lu, Z., Chu, M., Di, R., et al. (2022). Oar-miR-432 regulates fat differentiation and promotes the expression of BMP2 in ovine preadipocytes. *Front. Genet.* 13, 844747. doi:10.3389/fgene.2022.844747

John, B., Enright, A., Aravin, A., Tuschl, T., Sander, C., and Marks, D. (2004). Human MicroRNA targets. *PLoS. Biol.* 2 (11), e363. doi:10.1371/journal.pbio.0020363

Kai, X., Zhao, X., Ao, H., Chen, S., Yang, T., Tan, Z., et al. (2019). Transcriptome analysis of miRNA and mRNA in the livers of pigs with highly diverged backfat thickness. *Sci. Rep.* 9 (1), 16740. doi:10.1038/s41598-019-53377-x

Kern, F., Amand, J., Senatorov, I., Isakova, A., Backes, C., Meese, E., et al. (2020). miRSwitch: detecting microRNA arm shift and switch events. *Nucleic. acids. Res. 2020*, 48, (W1), W268–W274. doi:10.1093/nar/gkaa323

Kurtz, C., Fannin, E., Toth, C., Pearson, D., Vickers, K., and Sethupathy, P. (2015). Inhibition of miR-29 has a significant lipid-lowering benefit through suppression of lipogenic programs in liver. *Sci. Rep.* 5, 12911. doi:10.1038/srep12911

Langmead, B., Trapnell, C., Pop, M., and Salzberg, S. (2009). Ultrafast and memory-efficient alignment of short DNA sequences to the human genome. *Genome. Biol.* 10 (3), R25. doi:10.1186/gb-2009-10-3-r25

Lee, H., Jang, M., Kim, H., Kwak, W., Park, W., Hwang, J., et al. (2013). Comparative transcriptome analysis of adipose tissues reveals that ECM-Receptor interaction is involved in the de-pot-specific adipogenesis in cattle. *PLoS One* 8 (6), e66267. doi:10.1371/journal.pone.0066267

Li, B., Yang, J., Gong, Y., Xiao, Y., Zeng, Q., Xu, K., et al. (2021). Integrated analysis of liver transcriptome, miRNA, and proteome of Chinese indigenous breed ningxiang pig in three developmental stages uncovers significant miRNA-mRNA-Protein networks in lipid metabolism. *Front. Genet.* 12, 709521. doi:10.3389/fgene.2021.709521

Li, Q., Lu, Z., Jin, M., Fei, X., Quan, K., Liu, Y., et al. (2020). Verification and analysis of sheep tail type-associated PDGF-D gene polymorphisms. *Animals* 10 (1), 89. doi:10.3390/ani10010089

Liang, J., Teoh, N., Xu, L., Pok, S., Li, X., Chu, E. S. H., et al. (2018). Dietary cholesterol promotes steatohepatitis related hepatocellular carcinoma through dysregulated metabolism and calcium signaling. *Nat. Commun.* 9 (1), 4490. doi:10.1038/s41467-018-06931-6

Liang, R., Han, B., Li, Q., Yuan, Y., Li, J., and Sun, D. (2017). Using RNA sequencing to identify putative competing endogenous RNAs (ceRNAs) potentially regulating fat metabolism in bovine liver. *Sci. Rep.* 7 (1), 6396. doi:10.1038/s41598-017-06634-w

Lin, H., Wang, F., Yang, Y., and Huang, Y. (2019). MicroRNA-29a suppresses CD36 to ameliorate high fat diet-induced steatohepatitis and liver fibrosis in mice. *Cells* 8 (10), 1298. doi:10.3390/cells8101298

Lin, Y., Dan, H., and Lu, J. (2020). Overexpression of microRNA-136-3p alleviates myocardial injury in coronary artery disease via the rho A/ROCK signaling pathway. *Kidney. blood. Press. Res.* 45 (3), 477–496. doi:10.1159/000505849

Lin, Z., Tang, Y., Li, Z., Yu, C., Yang, C., Liu, L., et al. (2022). miR-24-3p dominates the proliferation and differentiation of chicken intramuscular preadipocytes by blocking ANXA6 expression. *Genes* 13 (4), 635. doi:10.3390/genes13040635

Lu, Z., Liu, J., Han, J., and Yang, B. (2020). Association between BMP2 functional polymorphisms and sheep tail type. *Anim. (Basel)* 10 (4), 739. doi:10.3390/ani10040739

Luo, R., Zhang, X., Wang, L., Zhang, L., Li, G., and Zheng, Z. (2021). GLIS1, a potential candidate gene affect fat depo-sition in sheep tail. *Mol. Biol. Rep.* 48 (5), 4925–4931. doi:10.1007/s11033-021-06468-w

Lv, Y., Yu, J., Sheng, Y., Huang, M., Kong, X., Di, W., et al. (2018). Glucocorticoids suppress the browning of adipose tissue via miR-19b in male mice. *Endocrinology* 159 (1), 310–322. doi:10.1210/en.2017-00566

Ma, L., Zhang, M., Jin, Y., Erdenee, S., Hu, L., Chen, H., et al. (2018). Comparative transcriptome profiling of mRNA and lncRNA related to tail adipose tissues of sheep. *Front. Genet.* 9, 365. doi:10.3389/fgene.2018.00365

Mortazavi, A., Williams, B., McCue, K., Schaeffer, L., and Wold, B. (2008). Mapping and quantifying mammalian transcriptomes by RNA-Seq. *Nat. Methods.* 5 (7), 621–628. doi:10.1038/nmeth.1226

Pan, Y., Jing, J., Qiao, L., Liu, J., An, L., Li, B., et al. (2018). MiRNA-seq reveals that miR-124-3p inhibits adi-pogenic differentiation of the stromal vascular fraction in sheep via targeting C/EBPα. *Domest. Anim. Endocrinol.* 65, 17–23. doi:10.1016/j.domaniend

Pasquier, C., and Gardès, J. (2016). Prediction of miRNA-disease associations with a vector space model. *Sci. Rep.* 6, 27036. doi:10.1038/srep27036

Peng, Y., Xiang, H., Chen, C., Zheng, R., Chai, J., Peng, J., et al. (2013). MiR-224 impairs adipocyte early differentiation and regulates fatty acid metabolism. *Int. J. Biochem. Cell. Biol.* 45 (8), 1585–1593. doi:10.1016/j.biocel.2013.04.029

Pflug, F., and Haeseler, v. (2018). TRUmiCount: Correctly counting absolute numbers of molecules using unique molecular identifiers. *Bioinformatics* 34 (18), 3137–3144. doi:10.1093/bioinformatics/bty283

Pinzani, M., Gentilini, A., Caligiuri, A., Franco, R., Pellegrini, G., Milani, S., et al. (1995). Transforming growth factor-beta 1 regulates platelet-derived growth factor receptor beta subunit in human liver fat-storing cells. *Hepatology* 21, 232–239. doi:10.1016/0270-9139(95)90433-6

Rao, X., Huang, X., Zhou, Z., and Lin, X. (2013). An improvement of the 2(-delta delta CT) method for quantitative re-al-time polymerase chain reaction data analysis. *Biostat. Bioinforma. Biomath.* 3 (3), 71–85.

Raudvere, U., Kolberg, L., Kuzmin, I., Arak, T., Adler, P., Peterson, H., et al. (2019). g: Profiler: a web server for functional enrichment analysis and conversions of gene lists (2019 update). *Nucleic. acids. Res.* 47 (W1), W191–W198. doi:10.1093/nar/gkz369

Rha, E., Gyeol Yoo, J. M. K., and Yoo, G. (2015). Volume measurement of various tissues using the image J software. *J. Craniofac Surg.* 26 (6), e505–e506. doi:10.1097/SCS.0000000000002022

Rouleau, S., Glouzon, J., Brumwell, A., Bisaillon, M., and Perreault, J. (2017). 3' UTR G-quadruplexes regulate miRNA binding. *RNA* 23 (8), 1172–1179. doi:10.1261/rna.060962.117

San, J., Du, Y., Wu, G., Xu, R., Yang, J., and Hu, J. (2021). Transcriptome analysis identifies signaling pathways related to meat quality in broiler chickens - the extracellular matrix (ECM) receptor interaction signaling pathway. *Poult. Sci.* 100 (6), 101135. doi:10.1016/j.psj.2021.101135

Seclaman, E., Balacescu, L., Balacescu, O., Bejinar, C., Udrescu, M., Marian, C., et al. (2019). MicroRNAs me-diate liver transcriptome changes upon soy diet intervention in mice. *J. Cell. Mol. Med.* 23 (3), 2263–2267. doi:10.1111/jcmm.14140

Sikorska, M., Siwek, M., Slawinska, A., and Dunislawska, A. (2021). miRNA profiling in the chicken liver under the influence of early microbiota stimulation with probiotic, prebiotic, and synbiotic. *Genes (Basel).* 12 (5), 685. doi:10.3390/genes12050685

Singh, S., Golla, N., Sharma, D., Singh, D., and Onteru, S. K. (2019). Buffalo liver transcriptome analysis suggests immune tolerance as its key adaptive mechanism during early postpartum negative energy balance. *Funct. Integr. Genomics.* 19 (5), 759–773. doi:10.1007/s10142-019-00676-1

Soares, D. O., Amaral, N., Cruz, E. M. N., DE, M. E. L. O. M. A. I. A. B., and Malagoli, R. O. C. H. A. R. (2016). Noncoding RNA profiles in tobacco- and alcohol-associated diseases. *Genes* 8 (1), 6. doi:10.3390/genes8010006

Song, W., Wei, L., Du, Y., Wang, Y., and Jiang, S. (2018). Protective effect of ginsenoside metabolite compound K against di-abetic nephropathy by inhibiting NLRP3 inflammasome activation and NF-κB/p38 signaling pathway in high-fat di-et/streptozotocin-induced diabetic mice. *Int. Immunopharmacol.* 63, 227–238. doi:10.1016/j.intimp.2018.07.027

Sun, J., Zhang, B., Lan, X., Zhang, C., Lei, C., and Chen, H. (2014). Comparative transcriptome analysis reveals significant differences in MicroRNA expression and their target genes between adipose and muscular tissues in cattle. *PLoS. One.* 9 (7), e102142. doi:10.1371/journal.pone.0102142

Wang, H., Shao, Y., Yuan, F., Feng, H., Li, N., Zhang, H., et al. (2017). Fish oil feeding modulates the expression of hepatic MicroRNAs in a western-style diet-induced nonalcoholic fatty liver disease rat model. *Biomed. Res. Int.* 2017, 2503847. doi:10.1155/2017/2503847

Wang, L., Zhu, X., Sun, X., Yang, X., Chang, X., Xia, M., et al. (2019). FoxO3 reg-ulates hepatic triglyceride metabolism via modulation of the expression of sterol regulatory-element binding protein 1c. *Lipids. Health. Dis.* 18 (1), 197. doi:10.1186/s12944-019-1132-2

Wang, X., Yan, P., Liu, L., Luo, Y., Zhao, L., Liu, H., et al. (2020). MicroRNA expression profiling reveals potential roles for microRNA in the liver during pigeon (Columba livia) development. *Poult. Sci.* 99 (12), 6378–6389. doi:10.1016/j.psj.2020.09.039

Wang, Z., Gerstein, M., and Snyder, M. (2009). RNA-seq: A revolutionary tool for transcriptomics. *Nat. Rev. Genet.* 10 (1), 57–63. doi:10.1038/nrg2484

Wu, W., Xu, K., Li, M., Zhang, J., and Wang, Y. (2021). MicroRNA-29b/29c targeting CTRP6 influences porcine adipogenesis via the AKT/PKA/MAPK Signalling pathway. *Adipocyte* 10 (1), 264–274. doi:10.1080/21623945.2021.1917811

Xu, E., Zhang, L., Yang, H., Shen, L., Feng, Y., Ren, M., et al. (2019). Transcriptome profiling of the liver among the prenatal and postnatal stages in chickens. *Poult. Sci.* 98 (12), 7030–7040. doi:10.3382/ps/pez434

Yang, W., Tang, K., Wang, Y., and Zan, L. (2018). MiR-27a-5p increases steer fat deposition partly by targeting cal-cium-sensing receptor (CASR). *Sci. Rep.* 8 (1), 3012. doi:10.1038/s41598-018-20168-9

Zhang, Y., Wang, Y., Wang, H., Ma, X., and Zan, L. (2019). MicroRNA-224 impairs adipogenic differentiation of bovine preadipocytes by targeting LPL. *Mol. Cell. Probes.* 44, 29–36. doi:10.1016/j.mcp.2019.01.005

Zheng, F., Zhang, J., Luo, S., Yi, J., Wang, P., Zheng, Q., et al. (2016). miR-143 is associated with proliferation and apoptosis involving ERK5 in HeLa cells. *Oncol. Lett.* 12 (4), 3021–3027. doi:10.3892/ol.2016.5016

Zheng, Y., Jiang, S., Zhang, Y., Zhang, R., and Gong, D. (2015). Detection of miR-33 expression and the verification of its target genes in the fatty liver of geese. *Int. J. Mol. Sci.* 16 (6), 12737–12752. doi:10.3390/ijms160612737

Zhou, G., Wang, X., Yuan, C., Kang, D., Xu, X., Zhou, J. P., et al. (2017). In-tegrating miRNA and mRNA expression profiling uncovers miRNAs underlying fat deposition in sheep. *Biomed. Res. Int.* 2017, 1857580. doi:10.1155/2017/1857580

Frontiers in Genetics

Highlights genetic and genomic inquiry relating to all domains of life

The most cited genetics and heredity journal, which advances our understanding of genes from humans to plants and other model organisms. It highlights developments in the function and variability of the genome, and the use of genomic tools.

Discover the latest Research Topics

See more →

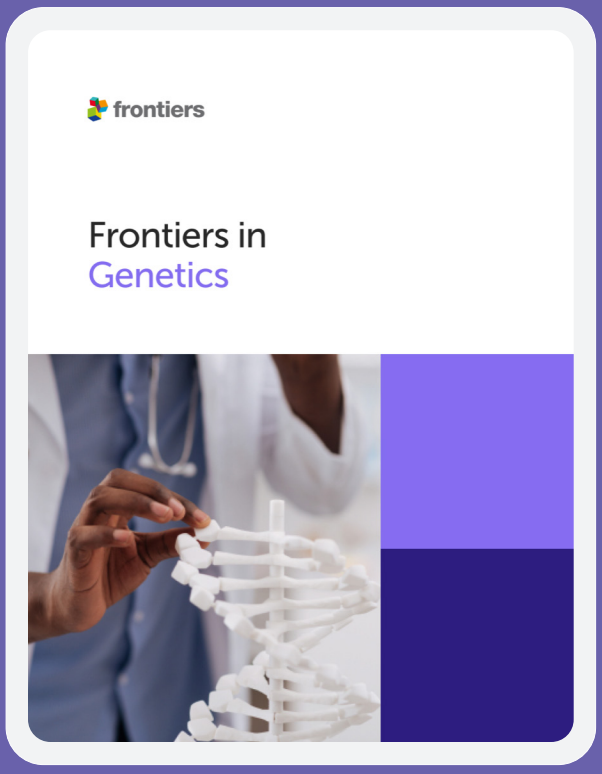

Frontiers

Avenue du Tribunal-Fédéral 34
1005 Lausanne, Switzerland
frontiersin.org

Contact us

+41 (0)21 510 17 00
frontiersin.org/about/contact